

Nikolaos Dervilis *Editor*

Special Topics in Structural Dynamics, Volume 5

Proceedings of the 36th IMAC, A Conference and Exposition
on Structural Dynamics 2018



@Seismicisolation

Springer

The Springer logo consists of a stylized horse head icon followed by the word "Springer" in a white, serif font.

Conference Proceedings of the Society for Experimental Mechanics Series

Series Editor

Kristin B. Zimmerman, Ph.D.
Society for Experimental Mechanics, Inc.,
Bethel, CT, USA

More information about this series at <http://www.springer.com/series/8922>

Nikolaos Dervilis
Editor

Special Topics in Structural Dynamics, Volume 5

Proceedings of the 36th IMAC, A Conference and Exposition
on Structural Dynamics 2018



@Seismicisolation

Editor

Nikolaos Dervilis
University of Sheffield
Sheffield, UK

ISSN 2191-5644 ISSN 2191-5652 (electronic)
Conference Proceedings of the Society for Experimental Mechanics Series
ISBN 978-3-319-75389-8 ISBN 978-3-319-75390-4 (eBook)
<https://doi.org/10.1007/978-3-319-75390-4>

Library of Congress Control Number: 2018939152

© The Society for Experimental Mechanics, Inc. 2019

This work is subject to copyright. All rights are reserved by the Publisher, whether the whole or part of the material is concerned, specifically the rights of translation, reprinting, reuse of illustrations, recitation, broadcasting, reproduction on microfilms or in any other physical way, and transmission or information storage and retrieval, electronic adaptation, computer software, or by similar or dissimilar methodology now known or hereafter developed.

The use of general descriptive names, registered names, trademarks, service marks, etc. in this publication does not imply, even in the absence of a specific statement, that such names are exempt from the relevant protective laws and regulations and therefore free for general use.

The publisher, the authors and the editors are safe to assume that the advice and information in this book are believed to be true and accurate at the date of publication. Neither the publisher nor the authors or the editors give a warranty, express or implied, with respect to the material contained herein or for any errors or omissions that may have been made. The publisher remains neutral with regard to jurisdictional claims in published maps and institutional affiliations.

Printed on acid-free paper

This Springer imprint is published by the registered company Springer International Publishing AG part of Springer Nature.
The registered company address is: Gewerbestrasse 11, 6330 Cham, Switzerland



Preface

Special Topics in Structural Dynamics represents one of nine volumes of technical papers presented at the 36th IMAC, A Conference and Exposition on Structural Dynamics, organized by the Society for Experimental Mechanics, and held in Orlando, Florida, February 12–15, 2018. The full proceedings also include volumes on Nonlinear Dynamics; Dynamics of Civil Structures; Model Validation and Uncertainty Quantification; Dynamics of Coupled Structures; Structural Health Monitoring, Photogrammetry and DIC; Rotating Machinery, Vibro-Acoustics and Laser Vibrometry; Sensors and Instrumentation, Aircraft/Aerospace and Energy Harvesting; and Topics in Modal Analysis and Testing.

Each collection presents early findings from experimental and computational investigations on an important area within structural dynamics. *Special Topics in Structural Dynamics* represents papers on enabling technologies for general dynamics and both modal analysis measurements and system identification, and damage detection.

The organizers would like to thank the authors, presenters, session organizers, and session chairs for their participation in this track.

University of Sheffield, Sheffield, UK

N. Dervilis

Contents

1	Harmonic Forcing of a Two-Segment Timoshenko Beam	1
	Arnaldo J. Mazzei, Jr. and Richard A. Scott	
2	Fastener Fatigue Analysis Using Time Domain Methods for Multiaxial Random Vibration	17
	Michael Ross, Brian Stevens, Moheimin Khan, Adam Brink, and James Freymiller	
3	Multi–input Multi–output Active Vibration Control for High Frequency Random Vibration	37
	Aabhas Singh, Matt Allen, and Washington J. DeLima	
4	A Method for Canceling Force Transducer Mass and Inertia Effects	49
	Garrett K. Lopp, Benjamin R. Pacini, and Randall L. Mayes	
5	Efficient Estimation of Clamped Step-Thickness Plates FRFs in Industrial Systems	61
	Yum Ji Chan, Chung-Yu Tai, and Yuan-You Li	
6	Modeling, Experimental Verification and Optimization of Seat Structure Per ECE R14	67
	Yunus Ozcelik, Semih Cakil, and Atıl Erdik	
7	ODS & Modal Testing Using a Transmissibility Chain	87
	Brian Schwarz, Patrick McHargue, and Mark Richardson	
8	Correlating Spectral Measurements	101
	Shawn Richardson, Jason Tyler, Brian Schwarz, and Mark Richardson	
9	A Differential Evolution Markov Chain Monte Carlo Algorithm for Bayesian Model Updating	115
	M. Sherri, I. Boulkaibet, T. Marwala, and M. I. Friswell	
10	Skin Performance in the Rollover Crashworthiness Analysis of Cutaway Bus	127
	MohammadReza Seyed, Grzegorz Dolzyk, Sungmoon Jung, and Jerzy Wekezer	
11	Across the Picket Fence: Influence of Sampling Frequency in Automatic Impact Modal Testing	137
	Daniel J. Alarcón, Sarah Schneider, Robert Kamenzky, and Peter Blaschke	
12	Estimation of Railway Track Longitudinal Profile Using Vehicle-Based Inertial Measurements	145
	Paraic Quirke, Eugene J. Obrien, Cathal Bowe, and Daniel Cantero	
13	Experimental Modal Analysis of Structures with Conventional Versus Contact-Free Suspension	149
	S. Schneider, T. T. Mallareddy, D. J. Alarcón, R. Kamenzky, and P. Blaschke	
14	Active Learning Approaches to Structural Health Monitoring	157
	L. Bull, G. Manson, K. Worden, and N. Dervilis	
15	Multimodal Damping of a Nonlinear Structure with a Passive Piezoelectric Network	161
	B. Lossouarn, J.-F. Deii, and G. Kerschen	
16	Probability Distribution of von Mises Stress in the Presence of Pre-load	165
	Daniel J. Segelman, Garth M. Reese, and Richard V. Field, Jr.	

17	Damage Detection Integrating ISHM and LWSHM Techniques	181
	Lucas Altamirando de Andrade da Rocha, Roberto Mendes Finzi Neto, and Valder Steffen, Jr.	
18	Structural Health Monitoring of Additively Manufactured Parts Using Fiber Bragg Gratings	195
	Carlisle Fauver, David Petrushenko, Elon Gordon, Michelle Lockhart, Scott Ouellette, and Alexandria Marchi	
19	Multipoint Control for Single Axis Vibration Testing	205
	Alan Williams, Vivian Cai, Michael Maestas, John Heit, and Stuart Taylor	
20	Driving a Motion Platform with a Vibration Control Software for Multi-axis Environmental Testing: Challenges and Solutions	215
	Umberto Musella, Ludovico Zanellati, Marco Grottoli, Francesco Celiberti, Bart Peeters, Francesco Marulo, and Patrick Guillaume	
21	The Yellow Frame: Experimental Studies and Remote Monitoring of the Structural Health Monitoring Benchmark Structure	233
	A. Mendler, C. E. Ventura, and S. Allahdadian	
22	Developing a Passive Vibration Absorber to Generate Traveling Waves in a Beam	245
	Seyedmostafa Motaharibidgoli, V. V. N. S. Malladi, and Pablo A. Tarazaga	
23	Experimental Assessment of the Effect of Different Tires on Comfort of Construction Truck Operators	249
	S. Cinquemani, M. Cutini, G. Abbati, G. Meloro, and E. Sabbioni	
24	Tool Wear Inspection of Polycrystalline Cubic Boron Nitride Inserts	259
	Chandula Wickramarachchi, T. E. McLeay, S. Ayvar-Soberanis, W. Leahy, and E. J. Cross	
25	A New Approach to Dynamic Analysis of a Multi-Span Beam Structure with Multiple Moving Oscillators	267
	Bingen Yang, Hao Gao, and Shbing Liu	



Chapter 1

Harmonic Forcing of a Two-Segment Timoshenko Beam

Arnaldo J. Mazzei, Jr. and Richard A. Scott

Abstract This work treats the lateral harmonic forcing, with spatial dependencies, of a two-segment beam. The segments are compact so Timoshenko theory is employed. Initially the external transverse load is assumed to be spatially constant. The goal is the determination of frequency response functions. A novel approach is used, in which material and geometric discontinuities are modeled by continuously varying functions. Here logistic functions are used so potential problems with slope discontinuities are avoided. The approach results in a single set of ordinary differential equations with variable coefficients, which is solved numerically, for specific parameter values, using MAPLE®. Accuracy of the approach is assessed using analytic and assumed mode Rayleigh-Ritz type solutions. Free-fixed and fixed-fixed boundary conditions are treated and good agreement is found. Finally, a spatially varying load is examined. Analytic solutions may not be readily available for these cases thus the new method is used in the investigation.

Keywords Layered cells beam · Layered structures resonances · Timoshenko non-homogeneous beam

Nomenclature

A_i ,	Beam segment cross section area
E_i ,	Beam segment material Young's modulus
G_i ,	Beam segment material shear modulus
k_i ,	Beam segment material shear coefficient
M ,	Bending moment
q ,	External force per unit length acting on the beam
f_1, f_2, f_3, f_4, f_5 ,	Non-dimensional functions for material/geometrical properties
I_i ,	Beam segment cross section area moment of inertia
L ,	Beam length
P ,	Compressive axial force acting on beam
t ,	Time
V ,	Shear force
w ,	Beam displacement in the y direction
Y ,	Non-dimensional beam displacement in the vertical direction
xyz ,	Inertial reference system (coordinates x, y, z)
x ,	Beam axial coordinate
γ ,	Shear strain
θ ,	Rotational angle of the beam cross section
ν ,	Non-dimensional frequency (Ω/Ω_0)
ξ ,	Non-dimensional spatial coordinate
ρ_i ,	Beam segment mass density

A. J. Mazzei, Jr. (✉)

Department of Mechanical Engineering, C. S. Mott Engineering and Science Center, Kettering University, Flint, MI, USA
e-mail: amazzei@kettering.edu

R. A. Scott

Department of Mechanical Engineering, University of Michigan, Ann Arbor, MI, USA

τ ,	Non-dimensional time
v_i ,	Beam segment material Poisson's ratio
Ω ,	Frequency
Ω_0 ,	Reference frequency

1.1 Introduction

This work augments a previous study conducted by the authors on vibrations of segmented Euler-Bernoulli beams [1]. Here Timoshenko beam theory is used for the modeling, expanding the study to cover a broader range of cases. The systems treated involve two-segment, non-homogeneous beams, subject to harmonic forcing. The goal is the determination of frequency response functions (FRFs). A couple of numerical approaches are used. The main method is developed wherein material and geometric discontinuities are modeled by continuously varying functions (here logistic functions). It results in a set of coupled ordinary differential equations with variable coefficients, which is solved numerically using MAPLE[®]¹ (for specific parameters). For comparison purposes, two extra approaches are discussed. An analytic solution is derived using differential equations for each segment. The constants involved in the solutions of these equations are determined, via MAPLE[®], using boundary and interface continuity conditions. Then the response, at a given location, is obtained as a function of the forcing frequency (FRF). Lastly, an assumed-modes solution is developed by means of Rayleigh-Ritz expansions. Different sets of boundary conditions, such as free-fixed and fixed-fixed, are treated. For the case of constant spatial external forcing, very good agreement is found between the numerical and analytical methods. The assumed modes approach led to good results when compared to the other two. Subsequently, a case with variable spatial forcing is solved using the continuous variation method.

Exact frequencies of homogeneous Timoshenko beams, with varying cross-sections, were discussed in Ref. [2]. Frequencies were calculated via a dynamic stiffness matrix approach and compared to known results.

Vibrations of Timoshenko beams with varying cross sections, subjected to both axial and tangential loads, were investigated in Ref. [3]. Natural frequencies were obtained using the Frobenius method for several cases, including the effect of non-uniformity, end masses and axial and tangential forces.

Non-uniform beam frequencies were also studied in Ref. [4], using Timoshenko (TB) and Euler-Bernoulli (EB) approaches. Efficacy of part by part modelling, i.e., utilizing a compatible approach, either TB or EB, for specific segments of the beam, and new approaches for Rayleigh–Ritz approximations were discussed. Computational solutions, for beams with rectangular cross-section, were validated by current literature results and FEM analyses.

1.2 Modeling

The two-segmented beam is shown in Fig. 1.1 and is comprised of two cells of different properties.

The modeling approach utilized here is described in Ref. [5] and is based on previous works on axially loaded beams by Bishop and Price [6] and Esmailzadeh and Ohadi [3]. The equations of motion for a shaft in bending under axial load can be derived via a Newton-Euler approach applied to a differential element of the beam at its deformed configuration, as seen in Fig. 1.2.

The figure shows the shear forces, bending moments and axial forces acting on the element. The axial forces are assumed to act perpendicular to the shear forces following a model given in Ref. [3] (see also follower force models given in Refs. [7–9]). On the right side of the element the axial force is offset by the shear deformation, whereas the direction of the shear force is not affected by the shear strain γ .

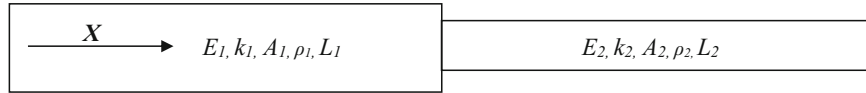
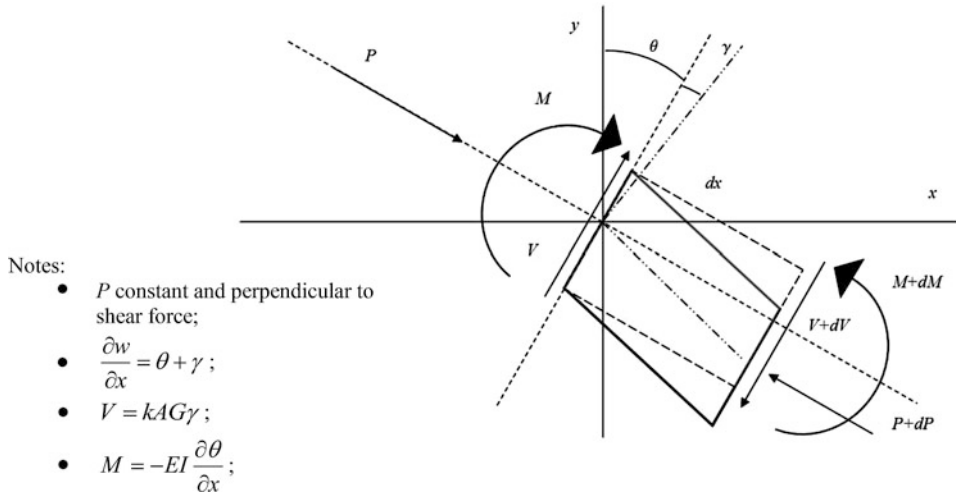


Fig. 1.1 Layered beam

¹www.maplesoft.com/products/Maple/.

**Fig. 1.2** Beam differential element

Assuming small angles and constant axial load P , the equations of motion can be written as:

$$\begin{aligned} \rho(x)A(x)dx \frac{\partial^2 w(x,t)}{\partial t^2} - \frac{\partial V}{\partial x}dx + P \frac{\partial \theta}{\partial x}dx - q(x,t)dx &= 0 \\ \rho(x)I(x)dx \frac{\partial^2 \theta(x,t)}{\partial t^2} + \frac{\partial M}{\partial x}dx - Vdx - P\gamma dx &= 0 \end{aligned} \quad (1.1)$$

Using a linearized curvature model, Eq. (1.1) can be re-written as:

$$\begin{aligned} \rho(x)A(x) \frac{\partial^2 w(x,t)}{\partial t^2} &= q(x,t) + \frac{\partial}{\partial x} \left[kA(x)G(x) \left(\frac{\partial w(x,t)}{\partial x} - \theta(x,t) \right) \right] - P \frac{\partial \theta(x,t)}{\partial x} \\ \rho(x)I(x) \frac{\partial^2 \theta(x,t)}{\partial t^2} &= \frac{\partial}{\partial x} \left[E(x)I(x) \left(\frac{\partial \theta(x,t)}{\partial x} \right) \right] + (P + kA(x)G(x)) \left(\frac{\partial w(x,t)}{\partial x} - \theta(x,t) \right) \end{aligned} \quad (1.2)$$

In Eq. (1.2) the shear force is given by: $V = kA(x)G(x)\gamma$, where k is the “shear coefficient” (see Ref. [10]), which relates the maximum shear stress to the average value in the cross section of the beam.

Non-dimensional versions of Eq. (1.2), for the case of zero axial loading, are developed next. By taking $\tau = \Omega_0 t$, $v = \Omega / \Omega_0$, $\xi = x/L$, $Y = w/L$, $E(x) = E_1 f_1(\xi)$, $kG(x) = k_1 G_1 f_5(\xi)$, $I(x) = I_1 f_2(\xi)$, $\rho(x) = \rho_1 f_3(\xi)$, $A(x) = A_1 f_4(\xi)$, and substituting, one obtains:

$$\begin{aligned} f_3(\xi) f_4(\xi) \frac{\partial^2 Y(\xi, \tau)}{\partial \tau^2} &= Q(\xi, \tau) + \alpha_1 \frac{\partial}{\partial \xi} \left(f_4(\xi) f_5(\xi) \left(\frac{\partial Y(\xi, \tau)}{\partial \xi} - \theta(\xi, \tau) \right) \right) \\ f_3(\xi) f_2(\xi) \frac{\partial^2 \theta(\xi, \tau)}{\partial \tau^2} &= \gamma_1 \frac{\partial}{\partial \xi} \left(f_1(\xi) f_2(\xi) \frac{\partial \theta(\xi, \tau)}{\partial \xi} \right) + (\alpha_1 \gamma_1 f_4(\xi) f_5(\xi)) \left(\frac{\partial Y(\xi, \tau)}{\partial \xi} - \theta(\xi, \tau) \right) \end{aligned} \quad (1.3)$$

where $Q(\xi, \tau) = \frac{q(x,t)}{\rho_1 \Omega_0^2 A_1 L}$, $\alpha_1 = \frac{k_1 G_1 A_1 L^2}{E_1 I_1}$, $\gamma_1 = \frac{A_1 L^2}{I_1}$ and Ω_0 is a reference frequency, $\Omega_0 = \sqrt{\frac{E_1 I_1}{\rho_1 A_1 L^4}}$.

Assuming harmonic forcing, $Q(\xi, \tau) = q_1(\xi) \exp(i\nu\tau)$, one can take $Y(\xi, \tau) = Z(\xi) \exp(i\nu\tau)$ and $\theta(\xi, \tau) = \phi(\xi) \exp(i\nu\tau)$, then:

$$\begin{aligned} f_3(\xi) f_4(\xi) \nu^2 Z(\xi) + \alpha_1 \frac{d}{d\xi} \left(f_4(\xi) f_5(\xi) \left(\frac{dZ(\xi)}{d\xi} - \phi(\xi) \right) \right) + q_1(\xi) &= 0 \\ f_3(\xi) f_2(\xi) \nu^2 \phi(\xi) + \gamma_1 \frac{d}{d\xi} \left(f_1(\xi) f_2(\xi) \frac{d\phi(\xi)}{d\xi} \right) + (\alpha_1 \gamma_1 f_4(\xi) f_5(\xi)) \left(\frac{dZ(\xi)}{d\xi} - \phi(\xi) \right) &= 0 \end{aligned} \quad (1.4)$$

1.3 Continuous Variation Model

In the continuous variation approach transitions from one material to another are modeled using logistic functions:

$$H(x) \approx \frac{1}{2} + \frac{1}{2} \tanh(\varepsilon x) = \frac{1}{1 + e^{-2\varepsilon x}} \quad (1.5)$$

where a larger ε corresponds to a sharper transition at $x = 0$.

Since analytic solutions may not be workable for Eq. (1.4), the method is as follows. Given the cells layout (material) and cross section variation, i.e., $f_1(\xi)$, $f_3(\xi)$, $f_2(\xi)$, $f_4(\xi)$ and $f_5(\xi)$, a MAPLE® routine is developed for obtaining numerical approximations to the frequency response function (FRF) of the system. It consists of using MAPLE®'s two-point boundary value solver to solve a forced motion problem. A forcing function $q_1(\xi)$ is assumed and the frequency ν is varied. By observing the mid-span deflection of the beam, resonant frequencies can be found on noting where change in signs occur. Higher modes can be obtained by extending the search range. Monitoring amplitudes results in the FRF for the system.

1.4 Numerical Results

Consider the beam shown in Fig. 1.1. Here the segment cross-sections are assumed to have the same geometry and joined at the center of the beam. The cross-section is taken to be a **S 24 X 121** (ASTM A6 – American Standard Beam)² and the following materials are used: Aluminum ($E_1 = 71 \text{ GPa}$, $\rho_1 = 2710 \text{ Kg/m}^3$, $v_1 = 0.33$, $G_1 = 26.69 \text{ GPa}$, $k_1 = 0.89$) and Silicon Carbide ($E_2 = 210 \text{ GPa}$, $\rho_2 = 3100 \text{ Kg/m}^3$, $v_2 = 0.16$, $G_2 = 90.52 \text{ GPa}$, $k_2 = 0.87$). These values are taken from Refs. [10, 11].

1.4.1 Continuously Varying Functions

For the continuous variation model and a uniform beam, the non-dimensional logistic functions and cross-section functions can be written, for example, as (see Fig. 1.3):

$$\begin{aligned} f_1(\xi) &= 1 + \frac{E_2 - E_1}{E_1} \left(\frac{1}{2} + \frac{1}{2} \tanh(500(\xi - \frac{1}{2})) \right), \quad f_2(\xi) = 1 \\ f_3(\xi) &= 1 + \frac{\rho_2 - \rho_1}{\rho_1} \left(\frac{1}{2} + \frac{1}{2} \tanh(500(\xi - \frac{1}{2})) \right), \quad f_4(\xi) = 1 \\ f_5(\xi) &= 1 + \frac{k_2 G_2 - k_1 G_1}{k_1 G_1} \left(\frac{1}{2} + \frac{1}{2} \tanh(500(\xi - \frac{1}{2})) \right) \end{aligned} \quad (1.6)$$

Assuming a value of 1 for the external forcing and using the approach given in Ref. [1], the resultant deflections for fixed-free boundary conditions are plotted below, for two distinct values of the frequency ν (see Fig. 1.4).

Using the figure, the first resonance frequency is taken to occur at $\nu = 2.50$. The second resonance, observed in the same manner, occurs at $\nu = 5.20$.

Amplitudes for the response at the center of the beam can be monitored from Eq. (1.4). This leads to the numerical FRF shown in Fig. 1.5.

Note that a similar problem is discussed in Ref. [1] using an Euler-Bernoulli model. For comparison purposes, the numerical FRFs are overlapped in Fig. 1.6. A good agreement is seen. Differences are expected to increase as the length of the beam is reduced.

For fixed-fixed boundary conditions the numerical FRF is shown in Fig. 1.7. First resonance is observed at $\nu = 5.00$.

²www.efunda.com/math/areas/RolledSteelBeamsS.cfm.

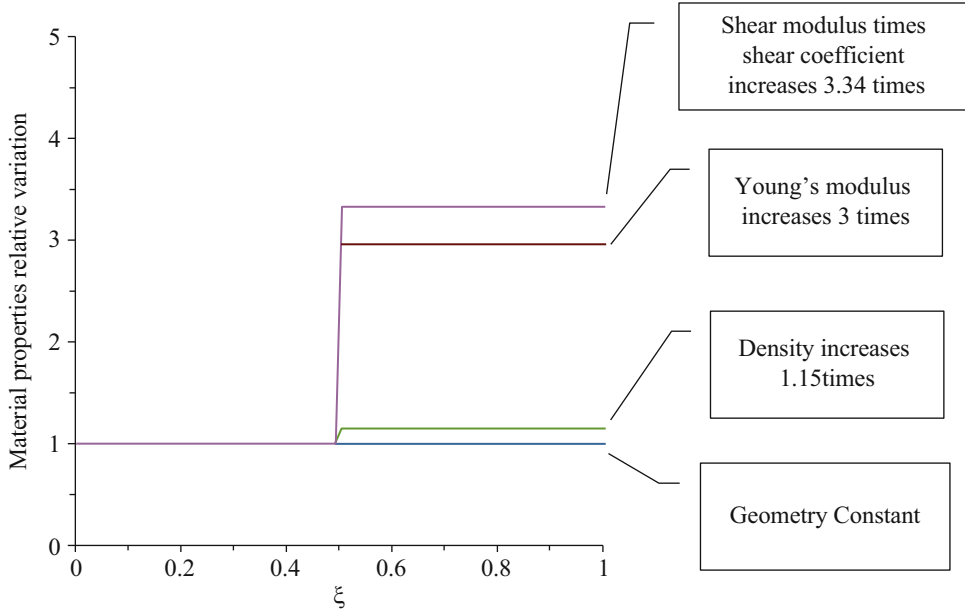


Fig. 1.3 Relative properties variation for two-cell Timoshenko beam

1.5 Accuracy Assessment

1.5.1 Analytical Approach

Analytical solutions to Eq. (1.4) can be sought using Timoshenko beam theory.

Note that for each segment of the beam, these equations can be written as:

$$\begin{aligned} f_3(\xi)f_4(\xi)\nu^2Z(\xi) + \alpha_1f_4(\xi)f_5(\xi)\left(\frac{d^2Z(\xi)}{d\xi^2} - \frac{d\phi(\xi)}{d\xi}\right) + q_1(\xi) &= 0 \\ f_3(\xi)f_2(\xi)\nu^2\phi(\xi) + \gamma_1f_1(\xi)f_2(\xi)\left(\frac{d^2\phi(\xi)}{d\xi^2}\right) + (\alpha_1\gamma_1f_4(\xi)f_5(\xi))\left(\frac{dZ(\xi)}{d\xi} - \phi(\xi)\right) &= 0 \end{aligned} \quad (1.7)$$

where the functions $f_i(\xi)$ are constant in each segment.

Solutions to this system of ODEs with constant coefficients, involve solutions to the homogeneous equations and particular integrals. Depending on the forcing function $q_1(\xi)$, tracking particular solutions can pose a problem. In this section attention is directed to obtaining solutions for the case of constant spatial forcing. (Variable spatial forcing is discussed later via the continuous variation model.)

Here this is done using MAPLE®. The solutions consist of exponential functions containing unknown coefficients, which must be determined based on the set of boundary conditions for the problem. In addition, solutions must match at the interface between the elements. Interface continuity requires matching of displacement, slope, moment and shear force.

These conditions provide a set of algebraic equations for the unknown coefficients. The FRFs can then be obtained by monitoring solutions, for different values of the forcing frequency ν , at a specific point of the beam (here this is taken at the center).

1.5.2 Analytical Results

Consider the free-fixed case. The boundary conditions are as follows (i subscript refers to the segment number).

The moment and shear free end at $\xi = 0$ gives: $\left.\frac{d\phi_1(\xi)}{d\xi}\right|_{\xi=0} = 0$ and $\left.\frac{dZ_1(\xi)}{d\xi}\right|_{\xi=0} = \phi_1(\xi)$. The conditions at the fixed end give: $Z_2(\xi) = 0$ and $\phi_2(\xi) = 0$. Interface continuity conditions are: $Z_1(\xi) = Z_2(\xi)$, $\xi = 0.5$ (displacement continuity),

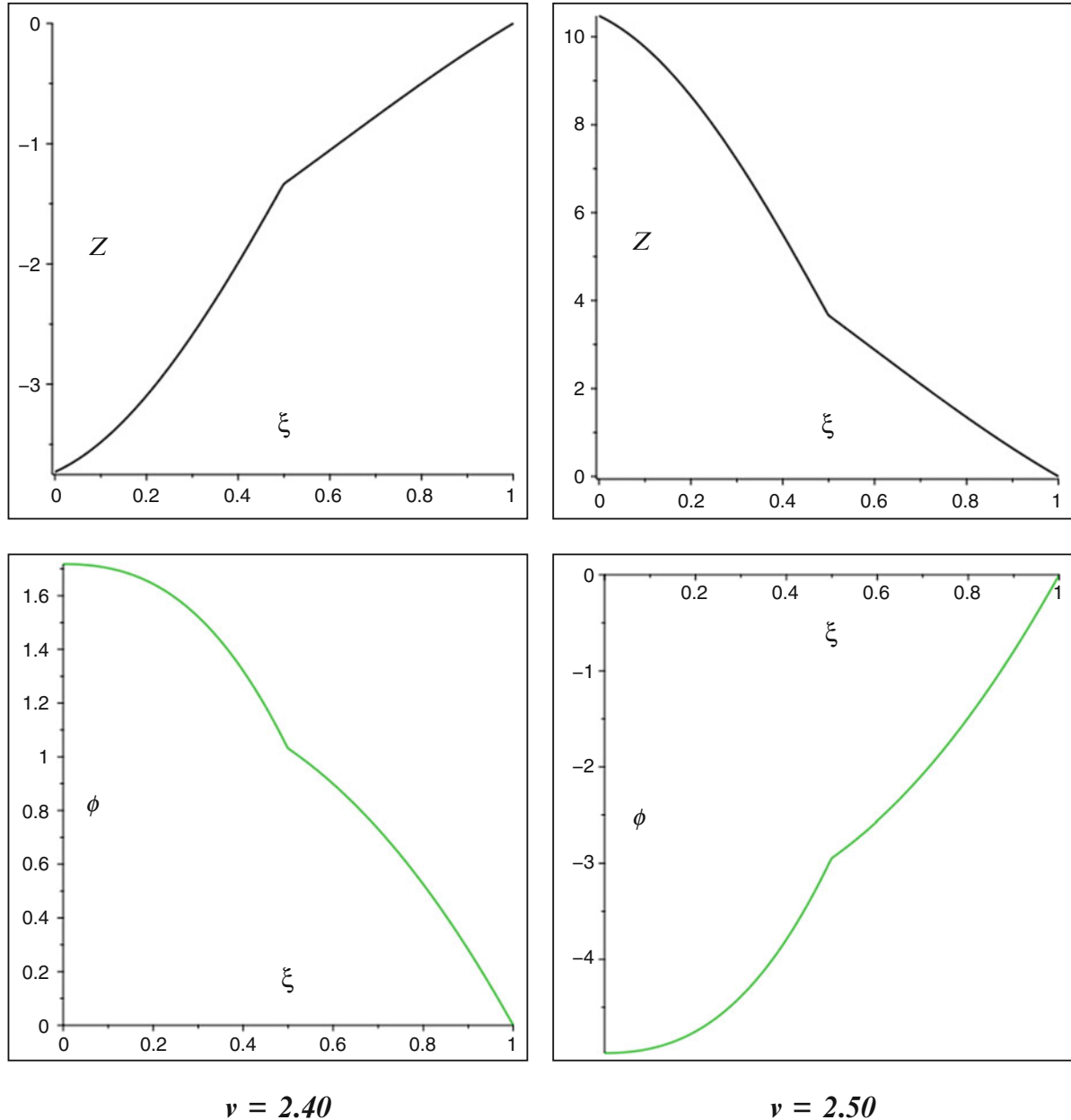


Fig. 1.4 Beam deflections for distinct values of ν – Free-Fixed: first resonance

$$\frac{dZ_1(\xi)}{d\xi} = \frac{dZ_2(\xi)}{d\xi}, \xi = 0.5 \text{ (slope continuity)}, \frac{d\phi_1(\xi)}{d\xi} = f_1 f_2 \frac{d\phi_2(\xi)}{d\xi}, \xi = 0.5 \text{ (moment continuity)} \text{ and } \frac{dZ_1(\xi)}{d\xi} - \phi_1 = f_4 f_5 \left(\frac{dZ_2(\xi)}{d\xi} - \phi_2 \right), \xi = 0.5 \text{ (shear continuity)}. q_1(\xi) \text{ is set to 1.}$$

The FRF for this case is shown in Fig. 1.8.

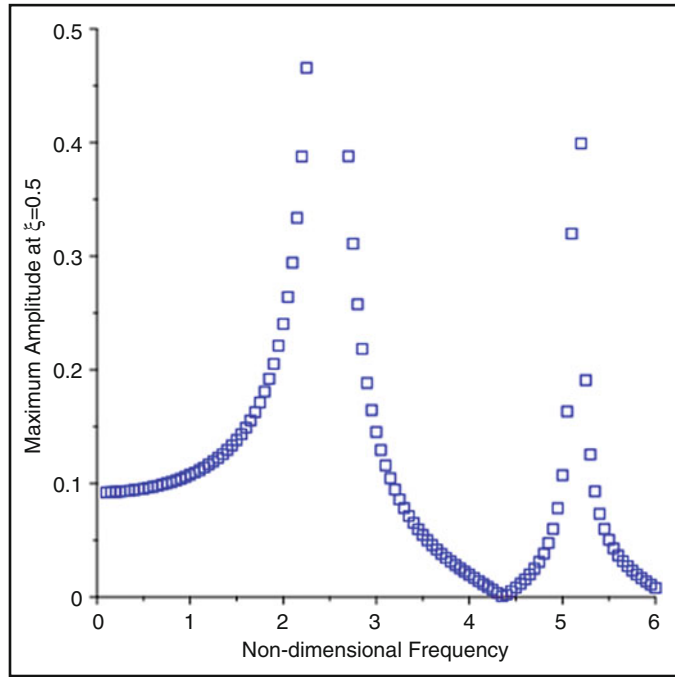
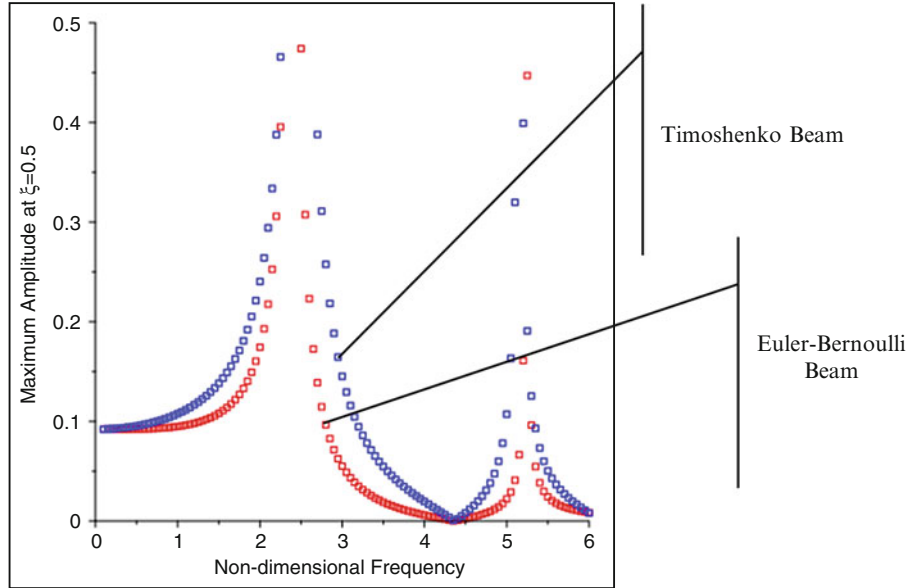
Next, consider the fixed-fixed case. Compared to the previous example, the only change in boundary conditions are at $\xi = 0$. The new set is: $Z_1(\xi) = 0$ and $\phi_1(\xi) = 0$. The FRF for this case is shown in Fig. 1.9.

Accuracy of the results given by the continuous variation model can be assessed by comparison (overlapping) of the FRFs. For the free-fixed case, the overlap is given in Fig. 1.10. It is seen that excellent agreement is obtained, the first two resonances are captured and the amplitude values correspond very well.

For the fixed-fixed case the overlapped is given in Fig. 1.11. Excellent agreement is also observed here.

These results lend confidence to the continuous variation model.

Note that the analytical method is complicated and, in the case of variable spatial forcing, solutions may be intractable. For this reason, an assumed modes method is discussed in the next section.

**Fig. 1.5** Numerical FRF segmented beam – free/fixed**Fig. 1.6** Numerical FRFs comparison for EB/TB beams – free/fixed

1.5.3 Assumed Modes Method

For the assumed modes approach, the solution to Eq. (1.1) is assumed to have the form of a Rayleigh-Ritz expansion:

$$w(x, t) = \sum_{i=1}^n U_i(t) \eta_i(x), \quad \theta(x, t) = \sum_{i=1}^n V_i(t) \lambda_i(x) \quad (1.8)$$

where the generalized coordinates U_i and V_i , in the linear combination of shape functions η_i and λ_i , are functions of time.

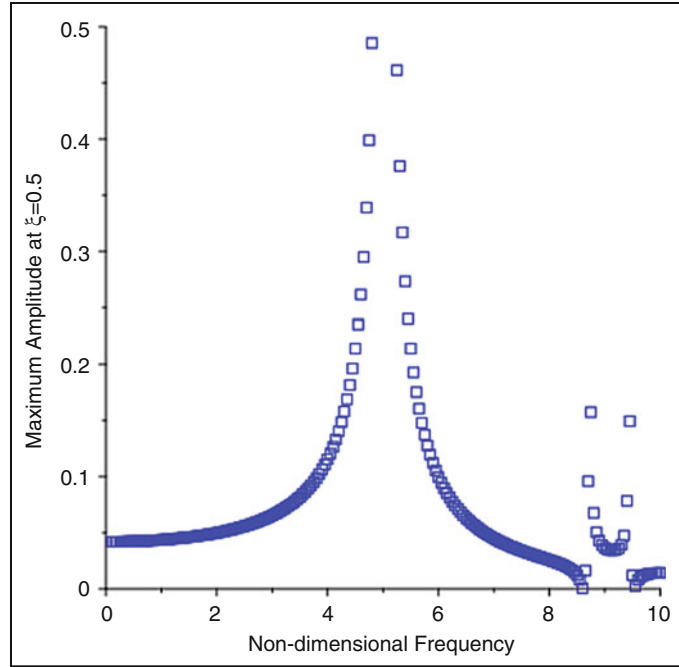


Fig. 1.7 Numerical FRF segmented beam – fixed/fixed

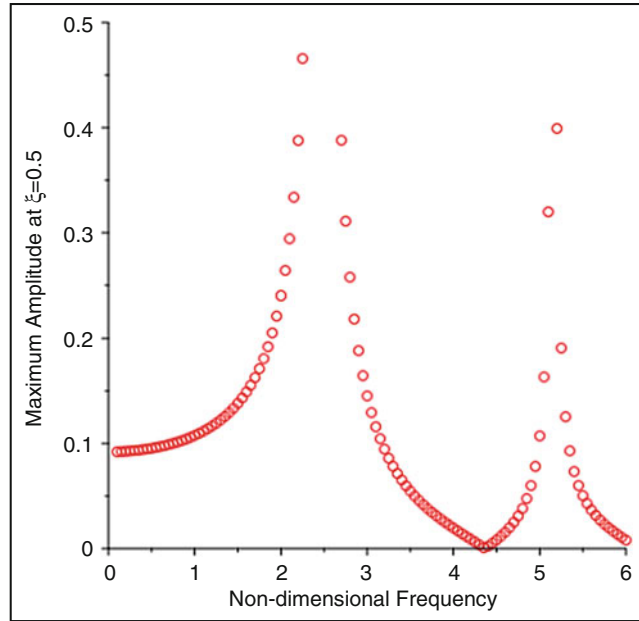


Fig. 1.8 Analytical FRF segmented beam – free/free

The shape functions must be chosen so they form a linearly independent set that possess derivatives up to the order appearing in the strain energy expression for the problem. They also must satisfy the prescribed boundary conditions.

The expressions for the kinetic (*KE*), strain energy (*PE*) and the external work done by the transverse load are:

$$PE = \int_0^{\frac{L}{2}} \left[E_1 I_1 \left(\frac{\partial \theta}{\partial x} \right)^2 + k_1 A_1 G_1 \left(\frac{\partial w}{\partial x} - \theta \right)^2 \right] dx + \int_{\frac{L}{2}}^L \left[E_2 I_2 \left(\frac{\partial \theta}{\partial x} \right)^2 + k_2 A_2 G_2 \left(\frac{\partial w}{\partial x} - \theta \right)^2 \right] dx \quad (1.9)$$

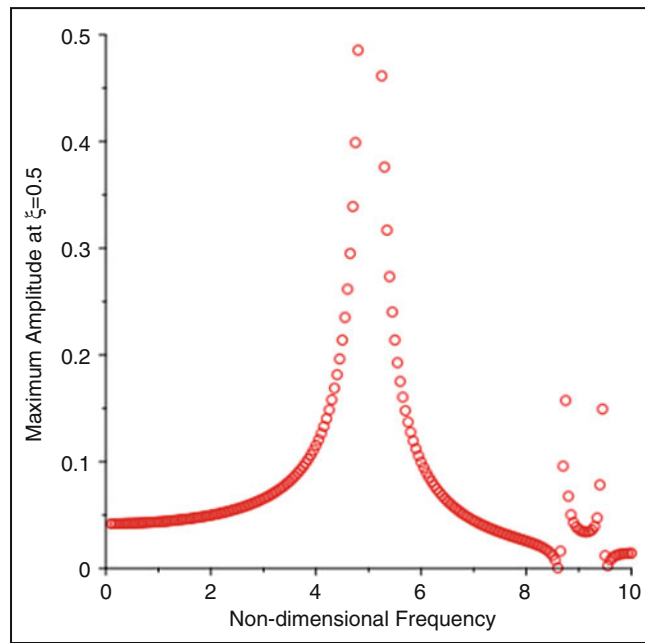


Fig. 1.9 Analytical FRF segmented beam – fixed/fixed

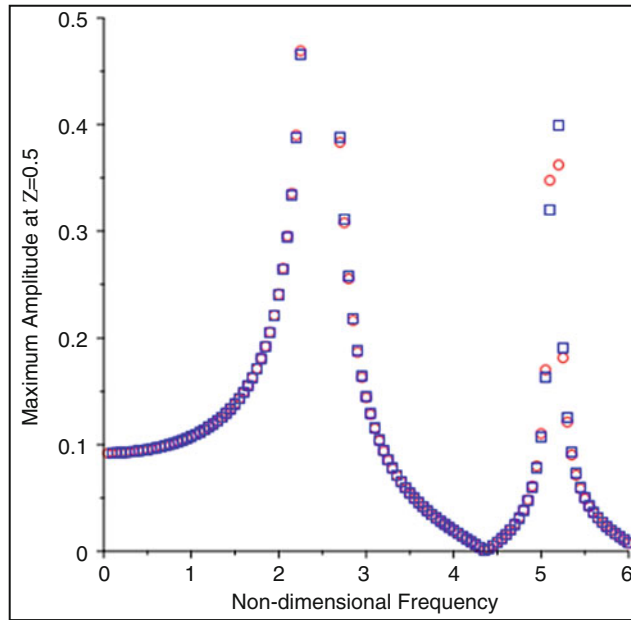


Fig. 1.10 FRFs comparison: analytical (○) and numerical (□) – free/fixed

$$KE = \int_0^{\frac{L}{2}} \left[\rho_1 A_1 \left(\frac{\partial w}{\partial t} \right)^2 + \rho_1 I_1 \left(\frac{\partial \theta}{\partial x} \right)^2 \right] dx + \int_{\frac{L}{2}}^L \left[\rho_2 A_2 \left(\frac{\partial w}{\partial t} \right)^2 + \rho_2 I_2 \left(\frac{\partial \theta}{\partial x} \right)^2 \right] dx \quad (1.10)$$

$$W = \int_0^{\frac{L}{2}} [q_1 w] dx + \int_{\frac{L}{2}}^L [q_2 w] dx + \int_0^{\frac{L}{2}} [q_1 \theta] dx + \int_{\frac{L}{2}}^L [q_2 \theta] dx \quad (1.11)$$

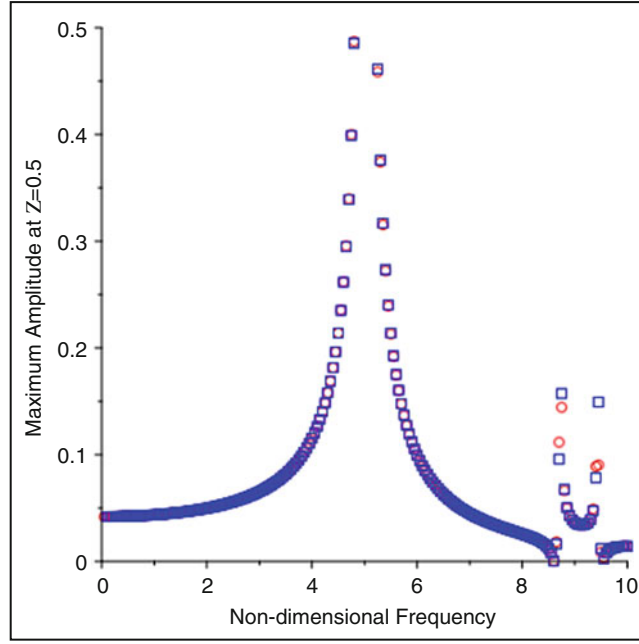


Fig. 1.11 FRFs comparison: analytical (○) and numerical (□) – fixed/fixed

Substituting Eq. (1.8) into these expressions, and using Lagrange's equations, leads to a set of n differential equations for the generalized coordinates (see Refs. [12] and for [13] details).

The discrete non-dimensional mass and stiffness matrices, for the differential equations set, can be obtained from (see Ref. [14]):

$$\begin{aligned} M^I_{i,j} &= \int_0^{\frac{1}{2}} \eta_i \eta_j \, dx + A_r \rho_r \int_{\frac{1}{2}}^1 \eta_i \eta_j \, dx, \quad M^{II}_{i,j} = \int_0^{\frac{1}{2}} \lambda_i \lambda_j \, dx + I_r \rho_r \int_{\frac{1}{2}}^1 \lambda_i \lambda_j \, dx, \\ K^I_{i,j} &= \int_0^{\frac{1}{2}} \eta'_i \eta'_j \, dx + k_r G_r A_r \int_{\frac{1}{2}}^1 \eta'_i \eta'_j \, dx, \quad K^{II}_{i,j} = - \int_0^{\frac{1}{2}} \eta'_i \lambda_j \, dx - k_r G_r A_r \int_{\frac{1}{2}}^1 \eta'_i \lambda_j \, dx, \\ K^{III}_{i,j} &= \int_0^{\frac{1}{2}} \lambda'_i \lambda'_j \, dx + E_r I_r \int_{\frac{1}{2}}^1 \lambda'_i \lambda'_j \, dx + \int_0^{\frac{1}{2}} \lambda_i \lambda_j \, dx + k_r G_r A_r \int_{\frac{1}{2}}^1 \lambda_i \lambda_j \, dx, \quad K^{IV}_{i,j} = - \int_0^{\frac{1}{2}} \eta'_j \lambda_i \, dx - k_r G_r A_r \int_{\frac{1}{2}}^1 \eta'_j \lambda_i \, dx \end{aligned} \quad (1.12)$$

If the external transverse loads are taken to be sinusoidal with frequency ν , the following expressions for calculating the generalized external forces can be used:

$$P_i^I = \left[\int_0^{\frac{1}{2}} p_1 \eta_i \, dx + \int_{\frac{1}{2}}^1 p_2 \eta_i \, dx \right] \sin(\nu \tau), \quad P_i^{II} = \left[\int_0^{\frac{1}{2}} p_1 \lambda_i \, dx + \int_{\frac{1}{2}}^1 p_2 \lambda_i \, dx \right] \sin(\nu \tau) \quad (1.13)$$

where p_i is the amplitude of the force acting on the i -segment.

The resulting system of equations can be written as:

$$\begin{bmatrix} [M^I] & [0] \\ [0] & [M^{II}] \end{bmatrix} \begin{Bmatrix} \{\ddot{U}_i\} \\ \{\ddot{V}_i\} \end{Bmatrix} + \begin{bmatrix} [K^I] & [K^{II}] \\ [K^{IV}] & [K^{III}] \end{bmatrix} \begin{Bmatrix} \{U_i\} \\ \{V_i\} \end{Bmatrix} = \begin{Bmatrix} \{P^I_i\} \\ \{P^{II}_i\} \end{Bmatrix} \quad (1.14)$$

The natural frequencies can be evaluated via an eigenvalue problem and the system response to external forcing estimated through modal analysis. The procedure is tackled using MAPLE®.

The procedure requires a choice of shape functions. Here these are taken to be beam characteristic orthogonal polynomials, with each polynomial satisfying the prescribed boundary conditions of the problem. They are generated by the Gram-Schmidt process [15] as demonstrated by Bhat [16].

For the free-fixed case, the first polynomial is taken to follow the static deflection of a homogeneous beam, under constant distributed load (q) and with these boundary conditions. Then, from Timoshenko theory:

$$-EI \frac{d\theta(x)}{dx} = M = -\frac{q}{2}x^2, \quad \frac{dw(x)}{dx} - \theta(x) = \frac{V}{kGA} = -\frac{q}{kGA}x \quad (1.15)$$

Employing the prescribed conditions gives, in non-dimensional form:

$$\eta_1(x) = c_1 \left[\frac{qL}{2kGA} (1 - \xi^2) + \frac{qL^3}{6EI} \left(\frac{1}{4}\xi^4 - \xi + \frac{3}{4} \right) \right], \quad \lambda_1(x) = d_1 \left[\frac{qL^3}{6EI} (\xi^3 - 1) \right] \quad (1.16)$$

The constants c_1 and d_1 are chosen such that:

$$\int_0^1 (\eta_k)^2 dx = 1, \quad \int_0^1 (\lambda_k)^2 dx = 1 \quad (1.17)$$

The remainder polynomials are generated by the Gram-Schmidt approach. In addition, the set is also normalized. They are divided by normalization parameters that are taken to be the inverse of the magnitude of their maximum values in the interval $\xi = 0 \dots 1$.

For example, an approximation with two polynomials gives:

$$\begin{aligned} \eta_1(\xi) &= 0.1339\xi^4 - 1.1012\xi^2 - 0.5356\xi + 1.5029 \\ \eta_2(\xi) &= (\xi - 0.2865)(0.1339\xi^4 - 1.1012\xi^2 - 0.5356\xi + 1.5029) \\ \lambda_1(\xi) &= 1.2472\xi^3 - 1.2472 \\ \lambda_2(\xi) &= (\xi - 0.3500)(1.2472\xi^3 - 1.2472) \end{aligned} \quad (1.18)$$

which leads to the following discrete differential equations of motion for the generalized coordinates α_i :

$$\begin{bmatrix} 0.4535 & 0.0130 & 0 & 0 \\ 0.0130 & 0.2434 & 0 & 0 \\ 0 & 0 & 0.6678 & 0.0212 \\ 0 & 0 & 0.0212 & 0.2844 \end{bmatrix} \begin{bmatrix} \ddot{U}_1 \\ \ddot{U}_2 \\ \ddot{V}_1 \\ \ddot{V}_2 \end{bmatrix} + \begin{bmatrix} 3.068 & 1.3837 & -1.4335 & -1.0084 \\ 1.3837 & 9.8932 & 1.2194 & -1.1612 \\ -1.4335 & 1.2194 & 6.2609 & 4.1049 \\ -1.0084 & -1.1612 & 4.1049 & 12.6211 \end{bmatrix} \begin{bmatrix} U_1 \\ U_2 \\ V_1 \\ V_2 \end{bmatrix} = \begin{bmatrix} 0.5954 \\ 0.1476 \\ -0.7500 \\ -0.1071 \end{bmatrix} \sin(\nu\tau) \quad (1.19)$$

The first natural frequencies are calculated as $\nu = 2.03$ and $\nu = 2.95$ (more polynomials are required for convergence).

Following the procedure with 18 polynomials and using a non-dimensional time $\tau = 100$, monitoring the amplitudes at $\xi = 0.5$ leads to the results shown in Fig. 1.12. The eigensolution gives the following first two frequencies: $\nu = 1.93$ and $\nu = 2.75$. A comparison (overlap) between the forced motion (continuous variation) and assumed modes approach is given in Fig. 1.13.

Note that the first resonance seen in the figures is $\nu = 2.75$ (assumed modes) or $\nu = 2.50$ (forced motion). The results differ by 10%.

For the fixed-fixed case, the polynomials are chosen as described above, using the static deflection equation under constant distributed loading and Timoshenko theory. This gives:

$$\eta_1(x) = c_1 \left[\frac{qL}{2kGA} (-\xi^2 + \xi) + \frac{qL^3}{24EI} (-\xi^4 + 2\xi^3 - \xi^2) \right], \quad \lambda_1(x) = d_1 \left[\frac{qL^3}{12EI} (-2\xi^3 + 3\xi^2 - \xi) \right] \quad (1.20)$$

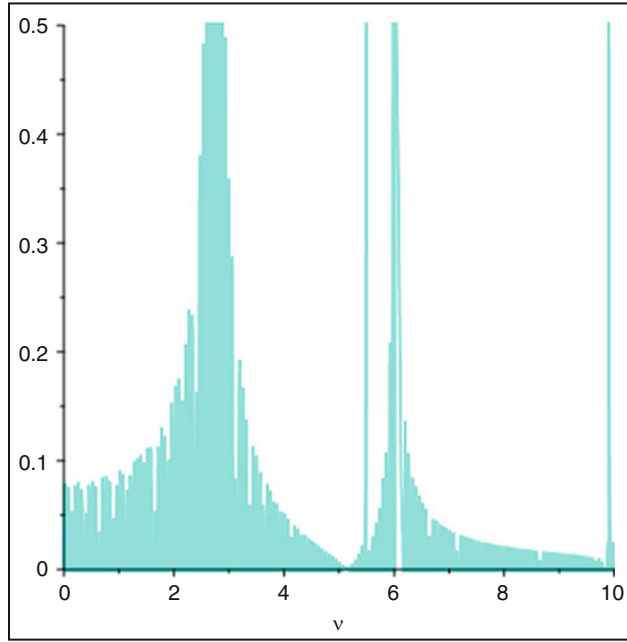


Fig. 1.12 Numerical FRF with 18 polynomials – free/fixed

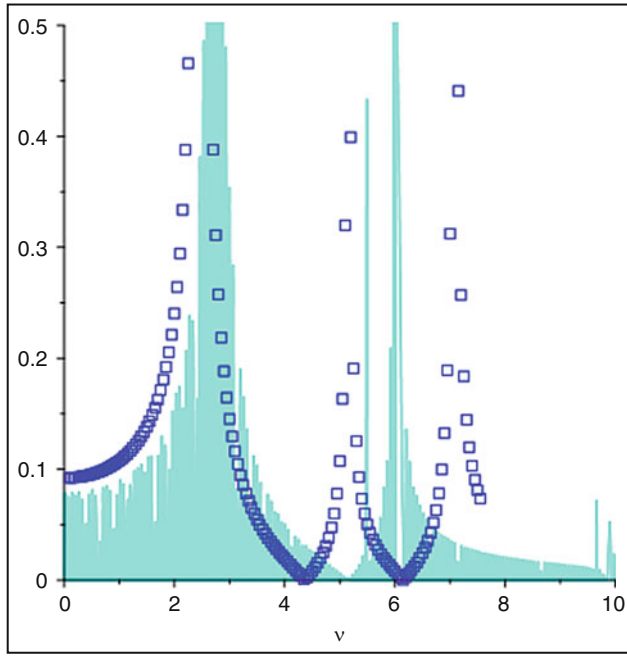


Fig. 1.13 Comparison of numerical FRFs – free/fixed

Using the approach with 18 polynomials, a non-dimensional time $\tau = 100$ and monitoring the amplitudes at $\xi = 0.5$, leads to the results shown in Fig. 1.14. The first two natural frequencies are $\nu = 4.24$ and $\nu = 6.51$. A comparison (overlap) between the forced motion and assumed modes approach is given in Fig. 1.15.

The difference between the approaches for the first resonance is about 15% ($\nu = 4.24$ – assumed modes and $\nu = 5.00$ – forced motion).

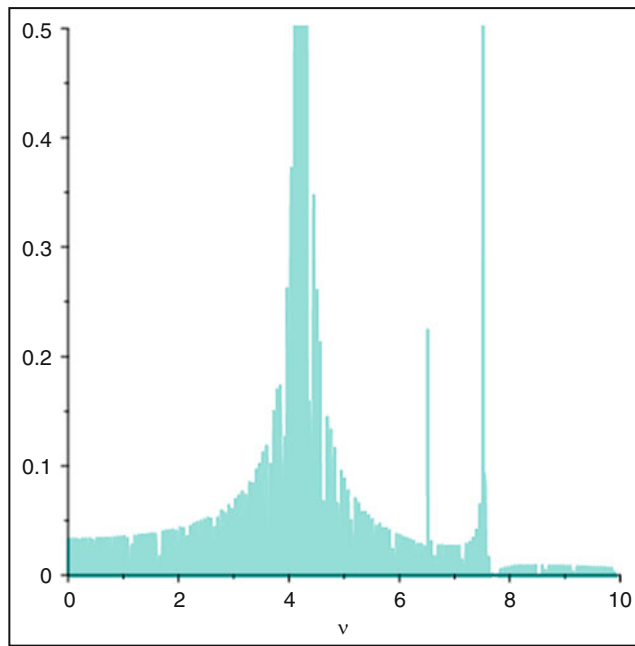


Fig. 1.14 Numerical FRF with 18 polynomials – fixed/fixed

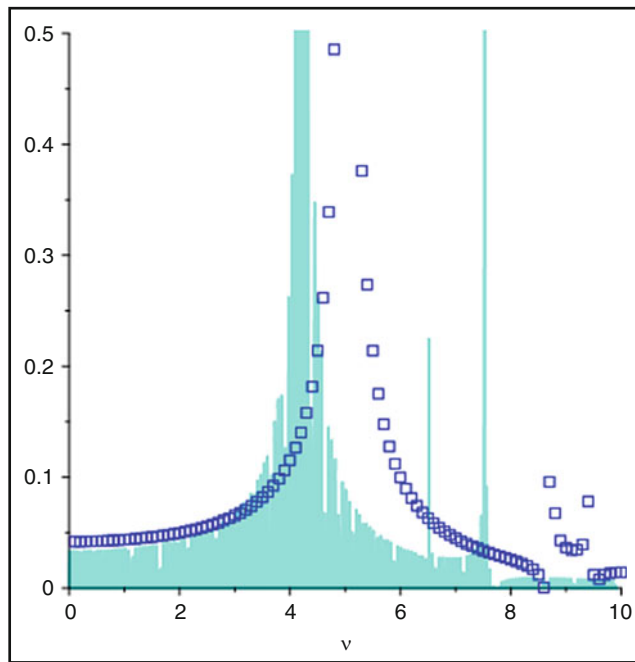


Fig. 1.15 Comparison of numerical FRFs – fixed/fixed

1.5.4 Spatially Varying External Forcing

One of the objectives of developing the continuous variation model is the ability to obtain solutions for analytically intractable problems. Consider next an example which includes spatial force variations. The results can be found using the model and, as demonstrated above, can give very accurate estimates for the FRFs.

Take, for example, variable forces equal in both segments and given by the exponential function: $q_1(\xi) = e^{-\xi^2}$. The FRFs given by the approach, for both sets of boundary conditions, are seen in Fig. 1.16.

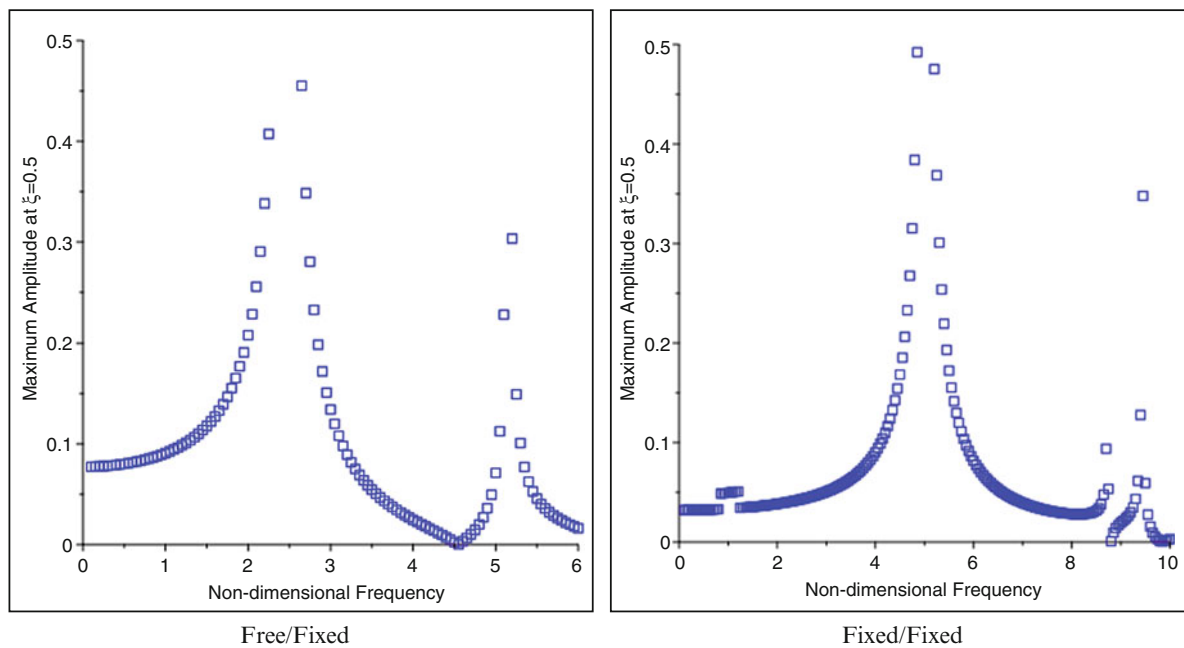


Fig. 1.16 FRF for varying spatial functions

1.6 Conclusions

A numerical approach was developed in which discontinuities were modeled by continuously varying functions (here chosen to be logistic functions). This led to a single set of ordinary differential equations with variable coefficients, which was solved for specific parameter values, using MAPLE®.

Accuracy was assessed by comparison with results obtained from an analytical approach. This model was obtained by determining solutions for each segment and then using interface continuity conditions and boundary conditions to obtain solutions. This is an arduous process and another approach to assessment was offered in the form of a Rayleigh-Ritz method.

Two sets of boundary conditions were investigated, namely, free-fixed and fixed-fixed. For spatially constant external forcing, the continuous variation approach compared very well with the analytic solutions. The Rayleigh-Ritz solutions compared well to the continuous variation ones; maximum differences were in the order of 15%.

Subsequently, the continuous variation approach was used to produce solutions for a case with external spatially varying force, which could be intractable analytically.

References

1. Mazzei, A.J., Scott, R.A.: Harmonic forcing of a two-segment Euler-Bernoulli beam. In: Dervilis, N. (ed.) Special Topics in Structural Dynamics, Volume 6: Proceedings of the 35th IMAC, a Conference and Exposition on Structural Dynamics 2017, pp. 1–15. Springer International Publishing, Cham (2017)
2. Eisenberger, M.: Dynamic stiffness matrix for variable cross-section Timoshenko beams. Commun. Numer. Methods Eng. **11**(6), 507–513 (1995)
3. Mazanoglu, K.: Natural frequency analyses of segmented Timoshenko–Euler beams using the Rayleigh–Ritz method. J. Vib. Control. **23**(13), 2135–2154 (2015)
4. Mazzei, A.J., Scott, R.A.: Resonances of compact tapered inhomogeneous axially loaded shafts. In: Allemand, R., De Clerck, J., Nieuwreijck, C., Wicks, A. (eds.) Special Topics in Structural Dynamics, Volume 6, pp. 535–542. Springer, New York (2013)
5. Bishop, R.E.D., Price, W.G.: The vibration characteristics of a beam with an axial force. J. Sound Vib. **59**(2), 237–244 (1978)
6. Esmailzadeh, E., Ohadi, A.R.: Vibration and stability analysis of non-uniform Timoshenko beams under axial and distributed tangential loads. J. Sound Vib. **236**(3), 443–456 (2000)
7. Saito, H., Otomi, K.: Vibration and stability of elastically supported beams carrying an attached mass under axial and tangential loads. J. Sound Vib. **62**(2), 257–266 (1979)
8. Irie, T., Yamada, G., Takahashi, I.: Vibration and stability of a non-uniform Timoshenko beam subjected to a follower force. J. Sound Vib. **70**(4), 503–512 (1980)

9. Kounadis, A.N., Katsikadelis, J.T.: Coupling effects on a cantilever subjected to a follower force. *J. Sound Vib.* **62**(1), 131–139 (1979)
10. Cowper, G.R.: The shear coefficient in Timoshenko's beam theory. *J. Appl. Mech.* **33**(2), 335–340 (1966)
11. Chiu, T.C., Erdogan, F.: One-dimensional wave propagation in a functionally graded elastic medium. *J. Sound Vib.* **222**(3), 453–487 (1999)
12. Craig, R.R., Kurdila, A., Craig, R.R.: *Fundamentals of Structural Dynamics*. Wiley, Hoboken (2006)
13. Kelly, S.G.: *Advanced Vibration Analysis*. CRC/Taylor & Francis, Boca Raton (2007)
14. Eslami, M.R.: *Finite Elements Methods in Mechanics*. Springer, Cham (2014)
15. Chihara, T.S.: *Introduction to Orthogonal Polynomials*. Gordon and Breach, London (1978)
16. Bhat, R.B.: Transverse vibrations of a rotating uniform cantilever beam with tip mass as predicted by using beam characteristic orthogonal polynomials in the Rayleigh-Ritz method. *J. Sound Vib.* **105**(2), 199–210 (1986)



Chapter 2

Fastener Fatigue Analysis Using Time Domain Methods for Multiaxial Random Vibration

Michael Ross, Brian Stevens, Moheimin Khan, Adam Brink, and James Freymiller

Abstract The success or failure of a structure can hinge on the proper selection of its fasteners. A predominant failure of a fastener during random vibration is that of fatigue. This generally occurs after the loss of the bolt pre-tension. Time domain methods for fatigue assessment of fasteners are used for typical environments in the Aeronautics industry. Also explored is if the multiaxial loading of random events creates proportional or non-proportional loading in the fasteners. This work finds that if the applied loads at a fastener jointed interface from a random vibration environment are such that the preload is greatly reduced, then it is essential to analyze fasteners with a multiaxial fatigue method.

Keywords Fasteners · Fatigue · Multiaxial · Non-proportional · Random vibration

2.1 Introduction

One of the more important structural aspects of any system is the fasteners and the joints included within it. Similar to other metallic components, fasteners often fail due to fatigue. In fact, fatigue has been cited as one of the major causes of in-service failure throughout engineering history [1], and it has been estimated that fatigue contributes to approximately 90% of all mechanical service failures [2]. Additionally, testing a system to fail in fatigue is untenable due to the time and economic expense, especially with accounting for variability. For these reasons, it quickly becomes necessary to model system fatigue failure numerically during the design process.

Fatigue crack initiation and growth occurs due to the application of fluctuating stresses, which are often significantly lower than the stress required for single passage failure, provided that the part experiences a sufficient number of cycles. Typical random vibration events for components mounted to an aircraft can generate an ample number of stress cycles in the component fasteners, and so fatigue becomes an important design consideration.

The cyclic-stress amplitude in a fastener is dependent on the preload. “Specifically, increased preload results in decreased cyclic stress-amplitude, particularly at loads below the clamping force imposed by the fastener” [3]. However, preload must only be increased to a point that does not overload the fastener system and exceed the strength capacity of the clamped materials or the fastener. The clamped materials may include an insert where increasing the preload could result in shear failure of the material threads around the insert.

The shear stress in a fastener is also dependent on the preload. If the preload is sufficient, then joint friction will prevent shear forces on the fastener. However, if the applied tensile forces are such that the joint is close to separation, then the fastener will resist shear loading. The studies in this work are such that the applied forces from the random vibration events have significantly reduced the preload, thus introducing the possibility of shear as a contributor to failure. The reduction in preload causes the frictional forces at the joint to decrease to a point where the fastener experiences a shear load.

Due to the combined tensile and shear loading on the fastener, a multiaxial stress state is then found in the fastener with reduced preload. It is shown that this creates a non-proportional loading. A non-proportional loading state is defined as a stress state where the principle stress tensor is time variant [4]. Modeling fatigue of the fastener with standard stress states that are essentially uniaxial, fail to predict the potential non-proportional fatigue failure.

This paper begins with addressing some typical modeling methods for fasteners in Sect. 2.2.1. Then, basic stress states are found for the fastener with standard machine design methods, such as those found in Shigley and Mischke [5] or Norton [6].

M. Ross (✉) · B. Stevens · M. Khan · A. Brink
Sandia National Laboratories, Albuquerque, NM, USA
e-mail: mross@sandia.gov

J. Freymiller
ATA Engineering Inc., Sandia Park, NM, USA

Typical fatigue predictions for fasteners are then found with these stress states, see Sect. 2.2.3. Multiaxial fatigue methods are then presented in Sect. 2.2.4. Credibility of the modeling method chosen and fastener fatigue is provided in Sect. 2.3. Finally, a test article is subjected to a random vibration environment in Sect. 2.4, where it is found that multiaxial non-proportional methods are best suited for fatigue predictions of fasteners in these numerical analyses.

2.2 Fasteners

The fasteners in question in this report were investigated for single passage failure and fatigue. This section provides the background on the calculations used for this work.

The typical joints analyzed are shown in Fig. 2.1. Each joint is comprised of a bolt that clamps two plates. The bolt is threaded into either a nut or a threaded insert. In the case of an insert, Plate 2 is threaded to accept the insert, see Fig. 2.1. In the case of a nut, Plate 2 simply has a through hole and acts the same as Plate 1. This work uses the case of an insert.

2.2.1 Modeling Approach

There are several methods for modeling fastener joints numerically. The predominant methods used are illustrated in Fig. 2.2 with the joining materials being separated for visualization purposes. These techniques range from representing the joint mechanics with a beam or spring and post processing stress states in the bolt and threads, to modeling the joint as a full 3D model including the threads. Typical system level models can have on the order of 10 million degrees of freedom with hundreds of fasteners that need to be analyzed. Therefore, including a complete model of the fastener and trying to employ high fidelity modeling on all aspects in the finite element model, such as friction at the threads, would be computational intractable. Therefore, the first three methods in Fig. 2.2: a beam, a spring, and a solid (no threads), have been explored for modeling the fastener. A valid method that was not explored in this work, would be to use a global-local modeling approach. Where the simplified model of the fastener-joint would provide input into a higher fidelity fastener-joint model, such as the *Full 3D* in Fig. 2.2.

Advantages of the spring and beam methods is that the analyst can obtain a realistic, fast, computational force/stress state. This is used to calculate items such as insert tear out during a post-processing procedure. An advantage of a beam over a spring is if the system has bolts that are long and could experience bending, then that bending is captured by the analysis. The spring can still model rotational motion from a rotational spring constant, but it may not capture a true long fastener bending effect.

Fasteners can fail in many ways, ranging from tensile failure of the bolt to insert pull out from the parent material. The following fastener analyses are explored in this work:

- bolt tension failure,
- bolt shear failure,
- bolt combined failure,
- bolt thread shear,
- insert thread shear,

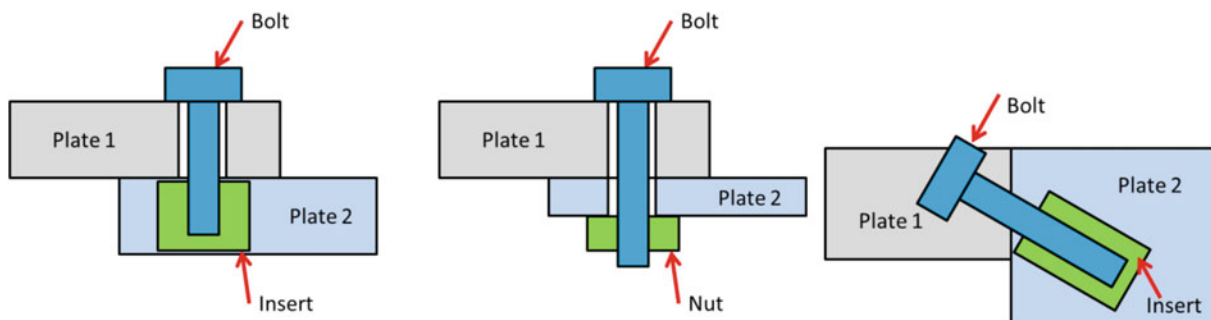


Fig. 2.1 Three types of joints that are common

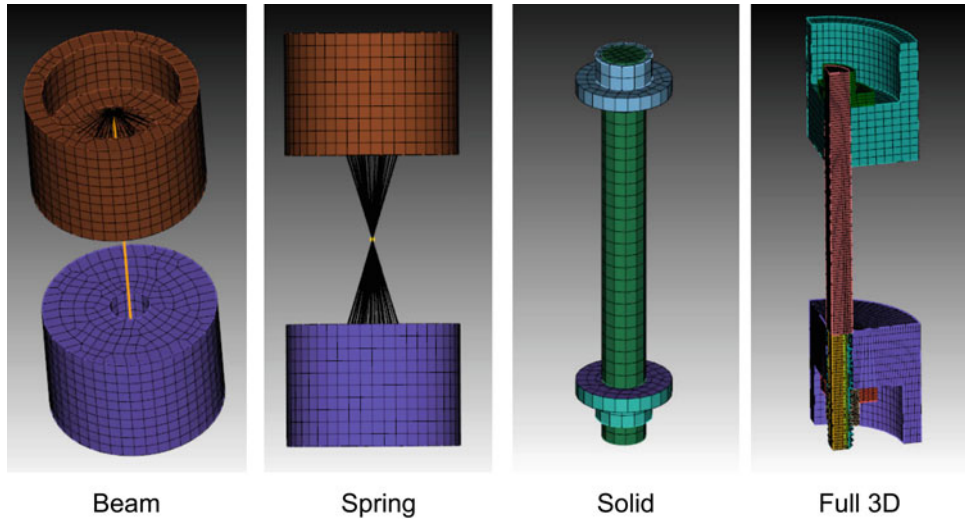


Fig. 2.2 Typical methods for modeling a fastener joint. The joining materials are separated for visualization purposes

- nut thread shear, and
- casing thread shear (insert pulling out of parent material).

In regards to all of these failure mechanisms, the axial and transverse loads on the fastener will be needed for the analyses, as discussed in Sect. 2.2.2. Ultimately, it was found that a beam or spring model of the joint is sufficient to run these analyses as discussed in Sect. 2.3.1.

Using a spring model for the joint enables the analyst to determine the applied axial and transverse loads in the bolt. Because the environments are transient analyses, these values change with time. The axial load in the bolt modeled as a spring is found from

$$F_{\text{axial}}(t) = k_b * u_{\text{axial}}(t), \quad (2.1)$$

where k_b is the axial stiffness of the bolt, discussed in Sect. 2.2.2, and $u_{\text{axial}}(t)$ is the relative axial displacement of the spring derived in the finite element analyses. However, the stiffness used in these calculations needs to be the same used in the finite element analyses. If the bolt is not aligned with the general coordinates of the system, then a cylindrical or spherical coordinate system can be used to assure that the correct axial displacement is found.

The applied shearing loads on the bolt can be found from the spring displacements in the transverse directions using a similar approach as the axial method. This provides two orthogonal loads, where the resultant would provide the complete shear load on the bolt. The shear force loads, $F_{\text{shear}1}$ and $F_{\text{shear}2}$, can be found from

$$F_{\text{shear}_i}(t) = k_{\text{shear}} * u_{\text{shear}_i}(t), \quad (2.2)$$

where subscript i is the two transverse directions (shear directions) on the bolt, and k_{shear} is the stiffness of the bolt in shear. The shear stiffness needs to be the same as used in the finite element analysis. The resultant shear force can be found from

$$F_{\text{shear}}(t) = \sqrt{F_{\text{shear}1}^2(t) + F_{\text{shear}2}^2(t)}. \quad (2.3)$$

A conservative approach in full system modeling is to remove any friction modeling at the lap joint; thus, the fastener resists all the shear. Consequently, the shear force in the fastener is generally a larger value in the model than reality if the joint does not separate (lose the preload). Typically, dowel pins and the frictional interface of the joint are used to resist shearing. However, that is not always the design solution, and fasteners will undergo shear loading.

The use of a spring model for the bolt fastener does break down in accuracy if the fastener is placed in significant bending. This can happen for long fasteners. If this is the case, it is recommended to use a beam modeling approach. In fact, a beam can provide the same information as the spring, plus better bending information. A beam provides the axial load and shearing loads in SIERRA SD [7] in terms of an element force variable, $e\text{force}$. Once again, the shearing force needs to be the resultant of the two shear forces from the element force in the beam.

2.2.2 Typical Fastener Stress Analyses

The fasteners in these analyses experience the following three environments: random vibration, shock, and quasi-static acceleration. When looking at the single passage failure, the greatest stress state found throughout time is used. To find the stress state the following fastener analyses are explored and discussed in the sections below: bolt tension stress, bolt shear stress, bolt thread shear, insert thread shear, nut thread shear, casing thread shear (insert pulling out of parent material).

The stress states for fastener analyses are post processed, given the axial force and shearing forces in the bolt. These forces are found from the finite element simulation as a function of time and dependent on the bolt modeling technique. As noted in Sect. 2.2.1, it is recommended to obtain these values from either a spring model of the bolt or a beam model of the bolt. These stress values will be a function of time and can be used for determining fatigue properties as discussed in Sect. 2.2.3.

2.2.2.1 Fastener Axial Stress

The axial stress of a fastener is more complicated than a simple rod in tension. An analyst needs to consider the preload, the flanges that the bolt is connecting take a portion of the load, the axial stress is better defined by the average of the minor and pitch bolt diameters, and the issue that the flanges may separate putting all the load on the bolt.

To begin the analysis, the preload tension in the fastener, F_i , needs to be determined. This can be found as [8]:

$$F_i = \frac{T}{K_t d_{bolt}}, \quad (2.4)$$

where T is the torque, K_t is torque coefficient, and d_{bolt} is the bolt diameter. The torque coefficient, K_t , also known as the nut factor, is a factor applied to account for the effects of friction. Typically, the torque coefficient for UNS Standard threads with coefficients of friction at 0.15 is 0.22 [6].

When the bolt is preloaded, the bolt is under tension and the flanges are compressed. In a preload state, the bolt carries only a portion of the applied load. The other portion of the applied loading is offset by the release of the compressive energy introduced to the flanges during the initial preload. Essentially, a portion of the work is performed by the joint and a portion by the bolt.

This is the ideal situation; therefore, the initial preload is introduced so that the compression in the flanges is preferably never completely relieved and hence the flange faces never separate. However, there is a potential for this separation. If the flanges completely separate, then the bolt must carry the entire load. The separation load can be determined by:

$$P_o = \frac{F_i}{1 - C}, \text{ where } C = \frac{k_b}{k_b + k_m}, \quad (2.5)$$

k_b is the bolt stiffness Eq. (2.6), and k_m is the material stiffness of the material surrounding the bolt Eq. (2.8). The bolt stiffness is simply found from [6]:

$$k_b = \frac{A_t E_b}{L}, \quad (2.6)$$

where A_t is tensile stress area, E_b is the bolt modulus of elasticity, and L is the length of the bolt under load, see Fig. 2.3. The tensile stress area is found in tables or from the equation:

$$A_t = \frac{\pi}{4} \left(\frac{d_p + d_r}{2} \right)^2, \quad (2.7)$$

where d_p is the pitch diameter and d_r is the minor diameter.

Several methods exist for estimating the stiffness of the joint material's load effected region. This report uses the method reported in Chambers [8] for bolts depicted in Fig. 2.3. The material stiffness is defined as:

$$k_m = \frac{\pi E_m d_b}{\ln \left[5 \left(\frac{2L + 0.5d_b}{2L + 2.5d_b} \right) \right]} \quad (2.8)$$

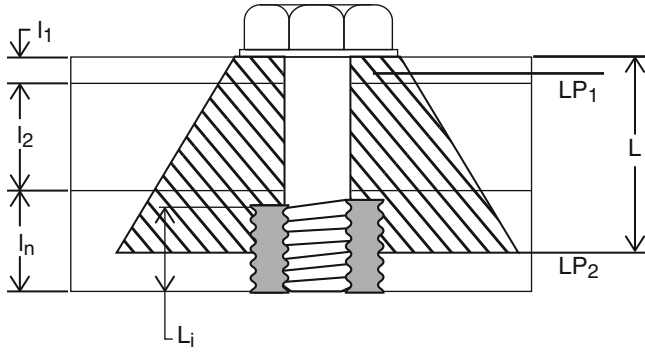


Fig. 2.3 Fastener and joint configuration for joints connected with inserts. (Figure from [8])

where

$$L = l_1 + l_2 + (l_n + \frac{L_i}{2}), \quad (2.9)$$

$$E_m = \frac{L}{\frac{l_1}{E_1} + \frac{l_2}{E_2} + \frac{l_n - L_i/2}{E_n}}, \quad (2.10)$$

where d_b is the nominal bolt diameter, E_i are the material modulus of elasticities corresponding to material 1, 2, and n, and dimensions (l_1 , l_2 , l_n , etc.) are shown in Fig. 2.3.

The tension load in the bolt, $F_t(t)$, can be determined with the use of the preload, the required load for separation, and the axial load in the bolt.

if $F_{axial}(t) < P_o$, then

$$F_t(t) = F_i + CF_{axial}(t), \quad (2.11)$$

else

$$F_t(t) = F_{axial}(t),$$

where $F_{axial}(t)$ is the applied axial load in the bolt found from the finite element analysis.

The tensile stress in the bolt can be found given the axial load, Eq. (2.11), and the tensile stress area of the bolt, Eq. (2.7).

$$\sigma_t(t) = \frac{F_t(t)}{A_t}. \quad (2.12)$$

Margin of Safety for Ultimate Axial Stress

A margin of safety can be found for single passage failure of the bolt in axial stress from

$$MS_{tensile}(t) = \frac{\sigma_{allow}}{FS(\sigma_t(t))} - 1, \quad (2.13)$$

where σ_{allow} is either the yield or ultimate stress of the material, and FS is the factor of safety. The lowest margin is reported and corresponds to the highest tensile stress in the bolt found during the transient analyses.

2.2.2.2 Parent Material Thread Shear/Insert Pull-Out

If the parent material is significantly weaker than the insert material, then another possible mechanism of failure is the shear failure of the parent material's internal threads. The shear area of the parent material is calculated from the properties of the casing's internal thread where it mates with the insert's external thread. The area for the shear stress of the internal threads of the parent material is found from:

$$A_{par} = \pi n_n L_e D_s \left(\frac{1}{2n_n} + 0.57735(D_s - E_n) \right), \quad (2.14)$$

where n_n is the number of threads per inch, L_e is the length of thread engagement, D_s is the minimum major diameter of the external threads, and E_n is the maximum pitch diameter of the mating external threads [9].

The shear stress calculation in the parent material near at the threads at the insert is based on the axial load in the bolt, see Eq. (2.11), and the thread shear area, see Eq. (2.14).

$$\tau_{par}(t) = \frac{F_t(t)}{A_{par}}. \quad (2.15)$$

Margin of Safety for Ultimate Parent Material Thread Shear Stress

A margin of safety can be found for single passage failure of the parent material threads near the insert using:

$$MS_{par}(t) = \frac{\sigma_{uts}}{FS(\tau_{par}(t))} - 1, \quad (2.16)$$

where σ_{uts} is the ultimate shear strength that can be defined as $\sigma_{uts} = 0.577\sigma_{allow}$. The lowest margin is reported and corresponds to the highest thread shear stress in the parent material found during the transient analyses.

2.2.2.3 Bolt Thread Shear

Another possible mechanism for failure is if the bolt threads shear. The area used to calculate the thread shear stress in the bolt is found from the following:

$$A_{thd} = \pi n_e L_e K_n \left(\frac{1}{2n_e} + 0.57735(E_s - K_n) \right), \quad (2.17)$$

where n_e is the number of threads per inch, L_e is the length of thread engagement, K_n is the maximum minor diameter of the internal threads and E_s is the minimum pitch diameter of the mating internal threads [9].

The shear stress calculation in the bolt threads is based on the axial load in the bolt, see Eq. (2.11), and the thread shear area, see Eq. (2.17).

$$\tau_{thd}(t) = \frac{F_t(t)}{A_{thd}}. \quad (2.18)$$

Margin of Safety for Bolt Thread Shear

A margin of safety can be found for single passage failure of the bolt threads in shear from

$$MS_{thd}(t) = \frac{\sigma_{uts}}{FS(\tau_{thd}(t))} - 1, \quad (2.19)$$

where σ_{uts} is the ultimate shear yield strength that can be defined as $\sigma_{uts} = 0.577\sigma_{allow}$. The lowest margin is reported and corresponds to the highest thread shear stress in the bolt found during the transient analyses.

2.2.2.4 Insert/Nut Internal Thread Shear

A bolt can also fail by stripping the nut or insert threads. Typically, a nut or insert is chosen such that it has a higher material strength than the surrounding material, and will not be the weakest section of the joint. The area used to calculate the insert/nut internal thread shear is found from the following:

$$A_{int} = \pi n_i L_e D_s \left(\frac{1}{2n_e} + 0.57735(D_s - E_n) \right), \quad (2.20)$$

where n_i is the number of threads per inch, L_e is the length of thread engagement, D_s is the minimum major diameter of the external threads, and E_n is the maximum pitch diameter of the mating external threads [9].

The shear stress calculation in the insert/nut internal threads is based on the axial load in the bolt, see Eq. (2.11), and the insert/nut internal thread shear area, see Eq. (2.20).

$$\tau_{int}(t) = \frac{F_t(t)}{A_{int}}. \quad (2.21)$$

Margin of Safety for Insert/Nut Thread Shear

A margin of safety can be found for single passage failure of the insert/nut internal threads in shear from

$$MS_{int}(t) = \frac{\sigma_{uts}}{FS(\tau_{int}(t))} - 1, \quad (2.22)$$

where σ_{uts} is the ultimate shear yield strength that can be defined as $\sigma_{uts} = 0.577\sigma_{allow}$. The lowest margin is reported and corresponds to the highest shear stress in the insert/nut internal threads found during the transient analyses.

2.2.2.5 Insert External Thread Shear

The area used to calculate the insert external thread shear stress is found from the following:

$$A_{ext} = \pi n_e L_e K_n \left(\frac{1}{2n_e} + 0.57735(E_s - K_n) \right), \quad (2.23)$$

where n_e is the number of threads per inch, L_e is the length of thread engagement, K_n is the maximum minor diameter of the internal threads and E_s is the minimum pitch diameter of the mating internal threads [9].

The shear stress calculation in the insert external threads is based on the axial load in the bolt, see Eq. (2.11), and the insert external shear area, see Eq. (2.23).

$$\tau_{ext}(t) = \frac{F_t(t)}{A_{ext}}. \quad (2.24)$$

Margin of Safety for Insert External Thread Shear

A margin of safety can be found for single passage failure of the insert internal or nut threads in shear from

$$MS_{ext}(t) = \frac{\sigma_{uts}}{FS(\tau_{ext}(t))} - 1, \quad (2.25)$$

where σ_{uts} is the ultimate shear yield strength that can be defined as $\sigma_{uts} = 0.577\sigma_{allow}$. The lowest margin is reported and corresponds to the highest shear stress in the external threads of the insert found during the transient analyses.

2.2.2.6 Bolt Shear Stress

The next area of concern is if the bolts will shear. It is assumed that the torsional stress caused by the preload torque has relaxed over time. This is typical, especially if there is any vibration present (transportation, etc.) [6]. Thus, the only shear load is from the applied loads, Eq. (2.3). The shear area, A_{shear} , is calculated using the nominal diameter of the bolt. The shear stress is then found from:

$$\tau_{shear}(t) = \frac{F_{shear}(t)}{A_{shear}}. \quad (2.26)$$

Margin of Safety for Shear Stress in the Fastener

A margin of safety can be found for single passage failure of the shear stress in the fastener from

$$MS_{shear}(t) = \frac{\sigma_{uts}}{FS(\tau_{shear}(t))} - 1, \quad (2.27)$$

where σ_{uts} is the ultimate shear strength that can be defined as $\sigma_{uts} = 0.577\sigma_{allow}$. The lowest margin is reported and corresponds to the highest shear stress in the fastener found during the transient analyses.

2.2.2.7 Tear-Out Analysis

Another possible mechanism of failure is shear tear out of the flange materials. This is possible when the bolt is positioned near the free edge of one or more of the abutment components and is loaded in shear. The bolt fails the flange material by shearing (or tearing) the material between the hole and the free edge of the flange. The available shear tear area is defined as [8]

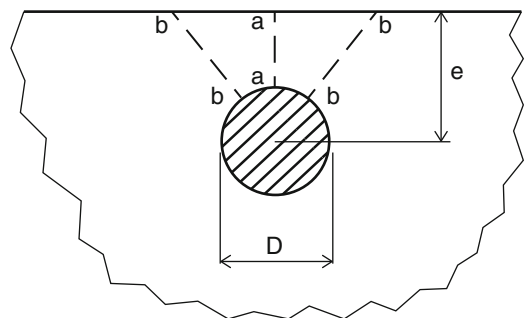
$$A_{tear} = 2t(e - \frac{D}{2}), \quad (2.28)$$

where t is the thickness of the sheet, e is the perpendicular distance from the hole centerline to the free edge of the sheet, and D is the nominal fastener diameter (see Fig. 2.4).

The shear stress in this scenario is due to the resultant shear force on the bolt, Eq. (2.3), and the available shear tear area, Eq. (2.28).

$$\tau_{tear}(t) = \frac{F_{shear}(t)}{A_{tear}}. \quad (2.29)$$

Fig. 2.4 Shear tear out of sheet edge. (Figure from [8])



Margin of Safety for Tear-out of the Material

A margin of safety can be found for single passage failure of the tear-out of the material from

$$MS_{tear}(t) = \frac{\sigma_{uts}}{FS(\tau_{tear}(t))} - 1, \quad (2.30)$$

where σ_{uts} is the ultimate shear strength that can be defined as $\sigma_{uts} = 0.577\sigma_{allow}$.

2.2.3 Typical Fastener Fatigue Approach

Fatigue is caused by a fluctuation of the applied stress with a sufficiently large number of cycles. Once the stress state as a function of time is known, fatigue calculations can be performed in a typical high-cycle fatigue methodology with some modifications to accommodate for fasteners in multiaxial stress states. High cycle fatigue is used, because the system under study for this analysis experienced a large number of cycles ($> 10^5$ cycles) and remained in the elastic regime of the bolt material.

The method for fatigue begins with cycle counting the stress state that is a function of time, $\sigma(t)$ or $\tau(t)$. In the time domain with uniaxial loading, rainflow counting techniques are well established [10] and used in this work. For each cycle, the rainflow algorithm provides a peak stress and an amplitude. This information provides a stress ratio for each cycle, defined as

$$R = \frac{\sigma_{min}}{\sigma_{max}}, \quad (2.31)$$

where σ_{min} is the minimum stress and σ_{max} is the maximum stress in the particular cycle. This is an important factor for bolts that are preloaded. Thus, the cycle counting from the rainflow algorithm provides a number of cycles, the stress state at each cycle, and the stress ratio.

Next, a stress or strain to cycle (S/N) curve is needed for the bolt material. This can be obtained from either experiments or literature. The work here uses the S/N curve data from MMPDS-11 (formally MIL-HDBK-5). In the data, it is important to know if it accounts for different stress ratios or the applicable range of the stress ratio. If the S/N curve does not accommodate the high stress ratio typically found with preloaded bolts, this work uses a Goodman modification [6] to generate an equivalent stress, σ_{eff} , with an $R = -1$ (fully reversed stress data).

$$\sigma_{eff} = \sigma_a \left[\frac{\sigma_{max}}{\sigma_{max} - \sigma_m} \right], \quad (2.32)$$

where σ_{max} is the maximum stress from the rainflow particular cycle, σ_a is the alternating stress at that cycle, and σ_m is the mean stress at that cycle.

The S/N curve data for the material will then provide a fatigue life in cycles for that particular equivalent stress level or max stress with R . This number of life cycles for a particular stress is commonly noted as N_i . The simulation and rainflow counting provide a cycle count for the same stress level, n_i . Cumulative damage is done with the popular Palmgren-Miner rule [11] to obtain a damage metric,

$$D = \sum_{i=1}^k \frac{n_i}{N_i}, \quad (2.33)$$

where k is the number of stress events. In this work, a $D \geq 0.5$ is indicative of fatigue failure, following customer requirements derived from Steinberg [12].

For each of the stress states, noted in Sect. 2.2.2, a damage metric, D , can be found. However, the S/N curves are typically based on a uniaxial tensile test. The stress states that are not in tension, such as thread shear, need a method to create an equivalent tensile stress state from the current stress state for comparisons to typical S/N curves.

Following work by Anes et al. [13], a stress scale factor, ssf , is used. The ssf relates a pure shear stress state to a tension S/N results based on various multiaxial fatigue criterions [13]. By multiplying various shear stress states with the ssf and equivalent tension stress state is found that can be compared to typical uniaxial tension S/N data. The ssf for various criterions

Table 2.1 Stress scale factors for selected multiaxial fatigue criteria as noted in Anes et al. [13]. These are for going from shear stress to tensile stress; hence, the values are greater than one

Model	Stress scale factor, <i>ssf</i>
von Mises	1.733
Crossland	4.386
Matake	1.486
Dang Van	2.174
Papadopoulos	4.386
Carpinteri-Spagnoli	1.531

is provided in Table 2.1. These are for going from a shear stress to a tension stress, and as expected the *ssf* will be greater than one. The values in Table 2.1 are material specific, and for the bolts in this study the fatigue limit ratio was 1.53, and the ultimate stress was 125 ksi.

One simple check that is also performed is if the preload is overcome and the joint separates. An increase in preload creates a decrease in cyclic stress amplitudes. A separation of the joint can lead to fretting and fatigue of the joint.

Finally, surface conditions are an important factor in the analysis of the fastener member. If the S/N curve data does not match the surface conditions of the fastener under study, then a surface factor is applied. As an example, a threaded fastener with rolled threads will use a fatigue stress concentration of 2.2 for SAE grades 0–2 [14].

2.2.4 Multiaxial Fatigue Models

The fastener analyses previously mentioned in Sect. 2.2.2 follow machine design methods such as Shigley and Mitchell [5] or Norton [6]. However, in fatigue it has been found that a multiaxial stress state can reduce the fatigue life [4, 13]. This section provides a simple method to determine if the fastener is experiencing non-proportional loading and then provides three common methods for multiaxial fatigue models: von Mises, Findley, and McDiarmid [4]. In each of these models, an equivalent stress amplitude is found throughout time that can be related to a tensile test. These methods use the stress tensor throughout time in the fastener to obtain this equivalent stress. Once the equivalent stress is found, then fatigue can proceed as discussed in Sect. 2.2.3.

The previously described fatigue methods assume that the stresses can be a simple scaling of a ‘unit’ uniaxial load case. Clearly, in a random vibration simulation in the three cartesian directions, the external loading is not uniaxial; however, local stress variations may in fact be dominated by uniaxial behavior. Therefore, a simple method is used to determine if the stress state can be considered uniaxial. Further, the method also distinguishes between what is commonly termed proportional and non-proportional loading. Proportional loading results in additional strain hardening. Non-proportional loading theories assume that combinations of shear and direct loading will increase fatigue crack propagation or growth. These are defined by Socie and Marquis as

Proportional loading, which is defined as any state of time varying stress where the orientation of the principal stress axes remained fixed with respect to the axes of the component. Thus, nonproportional loading is defined as any state of time varying stress where the orientation of the principal stress axes changes with respect to the axes of the component. [4]

2.2.4.1 Biaxiality Ratio for Loading Condition

Given the current stress state in the fastener as a function of time, a ratio between the third and first principal stress is believed to be indicative of the loading condition. This ratio is termed *biaxiality ratio*. If the *biaxiality ratio* is zero, then uniaxial fatigue methods would be appropriate. If it is constant throughout time, then multiaxial proportional fatigue methods would be appropriate. Finally, if it is variable, then multiaxial non-proportional methods should be used.

2.2.4.2 Von Mises Equivalent Stress

A simple and very popular multiaxial fatigue model is the von Mises yield criterion. It is a method that is appropriate for proportional loading, but not non-proportional loading [4]. For bolts subjected to the combination of simultaneous tension and shear, the von Mises Stress can be found in the bolt. This calculation requires the tensile stress, Eq. (2.12), and the shear stress, Eq. (2.26) in the bolt.

$$\tau_{vm}(t) = \sqrt{\sigma_t^2(t) + 3\tau_{shear}^2(t)}. \quad (2.34)$$

This is the equivalent stress that can then be processed for fatigue.

2.2.4.3 Findley Equivalent Stress

The Findley method is a critical plane method, where fatigue crack initiation and growth are dependent on both alternating shear stress and normal stress acting on a particular plane [4]. The Findley method believes failure will occur on the plane with the maximum sum of the two

$$\left(\frac{\Delta\tau}{2} + k\sigma_n \right)_{max} = f, \quad (2.35)$$

where k describes the influence of the normal stress and f is the fatigue life. The constant k is found from the ratio of fatigue strengths between axial loading and torsional loading from fully reversed tests [4],

$$\frac{\sigma_{a,R=-1}}{\tau_{R=-1}} = \frac{2}{1 + \frac{k}{\sqrt{1+k^2}}}. \quad (2.36)$$

An equivalent stress for the Findley method is found at each time step by

$$\sigma_{findley}(t) = \left(\frac{\Delta\tau}{2k} + \sigma_n \right)_{max}. \quad (2.37)$$

This equivalent stress can then be processed for fatigue with comparisons to axial tests.

2.2.4.4 McDiarmid Equivalent Stress

The McDiarmid method is also based on the critical plane approach. The criterion is based on the shear stress amplitude, $\frac{\Delta\tau_{max}}{2}$, on the plane of maximum range of shear stress and the normal stress, $\sigma_{n,max}$, on the same plane. The criterion takes the form

$$\frac{\Delta\tau_{max}}{2t_{A,B}} + \frac{\sigma_{n,max}}{2\sigma_u} = 1, \quad (2.38)$$

where $t_{A,B}$ is the shear fatigue strength for case A or case B crack growth, and σ_u is the ultimate tensile strength. This equation is typically combined with the Basquin's equation for fatigue predictions,

$$\frac{\Delta\tau_{max}}{2} \left(\frac{\sigma_u}{t_{A,B}} \right) + \frac{\sigma_{n,max}}{2} = \sigma'_f (2N_f)^b, \quad (2.39)$$

where σ'_f is the fatigue strength coefficient. The left hand side of Eq. (2.39) is the equivalent stress used in this work for the McDiarmid method. For this particular multiaxial method, the Basquin equation for fatigue calculations is used in this work.

2.3 Credibility

2.3.1 Fastener Modeling Credibility

This section explores the use of two different modeling techniques for a simple lap joint problem shown in Fig. 2.5. The lap joint consists of two mating aluminum surfaces with a steel alloy 1/4 – in bolt into an insert in the bottom mating surface.

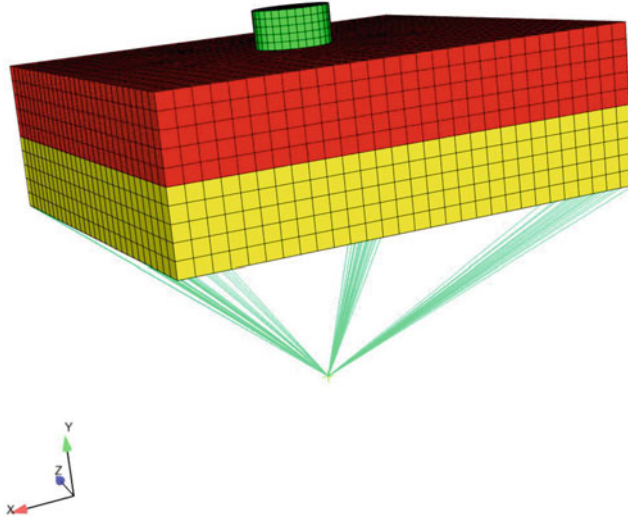
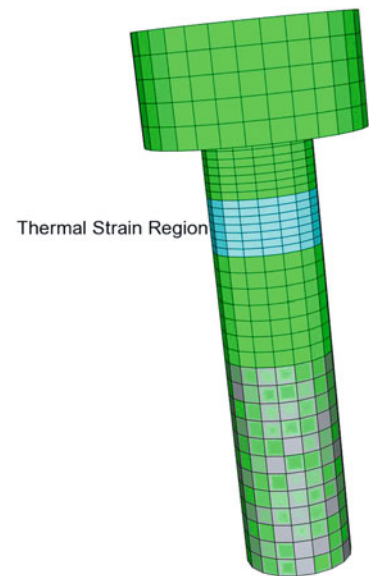


Fig. 2.5 Simple lap joint with a bolt and insert used for exploring different modeling techniques

Fig. 2.6 One method for modeling the bolt is to use solid elements and apply a thermal strain to a portion of the bolt. The insert is shown in the grey and green portion



Three models are explored in this section to determine an efficient and accurate method of modeling the joints going forward: solid element of the fastener, a spring element for the fastener, and a beam element for the fastener. The first method is to model the bolt with solid elements, see Fig. 2.6. In the code used for these analyses, SIERRA SD, the bolt can be preloaded with a thermal strain in a section of the bolt.

The propensity for fatigue failure and fretting is greatest when the joint begins to separate. At the point just before joint separation, the contact patch between the mating surfaces would be very minimal. As this is the worst case scenario, the models in this study use a contact patch represented by a spring that is rigidly tied to the nodes at the matching interfaces bolt holes.

The second method of modeling the bolt is with the spring element rigidly tied to the holes of the two mating surfaces, as depicted in Fig. 2.7. This is a simpler method and more efficient method; however, the bolt preload cannot be applied in the finite element model with the code being used. The bolt preload is post-processed as discussed in Sect. 2.2.2. A beam element can also be used, and has shown similar results.

Finally, the third method of modeling the bolt in the lap joint with an insert is to use a beam, see Fig. 2.8. The bottom of the beam is rigidly tied to the insert location and the top of the beam is rigidly tied to the contact surface where the head of the bolt or washer would be.

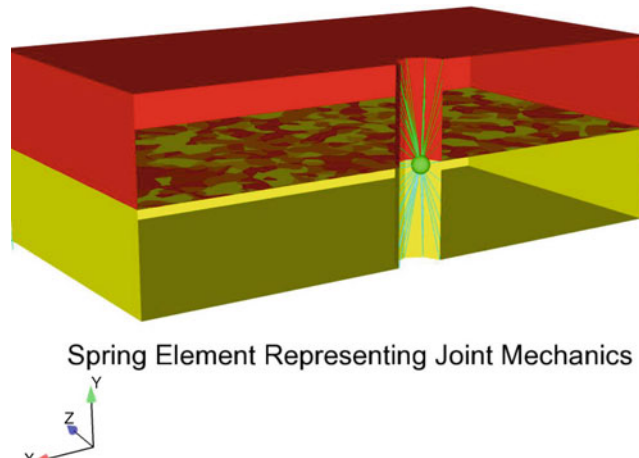


Fig. 2.7 Another method for modeling the bolt is to use springs that are rigidly tied to the fastener holes of the two mating surfaces

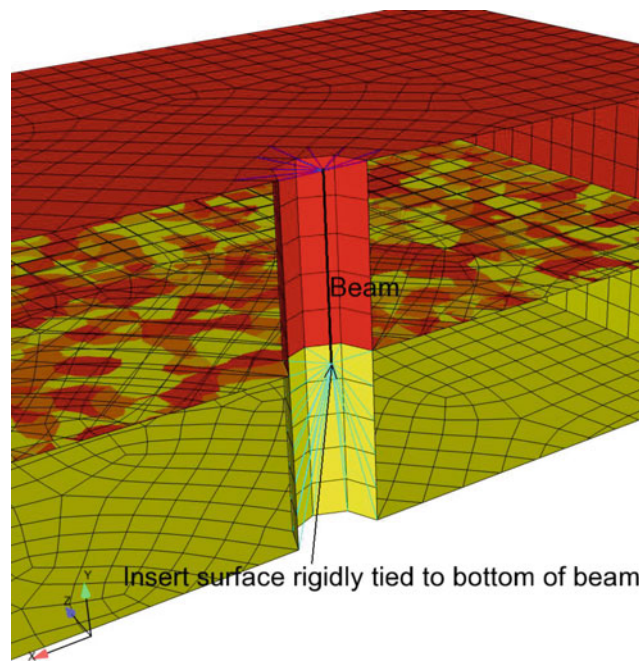


Fig. 2.8 Another method for modeling the bolt is to use a beam that is rigidly tied to the insert and at the top of the joint where the washer would be at the bolt head

2.3.1.1 Modal Comparison

As with any dynamics analysis, this study begins by looking at the modes of the simple models. The realistic modes are depicted in Fig. 2.9 for the model of the solid and the spring. Table 2.2 provides the difference of the modes between the different methods. As can be seen, there is not a significant amount of difference between these methods. The slight variation noted in the modes is more than likely eclipsed by the variability of the joint system.

2.3.1.2 Axial Load in Bolt

The majority of the calculations for fastener analyses are dependent on the axial force in the bolt, see Sect. 2.2.2. To assess the differences in the modeling techniques, a tensile traction that is ramped up from 0 to 555 psi in 0.05 s. is applied to the top

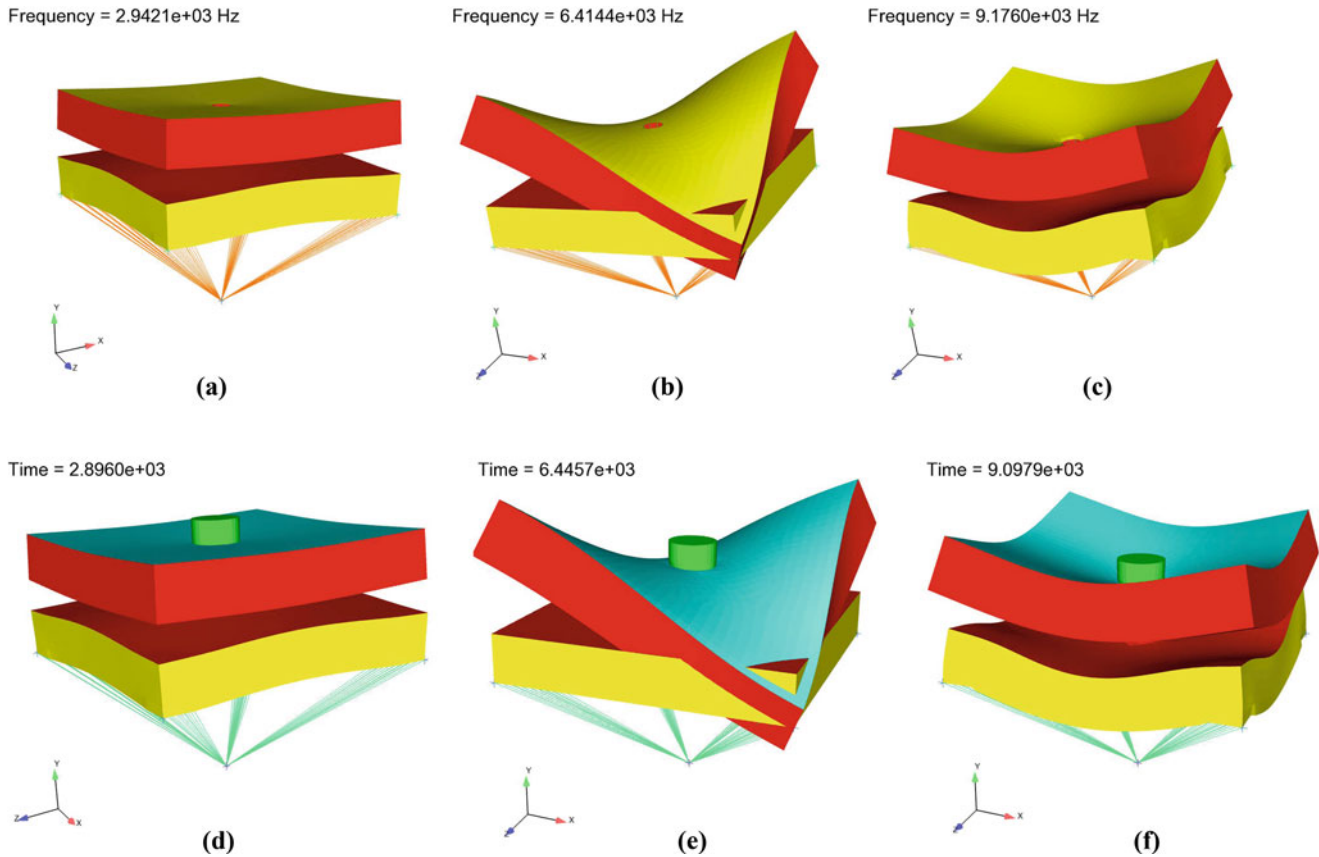


Fig. 2.9 Modal comparisons of the modeling techniques for the lap joint with an insert. (a) Spring mode 1. (b) Spring mode 2. (c) Spring mode 3. (d) Solid mode 1. (e) Solid mode 2. (f) Solid mode 3

Table 2.2 Modal comparisons of the modeling techniques for the lap joint with an insert

Mode	Beam frequency (Hz)	Spring frequency (Hz)	Solid frequency (Hz)	Difference spring vs. solid
1	2944.0	2942.1	2896.0	1.6%
2	6420.3	6414.4	6445.7	-0.5%
3	9163.2	9176.0	9097.9	0.9%

of lap joint. With a top area of the lap joint that is roughly 9 in.², this should apply an axial force around 5,000 lb to the bolt, if the lap joint stiffness is not included, see Sect. 2.2.2.

Figure 2.10 illustrates the axial force in the bolt using the three different modeling techniques. For the solid model, the preload was determined based on the thermal strain applied. The thermal strain was applied for a particular band of elements to get a preload around 3,000 lb. The spring and beam models can be calculated with and without a joint stiffness parameter, C . This is defined in Sect. 2.2.2 and Eq. (2.5). The joint stiffness parameter accounts for the fact that the bolt only carries a portion of the tensile load until separation (loss of preload). When the bolt is preloaded, the bolt is under tension and the abutments (flanges) are compressed. In a preload, the bolt carries only a portion of the load. The other portion of the loading is offset by the release of the compressive energy introduced to the flanges during the initial torquing (preload). Essentially, a portion of the work is performed by the joint and a portion by the bolt. As can be seen in Fig. 2.10, the three methods essentially provide the same axial force with the spring and the beam techniques being slightly more conservative.

2.3.1.3 Stress State of Mating Lap Joint Aluminum Materials

The final area explored in this simple study is the stress state around the mating lap joint materials. The largest discrepancy is noted on the top mating surface. This is due to the different boundary conditions used for representing the top of the bolt and its effects. Though there are different boundary conditions, if an element around two radius from the hole/boundary condition is explored, then the methods are almost identical, as seen in Fig. 2.11.

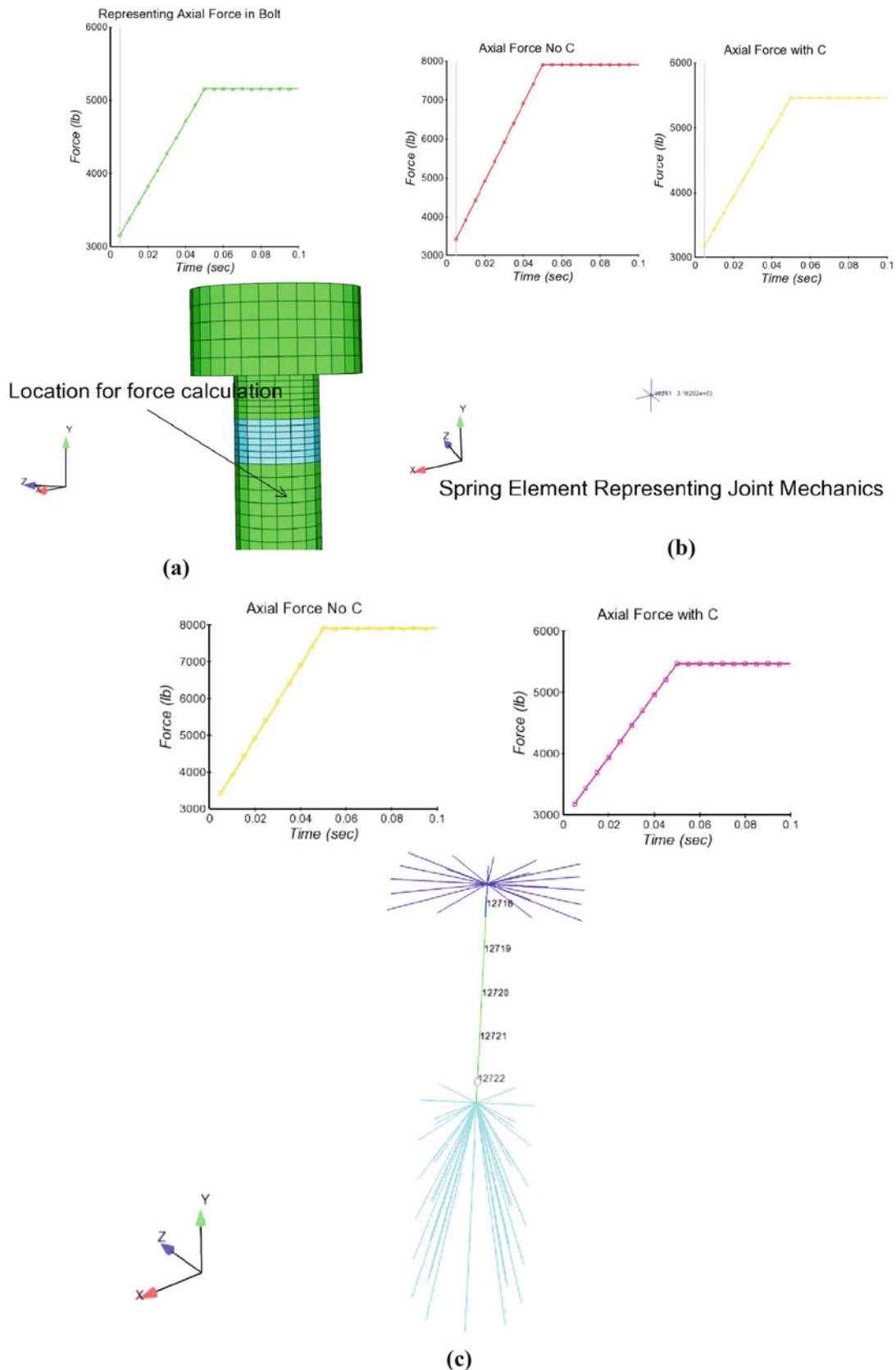


Fig. 2.10 Axial force in bolt comparisons of the modeling techniques for the lap joint with an insert. (a) Solid model. (b) Spring model. (c) Beam model

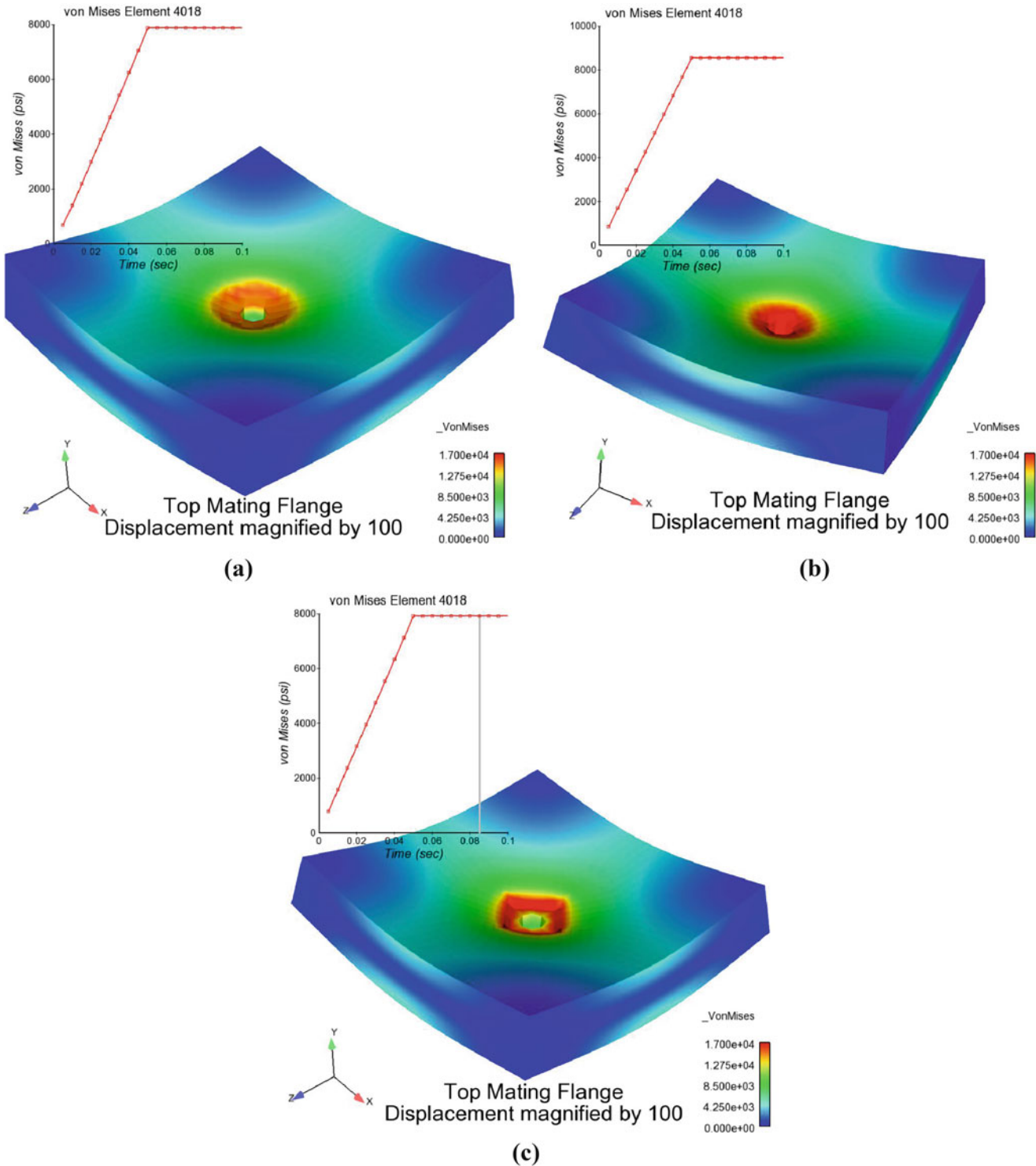


Fig. 2.11 Von Mises stress comparisons of the modeling techniques for the top mating surface of the lap joint with an insert. **(a)** Solid model. **(b)** Spring model. **(c)** Beam model

2.3.2 Fastener Fatigue Credibility

If the modeling of the fastener and the algorithms/coding of the stresses in the fastener are found acceptable, then the final piece of the puzzle for credibility would be assuring that the algorithms/coding of the fatigue methods is correct. To check the majority of the fatigue codes (cycle counting, damage accumulation, and S/N curve derivation) a fastener under axial loading is modeled and compared to work by Wentzel and Huang [15]. Good agreement is shown with Wentzel and Huang's axial fatigue experiment for an ISO-metric M14 bolt as seen in Fig. 2.12. The beam, spring, and solid methods of modeling the bolts as noted in Fig. 2.2 show basically the same result.

2.4 Results

In an effort to explore the effects of different fatigue methods for fasteners, a simple test article was simulated for a random vibration environment. The test article is shown in Fig. 2.13. The test article is bolted to a fixture that would be bolted to a shaker table. An applied acceleration is applied to the base of the fixture replicating the shaker table. The random vibration environment was a typical transportation environment and simulated in all three cartesian directions at the same time. The random vibration environment was scaled until a damage metric, D , of 0.18 was found for one of the fasteners in tension.

There are 36 bolts attaching the test article to the fixture. The test article and the fixture are aluminum. The fasteners analyzed are 5/16 – 24 UNJF-3A, alloy steel (AISI 4340) with properties shown in Table 2.3. The insert is of the same material with an external thread of 1/2 – 13 UNC.

The simulations were run in a transient manner that was compared with frequency domain random vibration simulation to assure the time duration was sufficient to capture the system's response in a random process. The damage metric, D , for each method was then appropriately scaled to the duration of the environment. The damage metric for each fatigue calculation is shown in Table 2.4 with the maximum D found from the 36 bolts.

Table 2.4 shows that the fastener would fail in fatigue under the Findley and McDiarmid methods, but not the other analyses. The biaxiality, an indication of loading condition (see Sect. 2.2.4), is shown in Fig. 2.14 for the bolt that had the largest fatigue damage. The biaxiality shows that the bolt is in a multiaxial non-proportional loading condition. Figure 2.15 provides the stress state for the tensile stress and the equivalent Findley stress; clearly indicating a larger stress state with Findley.

2.5 Conclusion

If the applied loads at a fastener jointed interface from a random vibration environment are such that the preload is greatly reduced, then it is essential to analyze fasteners with a multiaxial fatigue methods, such as Findley or McDiarmid. The current practice of using uniaxial stress states for fasteners could greatly under predict the fatigue failure of the fastener.

This work provided typical uniaxial stress state derivations for a fastener. It then provided a time domain method for analyzing these uniaxial stress states for fatigue. Multiaxial fatigue methods were then explored for fasteners given the stress tensor in the fastener as a function of time. These derivations were then explored on a test article under random vibration environments to show the relevance of using multiaxial fatigue methods. Future work would include experimentally testing these numerical results.

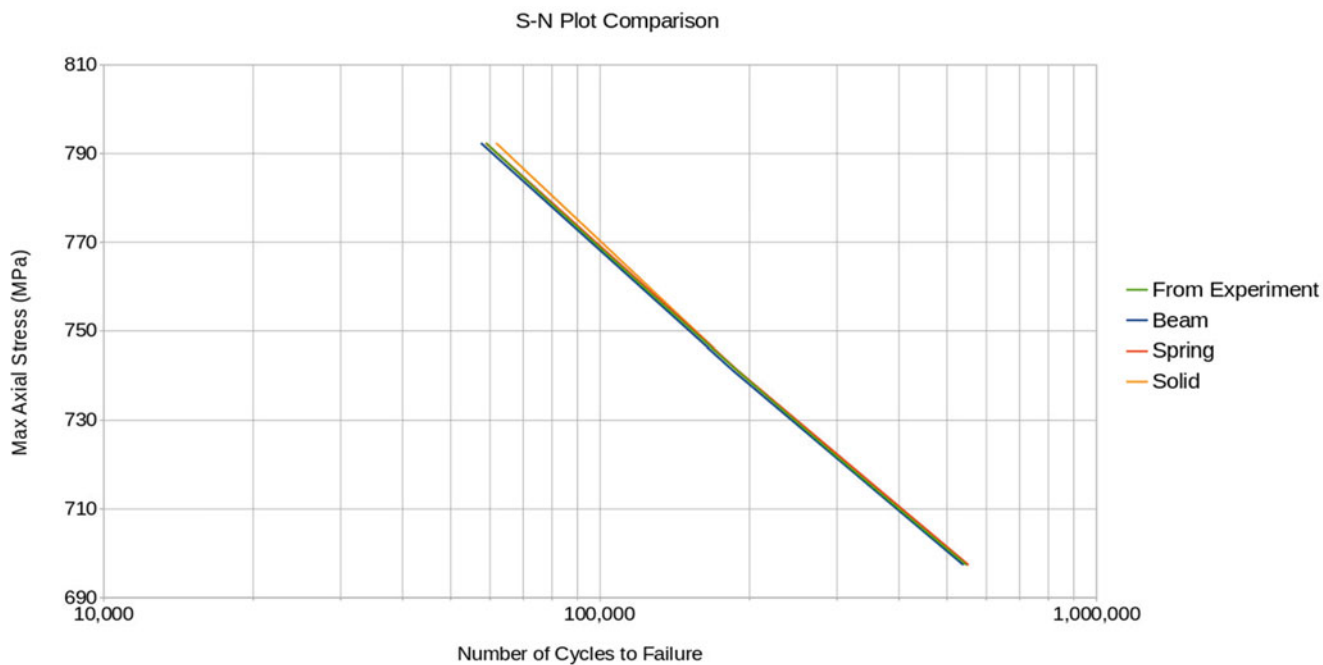


Fig. 2.12 Comparison between simulations and from Wentzel and Huang's experiment [15] for a M14 bolt

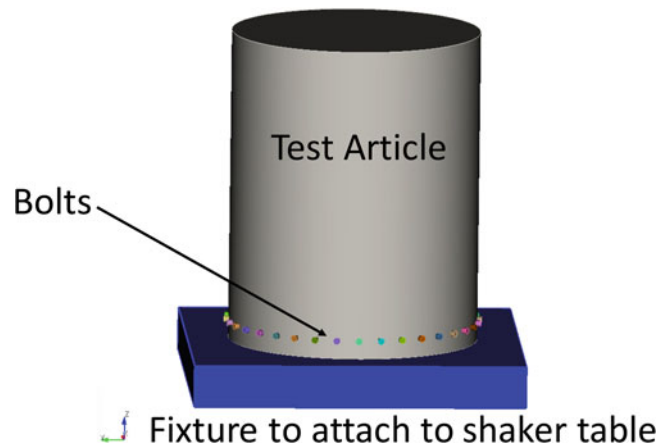


Fig. 2.13 Test article used to explore different fatigue methods for fasteners

Table 2.3 Material properties for the 5/16 – 24 UNJF-3A Fasteners used in this analysis

Property	Value
Fatigue strength axial	60.0 ksi
Fatigue strength shear	40.8 ksi
Fatigue strength coefficient	178.8 ksi
Torque preload	115 lbf-in
Ultimate stress	125 ksi

Table 2.4 The maximum fatigue methods damage metric, D , found from the 36 bolts for the random vibration environment

Fatigue analysis	Damage metric, D
Tensile stress	0.18
Shear stress in bolt	1.2×10^{-10}
Insert pull-out	4.82×10^{-6}
Bolt thread shear	1.37×10^{-8}
Insert internal thread shear	1.0×10^{-20}
Insert external thread shear	1.0×10^{-20}
<i>Multiaxial methods</i>	
von Mises	0.23
Findley	7.82
McDiarmid	3.07

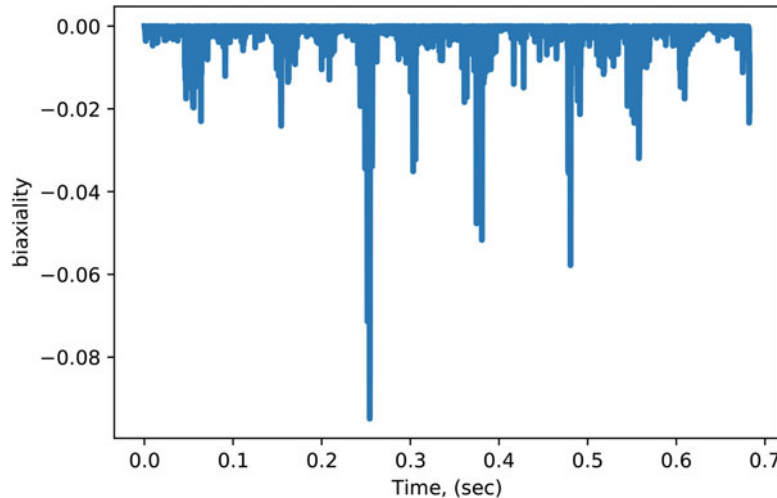


Fig. 2.14 Biaxiality as a function of time for the bolt with the most fatigue damage. The non-constant nature of the biaxiality shows the need for analyzing fatigue with non-proportional appropriate methods, such as Findley or McDiarmid

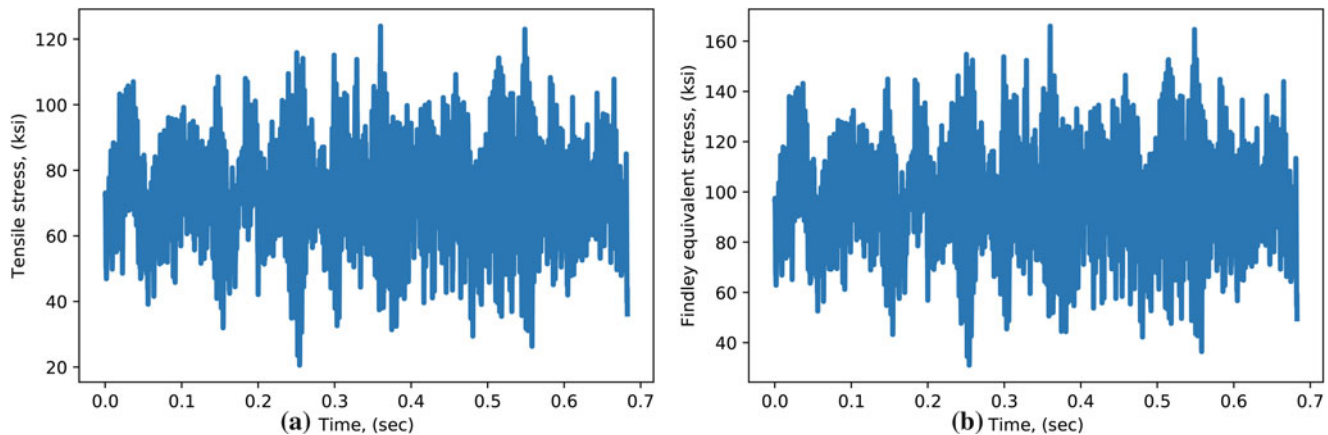


Fig. 2.15 Stress comparisons of the tensile stress in the fastener and the equivalent Findley stress. **(a)** Tensile. **(b)** Findley

Acknowledgements Sandia National Laboratories is a multimission laboratory managed and operated by National Technology and Engineering Solutions of Sandia LLC, a wholly owned subsidiary of Honeywell International Inc. for the U.S. Department of Energy's National Nuclear Security Administration under contract DE-NA0003525. Sandia Report SAND2017-11320C.

References

1. Wirsching, P.H., Paez, T.L., Ortiz, K.: Random Vibrations: Theory and Practice. Dover Books, New York (1995)
2. Campbell, F.C. (eds.): Elements of Metallurgy and Engineering Alloys. ASM International, Materials Park (2008)
3. Hudgins, A., James, B.: Fatigue of threaded fasteners. *Adv. Mater. Process.* **172**, 18–22 (2014)
4. Socie, D.F., Marquis, G.B.: Multiaxial Fatigue. Society of Automotive Engineers, Inc., Warrendale (2000)
5. Shigley, J.E., Mitchell, L.D.: Mechanical Engineering Design, 4th edn. McGraw-Hill, New York (1983)
6. Norton, R.L.: Machine Design: An Integrated Approach. Prentice-Hall, Upper Saddle River (1998)
7. Sierra Structural Dynamics Development Team: Sierra structural dynamics – user's notes. Technical report SAND2017-3553, Sandia National Laboratories (2017)
8. Chambers, J.A.: Preloaded joint analysis methodology for space flight systems. Technical report 106943, NASA (1995)
9. Oberg, F.J.E.: Machinery's Handbook. Industrial Press, New York (2008)
10. Downing, S.D., Socie, D.F.: Simple rainflow counting algorithms. *Int. J. Fatigue* **4**, 31–40 (1982)
11. Miner, M.A.: Cumulative damage in fatigue. *J. Appl. Mech.* **12**, A159–A164 (1945)
12. Steinberg, D.S.: Vibration Analysis for Electronic Equipment, 3rd edn. Wiley, New York (2000)
13. Anes, V., Reis, L., Li, B., Fonte, M., de Freitas, M.: New approach for analysis of complex multiaxial loading paths. *Int. J. Fatigue* **62**, 21–33 (2014)
14. Lindeburg, M.R.: Mechanical Engineering Reference Manuals for the PE Exam, 11th edn. Professional Publications, Belmont (2001)
15. Wentzel, H., Huang, X.: Experimental characterization of the bending fatigue strength of threaded fasteners. *Int. J. Fatigue* **72**, 102–108 (2015)



Chapter 3

Multi-input Multi-output Active Vibration Control for High Frequency Random Vibration

Aabhas Singh, Matt Allen, and Washington J. DeLima

Abstract Electromagnetic shakers and closed loop control systems are commonly used in qualification tests for environmental vibration conditions. However, at high frequencies shakers have resonances and anti-resonances. Resonances can be beneficial in that the shaker needs to exert less force to achieve the desired environment, but they can make it more challenging for the control system to match the desired environment. Anti-resonances are more problematic because they represent frequencies where the voltage input to the shaker causes little motion (at some locations on the slip table or adapter plate). Hence, these can cause the system to require driver voltage levels above the controller capacity and cause the test to abort. Furthermore, an anti-resonance is in essence a motion that is unobserved at the point(s) of interest, and hence they may lead to damage if internal components experience much higher vibration levels than the control accelerometer. This paper proposes and characterizes a hybrid shaker system that would use a piezoelectric actuator in addition to the electromagnetic shaker to create a MIMO control system. It is hoped that the additional control effort introduced by the piezoelectric actuator could be used to expand the frequency range over which the desired environment can be achieved.

Keywords Modal Test · Model calibration

3.1 Introduction

Electromagnetic shakers are commonly used to replicate the motion of a test part under environmental vibration conditions. To do so, modern shakers must be capable of large displacements and high force levels and as a result, are large and have low frequency resonances, often hindering high frequency vibration tests. At higher frequencies above the first resonance of the shaker, uncontrollable modes of the shaker armature are excited, which can make it difficult or impossible to replicate the desired environment and which could result in damage to the shaker armature. These high-frequency modes can be highly variable between shakers, as shown recently by DeLima and Ambrose [1], who measured the driver voltage necessary to achieve a desired environment for four shakers (UD-T2000[®]) as a function of the forcing frequency, a result that is repeated in Fig. 3.1. As expected, at resonance there is a dip in the driver voltage, since the force required to excite the structure is minimized. However, at higher frequencies the behavior of the four shakers becomes erratic, deviating significantly from each other. In addition, at higher frequencies, the driver voltages peak, indicating anti-resonances or frequencies in which the test part moves little in response to the input force, so one must increase the voltage significantly to obtain the desired motion and the necessary voltage may be outside the capability of the shaker.

This paper evaluates the potential to add piezoelectric actuators to a traditional electromagnetic shaker, so that a multi-input multi-output control scheme can be used to extend random test vibrations to higher frequencies without the potential of damaging the shaker structure. Past work to surpass these limitations of the shaker researched the sole use of piezo actuators to force test articles to a desired environment. This proved successful at high frequencies given that piezo actuators can

Honeywell Federal Manufacturing & Technologies, LLC manages and operates the Department of Energy's Kansas City National Security Campus under contract DE-NA-0002839.

A. Singh (✉) · M. Allen
University of Wisconsin – Madison, Madison, WI, USA
e-mail: Singh36@wisc.edu; msallen@engr.wisc.edu

W. J. DeLima
Honeywell, Kansas City, MO, USA
e-mail: wdelima@kcp.com

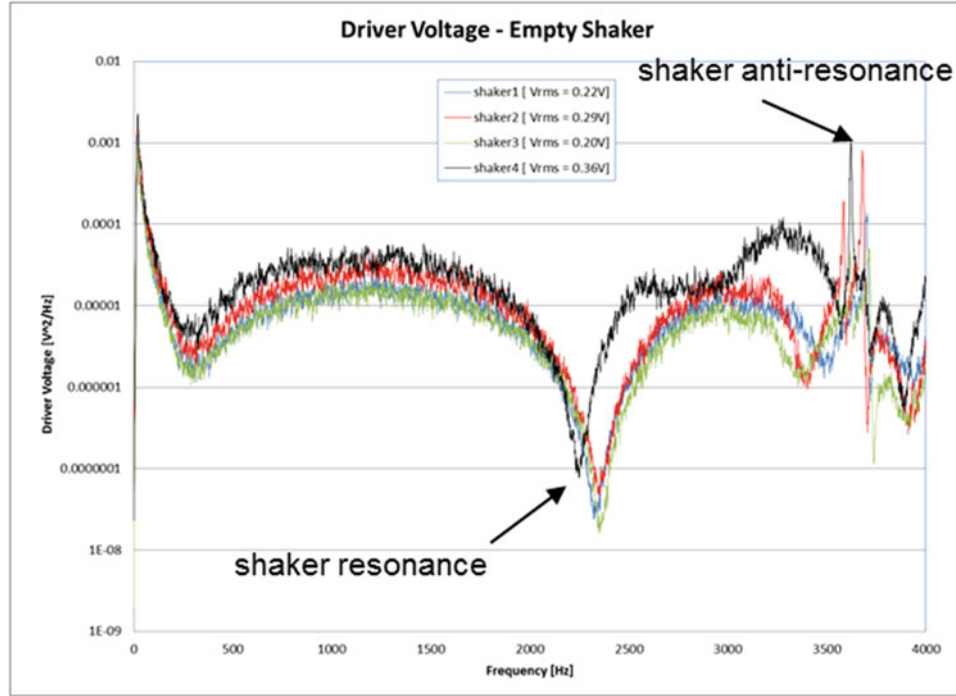


Fig. 3.1 Experimental setup for the shaker test [1]

support large-weight articles and render large forces [2]. However, the stroke length limitations of piezo actuators limit the displacement imposed on the test article. This work seeks to use MIMO control so that a traditional shaker and a piezo actuator can be used simultaneously, each working in the frequency range in which it is most effective, in hopes of reproducing the complete environment in a single test.

Prior to designing the control scheme, extensive modeling is required to understand the effects of coupling between the piezoelectric actuator and electrodynamic shaker motion. Piezoelectric actuators are somewhat fragile (made from brittle ceramic) so care must be taken to assure that the piezo actuator is not stressed beyond its limits. As a result, this work will validate three models for the piezo/shaker with varying degrees of fidelity to gauge their effectiveness to provide the desired forces and survive the vibration environment: (1) a two degree of freedom model for the shaker, (2) a two degree of freedom model for the piezo actuator, and (3) a three degree of freedom model for the assembly.

The following sections discuss the tests that were used to characterize each of the components and the model calibrations done to equate to the test data.

3.2 Experimental Characterization & Modeling of Shaker

The electrodynamic shaker and piezoelectric actuator system under investigation consists of a Brüel Kjær LDS V830–335 Metric Shaker coupled with the CEDRAT PPA40XL Actuator. Prior to creating the models, both components were characterized through modal analysis, and then the two models were assembled to evaluate the effectiveness of the coupled model. The modal test of the shaker was performed using 25 input points that followed the bolt pattern on the plate and two output points (accelerometers) as depicted in Fig. 3.2.

As with the experimental analysis done by DeLima et al. [1], the frequency bandwidth was limited to approximately 4 kHz. Frequency Response Functions (FRFs) were measured for four DOF at two points on the plate: a triaxial accelerometer at point 19, and a uniaxial accelerometer (Z direction) at point 20. The mode shapes of the shaker and the plate are obtained using the FRFs with modal parameter identification using the Algorithm for Mode Isolation (AMI) [3], resulting in eight modes listed in Table 3.1.

The mode of primary interest is the first axial mode of the shaker, which was found to be at 2145.7 Hz and whose mode shape is shown below. Note that measurements were only taken on the shaker adapter plate, so it is impossible to characterize

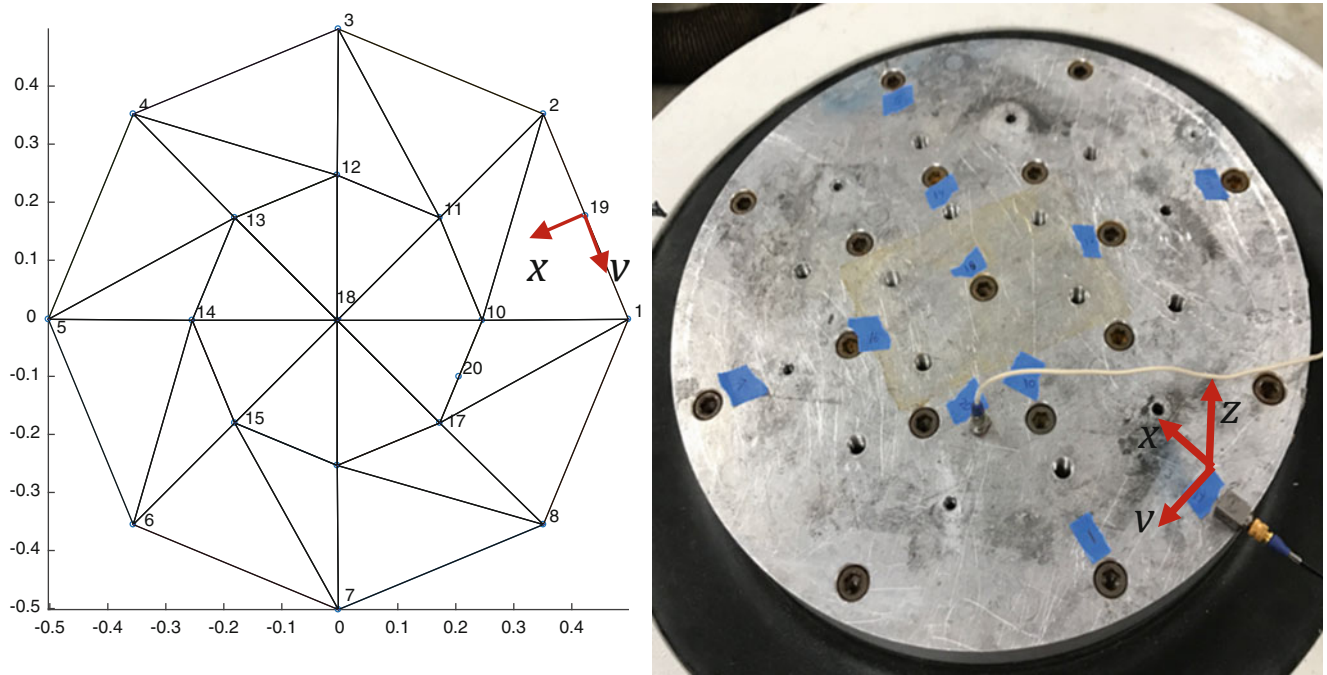


Fig. 3.2 Experimental setup for the shaker test

Table 3.1 Modes and the identified resonant frequencies and damping ratios

Mode	Resonant frequency (Hz)	Damping ratio (%)	Mode shape description
1	1373	0.604	Y-axis rocking of top plate
2	2145.7	0.216	1st drum mode of top plate/assumed axial mode of shaker
3	2161.4	0.429	X-axis rocking of top plate with minor bending
4	2181	0.665	Y-axis rocking of top plate with minor bending
5	2627.5	1.30	1st torsion (“potato chip”) of top plate, two radial node lines
6	3290.5	1.09	1st drum mode of top plate, about center of mass
7	3845.5	0.782	2nd torsion of top plate, three radial node lines
8	4160	0.602	1st drum mode of top plate with edge distortion

them separately with complete certainty. After the second mode, all of the modes involve zero motion of the center of the shaker plate until the 3290.5 Hz mode, suggesting that the 2DOF model of the shaker could be effective up until near that frequency (Fig. 3.3).

3.2.1 2DOF Electrodynami c Shaker Model

The model for the electrodynamical shaker is based on the work by Waimer et al. [4]. The simplest model is a 2DOF lumped parameter model as shown in Fig. 3.4. A two-mass system is the lowest order system that could exhibit the anti-resonances seen in the experiments by DeLima and Ambrose. Unlike Waimer, this model does not incorporate rotational shaker modes, given that the shaker is expected to be run at low frequencies, mitigating the non-axial modes.

A few parameters of the shaker are known from test and/or the manufacturer’s specifications, and are noted in Table 3.2.

It is assumed that the system is lightly damped, with 0.2% modal damping for its axial mode. The natural frequency of the armature was measured and found to be approximately 2146 Hz. However, we do not have enough information to know how to divide the armature mass between the top plate and the internals of the shaker armature. Hence, in order to create this first model, the mass was simply divided such that 89% of the mass was placed on the top plate and 11% on the bottom

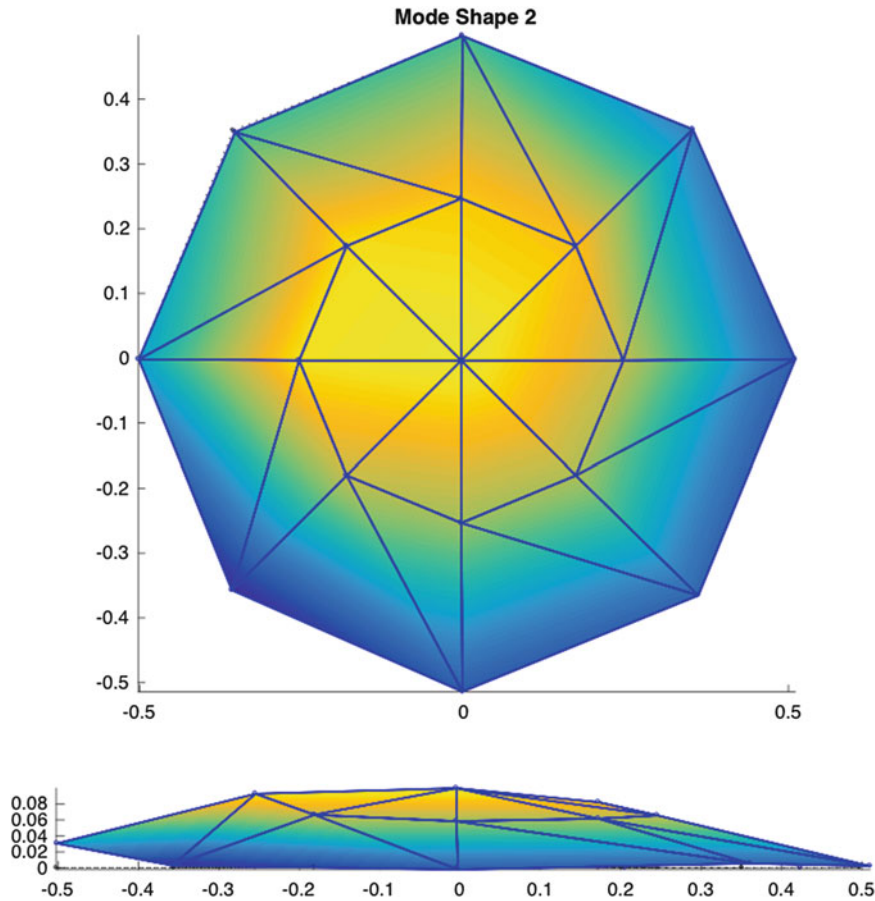
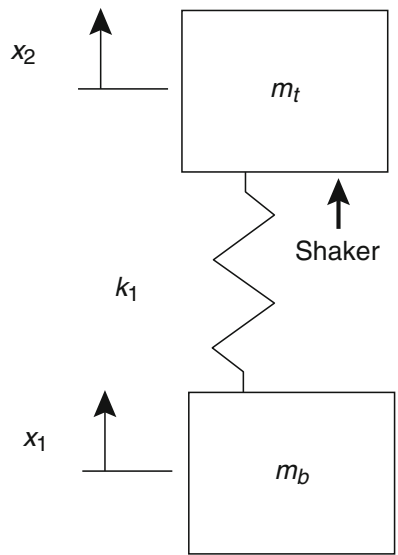


Fig. 3.3 Mode shape of mode 2 at 2145.7 Hz

Fig. 3.4 2DOF model of the shaker armature



in an effort to equate to experimental data. Then the stiffness was tuned such that the fundamental resonance frequency of the model matched the experimental resonance as shown in Table 3.3. Hence, the 2DOF system can be represented with the following parameters:

In the interest of brevity, no measurements are shown to confirm this model, but it will be confirmed in conjunction with the piezo model in Sect. 3.4.

Table 3.2 Notable LDS shaker parameters

LDS V830–335 shaker parameters	
Armature diameter	335 mm
Experimental armature resonance	2.146 kHz
Armature mass	12.83 kg
Usable frequency range	0–3 khz

Table 3.3 Shaker model parameters

Upper shaker mass	11.41 kg
Lower shaker mass	1.42 kg
Armature stiffness	3e8 N/m
Percent damping	0.05%

Table 3.4 Modes and the identified resonant frequencies and damping ratios.

Mode	Resonant frequency (Hz)	Percent damping
1	2562.5	0.302
2	2592	0.170
3	2727.1	1.117
4	2743.6	0.437

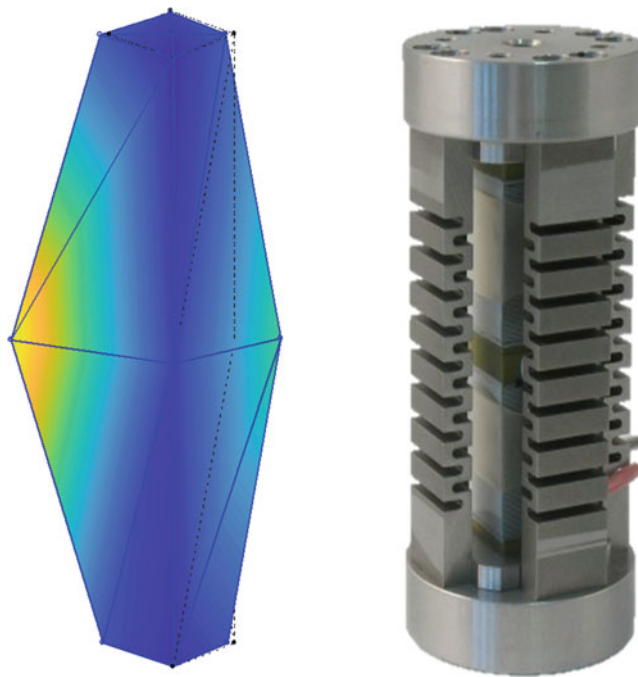


Fig. 3.5 2.59 kHz mode of the piezo

3.3 Experimental Characterization & Modeling of Piezoelectric Actuator

A modal test of the piezo actuator was also performed, with one of the primary goals being to see what resonances it might have that could be excited in a test and hence could damage the piezo. As a first step, the CEDRAT piezo actuator was characterized in free-free conditions by laying the actuator on a foam pad. A modal hammer test was performed with 14 input points and a tri-axial accelerometer output at the top of the piezo, from which four modes were identified within the frequency range of interest; their properties are shown in Table 3.4.

All four modes in this range correspond to bending of one of the four springs on the piezo, as seen with mode 2 below. The identified shapes suggest that these modes may be negligible if the motion is primarily axial, although this frequency range should be monitored to make sure that these lightly damped modes aren't excited. No other modes were observed in the frequency range of interest (Fig. 3.5).

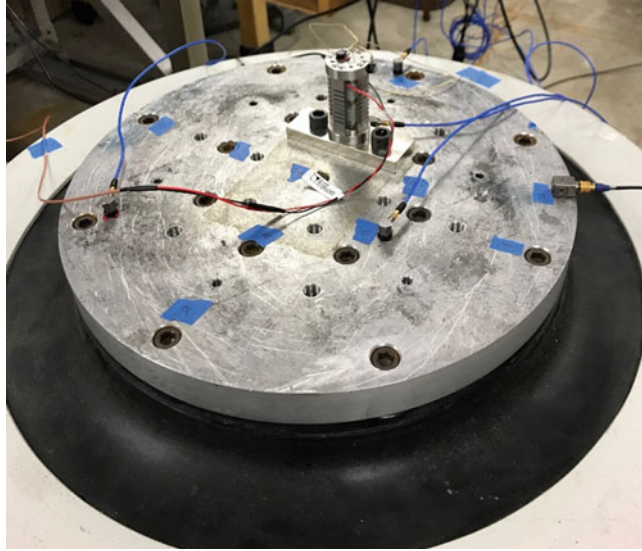


Fig. 3.6 Experimental setup used to test the piezo actuator on the shaker. Two other setups were also used that are not shown: (1) Bare piezo actuator mounted on foam, (2) Piezo actuator with a steel mass mounted to one end, mounted on foam

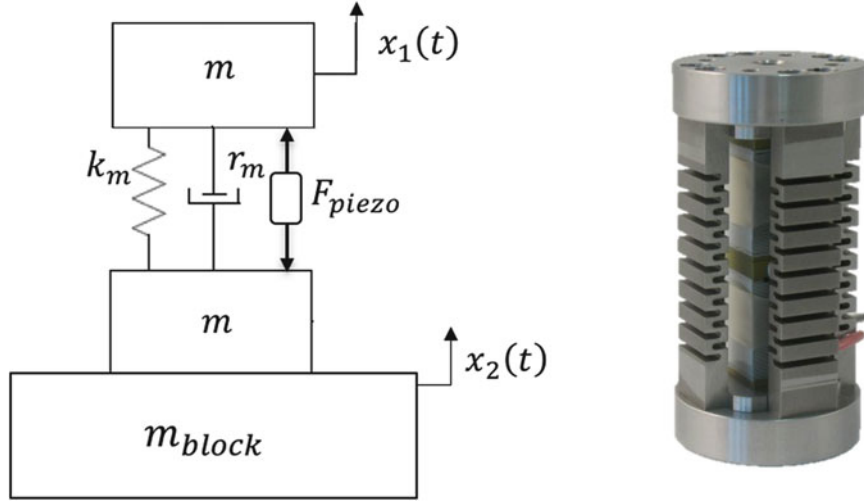


Fig. 3.7 2DOF Piezo/blocked model

In addition to modal tests done to understand the dynamics of the actuator in isolation, the piezo actuator was run at low input voltage with free – free conditions to model its ability to generate force. Free – blocked conditions were then added to validate the model predicted simulations. Lastly, the piezo actuator was bolted to the shaker using a fixture and each component was then excited separately to correlate to the coupled model as depicted in Fig. 3.6.

3.3.1 2DOF Piezo Actuator Model

The simplest model of the piezoelectric actuator is a 2DOF model, as discussed in the CEDRAT Catalog [5] and shown in Fig. 3.7 below.

The parameters given in the Cedrat catalog were found to not reproduce our measurements precisely, so the parameters were tuned to match the experimental characterization of the piezo and validated using additional free – blocked case studies, as described below. Given a 2DOF system depicting the top of the piezo and the bottom of the piezo with a mass attached (m_{block}), the system transfer functions can be presented by the following equations of motion:

Table 3.5 CEDRAT piezo model parameters

Parameters	Catalog values	Model values
Mass (m)	0.0319 kg	0.0319 kg
Force factor (N)	39.14 N/V	39.14 N/V
Resistance (r_m)	136.11	136.11
Stiffness (k_m)	155.08 N/ μm	217.11 N/ μm
Quality factor (Q)	20	20
Resonance (w_r)	13600 Hz	13600 Hz

$$M\ddot{s} + C\dot{s} + Ks = F \quad (3.1)$$

$$M = \begin{bmatrix} m & 0 \\ 0 & m + m_{block} \end{bmatrix}, \quad C = \begin{bmatrix} r_m & -r_m \\ -r_m & r_m \end{bmatrix}$$

$$K = \begin{bmatrix} k_m & -k_m \\ -k_m & k_m \end{bmatrix}, \quad F = \begin{Bmatrix} F_{piezo} \\ -F_{piezo} \end{Bmatrix}, \quad s = \begin{Bmatrix} x_1 \\ x_2 \end{Bmatrix}$$

Given the input force of the piezo actuator, the transfer functions can be represented for each DOF by the following equations (Table 3.5)

$$H_1(\omega) = \frac{a}{V} = \frac{\omega^2 N}{2k_m + i2r_m\omega - m\omega^2} \quad (3.2)$$

$$H_2(\omega) = \frac{a}{V} = \frac{-\omega^2 N}{2k_m + i2r_m\omega - m\omega^2} \quad (3.3)$$

To gauge the effectiveness of the model, using the above equations and the parameters in Table 3.1, the piezo electric model was evaluated against three case studies: (1) no blocked mass, (2) 0.34 kg block, and (3) 1.95 kg block. The values per the catalog were used in modeling the piezo actuator, with the exception of the axial stiffness of the piezo. Initially the curves showed a uniform offset, so the model stiffness was increased from the catalog value by 40% to bring the curves into agreement (Fig. 3.8).

After these adjustments to the model parameters, the model now accurately reflects the acceleration transfer function up to about 2 kHz for all cases. At about 4–5 kHz the blocks exhibit a resonances that weren't included in the model, and so model can't be checked beyond that point. The measurements are all below the first elastic resonance of the piezo, which is nominally at 13.6 kHz for the no block case, and so these measurements do not allow validating the stiffness rigorously. We presume that the model is sufficiently accurate to move forward.

3.4 Coupled Model

The coupled component model features the conjunction of both models depicted in Sects. 3.2 and 3.3. The dynamics at the junction between the actuator and shaker are neglected to result in a 3DOF model given by: (1) Top of the piezo actuator, (2) junction between piezo and upper shaker armature, and (3) lower shaker armature as shown in Fig. 3.9. Non-axial motion is not captured in this model.

The 3DOF model maintains the parameters of the previous models and imposes the forcing of either the piezo, the shaker, or both on the model. The motion of the model hybrid system is governed by the following equation:

$$M\ddot{s} + C\dot{s} + Ks = F \quad (3.4)$$

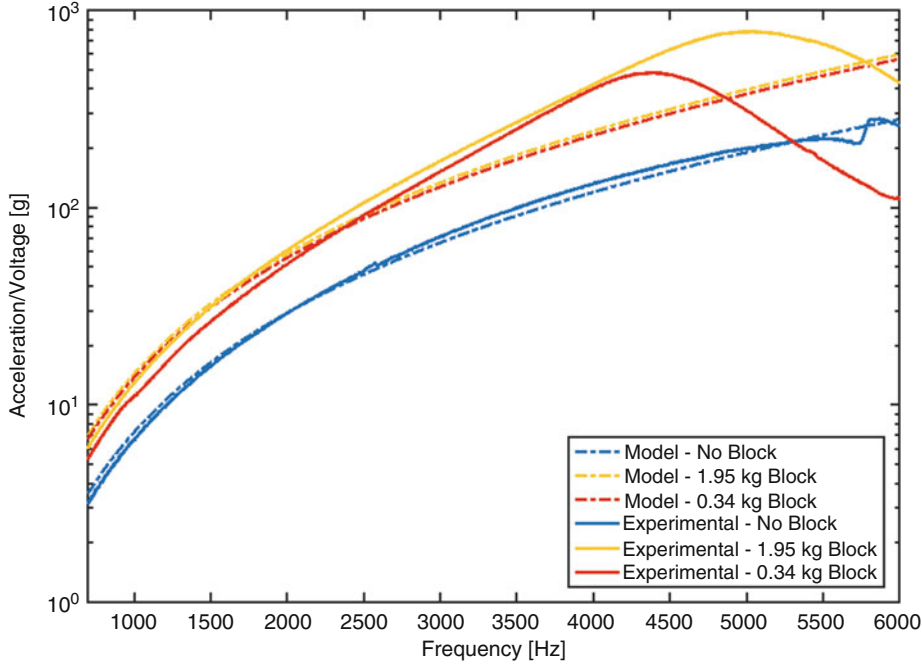
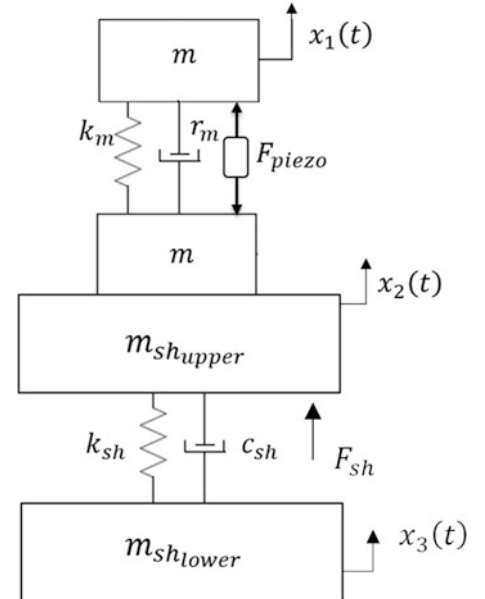


Fig. 3.8 Experimental vs. model results for motion at the top of the piezo actuator given an input voltage to the piezo actuator

Fig. 3.9 3DOF model for the hybrid shaker – piezo system



$$M = \begin{bmatrix} m & 0 & 0 \\ 0 & m_{shupper} + m & 0 \\ 0 & 0 & m_{shlower} \end{bmatrix}, \quad C = \begin{bmatrix} r_m & -r_m & 0 \\ -r_m & r_m + c_{sh} & -c_{sh} \\ 0 & -c_{sh} & c_{sh} \end{bmatrix}$$

$$K = \begin{bmatrix} k_m & -k_m & 0 \\ -k_m & k_m + k_{sh} & -k_{sh} \\ 0 & -k_{sh} & k_{sh} \end{bmatrix}, \quad F = \begin{Bmatrix} F_{piezo} \\ -F_{piezo} + F_{sh} \\ 0 \end{Bmatrix}, \quad s = \begin{Bmatrix} x_1 \\ x_2 \\ x_3 \end{Bmatrix}$$

As a result, the model can then be compared to the experimental data of the piezo actuator on the shaker for two cases: (0) when the piezo was excited, and the shaker was off, and (1) when the piezo was off, and the shaker was excited. Any

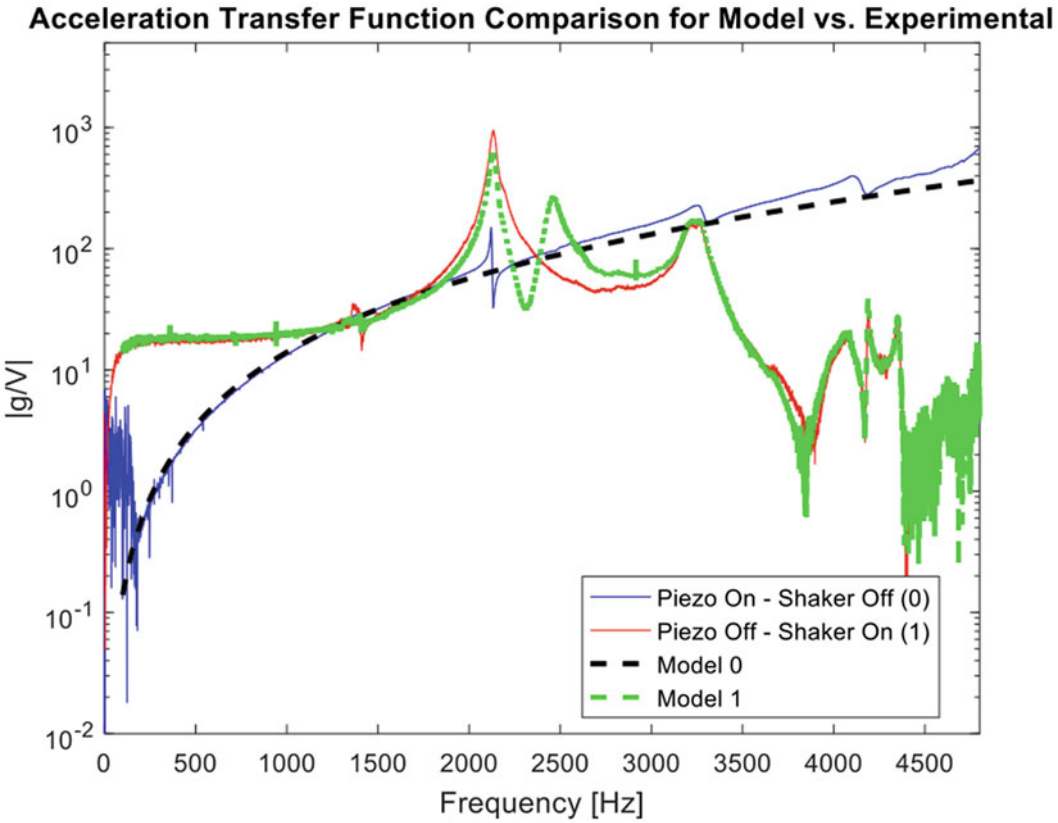


Fig. 3.10 3DOF model in comparison to the experimental acceleration data

combination of the two cases can be used in union to result in a desired environment. In all cases, the acceleration at the top of the piezo was compared between experimental and model data to determine if the model captures the force transmissibility from the shaker to the piezo.

In the first case, the piezo was excited with a 200 mV pseudorandom input. In essence, this is another blocked case for the piezo model, with the shaker providing the foundation. However, In the second case, the shaker was excited with a 50 mV pseudorandom input. Unlike the piezo actuator, there is no empirical value for the force factor of the shaker. Given that the force of the shaker is unknown, the acceleration at the top of the plate and the armature mass was used to determine the force of the shaker using $F_{sh} = m_{sh}\ddot{x}_2$ where m_{sh} is the armature mass, assuming no energy loss between the joints connecting the plate to the shaker. The results of both cases are shown in Fig. 3.10, comparing the model prediction to the experimental data at the top of the piezo actuator.

Within the range of interest, both models accurately capture the profile of the experimental data. Case one with the piezo actuator on and the shaker off is very accurately replicated by the model (recall that the stiffness factor for the piezo was scaled from the catalog value by 40% when tuning in the prior section). However, as expected, it cannot capture the additional resonances of the shaker, at the top of the piezo actuator. On the other hand, Model 1 is found to replicate the results for the case where the shaker is energized and the piezo is off but introduces an additional resonance at 2400 Hz. This resonance is thought to come about due to dynamics of the mounting plate located at the interface between the piezo actuator and the shaker, which is not accounted for within the model. In any event, this confirms that these models are able to reproduce the force generating ability of the piezo actuator and shaker, and hence they can now be used to determine what environments this combination of actuators can produce.

The second purpose for creating these models was to predict the stress in the piezo actuator to assure that it would not be damaged in the environments of interest. To do this, the strain of the piezo actuator in both cases was evaluated against experimental measurements. The displacements of the two masses in the piezo model were used to calculate the strain, which was then compared with measurements from a strain gauge mounted on the piezo as depicted below in Fig. 3.11.

As with the acceleration FRFs, both models accurately reflect the experimental strain of the piezo actuator. Model 0 simply shows that the strain magnitude achieved by the piezo matches that predicted by the model and both are essentially static in the frequency range of interest. Model 1 (piezo off/shaker on) captures the key resonance in the system at 2.146 kHz,

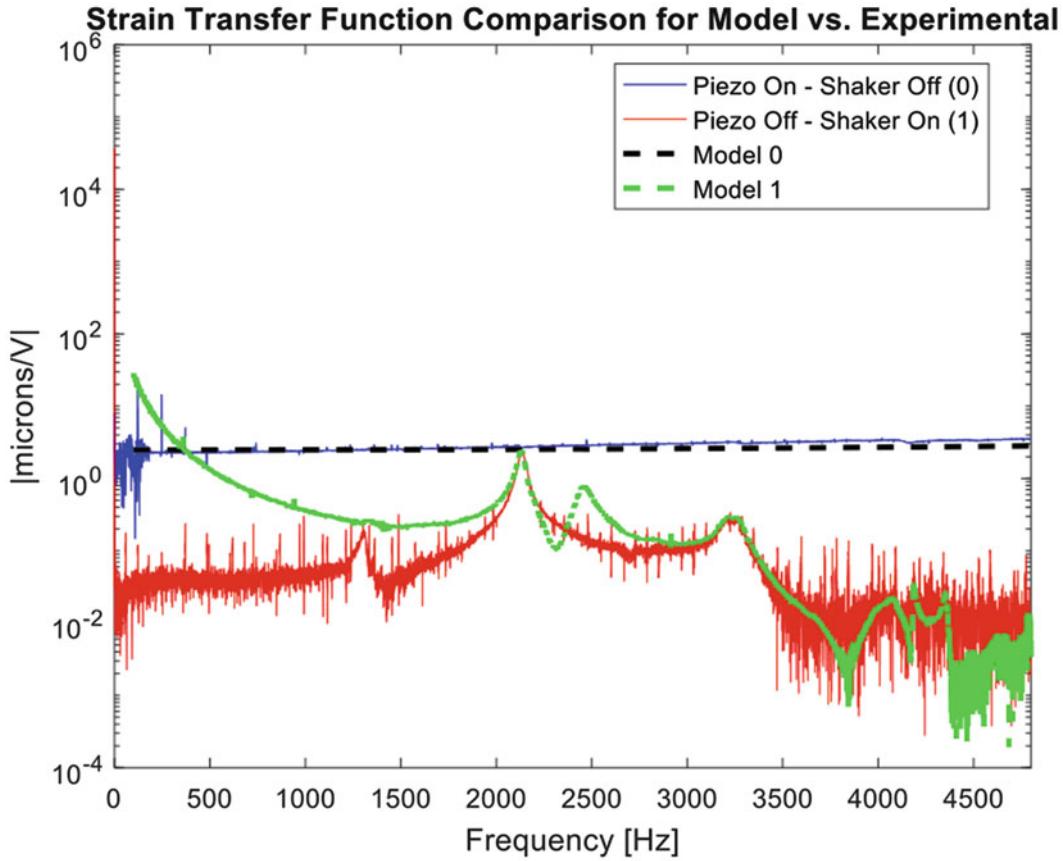


Fig. 3.11 3DOF model in comparison to the experimental strain data of the piezo actuator

showing excellent agreement near that mode, and since this is the primary mode of interest at the moment the model is judged successful. However, Model 1 shows an error that manifests itself as an over – prediction in the strain at low frequencies for which the cause is not yet known. These models have now been shown to reproduce the ability of the actuators to generate force and the strain in the piezo due to each actuator. However, we have not yet verified that superposition is valid for this configuration nor has the linearity of the system been verified. Further testing is underway in which both actuators are used simultaneously to see whether the response and strains predicted obey superposition when both the piezo actuator and shaker are active.

The purpose of the shaker/piezo actuator hybrid system is to excite a test article to a certain environment, while not exceeding the limitations in the test hardware. An effective method to evaluate the effectiveness of this system is to estimate the voltage required to excite the test article to a certain acceleration and calculate the effective strain of the piezo actuator, such that it does not exceed hardware strain limitations. Assuming a desired 8 g rms environment, the model reveals that approximately 10 V must be supplied to the shaker to create this environment for the desired frequency range (0 Hz – 4 kHz) as detailed in the equations below:

$$rms \left(V_0 * H_a \left[\frac{g}{V} \right] \right) = a_{desired} \quad (3.5)$$

where V_0 is the required voltage to produce the desired acceleration ($a_{desired}$) using the experimental FRF data. Likewise, the maximum effective strain of the piezo actuator can be found in a similar manner by using the voltage obtained in Eq. 3.5 to evaluate the max strain in Eq. 3.6.

$$\varepsilon_{max} = \max \left(V_0 * H_{strain} \left[\frac{\mu m}{V} \right] \right) \quad (3.6)$$

Table 3.6 Max piezo strain to produce a desired environment

	Case 0 (Piezo on, shaker off)	Case 1 (Piezo off, shaker on)
Environment	8 g rms	8 g rms
Voltage required	6.16 V	9.96 V
Max piezo strain	12.431 microns	45.009 microns

Using this methodology, the maximum strain given a desired acceleration of 8 g rms, for both cases is evaluated. For the first case with the shaker off and the piezo on, the maximum strain produced within the piezo is 12 microns, whereas for the second case with the shaker on and the piezo off, the maximum strain produced within the piezo is 45 microns. This is summarized in the table below (Table 3.6).

As evident, the second case exceeds the maximum strain allowed within the piezo of 44 microns [5]. Furthermore, even though the first case remains within the strain limitations of the piezo actuator, the voltage required exceeds the piezo limitations. The piezo itself is limited to 85 V, but the 20x multiplicity of the amplifier with the 6.16 V to the amplifier well exceeds this limitation. Hence, moving forward it will be necessary to limit each actuator to a subset of the frequency band (i.e. use the shaker from 0-3 kHz and the piezo actuator from 3–5 kHz) in order to hopefully keep within the limitations of the piezo.

3.5 Conclusion

This work has explored the characterization of an electromagnetic shaker and piezoelectric actuator to create a hybrid system that could hopefully allow more faithful reconstruction of high frequency vibration environments. Tests were performed on each of the structures to establish low-order models and to understand what frequency range each model might be valid for. The models were then combined to create a model for the hybrid piezo/shaker system, and the resulting model was found to properly replicate the experimental data with the piezo actuator forcing the system and the shaker off, or with the actuator off and the shaker on. However, the measurements did show additional resonances that were not captured by the model, presumably due to additional modes in the experimental data. So far these modes are not dominant contributors to the environment or strain in the piezo, so they have been ignored but they certainly could be included in future models.

Future work will seek to validate the model with a superposition of forces to better correlate test cases where both the shaker and the piezo actuator are exciting the system. With the validation of the model, control schemes will be explored to evaluate the effectiveness in the mitigation of shaker anti-resonances and the ability to produce desired test environments through a closed loop configuration coupled with a vibration controller.

References

1. DeLima, W.J., Ambrose, M.N.: Chapter 6: Experimental characterization and simulation of vibration environmental test, Kansas City. In: Topic in Modal Analysis, vol. 10, Proceedings pg 33rd IMAC – Conference & Exposition on Structural Dynamics, Orlando (2015)
2. Jepsen, R., Romero, E.: Testing in a combined vibration and acceleration environment. In: IMAC – XXIII Conference & Exposition on Structural Dynamics, Orlando (2005)
3. Allen, M.S., Ginsberg, J.H.: A global, SIMO implementation of the algorithm of mode isolation and application to analytical and experimental data. *Mech. Syst. Signal Process.* **20**(5), 1090–1111 (2006)
4. Waimer, S., Manzato, S., Peeters, B., Wagner, M., Guillaume, P.: A multiphysical modelling approach for virtual shaker testing correlated with experimental test results. In: Conference Proceedings of the Society for Experimental Mechanics Series, Orlando (2016)
5. CEDRAT TECHNOLOGIES: Products catalog, Cedrat Technologies, France (2016)



Chapter 4

A Method for Canceling Force Transducer Mass and Inertia Effects

Garrett K. Lopp, Benjamin R. Pacini, and Randall L. Mayes

Abstract Experimental modal analysis via shaker testing introduces errors in the measured structural response that can be attributed to the force transducer assembly fixed on the vibrating structure. Previous studies developed transducer mass-cancellation techniques for systems with translational degrees of freedom; however, studies addressing this problem when rotations cannot be neglected are sparse. In situations where rotations cannot be neglected, the apparent mass of the transducer is dependent on its geometry and is not the same in all directions. This paper investigates a method for correcting the measured system response that is contaminated with the effects of the attached force transducer mass and inertia. Experimental modal substructuring facilitated estimations of the translational and rotational mode shapes at the transducer connection point, thus enabling removal of an analytical transducer model from the measured test structure resulting in the corrected response. A numerical analysis showed the feasibility of the proposed approach in estimating the correct modal frequencies and forced response. To provide further validation, an experimental analysis showed the proposed approach applied to results obtained from a shaker test more accurately reflected results obtained from a hammer test.

Keywords Transducer removal · Experimental substructuring · Instrumentation error · Decoupling · Modal analysis

4.1 Introduction

Conducting a modal test with a vibration shaker offers many benefits over impact testing; however, one drawback includes the requirement of a force transducer fixed on the vibrating structure. If the structure is relatively lightweight, the presence of this transducer can alter the structure's mass distribution, thus affecting the dynamic response and driving down the modal frequency estimates. The mass-cancellation procedure for transducers at drive-point measurements has been well-known for some time [1]. More recently, methods have been developed to extend the correction for transfer measurements [2–8]. Although showing success, these methods mainly focus on eliminating the translation degree-of-freedom (DOF) mass effects from the dynamic response. For systems where rotations cannot be neglected, such as beam- and plate-like structures, 75% of the frequency response function (FRF) matrix corresponds to rotation-based quantities, so the transducer's moment of inertia can also pollute the dynamic response [9]. The focus of the current paper is to develop a suitable approach capable of correcting for both the transducer mass and moment of inertia on the measured response.

The proposed approach utilizes concepts from an experimental modal substructuring approach introduced by Allen et al that utilizes a fixture attached to a test article for the purpose of combining with an analytical model of a separate substructure [10, 11]. Inclusion of this fixture mass-loads the test article interface which leads to an improved modal basis and more accurate modal parameter estimates when combining with the analytical substructure. The fixture is of simple geometry so that an accurate analytical model facilitates the removal of the fixture effects from the final combined system. The current paper adopts this concept by incorporating an analytical model of a local section of the test structure containing

Sandia is a multimission laboratory managed and operated by National Technology and Engineering Solutions of Sandia, LLC., a wholly owned subsidiary of Honeywell International, Inc., for the U.S. Department of Energy National Nuclear Security Administration under contract DE-NA-0003525.

G. K. Lopp
Department of Mechanical and Aerospace Engineering, University of Central Florida, Orlando, FL, USA

B. R. Pacini (✉) · R. L. Mayes
Structural Dynamics Department, Sandia National Laboratories, Albuquerque, NM, USA
e-mail: brpacin@sandia.gov

the attached force transducer. Rather than using the local analytical model to remove the effects of the substructure from the system response, the model is instead used in an expansion process to estimate the mode shapes corresponding to both translation and rotation degrees of freedom at the transducer connection point. An accurate estimation of these connection point mode shapes, combined with a rigid body model of the force transducer, enables immediately the removal of the force transducer from the system.

The remainder of the paper is composed as follows: Sect. 4.2 develops the substructuring theory used to remove the transducer effects. Also provided is a discussion on modeling the force transducer as a general rigid body. Section 4.3 introduces the test structure utilized in this work. Simulations are then performed on a 2-D finite element (FE) model with an attached force transducer to test the performance of the correction procedure. The results are then compared in terms of the modal frequencies and the forced response to a similar model without the transducer. Section 4.4 provides experimental validation of the proposed approach by correcting the response obtained from a shaker test. The results are then compared to a hammer test on the same structure without the force transducer assembly.

4.2 Theoretical Development

4.2.1 Transducer Removal

Consider the T-Beam structure shown in Fig. 4.1. When performing a shaker vibration test, the effects of the mass and moment of inertia of the attached force transducer on the test structure, specified here as CT , pollute the measured data. The approach presented here assumes the force transducer, specified here as component T , is a rigid body with mass and moment of inertia terms that can be determined leading to an analytical mass matrix. Subtracting the mass matrix of the force transducer from the measured system recovers the true system without the transducer, specified here as system C . The equations of motion governing this process are

$$\begin{aligned} \begin{bmatrix} \mathbf{M}_{CT} & \mathbf{0} \\ \mathbf{0} & -\mathbf{M}_T \end{bmatrix} \begin{Bmatrix} \ddot{\mathbf{u}}_{CT} \\ \ddot{\mathbf{u}}_T \end{Bmatrix} + \begin{bmatrix} \mathbf{C}_{CT} & \mathbf{0} \\ \mathbf{0} & \mathbf{0} \end{bmatrix} \begin{Bmatrix} \dot{\mathbf{u}}_{CT} \\ \dot{\mathbf{u}}_T \end{Bmatrix} + \begin{bmatrix} \mathbf{K}_{CT} & \mathbf{0} \\ \mathbf{0} & \mathbf{0} \end{bmatrix} \begin{Bmatrix} \mathbf{u}_{CT} \\ \mathbf{u}_T \end{Bmatrix} \\ = \begin{Bmatrix} \mathbf{f}_{CT} \\ \mathbf{0} \end{Bmatrix} + \begin{Bmatrix} \mathbf{g}_{CT} \\ \mathbf{g}_T \end{Bmatrix} \end{aligned} \quad (4.1)$$

where \mathbf{u} is the 3-D response vector containing both translations and rotations at each element node; \mathbf{M} , \mathbf{C} , and \mathbf{K} are the mass, damping, and stiffness matrices of the corresponding substructure; \mathbf{f} is the external force vector and \mathbf{g} is the vector of connecting forces between substructures. The subscripts CT and T refer to quantities associated with the test structure CT and transducer T , respectively. The above equations are also subject to compatibility and equilibrium constraints at the transducer connection point where the motion between the transducer and the system are equal and the reaction forces are equal and opposite. These constraints are

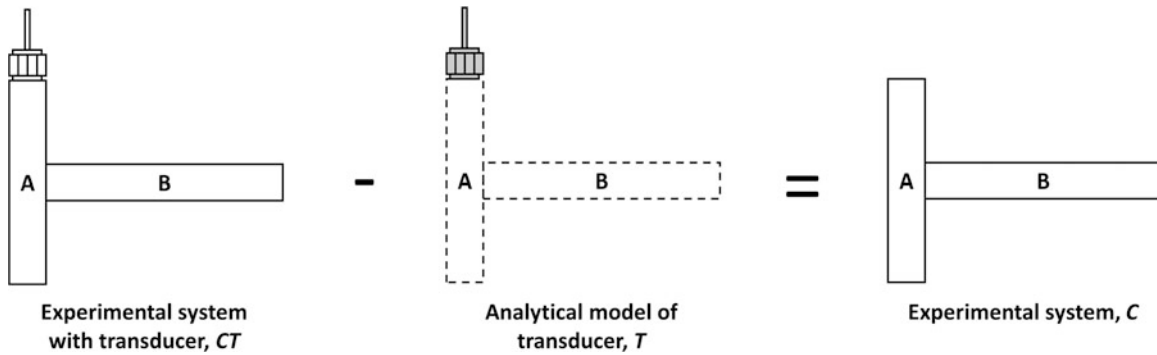


Fig. 4.1 Example of transducer removal from the experimental system

$$\mathbf{B} \begin{Bmatrix} \mathbf{u}_{CT} \\ \mathbf{u}_T \end{Bmatrix} = 0 \quad (4.2)$$

$$\mathbf{L}^T \begin{Bmatrix} \mathbf{g}_{CT} \\ \mathbf{g}_T \end{Bmatrix} = 0 \quad (4.3)$$

where \mathbf{B} is the matrix enforcing the compatibility constraint and \mathbf{L} is the matrix enforcing the force equilibrium constraint. The force transducer can be idealized with a simple geometry allowing for an analytical calculation of the mass matrix \mathbf{M}_T ; however, the spatial model for CT is unknown. Instead, a modal model for CT is derived from a modal test. This requires transforming the above equations of motion into the modal coordinate system using the modal frequencies and mass-normalized mode shapes ($\omega_{CT,r}$ and $\phi_{CT,r}$) for the total number of modes R_{CT} retained for the test structure, as well as the mass-normalized transducer rigid body modes ($\omega_{T,r} = 0$ and ϕ_T) for the total number of modes R_T included in the transducer model. In the general case of 3-D motion, there will be six transducer rigid body modes corresponding to three translations and three rotations. The transformation to the modal coordinate system is

$$\begin{Bmatrix} \mathbf{u}_{CT} \\ \mathbf{u}_T \end{Bmatrix} = \begin{bmatrix} \Phi_{CT} & \mathbf{0} \\ \mathbf{0} & \Phi_T \end{bmatrix} \begin{Bmatrix} \mathbf{q}_{CT} \\ \mathbf{q}_T \end{Bmatrix} \quad (4.4)$$

with the associated modal equations of motion

$$\begin{aligned} & \begin{bmatrix} \mathbf{I}_{CT} & \mathbf{0} \\ \mathbf{0} & -\mathbf{I}_T \end{bmatrix} \begin{Bmatrix} \ddot{\mathbf{q}}_{CT} \\ \ddot{\mathbf{q}}_T \end{Bmatrix} + \begin{bmatrix} [2\zeta_r \omega_r]_{CT} & \mathbf{0} \\ \mathbf{0} & \mathbf{0} \end{bmatrix} \begin{Bmatrix} \dot{\mathbf{q}}_{CT} \\ \dot{\mathbf{q}}_T \end{Bmatrix} + \begin{bmatrix} [\omega_r^2]_{CT} & \mathbf{0} \\ \mathbf{0} & \mathbf{0} \end{bmatrix} \begin{Bmatrix} \mathbf{q}_{CT} \\ \mathbf{q}_T \end{Bmatrix} \\ &= \begin{Bmatrix} \Phi_{CT}^T \mathbf{f}_{CT} \\ \mathbf{0} \end{Bmatrix} + \begin{bmatrix} \Phi_{CT}^T & \mathbf{0} \\ \mathbf{0} & \Phi_T^T \end{bmatrix} \begin{Bmatrix} \mathbf{g}_{CT} \\ \mathbf{g}_T \end{Bmatrix} \end{aligned} \quad (4.5)$$

The corresponding modal constraint equations are then

$$\mathbf{B} \begin{bmatrix} \Phi_{CT} & \mathbf{0} \\ \mathbf{0} & \Phi_T \end{bmatrix} \begin{Bmatrix} \mathbf{q}_{CT} \\ \mathbf{q}_T \end{Bmatrix} = \mathbf{B}_p \begin{Bmatrix} \mathbf{q}_{CT} \\ \mathbf{q}_T \end{Bmatrix} = 0 \quad (4.6)$$

$$\mathbf{L}_p^T \begin{bmatrix} \Phi_{CT}^T & \mathbf{0} \\ \mathbf{0} & \Phi_T^T \end{bmatrix} \begin{Bmatrix} \mathbf{g}_{CT} \\ \mathbf{g}_T \end{Bmatrix} = \mathbf{L}_p^T \begin{Bmatrix} \mathbf{g}_{p,CT} \\ \mathbf{g}_{p,T} \end{Bmatrix} = 0 \quad (4.7)$$

where the p subscripts denote modal quantities. Enforcing the modal compatibility constraint of Eq. 4.6 requires knowledge of the mode shapes of system CT , including rotational degrees of freedom, at the transducer connection point (i.e., $\Phi_{CT,T}$ must be fully known); such knowledge may not be available in a typical modal test. Instead, enforcing these modal constraints between the experimental system and the analytical transducer model requires a separate approach. The approach proposed here assumes that a simple analytical model AT can adequately describe the motion of a local section of the experimental system containing the force transducer attachment (e.g., the vertical beam in Fig. 4.1). By measuring translations on this local system, the analytical model then generates information regarding motion at the transducer connection point. This process begins by first constraining the measurement points, denoted with the m subscript, between AT and CT such that

$$\mathbf{u}_{AT,m} = \mathbf{u}_{CT,m} \quad (4.8)$$

or in the modal coordinate system

$$\Phi_{AT,m} \mathbf{q}_{AT} = \Phi_{CT,m} \mathbf{q}_{CT} \quad (4.9)$$

Taking the pseudo-inverse (denoted with the \dagger superscript) of the analytical mode shape matrix at the measurement points produces a least-squares fit for the modal motion of AT in terms of the modal response of CT

$$\mathbf{q}_{AT} = \Phi_{AT,m}^\dagger \Phi_{CT,m} \mathbf{q}_{CT} \quad (4.10)$$

The application of the pseudo-inverse requires at least as many measurements on AT as there are modes included in the model (i.e., $m > R_{AT}$). This process is the basis of the modal constraints for fixture and subsystem (*MCFS*) substructure constraint approach [10, 11]; however, rather than using these modal constraints to remove AT from system CT , the analytical mode shapes of AT allow for an expansion of the modal response to estimate the motion at the transducer connection point

$$\mathbf{u}_{AT,T} = \Phi_{AT,T} \mathbf{q}_{AT} \quad (4.11)$$

Substituting \mathbf{q}_{AT} from Eq. 4.10 into the above equation leads to

$$\mathbf{u}_{AT,T} = \underbrace{\left[\Phi_{AT,T} \Phi_{AT,m}^{\dagger} \Phi_{CT,m} \right]}_{\hat{\Phi}_{CT,T}} \mathbf{q}_{CT} = \hat{\mathbf{u}}_{CT,T} \quad (4.12)$$

The bracketed terms are the estimated CT mode shapes that correspond to the transducer connection point degrees of freedom $\hat{\Phi}_{CT,T}$ and are generated using a combination of the CT measured mode shapes and the AT analytical mode shapes. Essentially, this process can then be thought of as first applying a modal filter to obtain the modal response of system AT from the translation measurements on system CT , followed by a model expansion to obtain the motion (translations and rotations) at the transducer connection point. This process allows for the motion of the force transducer to be constrained to system AT at the transducer connection point

$$\mathbf{u}_{AT,T} = \mathbf{u}_T \quad (4.13)$$

or rewritten in terms of the modal response of T

$$\mathbf{u}_{AT,T} = \Phi_T \mathbf{q}_T \quad (4.14)$$

Inserting the above equation into Eq. 4.12 and rearranging leads to an equation constraining the transducer modal response with that of the measured system

$$\hat{\Phi}_{CT,T} \mathbf{q}_{CT} - \Phi_T \mathbf{q}_T = \mathbf{0} \quad (4.15)$$

The constraints can be written in terms of the modal constraint matrix \mathbf{B}_p such that

$$\underbrace{\begin{bmatrix} \hat{\Phi}_{CT,T} & -\Phi_T \end{bmatrix}}_{\mathbf{B}_p} \begin{Bmatrix} \mathbf{q}_{CT} \\ \mathbf{q}_T \end{Bmatrix} = \mathbf{0} \quad (4.16)$$

where \mathbf{B}_p enforces as many constraints as the number of rigid body modes included in the transducer model. Comparing \mathbf{B}_p from the above equation with that presented in Eq. 4.6 shows that the above method constrains the estimated DOFs on CT with the force transducer DOFs at the connection point. Furthermore, from Eq. 4.5, there are $R_{CT} + R_T$ equations and, using all the rigid body modes of the transducer, there are R_T constraints, thus requiring a transformation to an unconstrained set of modes. Choosing this set simply as the modes of CT , the transformation is

$$\begin{Bmatrix} \mathbf{q}_{CT} \\ \mathbf{q}_T \end{Bmatrix} = \underbrace{\begin{bmatrix} \mathbf{I}_{CT} \\ \Phi_T^{-1} \hat{\Phi}_{CT,T} \end{bmatrix}}_{\mathbf{L}_p} \mathbf{q}_{CT} \quad (4.17)$$

where \mathbf{L}_p is the transformation matrix that is in the null space of \mathbf{B}_p , thus always satisfying the constraints of Eq. 4.16. Inserting \mathbf{L}_p back into Eq. 4.7 results in

$$\Phi_{CT}^T \mathbf{g}_{CT} + \hat{\Phi}_{CT,T}^T \mathbf{g}_T = \mathbf{0} \quad (4.18)$$

If the interface mode shape estimates are perfect, this results in the complete cancellation of the interface forces and the transducer effects are fully removed in the corrected system. In general, there will be some errors in the mode shape estimates resulting in a residual force acting on the corrected system, thus resulting in slight errors remaining in the corrected response. Inserting the transformation of Eq. 4.17 into Eq. 4.5 and premultiplying by \mathbf{L}_p^T results in the unconstrained equations

$$\tilde{\mathbf{M}}\ddot{\mathbf{q}}_{CT} + \tilde{\mathbf{C}}\dot{\mathbf{q}}_{CT} + \tilde{\mathbf{K}}\mathbf{q}_{CT} = \tilde{\mathbf{f}} + \tilde{\mathbf{g}} \quad (4.19)$$

where

$$\tilde{\mathbf{M}} = \mathbf{L}_p^T \begin{bmatrix} \mathbf{I}_C & \mathbf{0} \\ \mathbf{0} & -\mathbf{I}_T \end{bmatrix} \mathbf{L}_p = \mathbf{I}_{CT} - \hat{\Phi}_{CT,T}^T [\Phi_T \Phi_T^T]^{-1} \hat{\Phi}_{CT,T} \quad (4.20)$$

$$\tilde{\mathbf{C}} = \mathbf{L}_p^T \begin{bmatrix} [2\xi_r \omega_r]_{CT} & \mathbf{0} \\ \mathbf{0} & \mathbf{0} \end{bmatrix} \mathbf{L}_p = [2\xi_r \omega_r]_{CT} \quad (4.21)$$

$$\tilde{\mathbf{K}} = \mathbf{L}_p^T \begin{bmatrix} [\omega_r^2]_{CT} & \mathbf{0} \\ \mathbf{0} & \mathbf{0} \end{bmatrix} \mathbf{L}_p = [\omega_r^2]_{CT} \quad (4.22)$$

$$\tilde{\mathbf{f}} = \mathbf{L}_p^T \left\{ \begin{array}{c} \Phi_{CT}^T \mathbf{f}_{CT} \\ \mathbf{0} \end{array} \right\} = \Phi_{CT}^T \mathbf{f}_{CT} \quad (4.23)$$

$$\tilde{\mathbf{g}} = \mathbf{L}_p^T \begin{bmatrix} \Phi_{CT}^T & \mathbf{0} \\ \mathbf{0} & \Phi_T^T \end{bmatrix} \left\{ \begin{array}{c} \mathbf{g}_{CT} \\ \mathbf{g}_T \end{array} \right\} = \mathbf{0} \quad (4.24)$$

The updated modal damping matrix $\tilde{\mathbf{C}}$, stiffness matrix $\tilde{\mathbf{K}}$, and modal force vector $\tilde{\mathbf{f}}$ remain unchanged from the initial measured system; however, the modal mass matrix $\tilde{\mathbf{M}}$ is reduced by an amount that corresponds to the removal of the force transducer. Expanding this mass matrix further results in

$$\tilde{\mathbf{M}} = \mathbf{I}_{CT} - \Phi_{CT,m}^T \left[(\Phi_{AT,T} \Phi_{AT,m}^\dagger)^T (\Phi_T \Phi_T^T)^{-1} \Phi_{AT,T} \Phi_{AT,m}^\dagger \right] \Phi_{CT,m} \quad (4.25)$$

The bracketed term in the above equation is pre- and post-multiplied by $\Phi_{CT,m}^T$ and $\Phi_{CT,m}$, indicating mass is removed from the measurement locations on CT . Essentially, the above process utilizes the analytical modes of AT and T to eliminate the requirement for directly measuring mode shapes corresponding to the rotation degrees of freedom at the transducer connection point. The force transducer mass and moment of inertia are then distributed as an equivalent mass at the translation measurement locations, thus allowing for immediate removal from the system. Finally, the eigensolution of Eq. 4.19 recovers the corrected modal frequencies ω_C of the system without the transducer. Using the mode shape $\tilde{\Phi}$ associated with the eigensolution of Eq. 4.19 and the original measured mode shape recovers the corrected mode shape such that

$$\Phi_C = \Phi_{CT} \tilde{\Phi} \quad (4.26)$$

4.2.2 Transducer Model

The current approach utilizes the mass-normalized rigid body modes of the force transducer and requires a model that accurately describes the rigid body dynamics. This analysis assumes the transducer behaves as a general rigid body connected to a single point on the surface of the structure with the transducer center of mass offset a distance $r_T = (x_T, y_T, z_T)$. The physical DOF mass matrix of a general rigid body with respect to the connection point on the surface of the structure is

$$\mathbf{M}_T = \begin{bmatrix} m_T & 0 & 0 & 0 & m_T z_T & -m_T y_T \\ 0 & m_T & 0 & -m_T z_T & 0 & m_T x_T \\ 0 & 0 & m_T & m_T y_T & -m_T x_T & 0 \\ 0 & -m_T z_T & m_T y_T & I_{xx} & -I_{xy} & -I_{xz} \\ m_T z_T & 0 & -m_T x_T & -I_{xy} & I_{yy} & -I_{yz} \\ -m_T y_T & m_T x_T & 0 & -I_{xz} & -I_{yz} & I_{zz} \end{bmatrix} \quad (4.27)$$

where m_T is the mass of the force transducer, I_{xx} , I_{yy} , and I_{zz} are the moments of inertia, and I_{xy} , I_{yz} , I_{xz} are the products of inertia about the coordinate system located at the connection point on the structure surface. Also note that only half of the transducer mass contributes to the force measurement as the terminal is located approximately halfway along the transducer thickness. In the above mass matrix, only half of the transducer mass needs to be included in the direction in-line with the applied force; for the perpendicular directions, the total mass of the transducer should be used. Furthermore, the geometry of the transducer used in the proceeding sections is idealized as a solid uniform cylinder allowing analytical calculations of the inertia terms. The transducer mass-normalized rigid body modes can then be determined.

4.3 Numerical Simulations

4.3.1 System of Interest

To test the proposed approach, the T-beam system shown in Fig. 4.2 was utilized with the corresponding parameters recorded in Table 4.1. This analysis assumes the out-of-plane motion is negligible, thus reducing the system to 2-D that results in the transducer mass matrix

$$\mathbf{M}_T = \begin{bmatrix} m_T & 0 & -m_T y_T \\ 0 & m_T/2 & 0 \\ -m_T y_T & 0 & I_{zz} \end{bmatrix} \quad (4.28)$$

Note here the inclusion of only half of the transducer mass in the direction of the applied force for reasons previously discussed.

4.3.2 Results

The numerical analysis utilized a FE model for the system with 2-D beam elements where beams A and B contained 20 and 40 elements, respectively. Obtaining an adequate estimate of the mode shapes at the transducer connection point ($\hat{\Phi}_{CT,T}$ in Eq. 4.12) requires a sufficient number of modes of the analytical beam AT to capture the modal motion of the local section of system CT that contains the transducer. Figure 4.3 shows the first 10 mode shapes (3 rigid body modes and 7 elastic modes)

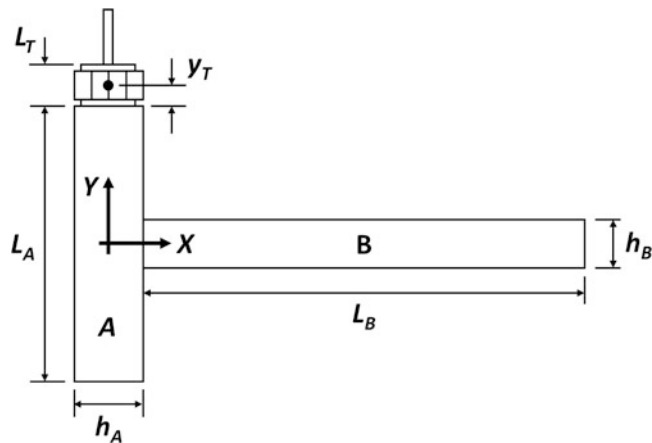


Fig. 4.2 System of interest with attached transducer

Table 4.1 T-beam system parameters

Beam A		Beam B		Transducer T	
Material		Material		Mass	Inertia
$L_A \times w_A \times h_A$	$4.5 \times 1 \times 1 \text{ in}^3$	$L_B \times w_B \times h_B$	$12 \times 1 \times 0.75 \text{ in}^3$	0.05 lb	0.0065 lb in ²

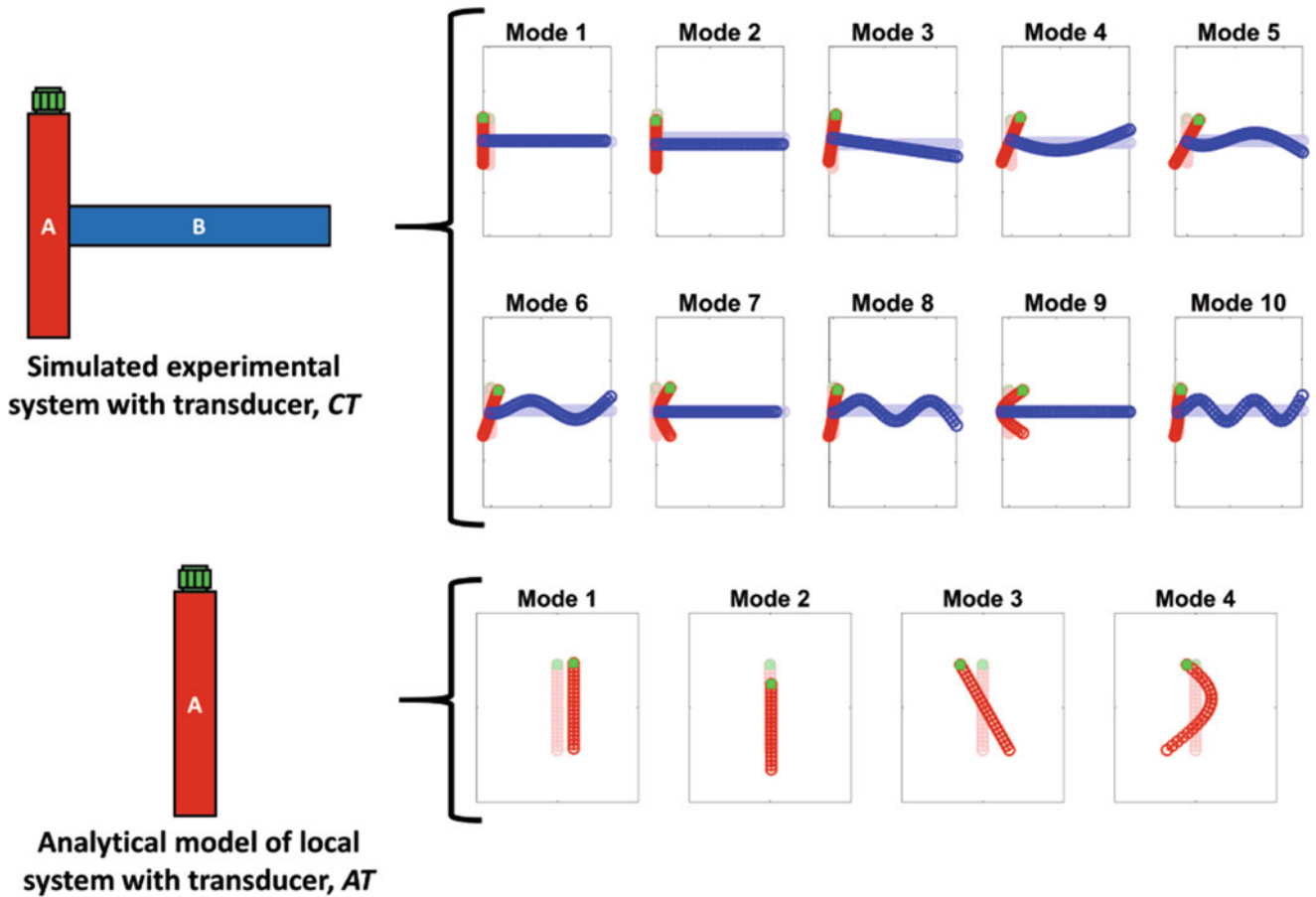


Fig. 4.3 Mode shapes generated from the FE model for the (top) simulated experimental system with the attached transducer and the (bottom) analytical model of the local section of the system that contains the transducer

of CT and the first 4 mode shapes (3 rigid body modes and 1 elastic mode) of AT . The vertical beam A in the CT mode shapes shows mostly rigid body motion for each mode, as well as first beam bending motion present in CT modes 7 and 9. Therefore, the first 4 modes of AT were chosen to form a sufficient modal basis to capture this motion.

To simulate an experimental test, in-plane translation measurements were recorded at 3 locations along AT , two at the beam tips and one at the beam center. Figure 4.4 shows an example of the process used to estimate the mode shapes at the transducer connection point for mode 7 of CT . The translations measured by the accelerometers (shown as blue squares) generate the mode shapes $\Phi_{CT,m}$ measured on the vertical section of the test structure. Similar to Eq. 4.12, using the full set of analytical mode shapes of AT leads to estimates of the mode shapes of the entire vertical section

$$\hat{\Phi}_{CT} = \Phi_{AT} \Phi_{AT,m}^\dagger \Phi_{CT,m} \quad (4.29)$$

Figure 4.4 also shows the estimated mode shape (red curve) for mode 7 of CT . This estimated shape includes both translation and rotation information at every point along the vertical beam, including the transducer connection point, thus allowing for the removal of the transducer mass and moment of inertia from each mode included in the system.

The transducer was then removed from the simulated experimental system CT using the process described in the previous section. The simulated experiment assumed all the modes of CT under 10 kHz are “measured” exactly with the first 10 modes falling within this frequency band. The first 4 modes of AT were then used in the transducer removal procedure. A FE model of the system without the transducer was used as the truth baseline and the corresponding modal frequencies are compared to the system with the attached transducer, both before and after the correction procedure, and recorded in Table 4.2. As expected, the presence of the force transducer drives down the modal frequencies with a maximum error of 5.36% for the 9th mode. After correcting for the transducer, the frequencies more accurately reflect the truth case with the maximum error reduced to just 0.56%.

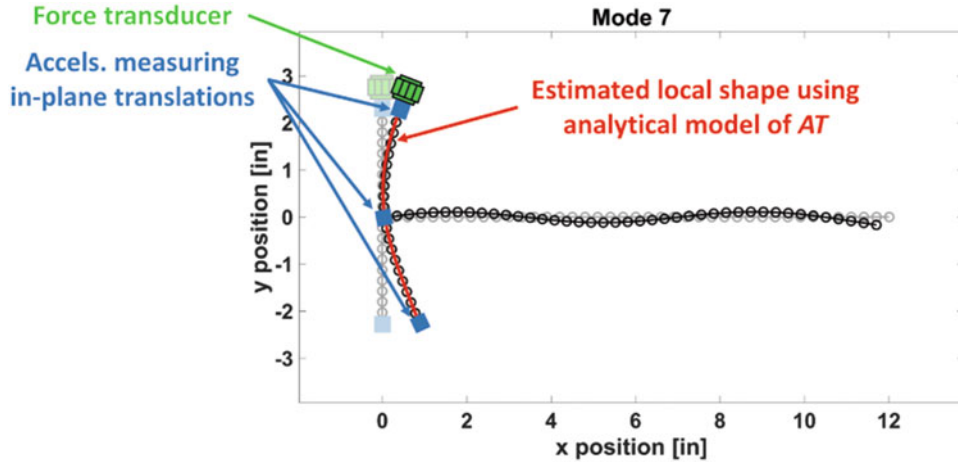


Fig. 4.4 Example of the estimated mode shape (red) for mode 7 of CT. This shape was obtained using x-, y-translation measurements at three locations (blue squares) on the local section of the CT containing the force transducer

Table 4.2 Modal frequency comparison between the baseline case without the attached transducer and the cases with the attached transducer, both uncorrected and corrected

Flexible mode #	f_n actual: FEM [Hz]	f_n with transducer: uncorrected [Hz]	% Error	f_n with transducer: corrected [Hz]	% Error
1	723.17	708.42	-2.04	723.15	0.00
2	1723.7	1663.8	-3.48	1723.3	-0.03
3	3334.8	3290.1	-1.34	3333.6	-0.04
4	5340.7	5143.4	-3.69	5351.9	0.21
5	6033.2	6011.3	-0.36	6031.0	-0.04
6	9311.5	8812.5	-5.36	9363.3	0.56
7	9735.8	9723.5	-0.13	9731.4	-0.05

Analysis of the forced response also shows the effectiveness of the proposed approach. Figure 4.5a shows the drive-point FRF for each of the three cases with modal damping $\zeta = 0.1\%$ assigned for all modes. For the uncorrected system, the first three resonances and anti-resonances show clear shifts to lower frequencies. For the corrected case, the resonance peaks show excellent agreement to the truth case for all modes, although the anti-resonance locations begin to deviate after 7 kHz. As a general rule of thumb for modal substructuring, modal information should be included for 1.5–2 times the frequency band of interest for the final assembly [10]. As modal information up to 10 kHz was included in this analysis, one would expect accurate results up to 5–6.7 kHz, which is indeed the case. Figure 4.5b shows the complex mode indicator function (CMIF) for this single forcing configuration. Again, the uncorrected system shows clear downward shifts for the resonance frequencies. Interestingly, two spurious peaks are also present and correspond to the axial modes of the system. The presence of these peaks indicates the presence of the transducer breaks the symmetry of the structure, leading to an appreciable effect on the axial modes shapes that allows a transverse load to excite these modes. The corrected system again shows excellent agreement for all modes in the frequency band. The two spurious peaks were reduced in magnitude, though not fully eliminated. Although not shown here, increasing both the number of modes in the analytical model AT and measurement points showed further reductions for these peaks.

4.4 Experimental Results

Two separate modal tests were then performed to provide further validation for the proposed approach. Figure 4.6a shows the first test configuration, a hammer test that serves as the truth baseline without the attached transducer assembly. Figure 4.6b shows the second test configuration, a shaker test with the attached force transducer assembly. Excitation was provided up to 2.5 kHz to excite the first two in-plane bending modes. The response was measured with nine triaxial accelerometers mounted on the structure, including five on the horizontal beam with the attached transducer.

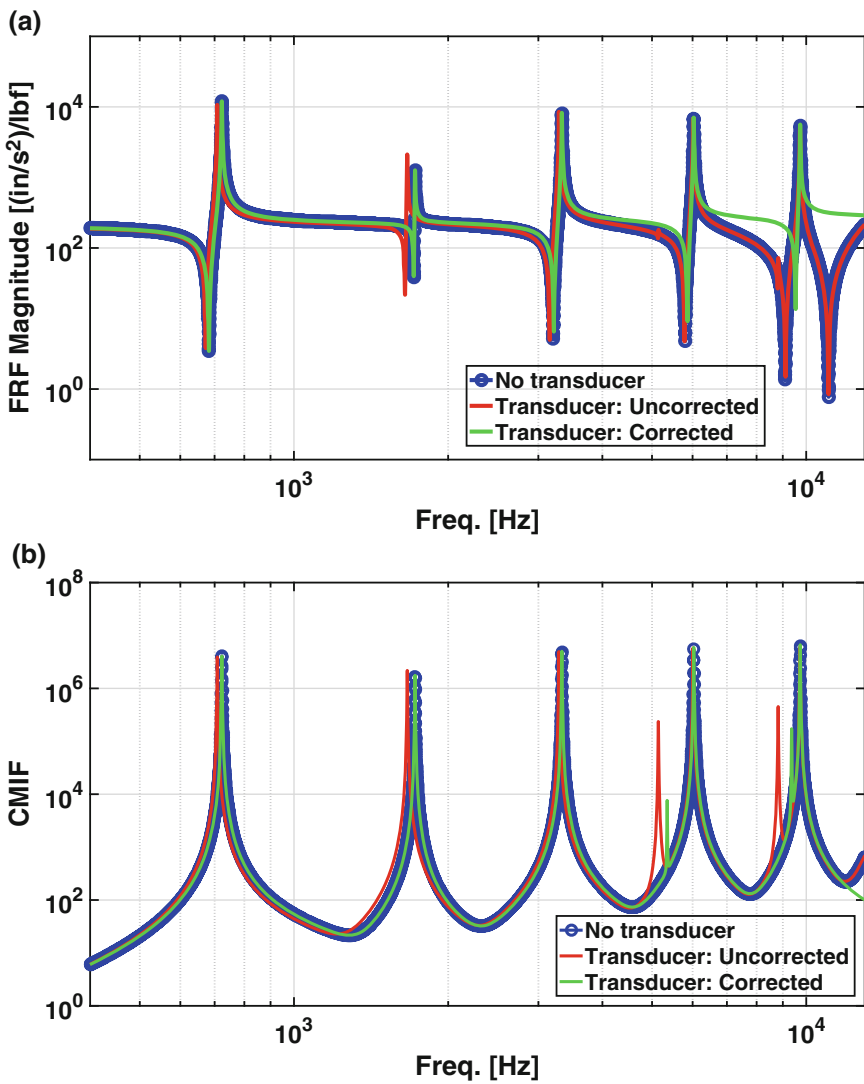


Fig. 4.5 Frequency response for the truth baseline with no transducer (blue circles) and the system with the transducer, both uncorrected (red) and corrected using the proposed approach (green). **(a)** Drive-point FRF. **(b)** Complex mode indicator function

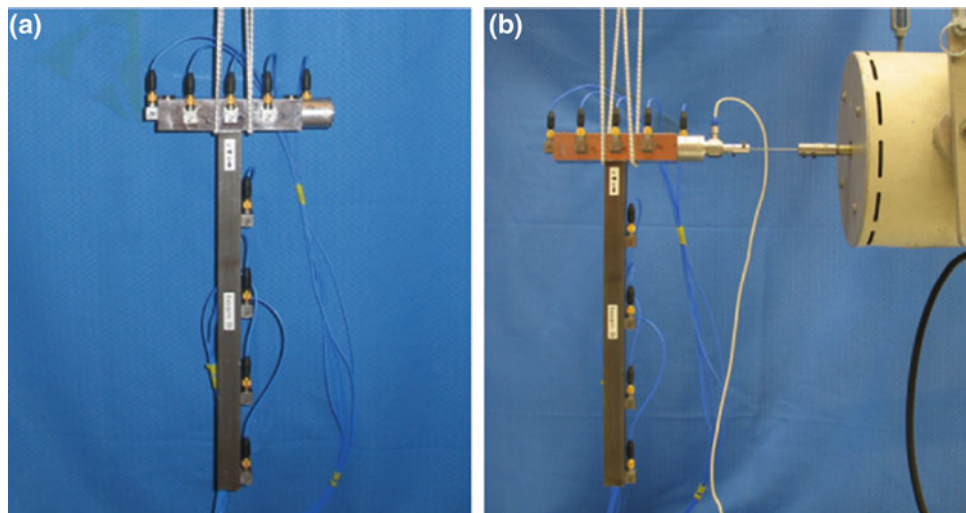


Fig. 4.6 Modal test configurations used to provide experimental validation **(a)** Hammer test setup used as the truth baseline without the attached force transducer assembly **(b)** Shaker test setup used to apply the transducer correction procedure

Table 4.3 Modal frequency comparison between the baseline case without the attached transducer and the cases with the attached transducer, both uncorrected and corrected

Mode #	Hammer: f_n truth [Hz]	Shaker: f_n uncorrected [Hz]	% Error	Shaker: f_n corrected [Hz]	% Error
1	625.8	598.0	-4.44	634.6	1.41
2	1449	1344	-7.81	1442	-0.48

The force transducer assembly consisted of not only the force transducer, but also a stinger adapter that also has a mass and moment of inertia, idealized here as a solid cylinder, requiring removal from the system. A drive-cap was placed over an accelerometer used for drive-point measurements that introduces an offset of the transducer assembly from the test structure. This offset increases the moment of inertia of the transducer assembly about the connection point and is accounted for during the correction procedure. Similar to the numerical simulations, the first 4 modes of the FE model shown in Fig. 4.3 were used for the horizontal beam to estimate the connection point mode shapes. Furthermore, the correction procedure utilized only three of the accelerometers located on the horizontal beam, the two located at the beam tips and the one located at the center of the beam closest to the vertical beam connection.

Table 4.3 shows a comparison of the modal frequencies. For the uncorrected shaker test, the first two modal frequencies showed downward shifts with errors of -4.44% and -7.81% for modes 1 and 2, respectively. After application of the correction procedure, the modal frequencies shifted upwards towards their true values with reduced errors of 1.41% and -0.48%.

The forced response was also analyzed for each of the cases. Figure 4.7a shows the drive-point FRFs where the uncorrected shaker response clearly shows the downward shifts for both the resonance and anti-resonance frequencies, as well as deviations in the peak response magnitudes. The corrected response shows drastic improvements for both the resonance and anti-resonance frequencies, as well as the peak magnitudes, though some deviations still exist. Figure 4.7b shows the CMIF where both the measured and synthesized singular values are shown for the hammer and uncorrected shaker tests. An out-of-plane bending mode can also be seen near 960 Hz, though was not synthesized in the modal parameter extraction process. The CMIF for the corrected shaker test shows excellent agreement with the hammer test, though again with some deviations in resonance frequency and the corresponding magnitude of the singular values. These deviations can most likely be attributed to the modeling of the force transducer assembly where both the force transducer, and the stinger adapter, were idealized as uniform cylinders; the associated cables and connector can also introduce mass and inertia that may not be negligible. Furthermore, it may be difficult to model completely the force transducer assembly and the response from a hammer test may not be available to compare the corrected shaker response. For such a case, one approach may be to develop a system with a simple geometry, such as the T-beam system used in this work, for the purpose of tuning the mass matrix of the force transducer assembly so that the corrected response from a shaker test matches more accurately the hammer test response. Such a calibration procedure will then garner more confidence when applying the correction for the same transducer assembly used on more complicated test structures.

4.5 Conclusions and Future Work

The objective of this paper was to correct for the force transducer mass and moment of inertia effects during shaker tests. Utilizing concepts in experimental modal substructuring, this method relies on constraining the translation measurements on a local section of the test structure containing the transducer to an analytical model of this same section. Such constraints then enabled an estimation of the mode shapes for all degrees of freedom, including translations and rotations, at the transducer connection point. Knowledge of these connection point mode shapes allowed for the immediate removal of an analytical rigid body modal model of the transducer from the system, thus correcting the system dynamics. In the modal equations of motion, the removal of transducer mass and moment of inertia at the connection point manifests itself as the removal of an equivalent mass distributed across the measurement locations. Both numerical and experimental analysis on a T-Beam structure showed the feasibility of the proposed approach in correcting for both the modal frequency estimates, as well as the forced response.

Although the scope of the paper focused on the removal of the force transducer, the proposed approach may also be extended to remove the effects of other attached transducers, such as accelerometers, if necessary. If an analytical model for the entire test structure is known, e.g., when performing a modal test for model correlation, the proposed approach can enable

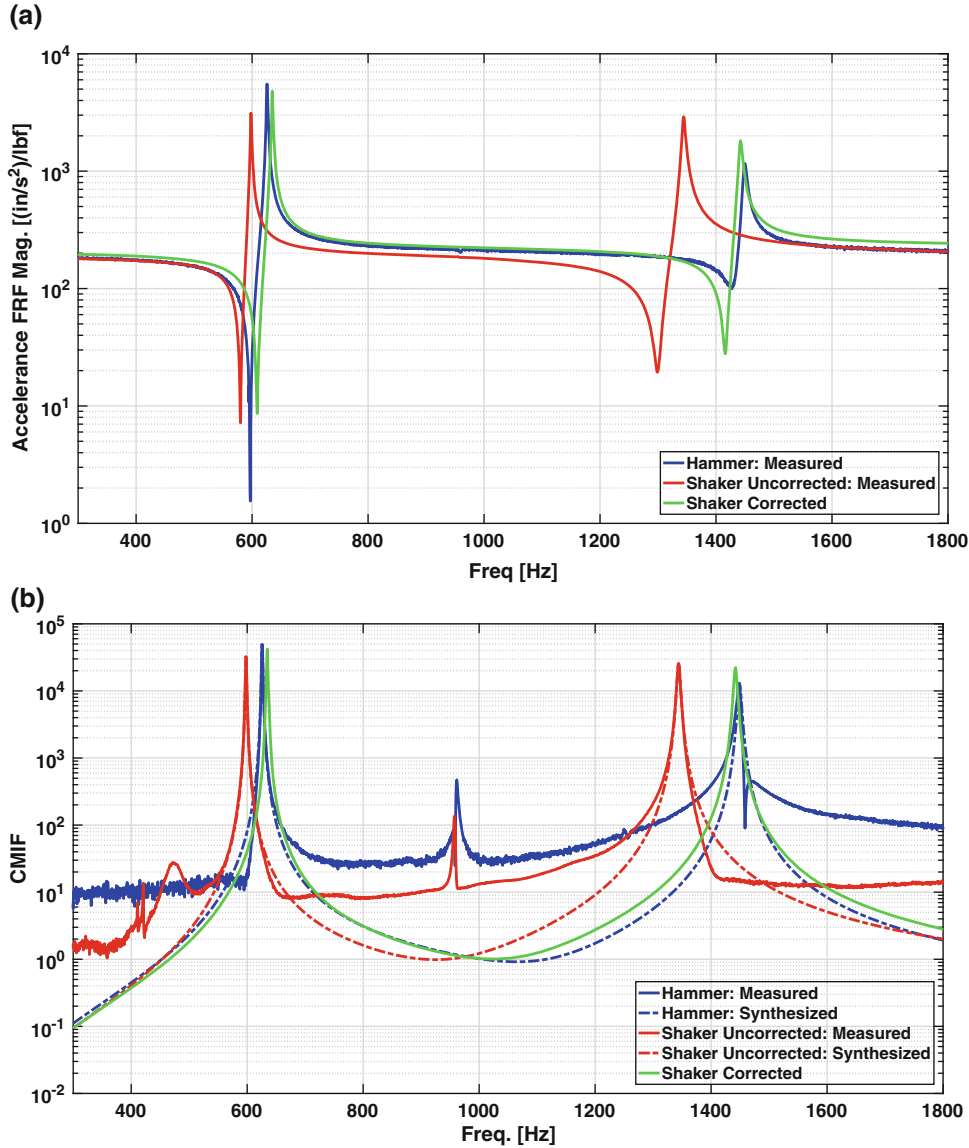


Fig. 4.7 Frequency response for the two test configurations: the hammer test (blue) used as the truth baseline, and the shaker test with the attached force transducer assembly, both uncorrected (red) and corrected using the proposed approach (green). **(a)** Experimental drive-point FRF. **(b)** Experimental CMIF with the measured (solid) and synthesized (dashed) values shown

full mode shape estimations at each transducer connection point allowing for the removal of all transducers simultaneously. Furthermore, it is imperative the analytical model of the local section forms a sufficient modal basis for estimating the transducer connection point mode shapes. The proposed approach does not rely on knowledge of the frequencies of the analytical model, so if an accurate model does not exist and is unable to be developed, one method to bypass this issue may be to estimate the mode shapes by curve-fitting polynomials through the measurement locations.

Acknowledgements Notice: This manuscript has been authored by National Technology and Engineering Solutions of Sandia, LLC, under Contract No. DE-NA0003525 with the U.S. Department of Energy/National Nuclear Security Administration. The United States Government retains and the publisher, by accepting the article for publication, acknowledges that the United States Government retains a non-exclusive, paid-up, irrevocable, world-wide license to publish or reproduce the published form of this manuscript, or allow others to do so, for United States Government purposes.

References

1. Ewins, D.J.: Modal Testing: Theory, Practice, and Application. Research Studies Press, Baldock (2000)
2. Decker, J., Witfeld, H.: Correction of transducer-loading effects in experimental modal analysis. In: Proceedings of the 13th International Modal Analysis Conference (1995)
3. Silva, J.M.M., Maia, N.M.M., Ribeiro, A.M.R.: Some applications of coupling/uncoupling techniques in structural dynamics – part 1: Solving the mass cancellation problem. In: Proceedings of the 15th International Modal Analysis Conference, Orlando (1997)
4. Ashory, M.: Correction of mass-loading effects of transducers and suspension effects in modal testing. In: Proceedings of the 16th International Modal Analysis Conference, Santa Barbara (1998)
5. Silva, J.M.M., Maia, N.M.M., Ribeiro, A.M.R.: Cancellation of mass-loading effects of transducers and evaluation of unmeasured frequency response functions. *J. Sound Vib.* **236**(5), 761–779 (2000)
6. Cakar, O., Sanliturk, K.: Elimination of transducer mass loading effects from frequency response functions. *Mech. Syst. Signal Process.* **19**(1), 87–104 (2005)
7. Bi, S., Ren, J., Wang, W., Zong, G.: Elimination of transducer mass loading effects in shaker modal testing. *Mech. Syst. Signal Process.* **38**(2), 265–275 (2013)
8. Zamani, P., Anbouhi, A.T., Ashory, M.R., Khatibi, M.M., Nejad, R.M.: Cancelation of transducer effects from frequency response functions: experimental case study on the steel plate. *Adv. Mech. Eng.* **8**(4), 1–12 (2016)
9. McConnell, K.G., Cappa, P.: Transducer inertia and stinger stiffness effects on FRF measurements. *Mech. Syst. Signal Process.* **14**(4), 625–636 (2000)
10. Allen, M.S., Mayes, R.L.: Comparison of FRF and modal methods for combining experimental and analytical substructures. In Proceedings of the 25th International Modal Analysis Conference, Orlando (2007)
11. Allen, M.S., Mayes, R.L., Bergman, E.J.: Experimental modal substructuring to couple and uncouple substructures with flexible fixtures and multi-point connections. *J. Sound Vib.* **329**(23), 4891–4906 (2010)



Chapter 5

Efficient Estimation of Clamped Step-Thickness Plates FRFs in Industrial Systems

Yum Ji Chan, Chung-Yu Tai, and Yuan-You Li

Abstract Frequency response functions (FRFs) of thin workpieces, which are typically clamped step-thickness cantilever plates, are needed at every stage in order to avoid chatter (cutting-related instability). Due to variability of machining procedure, FRF estimation is proposed to be carried out at the embedded computer at machine tool, which has limited computing power. A combination of Reissner-Mindlin plate theory and Rayleigh-Ritz method are used to form small system matrices to estimate FRFs. Mode shapes of uniform-thickness Timoshenko beams are taken as the admissible functions. Example shows that a system with approximately 500 DOFs, which is much smaller than a full finite-element model with 10,000's of DOFs, can estimate the first four natural frequencies with a similar error level during every step of cut. Additionally, experimental natural frequencies are used to estimate the contact stiffness at the vice. As a result, the change in those natural frequencies during machining are determined accurately.

Keywords Cantilevered plate · Stepped-thickness plate · Mindlin plate · Rayleigh-Ritz method · Clamping stiffness

5.1 Introduction

Chatter instability [1] is an undesirable phenomenon in machining, and is the joint result of insufficient dynamic stiffness and periodic cutting force. While textbook cases of chatter instability are focused on the vibration of the tool, the cause of such instability can be traced to the workpiece if the workpiece stiffness is lower than that of the tool [2], especially in modern-day heavy cutting on thin-wall structures typically found in aerospace components. The likelihood of chatter instability can be estimated using frequency response functions (FRFs). However, the geometry of a thin-walled plate changes after each machining pass. The computational effort would be significant since FRFs have to be determined at each pass, and on top of that, machining parameters may undergo constant optimization and the vice clamping stiffness is unknown at the design stage. Therefore, much of the dynamic analysis has to be carried out at the machining centre, which has limited computational power and commercial software is unavailable.

This study aims at modelling the variation of natural frequencies of workpieces in the cutting processes using restricted computational resources. Although the plates encountered in aerospace part manufacturing are thin in a manufacturing context, these plates are classified as thick in mechanics due to their aspect ratio, and the Mindlin plate theory should be used. Due to computational efficiency, the Rayleigh-Ritz method [3] is preferred over the Finite element method [4]. It is noted that there were few studies dealing with Mindlin plates [5], while none of them involve cantilever-type boundary conditions. In the study, the clamp stiffness is determined using the model updating approach [6].

Y. J. Chan (✉) · Y.-Y. Li
Mechanical Engineering Department, National Chung Hsing University, Taichung, Taiwan
e-mail: yjchan@nchu.edu.tw

C.-Y. Tai
Intelligent Machinery Technology Center, Industrial Technology Research Institute (ITRI), Taichung, Taiwan
e-mail: Harkat_Tai@itri.org.tw

5.2 Methodology

A rectangular plate with length a , width b and initial thickness t is considered. The displacement of the middle plane of the plate and the rotations of the cross-section are described as z , θ_x and θ_y , respectively. By the use of non-dimensional coordinates $\xi = x/a$ and $\eta = y/b$, the maximum strain energy and maximum kinetic energy of the plate are given as [7]

$$U_{max} = \frac{1}{2} \frac{Db}{a^3} \int_0^1 \int_0^1 \left\{ \left(\frac{\partial \theta_x}{\partial \xi} + \lambda^2 \frac{\partial \theta_y}{\partial \eta} \right)^2 - 2(1-\nu) \lambda^2 \left[\frac{\partial \theta_x}{\partial \xi} \frac{\partial \theta_y}{\partial \eta} - \frac{1}{4} \left(\frac{\partial \theta_y}{\partial \xi} + \frac{\partial \theta_x}{\partial \eta} \right)^2 \right] \right. \\ \left. + \frac{\kappa G h}{D} a^2 \left[\left(\theta_x + \frac{\partial Z}{\partial \xi} \right)^2 + \lambda^2 \left(\theta_y + \frac{\partial Z}{\partial \eta} \right)^2 \right] \right\} d\xi d\eta \quad (5.1)$$

$$T_{max} = \frac{1}{2} \rho h \omega^2 ab \int_0^1 \int_0^1 \left[Z^2 + \frac{1}{12} \gamma^2 \left(\frac{\theta_x^2}{\lambda^2} + \theta_y^2 \right) \right] d\xi d\eta \quad (5.2)$$

where $D = Et^3/12(1-\nu^2)$, $\lambda = a/b$ and $\gamma = h/b$. Similar equations can be established for thick plates with thickness step at $a\alpha$. For example,

$$V_{max} = \frac{1}{2} \frac{D_1 b}{a^3} \int_0^\alpha \int_0^1 \left\{ \bar{U}_b + \frac{\kappa G h}{D_1} a^2 \left[\left(\theta_x + \frac{\partial Z}{\partial \xi} \right)^2 + \lambda^2 \left(\theta_y + \frac{\partial Z}{\partial \eta} \right)^2 \right] \right\} d\eta d\xi \\ + \frac{1}{2} \frac{D_2 b}{a^3} \int_\alpha^1 \int_0^1 \left\{ \bar{U}_b + \frac{\kappa G h}{D_2} a^2 \left[\left(\theta_x + \frac{\partial Z}{\partial \xi} \right)^2 + \lambda^2 \left(\theta_y + \frac{\partial Z}{\partial \eta} \right)^2 \right] \right\} d\eta d\xi \quad (5.3)$$

where $\bar{U}_b = \left(\frac{\partial \theta_x}{\partial \xi} + \lambda^2 \frac{\partial \theta_y}{\partial \eta} \right)^2 - 2(1-\nu) \lambda^2 \left[\frac{\partial \theta_x}{\partial \xi} \frac{\partial \theta_y}{\partial \eta} - \frac{1}{4} \left(\frac{\partial \theta_y}{\partial \xi} + \frac{\partial \theta_x}{\partial \eta} \right)^2 \right]$, $D_1 = \frac{Et_1^3}{12(1-\mu^2)}$ and $D_2 = \frac{Et_2^3}{12(1-\mu^2)}$.

In the Rayleigh-Ritz method, the displacement is assumed to be a weighted sum of assumed functions. In this study, separation of variables is assumed:

$$Z(\xi, \eta) = \sum_{i=1}^{\infty} \sum_{j=1}^{\infty} p_{ij} Z_{Mi}(\xi) Z_{Mj}(\eta), \quad \theta_x(\xi, \eta) = \sum_{i=1}^{\infty} \sum_{j=1}^{\infty} q_{ij} \theta_{Mi}(\xi) Z_{Mj}(\eta) \\ \theta_y(\xi, \eta) = \sum_{i=1}^{\infty} \sum_{j=1}^{\infty} r_{ij} Z_{Mi}(\xi) \theta_{Mj}(\eta) \quad (5.4)$$

Timoshenko beam shape functions from Ref. [8] are taken to construct admissible functions in each direction. Admissible functions for deflection and rotation of Timoshenko beams in terms of ξ are denoted Z_{Ti} and θ_{Ti} , respectively:

$$Z_{Ti}(\xi) = C_0^i + C_1^i \xi + C_2^i \frac{\xi^2}{2} + C_3^i \left(\frac{\xi^3}{6} - R\xi \right) + \left[R\xi(i\pi)^2 + 1 \right] \sin(i\pi\xi) \\ \theta_{Ti}(\xi) = C_1^i + C_2^i \xi + C_3^i \frac{\xi^2}{2} + (i\pi) \cos(i\pi\xi)$$

where $R = EI/GAk^2$. κ is known as the shear correction coefficient and is taken as 5/6 in this study. Also, C_j^i ($j = 0, 1, 2, 3$) depends on boundary conditions given in Table 5.1. For Free-Free boundary conditions, two admissible functions are added to represent rigid-body like motion:

$$z_{T1} = 1, \theta_{T1} = 0 \text{ and } z_{T2} = \xi - 0.5, \theta_{T2} = 1$$

After establishing the admissible functions, stiffness and mass matrices can be built according to the Rayleigh-Ritz method.

Table 5.1 Polynomial coefficients in the static Timoshenko beam functions

	C_0^i	C_1^i	C_2^i	C_3^i
C-F	0	$-i\pi$	$-(-1)^i(i\pi)^3$	$(-1)^i(i\pi)^3$
F-F	0	0	0	0

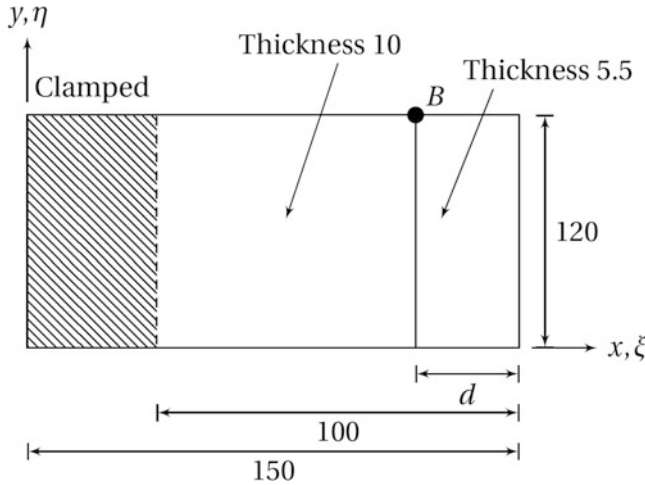


Fig. 5.1 Schematic of stepped-thickness cantilever plate under investigation

5.3 Results

5.3.1 Natural Frequency Estimation

The performance of the proposed method is demonstrated through comparing the natural frequency estimation error with that of the finite element model. Geometric parameters of the stepped-thickness plates in the study are shown in Fig. 5.1. An aluminium plate with an initial thickness of 10 mm is machined to 5.5 mm. The depth of each cutting pass is 20 mm, such that $d = \{20, 40, 60, 80\}$ mm. The point receptance at Point B (located at the thickness step) is sought first in ANSYS. The results shown in Fig. 5.2 show that the natural frequency fluctuates during machining. In other words, natural frequency of the plate in each stage of machining need to be modelled separately, in order to obtain accurate FRFs.

In the next step, a plate model is built using the Rayleigh-Ritz method. 14 admissible functions are used in the x direction and 12 are used in the y -direction, resulting in system matrices of about 500×500 . The natural frequencies obtained from ANSYS and the Rayleigh-Ritz method are compared with a set of converged results. From Fig. 5.3, it can be seen that the natural frequency error obtained from the Rayleigh-Ritz method are comparable with (and in many cases, lower than) those from the ANSYS results, although the number of degrees of freedom in the Rayleigh-Ritz method are 1/10 of those from ANSYS.

5.3.2 Clamping Stiffness Identification

Additional to simulations, experiments were carried out on a stepped-thickness plate (Fig. 5.4). The length (span) and width of the cantilever plate are 102.9 mm and 100 mm, respectively. The plate is clamped on a machine tool table using a hydraulic vise. It is found that the experimental natural frequencies are much lower than those obtained from the last section. It is speculated that the difference is attributed to non-ideal clamping conditions.

The restrained boundary conditions provided by the clamp is modelled using a spring bed. Model updating with the sensitivity method was carried out using the natural frequencies as the output parameter. Identification results show that the spring bed stiffness is quite stable, with an average of 3×10^{12} N/m³ (Fig. 5.5).

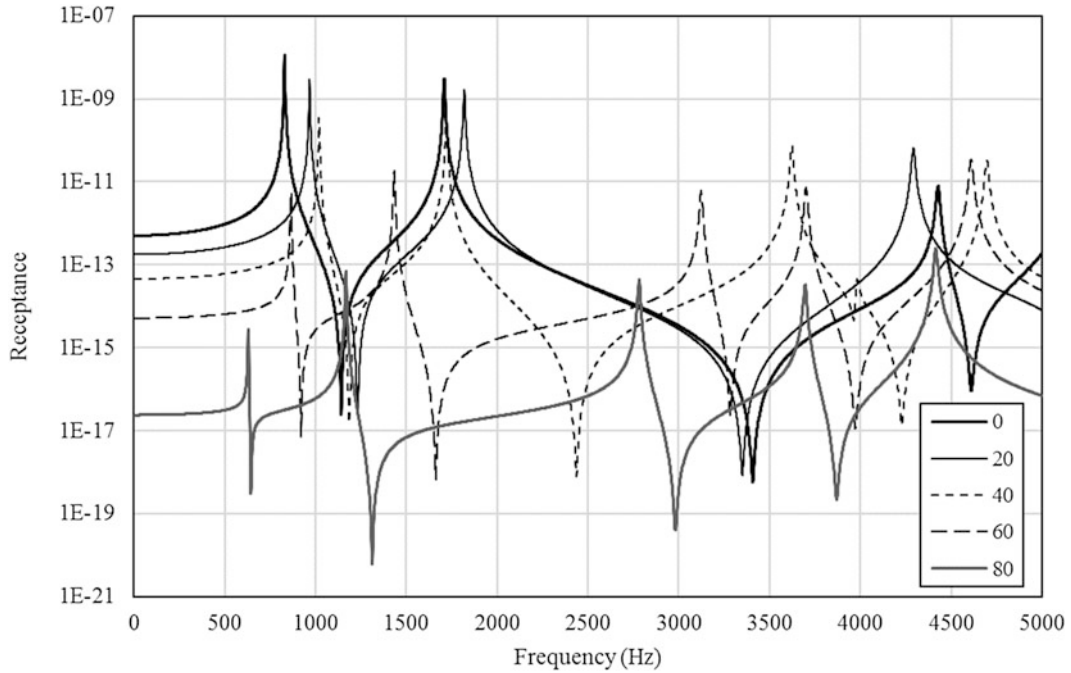


Fig. 5.2 Point receptance of cantilevered plate under various values of d (in mm)

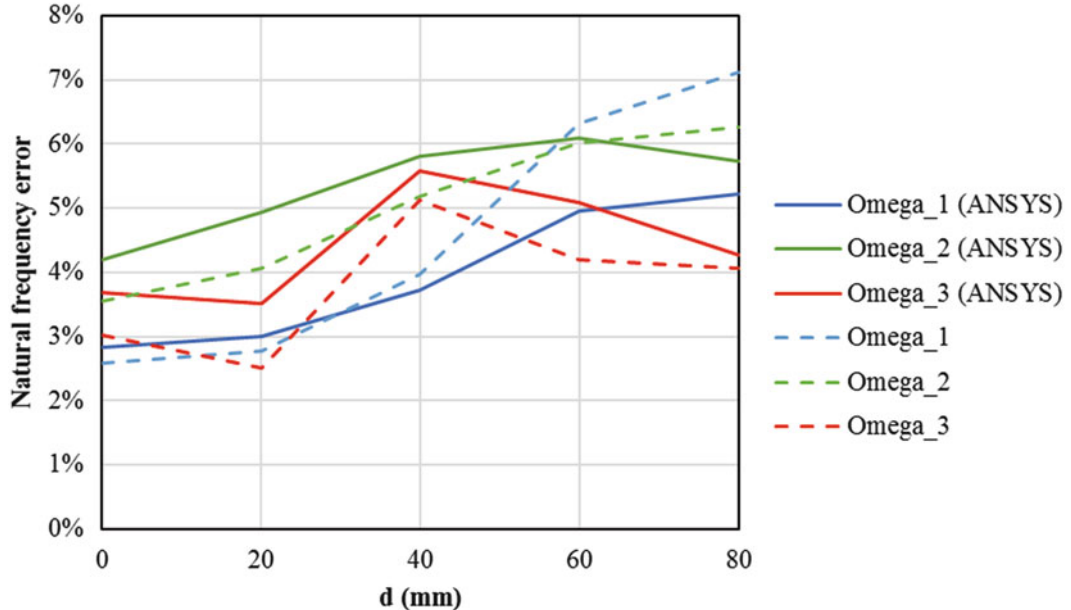


Fig. 5.3 Natural frequency estimation error using ANSYS and Rayleigh-Ritz method

5.4 Conclusions

Natural frequencies of a cantilevered plate drift during machining, thus an algorithm that determine dynamic properties for such plates under restricted computation resources is required. A model for stepped-thickness thick cantilever plates has been constructed using a combination of Mindlin theory and the Rayleigh-Ritz method. The proposed method can attain the order of error on natural frequency of the ANSYS model with smaller system matrices. Experimental validation was carried out, and the difference between simulation and experimental results is traced to non-ideal boundary conditions at the clamped end.

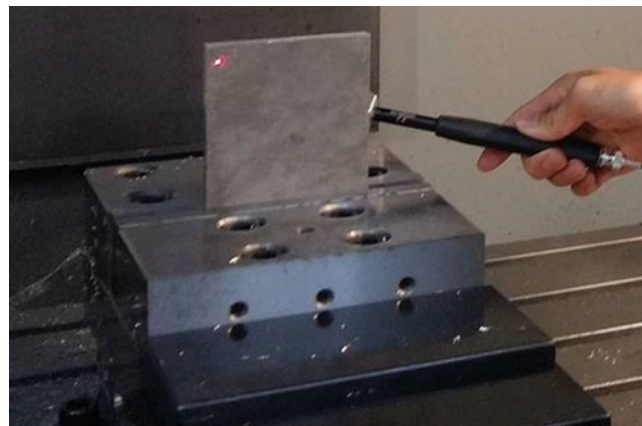


Fig. 5.4 Layout of experiment

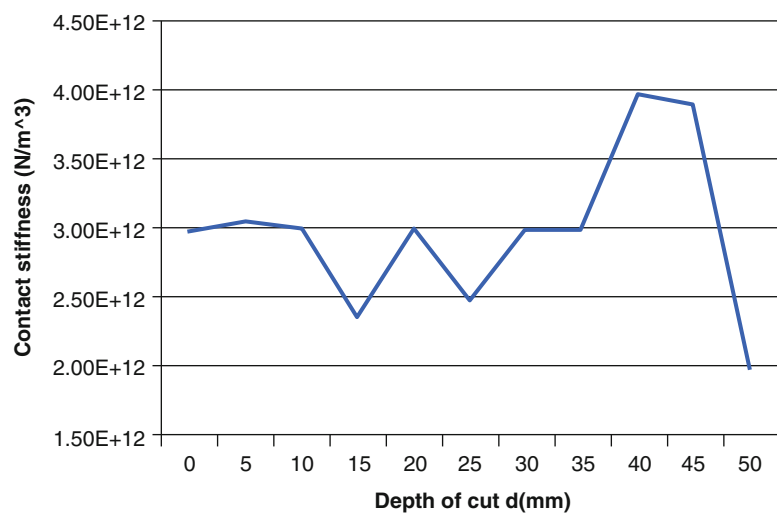


Fig. 5.5 Identified contact stiffness

References

1. Stone, B.: Chatter and Machine Tools. Springer International, Cham (2014)
2. Kolluru, K., Axinte, D.: Coupled interaction of dynamic responses of tool and workpiece in thin wall milling. *J. Mater. Process. Technol.* **213**(9), 1565–1574 (2013)
3. Ilanko, S., Monterrubio, L.E.: The Rayleigh-Ritz Method for Structural Analysis. ISTE, London (2014)
4. Ferreira, A.: MATLAB Codes for FInite Element Analysis: Solids and Structures. Springer, Berlin (2009)
5. Xiang, Y., Wang, C.: Exact buckling and vibration solutions for stepped rectangular plates. *J. Sound Vib.* **250**(3), 503–517 (2002)
6. Mottershead, J.E., Link, M., Friswell, M.I.: The sensitivity method in finite element model updating: a tutorial. *Mech. Syst. Signal Process.* **25**(7), 2275–2296 (2011)
7. Liew, K., Xiang, Y., Kitipornchai, S.: Transverse vibration of thick rectangular plates-I. Comprehensive sets of boundary conditions. *Comput. Struct.* **49**(1), 1–29 (1993)
8. Cheung, Y., Zhou, D.: Vibrations of moderately thick rectangular plates in terms of a set of static Timoshenko beam functions. *Comput. Struct.* **78**(6), 757–768 (2000)



Chapter 6

Modeling, Experimental Verification and Optimization of Seat Structure Per ECE R14

Yunus Ozcelik, Semih Cakil, and Atıl Erdik

Abstract Up to date concerns of automotive authorities are environmental sustainability, fuel efficiency and CO₂ emission. Lightweight component design is a key solution for those concerns. In a passenger vehicle, total weight of the seat structures is comparably high due to their quantity per vehicle. Therefore, seat structure has been chosen for lightweight design. Moreover, seat structure, seat belts and seat-belt anchorages are vital components of vehicles considering passenger safety in case of an accident. Thus, these components have to pass safety tests defined in European regulation ECE-R14. In order to reduce the number and cost of the regulation tests, a virtual test model is carried out using nonlinear finite element methods. Additionally, thickness and topology optimizations are performed to investigate light weighting opportunities on seat structure. Explicit and implicit methods are used to obtain virtual test model by using Radioss and ANSYS, respectively. The required validation process is carried out by performing seat pull test according to ECE R-14 regulations. Seat back displacement data is collected during the experiment. After comparison of the experiment result with both implicit and explicit analyses results, the proper virtual test model is chosen by taking computation time and accuracy into account. The validated model is used to optimize thickness and topology. The final design after optimization is evaluated in virtual test environment per ECE R14 regulation.

Keywords Bus Seat Design · ECE-R14 · Implicit & Explicit Analysis · Experimental Verification · Topology Optimization

6.1 Introduction

In recent years, intense pressures to reduce fuel consumption and carbon emissions in the automotive industry have been increased by national and international regulations. Among those are the first Greenhouse Gas (GHG) regulations for heavy-duty engines and vehicles developed by the Environmental Protection Agency (EPA) and the National Highway Traffic Safety Administration (NHTSA) in the United States. According to EPA, by 2018 the regulations should create an average reduction in GHG emissions per vehicle by 17 percent. The dramatic decrease in oil consumption aimed by the regulations is expected to result in a reduction of more than 3.1 billion metric tons of CO₂ emissions through 2025 [1].

Lorries, buses and coaches make a major contribution to CO₂ emissions in EU. Unfortunately, this is thought to increase another 10% between 2010 and 2030 [2]. While up to date fuel efficiency standards and a carbon dioxide monitoring scheme are not set in EU as in the case of cars and vans, other parts of the world, such as the United States, China, Japan and Canada, have already introduced standards. According to the post-2020 strategy for lorries, buses and coaches reported by EU Commission, EU is working on the certification of carbon dioxide emissions and fuel consumption of these vehicles and on the monitoring and reporting of such certified data [1].

Mentioned regulations and strategies orient automotive and part manufacturers to focus on the reduction in fuel consumption by various ways. Two main approaches dominate the industry. First approach aims to improve engine technologies by either enhancing the internal combustion engine efficiency or completely switching to hybrid or electricity power. The latter might be a long term solution, as it requires additional significant changes in automotive ecosystem. Second approach rather focuses on weight reduction by design improvement/optimization and/or material change. Due to the ease of application compared to the first approach, results can be appreciated in a shorter term.

Y. Ozcelik (✉) · S. Cakil
Borusan Arge, Istanbul, Turkey

A. Erdik
Otokar, Sakarya, Turkey

Table 6.1 ECE R14 traction forces for M1, M2 and M3 vehicles

Vehicle class	Number of anchorage	Lower belt pull force [N]	Upper belt pull force [N]
M1	2	22,250 + mseat*20 g	—
M1	3	13,500 + mseat*20 g	13,500
M2 (<5000 kg)	2	11,000 + mseat*10 g	—
M2 (<5000 kg)	3	6750 + mseat*10 g	6750
M3 (>5000 kg)	2	7400 + mseat*6.6 g	—
M3(>5000 kg)	3	4500 + mseat*6.6 g	4500

In order to achieve a considerable weight reduction in mass transport vehicles, the focus should be on the most commonly used components. From this perspective, passenger seat structure come to the forefront. Passenger seat structures weight nearly 500 kg in a 59 seated bus. Therefore, even a slight reduction in passenger seat offers an important potential for reducing the fuel consumption and carbon dioxide emissions through vehicle lightening.

In EU, every year approximately 20,000 buses and coaches are involved in accidents that result in nearly 30,000 causalities with over 150 fatal injuries [3]. One of the most influential components in case of an accident is seat with restraint systems. In order to minimize the risk of injury, strict safety regulations for seat systems are set by international authorities. There are two regulations which are directly related to seat structure and seatbelt anchorages.

First regulation is ECE R80, which is applicable for the mass transport vehicles with the capacity of 16 or more persons and with forward facing seats with a reference height of at least 1 m. Two types of tests are described by the regulation. Seat shall be subject to the test requirements of either dynamic test or static test. This regulation requires that the seat remains in an appointed zone in case of a crash where the vehicle is exposed to a predefined deceleration [4].

Second regulation, ECE R14 determines the conformity of the seat structure and seat belt anchorages for motor vehicles. Within the scope of conformity tests specified in the regulation, the forces shown in Table 6.1 are applied statically to the seat belts with the help of certain pulling apparatuses. Two types of seatbelts with regard to number of anchorage are presented; whereas two point seatbelts secure only lap region, three point seatbelts secure both lap and shoulder regions. Integrity of the seat structure and seat belt anchorages should be assured to comply with ECE R14. An additional requirement states that seatbelt anchorages should remain within a limited zone in case of three point seatbelts.

Several studies have been conducted to simulate seat belt anchorage according to ECE R-14. Hessenberger et al. [5] examined strength of seat belt anchorage using ABAQUS and LS-Dyna. In ABAQUS, the test was modeled by quasi-static implicit finite element techniques, since the loads are applied slowly. In LS-Dyna, however, explicit finite element techniques were used to simulate seat belt anchorage per ECE R-14. Although both methods yielded desirable correlation with each other, LS-Dyna has some advantages over ABAQUS to model seat belt and contacts. Singh et al. [6] studied modeling of automotive seat(s?) for dynamic sled testing. Dynamic sled testing was simulated using Altair Hypermesh, a commercial tool for meshing, and LS-Dyna, an explicit finite element solver. Singh et al. evaluated safety of automotive seat per results of the simulation. Pathy et al. [7] solved roof-crash and set-pull problems using LS-Dyna implicit solver by means of recent developments and improvements to LS-Dyna implicit solver. Computation time took 5 h 45 min for explicit model, while it took 6 h 10 min for implicit model as per the study. Also, localized buckling in the seat structure induces a highly nonlinear problem to be solved. Vatambe [8] simulated automotive seat(s?) per Federal Motor Vehicle Safety Standards (FMVSS) 207/210. The automotive seat was modeled with shell element using Hypermesh software as per FMVSS 207/210 regulations. LS-Dyna, an explicit finite element solver, was used in this study. According to the study, changing the body block material from steel to aluminum has advantages in terms of energy absorption, since aluminum has a higher specific energy absorption capability than the corresponding steel. Moreover, this material change reduces both weight of the automotive seat and maximum stresses on the component. Arslan et al. [9] designed new seat anchorages for commercial vehicles per ECE R-14 regulation. In this work, Hypermesh and LS-Dyna were used to create and solve the explicit finite element model, respectively. Based on the ratio of maximum Von Mises stress to material yield strength, iterative simulations were carried out to design a new automotive seat anchorage. Finally, the new design was tested and approved by the certified institute.

Optimization of topology and size is a key topic to get lightweight products. Some researchers studied topology and size optimization on seat structure. Yuce et al. [10] designed new lightweight passenger seat using Radioss, a commercial explicit finite element solver. Topology and free size optimization techniques were used to get lightweight passenger seat. After solving (the) baseline model, high and low stress areas on the model were observed using Hyperview. After that, low-stress

regions were removed to reduce weight. Moreover, high strength steel was used instead of low strength steel in the passenger seat. This allowed reducing thickness of the seat components, which yielded lightweight passenger seat. Sarisac and Kaya [11] carried out the study about designing passenger seat structure components using topology and size optimization. Seat structure model was prepared and solved using Hypermesh and Radioss, respectively. Topology optimization was conducted using Optistruct, a commercial linear, nonlinear and structural optimization solver [12]. Furthermore, size optimization was done using Hyperstudy, a design exploration tool [13].

6.2 Modeling of the Bus Seat

In this section, components of the seat structure are introduced to clarify the seat structure design. Moreover, implicit and explicit modeling techniques for bus seat per ECE R-14 are discussed extensively. Besides, solution techniques of both implicit and explicit are discussed. At the end, mentioned methods are compared in terms of computation time and seat back displacement.

6.2.1 Describing of the Seat Structure

Metal frame of the seat structure consists of numerous components. Alphanumeric and numeric codes for seat components used in this work are given in Fig. 6.1.

In the current design, materials and thickness of the components are summarized in Table 6.2.

After this point, only numeric codes designated to components will be used to reduce complexity.

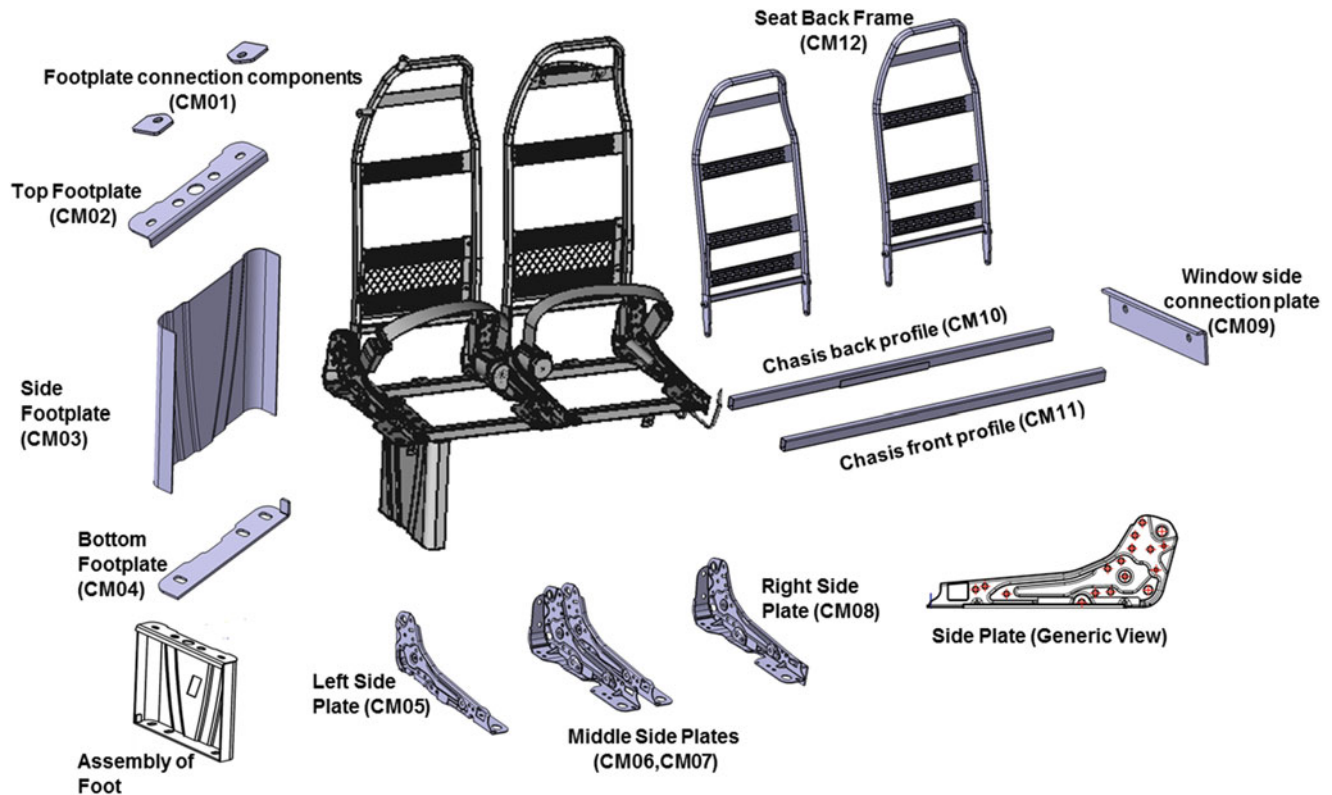


Fig. 6.1 Components of the seat structure

Table 6.2 Materials and thickness of seat structure components

Alphanumeric name	Numeric name	Material	Thickness [mm]
Footplate connection comp.	CM01	MAT1	4
Top footplate	CM02	MAT2	3
Side footplate	CM03	MAT1	2
Bottom footplate	CM04	MAT1	4
Left side plate	CM05	MAT2	2.5
Middle side plates	CM06	MAT2	2.5
Right side plates	CM07	MAT2	2.5
Window side connection	CM08	MAT1	4
Chasis back profile	CM09	MAT1	2
Chasis front profile	CM10	MAT1	2

6.2.2 Implicit Modeling Technique

In this section, solution methodology of implicit technique are introduced. Besides, implicit modeling of the seat structure is examined in detail.

Newmark method, a single step implicit numerical integration method, is one of the most widely used numerical integration methods to determine the response of dynamic system [14]. Newmark method is introduced to solve both linear and nonlinear systems under blast and seismic loading [15]. Consider the governing equation for a dynamic system as [16]

$$M \{ \ddot{X} \} + C \{ \dot{X} \} + \{ F_s \} = P, \quad (6.1)$$

where, M and C are mass and damping matrices, respectively. $\{F_s\}$ is an internal spring force, which is nonlinear. P is the external force. Since this method intends to solve a nonlinear system Newton-Raphson technique is used in order to find the rate of change of stiffness in infinitesimal displacement increment [17]. Thus, Jacobian matrix can be written as

$$k_T = \begin{pmatrix} \frac{\partial F_{s1}}{\partial x_1} & \dots & \frac{\partial F_{s1}}{\partial x_n} \\ \vdots & \ddots & \vdots \\ \frac{\partial F_{sn}}{\partial x_1} & \dots & \frac{\partial F_{sn}}{\partial x_n} \end{pmatrix}. \quad (6.2)$$

Flowchart of Newmark method for nonlinear system is given in Fig. 6.2.

Inherently, Newmark method introduces numerical damping that is controlled by α and β constants. Numerical damping damps out artificial components of higher modes [17].

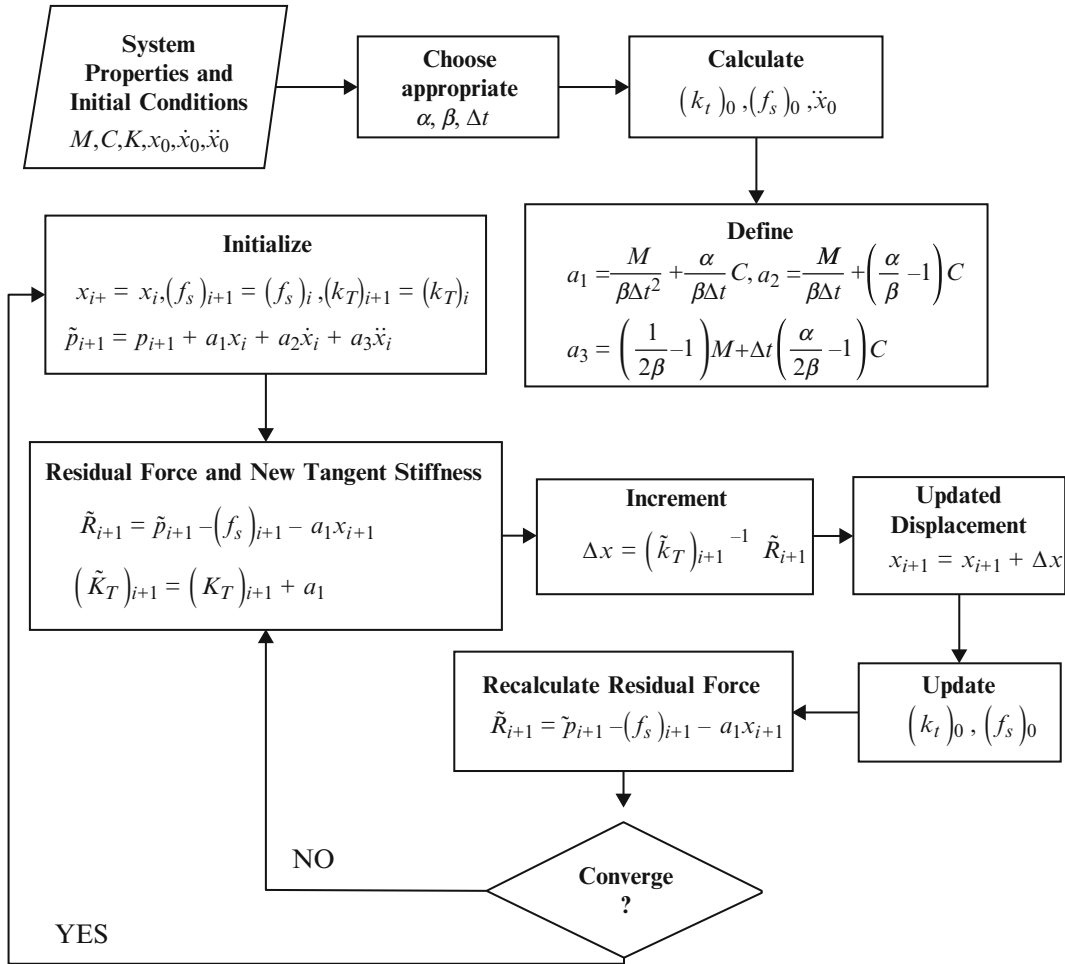
ANSYS, a commercial finite element software, is used to simulate seat structure as per ECE R14 regulation for an implicit modeling. Naturally, almost of the whole seat structure is made up of sheet metal. Since the ratio of a typical dimension to a thickness of seat structure is higher than 10, seat structure can be modeled by shell elements with a negligible error [18]. As can be seen from Fig. 6.3, the 2D analysis model is constructed by extracting the middle plane of original 3D geometry using ANSYS SpaceClaim, a modeling software. Moreover, weight and stiffness of foam components of the seat structure are neglected for implicit analysis in order to reduce complexity.

Since the seat structure may deform plastically after application of load, elastic-plastic material model is used to get accurate results. In ANSYS, the elastic-plastic material can be generated from true stress-strain data. Therefore, tensile testing is applied to a number of specimens having different thickness. Since the result of tensile testing gives engineering stress-strain data, conversion of engineering stress-strain to true stress-strain can be done using

$$\varepsilon_{true} = \ln(1 + \varepsilon_{eng}), \quad (6.3)$$

$$\sigma_{true} = \sigma_{eng} e^{\varepsilon_{true}}, \quad (6.4)$$

where, ε_{true} , ε_{eng} , σ_{true} and σ_{eng} are true strain, engineering strain, true stress and engineering stress, respectively. Averaged true stress-strain curves of MAT01 and MAT02 are given in Fig. 6.4.

**Fig. 6.2** Flowchart of newmark method

Frictionless contact, which acts as a nonlinear touch contact, is defined between seat structure and frame. Moreover, welded locations are modeled using “*Multipoint Constrained (MPC)*” type contact in ANSYS. Furthermore, bolted locations are modeled using preloaded line body, whose properties are given in Table 6.3. Bilinear material model is chosen to model bolt material. Yield strength of bolt is selected as an average of minimum and maximum yield strengths of bolt given in Table 6.3. Stress-strain curve of the bolt material model is shown in Fig. 6.5.

The seat structure is meshed with Shell 181 element type in ANSYS. Shell 181 is suitable for analyzing thin to moderately thick shell structures. It is a four-noded element with six degrees of freedom at each node (three translational and three rotational). Moreover, it is suitable for nonlinear applications such as large rotation and large strain problems [21].

Element test is important to verify elements and material model. Therefore, simple tensile testing simulation is done with Shell 181 element and MAT01. Consider the specimen being 100 mm in length and 6 mm in gauge width and 2 mm in thickness (see Fig. 6.6). One end is fixed while the other end is exposed to displacement as an input. Engineering stress is obtained by dividing reaction force to initial gauge area while engineering strain is the ratio of gauge expansion to initial gauge length. The problem is solved for both linear and nonlinear (geometric nonlinearity) cases. As can be seen from Fig. 6.7, although linear analysis yields an enormous error, the nonlinear analysis yields accurate results compared to input material curve. Therefore, Shell 181 element type gives accurate results for large strain problems when geometric nonlinearity option is activated in ANSYS.

Frequency content of input force curve and natural frequencies of the seat structure are vital parameters to determine the accuracy of the quasi-static simulation. Figure 6.8 shows input force curve and Fast Fourier Transform (FFT) of (the) force curve. Accordingly, the dominant frequency of the input signal is around 0.39 Hz. The fundamental natural frequency of the seat structure is calculated as 23.2 Hz, which is well above the dominant frequency of (the) input signal. Therefore, it

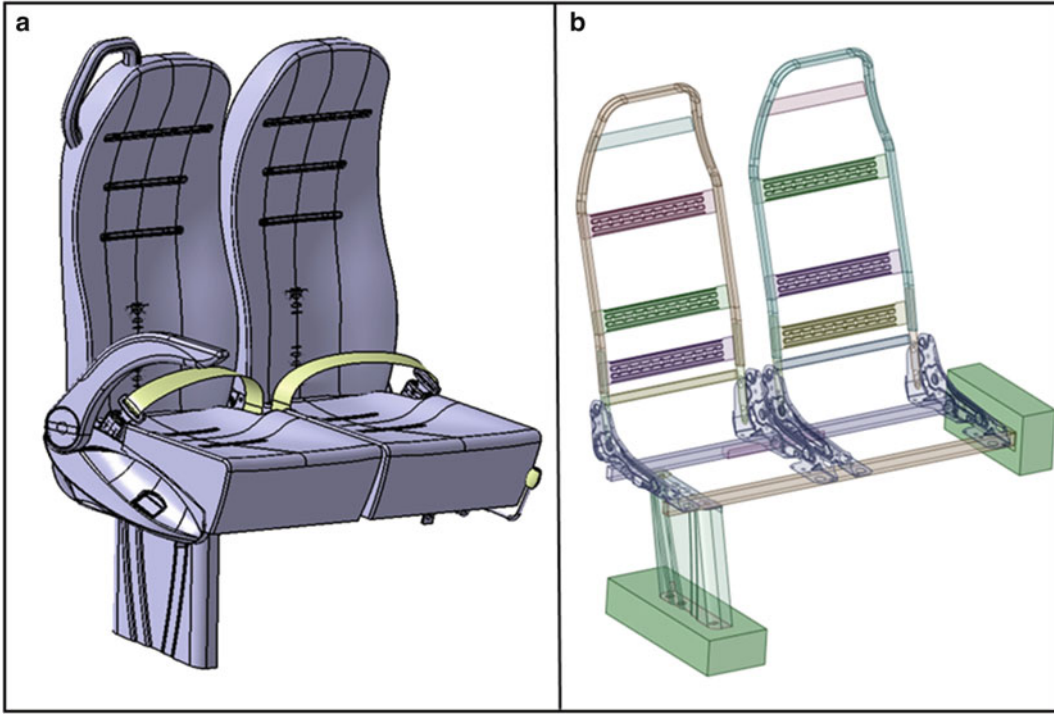


Fig. 6.3 Geometry of seat structure **(a)** 3D model **(b)** 2D analysis model

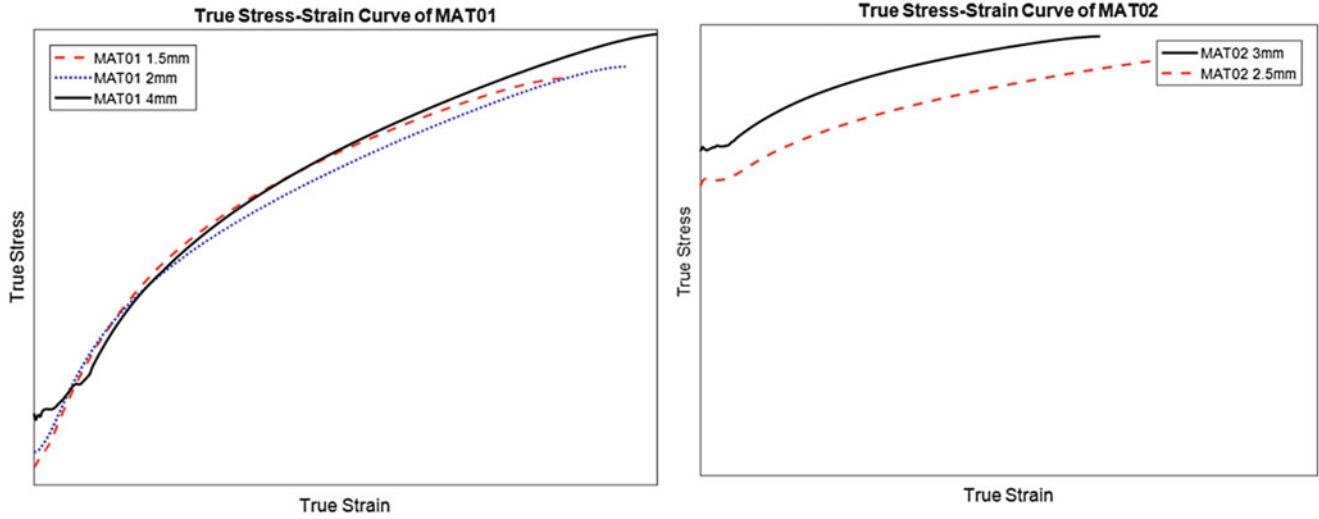


Fig. 6.4 True stress-strain of MAT01 and MAT02 with various thickness

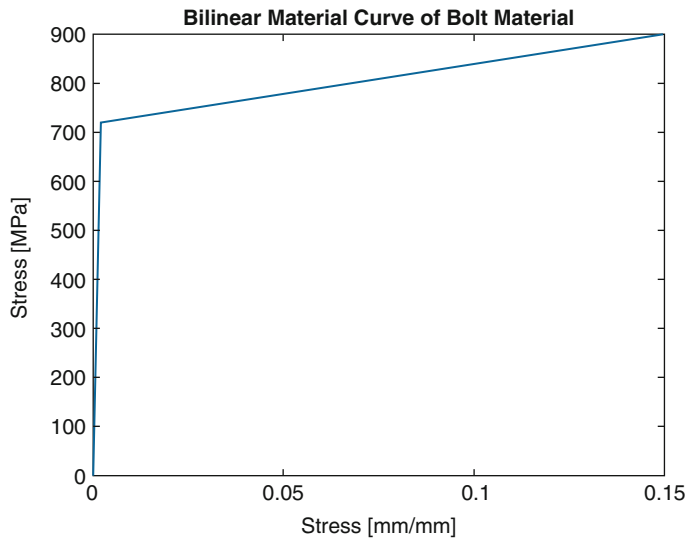
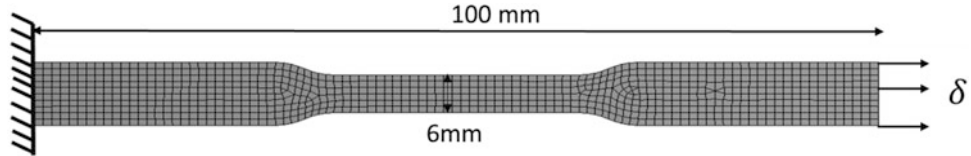
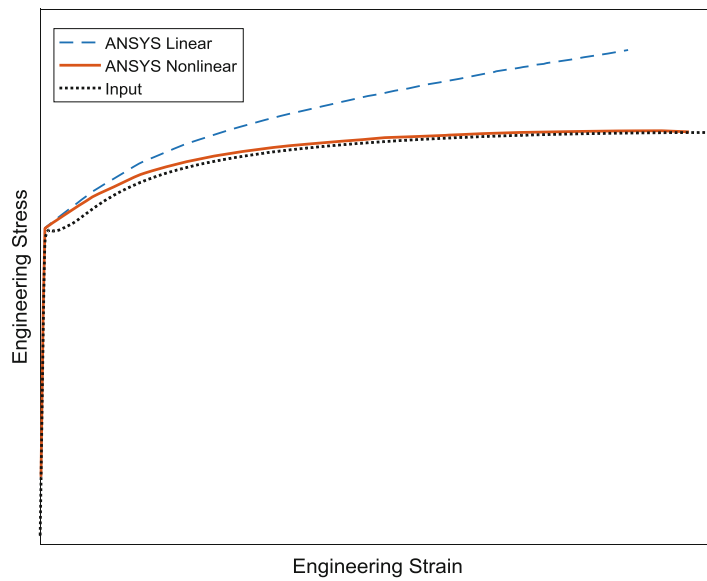
Table 6.3 Class 8.8 M10 bolt properties

Bolt type	Min. yield strength [19]	Max. yield strength [19]	Pretension [20]
Class 8.8	640 MPa	800 MPa	15 kN

can be said that quasi-static analysis can yield as accurate results as obtained with transient analysis. The main advantage of quasi-static simulation is that computation time can be reduced significantly.

Quasi-static simulation is conducted using ANSYS including geometric nonlinearity. Deformation history of the seat back is given in Fig. 6.9. The seat structure maintains its integrity after load application as per analysis results.

In this section, implicit solution techniques and details of ANSYS simulation were extensively discussed. Comparison of implicit simulation and test results is given in Sect. 6.2.4.

**Fig. 6.5** Stress-strain curve of bolt material**Fig. 6.6** Tensile testing simulation**Fig. 6.7** Engineering stress-strain curve

6.2.3 Explicit Modeling Technique

In this section, solution methodology of the explicit technique is introduced. Besides, explicit modeling of the seat structure is examined in detail.

The equation of motions is given as

$$M \left\{ \frac{d^2 u}{dt^2} \right\}_n + C \left\{ \frac{du}{dt} \right\}_n + K \{U\}_n = \{F_{ext}\}_n, \quad (6.5)$$

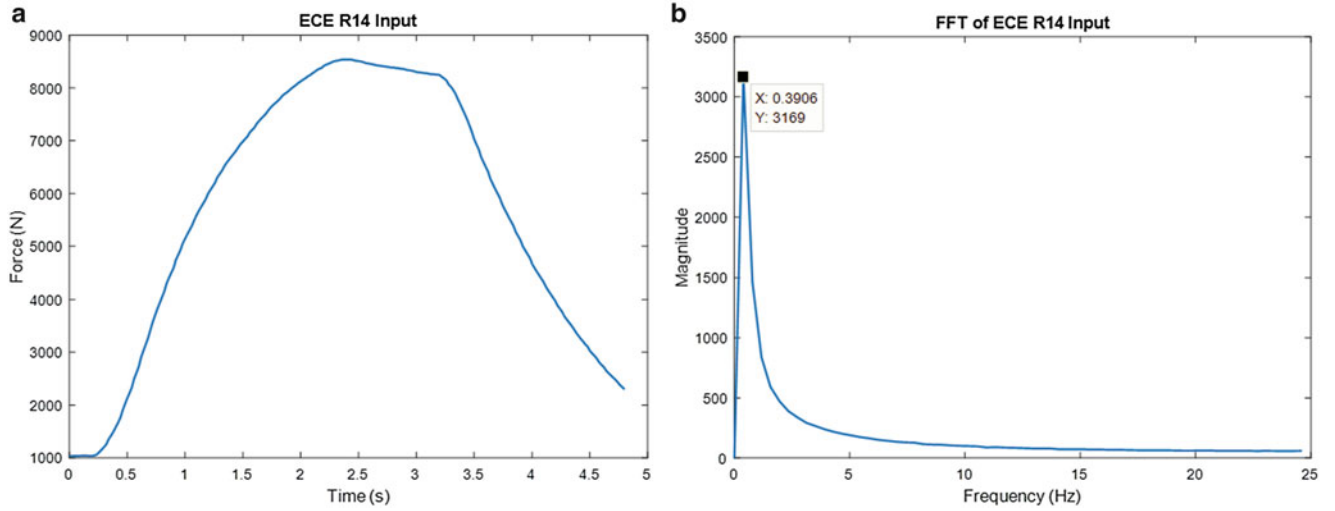


Fig. 6.8 (a) Force curve (b) FFT of force curve

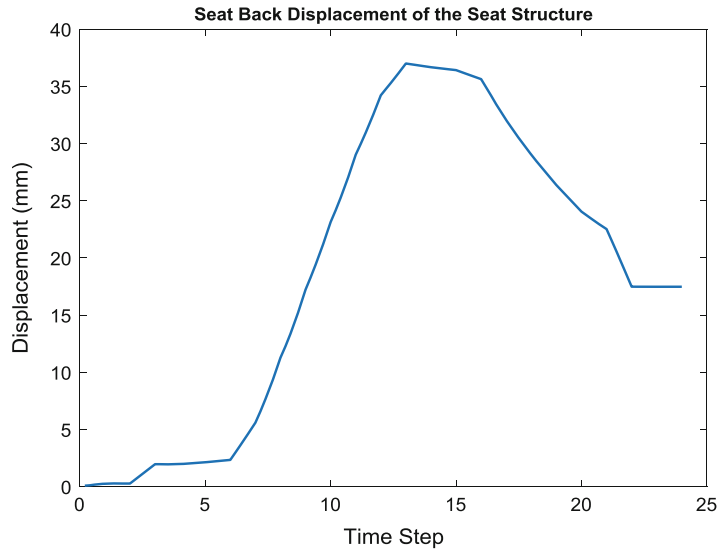


Fig. 6.9 Seat back deformation (implicit)

where, M , C , K are mass, damping and stiffness matrices, respectively. n is a time level index, F_{ext} is an external force. u is the displacement to be determined. One of the most widely used explicit schemas is central difference algorithm [22]. Second order central difference operator is given as [22]

$$\left\{ \frac{du}{dt} \right\}_n = \frac{\{U\}_{n+1} - \{U\}_{n-1}}{2\Delta t}, \quad (6.6)$$

$$\left\{ \frac{d^2u}{dt^2} \right\}_n = \frac{\{U\}_{n+1} - 2\{U\}_n + \{U\}_{n-1}}{\Delta t^2}, \quad (6.7)$$

where, Δt is time increment between successive time steps. Substitute Eq. (6.6) and Eq. (6.7) into Eq. (6.5), the governing equation becomes

$$\left(\frac{1}{\Delta t^2} M + \frac{1}{2\Delta t} C \right) \{U\}_{n+1} = \{F_{ext}\}_n - K\{U\}_n + \frac{1}{\Delta t^2} M (2\{U\}_n - \{U\}_{n-1}) + \frac{C}{2\Delta t} \{U\}_{n-1}. \quad (6.8)$$

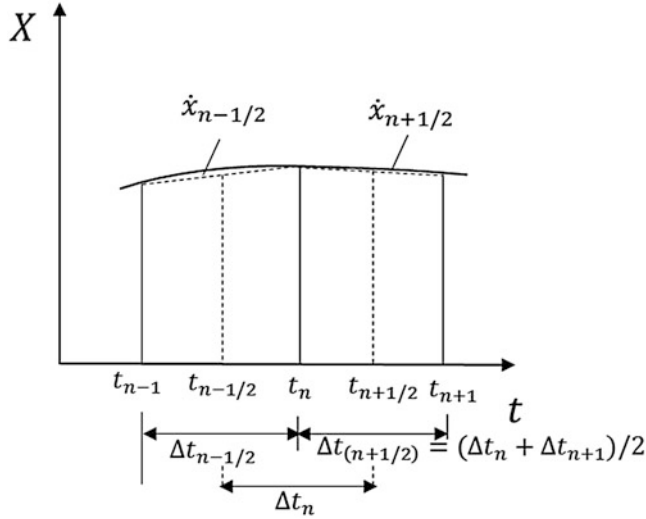


Fig. 6.10 Two-step central difference formulation

Equation (6.8) has no computational advantage, since LHS of the equation still requires matrix inversion procedure. In order to eliminate matrix inversion, however, most of the algorithms use two-step formulation (see Fig. 6.10).

As can be seen from Fig. 6.10, velocity and acceleration are given as [23]

$$\dot{u}_{n+1/2} = \frac{1}{\Delta t_{n+1/2}} (u_{n+1} - u_n), \quad (6.9)$$

$$\ddot{u}_n = \frac{1}{\Delta t} (\dot{u}_{n+1/2} - \dot{u}_{n-1/2}). \quad (6.10)$$

Recast equation of motion for nonlinear case,

$$M\{\ddot{U}\}_n + C\{\dot{U}\}_{n-1/2} = \{F_{ext}\}_n - \{F_{int}\}_n, \quad (6.11)$$

where, F_{int} is the internal force.

Using Eq. (6.9), Eq. (6.10) and Eq. (6.11), updated acceleration, velocity and displacement terms are given as

$$\{\ddot{U}\}_n = M^{-1} \left(\{F_{ext}\}_n - \{F_{int}\}_n - C\{\dot{U}\}_{n-1/2} \right), \quad (6.12)$$

$$\{\dot{U}\}_{n+1/2} = \{\dot{U}\}_{n-1/2} + \Delta t_n \{\ddot{U}\}_n, \quad (6.13)$$

$$\{U\}_{n+1} = \{U\}_n + \Delta t_{n+1/2} \{\dot{U}\}_{n+1/2}. \quad (6.14)$$

It is noted that initial condition for Eqs. (6.12, 6.13 and 6.14) are given as

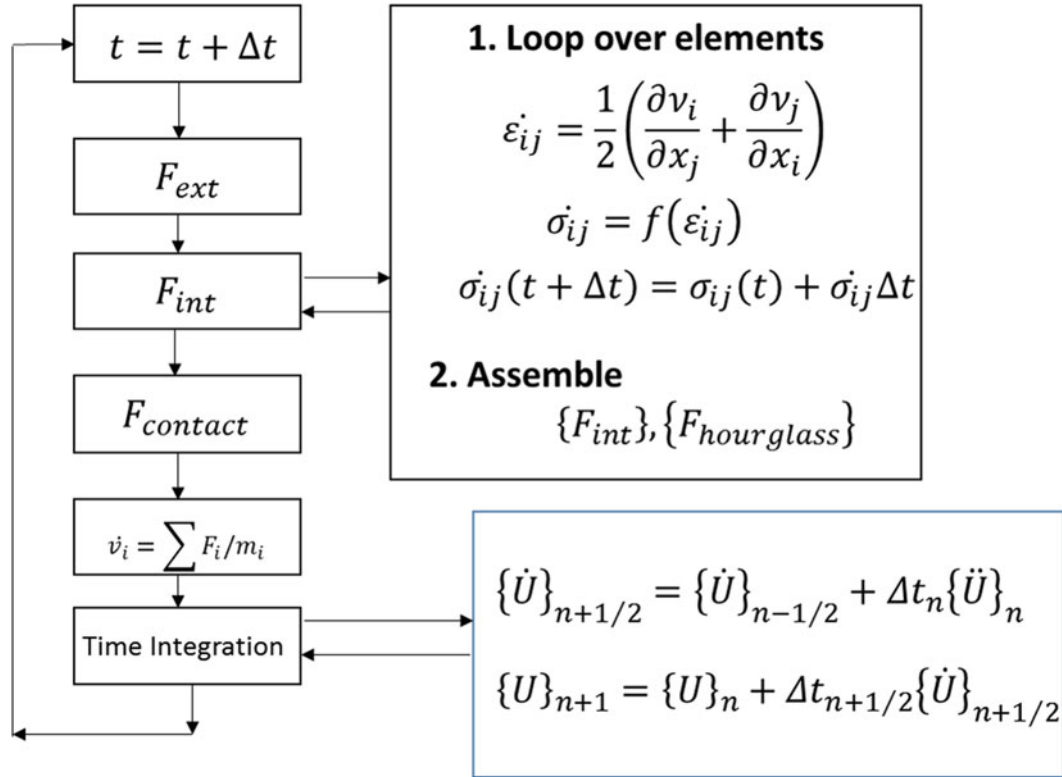
$$\{U\}_0 = \{\bar{U}\}_0 + \{U\}_{stat}, \quad (6.15)$$

$$\{v_0\} = \frac{1}{2} \left(\{\dot{U}\}_{-1/2} + \{\dot{U}\}_{1/2} \right), \quad (6.16)$$

where, $\{\bar{U}\}_0$ is initial displacement and $\{U\}_{stat}$ is static displacement.

Table 6.4 Speed of sound and characteristic length of some element types

Element type	Speed of sound	Characteristic length
Beam [24]	$\sqrt{E/\rho}$	Length of the element
Shell (quad) [24]	$\sqrt{\frac{E}{\rho(1-\nu^2)}}$	$\frac{\text{Area of the element}}{\text{Max.Length}}$
Shell (triangular) [24]		$\frac{2*\text{Area of the element}}{\text{Max.Length}}$
3D quad [25]	$\sqrt{\frac{E(1-\nu)}{\rho(1+\nu)(1-2\nu)}}$	$\frac{\text{Volume of the element}}{\text{Max.side area}}$
3D tetrahedral [25]		Minimum altitude

**Fig. 6.11** General flow chart for explicit analysis

As seen from Eq. (6.12), inversion of mass matrix is trivial which gives a computational advantage. Furthermore, as per von-Neumann, central difference method is conditionally stable if the following criteria is satisfied [22]

$$(\Delta t)_{\max} \leq \frac{l}{c} = \frac{l}{\sqrt{E/\rho}}. \quad (6.17)$$

where, l is characteristic length, c is the speed of sound, which can be expressed in terms of Young's modulus (E) and density (ρ) of the material. The physical meaning of Eq. (6.17) is that time step should be small enough so that the information does not propagate across more than one element per time step. For example, consider steel material of which Young's Modulus and density are 210 GPa and 7800 kg/m³, respectively. When time step is one microsecond, then the maximum characteristic length of the element should be 5 mm. Besides, the characteristic length and speed of sound depend on element types. Summary tables for the speed of sound and characteristic length are given in Table 6.4.

Solution methodology of explicit method is given in Fig. 6.11.

The seat structure simulation model is prepared using Hypermesh and Hypercrash. MAT01 and MAT02 is taken as an elastic-plastic material for this analysis. In addition to the implicit model, foam and seat belt is included into the simulation model. Foam is modeled using LAW70 material card in Hypercrash. Automatic seat belt fitting interface of Hypercrash is employed to get closer response to test result. The welded region is represented using node to node spot weld with no failure. This approach gives suitable results since no weld failure occurs after ECE R14 testing. Bolts and nuts in the seat

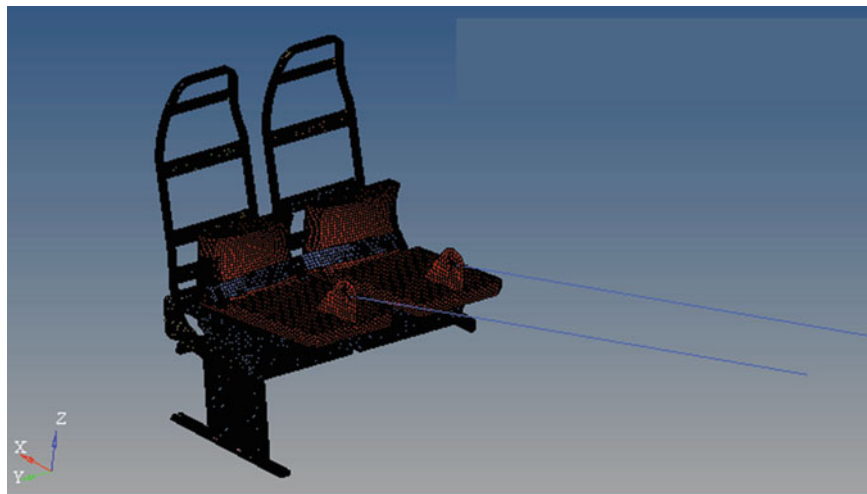


Fig. 6.12 The seat structure in Hypercrash

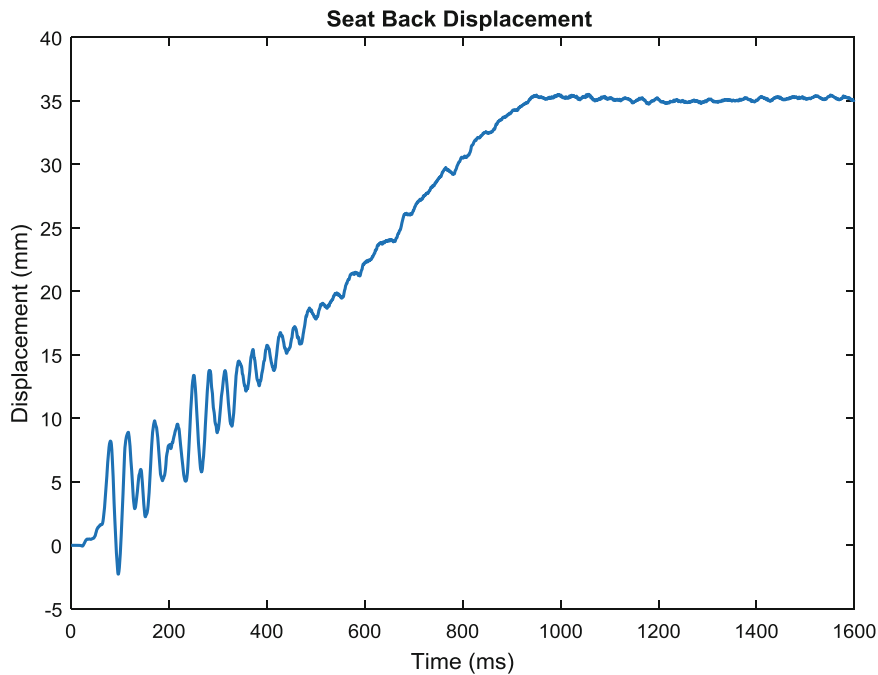


Fig. 6.13 Seat back deformation (explicit)

structure are represented by beam elements. Besides, foam is modeled with solid element while the remaining components are represented by shell elements. Figure 6.12 shows the seat structure in Hypercrash. It is noted that seat belt and pulling components, shown dark blue and red in Fig. 6.12, are available only in the explicit model.

The finite element model is solved using Radioss, an explicit finite element solver. The seat back displacement is shown in Fig. 6.13. Initial oscillations, which are characteristics of explicit analysis, are due to initial alignment of seat belt and pulling components. It should be noted that explicit analysis was not run till end due to the long solution time. Nevertheless the desired results are already obtained after applied force reaches a maximum value.

In this part, solution method, stability condition, explicit seat structure model as well as seat back displacement were summarized.

6.2.4 Comparison of Implicit and Explicit Analyses

In this part, the differences between implicit and explicit analyses are explained. Moreover, results of both implicit and explicit analyses are discussed.

Explicit and implicit analysis refer to two type integration schema to solve dynamic problems. Those schemas are described in previous sections. As can be seen from Fig. 6.14, the implicit analysis is well suited to static linear, some level of plasticity and buckling while explicit analysis is more suitable for dynamic analysis including buckling, damage and rapture. As an example, crashworthiness analysis, manufacturing process simulations (deep drawing, extrusion), bird-strike, blade out and bus roll over simulations are done using explicit analysis. Moreover, analysis type should be correctly chosen for a given problem. Otherwise, computation time can be long or the problem cannot be solved due to convergence problems. Figure 6.15 shows a general view of CPU cost of both implicit and explicit analysis types in terms of complexity.

Figure 6.16 shows a comparison of implicit quasi-static simulations and explicit solutions. It is noted that time domain in the explicit simulation is converted to time step by multiplying with a shift factor. Although there is a slight difference between implicit and explicit solutions, the computation time is different. Computation time for implicit analysis takes about 15 h while it takes about 23 h for explicit analysis. It is noted that both analyses were conducted using the same computer with 12 cores.

In the light of above information, both methods give similar seat back displacement. However, the implicit method is more advantageous in terms of computation time.

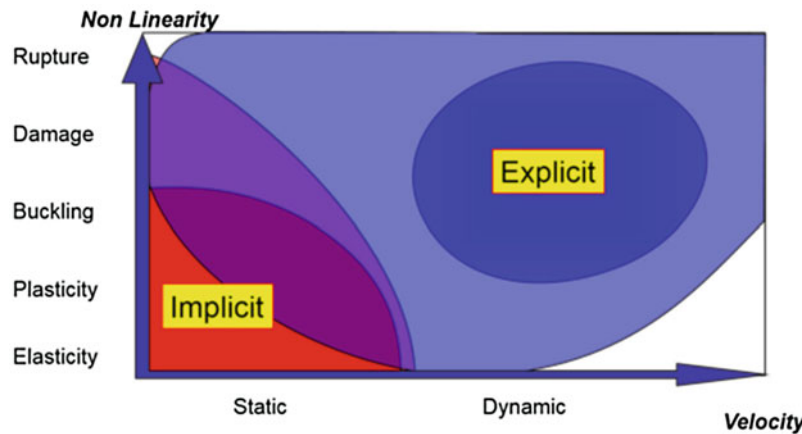


Fig. 6.14 Range of implicit and explicit analyses [26]

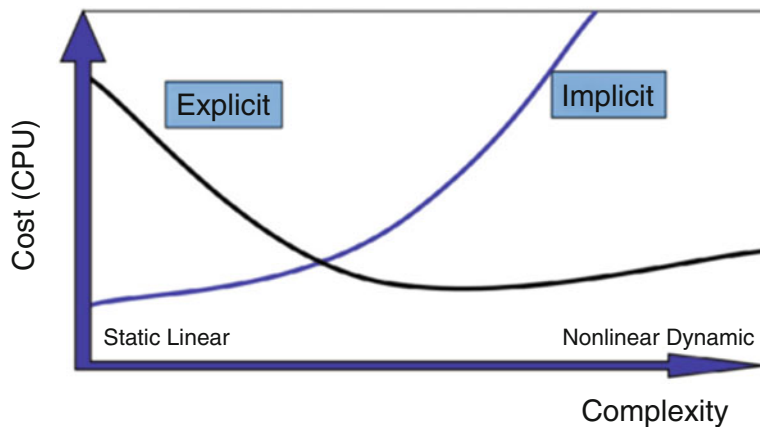


Fig. 6.15 CPU cost of implicit and explicit analyses [26]

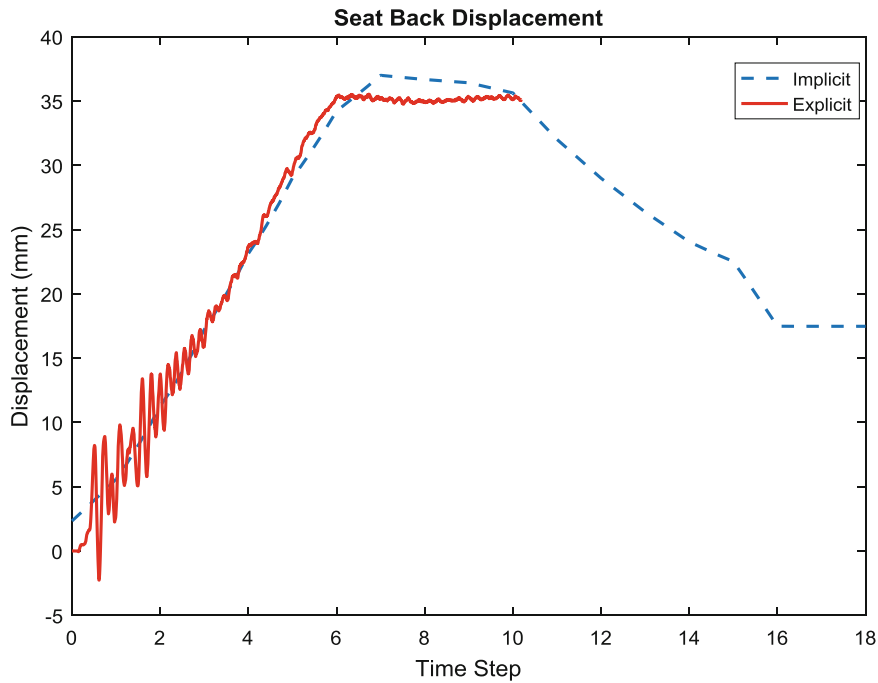


Fig. 6.16 Implicit vs explicit comparison

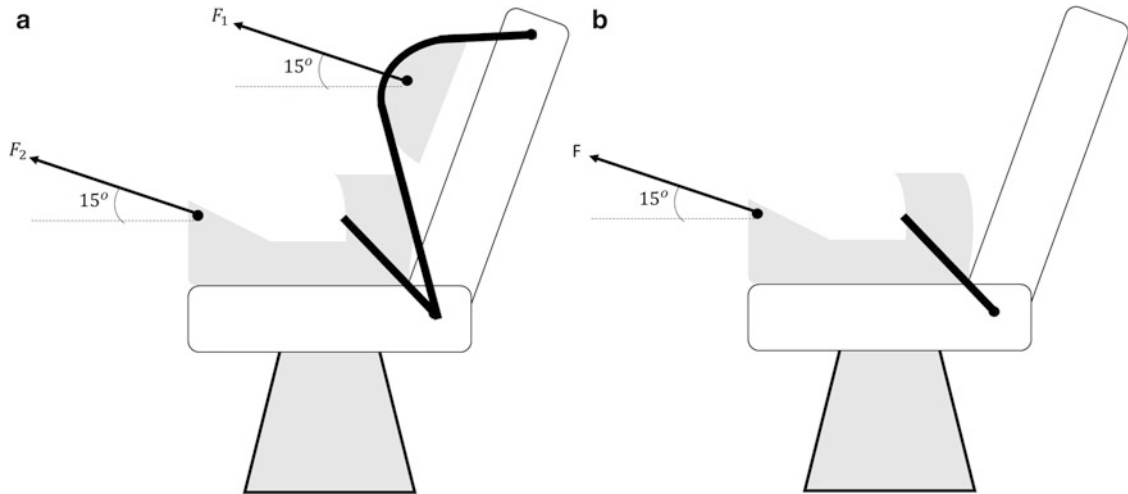


Fig. 6.17 (a) Three point seatbelt test schematics (b) two point seatbelt test schematics

6.3 Experimental Verification

ECE R14 regulation tests were performed in a TUV certified test laboratory in order to correlate FEM results and test results. Test schematics for both three point and two point seatbelt tests are shown in Fig. 6.17. Seat structure should be mounted on a frame which is identical to the bus frame where the tested seat will be used. Angle of seatback frame has to be set to a reference position defined by seat design. All other components should be assembled according to the reference design by applying design torque values. The direction of pulling force is arranged to make an angle of 15° with ground plane. Instrumented test setup is shown in Fig. 6.18. At the beginning of the test, a preload of 1 kN is applied to ensure the tightness of seatbelt and pulling chain. Since current study focuses on seats with two point seatbelts, only a lap block force of 8.5 kN is applied to the seat structure as in Fig. 6.17. Max load is reached in 0.5 s after test start. Although resistance for 0.2 s is accepted according to the regulation, maximum load is applied for 2 s. Seat back displacements of both window side and aisle side are measured during the test.



Fig. 6.18 ECE R14 test platform

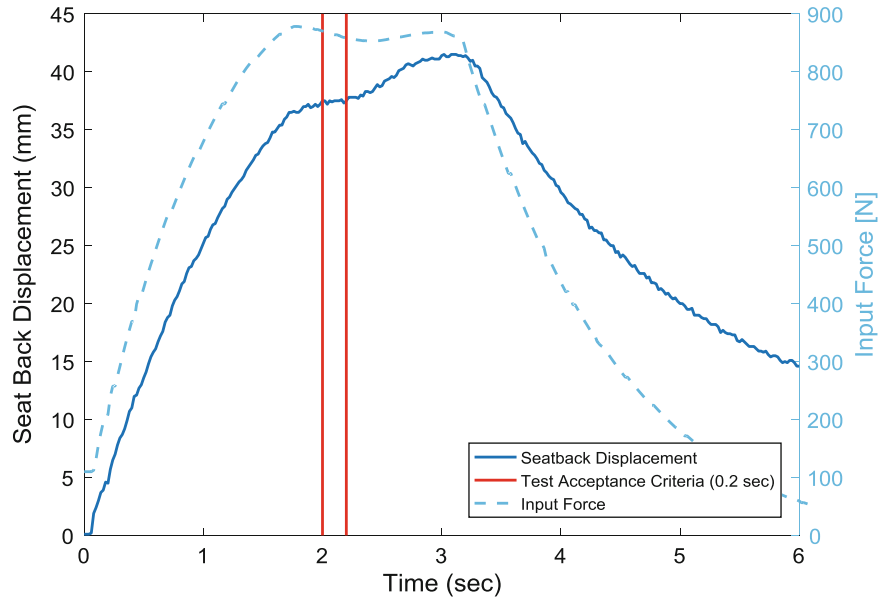


Fig. 6.19 Seat back displacement & applied force during the test

Test results for aisle side seat are presented in Fig. 6.19. Seatback displacement value tends to increase with increasing input load. The region limited within the lines perpendicular to y-axis shows the acceptance region, which corresponds to a time interval of 0.2 s. Test results and FEM results are graphed in Fig. 6.20. Trends of the test result curve and FEM result curves do not overlap between the time steps 8 and 13 corresponding to 2.5th sec and 4.5th sec of the test. However curves match each other in the acceptance region, so FEM and test results may be considered to be in correlation with a slight underestimation by FEM approach.

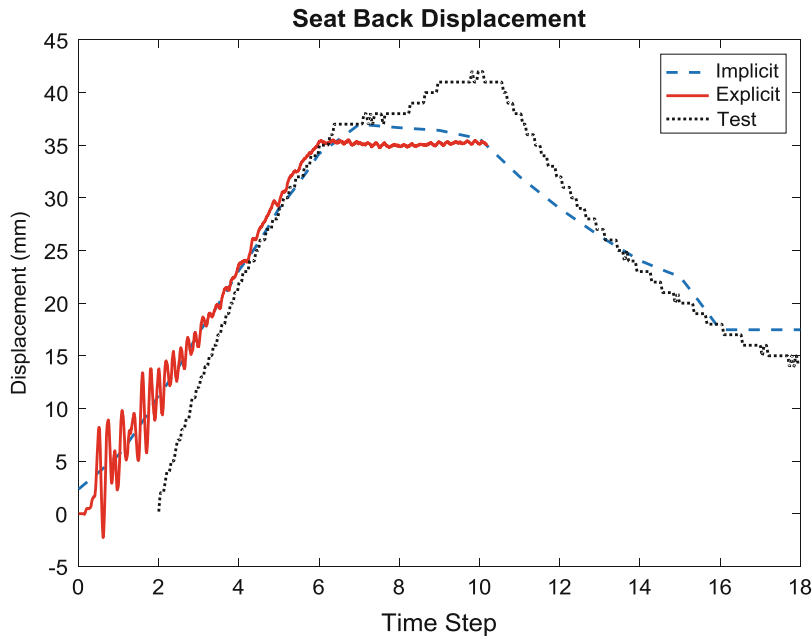


Fig. 6.20 Comparison of simulations and test results

6.4 Topology and Size Optimization

Topology optimization is a mathematical method that optimizes structure within a given space or block for defined loads, constraints, boundary conditions with minimizing or maximizing the objective function such as compliance, maximum stress or fundamental frequency [27]. In other words, topology optimization is a kind of optimization that constructs a structure from a block of material. Furthermore, size optimization generally refers to optimization of thickness of the components that can withstand applied loads. Both topology and size optimizations are carried out using ANSYS. Topology and size optimizations are vital for the design of functional lightweight components. Also, complicated geometry resulting from topology optimization that cannot be produced by classical manufacturing types can be produced by additive manufacturing.

CM03 component is selected for topology optimization since the component has a larger area without any features such as hole and rib. All areas of CM03 are defined as design space except locations where loads applied and boundary condition exists. The objective function of the optimization is to minimize compliance. ANSYS Topology Optimization tool is used to optimize CM03. Figure 6.21 shows new geometry after topology optimization.

After topology optimization, size optimization is carried out to reduce the weight of the seat structure. Sensitivity analysis is conducted to determine which components are more sensitive to seat back displacement. To do this, the thickness of each component namely CM02, CM03, CM04, CM05 and CM09 is reduced by 10% and analyses are repeated for each reduction. It is concluded from Fig. 6.22 that seat back displacement is most sensitive to CM04.

In the light of optimization results, two lightweight prototypes were manufactured and tested. One prototype is produced by taking into account only size optimization results while both optimization results are considered for the second one.

The first prototype has a thickness reduction as well as a minor modification on CM04 base design. The free edge of CM04 is bended to increase bending stiffness as shown in Fig. 6.23. Parametric analyses are conducted using ANSYS Parametric toolbox. After several iterative simulations, new thicknesses of the components can be computed (see Table 6.5). Since seat back displacement is most sensitive to CM04 (see Fig. 6.1 for baseline model), an edge bend feature was added to decrease seat back displacement of the seat structure (see Fig. 6.23 for new design). The second prototype includes the changes in the first prototype and additional changes resulting from topology optimization. Middle region of CM03 is cut out on the basis of topology optimization result shown in Fig. 6.21. The new design is shown in Fig. 6.24.

Two prototypes are tested as per ECE R14 regulation and both are shown to meet the requirements of the regulation successfully with a remarkable weight reduction. The weight of the seat structure is reduced by 8% for the first prototype while reduction is about 10% for the second prototype. Both prototypes maintain their structural integrity. Seat back

Fig. 6.21 Geometry of CM03 after topology optimization

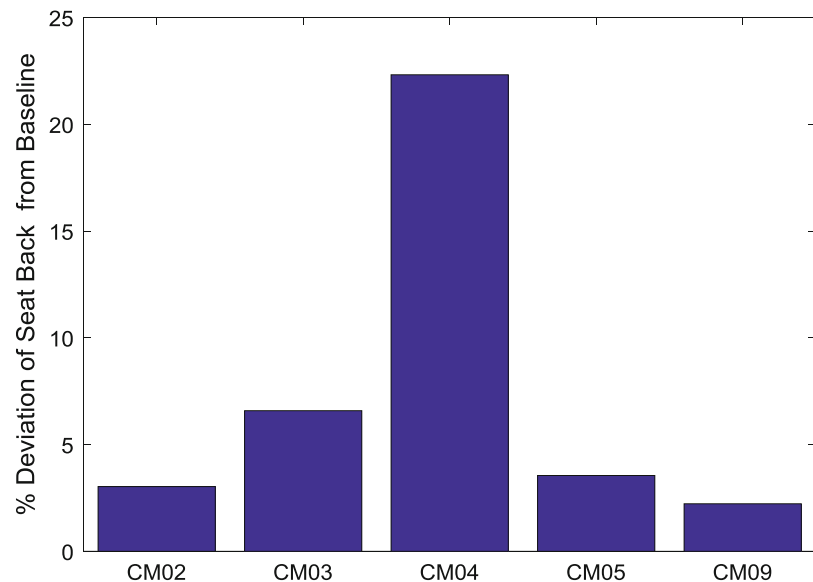


Fig. 6.22 Sensitivity study of several components

Table 6.5 New thickness of the seat structure

Components	CM02	CM03	CM04	CM05, CM06, CM07, CM08	CM09
Baseline thickness	3 mm	4 mm	2 mm	2.5 mm	4 mm
New thickness	2 mm	3 mm	1.8 mm	2 mm	3 mm

displacement is about 31 mm for the first prototype while it is 38 mm for the second prototype. Stiffness behavior of the prototypes and base design during the tests can be seen in Fig. 6.25. Prototype 1 has a considerably higher structural stiffness compared to base design. This improvement on stiffness can be explained by the addition of a flange on the CM04. Prototype 2 has a reduced structural stiffness due to removal of material from the middle region of CM03.



Fig. 6.23 Edge bend feature of CM04



Fig. 6.24 New design of CM03 obtained by cutting out of mid region

6.5 Conclusion

Lightweight component design is a vital issue to reduce CO₂ emission since automotive industry is regulated by national and international regulations such as ECE R14. Seat structure is among the most suitable automobile components for lightweight design, as seats are numerous in a mass transport vehicle. Therefore, lightweight seat structure design offers a promising approach to overcome the challenges of fuel consumption and CO₂ emission.

Implicit and explicit analysis techniques are discussed to get a virtual test environment using finite element methods. Firstly, implicit modeling of the seat structure is carried out to compute seatback displacement. ANSYS is used for implicit analysis. Secondly, the seat structure is represented by using Hypermesh and Hypercrash. Then, the seatback displacement is calculated using explicit solver, Radioss. In explicit model, seat belt and pulling devices are also included in the simulation model. Besides, the test is conducted as per ECE R 14 in order to validate both implicit and explicit models. According to test results, both methods accurately compute seatback displacement. However, implicit modeling of the seat structure has advantages in terms of computation time. Therefore, it is concluded that implicit model of the seat structure is accurate and the computation time is less than that of the explicit model.

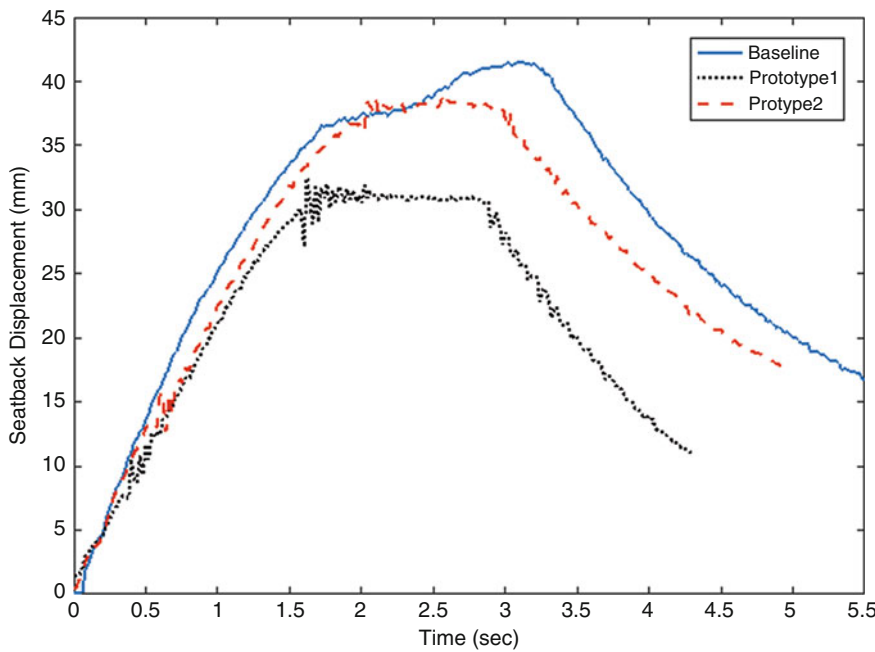


Fig. 6.25 ECE R14 test results of the base design and prototypes

Topology optimization is a key concept to design lightweight components. Topology optimization is conducted with the validated model using ANSYS Topology Optimization module. Moreover, size optimization is carried out to find optimum thickness of the components used in seat structure. Two prototypes are manufactured according to size and topology optimization results. Tests in the frame of ECE R14 regulations are applied to the prototypes. Both prototypes are shown to maintain structural integrity as expected according to the analysis results. Therefore, virtual test environment, created by finite element methods, reduces number of iterations. Finally, weight of the seat structure is shown to be successfully reduced by 10%, which will reduce weight of raw material used to manufacture seat structure and eventually fuel consumption and CO₂ emission.

References

1. A European Strategy for Low-Emission Mobility.: Available at http://europa.eu/rapid/press-release_MEMO-16-2497_en.htm?locale=en (2016). Accessed June 2017
2. P. Capros, A. De Vita et al.: EU Reference Scenario 2016: Energy, Transport and GHG emissions trends to 2050. European Commission, Greece (2016)
3. Road Safety.: Available at https://ec.europa.eu/transport/road_safety/specialist/knowledge/vehicle/safety_design_needs/buses_and_coaches_en (2017). Accessed 1 Jan 2017
4. Proposal for Amendments to ECE Regulation No.14, UNECE, 2011
5. Hessenberger, K.: Strength analysis of seat belt anchorage according to ECE R14 and FMVSS. In: 4th European LD-Dyna Users Conference, Germany, vol. 2223, pp. 15–20, May 2003
6. Singh, V., Ahmed, S.S.: Automotive seat modeling and simulation for occupant safety using dynamic sled testing. Int. J. Eng. Res. Technol. **3**(7), 1501–1505 (2014)
7. Pathy, S., Borrrell, T.: Quasi-static simulations using implicit LS-DYNA. In: 14th International LS-DYNA Users Conference, USA, pp. 1–8, 2016
8. Vatambe, A.: Simulation and validation of automotive seat using the regulation Fmvss 207/210. US-Hungarian Sci. Technol. Joint. **12**(1), 385–392 (2015)
9. Arslan, A., Kaptanoglu, M.: Development of seat anchorages of a commercial vehicle which are satisfying the requirements of ECE R-14 regulation. Otomotiv Teknol. **1**, 13–15 (2010)
10. Yüce, C., Karpat, F., Yavuz, N., Kaynakli, Ö., Dolaylar, E., Sendeniz, G.: Prototyping a new lightweight passenger seat. In: Proceedings of the ASME 2013 International Mechanical Engineering Congress & Exposition IMECE2013, USA, vol. 13, p. V013T14A034 (2013)
11. Sarisac, S., Kaya, N.: Design with topography and size optimization for passenger seat structure components. Otomotiv Teknol. Kongresi. **1**, 792–795 (2016)
12. Altair Optistruct. [Online]. (2017). Available: <http://www.altairhyperworks.com/product/OptiStruct>

13. Hyperstudy Overview. [Online]. (2017). Available: <http://www.hyperworks.fr/product/HyperStudy>
14. Roy, D., Dash, M.K.: Explorations of a family of stochastic Newmark methods in engineering dynamics. *Comput. Methods Appl. Mech. Eng.* **194**(45–47), 4758–4796 (2005)
15. Newmark, N.M.: A method of computation for structural dynamics. *J. Eng. Mech. Div.* **85**(7), 67–94 (1959)
16. Chopra, A.K.: *Dynamics of Structures*, 4th edn. Pearson, USA
17. Ozcelik, Y.: Modeling and Experimental Verification of Dynamic Characteristic of the Antenna Structure Under Mechanical Shock Using Mdof Models (2015), Turkey
18. Eduard Ventsel, T.K.: *Thin plates and Shells theory, analysis, and applications*, 1st edn. Marcel Dekker, New York (2001)
19. Bolt Depot.: Available at <https://www.boltdepot.com/fastener-information/materials-and-grades/bolt-grade-chart.aspx> (2016). Accessed 1 Jan 2017
20. Guideline for Tightening Torque.: Available at http://german.deltaregis.com/doc/Cat_Torque_Guideline_EN.pdf (2017). Accessed May 2017
21. ANSYS Inc.: Shell 181 Element Type, ANSYS 18 Help Viewer, 2017
22. Gokhale, N.S., Deshpande, S.S., Bedekar, S.V., Thite, A.N.: *Practical Finite Element Analysis*, 1st edn. Finite to Infinite, Pune (2008)
23. LS Dyna Support.: Available at <http://www.dynasupport.com/tutorial/ls-dyna-users-guide/time-integration> (2016). Accessed 1 Jan 2017
24. A. Inc.: ANSYS LS-DYNA in Mechanical APDL., ANSYS Inc., USA, pp. 1–54 (2013)
25. LS Dyna Time Step Size.: Available at <http://www.dynasupport.com/tutorial/ls-dyna-users-guide/time-step-size> (2016). Accessed 1 Jan 2017
26. Goelke, M.: Crash Analysis with RADIOSS – A Study Guide, 1st edn., Altair University, USA (2016)
27. Topology Optimization.: Available at https://en.wikipedia.org/wiki/Topology_optimization (2017). Accessed 1 Jan 2017



Chapter 7

ODS & Modal Testing Using a Transmissibility Chain

Brian Schwarz, Patrick McHargue, and Mark Richardson

Abstract In this paper, we show how Operating Deflection Shapes (ODS's) and mode shapes can be obtained experimentally from measurements that are made using **only two sensors** and **two short wires** to connect them to a multi-channel acquisition system. This new test procedure is depicted in Fig. 7.1. Not only is the equipment required to do a test much more cost effective, but this method can be used to test **any sized test article**, especially large ones.

The testing method introduced here involves moving a pair of sensors along together in a prescribed manor, and calculating the Transmissibility between them. The resulting chain of Transmissibility's is then post-processed to obtain a **single reference set** of cross-channel measurements, from which ODS's and mode shapes can be extracted.

A “**round trip**” example is used to show how an original set of modal parameters can be recovered by curve fitting a **single reference set** of output-only Cross spectra, and a **single reference set** of FRFs.

Keywords Fourier spectrum (DFT) · Auto power spectrum (APS) · Cross power spectrum (XPS) · Frequency Response Function (FRF) · Operating Deflection Shape (ODS) · Experimental Mode Shape (EMA Mode) · Operational Mode Shape (OMA Mode) · Modal Assurance Criterion (MAC) · Shape Difference Indicator (SDI)

7.1 Introduction

To obtain the experimental ODS's or mode shapes of a machine or structure, each degree-of-freedom (DOF) of a shape must contain the **correct magnitude & phase relative to all other DOFs**. If all of the sensor data is **simultaneously acquired**, each shape component will contain the correct magnitude & phase. However, simultaneous acquisition requires that all of the sensors be connected to a multi-channel acquisition system that can simultaneously acquire the data from all channels.

ODS's and mode shapes can be obtained from a set of cross-channel measurements if a **fixed reference sensor** is used, but the reference sensor must remain fixed throughout the test. For large test articles, the wire from the reference sensor to the acquisition system could be very long. Or, in a roving impact test, the wire from the instrumented hammer to the acquisition system could also be long (Fig. 7.1).

Operational modal parameters (frequencies, damping, mode shapes) are obtained by curve fitting a **single reference set** of output-only Cross spectra. An **experimental modal model** (a set of mode shapes containing the mass, stiffness and damping properties of the structure) is obtained by curve fitting a **single reference set** of calibrated FRFs.

An output-only Cross spectrum is a cross-channel frequency-based measurement that is defined as the Fourier spectrum of one response multiplied by the complex conjugate of the Fourier spectrum of the other response. An FRF is a cross-channel frequency-based measurement that is defined as the Fourier spectrum of a structural response (in displacement, velocity, or acceleration units) divided by the Fourier spectrum of an excitation force that caused the response.

A Transmissibility is also a cross-channel frequency-based measurement function. It is defined as the Fourier spectrum of one response divided by the Fourier spectrum on another response, as illustrated in Fig. 7.2.

B. Schwarz · P. McHargue · M. Richardson (✉)
Vibrant Technology, Inc., Centennial, CO, USA
e-mail: mark.richardson@vibetech.com

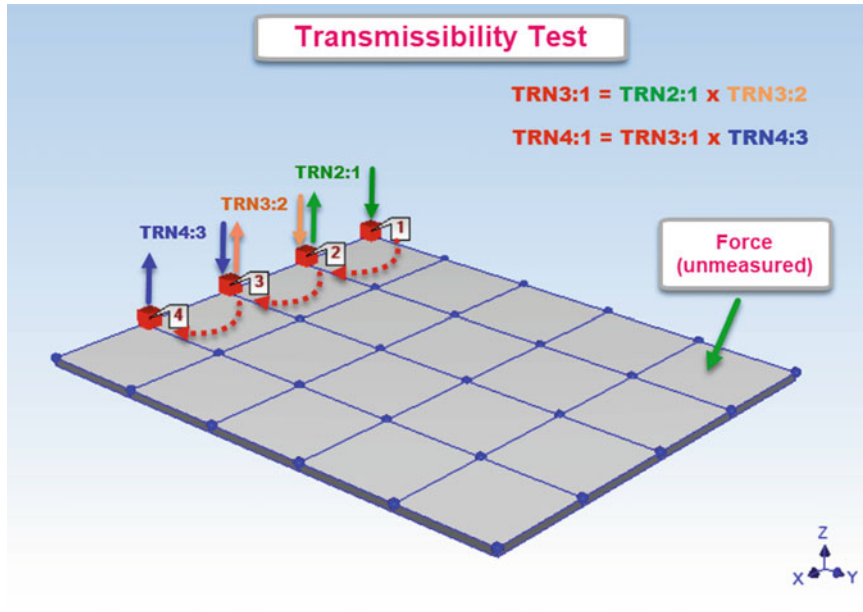


Fig. 7.1 Transmissibility chain measurement

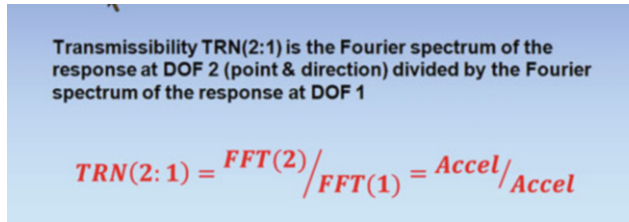


Fig. 7.2 Transmissibility

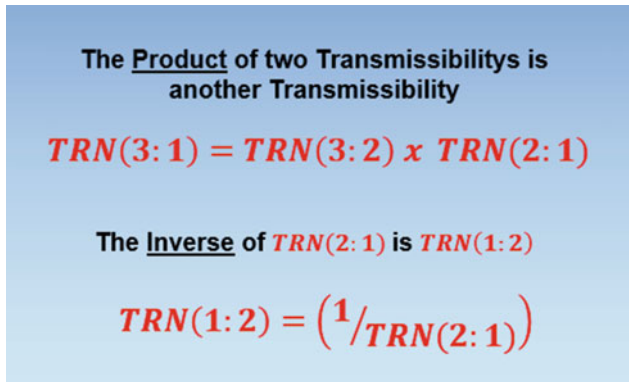


Fig. 7.3 Transmissibility properties

7.2 Transmissibility Properties

Transmissibility's have two unique properties that make them useful for recursive post-processing. Multiplying the Transmissibility between DOF 1 & DOF 2 by the Transmissibility between DOF 2 & DOF 3 gives the Transmissibility between DOF 1 & DOF 3. This property will be used to create a **Transmissibility Chain**, as depicted in Fig. 7.4.

The inverse property of Transmissibility's will also be used to measure Transmissibility's using a simple test procedure called a **Slinky Test**. A **Slinky Test** is depicted in Fig. 7.8 (Fig. 7.3).

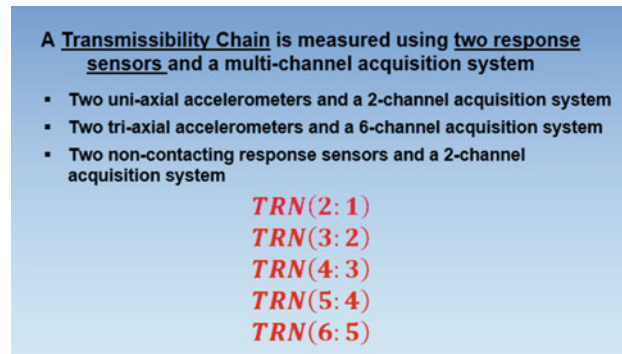


Fig. 7.4 1D or 3D chain measurement

7.3 Transmissibility Chain Measurement

In this new test procedure, Transmissibility's are measured in a chain fashion as depicted in Fig. 7.1. The three measurements shown in Fig. 7.1 are made with two sensors, (for example accelerometers), and a 2-channel acquisition system.

The sensor data used in the **denominator** of a Transmissibility is called the **Input**, and the sensor used in the **numerator** is called the **Output**. The test procedure is as follows;

1. Attach the sensors to points 1 & 2
2. Acquire vibration data with **point 1 designated as Input** and **point 2 designated as Output**
3. Calculate **TRN(2:1)**
4. Attach the sensors to points 2 & 3
5. Acquire vibration data with **point 2 designated as Input** and **point 3 designated as Output**
6. Calculate **TRN(3:2)**
7. Attach the sensors to points 3 & 4
8. Acquire vibration data with **point 3 designated as Input** and **point 4 designated as Output**
9. Calculate **TRN(4:3)**

A chain can be measured using either **uni-axial** or **tri-axial** sensors, as described in Fig. 7.4. Tri-axial sensors will measure 3D motion of the surface at each test point. This has the advantage of yielding ODS's and mode shapes that describe the **3D motion of the structure** at each point.

7.4 Benefits of Chain Measurement

The benefits of measuring a chain of Transmissibility's are listed in Fig. 7.5. This type of testing has its greatest advantage for testing running machines or vehicles, where the excitation forces are distributed and un-measureable. In other applications, excitation can be provided either with an impactor or with shakers, but only the responses are acquired, not the excitation forces.

7.5 Seeding the Chain

Once the Transmissibility Chain has been acquired for all points & directions (DOFs) on the structure, it can be “seeded” using either a Cross spectrum, an FRF, or an Auto spectrum.

- Seeding with a Cross spectrum (XPS) yields a **single reference set** of Cross spectra
- Seeding with an FRF yields a **single reference set** of FRFs
- Seeding with an Auto spectrum (APS) yields a **single reference set** of ODS FRFs
- Seeding the Chain with a calibrated measurement yields a **single reference set** of calibrated measurements

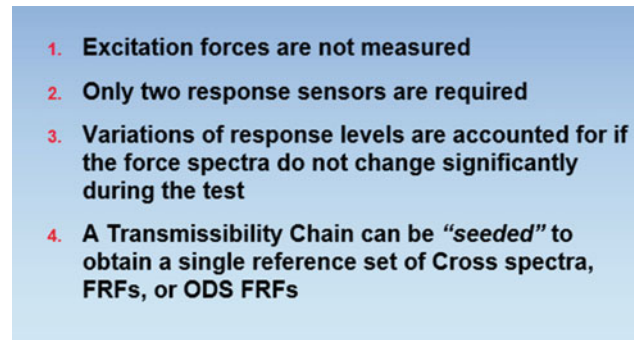


Fig. 7.5 Benefits of chain measurement

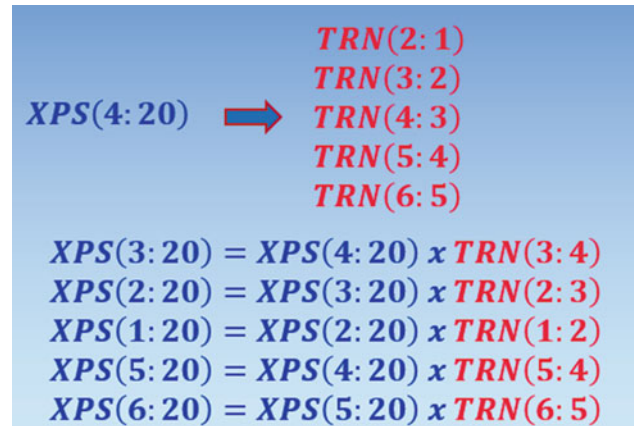


Fig. 7.6 Seeding with a Cross Spectrum.

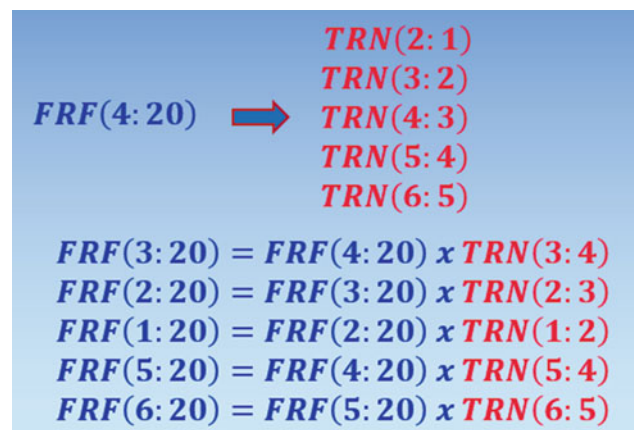


Fig. 7.7 Seeding with an FRF

Notice in Fig. 7.6 that the **reference DOF** of the Cross Spectrum is not used, so it can be from anywhere on the machine or structure. The only requirement for seeding a chain is that the **Output DOF of the seed XPS matches with a DOF of one of the Transmissibility's** in the Chain. Notice also that the Inverse property of the Transmissibility's is used during the recursive operation to “*walk along*” the Transmissibility Chain in both directions.

Seeding a Chain with FRFs is depicted in Fig. 7.7. Again, the FRF seed can be measured from force Input anywhere on the structure. The only requirement is that the **Output DOF of the seed FRF matches with a DOF of one of the Transmissibility's**.

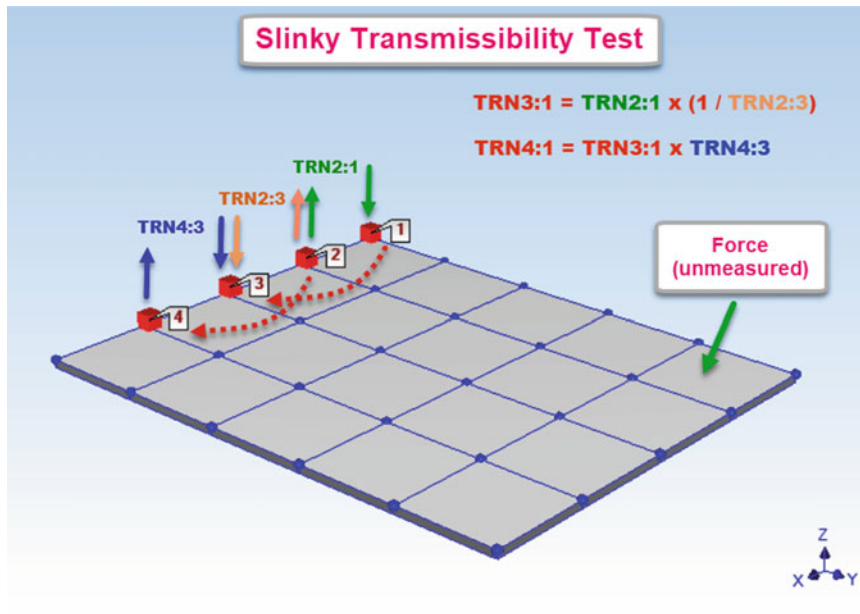


Fig. 7.8 Slinky test

7.6 Slinky Test

There is faster, easier way to acquire a Transmissibility Chain than the one depicted in Fig. 7.1. We call it a ***Slinky Test***, and it is depicted in Fig. 7.8. Notice in Fig. 7.8 that ***only one sensor has to be moved*** between acquisitions. Each time a sensor is moved it “***hops over***” the other sensor to the next test point on the structure, in a manner similar to the way a ***slinky spring*** walks down a stairway.

Comparing the test in Fig. 7.1 with the Slinky Test in Fig. 7.8, ***six sensor moves*** were made in Fig. 7.1 to measure three Transmissibility’s, whereas ***only two sensor moves*** were required in Fig. 7.8 to measure the same number of Transmissibility’s.

7.7 Round Trip Simulation

In order to verify the Transmissibility Chain testing method, a ***round trip simulation*** of a test was done using a modal model of the plate structure shown in Figs. 7.1 and 7.8. The modal model will be used to simulate random vibration of the plate. Then, Transmissibility’s will be “***acquired***” from the responses, and seeded to calculate single reference Cross spectra and FRFs. Finally, the original mode shapes will be recovered by curve fitting the Cross spectra and the FRFs.

To obtain the modal model, a **Roving Impact Test** was performed on the aluminum plate. A uni-axial accelerometer was attached to Point 1 as a reference, the plate was impacted with an instrumented hammer at each point, ***and a calibrated FRF*** was calculated between each impact point and the reference response.

An ODS display at one of the resonance peaks in the FRFs is shown in Fig. 7.9.

Next, the FRFs were curve fit to obtain Residue mode shapes for the five modes with resonance peaks in the FRF. The mode shapes are shown in Fig. 7.10.

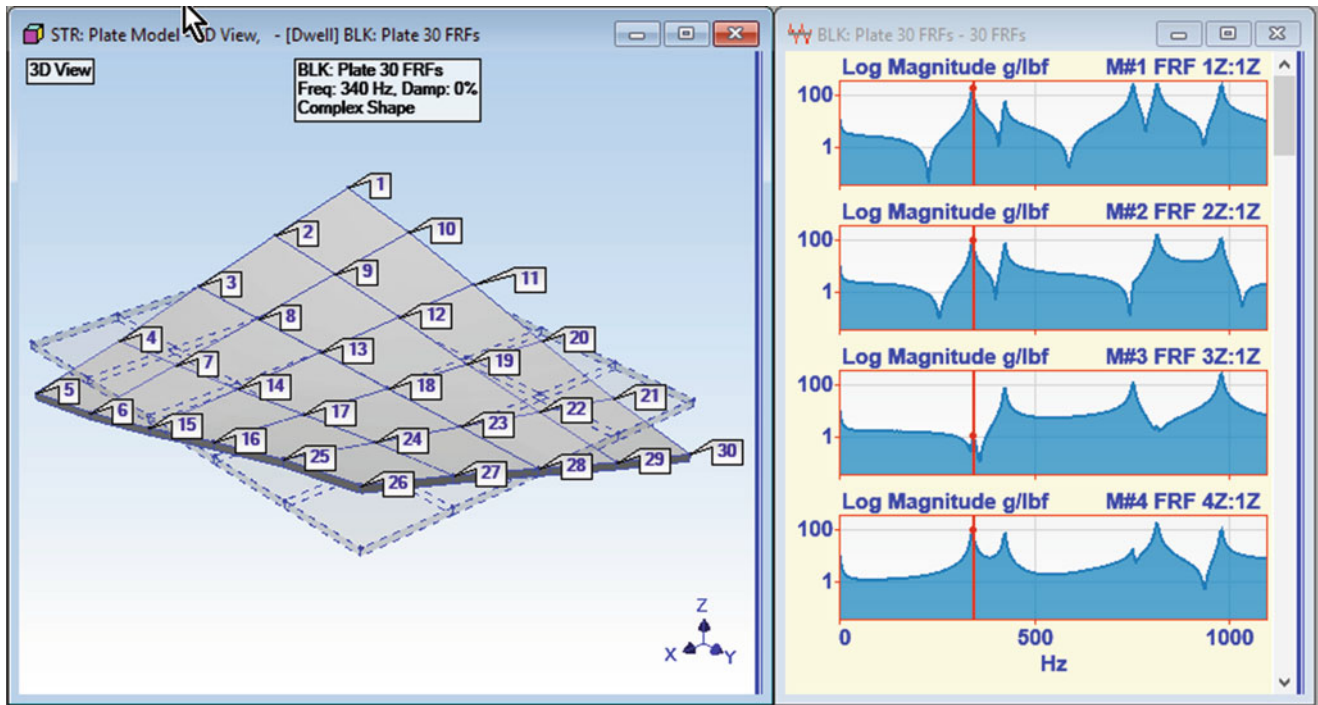


Fig. 7.9 ODS at a resonance peak in the FRFs

7.8 Burst Random Responses

The following steps were used to calculate time domain responses of the plate at all 30 points due to random excitation of the plate;

1. A sequence of ***ten burst random excitation waveforms*** was created as ***a simulated force Input*** to the plate at DOF 1Z.
2. The modal model (of calibrated mode shapes) was used to synthesize FRFs between 1Z and the 30 response DOFs of the plate.
3. The synthesized FRFs were multiplied by the Fourier spectrum of the Input force to obtain the Fourier spectrum of the Outputs, which were then transformed to the time domain waveforms shown in Fig. 7.11.

This process is referred to as **Multi-Input Multi-Output (MIMO) Modeling & Simulation**. Any type of forcing function can be used with MIMO simulation, but a burst random force sequence was used to ***eliminate leakage*** in the response Fourier spectra.

A ***pure random Input*** would more accurately simulate real world excitation of a machine or structure. However, in this case burst random excitation was used to minimize errors so that the original mode shapes could be recovered by post-processing the Transmissibility Chain.

Some of the burst random responses are shown in Fig. 7.11. Notice that the burst random length was chosen so that the structural responses would decay to “***nearly zero***” by the end of each burst sequence.

In real-world testing applications, the burst length will depend on the damping in the structure, which is always reflected in the damping of the resonances or modes.

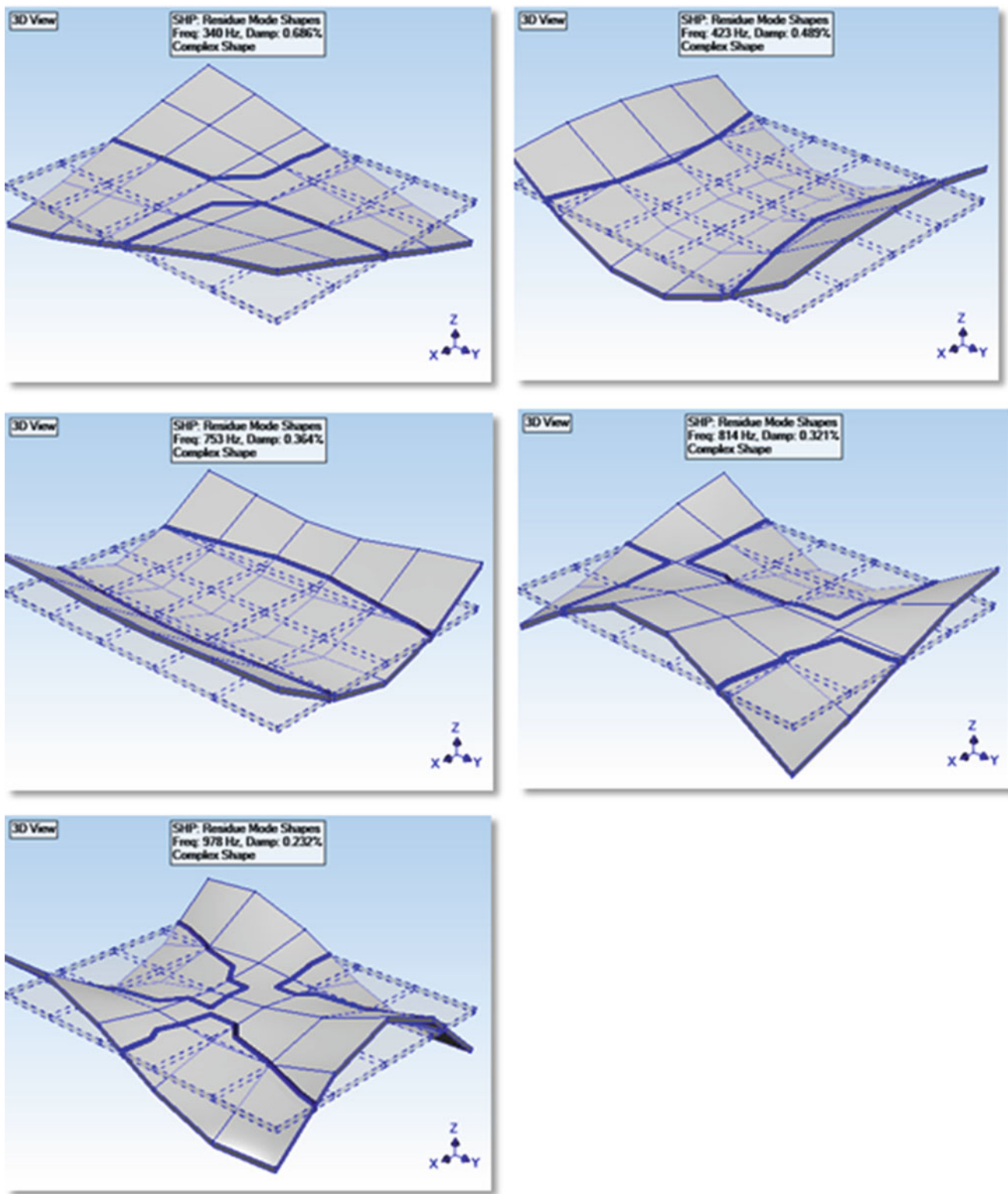


Fig. 7.10 Mode shapes of the plate

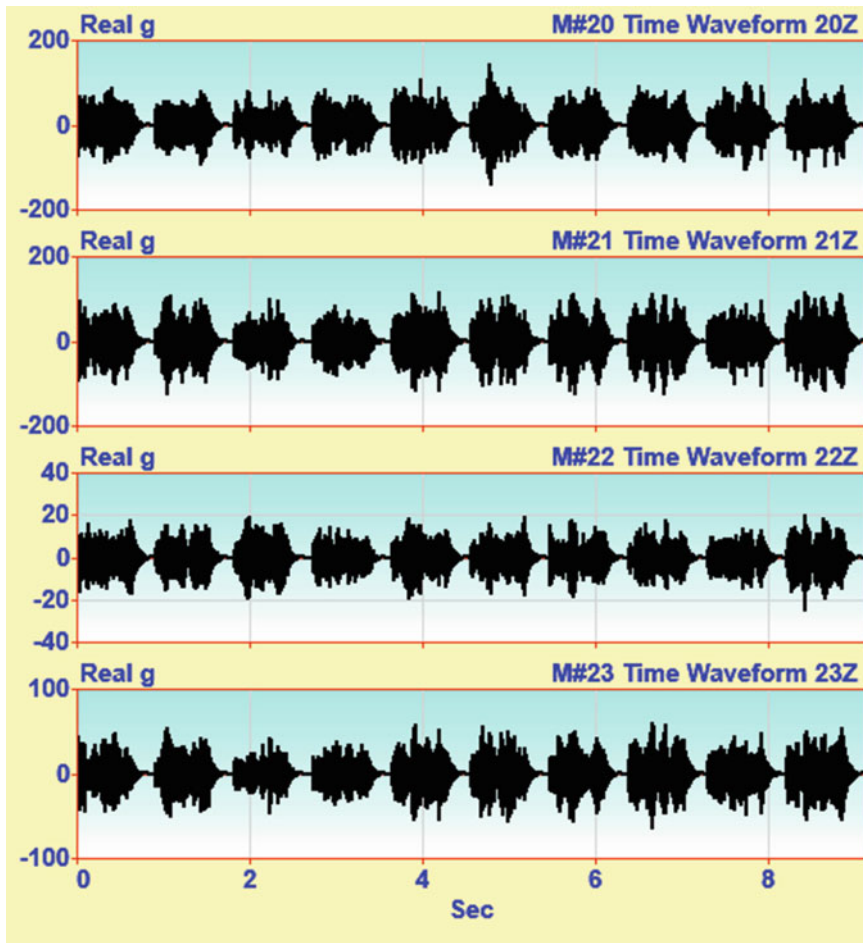


Fig. 7.11 Burst random responses

7.9 Calculating a Transmissibility Chain

A Transmissibility Chain was calculated from time waveforms that were “*acquired*” from the burst random responses, shown in Fig. 7.11. Each Transmissibility was calculated using the first response as an **Input** and the second as an **Output**, as indicated by the arrows in Fig. 7.1.

A chain of 29 Transmissibility’s was calculated between each pair of points on the aluminum plate, as depicted in Fig. 7.4. Some of the Transmissibility’s are displayed in Fig. 7.12.

It must be emphasized that the peaks in a Transmissibility are *not resonance peaks*. Hence, ODS’s or mode shapes cannot be obtained directly from Transmissibility’s. **Transmissibility’s cannot be curve fit using an FRF-based curve fitting method.** A Transmissibility is a different complex waveform than an FRF.

7.10 Calculating Single Reference Cross Spectra

The Transmissibility Chain of 29 Transmissibility’s was *seeded*, as depicted in Fig. 7.6, using the **Cross spectrum 1Z:1Z**. This yielded a *single reference set of Cross spectra*, some of which are shown in Fig. 7.13.

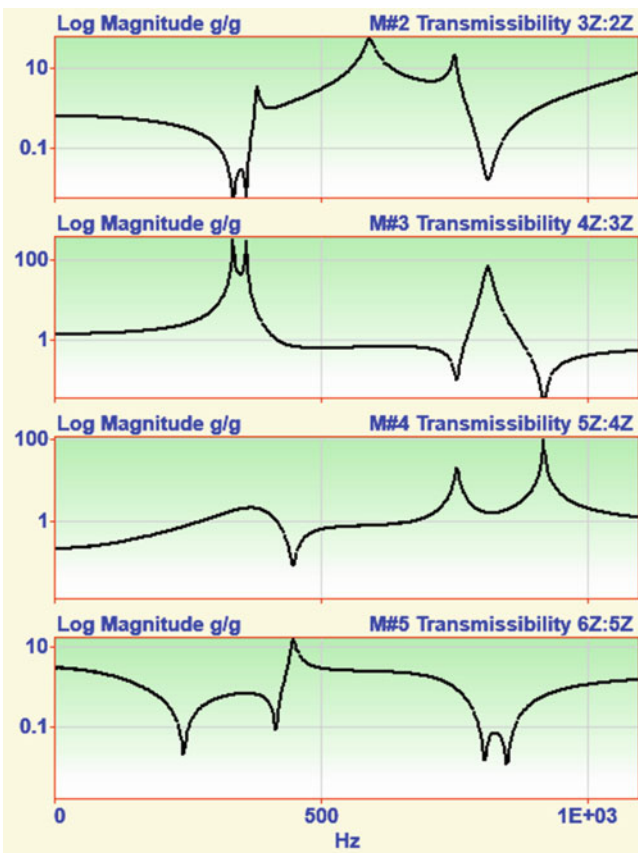


Fig. 7.12 Transmissibility chain

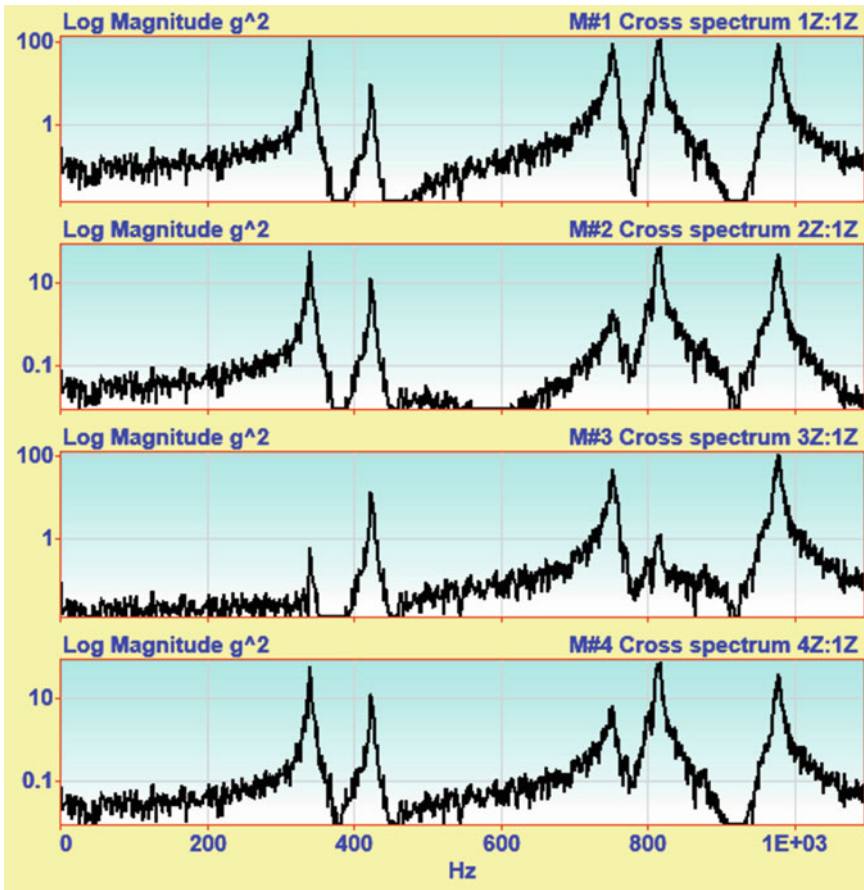


Fig. 7.13 Single reference set of cross spectra

7.11 Calculating Single Reference FRFs

The Transmissibility Chain of 29 Transmissibility's was also *seeded*, as depicted in Fig. 7.7, using the **driving point FRF 1Z:1Z**. This yielded a *single reference set of FRFs*, some of which are shown in Fig. 7.14.

7.12 Curve Fitting Results

The single reference set of 30 Cross spectra was curve fit using a deconvolution window followed by an FRF-based curve fitter. The resulting modal frequency & damping estimates are compared with the original modal parameters in Fig. 7.15. When paired with the original mode shapes, the mode shapes obtained by curve fitting the Cross spectra all had **MAC values of 1.0**. A MAC value *equal to 1.0* indicates that the two mode shapes are co-linear.

The single reference set of 30 FRFs was also curve fit. The resulting modal frequency & damping estimates are compared with the original modal parameters in Fig. 7.16. When paired with the original mode shapes, the mode shapes obtained by curve fitting the FRFs all had **SDI values equal to 1.0**.

The Shape Difference Indicator (SDI) [1] measures the true difference between two shapes, whereas the Modal Assurance Criterion (MAC) [2] measures the co-linearity of two shapes. Curve fitting a set of Cross spectra yielded mode shapes that were *co-linear with* the original Residue mode shapes. Curve fitting a set of FRFs yielded mode shapes that were *equal to* the original mode shapes.

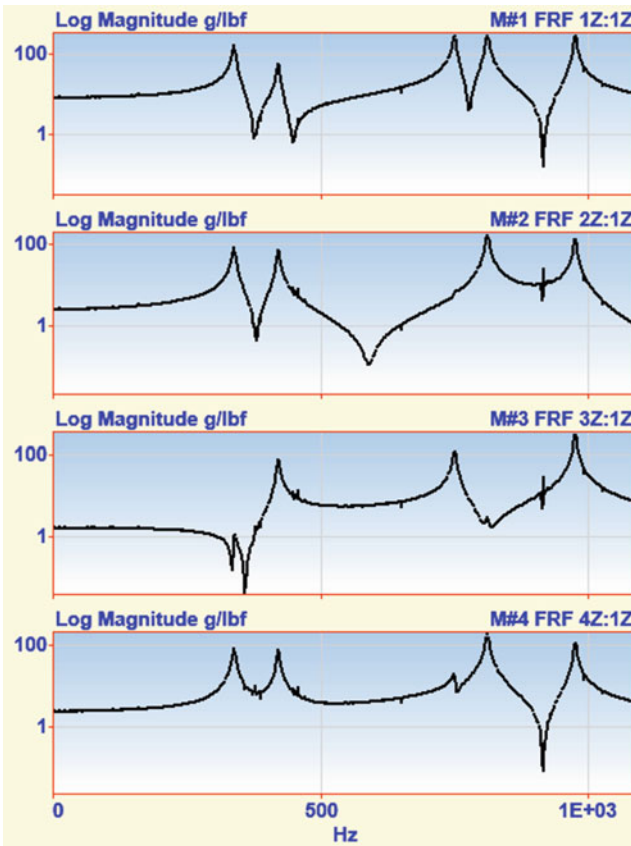


Fig. 7.14 Single reference et of FRFs

Mode Number	Original Frequency (Hz)	XPS Frequency (Hz)	Original Damping (Hz)	XPS Damping (Hz)
1	340.0	339.6	2.333	1.648
2	423.0	422.8	2.070	1.501
3	752.6	752.0	2.740	3.248
4	813.8	814.2	2.610	2.623
5	978.2	977.0	2.266	2.729

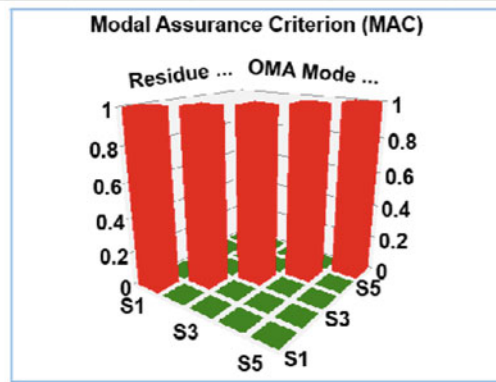


Fig. 7.15 XPS versus original modal parameters

Mode Number	Original Frequency (Hz)	FRF Frequency (Hz)	Original Damping (Hz)	FRF Damping (Hz)
1	340.0	340.0	2.333	2.316
2	423.0	423.0	2.07	2.082
3	752.6	752.6	2.74	2.734
4	813.8	813.8	2.61	2.629
5	978.2	978.2	2.266	2.244

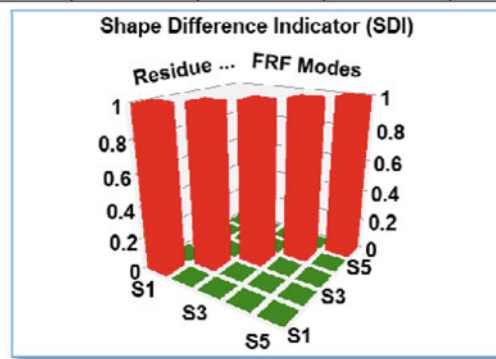


Fig. 7.16 FRFs versus original modal parameters

7.13 Conclusion

In order to obtain experimental ODS's or mode shapes, a ***single reference set*** of measurements is required. This means that ***one sensor must remain fixed*** throughout the test. To test a large structure, a long wire may be required to connect one of the sensors to the acquisition system.

In this paper, a new test procedure was introduced, which is based on the measurement of a Transmissibility Chain. A primary benefit of this testing method is that any machine or structure can be tested using two response sensors, a 2-channel acquisition system, and ***two short wires*** from the sensors to the acquisition system.

Another benefit of this method is that ***only structural responses are measured. The excitation forces do not have to be measured***. Hence, this method can be used to test running machinery, large or small, and to test large structures such as road bridges and buildings. In both of these cases, the excitation is distributed and un-measurable.

A ***Slinky Testing method*** was also introduced, which makes measurement of a Transmissibility Chain even easier. This simple method of ***hopping one sensor over the other*** between measurements is straightforward to implement.

It was shown with a ***round trip*** example how modal parameters can be recovered by curve fitting a single reference set of Cross spectra and a single reference set of FRFs. Starting with an experimental modal model of an aluminum plate, MIMO simulation was used to calculate its responses to a burst random excitation force.

The plate responses were used to calculate a Transmissibility Chain. Then, the Chain was ***seeded*** with a Cross spectrum to yield a ***single reference set of Cross spectra***. The same Chain was also seeded with an FRF to yield a ***single reference set of FRFs***. The modal parameters obtained from curve fitting both the Cross spectra and the FRFs closely matched the parameters of the original modal model.

There is one drawback to this method, however. If the seeding function, or any Transmissibility in the Chain, has errors in it, those errors will be propagated in the direction of calculation in the Chain. In Fig. 7.17, it is shown how the noise error in the seed (***FRF 1Z:1Z***) was propagated to the other FRFs.

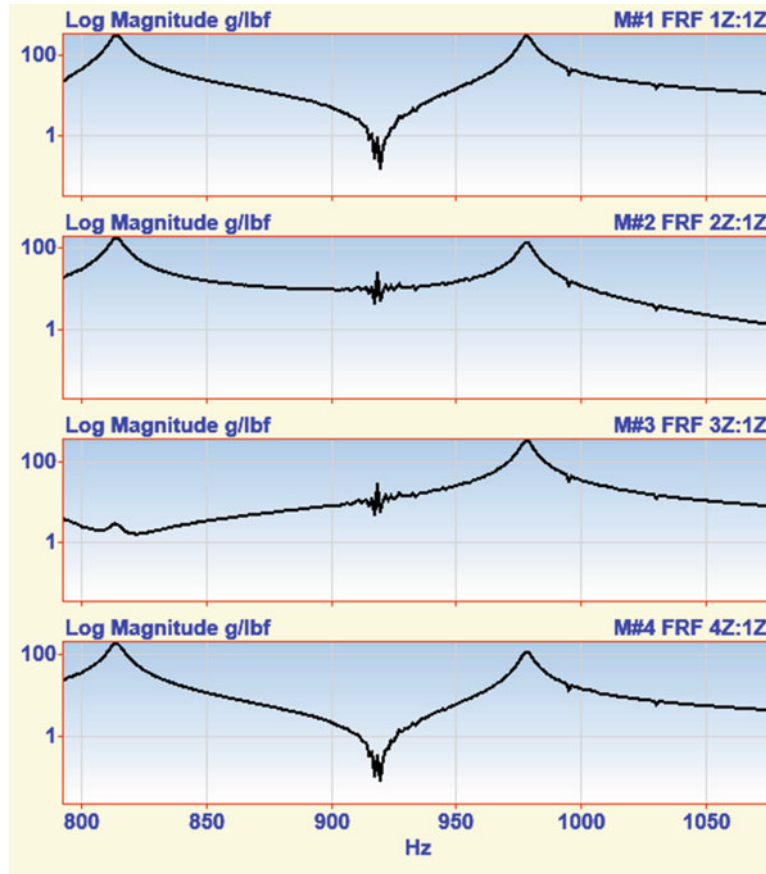


Fig. 7.17 Noise propagation

References

1. Richardson, S., Tyler, J., McHargue, P., Schwarz, B., Richardson, M.: A New Measure of Shape Difference. In: IMAC XXXII, February 3–6 (2014)
2. Richardson, S., Tyler, J., McHargue, P., Richardson, M.: Using Modal Parameters for Structural Health Monitoring. In: IMAC XXXV, January 30–February 2 (2017)
3. Allemand, R.J.: The modal assurance criterion (MAC): twenty years of use and abuse. In: Proceedings of the International Modal Analysis Conference (2002)



Chapter 8

Correlating Spectral Measurements

Shawn Richardson, Jason Tyler, Brian Schwarz, and Mark Richardson

Abstract In a recent paper (Richardson et al. (2014) A new measure of shape difference, In: IMAC XXXII, February 3–6), we introduced a new metric for comparing two operating .deflection shapes called the ***Shape Difference Indicator (SDI)***. In another previous paper (Richardson et al. (2017) Using modal parameters for structural health monitoring, In: IMAC XXXV, January 30–February 2), we used SDI to measure the difference in modal frequencies resulting from a joint stiffness change in a mechanical structure.

In this paper we use SDI in two new ways. In the first application, SDI is used to ensure that a repeatable impact is applied to a structure during a Roving Response ODS or Modal test. In the second application, SDI is used to measure the difference between ***currently acquired and Baseline*** Auto spectrum measurements over prescribed frequency band.

We have implemented SDI together with a search method for ranking ***currently acquired and archived data*** based upon their numerical differences. We call this new method Fault Correlation Tools (FaCTs™). FaCTs™ is useful in multiple applications, including route-based machine condition monitoring, structural health monitoring, production qualification testing, machinery recertification following scheduled maintenance, and noise & vibration monitoring in public places such as building construction sites to comply with local ordinances.

Keywords Fourier spectrum (FFT) · Auto power spectrum (APS) · Cross power spectrum (XPS) · Frequency Response Function (FRF) · Operating Deflection Shape (ODS) · Modal Assurance Criterion (MAC) · Shape Difference Indicator (SDI)

8.1 Introduction

SDI has been previously used for correlating two complex shapes, either ODS's or mode shapes [2, 3] It was also used for correlating shapes with modal frequencies as their shape components to detect and quantify joint stiffness changes [4]. In this paper, SDI will again be used to measure the difference between two shapes, but in a different sense. SDI will be used to measure the difference between multiple FRFs, and also to measure the difference between multiple Auto spectra in several frequency bands.

In its first application, SDI will be used to compare three reference FRF measurements with three **Baseline FRFs**. This comparison is done at the same frequency in the two blocks of measurements. An ODS is defined as structural deflection at a single frequency sample. Therefore, we have named this comparison of two blocks of data **ODS Correlation**,

ODS Correlation can be used throughout a Roving Response Impact test to ensure that the structure is impacted at the same impact location & direction, (degree-of-freedom or DOF). ODS Correlation can also be used to ensure that removable sensors are attached at the correct DOFs during a route-based condition-monitoring program.

In its second application, SDI is used to measure the difference between pairs of Auto spectra in multiple prescribed frequency bands. We call this comparison **Measurement Pairs Correlation**. Rather than use the conventional approach of comparing peak spectrum values with handbook values, Measurement Pairs Correlation numerically compares the “***shape***” of an Auto spectrum in a frequency band with the “***shape***” of another Auto spectrum with a matching DOF in the same frequency band.

S. Richardson · J. Tyler · B. Schwarz · M. Richardson (✉)
Vibrant Technology, Inc., Centennial, CO, USA
e-mail: mark.richardson@vibetech.com

Measurement Pairs Correlation will be used to correlate a block of **Baseline Auto spectra** with blocks of currently acquired Auto spectra thus creating a table of SDI values. FaCTs™ will then be applied to the archived SDI values to indicate a change in the operating condition of a rotating machine, and to identify a pre-defined unbalance condition in the machine.

8.2 Review of MAC and SDI

SDI is similar to MAC, which was originally developed to provide a numerical comparison between two mode shapes [5]. Like MAC, SDI is a **correlation coefficient** with values that range between 0 and 1. A value **equal to 1** indicates no difference between two shapes. A value **less than 1** indicates that two shapes are different.

The mathematical formulas utilized by these two metrics were presented in a previous paper [3]. Both are briefly reviewed here to point out their differences.

MAC was developed as a metric for correlating two mode shapes [5]. SDI was developed for a similar purpose, but it has different properties.

1. MAC indicates the **co-linearity** of two shapes. If two shapes lie on the same straight line, $\text{MAC} = 1$
2. MAC cannot measure the difference between two numbers. $\text{MAC} = 1$ if two shapes have only one component

Summarizing the MAC properties, if **MAC = 1**, then two shapes lie on the same straight line. If **MAC < 1**, then two shapes do not lie on the same straight line.

In contrast to MAC, if **SDI = 1**, then two shapes have **identical shape components**. If **SDI < 1**, then two shapes have **different shape components**. Several examples illustrate typical SDI values between two shapes {A} & {B}.

- If $\{A\}=\{B\}$, $\text{SDI} = 1$
- If $\{A\}=\{0\}$ or $\{B\}=\{0\}$, $\text{SDI} = 0$
- If $\{A\}=2\{B\}$, $\text{SDI} = 0.64$
- If $\{A\}=10\{B\}$, $\text{SDI} = 0.04$

Figure 8.1 is a plot of MAC for two shapes {A} & {B}. It shows that if vector {B} has values that **lie anywhere along the line** defined by vector $\{A\} = \{1, 1\}$, then MAC has a value of “1”.

Figure 8.2 is a plot of SDI for the same two shapes {A} & {B}. It shows that there are **only two values** of vector {B} where SDI has a value of “1”; $\{B\} = \{1, 1\}$ and $\{B\} = \{-1, -1\}$.

SDI has two unique properties, which make it more useful for measuring the difference between two vectors.

1. $\text{SDI} = 1$ under only two conditions, when $B = + - A$
2. SDI can measure the difference between **two scalars (two numbers)**

For these reasons, we will use SDI as the preferred metric for quantifying the **difference between two “shapes”** (or **vectors**) of spectral data.

8.3 Two Types of Measurement Correlation

SDI can be used to measure the difference between two sets of spectrum measurements at **a single frequency**, or it can be used to measure the difference between a pair of spectra over a band of frequencies. We call the first type of correlation **ODS Correlation**, and the second type **Measurement Pairs Correlation**.

8.3.1 ODS Correlation

Two (or more) spectral measurements can be correlated by measuring the difference between their values, **sample by sample**. We call this type of correlation **ODS Correlation** because the values at any frequency sample in a set of experimental Cross spectra, FRFs, or ODS FRFs can be displayed on a model of the test article as an ODS, (or deformation shape) of the structure at that frequency.

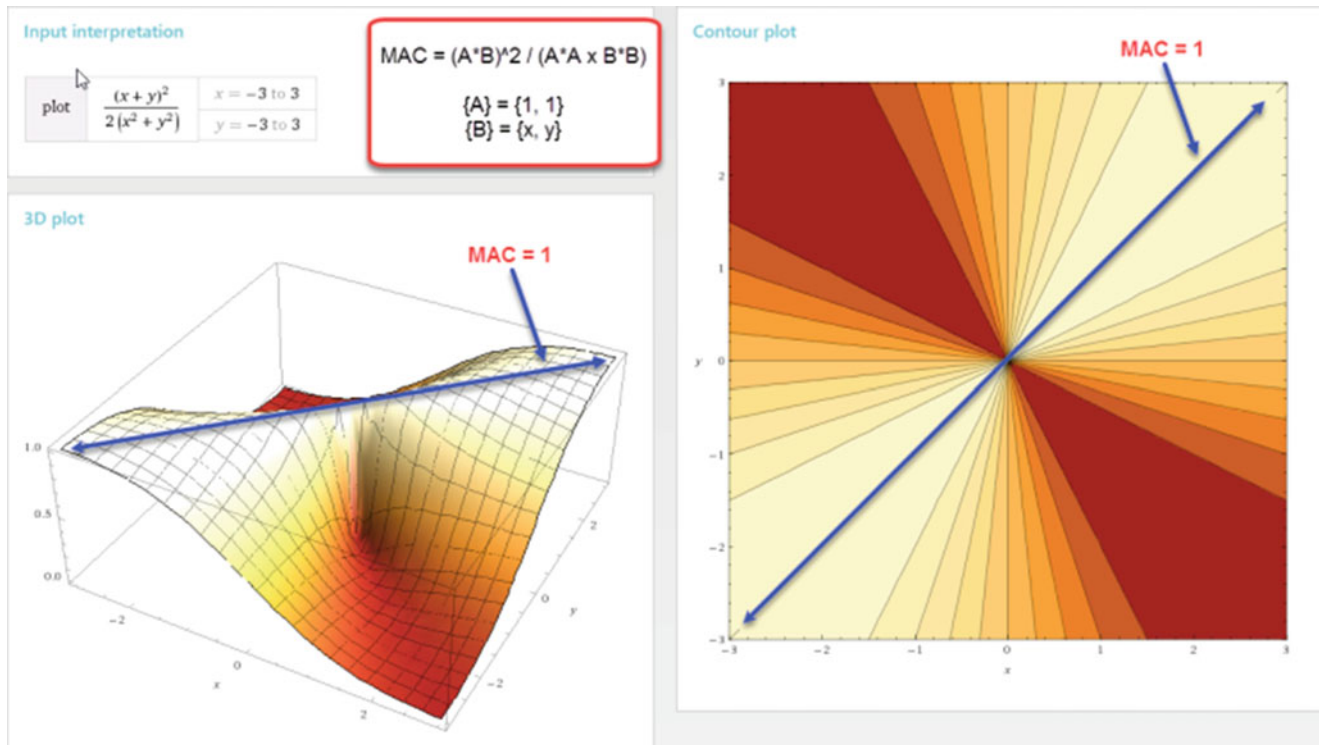


Fig. 8.1 MAC plot of Shape {A} vs. Shape {B}

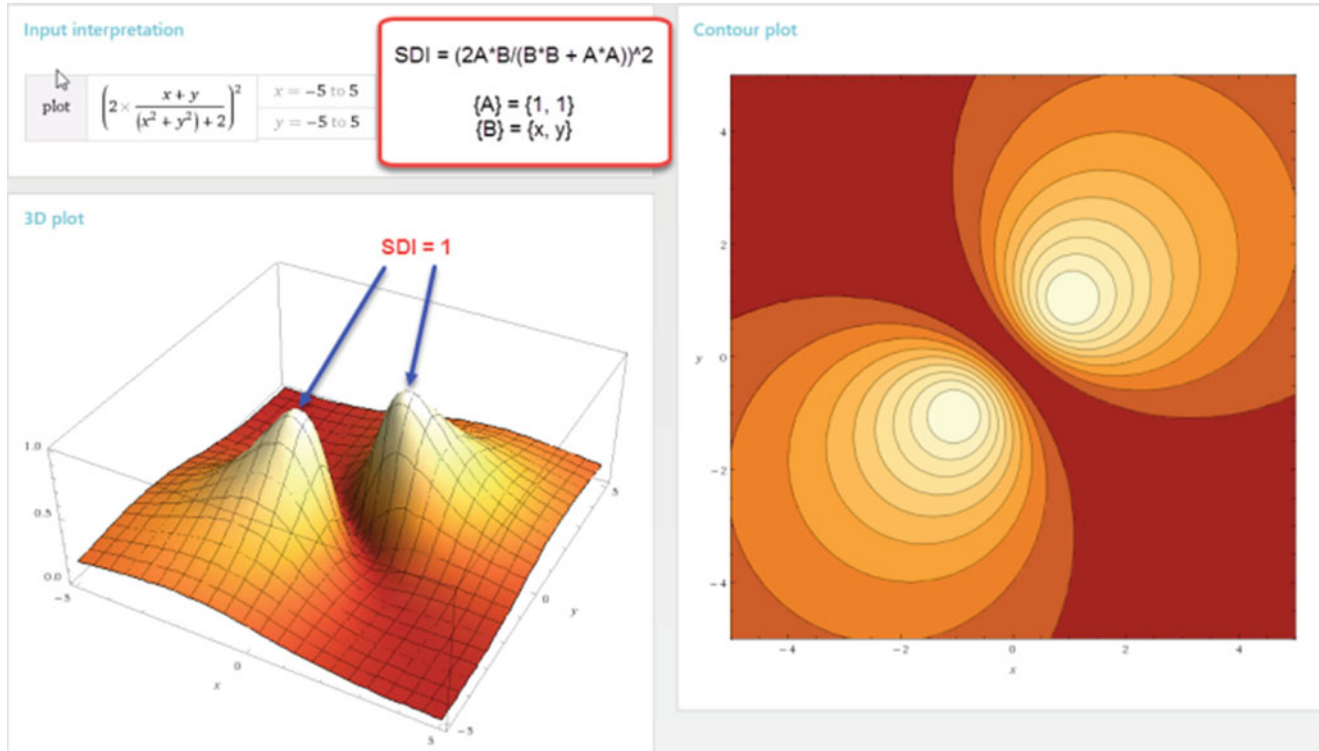


Fig. 8.2 SDI plot of Shape {A} vs. Shape {B}

In **ODS Correlation**, an SDI value is calculated *for each frequency sample* in the band over which two blocks of measurements are compared. An example is shown in Fig. 8.4.

8.3.2 Measurement Pairs Correlation

In Measurement Pairs Correlation, SDI is used to measure the difference between a pair of spectral measurements *over a band of frequencies*. The pair of spectra is assumed to have been calculated from data taken at the same DOF on the machine or structure.

- If two spectra have the *same value* at each sample in a band of frequencies, then $SDI = 1$
- If two spectra have *different values* at each sample in a band of frequencies, then $SDI < 1$

SDI measures the difference between the “*shapes*” of the two spectra, over the same band of frequencies.

MAC has also been used to measure the difference between two FRFs, and has therefore been called the **Frequency Response Assurance Criterion** (or **FRAC**),

If two blocks of spectral measurements with matching DOFs are correlated, a table of SDI values is created, with one SDI value for each matching pair. Each SDI value is a measure of the difference between the values of a spectrum in one block versus the values of the spectrum with a matching DOF in a second block, over the same band of frequencies.

8.4 Repeatable Impact

Like MAC and Coherence, SDI has values between 0 and 1. Like both of these other metrics, SDI can also be used as part of a testing procedure to insure that repeatable measurements are being made.

A popular way to perform an ODS or Modal test on a machine or structure is to test it using an instrumented impact hammer, a tri-axial accelerometer, and a 4-channel acquisition system. This is also called a “*bump test*” when it is done on an operating machine.

Impacting a structure is a good way to excite its resonances because the impact force will excite a broad band of frequencies. There are two ways to perform an impact test.

8.4.1 Roving Impact Test

This is the most popular type of impact test. In this test, the accelerometer is attached at a single point, and a different DOF is impacted with the hammer for each acquisition of data.

8.4.2 Roving Response Test

In this test, the structure is *impacted at the same DOF*, and the response sensor (for example, a tri-axial accelerometer) is moved to a new point prior to each acquisition of data.

The advantage of a Roving Response test is that if a tri-axial sensor is used, 3D ODS's and mode shapes can be obtained from the data. In other words, the *3D deformation of the structure* at each Roving Response point is obtained at each frequency.

To obtain a valid set of measurements from a Roving Response test, the structure *must be impacted at the same DOF* throughout the test.

8.4.3 Impact Repeatability Check

ODS Correlation can be used during a Roving Response test to insure that the structure is *always impacted at or near same DOF*. Using another (*fixed*) **reference** accelerometer, an impact Repeatability Check involves the following steps;

1. Attach the **reference accelerometer** anywhere on the structure. The accelerometer can be uni-axial or tri-axial,
2. Impact the structure at the fixed DOF chosen for the Roving Response test, and calculate one or more **Baseline FRFs** between the impact DOF and the DOFs of the reference accelerometer.
3. During the Roving Response test, each time an FRF is calculated between the impact DOF and the Roving Sensor, also calculate one or more **Repeatable FRFs** between the impact DOF and the reference accelerometer.
4. Calculate and display the **ODS Correlation** between the **Repeatable FRFs** and the **Baseline FRFs**.

To illustrate a Repeatability Check, a tri-axial accelerometer was attached as a **reference accelerometer** to the beam structure shown in Fig. 8.3. The beam was then impacted with an instrumented hammer at Point 1, and three **Baseline FRFs** were calculated between the impact force and the three responses of the **reference accelerometer**. These three **Baseline FRFs** were the result of impacting the structure at Point 1.

Figure 8.4 shows the results of impacting *at or near* Point 1 a second time. The FRFs and Coherences from the second impact measurement are shown on the left, and the Baseline FRFs and **ODS Correlation** are shown on the right.

In Fig. 8.4, the **ODS Correlation** (SDI values) with the Baseline FRFs is *close to “1”* for most of the frequencies. This means that the second set of FRFs was calculated from data that resulted from an impact applied *at or near* Point 1.

The results of impacting at Points 2 & 3 are shown in Figs. 8.5 and 8.6 respectively. Notice that in both cases, the ODS Correlation is *less than “1”* for many frequencies. Those FRF measurements *did not correlate well* with the Baseline FRFs at the frequencies with low SDI values. Of course this is expected since those impacts were not applied *at or near* Point 1.

Notice however that some ODS Correlation values are *close to “1”* for some frequencies in Figs. 8.5 and 8.6. This means that the FRFs calculated from impacting at Points 2 & 3 *did correlate well* with the Baseline FRFs at some frequencies. At those frequencies where the ODS Correlation values are *close to “1”*, it can be assumed that the structural response is *dominated by resonances* that have mode shape components similar in value to the mode shape components in the Baseline FRFs.

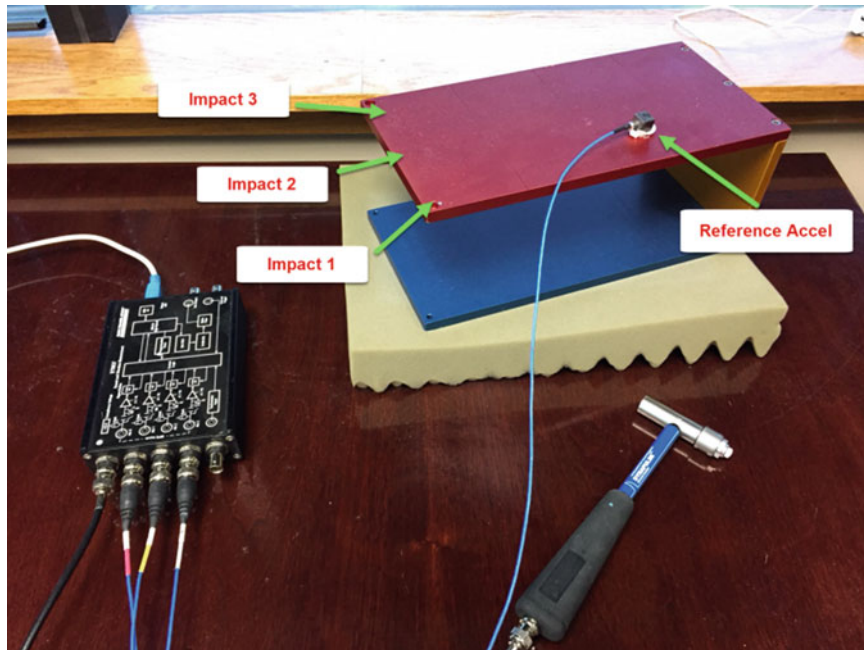


Fig. 8.3 Repeatability check

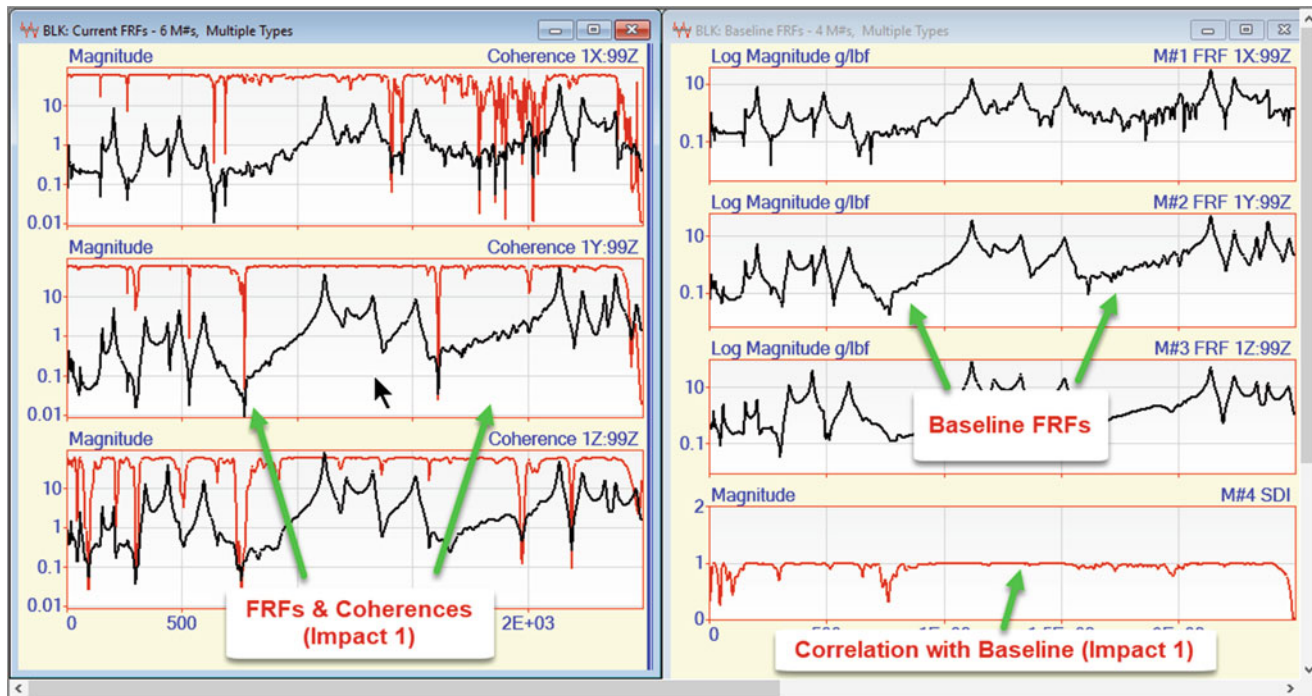


Fig. 8.4 Impact 1

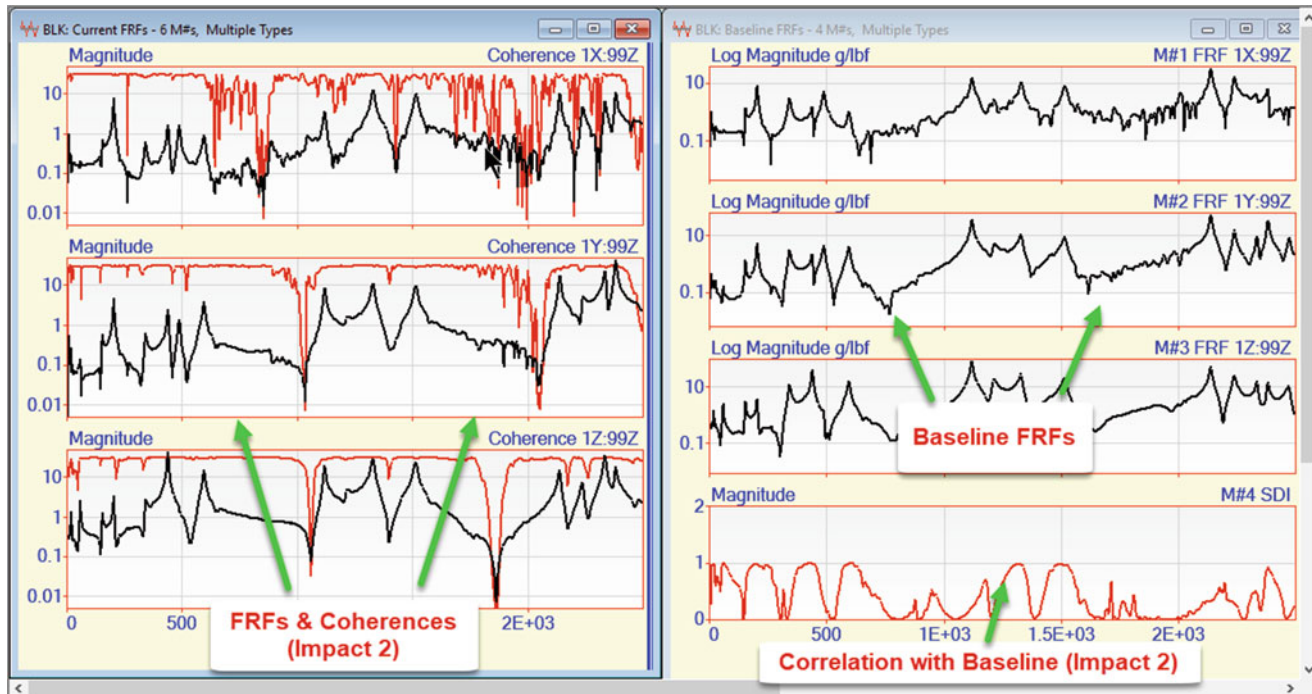


Fig. 8.5 Impact 2

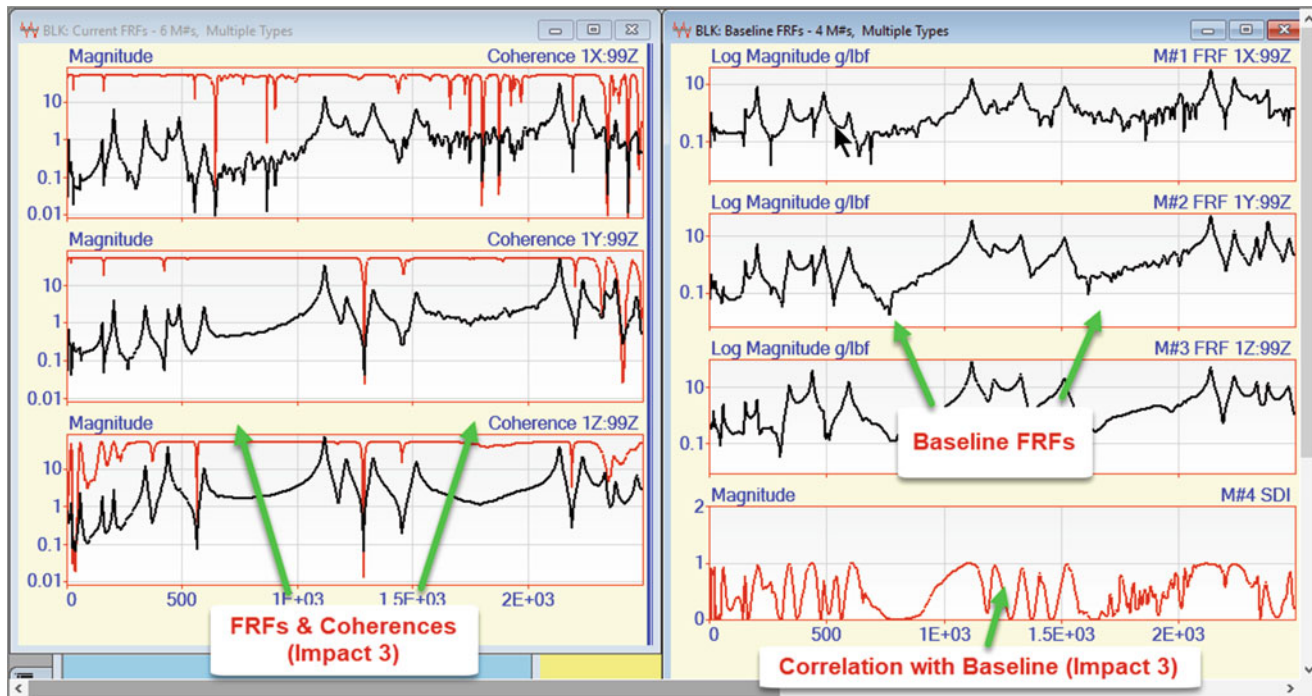


Fig. 8.6 Impact 3

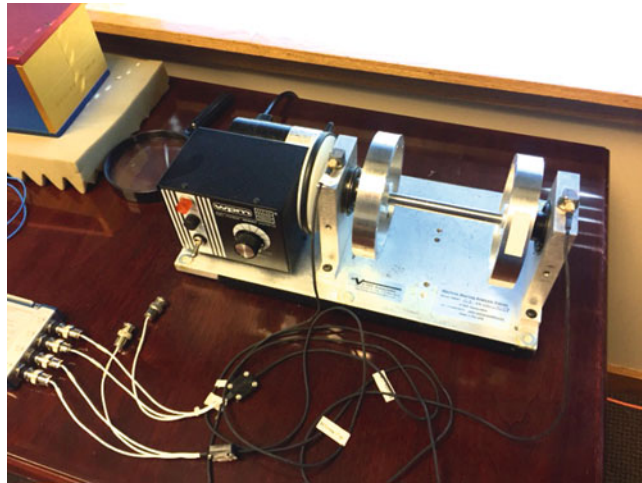


Fig. 8.7 Rotating machine simulator

8.5 Correlating Auto Spectra

In this second application, Measurement Pairs Correlation is combined with the FaCTs™ search method to indicate both a change in the operating condition of a rotating machine, and to identify a known unbalance condition in the machine.

To illustrate the combined use of **Measurement Pairs Correlation** and FaCTs™, *four Auto spectra* were calculated from two tri-axial accelerometers mounted on the bearing blocks of the rotating machine trainer shown in Fig. 8.7.

A 4-channel acquisition system was used to acquire the accelerometer data, and only the horizontal (X) and vertical (Z) vibration signals were acquired from the machine. The axial (Y) direction was not acquired. The model in Fig. 8.8 shows the horizontal (X) and vertical (Z) measurement directions of the two accelerometers attached with magnets to the two bearing blocks.

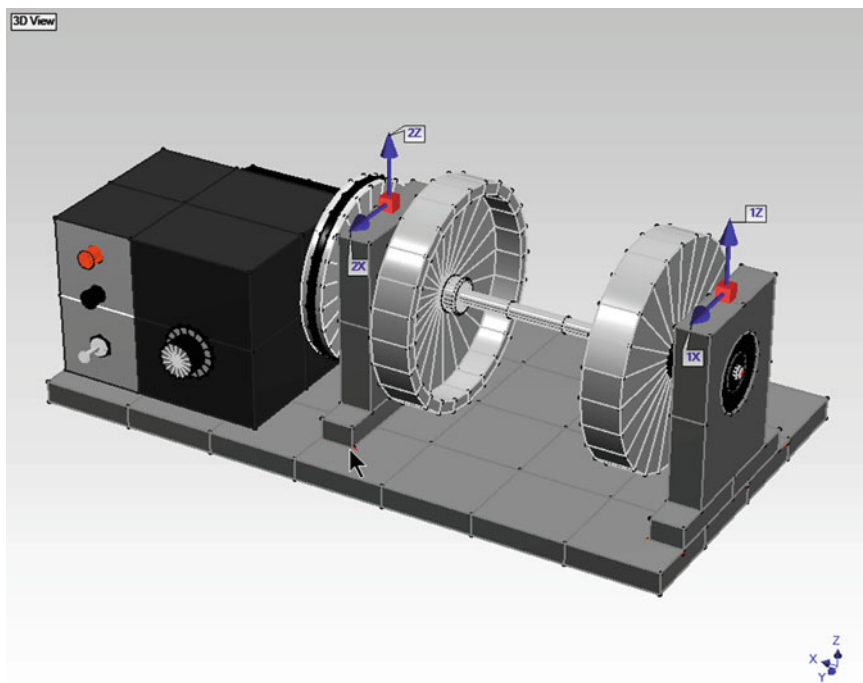


Fig. 8.8 Model showing four measurement directions

8.5.1 Baseline Auto Spectra

A Baseline set of Auto spectra was calculated from data that was acquired while the machine was operating in a balanced condition. In a machine condition monitoring program, these Baseline measurements would be archived in a database.

The four Baseline Auto spectra are shown in Fig. 8.9. Several order-related peaks are evident in the spectra.

The large peak at 1984 RPM is the first-order peak, or rotor speed of the machine. This peak is **dominant** in the horizontal (X) direction on both bearing blocks. The second large peak is **close to** a third-order peak, but is actually the motor speed, which is **2.85 times** the rotor speed. This peak is **dominant** in the vertical (Z) direction on both blocks.

Measurement Pairs Correlation was used to measure the difference between the four Baseline Auto spectra and a **current set** of Auto spectra over three different frequency bands, **each band enclosing an order peak**. Each band was **1000 RPM wide**.

Applying Measurement Pairs Correlation over three frequency bands of spectrum data would typically be used to identify machine faults that manifest more quickly as changes in and around the frequencies of higher machine orders.

Measurement Pairs Correlation yields a table of SDI values, one for **each frequency band**, and **each pair of Auto spectra with matching DOFs**. Each time a new set of data was acquired from the rotating machine and post-processed, another table of SDI values was archived in an archival database.

FaCTs™ was used to correlate **current tables of SDI values** with a **Baseline set of SDI values**. Two different examples will illustrate the combined use of Measurement Pairs Correlation and FaCTs™.

Example 1 Machine Warm Up

In this example, the machine was started and a Baseline set of Auto spectra was calculated. The machine was allowed to run for a while and SDI tables measuring the difference between the current and Baseline Auto spectra were stored into the archival database. The results are shown in Fig. 8.10.

The trend plot shows the SDI values decreasing as new data is acquired, indication that the four Auto spectra are changing relative to the Baseline Auto spectra. Each time new data is acquired, a new set of SDI values appears on the right side of the trend plot.

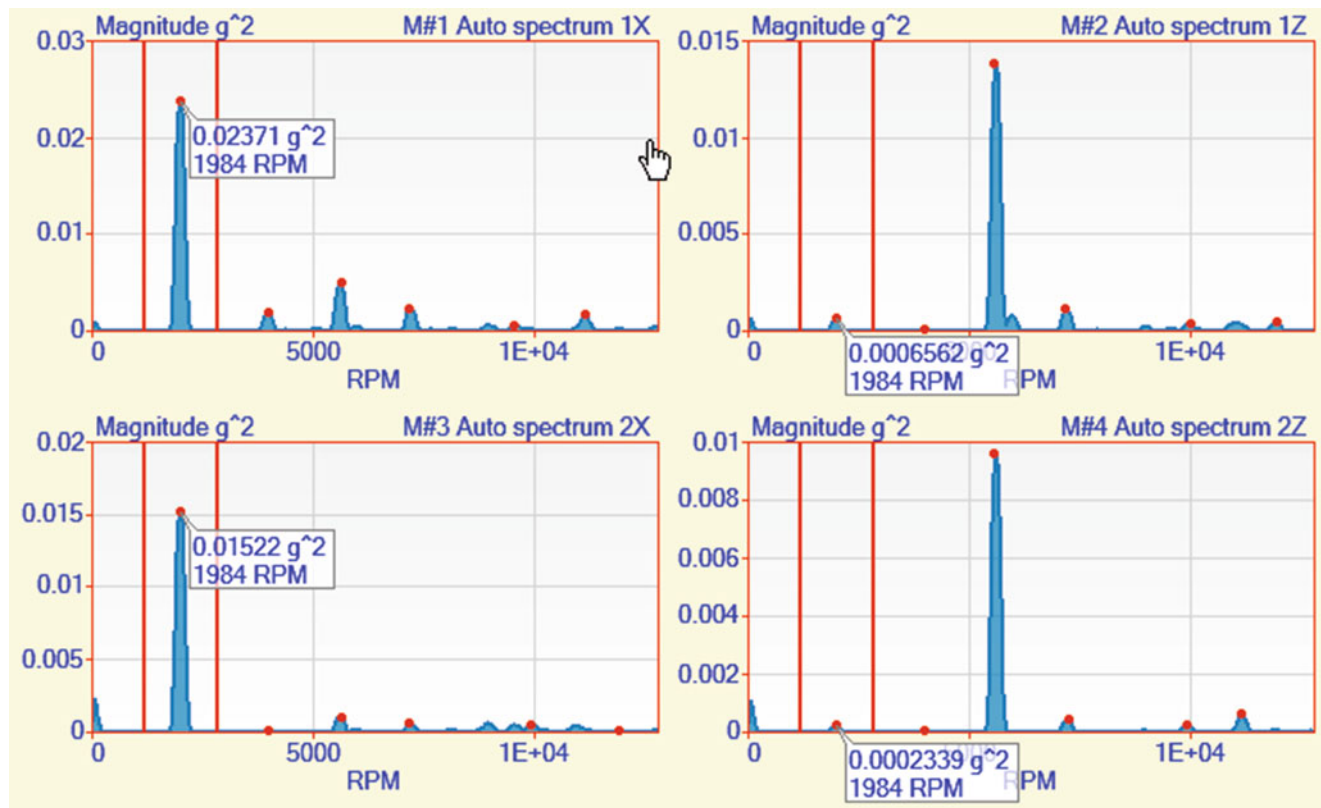


Fig. 8.9 Baseline auto spectra

For this case a **Baseline table of SDI values** was also saved in the database when the machine was started. As the machine warms up, the FaCTs™ bars in Fig. 8.10 have all dropped below a **value of “I”**, indicating that the SDI values for all three frequency bands of Auto spectrum data have undergone a change relative to the Baseline Auto spectra.

The three FaCTs bars clearly indicate that the operating condition of the machine has changed. The change can be attributed to a warming of the belt between the motor and the rotor causing belt slippage. The warm up caused the order peaks (rotor vibration caused by the motor) to **migrate in their frequency bands**. When correlated with its matching Baseline Auto spectrum, the peak migration in each current Auto spectrum caused a drop in the SDI value for each frequency band.

Figure 8.11 shows the FaCTs™ bars and SDI trend plot *after new Baseline spectra and new Baseline SDI values* have been calculated. With new Baselines, the FaCTs™ bars return to values that are **close to “I”**.

Example 2 Unbalance

In this second example, a small unbalance weight was added to the outboard rotor, and Auto spectra were again calculated from the vertical & horizontal acceleration data acquired from the two bearing blocks. Measurement Pairs Correlation was used to correlate the Auto spectra **after the unbalance weight was added** with Baseline Auto spectra from **before the weight was added**.

The trend plot of SDI values in Fig. 8.12 has much lower values in it, indicating that the unbalance caused the Auto spectra in all three frequency bands to be substantially different than the Baseline spectra of the balanced machine.

Three events are marked with vertical lines in the trend plot. They were marked when the **machine was in an unbalanced condition**. Three FaCTs™ bars were defined to correlate current SDI values with the three unbalanced machine events. The most current SDI values are displayed on the right side of the trend plot.

All three FaCTs™ bars are **close to “I”** in value, clearly showing that the data currently acquired from the unbalanced machine **strongly correlates** with the three prior unbalance events.

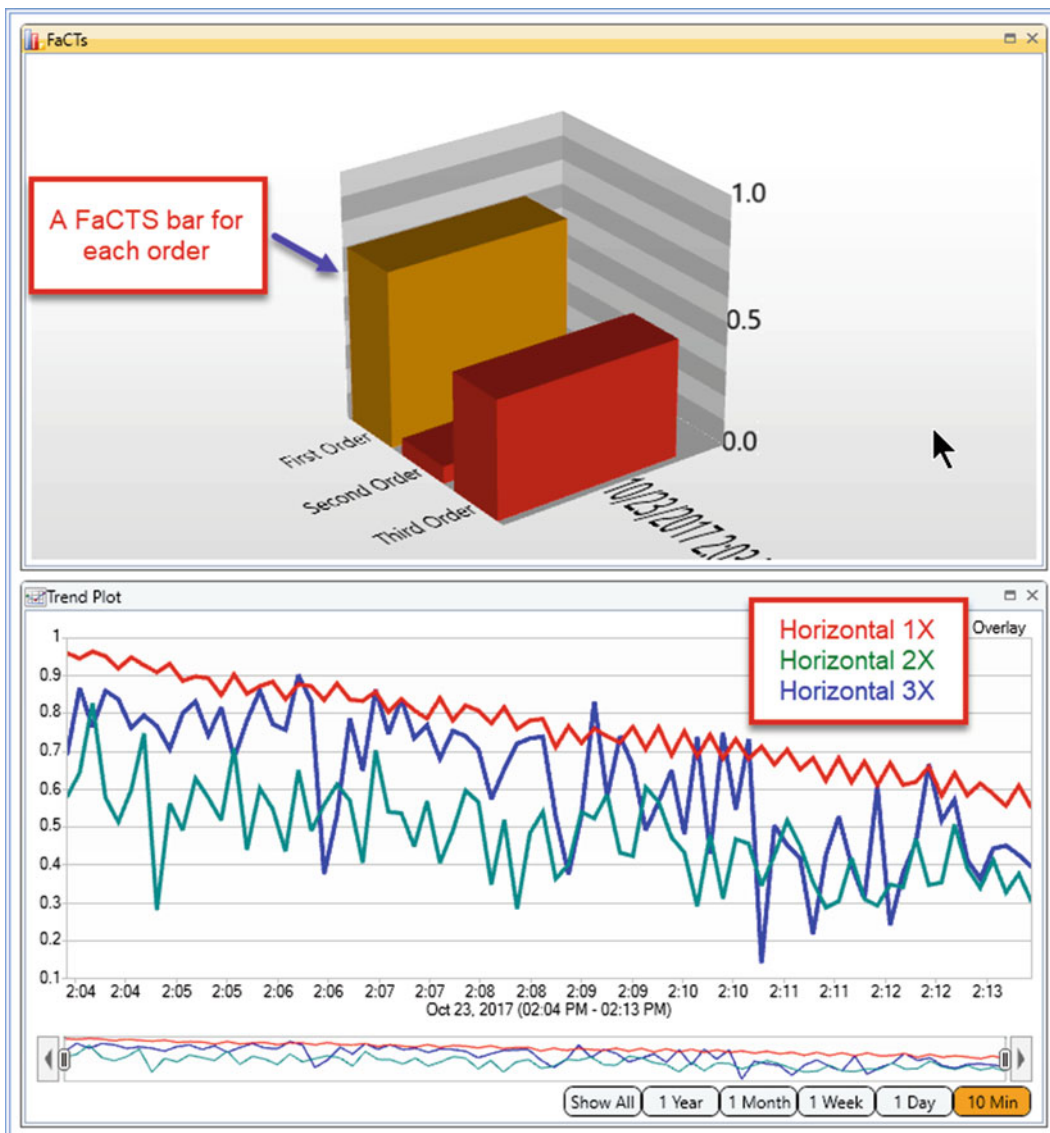


Fig. 8.10 FaCTS and SDI trend during warm up

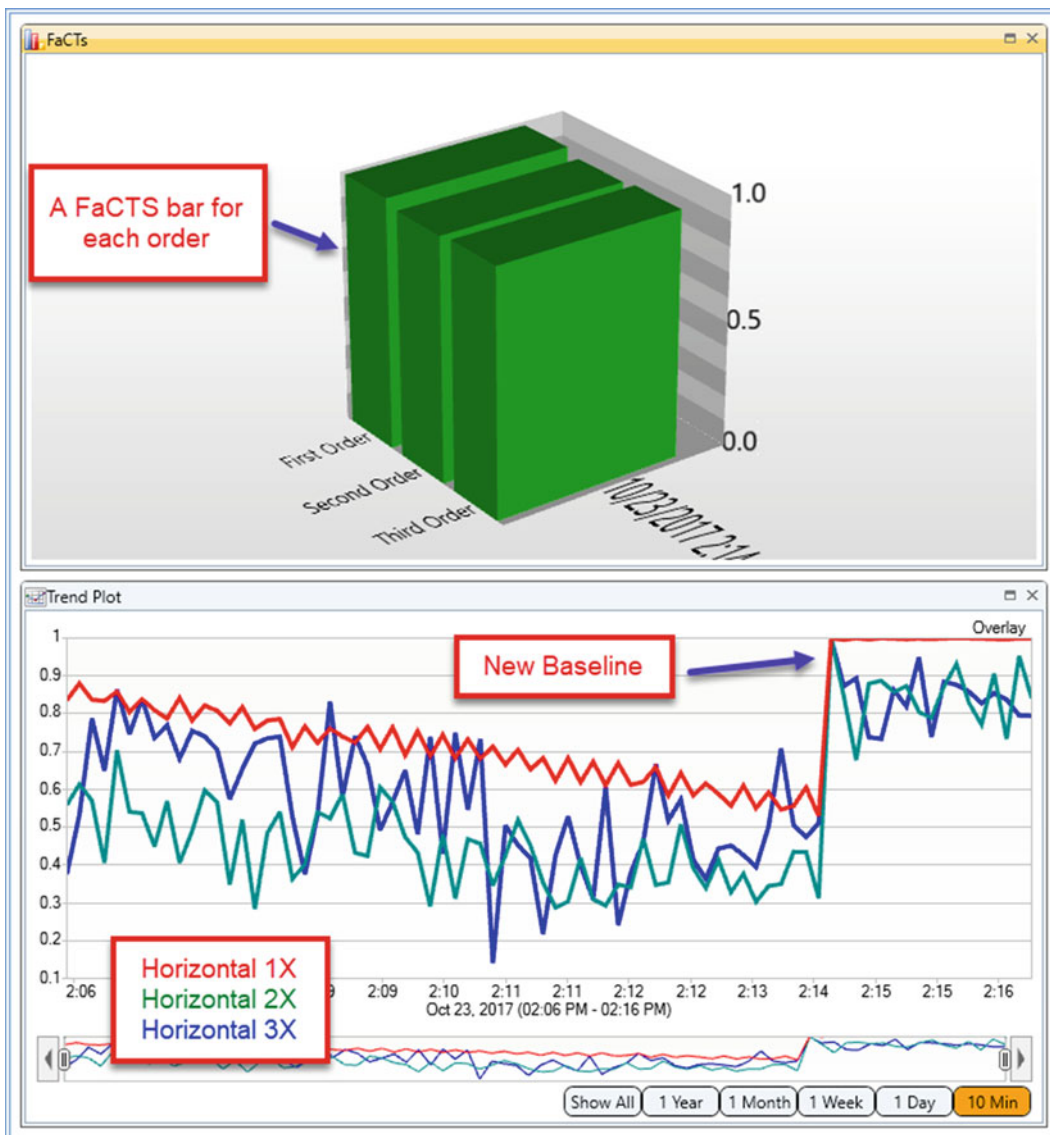


Fig. 8.11 FaCTS and SDI trend after a new baselines

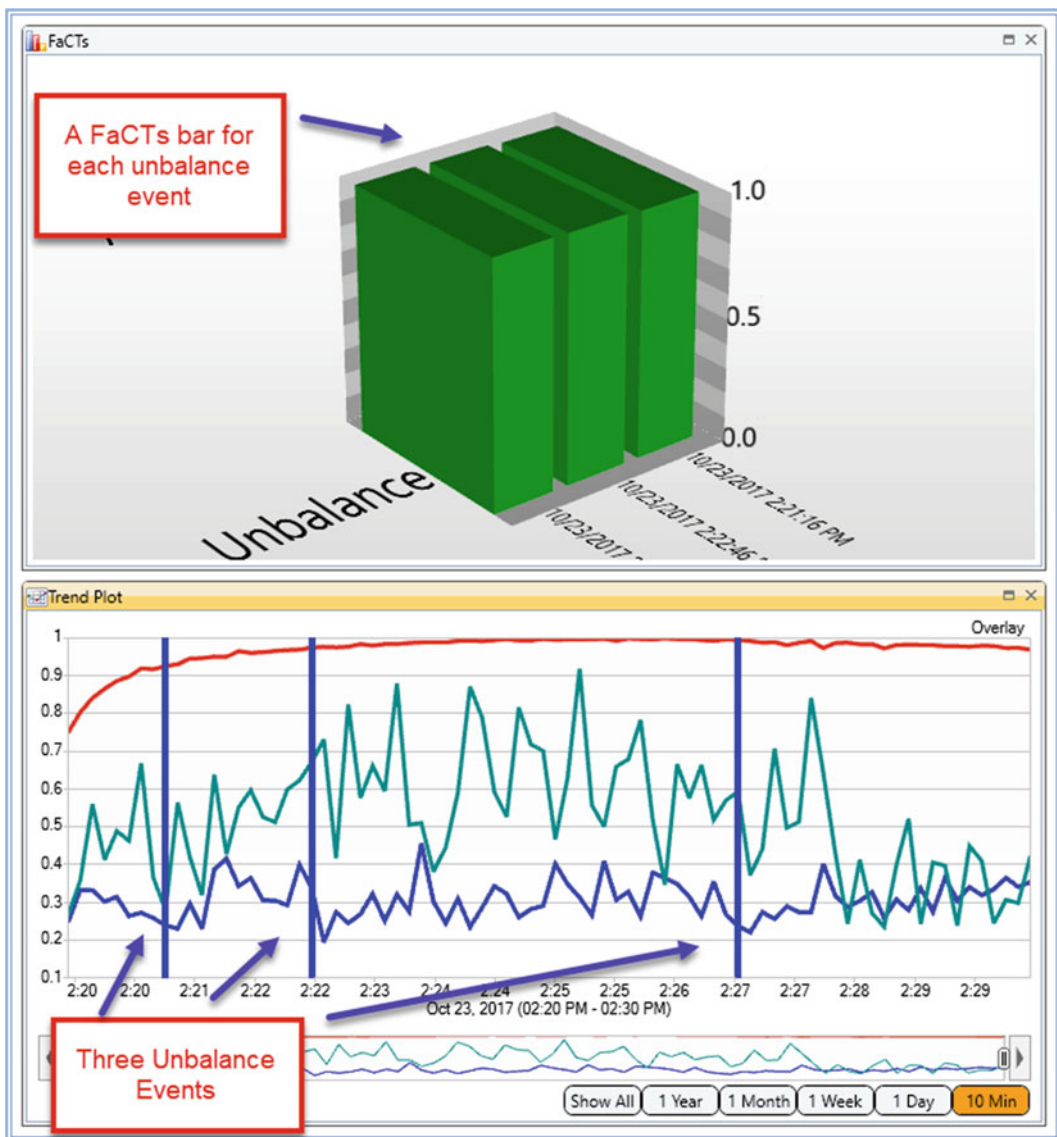


Fig. 8.12 FaCTs bars identifying unbalance

8.6 Conclusion

Two new uses of the SDI metric were demonstrated in this paper. In the first application, it was shown how **ODS Correlation** can be used during a Roving Response Impact test to indicate that a repeatable impact is applied to the structure during the test. ODS Correlation values between three reference FRFs and three Baseline FRFs were used to indicate repeatability.

The ODS Correlation calculation can be applied between any two sets of spectral measurements, containing any number of spectra.

In the second application, it was shown how **Measurement Pairs Correlation** was combined with the FaCTs™ database search method to indicate a changing operating condition in a rotating machine, and also to identify a previously defined unbalance condition in the machine.

Measurement Pairs Correlation was applied to four Auto spectra calculated from accelerometer data acquired from a rotating machine. Current Auto spectra were correlated with Baseline spectra in three different frequency bands. This correlation resulted in a table of 12 SDI values, one for each pair of spectra and each frequency band. Tables of SDI values were stored in an archival data base as the machine ran.

Three FaCTs™ bars were defined for correlating Baseline SDI values with current SDI values, for each frequency band. It was shown how the FaCTs™ bars indicated a slowly changing belt slippage condition due to warm up of the machine.

In the second example, three FaCTs™ bars were defined for correlating three marked unbalance events with current SDI data. In this example, FaCTs™ strongly correlated the current data from the unbalanced machine with the three prior unbalance events.

Measurement Pairs Correlation combined with FaCTs™ can be used in a number of route-based or continuous monitoring applications,

1. To indicate ***slowly occurring changes*** in the spectra of a machine or structure from monitored data
2. To ***identify specific mechanical faults*** which have been previously associated with data already stored in an archived database
3. In ***qualification testing***, where spectral measurements made on a test article are correlated with Baseline measurements to determine its ***pass-fail*** condition

References

1. Ganeriwala, S.N., Schwarz, B., Richardson, M.: Using operating deflection shapes to detect unbalance in rotating equipment. In: IMAC XXVII, Orlando 2009
2. Richardson, S., Richardson, M., Tyler, J., McHargue, P.: Using operating data to locate & quantify unbalance in rotating machinery. In: IMAC XXXIV, January 25–28 2016
3. Richardson, S., Tyler, J., McHargue, P., Schwarz, B., Richardson, M.: A new measure of shape difference. In: IMAC XXXII, February 3–6 (2014)
4. Richardson, S., Tyler, J., McHargue, P., Richardson, M.: Using modal parameters for structural health monitoring. In: IMAC XXXV, January 30–February 2 (2017)
5. Allemand, R.J.: The modal assurance criterion (MAC): twenty years of use and abuse. In: Proceedings of the International Modal Analysis Conference (2002)



Chapter 9

A Differential Evolution Markov Chain Monte Carlo Algorithm for Bayesian Model Updating

M. Sherri, I. Boulkaibet, T. Marwala, and M. I. Friswell

Abstract The use of the Bayesian tools in system identification and model updating paradigms has been increased in the last 10 years. Usually, the Bayesian techniques can be implemented to incorporate the uncertainties associated with measurements as well as the prediction made by the finite element model (FEM) into the FEM updating procedure. In this case, the posterior distribution function describes the uncertainty in the FE model prediction and the experimental data. Due to the complexity of the modeled systems, the analytical solution for the posterior distribution function may not exist. This leads to the use of numerical methods, such as Markov Chain Monte Carlo techniques, to obtain approximate solutions for the posterior distribution function. In this paper, a Differential Evolution Markov Chain Monte Carlo (DE-MC) method is used to approximate the posterior function and update FEMs. The main idea of the DE-MC approach is to combine the Differential Evolution, which is an effective global optimization algorithm over real parameter space, with Markov Chain Monte Carlo (MCMC) techniques to generate samples from the posterior distribution function. In this paper, the DE-MC method is discussed in detail while the performance and the accuracy of this algorithm are investigated by updating two structural examples.

Keywords Bayesian model updating · Markov Chain Monte Carlo · Differential evolution · Finite element model · Posterior distribution function

9.1 Introduction

During the last 30 years, the application of the finite element method (FEM) [1–3] has exponentially increased where this numerical technique has become one of the most popular engineering tools in systems modelling and prediction. In the domain of structural dynamics, the FEM tools are widely applied to model complex systems where this technique can produce results with high accuracy, especially when the modelled system is simple. However, the results attained by the FEM can be relatively inaccurate and the mismatches between the FEM results and the results attained from experimental studies are relatively significant. This is due to the errors associated with the modelling process as well as the complexity of modelled structure, which may reduce the accuracy of the modelling process. Consequently, the model obtained by an FEM needs to be updated to reduce the errors between the experimental and modelled outputs. The procedure of minimizing the differences between the numerical results and the measured data is known as the finite element model updating (FEMU) [4, 5], where the FEMU methods can be divided into two main classes. In the first class, which is also known as the direct methods, the experimental data are directly equated to the FEM outputs resulting in a procedure that constrains the updating to the FE system matrices (mass, stiffness) only. This kind of approach may produce non-realistic results where the resulting updating parameters may not have physical meaning. In the second class, which is also known as the iterative (or indirect) approaches, the FEM outputs are not directly equated to the experimental data, but instead, an objective function is introduced and iteratively minimised to reduce the errors between the analytical and experimental results. Thus, the system matrices and the model output vary during the minimisation process, and realistic results are often expected at the end of the updating process.

M. Sherri (✉)

Department of Mechanical Engineering Science, University of Johannesburg, Auckland Park, South Africa

I. Boulkaibet · T. Marwala

Institute of Intelligent Systems, University of Johannesburg, Auckland Park, South Africa

M. I. Friswell

College of Engineering, Swansea University, Bay Campus, Swansea, UK

Generally, several sources of uncertainty are associated with the modelling process, such as the mathematical simplifications made during the modelling, where this kind of uncertainty may affect the accuracy of the modelling process. Moreover, the noise that contaminates the experimental results may also have a significant impact on the updating process. To deal with such uncertainty problems, the updating process is accomplished by another class of methods called the uncertainty quantification methods. The most common uncertainty quantification method is known as the Bayesian approach in which the unknown parameters and their uncertainty are identified by defining each unknown parameter with a probability density distribution (PDF). Recently, the use of the Bayesian methodology has massively increased in the domain of system identification and uncertainty quantification. In this approach, the uncertainties associated with the modelled structure are expressed in terms of probability distributions where the unknown parameters are defined as a random vector with a multi-variable probability density function, and the resulting function is known as the posterior PDF. Solving the posterior PDF helps in identifying the unknown parameters and their uncertainties. Unfortunately, the posterior PDF cannot be solved in an analytical way for sufficiently complex problems which is the case for the FEMU problems since the search space is usually nonlinear and high dimensional. In this case, sampling techniques are employed to identify these uncertain parameters. The most recognised sampling methods are these related to Markov chain Monte Carlo (MCMC) methods.

Generally, the MCMC methods are very useful tools that can efficiently cope with large search spaces and generate samples from complex distributions. These methods draw samples with an element of randomness while being guided by the values of the posterior distribution function. Then, the drawn samples are accepted or rejected according to the Metropolis criterion. Unfortunately, the updated models, with relatively large complexities, may have multiple optimal (or near optimal) solution, and this cannot be easily identified by simple MCMC algorithms. In this paper, another version of the MCMC algorithms, known as the Differential Evolution Markov Chain (DE-MC) [6, 7] algorithm, is used to update FEMs of structural systems. The DE-MC algorithm combines the abilities of the differential evolution algorithm [8, 9], which is one of the genetic algorithms for global optimization, with the Metropolis-Hastings algorithm. In this algorithm, multiple chains are run in parallel, and the exploration and exploitation of the search space in the current chain are achieved by the difference of two randomly selected chains, multiplied by the value of the difference with a preselected factor and then the result is added to the value of the current chain. The value of the current chain is then accepted or rejected according to the Metropolis criterion. In this paper, the efficiency, reliability and the limitations of the DE-MC algorithm are investigated when the Bayesian approach is applied for FEMU. This paper is organized as follows: in the next section, the Bayesian formulations are introduced. Section 9.3 describes the DE-MC algorithm while Sect. 9.4 presents the results when a simple mass-spring structure is updated. Section 9.5 presents the updating results of an unsymmetrical H-shaped Structure. The paper is concluded in Sect. 9.6.

9.2 Bayesian Formulations

In this paper, the Bayesian approach is adopted to compute the posterior distribution function in order to update the FEMs. The posterior function can be represented by Bayes rule [10–14]:

$$P(\boldsymbol{\theta} | \mathcal{D}, \mathcal{M}) \propto P(\mathcal{D} | \boldsymbol{\theta}, \mathcal{M}) P(\boldsymbol{\theta} | \mathcal{M}) \quad (9.1)$$

where \mathcal{M} describes the model class for the target system where each model class \mathcal{M} is defined by certain updating parameters $\boldsymbol{\theta} \in \Theta \subset \mathbb{R}^d$. The experimental data \mathcal{D} of the structural system, which is represented by the natural frequencies f_i^m and mode shapes ϕ_i^m , are used to improve the FEM results. $P(\boldsymbol{\theta} | \mathcal{M})$ is the prior probability distribution function (PDF) that represents the initial knowledge of the uncertain parameters given a specific model \mathcal{M} , and in the absence of the measured data \mathcal{D} . The function $P(\mathcal{D} | \boldsymbol{\theta}, \mathcal{M})$ is known as the likelihood function and represents the difference between the experimental data and the FEM results. Finally, the probability distribution function $P(\boldsymbol{\theta} | \mathcal{D}, \mathcal{M})$ is the posterior function of the unknown parameters given a model class \mathcal{M} and the measured data \mathcal{D} . The model class \mathcal{M} is used only when several classes are investigated for both model updating and model selection. In this paper, only one model class is considered, and therefore, the term \mathcal{M} is omitted in order to simplify the Bayesian formulations.

In this paper, the likelihood function is given by:

$$P(\mathcal{D} | \boldsymbol{\theta}) = \frac{1}{\left(\frac{2\pi}{\beta_c}\right)^{N_m/2} \prod_{i=1}^{N_m} f_i^m} \exp\left(-\frac{\beta_c}{2} \sum_i^{N_m} \left(\frac{f_i^m - f_i}{f_i^m}\right)^2\right) \quad (9.2)$$

where N_m is the number of measured modes, β_c is a constant, f_i^m and f_i are the i th analytical and measured natural frequencies. The initial knowledge of the updating parameters $\boldsymbol{\theta}$, which is defined by a prior PDF, is given by the following Gaussian distribution:

$$P(\boldsymbol{\theta}) = \frac{1}{(2\pi)^{Q/2} \prod_{i=1}^Q \frac{1}{\sqrt{\alpha_i}}} \exp \left(-\sum_i^Q \frac{\alpha_i}{2} \|\boldsymbol{\theta}^i - \boldsymbol{\theta}_0^i\|^2 \right) = \frac{1}{(2\pi)^{Q/2} \prod_{i=1}^Q \frac{1}{\sqrt{\alpha_i}}} \exp \left(-\frac{1}{2} (\boldsymbol{\theta} - \boldsymbol{\theta}_0)^T \Sigma^{-1} (\boldsymbol{\theta} - \boldsymbol{\theta}_0) \right) \quad (9.3)$$

where Q is the number of the uncertain parameters, $\boldsymbol{\theta}_0$ represents the mean value of the updating parameters, α_i , $i = 1, \dots, Q$ are the coefficients of the updating parameters and the Euclidean norm is given by the notation: $\|*\|$.

After substituting Eqs. (9.2) and (9.3) into the Bayesian inference defined by Eq. (9.1), the posterior $P(\boldsymbol{\theta} | \mathcal{D})$ of the unknown parameters $\boldsymbol{\theta}$ given the experimental data \mathcal{D} is characterized by:

$$P(\boldsymbol{\theta} | \mathcal{D}) \propto \frac{1}{Z_s(\alpha, \beta_c)} \exp \left(-\frac{\beta_c}{2} \sum_i^{N_m} \left(\frac{f_i^m - f_i}{f_i^m} \right)^2 - \sum_i^Q \frac{\alpha_i}{2} \|\boldsymbol{\theta}^i - \boldsymbol{\theta}_0^i\|^2 \right) \quad (9.4)$$

where

$$Z_s(\alpha, \beta_c) = \left(\frac{2\pi}{\beta_c} \right)^{N_m/2} \prod_{i=1}^{N_m} f_i^m (2\pi)^{Q/2} \prod_{i=1}^Q \frac{1}{\sqrt{\alpha_i}} \quad (9.5)$$

Generally, the complexity of the posterior PDF, which depends on the modal parameters of the analytical model, is related to the complexity of the analytical model, and for certain relatively complex structural models the analytical results for the posterior distribution are difficult to obtain due to the high dimensionality of the search space. In this case, sampling techniques [5, 10, 11, 13, 14] are the only practical approaches in order to approximate the posterior PDF. The main idea of sampling techniques is to generate a N_s sequence of vectors $\{\boldsymbol{\theta}_1, \boldsymbol{\theta}_2, \dots, \boldsymbol{\theta}_{N_s}\}$ and use these samples to approximate the future response of the unknown parameters at different time instances. The most recognized sampling techniques are Markov Chain Monte Carlo (MCMC) methods [5, 13–18]. In this paper, the combination of one of the basic MCMC algorithms, known as the Metropolis-Hastings algorithm, with one of the genetic algorithms, known as differential evolution (DE), is used to generate samples from the posterior PDF in order to update structural models.

9.3 The Differential Evolution Markov Chain Monte Carlo (DE-MC) Method

In this paper, the DE and MCMC methods, which are extremely popular methods in several scientific domains, are combined to improve the convergence of the sampling procedure. In this approach, multiple chains are run in parallel in order to improve the accuracy of the updating parameters, while these chains learn from each other instead of running all the chains independently. This may improve the efficiency of the searching procedure and avoid sampling in the vicinity of a local minimum. The new chains are then accepted or rejected according to the Metropolis-Hastings criterion.

The Metropolis-Hastings (M-H) [18–20] algorithm is one of the common MCMC methods that can be used to draw samples from multivariate probability distributions. To sample from the posterior PDF $P(\boldsymbol{\theta}|D)$, where $\boldsymbol{\theta} = \{\theta_1, \theta_2, \dots, \theta_d\}$ is a d -dimensional parameters vector, a proposal density distribution $q(\boldsymbol{\theta}^* | \boldsymbol{\theta}_{t-1})$ is used to generate a proposed random vector $\boldsymbol{\theta}^*$ given the value at the previous accepted vector $\boldsymbol{\theta}_{t-1}$ at the iteration $t-1$ of the algorithm. Next, the Metropolis criterion is used to accept or reject the proposed sample $\boldsymbol{\theta}^*$ as follows:

$$\alpha(\boldsymbol{\theta}^* | \boldsymbol{\theta}_{t-1}) = \min \left\{ 1, \frac{P(\boldsymbol{\theta}^* | D) q(\boldsymbol{\theta}_{t-1} | \boldsymbol{\theta}^*)}{P(\boldsymbol{\theta}_{t-1} | D) q(\boldsymbol{\theta}^* | \boldsymbol{\theta}_{t-1})} \right\} \quad (9.6)$$

On the other hand, the Differential Evolution (DE) [8] is a very effective genetic algorithm in solving various real-world global optimization problems. As one of the genetic algorithms, the DE algorithm begins by randomly initialising the population within certain search area, and then these initial values are evolved over the generations in order to find the global minimum. This can be achieved using genetic operators such as: mutation, selection, and crossover.

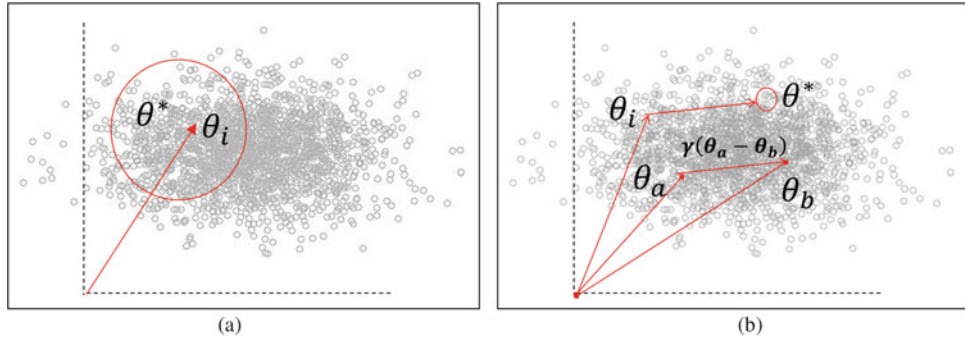


Fig. 9.1 Proposed vector generation in the M-H and DE-MC methods. (a) Metropolis-Hastings. (b) DE-MC

By integrating the Metropolis-Hastings criterion within the search abilities of the DE algorithm, the resulted MCMC method can be more efficient in determining where other chains can be employed to create the new candidates for the current chain. In the DE-MC algorithm, the new value of the chain is obtained by a simple mutation operation where the difference between two randomly selected chains (different from the current chain) is added to the current chain. Thus, the proposal for each chain depends on a weighted combination of other chains which can be easily defined as [6, 7]:

$$\theta^* = \theta_i + \gamma(\theta_a - \theta_b) + \epsilon \quad (9.7)$$

where θ^* represents the new proposed vector, θ_i is the current state of the i -th chain, θ_a and θ_b are randomly selected chains, γ is a tuning factor that always take a positive value and can be set to vary between $[0.4, 1]$. Note that the vectors: $\theta_i \neq \theta_a \neq \theta_b$. Finally, the noise ϵ , which is defined as a Gaussian distribution $\epsilon \sim N_p(\mathbf{0}, \sigma^2)$ with a very small variance vector σ^2 , is added to the proposed vector to avoid degeneracy problems. The factor γ can be seen as the magnitude that controls the jumping distribution. The main idea of the DE-MC algorithm can be illustrated in Fig. 9.1b.

Figure 9.1 explains the way to generate proposed vectors for the M-H method (Fig. 9.1a) and for the DE-MC method (Fig. 9.1b). As illustrated, the difference vector between the two randomly selected chains θ_a and θ_b represents the direction of the new proposed vector, where this difference is multiplied by the factor γ to define the moving distance. The moving distance is then added to the current chain θ_i to create the proposed vector. Note that, the DE-MC method has only one tuning factor γ in comparing to other versions of evolutionary MCMC methods. Finally, the new proposal θ^* of the i -th chain is accepted or rejected according to the Metropolis criterion which is given as:

$$r = \min \left\{ 1, \frac{P(\theta^*|D)}{P(\theta_i|D)} \right\} \quad (9.8)$$

The steps to update FEMs using the DE-MC algorithm are summarized as follows:

1. Initialize the population $\theta_{i,o}$, $i \in \{1, 2, \dots, N\}$.
2. Set the tuning factor γ . In this paper, $\gamma = 2.38/\sqrt{2d}$ and d is the dimension of the updating parameters.
3. Calculate the Posterior PDF for all chains.
4. For all chains $i \in \{1, 2, \dots, N\}$:
 - 4.1 Sample uniformly two random vectors θ_a, θ_b where $\theta_a \neq \theta_b \neq \theta_i$.
 - 4.2 Sample the random value ϵ with small variance $\epsilon \sim N_p(\mathbf{0}, \sigma^2)$.
 - 4.3 Calculate the proposed vector $\theta^* = \theta_i + \gamma(\theta_a - \theta_b) + \epsilon$.
 - 4.4 Calculate the Posterior PDF for the vector θ^* .
 - 4.5 Calculate the Metropolis ratio $r = \min \left\{ 1, \frac{P(\theta^*|D)}{P(\theta_i|D)} \right\}$
 - 4.6 Accept the proposed vector $\theta_i \leftarrow \theta^*$ with probability $\min(1, r)$, otherwise θ_i is unchanged.
5. Repeat the steps 4.1 to 4.6 until the number of samples required is achieved.

In next two sections, the DE-MC performance is highlighted when two structural examples are updated.

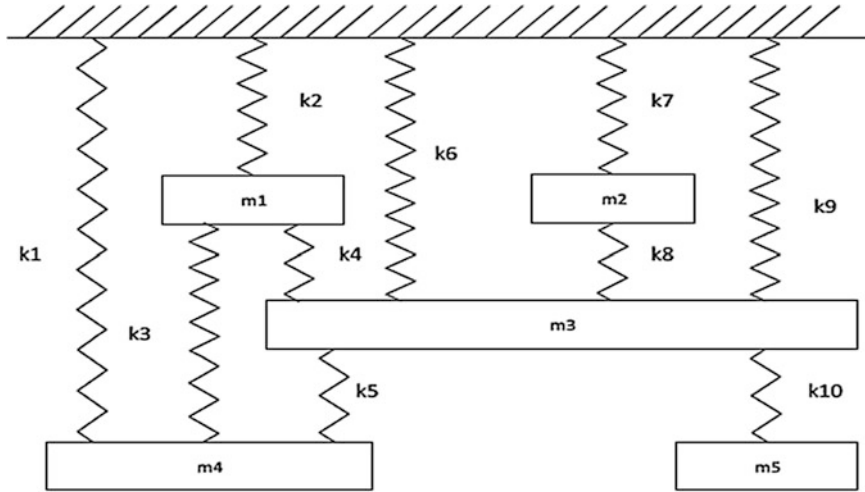


Fig. 9.2 The five degrees of freedom mass-spring system

Table 9.1 The updating parameters using DE-MC technique

Unknown parameters (N/m)

	Initial	Nominal values	Error (%)	DE-MC (μ_i)	Error (%)	$\frac{\sigma_i}{\mu_i}$ c.o.v (%)
θ_1	4600	4010	14.71	4004.4	0.14	1.03
θ_2	2580	2210	16.74	2197.6	0.56	1.71
θ_3	1680	2130	21.13	2109.4	0.97	2.07
θ_4	3100	2595	19.46	2600.9	0.23	2.32
θ_5	2350	2398	02.00	2410.4	0.52	1.77

Table 9.2 The updated natural frequencies and the errors obtained using the DE-MC

Modes	Nominal Frequency (Hz)	Initial Frequency (Hz)	Error (%)	Frequency DE-MC (Hz)	c.o.v (%)	Error (%)
1	3.507	3.577	1.97	3.507	0.118	0.00
2	5.149	5.371	4.30	5.149	0.126	0.00
3	7.083	7.239	2.21	7.082	0.119	0.02
4	8.892	9.030	1.56	8.894	0.140	0.03
5	9.426	9.412	0.16	9.426	0.117	0.00
TAE	_____	_____	1.98	_____	_____	0.012

9.4 Application 1: Simple Mass-Spring System

In this section, a five degrees of freedom mass-spring linear system, as presented in Fig. 9.2, is updated using the DE-MC algorithm.

The system contains 5 masses connected to each other using 10 springs (see Fig. 9.2). The deterministic values of the masses are: $m_1 = 2.7 \text{ kg}$, $m_2 = 1.7 \text{ kg}$, $m_3 = 6.1 \text{ kg}$, $m_4 = 5.3 \text{ kg}$ and $m_5 = 2.9 \text{ kg}$. The stiffness of the springs are: $k_3 = 3200 \text{ N/m}$, $k_5 = 1840 \text{ N/m}$, $k_7 = 2200 \text{ N/m}$, $k_9 = 2800 \text{ N/m}$ and $k_{10} = 2000 \text{ N/m}$. The spring stiffnesses k_1 , k_2 , k_4 , k_6 , and k_8 are considered as the uncertain parameters where the updating vector is: $\boldsymbol{\theta} = \{\theta_1, \theta_2, \theta_3, \theta_4, \theta_5\} = \{k_1, k_2, k_4, k_6, k_8\}$.

Since the DE-MC method is used for the updating procedure, the population used by the algorithm is selected to be $N = 10$. The updating vectors are bounded by $\boldsymbol{\theta}_{max}$ and $\boldsymbol{\theta}_{min}$ which are set to $\{4800, 2600, 2670, 3400, 2750\}$ and $\{3200, 1800, 1600, 1800, 2050\}$, respectively. The tuning factor is set to $\gamma = 2.38/\sqrt{2d}$ while $d = 5$, the initial vector of $\boldsymbol{\theta}$ is set to $\boldsymbol{\theta}_0 = \{4600, 2580, 1680, 3100, 2350\}$ and the number of generations (number of samples) is set to $N_s = 10000$. The obtained samples are illustrated in Fig. 9.3 while the updating parameters, as well as the initial and updated natural frequencies, are shown in Tables 9.1 and 9.2, respectively.

Figure 9.3 shows the scatter plots of the uncertain parameters using the DE-MC algorithm. The confidence ellipses (error ellipse) of the samples are also shown in the same figures (in red) where these ellipses visualize the regions that contain 95% of the obtained samples. As expected, the figure shows that the DE-MC algorithm has found the high probability area

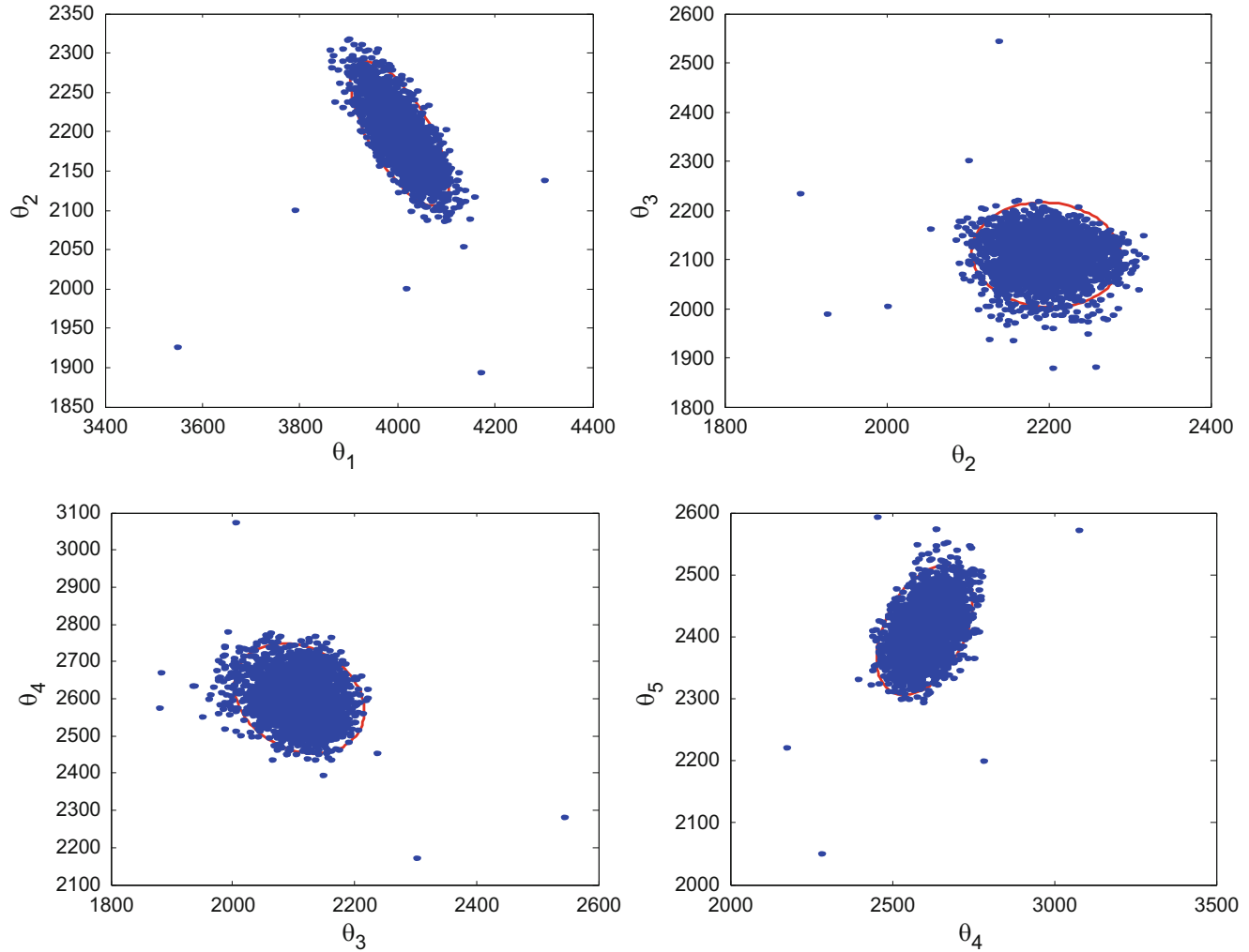


Fig. 9.3 The scatter plots of the samples using the DE-MC algorithm

after only few iterations. Table 9.1 contains the initial values, the nominal values and the updated values of the uncertain parameters. The coefficient of variation (c.o.v) values, which are estimated by dividing the standard deviations σ_i by the updated vectors θ_i (or μ_i), are also presented in Table 9.1 and used to measure the errors in the updating. It is clear that the obtained values of the c.o.v when the DE-MC algorithm is used to update the structure are small and less than 2.5% which means that the DE-MC algorithm performed well and was able to identify the areas with high probability. This also can be verified from the same table where the updating parameters are close the nominal values.

Table 9.2 contains the initial, nominal and updated natural frequencies. Furthermore, the absolute errors, which are estimated by $\frac{|f_i^m - f_i|}{f_i^m}$, the total average error (TAE), which is computed by $TAE = \frac{1}{N_m} \sum_{i=1}^{N_m} \frac{|f_i^m - f_i|}{f_i^m}$, $N_m = 5$, and the c.o.v values are also displayed. Obviously, the updated frequencies obtained by the DE-MC are better than the initial frequencies, and almost equal to the nominal frequencies.

The total average error of the FEM output was reduced from 1.98% to 0.012%. On the other hand, the values of the c.o.v for all updated frequencies are smaller than 0.15% which indicates that the DE-MC technique efficiently updated the structural system. Figure 9.4 shows the evaluation of the total average error at each iteration. The TAE in Fig. 9.4 is obtained as follows: first, the mean value of the samples at each iteration is computed as $\hat{\theta} = E(\theta) \approx \frac{1}{N_s} \sum_{j=1}^{N_s} \theta^j$ where i is the current iteration. Next, the mean value is used to compute the analytical frequencies of the FEM, and then the total average error is calculated as: $TAE(i) = \frac{1}{N_m} \sum_{j=1}^{N_m} \frac{|f_j^m - f_j|}{f_j^m}$. As a result, it is clear that the DE-MC algorithm converges efficiently after the first 2000 iterations.

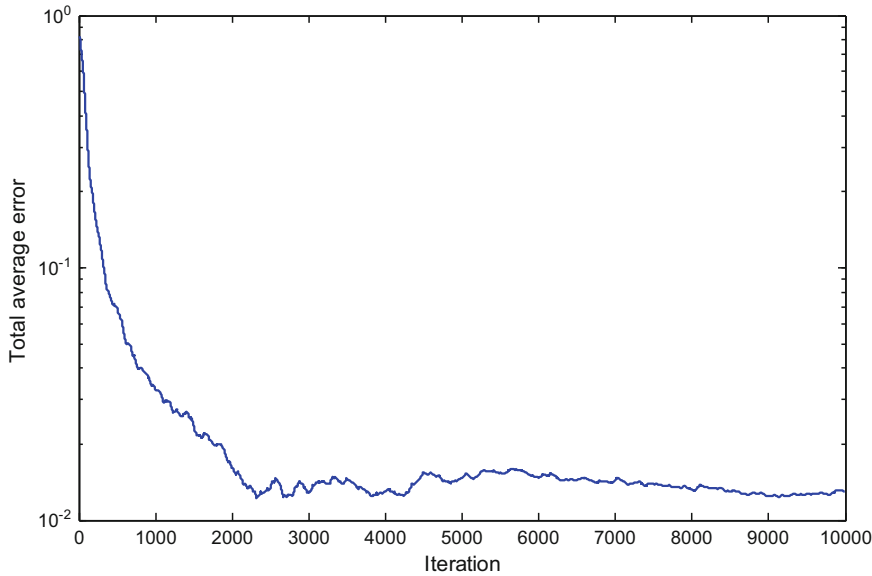


Fig. 9.4 The evaluation of the TAE using the DE-MC method

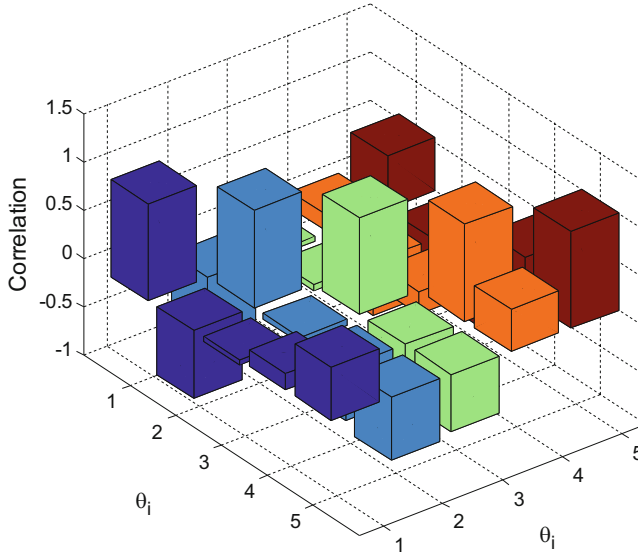


Fig. 9.5 The correlation between the updating parameters

Figure 9.5 illustrates the correlation between the updating parameters where all parameters are correlated (the values are different from zero). Moreover, the majority of these parameters are weakly correlated (small values <0.3) except the pairs (θ_1, θ_2) and (θ_4, θ_5) which are highly correlated (values >0.7).

In the next section, the DE-MC method is used to update an unsymmetrical H-shaped aluminum structure with real experimental data.

9.5 Application 2: The FEMU of the Unsymmetrical H-Shaped Structural System

In this section, the performance of the DE-MC algorithm is examined by updating an unsymmetrical H-shaped aluminum structure with real measured data. The FEM model of the H-shaped structure is presented in Fig. 9.6 where the structure is divided into 12 elements, and each element is modelled as an Euler-Bernoulli beam. The location displayed by a double arrow

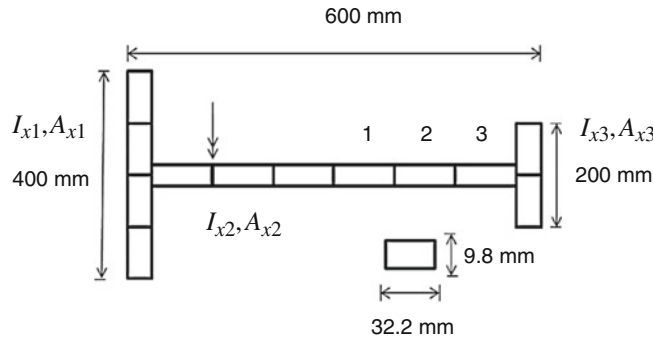


Fig. 9.6 The unsymmetrical H-shaped structure

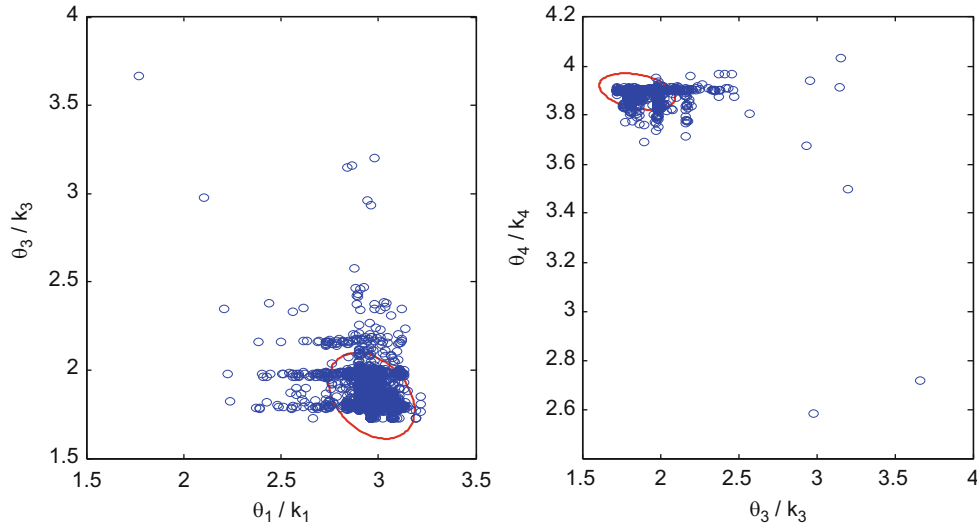


Fig. 9.7 The scatter plots of the samples using the DE-MC algorithm

at the middle beam indicates the position of excitation which is produced by an electromagnetic shaker. An accelerometer was used to measure the set of frequency-response functions. The initial analytical natural frequencies are 53.9, 117.3, 208.4, 254.0 and 445.0 Hz. In this example, the moments of inertia I_{xx} and the cross-sectional areas A_{xx} of the left, middle and right subsections of the H-shaped beam are selected to be updated in order to improve the analytical natural frequencies. Thus, the updating parameters are: $\boldsymbol{\theta} = \{I_{x1}, I_{x2}, I_{x3}, A_{x1}, A_{x2}, A_{x3}\}$.

The rest of the H-shaped structure parameters are given as follows: The Young's modulus is set to 7.2×10^{10} N/m² and the density is set to 2785 kg/m³. The updating parameters $\boldsymbol{\theta}$ are bounded by maximum and minimum vectors given by: $[4.73 \times 10^{-8}, 4.73 \times 10^{-8}, 4.73 \times 10^{-8}, 5.16 \times 10^{-4}, 5.16 \times 10^{-4}, 5.16 \times 10^{-4}]$ and $[0.73 \times 10^{-8}, 0.73 \times 10^{-8}, 0.73 \times 10^{-8}, 1.16 \times 10^{-4}, 1.16 \times 10^{-4}, 1.16 \times 10^{-4}]$, respectively. These boundaries are used to ensure that the updating parameters are physically realistic. The number of samples is set to $N_s = 5000$, the factor β_c of the likelihood function is set equal to 10, the coefficients α_i of the prior PDF are set to $\frac{1}{\sigma_i^2}$ where σ_i^2 is the variance of the i th uncertain parameters, and $\sigma = [5 \times 10^{-8}, 5 \times 10^{-8}, 5 \times 10^{-8}, 5 \times 10^{-4}, 5 \times 10^{-4}, 5 \times 10^{-4}]$.

Figure 9.7 illustrates the scatter plots of the updating parameters. The confidence ellipse that contains 95% of samples are also included in the figure. The updating parameters were normalized by dividing the parameters by $\mathbf{k} = [10^{-8}, 10^{-8}, 10^{-8}, 10^{-4}, 10^{-4}, 10^{-4}]$. As expected, the DE-MC algorithm was able to find the area with high probably after a few iterations. The rest of the updating parameters are shown in Table 9.3 as well as the initial values, the c.o.v values and the updating parameters obtained by the M-H algorithm [20, 21].

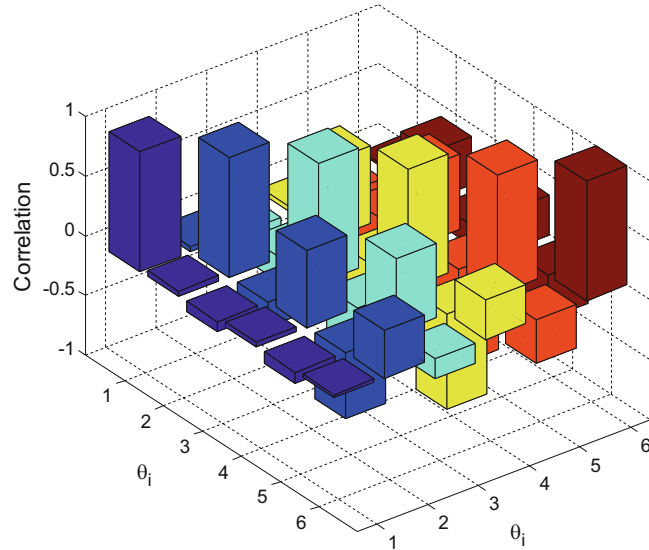
The results in Table 9.3 indicate that the updating parameters obtained by the DE-MC and M-H algorithms are different from the initial values which mean that the uncertain parameters have been successfully updated. Furthermore, the c.o.v values of the updating parameters obtained by the DE-MC algorithm are relatively small (<2.5%) with verifies that the algorithm was able to identify the areas with high probability in a reasonable amount of time; however, the c.o.v obtained by

Table 9.3 The initial parameters, the c.o.v values and the updating parameters using the DE-MC and M-H algorithms

	Initial	DE-MC (μ_i)	$\frac{\sigma_i}{\mu_i}$ (%)	M-H (μ_i)	$\frac{\sigma_i}{\mu_i}$ (%)
θ_1	2.7265×10^{-8}	2.8965×10^{-8}	5.76	2.31×10^{-8}	22.59
θ_2	2.7265×10^{-8}	2.9739×10^{-8}	1.91	2.68×10^{-8}	15.25
θ_3	2.7265×10^{-8}	1.7676×10^{-8}	1.67	2.17×10^{-8}	13.96
θ_4	3.1556×10^{-4}	3.8966×10^{-4}	0.65	2.85×10^{-4}	14.36
θ_5	3.1556×10^{-4}	2.1584×10^{-4}	2.93	2.83×10^{-4}	14.36
θ_6	3.1556×10^{-4}	2.9553×10^{-4}	0.026	2.77×10^{-4}	13.08

Table 9.4 Natural frequencies, c.o.v values and errors when DE-MC and M-H techniques are used for FEMU

Modes	Measured Frequency (Hz)	Initial Frequency (Hz)	Error (%)	Frequency DE-MC (Hz)	c.o.v (%)	Error (%)	Frequency M-H (Hz)	c.o.v (%)	Error (%)
1	53.90	51.04	5.31	52.56	0.30	2.49	53.92	3.96	0.04
2	117.30	115.79	1.29	119.42	0.35	1.81	122.05	4.28	4.05
3	208.40	199.88	4.09	210.46	0.54	0.99	210.93	4.95	1.22
4	254.00	245.76	3.25	253.37	0.41	0.25	258.94	4.81	1.94
5	445.00	387.53	12.92	435.71	0.63	2.09	410.33	4.74	7.79
TAE	_____	_____	5.37	_____	_____	1.53	_____	_____	3.01

**Fig. 9.8** The correlation between the updating parameters

the M-H algorithm are relatively high (>13.08%) which means that the M-H algorithm does not have the efficiency of the DE-MC algorithm.

Table 9.4 illustrates the updating frequencies using the DE-MC and M-H algorithms, the errors and the c.o.v values. As expected, the analytical frequencies obtained by the DE-MC algorithm are better than the initial frequencies as well as the frequencies obtained by the M-H algorithm. The DE-MC method has improved all natural frequencies and reduced the total average error (TAE) from 5.37% to 1.53%. Also, the c.o.v values obtained by the DE-MC method are relatively small (<0.65%).

Figure 9.8 shows the correlation of the updating parameters using the DE-MC parameters where the majority of these parameters are weakly correlated except the pairs (θ_2, θ_5) and (θ_4, θ_5), where the correlation between these pairs are relatively high (<0.7%).

The evaluation of total average error after each accepted (or rejected) sample is illustrated in Fig. 9.9. The result indicates that the DE-MC has a fast convergence rate and was able converge after 500 iterations.

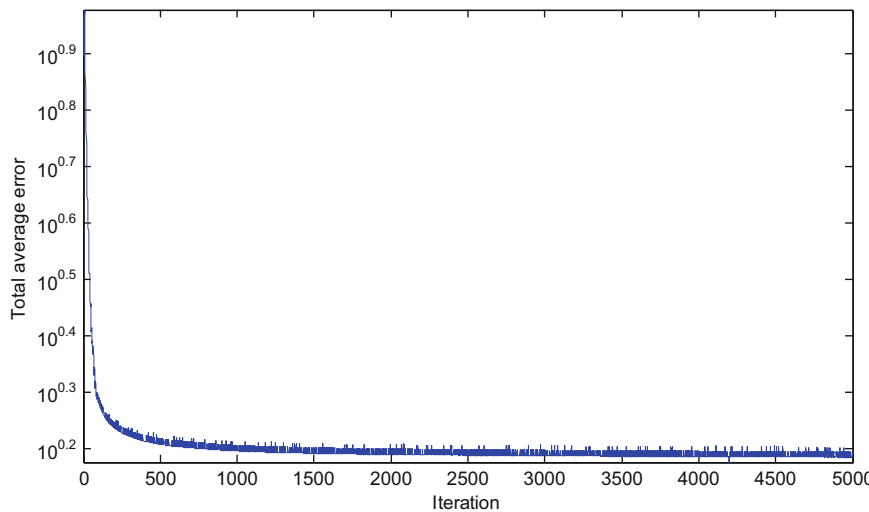


Fig. 9.9 The evaluation of the TAE using the DE-MC method

9.6 Conclusion

In this paper, the Differential Evolution Markov Chain (DE-MC) algorithm is used to approximate the Bayesian formulations in order to perform a finite element model updating procedure. In the DE-MC method, multi-chains are run in parallel which allows the chains to learn from each other in order to improve the sampling process where the jumping step depends on the difference between randomly selected chains. This method is investigated by updating two structural systems: the first one is a five DOF mass-spring linear system and the second one is the unsymmetrical H-shaped aluminum structure. In the first case, the total average error was reduced from 1.98% to 0.012%, while in the second case, the FEM updating of the unsymmetrical H-shaped structure, the total average error was reduced from 5.37% to 1.53%. Also the DE-MC algorithm appeared to have better results than the M-H algorithm when the unsymmetrical H-shaped structure is updated. In further work, the DE-MC algorithm will be modified and improved to include several steps such as the cross over and the exchange between the parallel chains. These changes may further improve the sampling procedure.

References

1. Zienkiewicz, O.C., Taylor, R.L.: *The Finite Element Method*, vol. 3. McGraw-hill, London (1977)
2. Hutton, D.: *Fundamentals of Finite Element Analysis*. McGraw-Hill, New York (2004)
3. Cook, R.D., Malcus, D.S., Plesha, M.E., Witt, R.J.: *Concepts and Applications of Finite Element Analysis*. Wiley, New Delhi (2007)
4. Friswell, M.I., Mottershead, J.E.: *Finite Element Model Updating in Structural Dynamics*, vol. 38. Springer Science & Business Media, Dordrecht (2013)
5. Marwala, T.: *Finite Element Model Updating Using Computational Intelligence Techniques: Applications to Structural Dynamics*. Springer Science & Business Media, London (2010)
6. Ter Braak, C.J.: A Markov Chain Monte Carlo version of the genetic algorithm differential evolution: easy Bayesian computing for real parameter spaces. *Stat. Comput.* **16**(3), 239–249 (2006)
7. ter Braak, C.J., Vrugt, J.A.: Differential evolution Markov chain with snooker updater and fewer chains. *Stat. Comput.* **18**(4), 435–446 (2008)
8. Storn, R., Price, K.: Differential evolution—a simple and efficient heuristic for global optimization over continuous spaces. *J. Glob. Optim.* **11**(4), 341–359 (1997)
9. Price, K., Storn, R.M., Lampinen, J.A.: *Differential Evolution: A Practical Approach to Global Optimization*. Springer Science & Business Media, Berlin Heidelberg (2006)
10. Bishop, C.M.: *Patern Recognition and Machine Learning*. Springer, Secaucus (2006)
11. Boulkaibet, I., Marwala, T., Mthembu, L., Friswell, M.I., Adhikari, S.: Sampling Techniques in Bayesian Finite Element Model Updating, in *Topics in Model Validation and Uncertainty Quantification*, vol. 4, pp. 75–83. Springer, New York (2012)
12. Yuen, K.-V.: *Bayesian Methods for Structural Dynamics and Civil Engineering*. Wiley, Singapore (2010)
13. Boulkaibet, I., Mthembu, L., Marwala, T., Friswell, M.I., Adhikari, S.: Finite element model updating using the shadow hybrid Monte Carlo technique. *Mech. Syst. Signal Process.* **52**, 115–132 (2015)
14. Boulkaibet, I., Mthembu, L., Marwala, T., Friswell, M.I., Adhikari, S.: Finite element model updating using Hamiltonian Monte Carlo techniques. *Inverse Probl. Sci. Eng.* **25**(7), 1042–1070 (2017)

15. Marwala, T., Sibisi, S.: Finite element model updating using Bayesian framework and modal properties. *J. Aircr.* **42**(1), 275–278 (2005)
16. Bishop, C.M.: *Neural Networks for Pattern Recognition*. Oxford University Press, Oxford (1995)
17. Ching, J., Leu, S.-S.: Bayesian updating of reliability of civil infrastructure facilities based on condition-state data and fault-tree model. *Reliab. Eng. Syst. Safety.* **94**(12), 1962–1974 (2009)
18. Metropolis, N., Rosenbluth, A.W., Rosenbluth, M.N., Teller, A.H., Teller, E.: Equation of state calculations by fast computing machines. *J. Chem. Phys.* **21**(6), 1087–1092 (1953)
19. Boulkaibet, I., Mthembu, L., Marwala, T., Friswell, M.I., Adhikari, S.: Finite Element Model Updating Using an Evolutionary Markov Chain Monte Carlo Algorithm, in *Dynamics of Civil Structures*, vol. 2, pp. 245–253. Springer, Cham (2015)
20. Marwala, T., Boulkaibet, I., Adhikari, S.: *Probabilistic Finite Element Model Updating Using Bayesian Statistics: Applications to Aeronautical and Mechanical Engineering*. Wiley, Chichester (2016)
21. Boulkaibet, I.: Finite element model updating using Markov Chain Monte Carlo techniques, PhD thesis, University of Johannesburg, (2014)



Chapter 10

Skin Performance in the Rollover Crashworthiness Analysis of Cutaway Bus

MohammadReza Seyed, Grzegorz Dolzyk, Sungmoon Jung, and Jerzy Wekezer

Abstract Rollovers are recognized as the most dangerous type of road accident. Among all accidents, they are the most challenging to analyze due to the complex nature of rollover accidents. The aim of this paper is to analyze the influence of the structural components, more specifically skin parts, on the safety of occupants during rollover crashes. Full scale experiments and components testing are needed to evaluate the safety of the passengers. As part of this study, full rollover test according to ECE R66 test procedure was conducted. Additionally, series of Finite Element (FE) analyses using LS-Dyna were performed to evaluate capabilities of skin parts to absorb the crash energy and its influence on the crush mechanism. Along with structural assessments, Anthropometric Test Devices (ATD) were used to evaluate the severity of the rollover crashes. Injury parameters such as Head Injury Criteria (HIC), chest acceleration, pelvic acceleration, and neck forces were measured for different rollover scenarios. The results showed that for the bus with high deformation of skin-cage structure the injury outcomes were lower than the injuries from the stiffer passenger compartment. Preliminary Results of this study are in conflict with the of UN ECE R66 safety assessment results, which indicate that stiffer buses are safer. Hence, further work needs to be carried out to find the links between an intrusion of skin and cage, and severity of injuries.

Keywords Rollover accidents · Structural analysis · Injury assessment · FE model

10.1 Introduction

The fact that rollover accidents are the most dangerous crash mode among road traffic accidents is recognized by many organizations and researchers throughout the world. Statistical data show that despite rollover accidents involved 2.1% of all accidents, they constitute 35% of all fatal crashes in the U.S [1]. Hence, the rollover crashworthiness analysis is needed to enhance the safety of occupants, and it remains among high priorities in automotive industries.

Rollover accidents are complex dynamic systems. In contrast to the frontal and side impact crash that happened in a millisecond, a rollover crash occurs over a second. In order to gain a better understanding of rollover mechanism, this event is classified into three phases included tripping phase (initiation phase), airborne phase, and ground impact phase (roof-to-ground phase) [2, 3]. A considerable amount of studies has already been completed to define the important rollover crashworthiness parameters. Researchers have utilized different experimental, numerical and statistical methodologies to assess the rollover safety from vehicle and occupant aspects. From vehicle aspect, the integrity of the structure and absorbing crash energy was assessed as the same time. An occupant view can help the researchers to quantify the human responses based on interactions of occupants and structural parts during an accident.

Over the last decades, steady increases in experimental and numerical analyses of rollover crashes have been seen. These studies have mostly focused on passenger cars where they quantified the rollover mechanism and kinematics of occupant to improve the safety of the vehicles during the rollover crashes [4]. For the heavy vehicles like bus, many rollover crashworthiness studies have been done without considering human responses in their assessments [5, 6]. Hence, further research is needed to identify the possible correlation of the structural performance and injury mechanism. In this study a series of numerical rollover tests were conducted based on UN ECE R66 to simulate the roof-to-ground phase of rollover crash.

M. Seyed (✉) · G. Dolzyk · S. Jung · J. Wekezer

Department of Civil and Environmental Engineering, Florida A&M University – Florida State University College of Engineering, Tallahassee, FL, USA

e-mail: reza.seyed@fsu.edu



Fig. 10.1 ECE R66 rollover test

It is well established that rollover accidents are associated with high risk of serious injury and death than other types of crashes. Over the years, many studies have been conducted to determine the patterns and nature of occupant injuries during the rollover. The main part of this study is to evaluate the structural performance of the cutaway bus with respect to the relative injury risk. Finite element simulations of a rollover crash involving two types of cutaway buses and Hybrid III ATD were conducted to determine the performance of the structural components during the rollover. More specifically the deformation of skin and steel cage components was quantified because they have a vital role to protect the occupants during the rollover crashes. The severity of each rollover scenarios was measured in terms of the injury outcomes and the degree of roof and wall intrusion. Then, the results were discussed from structural and occupants view. The preliminary results showed that the injury risks were decreased when the degree of roof and side wall intrusion were increased.

10.2 UN ECE R66 Rollover Test

Due to the complexity and chaotic nature of a rollover event, researchers inevitably are using simplified assumptions to simulate the rollover accidents. Hence, experimental tests are not a straightforward task and each test has its strengths and weaknesses to replicate the real rollover crash. The ECE R66 was first issued in 1987 in Europe to evaluate the strength of passenger compartment in the rollover event [5]. In this test procedure, a bus is placed on the flat table and slowly tilted to its unstable equilibrium position. Then, a bus falls under its own weight from 800 mm above the smooth, concrete ditch (Fig. 10.1). It should be noted that researchers highly criticized 800 mm drop height for the unrealistic kinematic response of the vehicle. They claimed that usually in real-world rollover accidents the drop height does not exceed 150 mm [7]. Although the ECE R66 rollover test is not fully dynamic test and only designed to measure the strength of the structure, it is highly repeatable and needs a small footprint area.

One of the important factors affecting occupant safety is the integrity of the passenger compartment within a vehicle during a rollover. Based on types of vehicles, different metrics have been used to quantify the survival space [8]. The structural performance in this test procedure is quantified by measuring the Deformation Index (DI) [9]. As in the Fig. 10.2 is shown, the residual space is the safety area which is defined to protect the occupants during the rollover accidents. The value for DI is calculated from Eq. (10.1) for front and rear section of the passenger compartment. The results of DI within the range $0 \leq DI < 1$ represent buses passing the rollover test, and means that the residual space remains intact. The value of $DI \geq 1$ corresponds to the wall structure intruded into the residual space, and the failure of the test.

$$DI = \frac{l}{d} \cdot \tan(\Delta\alpha_1) + \frac{(h-l)}{d} \cdot \tan(\Delta\alpha_2) \quad (10.1)$$

l – height from the floor to the plastic hinge in the sidewall, usually developing at the waist rail connection

h – height of the residual space (1250 mm)

d – horizontal distance from the side wall to the top corner of the residual space (400 mm)

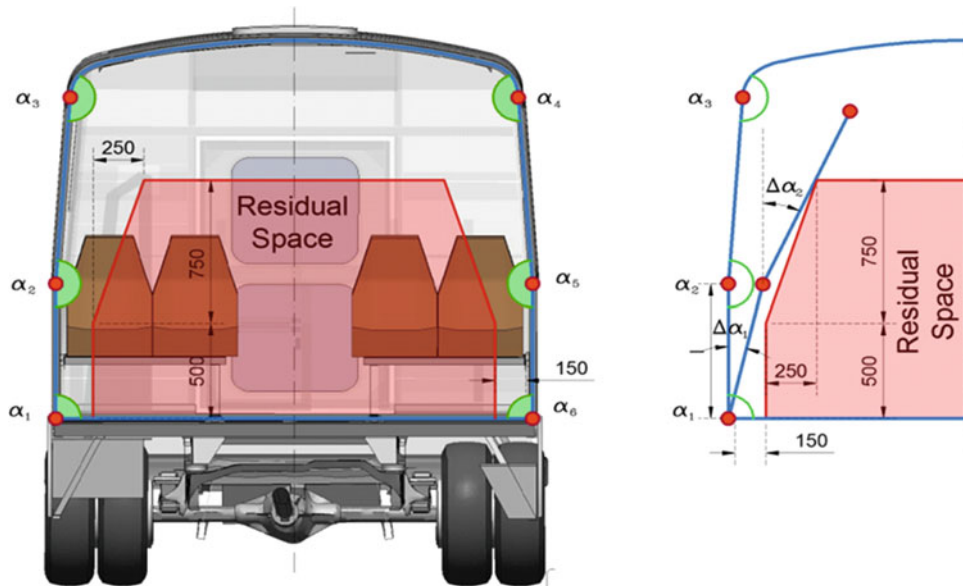


Fig. 10.2 Residual space and the DI concept [10]

Table 10.1 Two FE models of cutaway bus

Model	Commercial brand	Type of skin	Net weight (unloaded) kg
FRP-pw	Champion bus	Fiberglass/plywood & steel cage	4856
St-pw	Odyssey bus	Steel/plywood & steel cage	5987

10.3 Computational Model

Although FE model rollover analysis requires extensive experimental support in order to produce trustworthy and credible results, it provides a comprehensive understanding of structural behavior during a rollover crash. Based on the previous study, the major components responsible for bus structure behavior during a rollover crash are: steel cage and outer skin, front fiberglass cap, and floor chassis cab [11]. The numerical models of cutaway buses were developed by previous research at several stages [10–13]. Based on these studies, the validation and verification process of buses were conducted in three levels. The Unit level where the material properties of different parts such as skin, structural steel were extracted. Component levels where the specific test procedures were designed to assess the connection characteristics and deformation of structural parts. Next, as a validation of the entire structure, the location of the center of gravity and full scale rollover test were conducted to achieve the more reliable FE results.

In this study, two full scale FE models of cutaway buses were selected to assess the structural performance and injury outcomes. The general information of two cutaway bus model are shown in Table 10.1. The passenger compartment of these buses consists of two different structural panels. For the FRP-PW model, the steel cage was skinned with the two layers of fiberglass composite material and plywood. in the ST-PW model, the steel cage has covered by two layers of steel and plywood (Fig. 10.3). It should be noted that the primary experimental and FE analysis tests showed that inner skin has negligible effect on absorbing the crash energy.

The FE model of Hybrid III-50th male, which was developed by National Crash Analysis Center (NCAC), was also used to measure the kinematics of occupants. Although the Hybrid III does not originally design for rollover accidents, it is the most widely used ATD between researchers to define the injury risk [14]. The ATD was belted by a 2-point seatbelt and placed close to the impacted side wall. Injury parameters for different parts of the body such as head, neck, chest, and pelvic were measured and discussed in the following section. The injury outcomes can be described with several different injury metrics. While many different injury criteria [15], the Injury Assessment Reference Values (IARV) which more widely used for accidents were used in this paper.

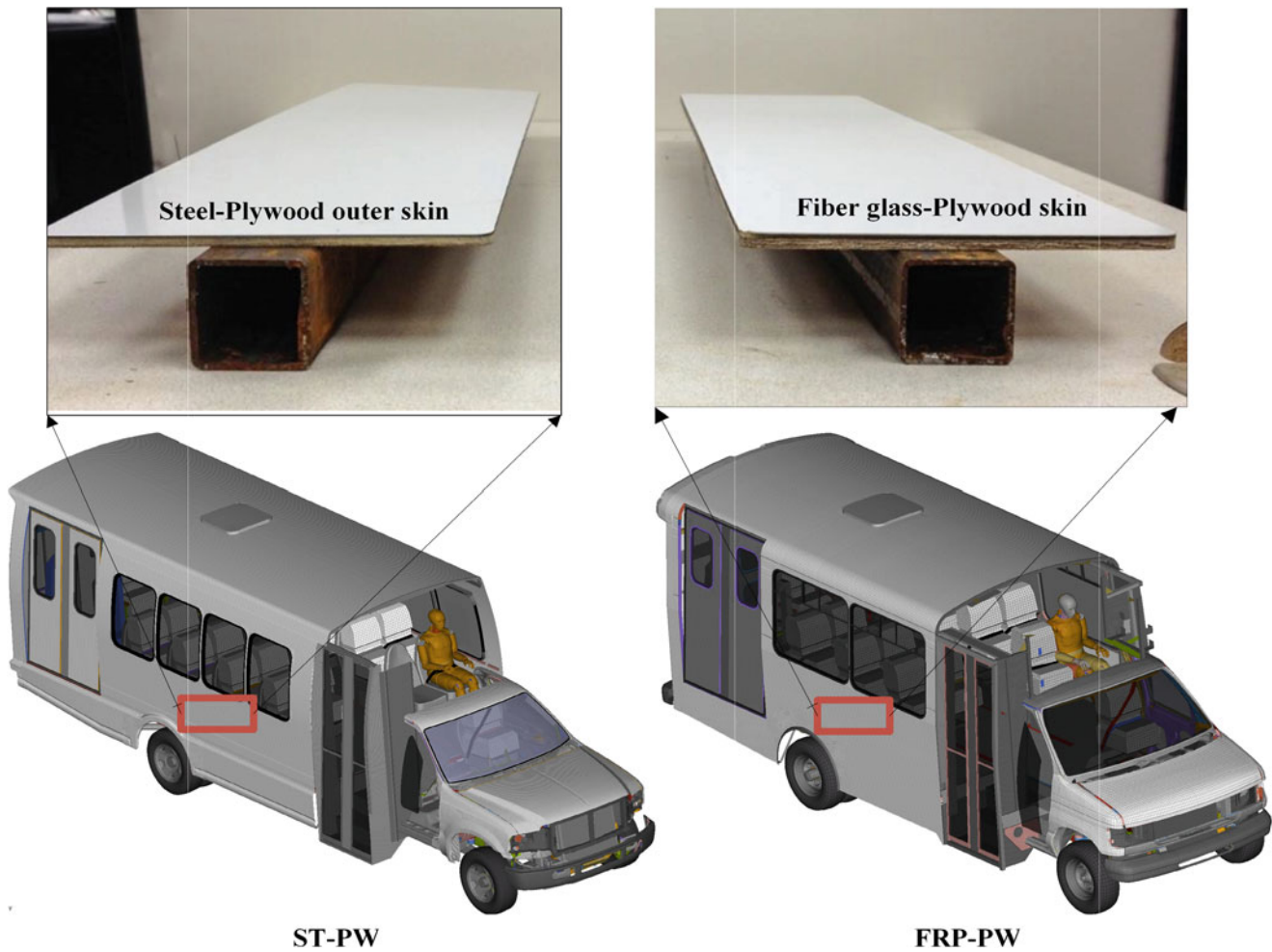


Fig. 10.3 Two numerical models of cutaway buses and the simplified section of the side wall for each model

Table 10.2 Specifications of rollover crash scenarios

Item	Description
Rollover test procedure	ECE R66 (tilt table test)
Drop heights	800 mm, 1000 mm, 1500 mm
Initial longitudinal and lateral velocity	0
Initial roll, yaw, pitch acceleration	0
Occupants model	Hybrid III 50th-male and water ballasts for other seats
Seatbelt	2-point

Different rollover scenarios were defined to evaluate the rollover crush mechanism and the injury risk. For each FE model, three rollover scenarios were designed, and deformations and important injury parameters were extracted. The details of the rollover test procedures are shown in Table 10.2.

10.4 Results and Discussion

In this section, the results of FE rollover crashworthiness analysis were discussed from vehicle and occupant view. Form vehicle aspect, structural performances of each bus were quantified with measuring the DI for front and rear section of passenger compartments. In the Figs. 10.4 and 10.5, the position of the buses at their maximum deformation are shown.

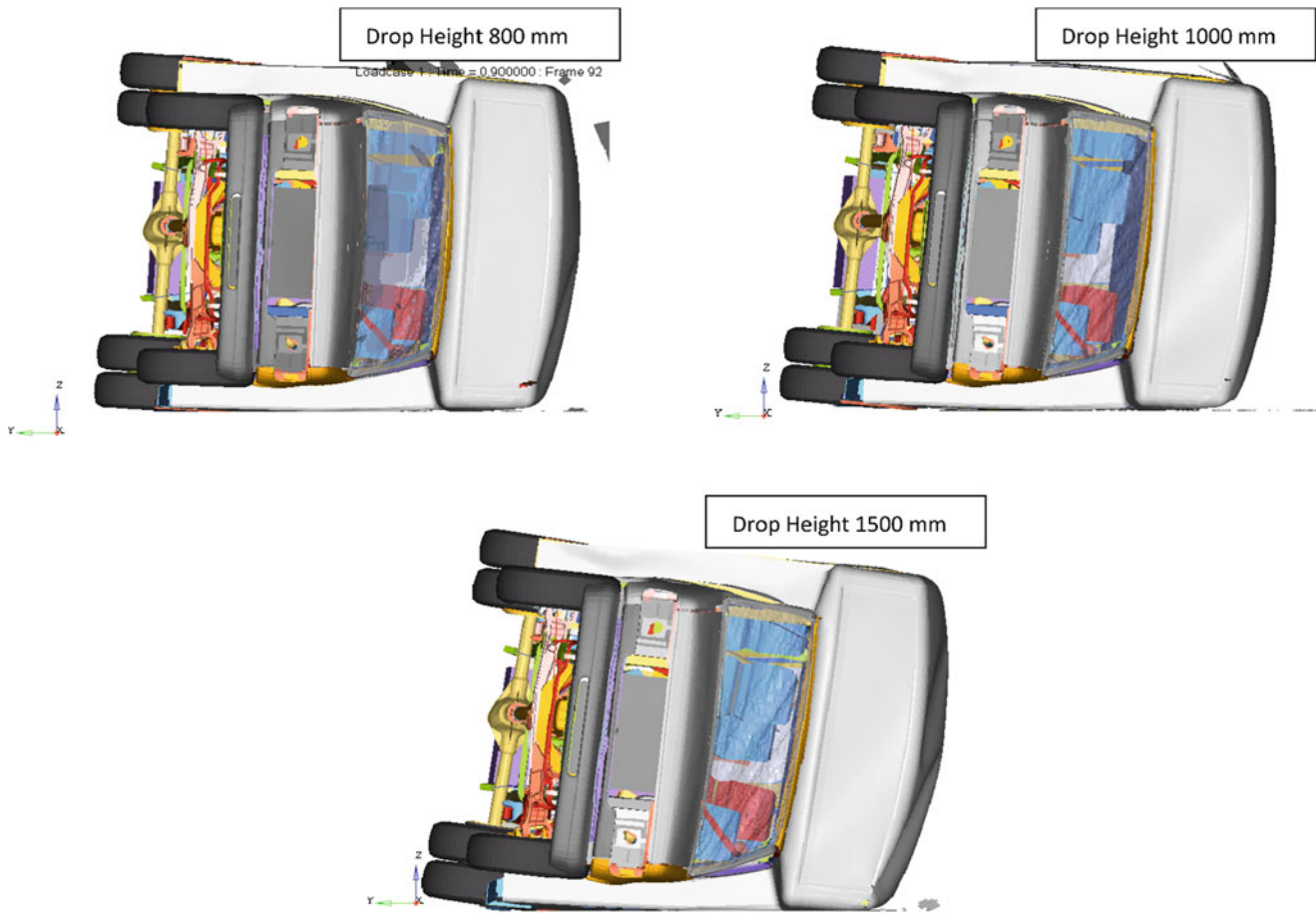


Fig. 10.4 Maximum deformation of FRP-PW model in rollover test at 800, 1000, and 1500 mm drop heights

From occupant view, injury parameters were measured to determine that whether occupant sustain fatal injuries during the rollover. The kinematics of ATD response during the rollover are plotted for different body regions (see Figs. 10.7 and 10.8 in the Appendix).

It can be seen that the structural component of FRP-PW model, particularly the skin and cage, did not deform significantly by changing the drop height. This means that, despite increasing the crash energy, the passenger compartment still kept its integrity (Fig. 10.4). The structural components of the side walls and roof experienced only minor deformations. The peak values in DI plots shows the maximum dynamic deformation of each section at the certain time. The results of DI indicate that the elastic and plastic deformation of both sections are very low for FRP-PW model.

For the ST-PW model, the substantial deformation can be observed in the Fig. 10.5. As a result, the amount of energy absorption of structural parts are more than the FRP-PW bus. This means that the small portion of the crash energy transferred to the ATD and consequently, the occupant did not experience severe injuries.

The results of injury measurements for ATDs in both buses are presented in Table 10.3. Injury criteria for head, chest, neck and pelvic were computed for each ATD. To measure the severity of the injuries, the occupant's responses were compared with the well-established Injury Assessment Reference Values. The results demonstrate that the severe injuries for the occupant inside the stiff bus were higher than the bus with high deformed structure.

According to the injury reference values, all injury measurements for ST-PW bus were below the upper limit which implies that a passenger did not sustain fatal injury. However, Fig. 10.6 shows that the DI $>> 1$ for front and rear section of ST-PW bus resulted in high amount of roof and side wall intrusion into the survival space. Recently, correlations between injury risk and structural performance are the most challenging topics. There is a continuing debate in the scientific literature regarding the relationship between roof crush and associated passenger injuries. Several studies have found a strong correlation between the amount of roof crush and the likelihood of serious injury in rollover crashes [16–18]. However, other researches have shown that there is no significant relationship between vehicle roof strength and injury outcome [19, 20]. To solve this

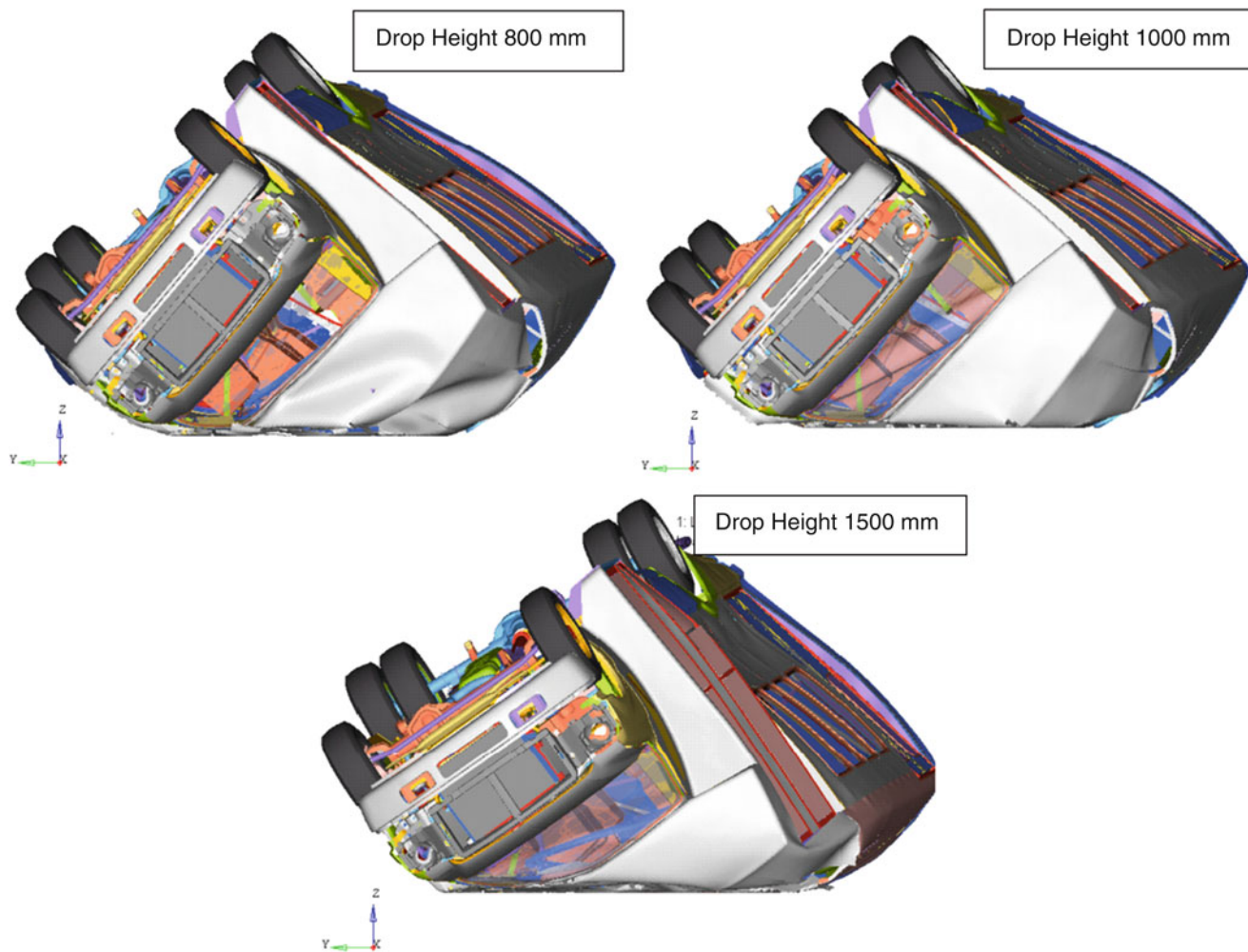


Fig. 10.5 Maximum deformation of ST-PW model in rollover test at 800, 1000, and 1500 mm drop heights

Table 10.3 Injury measurements for ATD in different rollover scenarios

Injury parameters	FRP-PW			ST-PW			Injury Assessment Reference Values (IARV)
	800 mm	1000 mm	1500 mm	800 mm	1000 mm	1500 mm	
HIC15	1845	2734	3653	514	193.9	62	700
Clip3ms (g)	25.87	26.36	30.9	29.8	32.9	27.1	60
Max pelvic acceleration (g)	27	31.5	34.68	28.8	30.8	22	130
Max neck force (N)	6867	8116	9225	4565	3276	1620	6050 ^a

^aThe total value of upper neck force from three directions

contradiction, comprehensive biomechanics research will be needed to improve the fidelity of the rollover crash analysis and quantifying the interaction of occupants with the bus's structure.

It should also be noted that statistical data about the real rollover accidents of cutaway buses are not available. Because in the database cutaway buses are categorized as other buses in their classification. As a result, researchers cannot use statistical models in their studies. Thereby, comparing findings from experimental and computational models with real rollover crash data may not be attainable for current research. Although crash avoidance is the main strategies for buses, due to the high fatality rate and complexity of this event, rollover crashworthy design should focus on both structural assessments and biomechanical aspect of rollover accidents.

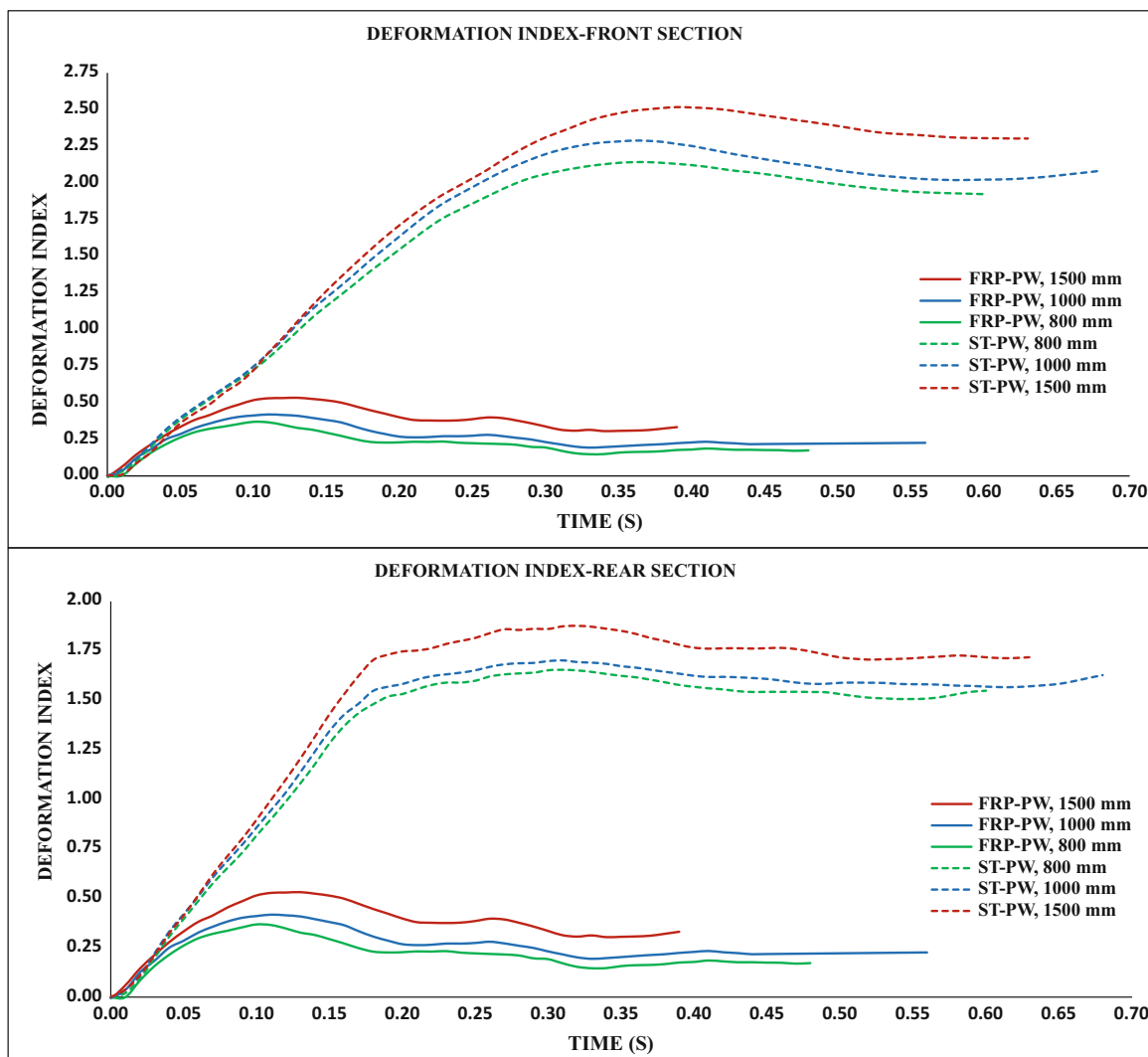


Fig. 10.6 DI measurements for two buses for different drop heights

10.5 Summary and Conclusion

In this study, series of FE rollover analyses were conducted involving two full scale FE model of cutaway buses and Hybrid III ATD. The ECE R66 rollover test procedure was selected to simulate the roof-to-ground impact phase. The structural performance especially skin-cage were quantified by the DI metric for all rollover tests. In addition, occupant responses for head, chest, neck, and pelvic were measured and compared with reference values to define the severity of injuries. Using an occupant model in crashworthiness analysis can provide a link between dynamic structural performance and occupant injury. The results showed that to protect the occupant from severe injuries optimized structural components are needed in order to manage the transferring crash energy. Moreover, ECE R66 rollover test may not be an adequate test procedure to assess the injury risk for occupants during a rollover crash.

Acknowledgment Funding for this study was provided by Florida Department of Transportation. All findings and views reported in this manuscript are based on the opinions of the authors and do not necessarily represent the consensus or views of the funding organization.

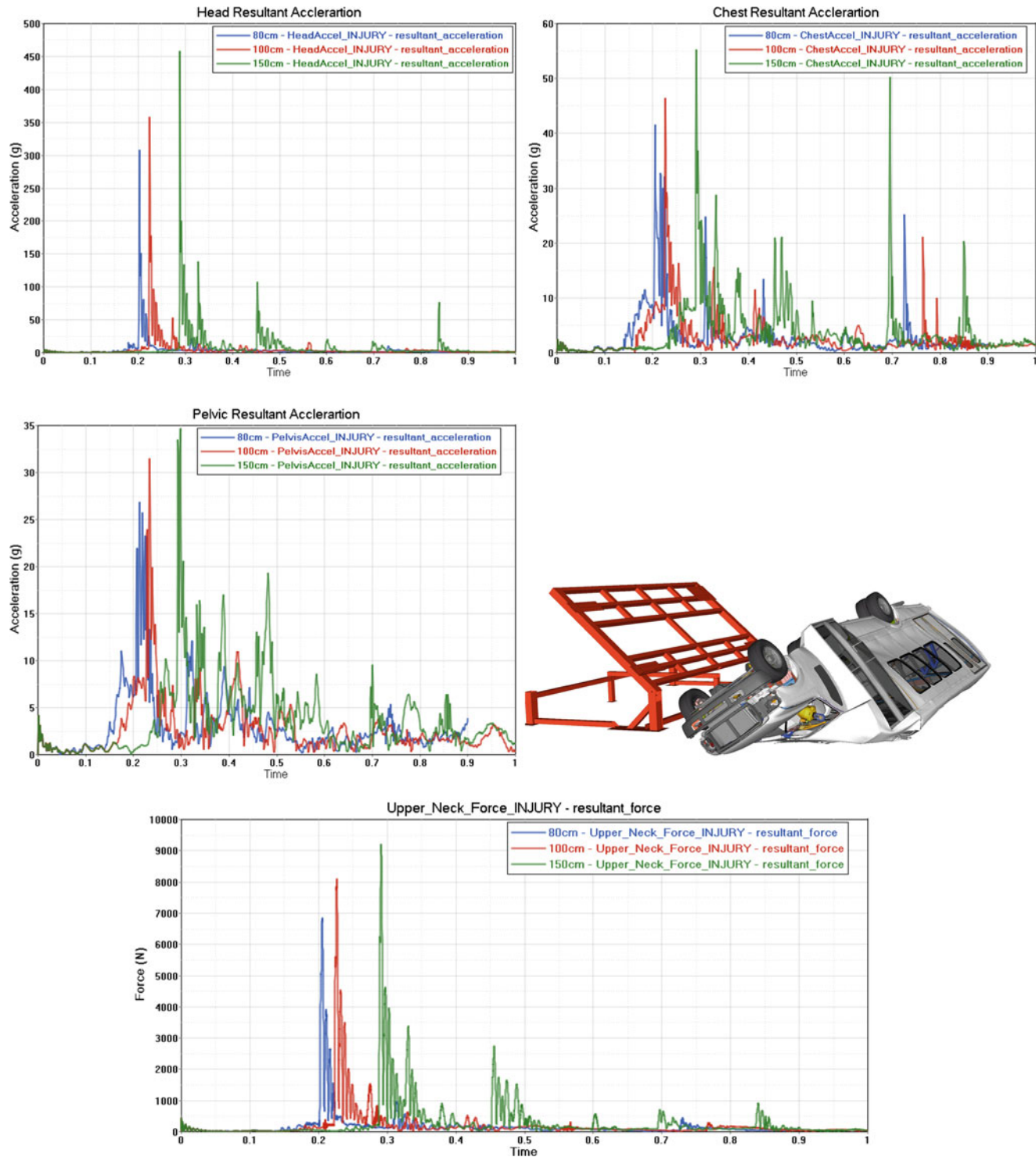


Fig. 10.7 ATD responses for head, chest, pelvic and neck in rollover tests of ST-PW FE model

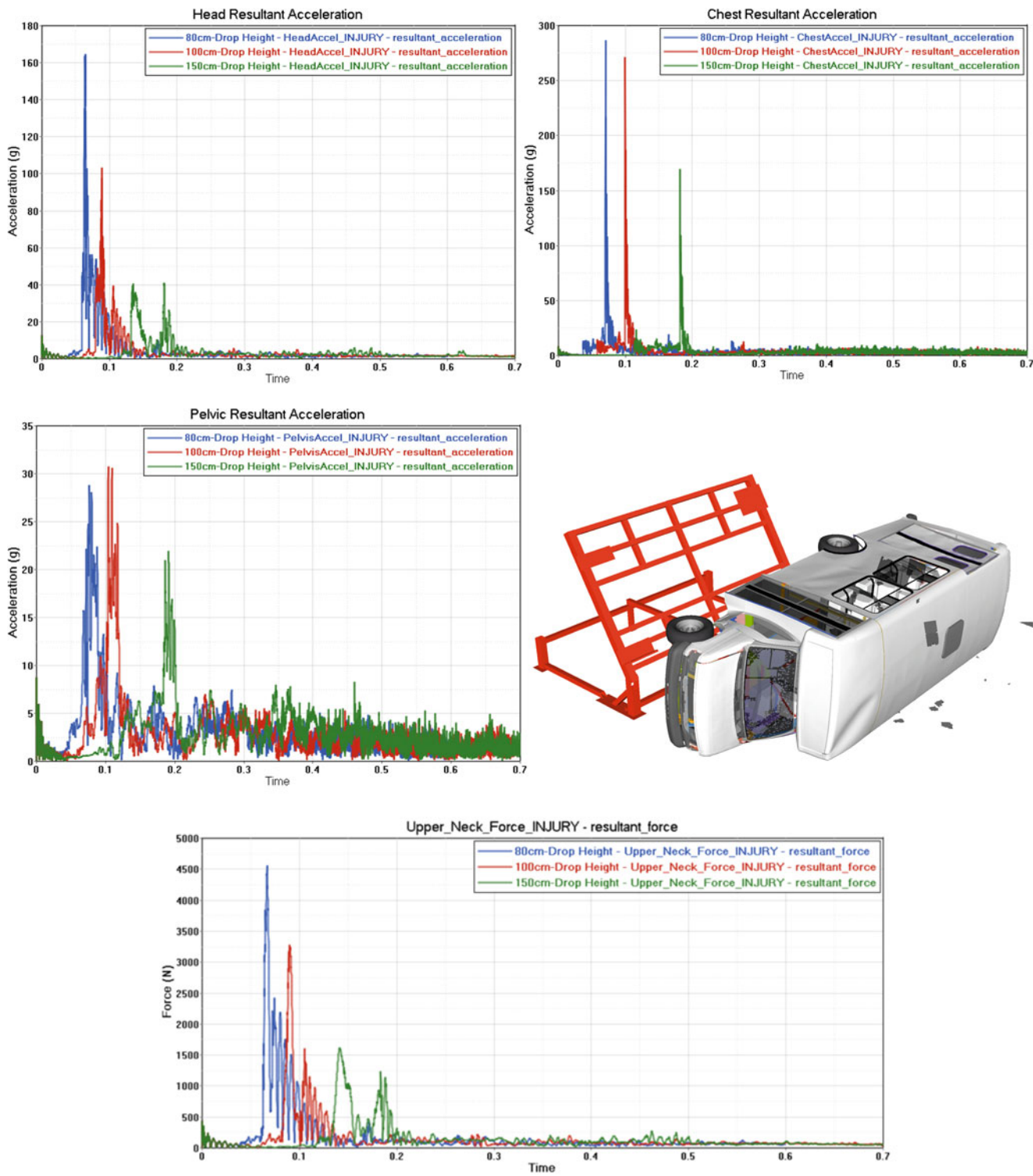


Fig. 10.8 ATD responses for head, chest, pelvic and neck in rollover tests of FRP-PW FE model

References

1. NHTSA, Traffic safety facts: 2012: A compilation of motor vehicle crash data from the fatality analysis reporting system and the general estimates system, vol. 812, (2012)
2. Parenteau, C.S., and Shah, M.: "Driver injuries in US single-event rollovers," SAE Technical Paper (2000)
3. Chou, C.C., Wagner, C.D., Yang, K.H., King, A.I., Hu, J., Hope, K., Arepally, S.: A review of math-based CAE tools for rollover simulations. *Int. J. Veh. Saf.* **3**(3), 236–275 (2008)
4. Chou, C.C., McCoy, R.W., Le, J.: A literature review of rollover test methodologies. *Int. J. Veh. Saf.* **1**(1–3), 200–237 (2005)
5. Liang, C., Le, G.-N.: Analysis of bus rollover protection under legislated standards using LS-DYNA software simulation techniques. *Int. J. Automot. Technol.* **11**(4), 495–506 (2010)
6. Belingardi, G., Gastaldin, D., Martella, P., Peroni, L.: Multibody analysis of M3 bus rollover: structural behaviour and passenger injury risk (2003)
7. Grzebieta, R., McIntosh, A., Bambach, M., Young, D.: Dynamic test protocol to assess rollover crashworthiness (2010)
8. Richardson, S., Grzebieta, R.H., Rechnitzer, G.: Proposal for a dynamic rollover protective system test. *Int. J. Crashworthiness*. **8**(2), 133–141 (2003)
9. F. D. o. T.-. FDOT: Crash and Safety Testing Standard for Paratransit Buses (2007)
10. Gepner, B., Bojanowski, C., Kwasniewski, L., Wekezer, J.: Effectiveness of ECE R66 and FMVSS 220 standards in rollover crashworthiness assessment of paratransit buses. *Int. J. Automot. Technol.* **15**(4), 581–591 (2014)
11. Bojanowski, C.: Verification, validation and optimization of finite element model of bus structure for rollover test, The Florida State University (2009)
12. Kwasniewski, L., Bojanowski, C., Siervogel, J., Wekezer, J.W., Cichocki, K.: Crash and safety assessment program for paratransit buses. *Int. J. Impact Eng.* **36**(2), 235–242 (2009)
13. Bojanowski, C., Kulak, R.F.: Multi-objective optimisation and sensitivity analysis of a paratransit bus structure for rollover and side impact tests. *Int. J. Crashworthiness*. **16**(6), 665–676 (2011)
14. Mertz, H.J., Irwin, A.L.: Anthropomorphic test devices and injury risk assessments. In: *Accidental Injury*, pp. 83–112. Springer, New York (2015)
15. Gabler, H.C., Weaver, A.A., Stitzel, J.D.: Automotive field data in injury biomechanics. In: *Accidental Injury*, pp. 33–49. Springer, New York (2015)
16. Atkinson, T., Cooper, J., Patel, B., Atkinson, P.: Considerations for rollover simulation, SAE Technical Paper (2004)
17. Brumbelow, M.L., Teoh, E.R., Zuby, D.S., McCartt, A.T.: Roof strength and injury risk in rollover crashes. *Traffic Inj. Prev.* **10**(3), 252–265 (2009)
18. Young, D., Grzebieta, R., McIntosh, A., Bambach, M., Frechede, B.: Diving versus roof intrusion: a review of rollover injury causation. *Int. J. Crashworthiness*. **12**(6), 609–628 (2007)
19. Padmanaban, J., Moffatt, E.A., Marth, D.R.: Factors influencing the likelihood of fatality and serious/fatal injury in single-vehicle rollover crashes, SAE Technical Paper (2005)
20. Funk, J.R., Cormier, J.M., Manoogian, S.J.: Comparison of risk factors for cervical spine, head, serious, and fatal injury in rollover crashes. *Accid. Anal. Prev.* **45**, 67–74 (2012)



Chapter 11

Across the Picket Fence: Influence of Sampling Frequency in Automatic Impact Modal Testing

Daniel J. Alarcón, Sarah Schneider, Robert Kamenzky, and Peter Blaschke

Abstract Automatic impact modal testing is a technique gaining momentum in recent years thanks to the popularization of Scanning Laser Doppler Vibrometry. These systems allow automatizing the output measurement of thousands of degrees of freedom in a short time. The use of automatic impact modal hammers allows automatizing the excitation input and broadband excitation without loading a structure with an extra mass or other drawbacks. However, the impact force repeatability is a prominent concern among test engineers, especially those who work with materials with non-proportional force/response ratios. Assessing the impact force repeatability of a given automatic modal hammer or test rig is necessary in order to ensure the right response level is measured impact after impact.

The assessment procedure can be misleading if not done right. Studying the automatic modal hammer repeatability under typical modal test conditions invariably leads to impact signals strongly distorted by the so called picket fence effect. This results in impacts sampled by only 3–4 data points; insufficient to accurately describe the actual impact force signals and the short contact times between hammer tip and structure. In the reality, the impacts are of larger magnitudes and shorter contact times than what is shown by the analyzer in typical test conditions.

This work studies the influence of the sampling frequency and the test structures used on the repeatability assessment of automatic impact modal hammers. Impact force signals are acquired in this work with enough resolution to eliminate the picket fence effect and truly evaluate how repeatable and reproducible automatic impacts are. The practicality of the procedure, which involves very large datasets and long testing times, is discussed. Guidelines are offered at the end of the paper for a successful repeatability and reproducibility assessment of automatic impact modal hammers.

Keywords Experimental modal analysis · Sampling · Automatic modal hammer · Impact modal testing · Validation

Nomenclature

DOF	Degree of Freedom
FFT	Fast Fourier Transformation
FRF	Frequency Response Function
LDV	Laser Doppler Vibrometry
R&R	Repeatability and Reproducibility
SAM	Scalable Automatic Modal Hammer

D. J. Alarcón (✉) · S. Schneider · R. Kamenzky
Technical University of Applied Sciences Wildau, Wildau, Germany
e-mail: daniel.alarcon@th-wildau.de

P. Blaschke
Technical University of Applied Sciences Wildau, Wildau, Germany
Noise-Vibration-Technology GmbH, Steinheim a.d. Murr, Germany
e-mail: peter-g.blaschke@th-wildau.de

11.1 Introduction

The last years have seen the advent of new response output measurement techniques. Piezoelectric accelerometers have been progressively replaced in many applications by Laser Doppler Vibrometers (LDV) and later by single-point or 3D Scanning LDV systems. The popularization of these techniques has had a special impact on the study of small, lightweight structures; where the attachment of accelerometers, no matter how small, is an issue. Attaching an accelerometer means heavily influencing the mass and the stiffness of structures such as composite material probes, thin plates, printed circuit boards, turbine blades, etc.

Scanning LDV systems allow automatizing the response output measurement of hundreds or thousands of degrees of freedom (DOFs) in a matter of minutes if the excitation input signal is automatized as well. Electrodynamic shakers have been traditionally used for that purpose with optimal results in larger structures, but their application in lightweight structures poses many challenges. Shaker excitation of smaller structures is an issue in regards to the stinger attachment and in general, in the experimental setup. As in the accelerometer case, these lightweight structures cannot be modified without dramatically changing their dynamic properties. Experience has shown that the practicality of shaker testing becomes also an issue when parts need to be quickly tested and interchanged, for example, in quality assurance applications.

Automatic impact modal excitation in combination with LDV has gained momentum in the recent years for the previously mentioned reasons. Authors such as Sauer et al. [1], Ritzmann and Meyeringh [2], Keil [3] and Rausch et al. [4] are successfully combining automatic impact modal excitation with LDV techniques for a variety of research purposes. These five mentioned works have all in common that, (1) the studied structures are relatively small and lightweight, (2) a large number of DOFs is needed, regardless of the purpose and (3) there is usually more than one structure to be tested.

Still, automatic impact modal excitation is a topic in ongoing research. Impact force repeatability is a prominent concern among test engineers, especially those devoted to the study of materials with non-proportional force/response ratios [5]. An automatic modal hammer with low force repeatability will oblige the test engineer to set more averages per DOF trying to smoothen the obtained FRFs, multiplying consequently the testing time by as many times as additional averages are needed. This means extra test hours and their respective cost in cases where thousands of DOFs are studied, and especially in case of lightly damped structures with long resonance fade-out times. Wear and tear issues related with the prolonged usage of the automatic modal hammer might arise as well. Due to these reasons, it is important to develop a methodology to assess the impact repeatability and reproducibility (R&R) of these test devices. If the test engineer is certain of the good R&R of their automatic impact hammer, test averages can be reduced along overall test times and costs. This work is centered on the issues the test engineer typically finds on this R&R assessment regarding data acquisition. In the last paragraphs of this work, the authors suggest a series of strategies for a successful R&R assessment overcoming the data acquisition difficulties.

11.2 Materials and Methods

The data for this work was acquired by impacting a thick, lightly-damped tempered steel plate with measures 90 mm × 100 mm × 18.1 mm and weights 1.26 kg. Its surface treatment is very adequate for the testing and of modal hammers, as it prevents the formation of dents on the plate surface. A mini modal impact hammer tip model 086E80 (PCB Piezotronics, Depew, NY, USA) was instrumented onto a Scalable Automatic Modal Hammer (SAM1) (Noise-Vibration-Technology, Steinheim a.d. Murr, Germany). Even though the NV-Tech SAM1 was used in this research, the issues and strategies described in this paper are valid for any kind of automatic modal hammer. The SAM1 rotation velocity and stop angle were set at 500 microsteps/second and 1.2° respectively. This resulted in impacts of around 90 N peak force value.

Data was sampled with two different pieces of equipment: (1) a data acquisition module vMeas (Maul-Theet GmbH, Berlin, Germany), able of a maximum sampling frequency of 52.7 kHz for a maximum bandwidth of 20 kHz; and (2) a National Instruments PCI-6110 (NI, Austin, TX, USA) able of a maximum sampling frequency of 250 kHz for a maximum bandwidth of 100 kHz. All measurements are triggered at the 5% of their time block length.

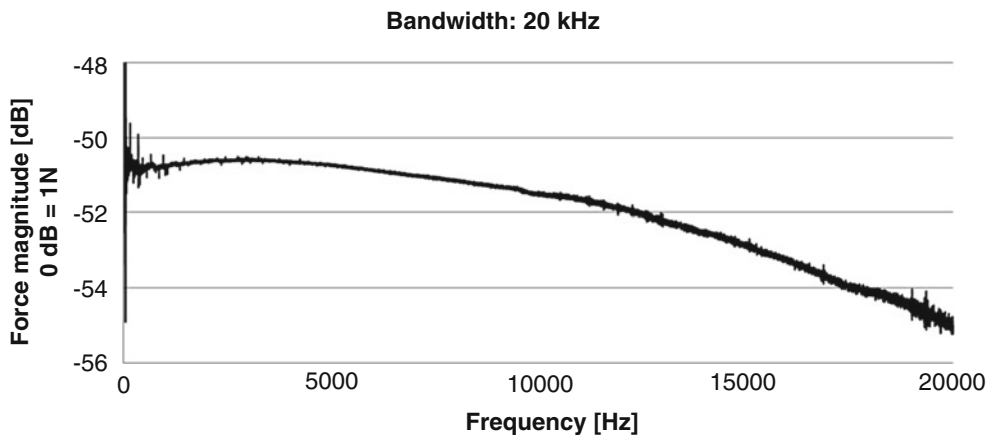


Fig. 11.1 Spectrum of an automatic hammer impact performed on the tempered steel plate described in the previous chapter. Special care was taken in minimizing the contact time between hammer tip and plate, resulting in an input power rolloff of 5 dB in the frequency range up to 20 kHz

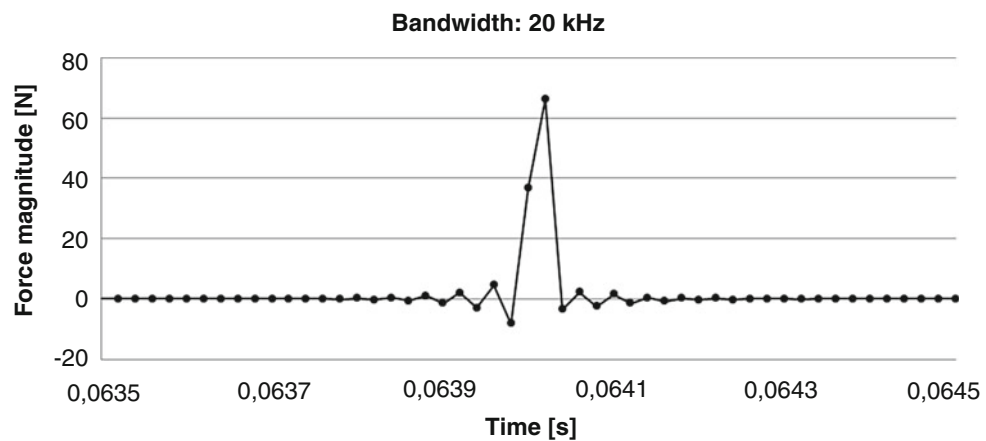


Fig. 11.2 Time signal of an automatic hammer impact performed on a tempered steel plate. The impact is sampled with only four data points. The picket fence effect hinders knowing the real peak force value

11.3 Results and Discussion: Effects of the Picket Fence Effect on the Assessment of the R&R of Automatic Impact Modal Hammers

It is of paramount importance both for manufacturers and end users of automatic impact modal hammers to assess the impact R&R of these devices. Until now, the assessment procedure has been typically performed under the test parameters required at the specific application where the hammer is to be applied; namely at frequency bands equal or lower than 20 kHz. Impact modal testing is rarely applied at bands higher than 20 kHz because no modal hammer in the market is yet capable of satisfactorily inputting enough excitation energy at bands higher than 20 kHz in normal test conditions. Properly exciting frequency bands higher than 20 kHz can only be achieved under special test conditions, e.g. when testing very stiff, non-responsive structures (Fig. 11.1) such as hammer calibrator masses [5] and achieving very short contact times between hammer tip and structure. Nonetheless, most of the tested structures in real working conditions never meet this requirement and assessing the R&R of automatic modal hammers below 20 kHz is common practice. This invariably yields unsatisfactory results as described in the next paragraphs.

A hammer impact sampled with a bandwidth of 20 kHz or less is invariably described by only 3–4 data points when impacting a non-responsive structure (Fig. 11.2). The picket fence effect is clearly visible in the figure, and it is suggestive that the real force peak value lays in between the two higher data points at a value higher than 64 N. Filter ring artifacts are also observed immediately before and after the impact [6].

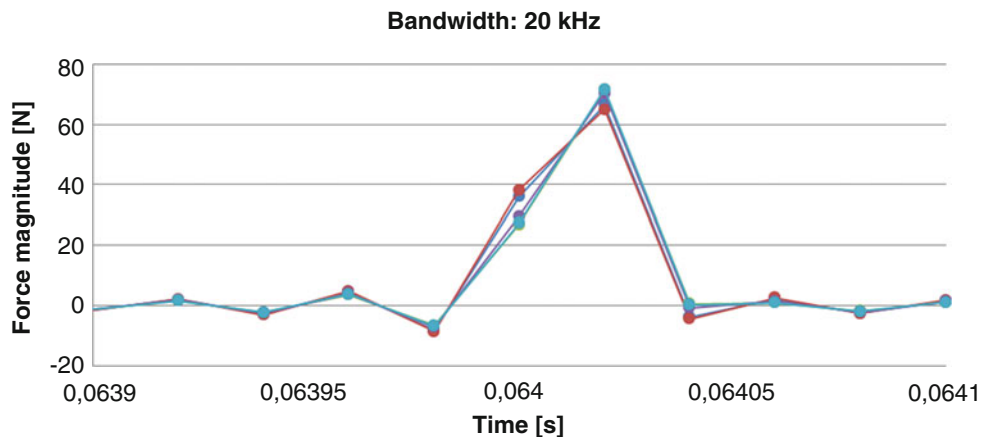


Fig. 11.3 Time signals of a sequence of five automatic hammer impacts performed on a tempered steel plate. Note the difference in peak values for all impacts due to the picket fence effect

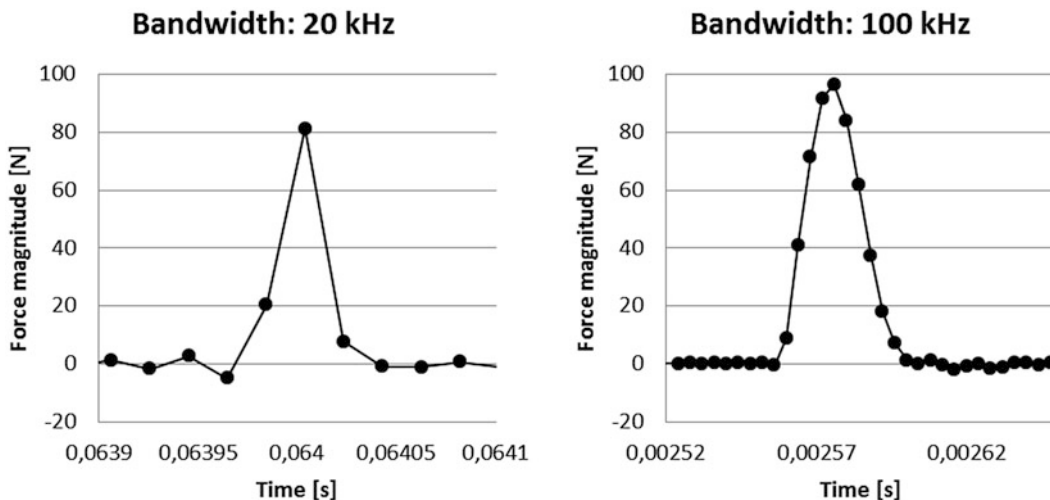


Fig. 11.4 Time signals of a single impact performed with an automatic modal hammer. Both signals have been acquired simultaneously with equipment working under different bandwidth settings. The plot at the left side has been acquired with a bandwidth of 20 kHz and 25,600 FFT lines. In this case, the resulting impact force is of 81 N and the contact time is 78 μ s. The plot at the right side has been acquired with a bandwidth of 100 kHz and 25,600 FFT lines. In this case, the resulting impact force is of 96 N and the contact time is 48 μ s

A sequence of repeated impacts was recorded with the same settings and measurement setup with an automatic modal hammer. The impact R&R assessment is affected by the picket fence effect, and it results in an apparently low R&R, with impacts ranging between 71 and 64 N, this is a difference of ± 3.5 N for a five impacts study (Fig. 11.3).

The picket fence effect has a profound effect on the obtained force peak value but also in the impact contact time (also known as “pulse” in the literature). Fig. 11.4 shows the same automatic hammer impact acquired simultaneously with the two data acquisition systems described in the previous chapter. One DAQ is set to measure with a bandwidth of 20 kHz and 25,600 FFT lines with a resulting measurement time block 1.28 s long. The other DAQ is set to measure with a bandwidth of 100 kHz and 25,600 FFT lines with a resulting measurement time block 0.256 s long. The measurement resolution is evidently better for the plot at the right side of the figure. The force impact peak value and the contact time between hammer tip and test plate are determined with a higher precision.

In Fig. 11.4 left, the hammer tip is shown to be in contact with the surface between $t = 0.06396$ s and $t = 0.06404$ s, resulting in a time difference of 78 μ s. In Fig. 11.4 right, the hammer tip is in contact with the surface between $t = 0.002556$ s and $t = 0.002604$ s, resulting in a time difference of 48 μ s. Some artifacts are still observed in this plot, where a slight vibration is seen right after the impact. This is actually the aliased resonance of the piezo-crystal inside the hammer tip. It is clearly observable in the spectrum when sampling with a bandwidth of 250 kHz.

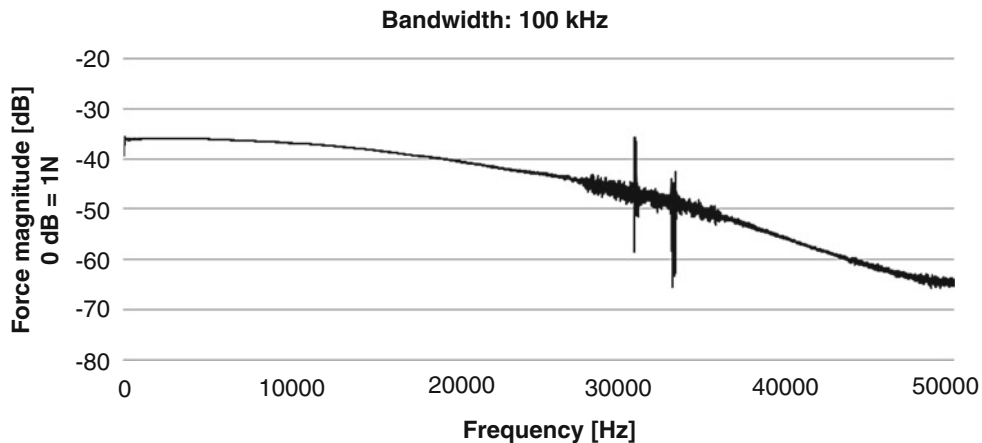


Fig. 11.5 Spectrum of the automatic hammer impact performed on a tempered steel plate shown in Fig. 11.5 right. When measuring with a bandwidth of 100 kHz, the recorded contact time between hammer tip and test plate surface is shown to be shorter and, consequently, a wider frequency band can be excited. With this procedure, the 20 dB rolloff happens at around 40 kHz

The picket fence effect therefore affects the measured contact time between hammer tip and structure, and this has a direct influence on the maximum frequency a hammer can be safely applied to. If the hammer tip is instrumented onto an automatic modal hammer and the sampling is adequate; results show that, for some specific cases, frequencies beyond 20 kHz can be safely excited above the 20 dB rolloff limit [7]. Figure 11.5 shows how the 20 dB rolloff is found at around 40 kHz for this structure. The presence of noise is an issue to be solved with a higher number of averages if needed.

Knowing the maximum frequency an automatic modal hammer can excite is useful to determine on which applications they can be safely used. Structures such as small turbine blades tend to present eigenfrequencies on the 10 kHz range, designed on purpose to avoid high cycle fatigue issues. The test engineer must be certain in these cases that the bandwidth required for the analysis can be excited.

11.4 Results and Discussion: Strategies for a Correct R&R Assessment of Automatic Impact Modal Hammers

This section proposes a series of strategies in order to avoid the aforementioned picket fence effect problems when assessing the R&R of an automatic impact modal hammer. The first strategy can be used with any kind of data acquisition system no matter its maximum sampling frequency. The second strategy has been thought for fast and cost-effective R&R assessments with minimum data treatment.

11.4.1 Autospectra Standard Deviation Plot

The assessment can be properly made if, for example, the corresponding spectra are analyzed instead (Fig. 11.6). A plot of the standard deviation for each FFT point for all five recorded spectra visualizes how the FFT standard deviation is distributed throughout the spectrum (Fig. 11.7). Later on, maximum deviation values can be specified in order to compare the performance of different automatic modal hammers in different working conditions. If an automatic modal hammer shows unstable values in the spectra standard deviation plots, it means appropriate technical measures need to be taken in order to bring the automatic hammer back to its ideal operation conditions.

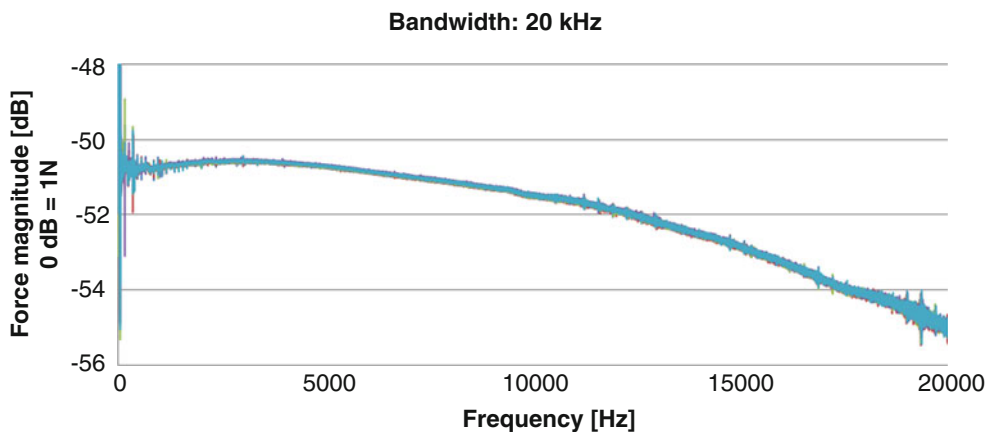


Fig. 11.6 Spectra of the sequence of five automatic hammer impacts performed on a tempered steel plate, previously shown in Fig. 11.3. The spectra show almost no differences among one another even though the time signals are affected by the picket fence effect

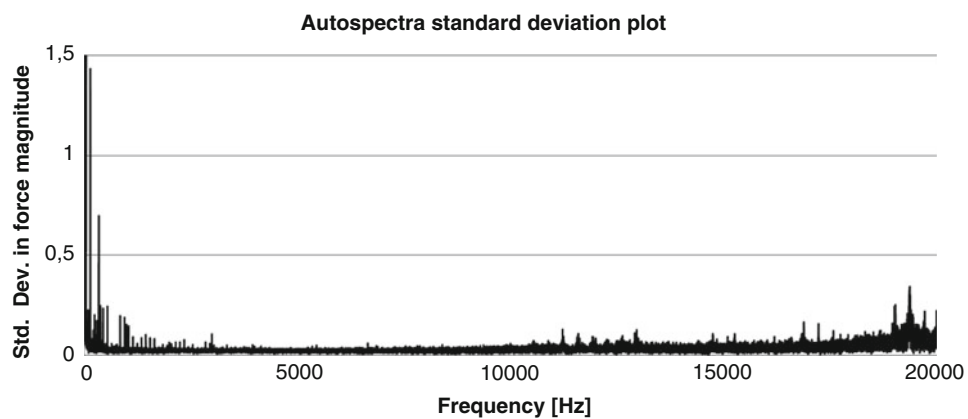


Fig. 11.7 Spectra standard deviation plot for the spectra seen in Fig. 11.6. The standard deviation of each FFT point has been calculated and plotted. Higher deviation values are expected in the noisy frequency regions

11.4.2 Recording of a Series of Impacts Over a Long Time Block

Another strategy can be effortlessly applied if hardware capable of sampling a bandwidth up to 100 kHz or higher is available. The maximum number of FFT lines is to be set in order to measure over a time block as long as possible. In the case of the hardware used in this work, 819,200 FFT lines are the maximum value and are used for the acquisition, resulting in a time block 8.19 s long. The SAM was set to impact at its fastest impact rate, of one impact every 0.6 s. This way, at least 11 impacts can fit in a single measurement (Fig. 11.8). Impact maximum and minimum values can be found directly at the acquisition software, although data has been in this case exported and processed in MATLAB 9.0 for a better visualization of the impacts. For this specific case, the automatic modal hammer impacted with peak values between 89.8 and 93.0 N, resulting in a difference of ± 1.85 N for this study. These values are more near to the reality and more precise than those previously obtained in Fig. 11.3. The data has been exported after the recording generating a file approximately 50 megabytes large.

The cause for the difference in force input peak values is thought to be that, with only 0.6 s between impacts, the test plate resonance has no time to completely fade out. The plate is still resonating when the next impact is performed, probably slightly distorting the results. The use of a heavier tempered steel block or a calibration mass could further improve these R&R results for the same hammer.

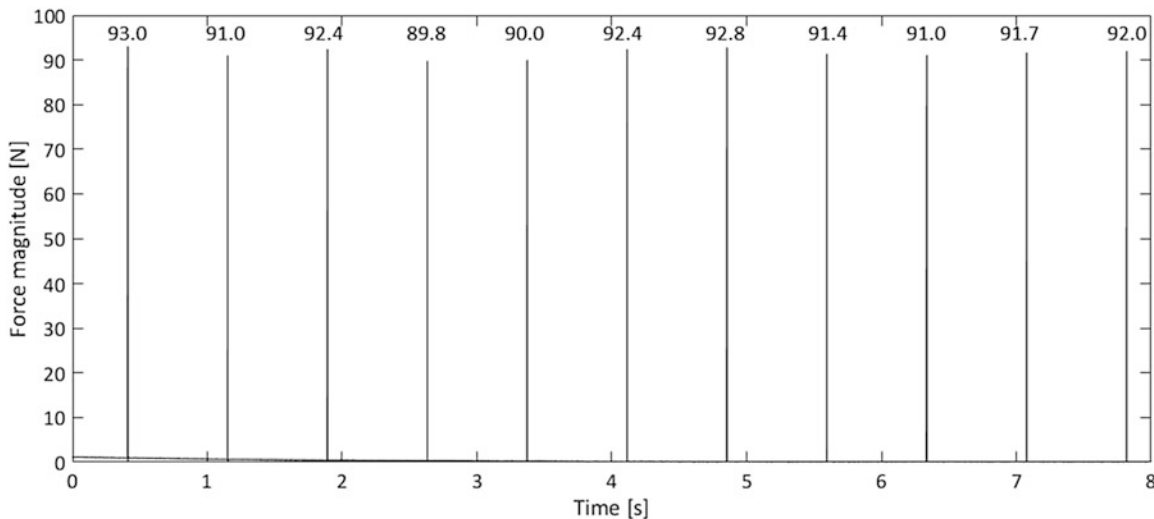


Fig. 11.8 Time signal of eleven consecutive automatic hammer impacts performed on a tempered steel plate. Acquiring a series of impacts over a long time block with a bandwidth of 100 kHz effortlessly provides a number of impact force peak values that can be later analyzed

11.5 Conclusions and Further Work

This work presents just some of the current issues present when trying to assess the R&R of the force peak value and pulse of automatic modal hammers. The findings of this study show that this assessment could be distorted and even misleading if the influence of a number of parameters such as the test structure, the hammer tip calibration and the data acquisition hardware (of which the sampling frequency is entirely dependent) are not accounted for. The test engineer has to find as well a compromise among several parameters:

- Sampling frequency: if it is low, the picket fence effect will distort the measurements, but it has to be high enough. 100 kHz were proven in this paper to set a good middle ground between very high resolutions and the use of multi-purpose acquisition equipment.
- Number of FFT lines: a low number means a shorter measurement block, which results in a more compact dataset. A high number of FFT lines means a longer measurement block and datasets that can stretch well into the hundreds of megabytes. This can make the data treatment and representation rather cumbersome when many datasets of hundreds of megabytes are involved and the

Further work could be devoted to a detailed study on the optimization of all these above mentioned parameters for a minimum R&R assessment time useful both for end users and automatic hammer manufacturers.

References

1. Sauer, J., et al.: Modal Shapes Extraction by Automated 3D Laser Scanning Vibrometry with High Spatial Resolution for Detailed FE Model Validation, Oral-only presentation at the EuroBrake 2017 Conference #EB2017-VDT-024, May 2017
2. Ritzmann, S., Meyerlingh, M.: Ermüdungstests an Triebwerksbaugruppen unter speziellen modalen Bedingungen, Proceedings of the 4th VDI Conference in Vibration Analysis and Identification, VDI-Berichte 2259, p. 149, March 2016
3. Keil, M.: Automatic Shim Damping Tests under Different Conditions and Setups – Comparison of Different Damping Estimation Methods, Oral-only presentation at the EuroBrake 2017 Conference #EB2017-VDT-017, May 2017
4. Rausch, C., et al.: Identification of Brake Disc Material Properties by Specimen Damping Measurement, Proceedings of the EuroBrake 2017 Conference, #EB2017-VDT-022, May 2017
5. The Modal Shop, Inc.: Impact Hammer Calibration System Models 9155D-961. Online resource [http://www.modalshop.com/filelibrary/Impact-Hammer-Calibrator-Datasheet-\(DS-0080\).pdf](http://www.modalshop.com/filelibrary/Impact-Hammer-Calibrator-Datasheet-(DS-0080).pdf) [Retrieved on 20th October 2017]
6. Avitabile, P., Peres, M.: Excitation Techniques – Do's and Don'ts, Presentation at the XXX International Modal Analysis Conference, February 2012
7. Avitabile, P.: Someone told me that you can't accept a FRF when the input spectrum has more than 20 dB rolloff *SEM Experimental Techniques*, pp. 1–2, October 2011



Chapter 12

Estimation of Railway Track Longitudinal Profile Using Vehicle-Based Inertial Measurements

Paraic Quirke, Eugene J. Obrien, Cathal Bowe, and Daniel Cantero

Abstract The emergence of systematic condition monitoring of railway infrastructure has the potential to reduce the cost of providing a safe network. The traditional ‘inspect and rectify’ style of maintenance planning is being increasingly complemented by a ‘monitor, predict and prevent’ approach. In order to facilitate this, the frequency of track measurement must be increased from the current periodic measurements using specialised instrumented vehicles. In recent years there has been an increased interest in the challenge of finding railway track longitudinal profile using the response of passing instrumented vehicles as a by-product of regular service. A method is presented where the inertial response of a train bogie is used as input to an optimisation technique that infers the track longitudinal profile. The method finds the track profile that generates a numerical output from a vehicle-track interaction model that best fits a measured response. Experimental data is used to validate the longitudinal profile estimation algorithm. An Irish Rail InterCity train was instrumented to capture in-service vehicle responses. During the testing period, the longitudinal profile of a section of this line featuring a known settlement issue was surveyed by traditional means, for reference. A calibrated vehicle is used in the optimisation algorithm to find the longitudinal profile that generates a numerical vehicle response best fitting the measured data. The known track settlement is found quite well using the calibrated vehicle, thereby validating the method. The reproducibility of the method is assessed. While improvements in accuracy and reproducibility are required to bring the method up to best practice standards, the information provided demonstrates the ability to find localised changes in track profile.

Keywords Railway track · Longitudinal profile · Drive by · Measurement · Vehicle track interaction · Cross entropy · Optimisation

12.1 Introduction

In any structural health monitoring system, the effectiveness of condition monitoring in identifying maintenance issues can benefit from real-time automated systems. This is especially true for railway track. This paper describes the field testing of a numerical method presented in OBrien *et al.* [1] using a calibrated vehicle model detailed in Quirke *et al.* [2]. This is an inverse technique whereby inertial measurements on an Irish Rail train are used to find the longitudinal track profile that generated the measurements. By installing the sensors on the train bogie, a loaded track profile is inferred by the method, considering both the track longitudinal profile and the variation in longitudinal track stiffness.

P. Quirke (✉)

Kilcullen Business Campus, Co. Kildare, Ireland

Iarnród Éireann Irish Rail, Technical Department, Engineering & New Works, Dublin, Ireland

School of Civil Engineering, University College Dublin, Dublin, Ireland

e-mail: pquirke@murphysurveys.ie

E. J. Obrien

School of Civil Engineering, University College Dublin, Dublin, Ireland

e-mail: eugene.obrien@ucd.ie

C. Bowe

Iarnród Éireann Irish Rail, Technical Department, Engineering & New Works, Dublin, Ireland

e-mail: cathal.bowe@irishrail.ie

D. Cantero

Department of Structural Engineering, Norwegian University of Science & Technology, Trondheim, Norway

e-mail: daniel.cantero@ntnu.no

Table 12.1 Properties of sensors

Sensor location	Type	Name	Range
Bogie – Bounce	Triaxial Accelerometer	Disynet-DA3802-015 g	±15 g
Bogie – Pitch	Triaxial Gyrometer	Crossbow VG400CC-200	±200 °/s

12.2 Field Testing

Vehicle response data was acquired using inertial sensors installed on the trailer (non-powered) bogie of an Irish Rail Hyundai Rotem InterCity fleet car. A tri-axial accelerometer and tri-axial gyrometer were installed as close to the bogie centre of mass as possible. The properties of both sensors used are listed in Table 12.1. A sampling frequency of 500 Hz was adopted for most of the testing. A Global Positioning System (GPS) antenna was used to detect train movement and approximately geolocate the measured data. Vehicle position was recorded at a frequency of 5 Hz. Testing took place on the Dublin-Belfast line from 13th January to 3rd February 2016. During this period, 57 return journeys were made on the line.

12.3 Model Description

A numerical vehicle model is used in the optimisation technique described in this paper to find track profiles that generate an inertial response on the vehicle bogie that best fits the measured data from the in-service train. A multi-body 2D car model is chosen over a 3D model to reduce the computational effort needed to run the simulations required in the optimisation procedure. The model uses rigid bars to represent the car body and bogies. Spring-damper combinations are used to model the behaviour of the primary and secondary suspensions.

Parameters for the Hyundai-Rotem train car are found through a calibration exercise carried out using data from the same measurement campaign. A full description of the model and the calibrated model parameters used in this study are given in Quirke *et al.* [2].

12.4 Methodology

The aim of this investigation is to find the longitudinal profile of a railway track from the measured inertial response of an in-service train. Measured data is used as input to a numerical optimisation method executed in Matlab. Multiple datasets are used to infer track longitudinal profiles though a section of track with a known settlement so that comparisons to surveyed track longitudinal profile can be made.

A section of track on the Dublin-Belfast railway line was identified for this study due to historical issues with track settlement there. The profile is shown in Fig. 12.1. A dip in the profile of approximately 80 mm over the 80 m section can be observed.

The raw data is filtered using a 6th order Butterworth bandpass filter (0.25–25 Hz) to remove the effects of sleeper spacing, drift, temperature and other noise in the signal. As detailed in Quirke *et al.* [2] a post-measurement calibration factor of 23.9 is required to account for the sensor offset from the bogie centre of mass.

Cross Entropy (CE) optimisation is used in this paper to find track longitudinal profile from the measured inertial response. The CE method uses Monte Carlo simulation to generate a population of trial solutions from a mean and standard deviation for each variable being sought. In this study a population of trial track longitudinal profiles is generated for both axles on the leading bogie of a vehicle model. Numerical outputs, generated by running the vehicle over the profiles in the population of estimates, are compared to measured data to find an elite set of profiles. This set is used to improve the population of estimates until the method converges to the solution.

In order to avoid local minima during the optimisation and thus converge to the global optimum, the dimensionality of the problem must be kept to a suitable level. This is controlled by limiting the number of variables considered at a given time. In this case each profile elevation is taken as a variable in the optimisation. To keep the dimensionality of the problem low, a limited number of elevations are considered. However, elevations are required at regular intervals to adequately define the longitudinal profile. Therefore, in order to infer a longitudinal profile over hundreds of metres the algorithm steps through the data in phases, inferring a small section of the profile in each phase. The inferred profile is then used to set the mean and

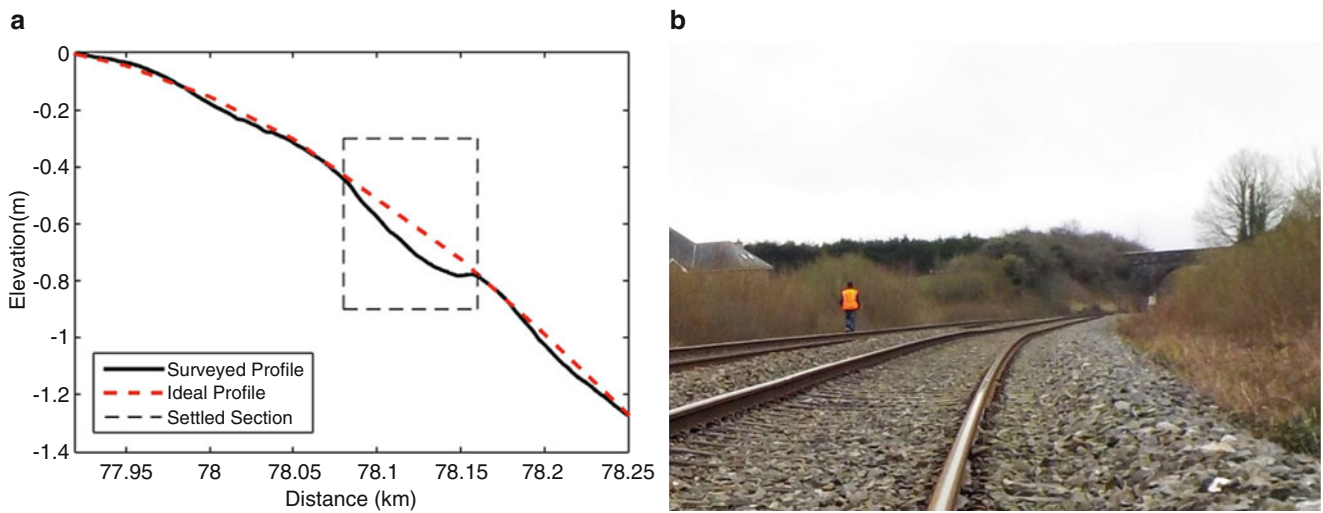


Fig. 12.1 (a) Level survey of track longitudinal profile; (b) Track settlement location (Photograph: C. Bowe)

standard deviation for the generation of profile estimates in the next phase. This stepping technique, and the vector transfer methodology required to enable it, are described in detail in OBrien *et al.* [2]. The elevation estimates for each profile in the population are ranked by minimising the value of an objective sub-function, O_i , where i is the scan number corresponding to the elevations in the profiles. The objective sub-function is calculated at each scan number, i , as follows:

$$O_i = W_A (\ddot{u}_{b1,i}^* - \ddot{u}_i^\circ)^2 + W_R (\dot{\theta}_{b1,i} - \dot{\theta}_i^\circ)^2$$

where W_A and W_R are weighting factors for the bogie vertical acceleration and angular velocity respectively. Measured signals are denoted with the superscript ‘ \circ ’. The weighting factors are required due to the different orders of magnitude of the bogie vertical acceleration and angular velocity. Weighting factors are calculated as the ratio of the sum of squared differences between the bogie acceleration and bogie angular velocity.

Convergence is achieved when the squared difference between the sum of standard deviations (for all scan numbers) for consecutive generations falls below a convergence threshold. As the standard deviation diminishes through the generations, there is less variance in the population of estimates, indicating that the process has converged to a solution. Tolerance limits are introduced as a positive and negative offset from the measured signals to ensure that, if exceeded by the model output, convergence is blocked and additional variance is introduced to the population of profiles in the next generation of estimates.

12.5 Results

Figure 12.2 presents the track profiles inferred from bogie inertial response data, measured through the case study section in 46 different runs. Aside from a surveyed dip at a track distance of 78.03 km, all other main features are detected. Generally, the magnitude of the elevation changes appear to be overestimated by the algorithm by a factor of about 2. Errors in the gyrometer calibration may be partially responsible for the poor match to the elevational profile in terms of magnitude. The use of a 2D vehicle model and possible inaccuracies in vehicle calibration, resulting in a poor representation of the vehicle dynamics, may also be a factor.

12.6 Conclusions

Cross Entropy optimisation is used to find the track longitudinal profile generating vehicle model responses that best match measured inertial response of an Irish Rail train. A novel approach of using tolerance limits is used, combined with suitable weighting of the optimisation objective function, to inject variance where required. The method presented in this paper can be

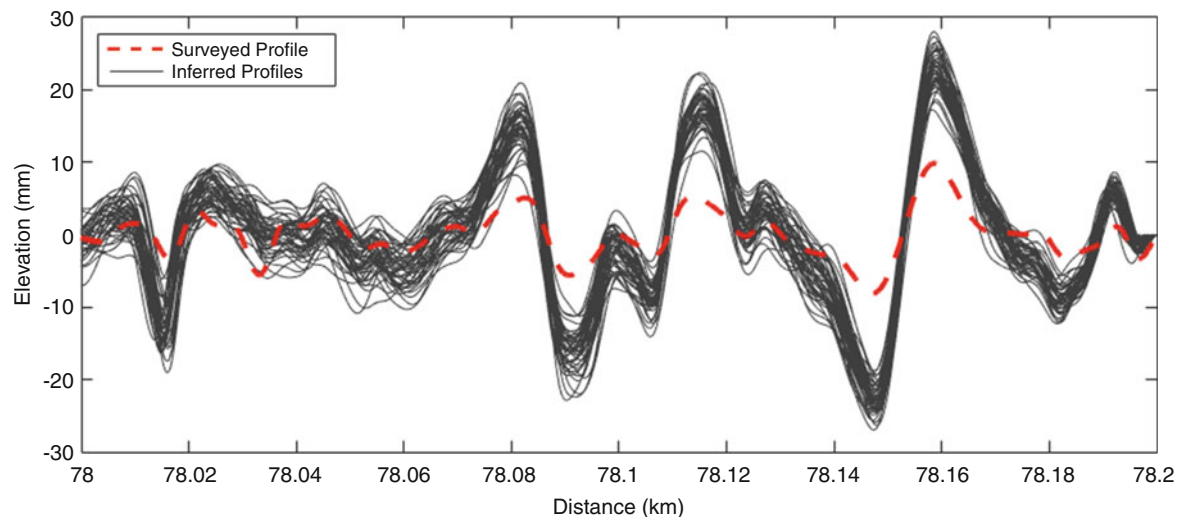


Fig. 12.2 Filtered inferred profiles, $r(x)$, for 46 runs, and filtered surveyed profile (3–25 m)

readily implemented using low-cost inertial sensors and simple numerical modelling. The method can give frequent updates of the track profile allowing the identification of differences in profiles produced suddenly or during prolonged periods of time.

References

1. O'Brien, E.J., Bowe, C., Quirke, P., Cantero, D.: Determination of longitudinal profile of railway track using vehicle-based inertial readings. *J Rail Rapid Transit.* **231**(5), 518–534 (2016)
2. Quirke P., O'Brien E.J., Bowe C., Cantero D.: Calibration of railway vehicle model using measured inertial response of in-service train for use in drive-by track monitoring system. Article under review (2017)



Chapter 13

Experimental Modal Analysis of Structures with Conventional Versus Contact-Free Suspension

S. Schneider, T. T. Mallareddy, D. J. Alarcón, R. Kamenzky, and P. Blaschke

Abstract The existence of free boundary conditions is frequently assumed for Experimental Modal Analysis (EMA) of a structure. However, free-free conditions can only be approximated because the structure must be supported in some manner. Therefore, comparing simulated data with experimental data can be deceiving, because these suspensions falsify modal parameters especially structural damping and stiffness. The current scenario of structural analysis is more towards focusing on modal updating or correlation, rather than the simulation results (FE) or the experimental results. So it is imperative to bridge the gap between FE and EMA, by carefully studying various parameters.

To overcome these drawbacks, levitation is suggested as a truly free-free suspension method. The levitation method was developed to allow a non-destructive, adaptable, and completely contactless approach for material testing: the structure under test is suspended on a thin film of pressurized air providing an aerodynamic bearing, levitating the specimen. Two suspension devices were constructed. Pressurized air is circulated into a casing with a single outlet (“air cushion”) or a fine grid of outlets (“air bed”).

A study was performed to investigate the influence of the support conditions on the modal parameters eigenfrequency and damping. Tested specimens were a brass plate, a stainless steel plate and two composite material probes. The tested suspension methods were (a) foam mat, (b) air cushion and (c) air bed. Modal tests were performed using a Scanning Laser Doppler Vibrometer (SLDV) and an automatic modal hammer for excitation. Evaluations of the measurements were performed manually.

The results showed that the detected eigenfrequencies of the metallic specimen have a variation below $\pm 0.3\%$ for the tested suspension methods. This variation is 10 times higher for the composite plates and lies between $\pm 3\%$. The damping ratios of the levitation suspensions show the different material behavior of metallic and composite specimen: damping ratios of metallic specimen lie between 0.05–0.5% whereas damping ratios of composite plates are ten times higher and lie between 0.3% and 3%. The damping ratios measured with the air cushion are smaller than the damping ratios for the air bed supporting the hypothesis that a laminar air film under the specimen leads to less additional damping.

The study shows that EMA can be performed on metallic and composite specimens using contact-less suspension methods. Especially for light-weight material specimens where EMA cannot be performed or where the results are not reliable, the contact-less suspension (levitation method) can be used.

Keywords Modal Analysis · Levitation · Free-free suspension · Composite materials · Automatic modal hammer

S. Schneider (✉) · T. T. Mallareddy · D. J. Alarcón · R. Kamenzky
Technical University of Applied Sciences Wildau, Wildau, Germany
e-mail: daniel.alarcon@th-wildau.de

P. Blaschke
Technical University of Applied Sciences Wildau, Wildau, Germany
NV Tech Design GmbH, Steinheim an der Murr, Germany

Nomenclature

EMA	Experimental Modal Analysis
FRF	Frequency Response Function
MAC	Modal Assurance Criterion
NVH	Noise, Vibration, Harshness
RTM	Resin Transfer Moulding
SAM	Scalable Automatic Modal Hammer
SLDV	Scanning Laser Doppler Vibrometer

13.1 Introduction

The existence of free boundary conditions is frequently assumed for the Experimental Modal Analysis (EMA) of a structure. However, free-free conditions can only be approximated because the structure must be supported in some manner. Usually, soft supports like foam mats are used to suspend the specimen, but the stiffness and damping of these supports will affect the modal parameters of the combined structural system [1].

The current scenario of structural analysis is more towards focusing on modal updating or correlation, rather than solely the finite element simulation results (FE) or the experimental results. So it is imperative to bridge the gap between FE and EMA, by carefully studying various parameters. Free boundary conditions are the desired support conditions for comparing the experimental results to the computational results. The free-free test environment is easily achieved in theoretical calculations but is usually compromised when measured experimentally due to the requirement to support the structure against gravity forces [2]. Therefore, comparing simulated data with experimental data can be deceiving, because these suspensions falsify modal parameters especially damping and stiffness.

To overcome these drawbacks, levitation is suggested as a truly free-free suspension method. The levitation method was developed to allow a non-destructive, adaptable, and completely contactless approach for material testing: the structure under test is suspended on a thin film of pressurized air providing an aerodynamic bearing by levitating the specimen. Two suspension devices were constructed. Pressurized air is circulated into a casing with a single outlet (“air cushion”) or a fine grid of outlets (“air bed”).

A study was performed to investigate the influence of three support conditions on the modal parameters eigenfrequency and damping ratio. Tested specimens were a brass plate, a stainless steel plate and two composite materials. The tested suspension methods were (a) foam mat, (b) air cushion and (c) air bed. Modal tests were performed using a Scanning Laser Doppler Vibrometer (SLDV) and an automatic modal hammer for excitation. Evaluations of the measurements were performed manually.

13.2 Materials and Methods

The EMA measurements of the steel plate and composite plates were performed with a Scanning Laser Doppler Vibrometer (SLDV) ScanSet (Maul Theet GmbH, Berlin, Germany) with laser head OFV-5000 (Polytec GmbH, Waldbronn, Germany) as a roving response sensor, Fig. 13.1 left. The EMA measurement of the brass plate was performed using a PSV-500-3D SLDV system (Polytec GmbH, Waldbronn, Germany), Fig. 13.1 right.

For EMA excitation the automatic modal hammer SAM (NV Tech Design, Steinheim, Germany) was used. The SAM was instrumented with a light impact hammer 086E80 (PCB Piezotronics, Inc., NY, US). The metallic specimens were tested with a measurement time of 1.28 s and a sample rate of 20 kHz (25,600 FFT-Lines), for the composite specimens a measurement time of 2.56 s and sample rate of 5 kHz (12,800 FFT lines) was used.

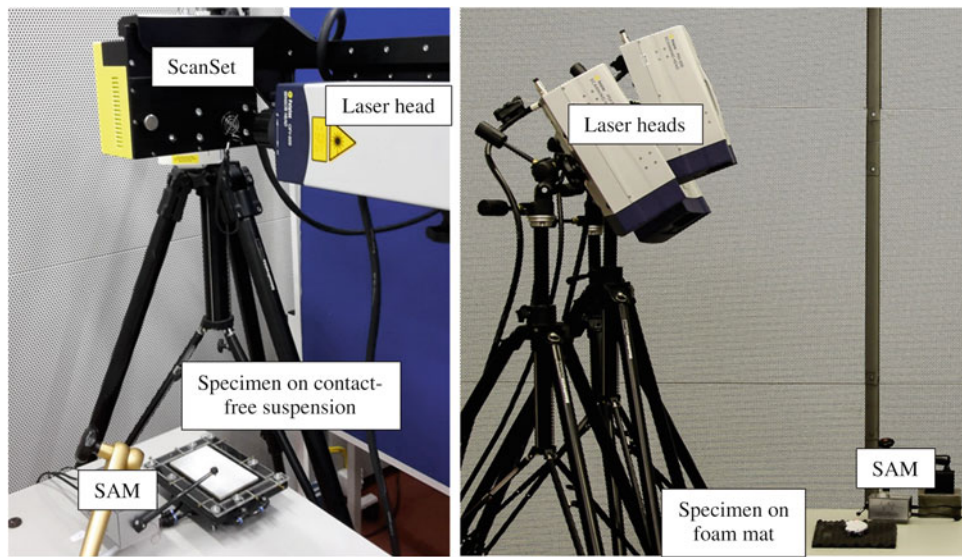


Fig. 13.1 Setup of the EMA measurements. A scalable automatic modal hammer (SAM) was used to excite the specimen. System response was measured with 1D SLDV (Left) or 3D SLDV (right)

Table 13.1 Material parameters and picture of the four specimen included in the study

Material	Stainless Steel	Brass	Composite RTM	Composite Sandwich
Weight in g	249.8	398	93.5	18.3
Dimensions (WxLxH) in mm	70x110x4	60x78x10	80x140x4	90x140x10
Specimen				

Measurements of eigenfrequencies and modal damping ratios were performed on four different materials and with three suspension methods. Table 13.1 shows the geometrical parameters of the used specimen. The composite specimens were provided from *Fraunhofer Institute for Applied Polymer Research / PYCO*, Teltow, Germany. The “Composite RTM” was manufactured using a Resin Transfer Moulding (RTM) process with 17 layers of glass fiber (269 g/m^3) and resin (Cytech 890) resulting in a fiber content of 40%. The “Composite Sandwich” is a nap core sandwich composite consisting of aramid hybrid yarn knitted fabric impregnated with the phenolic formaldehyde resin and a facing of Isovola Airpreg 8242.

Three suspension methods were used in this study (Fig. 13.2):

- (a) Foam mat,
- (b) Air cushion,
- (c) Air bed.

The EMA was performed using the hand-fit method in vModal (Maul Theet GmbH, Berlin, Germany) using a generally damped SDOF (Single Degree of Freedom) approach.

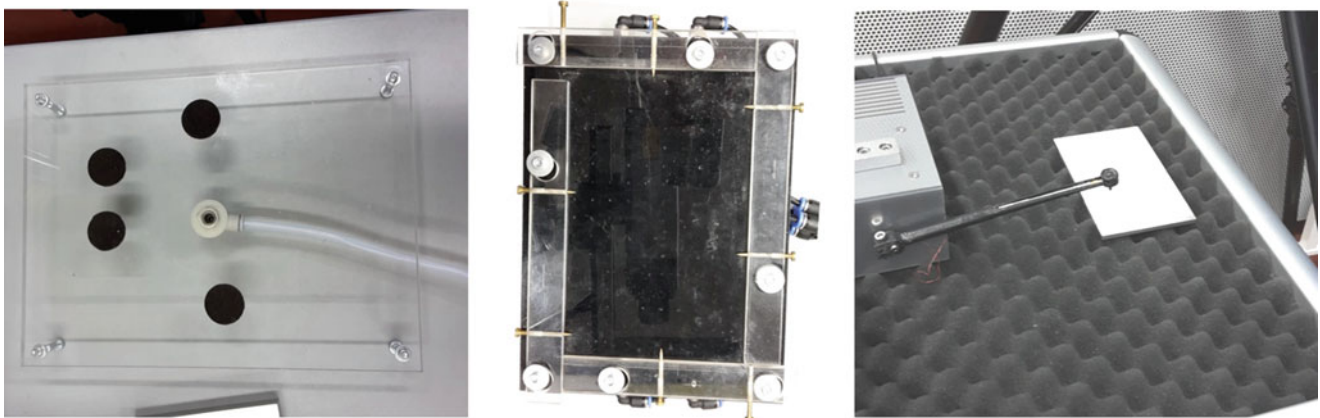


Fig. 13.2 Utilized suspension methods. Left: Air cushion with a single outlet for pressurized air. The adhesive felt stickers keep the specimen in the correct position. Center: Air bed with fine grid of holes for pressurized air. Pointed screws prevent the lateral movement of the specimen. Right: Foam mat with specimen and automatic modal hammer (SAM)

The “air cushion” consists of an acryl glass plate with a single outlet for pressurized air, Fig. 13.2 left. Lateral movement of the specimen was inhibited by circular felt adhesives. The “air bed” consists of a casing with a fine grid of opening holes, Fig. 13.2, center. Pointed screws prevent the specimen from moving. Air bed and air cushion were connected to a compressed air supply with 5 bar. An additional pressure valve at the suspension structure was used to regulate the required air pressure. A more detailed description of the levitation casings can be found in [3].

13.3 Results and Discussion

A grid of at least 5x8 measurement points was used on the rectangular specimens. Depending on the suspension, the output signals were of different quality resulting in the frequency response functions (FRF) given in Fig. 13.3. Especially the air cushion leads to much noisier FRFs.

Nonetheless it was possible to perform a manual fitting procedure for all data sets to analyze the eigenfrequencies and modal damping ratios. The Modal Assurance Criterion (MAC) proved the linear independency of the detected modes for all data sets.

The modal damping and eigenfrequencies were analyzed with a generally damped single degree of freedom (SDOF) method using a manual peak-picking method in the analyzing software. Figure 13.4 shows the results of the modal damping ratios of the first 6–12 modes for all specimens on all suspension methods.

It can be generally observed from Fig. 13.4, that the damping ratios for the contact-less suspensions (air cushion and air bed) are higher than the damping on the foam mat. Usually, the damping obtained from the air bed is the highest followed by the air cushion and foam mat. The damping ratios show the different material behavior of metallic and composite specimen: damping ratios of metallic specimen lie between 0.05% and 0.5% whereas damping ratios of composite plates are ten times higher and lie between 0.3% and 3%.

Another observation is related to the general distribution of damping ratio over mode number: the differences of damping ratios between conventional and contact-free suspension methods are higher in metallic structures than in composite materials. Calculating the damping value differences between contact-free and conventional suspensions leads to the results shown in Table 13.2.

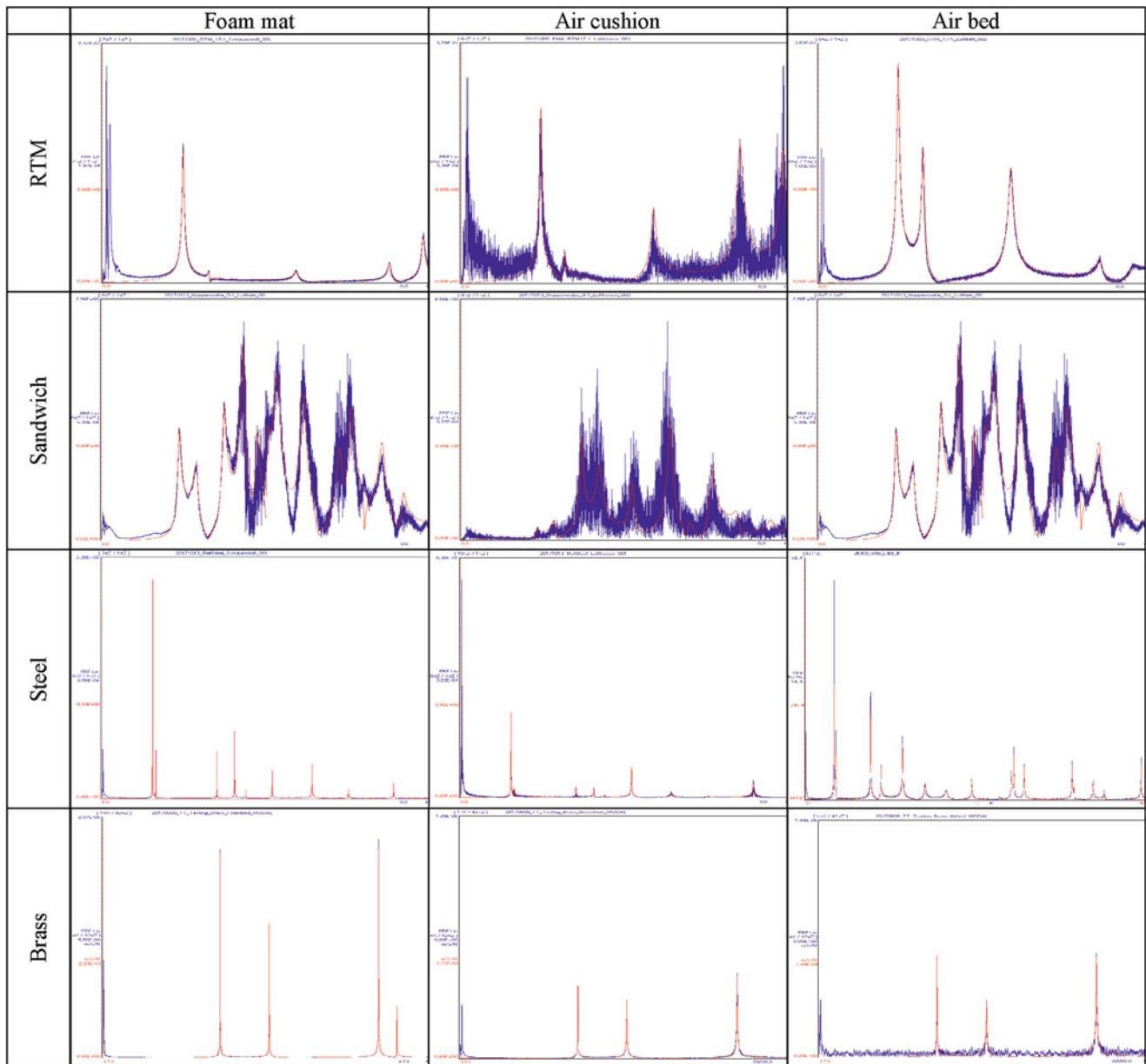


Fig. 13.3 FRF and hand fitted generally damped SDOF model of composite and metallic specimen on all tested suspension. The scaling of these FRF plots is different depending on the structure

To evaluate the detectability of eigenfrequencies, the eigenfrequencies were related to the mean eigenfrequencies of the three suspension values per structure. Figure 13.5 shows the percental variation of eigenfrequencies from the mean value.

The detected eigenfrequencies of the metallic specimen have a variation below $\pm 0,3\%$. This variation is up to 10 times higher for the composite plates and lies between $\pm 3\%$.

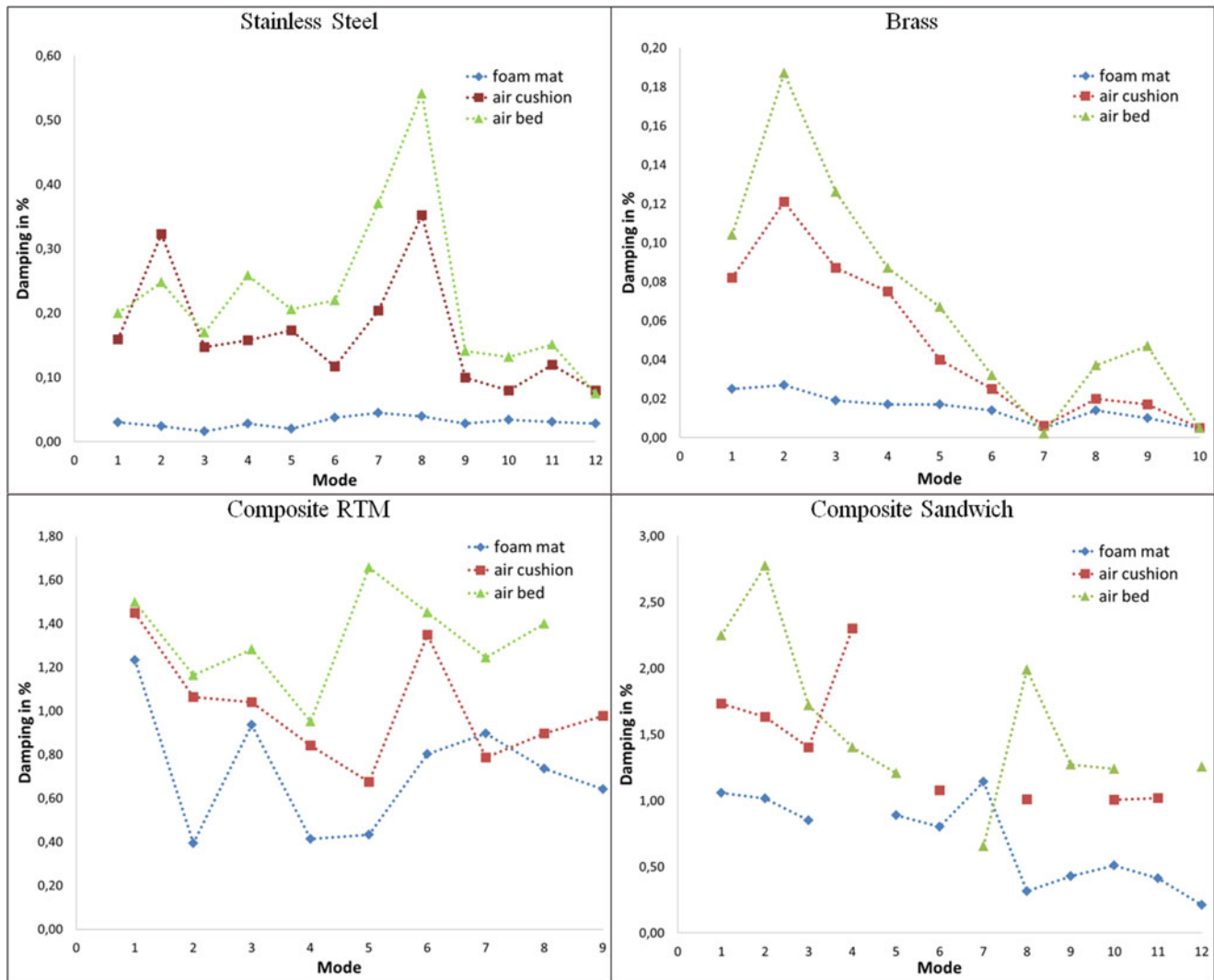


Fig. 13.4 Damping of metallic and composite specimens on three different suspensions

Table 13.2 Mean growth factor of damping ratio between contact-free and conventional suspensions

Specimen	Air cushion/foam mat	Air bed/foam mat
Steel	4.94	6.60
Brass	1.62	2.78
Composite RTM	0.54	1.10
Composite sandwich	0.99	1.94

13.4 Conclusion

In this study, the influence of contact-less suspension methods on the identification of eigenfrequency and modal damping using Experimental Modal Analysis was investigated.

The eigenfrequencies could be detected within a small variation range. Although the variation of detected eigenfrequencies is much higher for the composite plates than for the metallic plates (Fig. 13.5), the quantitative differences are low, Fig. 13.6.

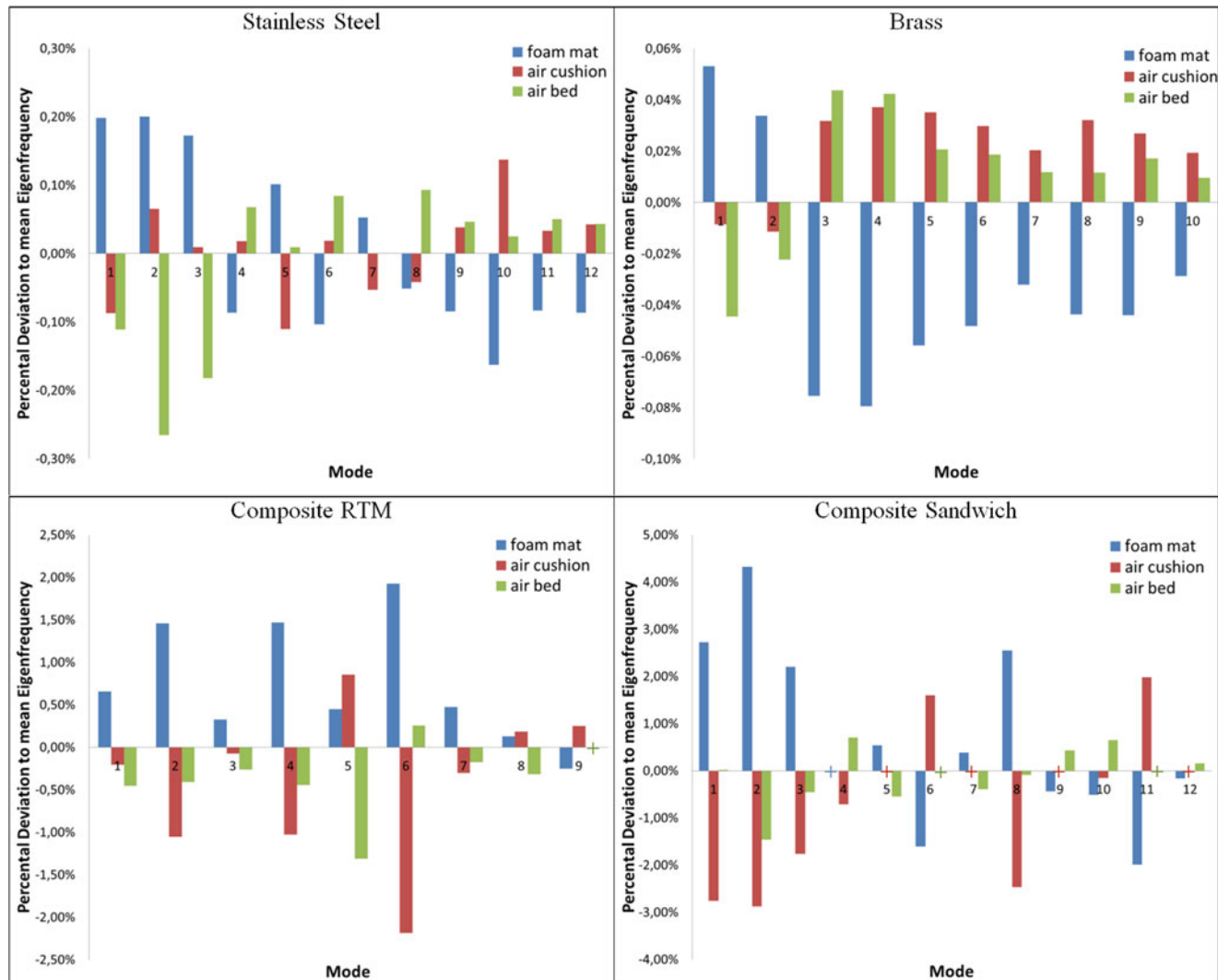


Fig. 13.5 Percental variation of eigenfrequencies related to the mean eigenfrequency of metallic and composite specimens on three different suspensions. Crosses mark where no mode/ no eigenfrequency could be detected

The contact-less suspension methods leads to additional damping in the test system. The factor of damping ratio increase lies between 1.6 and 6.6 (Table 13.2) for the metallic specimens and between 0.54 and 1.94 (Table 13.2) for the composite specimens, which is substantially different.

The study results lead to the conclusion that Experimental Modal Analysis can be performed on specimens with a contact-less suspension. However, this approach seems not to be beneficial compared to the standard technique for metallic specimen with a certain weight. For lightweight material structures such as most composite materials, a standard EMA measurement often is not possible because the structure cannot be excited properly. Further research on this topic is currently being performed, [4]. For these special cases where an EMA measurement cannot be performed or where the results are not reliable, the contact-less suspension (levitation method) can be used.

Further investigations will be concentrated on the origin of the additional damping by the air flow and how to minimize this influence. In the future, a more detailed study should be performed including more/different composite materials, the influence of specimen size and geometry and a comparison of modal parameters with numerical simulations.

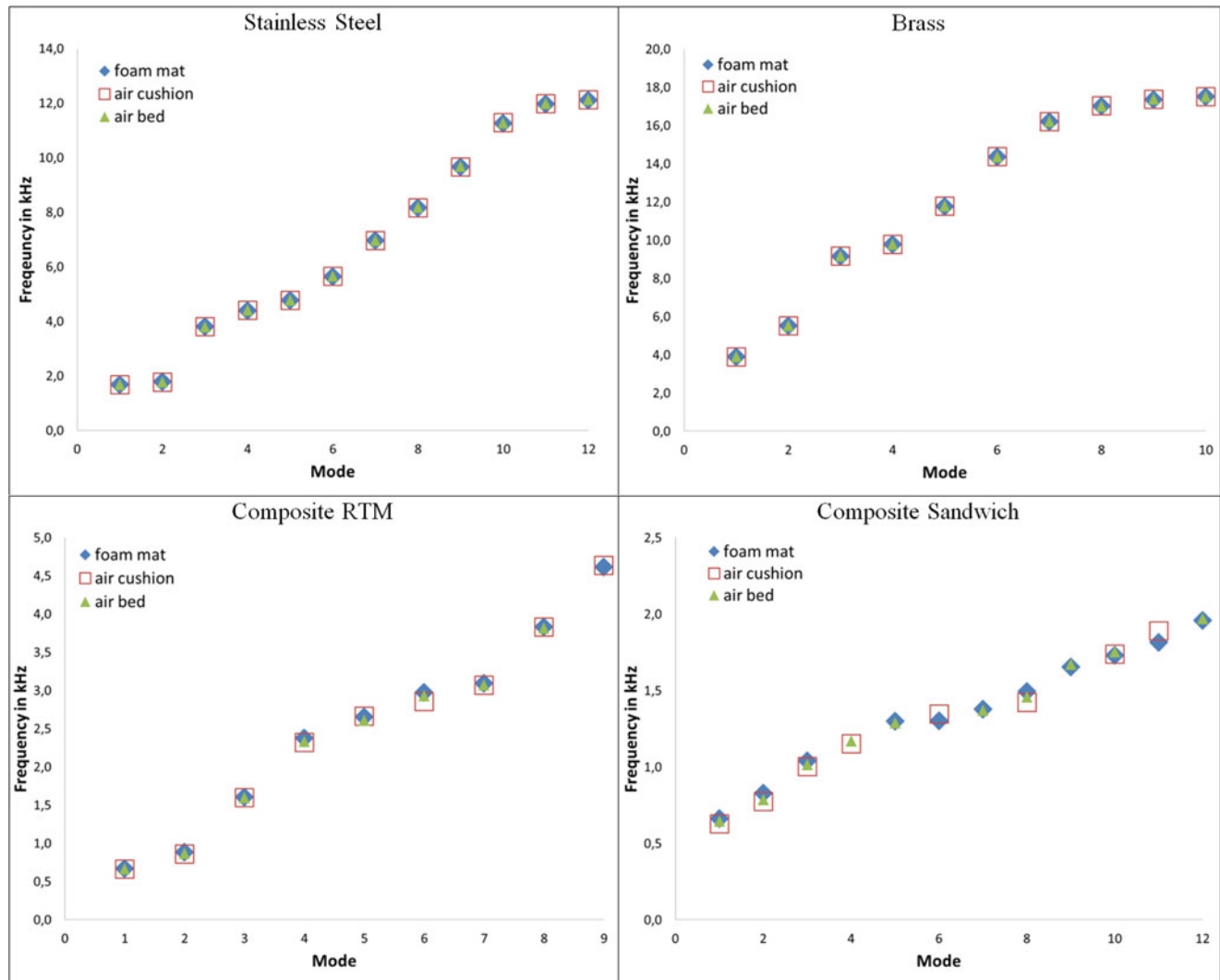


Fig. 13.6 Quantitative values of the detected eigenfrequencies on foam mat, air cushion and air bed

Acknowledgements This research is funded by means of European Funds for Regional Development.

References

1. Carne, T., Griffith, D., Casias, M.: Support conditions for experimental modal analysis. *Sound. Vib.* **41**, 10–15 (2007)
2. McConnell, K.: The Elusive Free-Free-Boundary Condition. Proceedings of the XXXV International Modal Analysis Conference, Garden Grove, CA (2016)
3. Kamenzky, R., Schneider, T., Schneider, S., Blaschke, P.: LEx- Levitation and Excitation method for Operational Modal Analysis. International Operational Modal Analysis Conference 2017, Ingolstadt, Germany (2017)
4. Mallareddy, T.T., Schneider, S., Blaschke, P.: Application of Advanced Hammer Excitation Technique on Light Weight Materials using Scalable Automatic Modal Hammer. Proceedings of the XXXVI International Modal Analysis Conference, Orlando, FL (2018)



Chapter 14

Active Learning Approaches to Structural Health Monitoring

L. Bull, G. Manson, K. Worden, and N. Dervilis

Abstract A critical issue for structural health monitoring (SHM) strategies based on pattern recognition models is a lack of diagnostic labels for system data. In an engineering context these labels are costly to obtain, and as a result, conventional supervised learning is not feasible. Active learning tools look to solve this issue by selecting a limited number of the most informative data to query for labels. This article demonstrates the relevance of active learning, using the algorithm proposed by Dasgupta and Hsu (the DH active learner). Results are provided for applications of this technique to engineering data from aircraft experiments.

Keywords Structural health monitoring · Active learning · Guided sampling · Semi-supervised learning · Machine learning

14.1 Active Learning

Active learning, or query learning, is motivated by scenarios in which it is relatively easy to amass large quantities of data but costly to obtain their labels [2]. Like supervised learning the goal is to ultimately learn a classifier; however, here the data are initially unlabelled—more precisely, the labels are hidden, and each of them can be revealed, but at a cost [3].

Consider the data (arriving as a stream or pool) $\mathcal{X} = \{\mathbf{x}_i\}_{i=1}^N$, each of which has a hidden label that can be queried from $\mathcal{Y} = \{y_i\}_{i=1}^N$. The idea is to find a classifier h that provides an accurate mapping of observations \mathcal{X} to labels \mathcal{Y} , while keeping queries to a minimum [2]. In summary, an active learner tries to get the most out of a limited budget n by choosing query points $\{\hat{\mathbf{x}}_i\}_{i=1}^n$ in an intelligent and adaptive manner [2]. The *generalised* steps behind active learning are summarised below and in Fig. 14.1, left.

1. Start with a pool of unlabelled data, these may arrive as a stream,
 $X \subset \mathcal{X}$.
2. By some querying regime establish which data carry the most information, budget n ,
 $\{\hat{\mathbf{x}}_i\}_{i=1}^n \subset X$.
3. Provide labels for these data,
 $\{\hat{y}_i\}_{i=1}^n \subset \mathcal{Y} \mid \{\hat{\mathbf{x}}_i\}_{i=1}^n$.
4. Train a classifier h on this informative subset,
 $h : \mathcal{X} \mapsto \mathcal{Y} \mid \{\hat{\mathbf{x}}_i\}, \{\hat{y}_i\}_{i=1}^n$.

14.2 The Two Faces of Active learning

Reference [2] offers an excellent definition (and comparison) of the two distinct narratives used to describe when active learning is useful. These approaches are summarised below:

L. Bull (✉) · G. Manson · K. Worden · N. Dervilis
Dynamics Research Group, Department of Mechanical Engineering, Sheffield, UK
e-mail: lbull1@sheffield.ac.uk

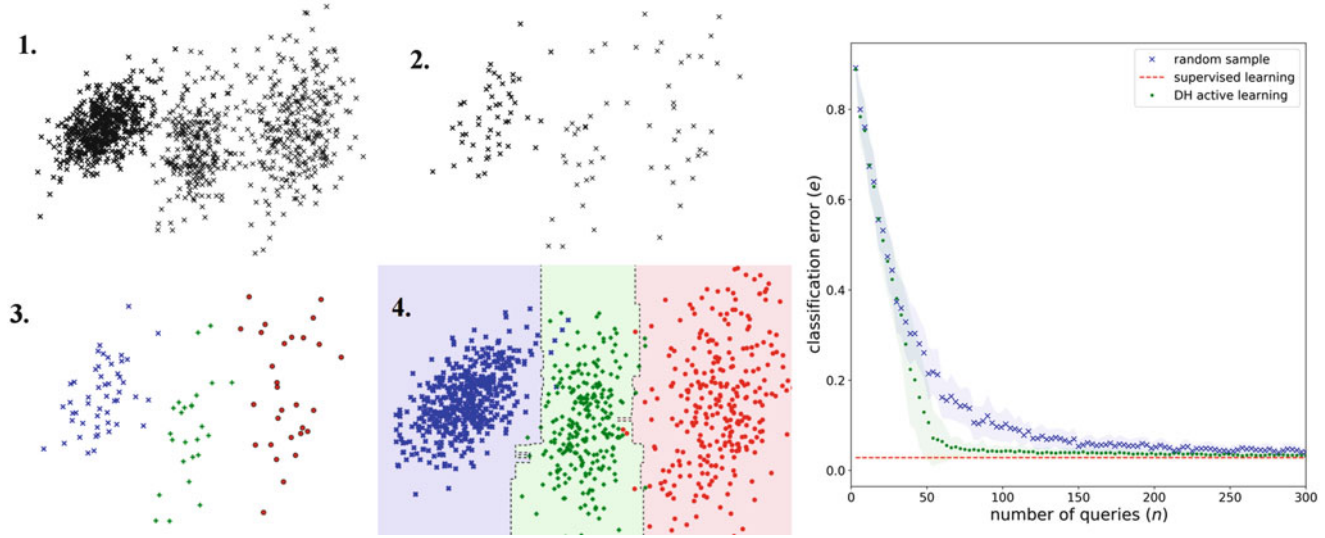


Fig. 14.1 Left: Visualisation of active learning steps. Right: The cluster adaptive DH learner—classification error for an increasing query budget n

14.2.1 Efficient Search Through Hypothesis Space

The hypothesis space \mathcal{H} is used to describe all the possible boundaries that a classifier can take. The version space is a subset of these hypotheses ($\mathcal{H}_t \in \mathcal{H}$ where $\mathcal{H}_t = \{h\}$) consistent with the labelled data seen so far [5]. As more labels are observed by the learner, the set of plausible hypotheses will shrink, restricting the current version space \mathcal{H}_t [5]. Using hypothesis space active learning, observations whose labels explicitly shrink the version space as fast as possible are queried [3], as these are assumed the most informative.

14.2.2 Exploiting Cluster Structure in Data

The second active learning regime exploits cluster structure in the data [4, 6]. In an ideal scenario, defined, separable clusters will exist that are pure in their labels. Following definition by unsupervised learning, a few informative points can be selected from each cluster; any remaining unlabelled points can then be assigned their majority label—this is a form of label propagation. Finally, a supervised classifier is trained on these data. These steps are typical of semi-supervised learning, as unlabelled instances are used to constrain the classifier. The main active learning element of cluster-based techniques is defined by the sampling procedure. Generally, queries are directed to clusters that appear most mixed in their labels, as these clusters are assumed the most informative [2].

14.3 Hierarchical Sampling for Active Learning

A technique is applied here that exploits cluster structure in data.

14.3.1 The DH Learner

Hierarchical sampling for active learning—applied via the DH algorithm—is an active learning tool proposed by Dasgupta and Hsu [3]. This technique utilises a cluster-based framework for guided sampling and label propagation. The heuristic is well defined in the original papers [2, 3]. Briefly, the algorithm starts with a hierarchical clustering of the input data; in the experiments here, agglomerative clustering is used. Sampling is initially random, but as learning proceeds, the algorithm

directs queries to partitions of the data that appear impure in their labels, as these data are assumed the most informative. Once the query budget n has been reached, labels are assumed for all data in clusters with a clear majority label. A standard supervised classifier is then trained on the labelled output data. In these tests bagged decision trees [1] are used.

14.3.2 Experiments and Discussion

The data used here describe an SHM classification problem for the wing of an aircraft. The goal is to train a damage location model, using data from $(\mathcal{X}, \mathcal{Y})$. Input vectors in \mathcal{X} are described by nine novelty indices, and the hidden targets \mathcal{Y} define which damage state has occurred. Damage was simulated by removing one of nine panels from the aircraft wing, so $\mathcal{Y} = \{y_i\}_{i=1}^{1782}$, where $y \in \{1, 2, 3, \dots, 9\}$. The performance of the DH learner is compared to two benchmark methods. Firstly, random sample learning, which queries data by a blind random sample (size n); a supervised classifier is then trained using this subset. Secondly, standard supervised learning, which uses all the labels in \mathcal{Y} ; this method is unaffected by n and should be considered the target performance.

Figure 14.1 (right hand side) shows classification error against an increasing query budget n . Curves are plotted for both benchmark methods and the DH active learner. After just 150 queries the DH learner provides misclassification errors very close to wholly supervised training, which requires all 1782 labels. Furthermore, after approximately 60 queries, the classification error for DH active learning is substantially lower than that for a random sample of the same budget n .

14.3.3 Conclusions

These results illustrate the advantages of applying active learning methods to real engineering data. Specifically, the use of cluster adaptive techniques for both guided sampling and label propagation. These mechanisms are particularly relevant to SHM applications, where the cost of labelling data is high. The details behind this work, along with algorithm implementation, are being submitted for journal publication. A MATLAB package for Dasgupta and Hsu's algorithm will also be made available via GitHub.

Acknowledgements The authors gratefully acknowledge the support of the UK Engineering and Physical Sciences Research Council (EPSRC) through Grant reference number EP/J016942/1.

References

1. Bishop, C.M.: Pattern Recognition and Machine Learning. Springer, New York (2006)
2. Dasgupta, S.: Two faces of active learning. *Theor. Comput. Sci.* **412**(19), 1767–1781 (2011)
3. Dasgupta, S., Hsu, D.: Hierarchical sampling for active learning. In: Proceedings of the 25th International Conference on Machine Learning, pp. 208–215. ACM (2008)
4. Hofmann, T., Buhmann, J.M.: Active data clustering. In: Advances in Neural Information Processing Systems, pp. 528–534 (1998)
5. Murphy, K.P.: Machine Learning: A Probabilistic Perspective. MIT Press, Cambridge (2012)
6. Settles, B.: Active learning literature survey. *Univ. Wis. Madison* **52**(55–66), 11 (2010)



Chapter 15

Multimodal Damping of a Nonlinear Structure with a Passive Piezoelectric Network

B. Lossouarn, J.-F. Deü, and G. Kerschen

Abstract This work proposes the implementation of a multimodal and fully passive piezoelectric tuned vibration absorber that mitigates several resonances of a nonlinear structure. By extending a principle of similarity, an analogous electrical network is designed in order to reproduce the dynamics of the mechanical structure. Several electrical resonances are simultaneously tuned to the mechanical resonances, thus providing the equivalent of a multimodal vibration absorber from electromechanical coupling through an array of piezoelectric patches. Furthermore, the use of a nonlinear capacitor in the analogous network generates an autonomous adjustment of the electrical resonance frequencies when the structure reaches the nonlinear domain. The interest of this method is proved experimentally by mitigating vibration over a wide frequency range that covers the first three modes of a beam with cubic nonlinearity.

Keywords Nonlinear absorber · Multimodal damping · Piezoelectric coupling · Resonant network · Passive control

15.1 Introduction

Considering piezoelectric tuned vibration absorbers, mechanical nonlinearities generate a detuning that seriously affects the damping performance. This limitation of the classical resonant piezoelectric shunt [1] was analyzed by Soltani et al. [2], who extended results obtained by Habib et al. in the case of a purely mechanical absorber [3]. In order to retrieve a correct tuning of the absorber, a solution consists in the introduction of an additional nonlinearity in the electrical circuit. The interest of such a nonlinear piezoelectric shunt has already been proven numerically and experimentally for vibration mitigation of a single nonlinear resonance [2, 4]. The objective is now to extend the method to multimodal structures by implementing a multi-resonant piezoelectric network [5] that is able to damp several resonances of a nonlinear structure.

15.2 Nonlinear Piezoelectric Tuned Vibration Absorber

The experimental setup is based on a cantilever beam involving a cubic nonlinearity. As shown in Fig. 15.1, a thin lamina is clamped at the left end of the beam, which generates the hardening nonlinearity. The structure is covered with an array of piezoelectric patches in order to mitigate vibration with a piezoelectric tuned vibration absorber [1]. A passive inductor is made by winding copper wire around a magnetic circuit in ferrite material and connected to the piezoelectric patches. A linear inductor allows reducing the vibration amplitude of the beam at low excitation but Fig. 15.2a shows that an increasing forcing amplitude leads to a complete detuning of the resonant shunt because of the mechanical nonlinearity. A solution to overcome this effect is to introduce in the absorber a nonlinearity similar to that of the primary structure [3]. Practically, it can be implemented with a nonlinear capacitor [2] or a nonlinear inductor [4]. Both solutions provide equivalent adaptive tuning by maintaining two equal peaks in the frequency response function. Such a result represented in Fig. 15.2b has already been proven experimentally by using a physical inductor subjected to magnetic saturation [4].

B. Lossouarn (✉) · J.-F. Deü

Laboratoire de Mécanique des Structures et des Systèmes Couplés, Conservatoire national des arts et métiers, Paris, France
e-mail: boris.lossouarn@cnam.fr

G. Kerschen

Department of Aerospace and Mechanical Engineering, University of Liège, Liège, Belgium

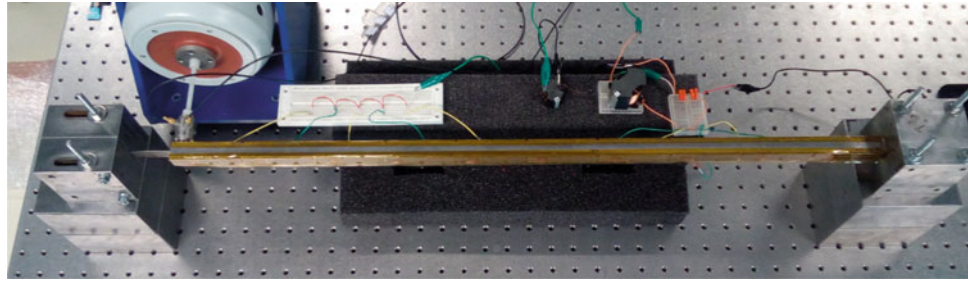


Fig. 15.1 Cantilever beam with additional clamping through a thin lamina

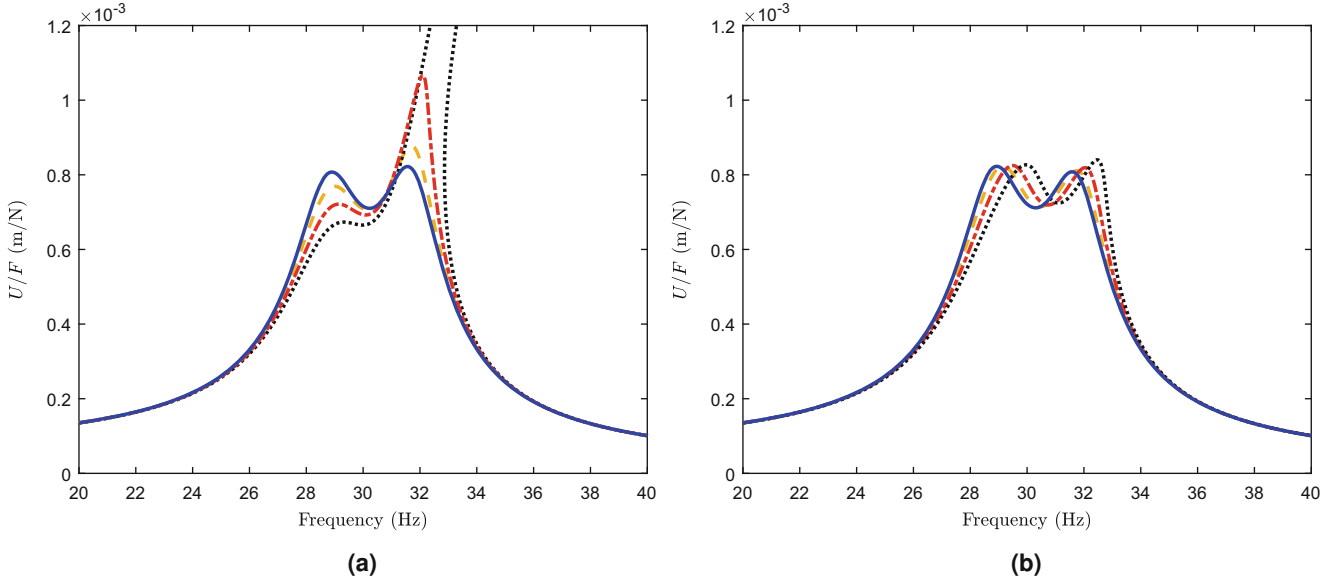


Fig. 15.2 Simulated frequency response functions for various forcing amplitudes, $F = 0.2 \text{ N}$ (—), $F = 0.4 \text{ N}$ (—), $F = 0.6 \text{ N}$ (— · —) and $F = 0.8 \text{ N}$ (···): (a) linear shunt, (b) nonlinear piezoelectric tuned vibration absorber

15.3 Multimodal Damping with an Analogous Piezoelectric Network

As the objective of the present work is to achieve vibration damping of several resonances, the array of piezoelectric patches is interconnected with electrical components in order to implement a multi-resonant electrical network. Actually, coupling a mechanical structure to its analogous electrical network generates electromechanical energy transfers over a broad frequency range. The electrical analogue of a beam [5] is considered for the present application. It is a fourth order transmission line made of inductors and transformers, as shown in Fig. 15.3. Capacitors are not explicitly represented because we directly benefit from the piezoelectric capacitance of the patches that couple the beam to the electrical network. Coupling the mechanical structure to its analogous electrical network gives the frequency response in Fig. 15.4, which shows the simultaneous vibration mitigation of the first three modes of the beam at low forcing amplitudes. Yet, higher amplitudes still lead to the undesired behavior illustrated in Fig. 15.2a if linear components are used in the electrical network. Contrary to a previous experimental validation based on a nonlinear inductor [4], a nonlinear capacitor is incorporated in the piezoelectric electrical network to ensure an equivalence with the nonlinear stiffness at the end of the beam. The analogy is not only valid in the linear domain but also in the nonlinear domain thanks to the principle of similarity developed in previous studies on nonlinear vibration absorbers [2, 3]. The damping performance are thus maintained, providing similar frequency response functions for higher forcing amplitudes.

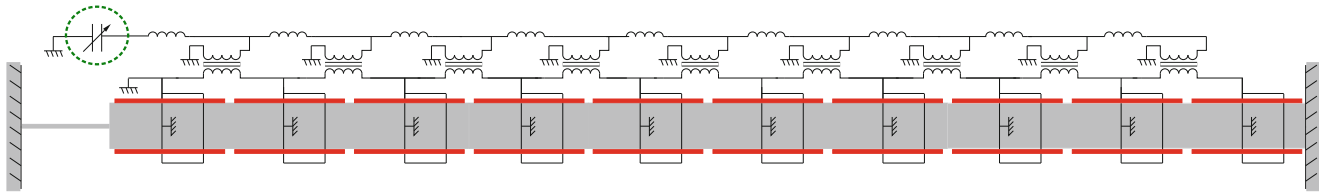


Fig. 15.3 Nonlinear beam coupled to its analogous electrical network through an array of piezoelectric patches

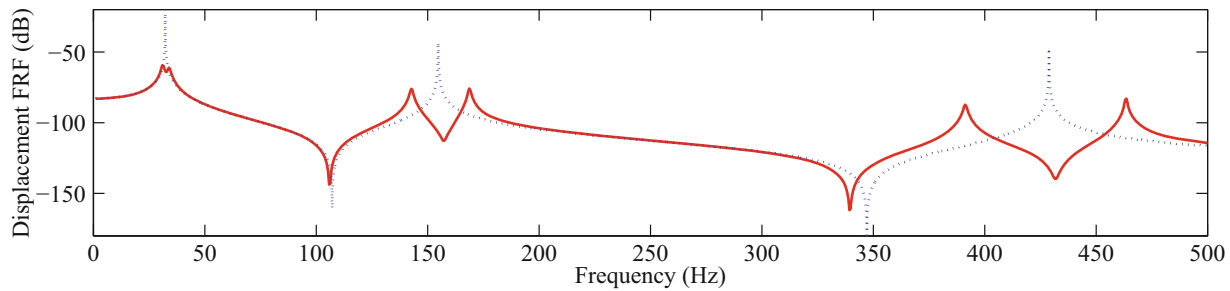


Fig. 15.4 Simulated frequency response function of the beam with short-circuited patches (···) and with the analogous electrical network (—)

15.4 Conclusions

This work aims to show that the principle of nonlinear similarity can be extended to multimodal damping with piezoelectric networks. To this end, an analogous electrical network is first assembled in order to reproduce the dynamics of the considered structure in the linear domain. A multimodal coupling offers vibration mitigation over a wide frequency range. For higher forcing amplitudes, it is shown experimentally that the mechanical nonlinearity induces a serious mistuning, especially for the first mode of the beam. A nonlinear capacitor is thus used in the electrical network in order to generate variable electrical resonances, which maintain a multimodal vibration reduction. This proves that broadband damping of a nonlinear structure can be achieved with a fully passive vibration absorber.

References

1. Hagood, N.W., von Flotow, A.: Damping of structural vibrations with piezoelectric materials and passive electrical networks. *J. Sound Vib.* **146**, 243–268 (1991)
2. Soltani, P., Kerschen, G.: The nonlinear piezoelectric tuned vibration absorber. *Smart Mater. Struct.* **24**, 075015 (2015)
3. Habib, G., Kerschen, G.: A principle of similarity for nonlinear vibration absorbers. *Physica D* **332**, 1–8 (2016)
4. Lossouarn, B., Deü, J.F., Kerschen, G.: Passive realization of a nonlinear piezoelectric tuned vibration absorber with a saturable inductor. In: Proceedings of the 9th European Nonlinear Dynamics Conference (2017)
5. Lossouarn, B., Deü, J.F., Aucejo, M.: Multimodal vibration damping of a beam with a periodic array of piezoelectric patches connected to a passive electrical network. *Smart Mater. Struct.* **24**, 115037 (2015)



Chapter 16

Probability Distribution of von Mises Stress in the Presence of Pre-load

Daniel J. Segalman, Garth M. Reese, and Richard V. Field, Jr.

Abstract Random vibration under preload is important in multiple endeavors, including those involving launch and re-entry. In these days of increasing reliance on predictive simulation, it is important to address this problem in a probabilistic manner – this is the appropriate flavor of quantification of margin and uncertainty in the context of random vibration. One of the quantities of particular interest in design is the probability distribution of von Mises stress. There are some methods in the literature that begin to address this problem, but they generally are extremely restricted and astonishingly, the most common restriction of these techniques is that they assume zero mean loads. The work presented here employs modal tools to suggest an approach for estimating the probability distributions for von Mises stress of a linear structure for the case of multiple independent Gaussian random loadings combined with a nonzero pre-load.

Keywords Random vibration · Von Mises stress · Gaussian · Pre-load · Stress process

Nomenclature

$F(t)$	Vector of random dynamic loads applied to structure
F_0	Vector of static loads applied to structure
d	The number of applied random dynamic forces
\mathcal{R}^d	The d -dimensional space of real numbers
S_{qq}	Cross spectral density matrix of modal displacements
$q(t)$	Column vector of modal displacements
$\sigma(x, t)$	Instantaneous stress at location x and time t
$\sigma_0(x)$	Static stress at location x
$\Psi(x)$	Matrix each of whose columns is the vector of stress components associated with that mode at that location (modal stresses)
$\Psi_n(x)$	The nth column of $\Psi(x)$
N_M	The number of vibration modes retained for analysis
$p(x, t)$	von Mises stress at location x and time t
A	6×6 matrix mapping used to map stress vectors to von Mises stress
$B(x)$	$\Psi^T(x) A \Psi(x)$

Sandia National Laboratories is a multi-mission laboratory managed and operated by National Technology and Engineering Solutions of Sandia, LLC., a wholly owned subsidiary of Honeywell International, Inc., for the U.S. Department of Energy's National Nuclear Security Administration under contract DE-NA-0003525.

D. J. Segalman (✉)
Department of Mechanical Engineering, Michigan State University, East Lansing, MI, USA
e-mail: segalman@egr.MSU.edu

G. M. Reese
Computational Solid Mechanics and Structural Dynamics, Sandia National Laboratories, Albuquerque, NM, USA
Richard V. Field, Jr.
Data Science & Applications, Sandia National Laboratories, Albuquerque, NM, USA
e-mail: rvfield@sandia.gov

Γ_{qq}	The zero-time lag covariance matrix of modal displacement: $E[qq^T]$
$p_{\text{RMS}}^2(x)$	Time average of the square of von Mises stress
Q	Element of decomposition $\Gamma_{qq} = Q X Q^T$
N_R	The rank of Γ_{qq}
$\hat{q}(t)$	$Q X \beta(t)$
$\beta(t)$	$X^{-1} Q^T q(t)$
C	$X Q^T B Q X$
$R(x)$	Defined in decomposition $C(x) = R(x) D^2(x) R^T(x)$
$D(x)$	Defined in decomposition $C(x) = R(x) D^2(x) R^T(x)$
N_P	The number of stress processes
$y(t, x)$	$R^T(x) \beta(t)$
Y_0^2	$p_0^2 - \gamma^T D^2 \gamma$
γ	$G(x) \sigma_0(x)$
G	$-D^{-2} R^T X^T Q^T \Psi^T A$
L	Length of beam in first and second example problems
ρ_B	Density of beam in first and second example problems
w	Half width of beam in first and second example problems
PDF	Probability Density Function
CDF	Cumulative Distribution Function

16.1 Introduction

Random vibration under preload is important in multiple endeavors, including those involving launch and re-entry. In these days of increasing reliance on predictive simulation, it is important to address this problem in a probabilistic manner – this is the appropriate flavor of quantification of margins and uncertainties in the context of random vibration. There are some methods in the literature that only begin to address this problem:

1. Miles' equation [1] addresses the accelerations seen by a single degree of freedom system supported by a randomly driven base. The attachment stresses are presumed to be proportional to the relative displacements. This is, of course, not suitable for real physical systems containing multiple degrees of freedom.
2. A method of Segalman et al. [2] facilitates estimating the RMS value of von Mises stresses under pre-load for arbitrary weakly stationary random dynamic loads, so long as the cross-spectral density matrix for load is available. This says nothing about probability distribution of von Mises stress.
3. Another method of Segalman et al. [3] does provide a method for calculating the probability distribution of von Mises stress so long as the applied random dynamic loads are stationary Gaussian and there is no pre-load.
4. Tibbits [4] extended the method of [3] to the case where there is pre-load, but where only one random dynamic stress load is applied. Though a major advance, this still does not admit re-entry type cases – where non-uniform random dynamic loads are distributed spatially about the structure.

None of these methods can be employed to address the severe conditions of random vibration applied to a structure also subject to preload – for which launch or re-entry would be paradigms – and generate probabilistic expressions for the von Mises stress likely to be encountered.

An effort to achieving such a method is described in this monograph. The development here is based on results reported in a technical document [5] prepared while the first author was a member of technical staff of Sandia National Laboratories.

16.2 Key Ingredients

The most important ingredient to this development is the partition of the applied loads into a system of random dynamic loads $F(t)$ and a set of static pre-loads F^0 . One might assume that the static loads are self-equilibrating, but the following

development does not require that condition. Also, critical to the following development is the assumption that the random dynamic load components $F(t)$ are stationary Gaussian processes with zero mean.

Let $F(t)$ be an \mathcal{R}^d -valued, weakly stationary Gaussian process of zero mean and having correlation matrix $r_{FF}(\tau) = E[F(t)F(t+\tau)^T]$, a $d \times d$ matrix. The matrix of two-sided spectral densities [6] is denoted by $S_{FF}(\omega)$ [6]

$$S_{FF}(\omega) = \frac{1}{2\pi} \int_{\mathcal{R}} r_{FF}(\tau) e^{-i\omega\tau} d\tau. \quad (16.1)$$

This matrix defines the characterization of the input needed for random vibration studies, assuming a linear structure.

From $S_{FF}(\omega)$ plus the structure's frequency response functions we can derive the cross spectral density matrix of modal displacement $S_{qq}(\omega)$. From $S_{qq}(\omega)$ we can evaluate the Γ_{qq} , the zero-time lag covariance matrix of modal displacement. (Γ_{qq} is defined mathematically below and a useful development can be found in Appendix A of [5]).

In the following section, we show how knowing Γ_{qq} and assuming that all loads are Gaussian processes, we may determine the statistics of von Mises stress of a linear structure, even in the presence of pre-load.

16.3 Separation of Stress Response Due to Static and Random Vibration Loads

At each location x in the structure, we can express the stress vector (discussed more below) in terms of modal amplitudes

$$\sigma(t, x) = \sigma_0(x) + \sum_n q_n(t) \Psi_n(x) = \sigma_0(x) + \Psi(x) q(t), \quad (16.2)$$

where q is a column vector of modal amplitudes with coordinates q_n and $\Psi(x)$ is a matrix each of whose columns is the vector of stress components associated with that mode at that location (modal stresses). Vector $\Psi_n(x)$ is the n th column of $\Psi(x)$. We have truncated the sum at N_M modes.

The square of the von Mises stress is

$$p^2(t, x) = (\Psi(x) q(t) + \sigma_0(x))^T A (\Psi(x) q(t) + \sigma_0(x)), \quad (16.3)$$

where

$$A = \begin{bmatrix} 1 & -1/2 & -1/2 & 0 & 0 & 0 \\ -1/2 & 1 & -1/2 & 0 & 0 & 0 \\ -1/2 & -1/2 & 1 & 0 & 0 & 0 \\ 0 & 0 & 0 & 3 & 0 & 0 \\ 0 & 0 & 0 & 0 & 3 & 0 \\ 0 & 0 & 0 & 0 & 0 & 3 \end{bmatrix} \quad (16.4)$$

We expand the argument in Eq. (16.3):

$$p^2(t, x) = (\Psi(x) q(t))^T A (\Psi(x) q(t)) + \sigma_0^T(x) A \sigma_0(x) + (\Psi(x) q(t))^T A \sigma_0(x) + \sigma_0^T(x) A (\Psi(x) q(t)). \quad (16.5)$$

Let $p_R^2(t, x)$ denote the component of squared von Mises stress due solely to random vibration, that is, the first term on the RHS of Eq. (16.5). Then

$$p_R^2(t, x) = (\Psi(x) q(t))^T A (\Psi(x) q(t)) = q(t)^T B(x) q(t), \quad (16.6)$$

where

$$B(x) = \Psi^T(x) A \Psi(x). \quad (16.7)$$

It follows that

$$E[p_R^2(t, x)] = B(x)_{ij} E[q_i q_j] = B(x)_{ij} (\Gamma_{qq})_{ij} = (B(x)^T \Gamma_{qq})_{jj} = \text{Tr}(B^T(x) \Gamma_{qq}) \quad (16.8)$$

where

$$\Gamma_{qq} = E[q(t) q^T(t)] \quad (16.9)$$

is the zero-time lag covariance matrix of modal amplitude. (Summation on repeated indices was employed in Eq. (16.8).) We note that Γ_{qq} has neither spatial or temporal dependence and that B has spatial dependence only. Also both matrices are symmetric, so the use of $(\cdot)^T$ in Eq. (16.8) is optional.

16.3.1 An Intermediate Result: RMS von Mises

Let's take the expected value of the right side of Eq. (16.5) to find

$$p_{\text{RMS}}^2(x) = E[p^2(t, x)] = E[q^T(t) B(x) q(t)] + 2 E[q^T(t)] \Psi^T(x) A \sigma_0(x) + \sigma_0^T(x) A \sigma_0(x), \quad (16.10)$$

but $E[q] = 0$, so the difference between the square of RMS von Mises stress in the absence of pre-stress (Eq. 16.8) and the square of von Mises stress in the presence of pre-stress (Eq. 16.10) is the square of von Mises stress of the pre-load alone ($\sigma_0^T A \sigma_0$). Examining the un-squared von Mises stress, we see that

$$p_{\text{RMS}}(x) = \sqrt{\text{Tr}(B^T(x) \Gamma_{qq}) + \sigma_0^T(x) A \sigma_0(x)} \leq \sqrt{\text{Tr}(B^T(x) \Gamma_{qq})} + \sqrt{\sigma_0^T(x) A \sigma_0(x)} \quad (16.11)$$

by the triangle inequality. Hence, the RMS von Mises stress is less than or equal to the sum of that due to random vibration and that due to preload.

16.3.2 Reduction to Stress Processes

Noting that matrix Γ_{qq} is square ($N_M \times N_M$) and positive semi-definite, we may decompose it

$$\Gamma_{qq} = Q X^2 Q^T, \quad (16.12)$$

where X is a diagonal matrix whose dimension (N_R) is the rank of Γ_{qq} and Q is a rectangular matrix having the property that

$$Q^T Q = I_{N_R} \quad (16.13)$$

where I_{N_R} is the identity matrix of rank N_R . Note that because Γ_{qq} has no time or spatial dependence, neither do Q or X .

This permits us a change of variables

$$\beta(t) = X^{-1} Q^T q(t) \quad (16.14)$$

where, by construction,

$$E[\beta(t) \beta(t)^T] = I_{N_R} \quad (16.15)$$

so that the elements of β are independent, identically distributed random processes. (Proof of this requires that we recall that X is a diagonal matrix and $\beta(t)$ is a linear mapping of $F(t)$ and therefore Gaussian.) While Q is not generally invertible, we may introduce the new random vector

$$\hat{q}(t) = Q X \beta(t). \quad (16.16)$$

It is shown in Appendix B of [5] that q and \hat{q} have identical first and second moments, and are therefore equivalent Gaussian random vectors. For the purpose of characterizing the statistics of von Mises stress, we could employ \hat{q} in Eq. (16.5) with the same legitimacy as employing q .

In our new coordinates β , the square of the von Mises stress *due solely to random vibration* is

$$p_R^2(t, x) = \beta^T(t) C(x) \beta(t), \quad (16.17)$$

where

$$C(x) = X^T Q^T B(x) Q X. \quad (16.18)$$

Matrix $C(x)$ is square, having dimensionality equal to the rank of Γ_{qq} but possibly much lower rank. The rank of C is the minimum of the rank of the matrices in the product on the right hand side of Eq. (16.18). Note that $\text{rank}(X) = \text{dimension}(X) = \text{rank}(\Gamma_{qq}) = N_R$ and $\text{rank}(B) \leq \text{rank}(A) = 5$.

We exploit the symmetry and the positive semi-definiteness of $C(x)$ in doing its singular value decomposition:

$$C(x) = R(x) D^2(x) R^T(x), \quad (16.19)$$

where the matrix $D(x)$ is diagonal and has dimension equal to the rank of N_P of $C(x)$, $R(x)$ is a rectangular matrix having property that $R^T R = I_{C(x)}$, and $I_{C(x)}$ is the identity matrix whose dimension is the rank of $C(x)$. We refer to N_P as the number of stress processes.

The square of the von Mises stress due solely to random vibration is now

$$p_R^2(t, x) = \beta^T(t) R(x) D^2(x) R^T(x) \beta(t). \quad (16.20)$$

This suggests yet another change of variables:

$$y(t, x) = R^T(x) \beta(t). \quad (16.21)$$

It is easily shown that the elements of y are independent, identically distributed (IID) Gaussian processes with unit variance. (This again employs the fact that X is a diagonal matrix and y is a linear function of F .) There are two obvious advantages of the above transformation: (1) it reduces the number of random variables of this problem to the rank of A (at most 5), and (2) it aligns the random variables in the directions of the axes of the ellipsoids of constant von Mises stress.

When Eq. (16.21) is substituted into Eq. (16.20), we obtain

$$p_R^2(t, x) = y(t, x)^T D(x)^2 y(t, x) = \sum_n y_n(t, x)^2 D_n(x)^2. \quad (16.22)$$

The above expression suggests the following terminology. We refer to the dimension of $D(x)$ as the number of independent ‘stress processes’ acting at the location x .

It is worthwhile to discuss how many modes should be retained in the above calculations. As in other cases of modal synthesis, one must include those modes whose frequency response functions significantly intersect the excitation spectrum. A conservative approach is to employ all modes through an upper bound of the frequencies in the power spectrum of the input loads. Since the largest computational effort involves the decomposition in Eq. (16.12), and that need be done only once per load case, the cost of such conservatism is not unreasonable.

Let us now return to calculation of the full von Mises stress, as presented in Eq. (16.5), but with our newer degrees of freedom, that is,

$$p^2(t, x) = y(t, x)^T D^2(x) y(t, x) + 2 \beta(t)^T \left(X^T Q^T \Psi(x)^T \right) A \sigma_0(x) + \sigma_0(x)^T A \sigma_0(x). \quad (16.23)$$

Approximating¹

$$\beta(t) \approx R(x)y(t, x) \quad (16.24)$$

at this location, we have

$$p^2(t, x) = y^T(t) D(x)^2 y(t) + 2y(t)^T \left(R(x)^T X Q^T \Psi(x)^T \right) A \sigma_0(x) + \sigma_0(x)^T A \sigma_0(x). \quad (16.25)$$

Defining a vector $\gamma(x)$ by

$$\gamma(x) = G(x) \sigma_0(x), \quad (16.26)$$

where

$$G(x) = -D(x)^{-2} R(x)^T X Q^T \Psi(x)^T A \quad (16.27)$$

and $p_0^2(x) = \sigma_0^T(x)A\sigma_0(x)$, Eq. (16.25) becomes

$$p^2(t, x) = y^T(t) D(x)^2 y(t) - 2y(t)^T D(x)^2 \gamma(x) + p_0(x)^2. \quad (16.28)$$

Obviously, this calls for completing the square

$$p^2(t, x) = (y(t) - \gamma(x))^T D(x)^2 (y(t) - \gamma(x)) + Y_0(x)^2 \quad (16.29)$$

where

$$Y_0(x)^2 = p_0(x)^2 - \gamma(x)^T D(x)^2 \gamma(x). \quad (16.30)$$

It appears that if $\sigma_0(x)$ is in the span of the vectors of $\Psi(x)$, $Y_0(x) = 0$. Otherwise $Y_0(x) > 0$.

The dimensions of the above matrices are presented in Tables 16.1 and 16.2. The dimensions themselves are discussed in Table 16.3.

Table 16.1 Global matrices

	Γ_{qq}	X	Q	A
Dimension	$N_M \times N_M$	$N_R \times N_R$	$N_M \times N_R$	6×6
Character		Diag.		Rank 5

Table 16.2 Local matrices

	Ψ	B	C	D	R	G	γ
Dimension	$6 \times N_M$	$N_M \times N_M$	$N_R \times N_R$	$N_P \times N_P$	$N_R \times N_P$	$N_P \times 6$	$N_P \times 1$
Character				Diag.			

Table 16.3 Dimensions

N_M	Number of modes employed
N_R	Rank of Γ_{qq} . $N_R \leq N_M$
N_P	Rank of C = number of random stress processes. $N_P \leq \text{rank}(A) = 5$

¹By this approximation, we mean that $y(t, x)^T \left(R(x)^T X Q^T \Psi(x)^T \right) A$ and $\beta(t)^T \left(X Q^T \Psi(x)^T \right) A$ have identical second moment properties.

16.4 Probabilistic Statements on von Mises Stress

The statistics of the von Mises stress are determined via appropriate integration over the joint probability distribution of the coordinates of $y(t, x)$ defined by Eq. (16.21).

16.4.1 A Previous Result from New Perspective

For instance we re-examine the mean square of the von Mises stress

$$\begin{aligned} E[p^2(t, x)] &= \int_{-\infty}^{\infty} \cdots \int_{-\infty}^{\infty} p^2(t, x) \prod_r \rho_r(y_r) dy_r = \int_{-\infty}^{\infty} \cdots \int_{-\infty}^{\infty} ((y - \gamma(x))^T D(x)^2 (y - \gamma(x)) + Y_0(x)^2) \prod_r \rho_r(y_r) dy_r \\ &= \text{Tr}(D(x)^2) + p_0(x)^2, \end{aligned} \quad (16.31)$$

where

$$\rho_r(y_r) = \frac{1}{\sqrt{2\pi}} e^{-y_r^2/2} \quad (16.32)$$

is the probability density function of a standard Gaussian random variable. For more detail on this derivation, please refer to Appendix C of [5]. We see that $D_r(x)^2$ is the contribution of the r th random process to $E[p(t, x)^2]$ at location x and the rank of D is N_P , the number of independent random processes contributing to the von Mises stress response at that location.

16.4.2 Probability Distributions of von Mises Stress

To determine the probability law for $p(x, t)$, it is useful to work with the square of the von Mises stress. Further, because von Mises stress is non-negative, it follows that for any Y , we have $P(p \leq Y) = P(p^2 \leq Y^2)$. The probability that the square of von Mises stress amplitude is less than or equal to a quantity Y^2 is

$$F_Y = P(p^2 \leq Y^2) = \begin{cases} 0 & \text{for } Y \leq Y_0 \\ \int_{Z(\{D\}, \gamma, Y_0, Y)} \prod \rho_r(y_r) dy_r & \text{for } Y > Y_0 \end{cases} \quad (16.33)$$

where $Z(\{D\}, \gamma, Y_0, Y)$ is the N_P -dimensional ellipsoid containing points y associated with the square of the von Mises stress less than or equal to Y^2 , that is

$$Z(\{D\}, \gamma, Y_0, Y) = \{y : ((y - \gamma)^T D^2 (y - \gamma)) \leq Y^2 - Y_0^2\} \quad (16.34)$$

and N_P is the rank of matrix D . Note that all the arguments of Z are functions of x only and that $Z(\{D\}, \gamma, Y_0, Y)$ is an ellipsoid centered at γ . The semi-axes of these ellipsoids are

$$A_r = \sqrt{\frac{Y^2 - Y_0^2}{D_r^2}} \quad (16.35)$$

See Fig. 16.1. (It is because von Mises stress is positive that the condition $p \leq Y$ is equivalent to $p^2 \leq Y^2$ and we are able to define Z without explicit use of square roots.)

The integral of Eq. (16.33) is generally impossible to evaluate exactly, but approximate quadrature is straight-forward. Here we employ a numerical quadrature similar to the heuristic used in explaining Riemann integration.

Fig. 16.1 Regions of constant von Mises stress are ellipsoids centered at locations γ

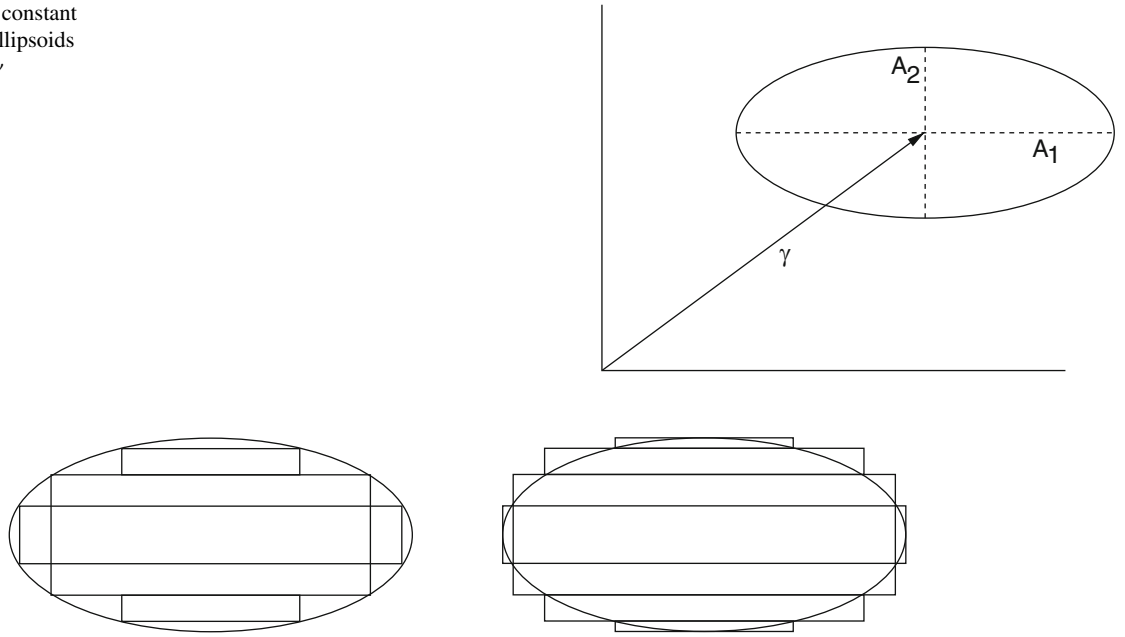


Fig. 16.2 Sets of boxes comprising subsets and supersets of the volume $Z(\{D\}, \gamma, Y_0, Y)$ for the case of $N_p = 2$

16.4.3 Quadrature by Boxes

One of the few domain types over which we can integrate Gaussian distributions is boxes in N space. Let B_λ be one such box, then

$$\int_{B_\lambda} \prod_{r=1}^{N_p} \rho_r(y_r) dy_r = \prod_{r=1}^{N_p} [\Phi(y_{r,\max}) - \Phi(y_{r,\min})], \quad (16.36)$$

where $y_{r,\max}$ and $y_{r,\min}$ define the boundaries of B_λ , and

$$\Phi(x) = \frac{1}{\sqrt{2\pi}} \int_{-\infty}^x \exp(-s^2/2) ds. \quad (16.37)$$

Note that Φ can also be expressed in terms of the error function, that is, $\Phi(x) = (1/2) (1 + \text{erf}(x/\sqrt{2}))$.

Because $Z(\{D\}, \gamma, Y_0, Y)$ is a convex volume, it is easy to devise sequences of sets of boxes that are fully contained in $Z(\{D\}, \gamma, Y_0, Y)$ but whose net volume converge to that of $Z(\{D\}, \gamma, Y_0, Y)$ from below. Similarly, it is straightforward to define sequences of sets all of which contain $Z(\{D\}, \gamma, Y_0, Y)$, and whose volumes converge to that of $Z(\{D\}, \gamma, Y_0, Y)$ from above (see Fig. 16.2).

For the following examples, the above integration over N -dimensional ellipsoids was performed via recursive calls to Matlab® function codes to obtain both upper and lower bounds for the integral defined by Eq. (16.33). (Listings can be found in Appendix D of [5].)

Credit should be given to Tibbits [4, 7] for creating approaches to the calculation of probability distribution for von Mises stress in the presence of pre-stress, but with some limitations. The approaches developed by Tibbits do not appear to accommodate the possibility of the number of random stress processes being less than the rank of the stress vector. The applications were limited to two dimensional problems where that assumption might more often be valid.

16.4.4 An Upper Bound for von Mises Probability

The recursive integrations associated with calculation of the probability distribution of von Mises stress where there are more than one random stress process present might be off-putting. Here we consider an obvious upper bound.

Let $B_U(\{D\}, \gamma, Y_0, Y)$ be the smallest N -box that entirely contains $Z(\{D\}, \gamma, Y_0, Y)$, that is

$$Z(\{D\}, \gamma, Y_0, Y) \subset B_U(\{D\}, \gamma, Y_0, Y). \quad (16.38)$$

The length of each side of the B_U will be twice a semi-axis of Z . Because of Eq. (16.38)

$$\int_{Z(\{D\}, \gamma, Y_0, Y)} \prod \rho_r(y_r) dy_r \leq \int_{B_U(\{D\}, \gamma, Y_0, Y)} \prod \rho_r(y_r) dy_r = \prod_{r=1}^{N_p} [\Phi(y_{r,\max}) - \Phi(y_{r,\min})], \quad (16.39)$$

where in this case $y_{r,\max}$ and $y_{r,\min}$ identify the coordinates at the corners of B_U .

16.4.5 Strategy for Implementation in a Finite Element Setting

Referring to Eqs. (16.33) and (16.34) and then backwards to Eqs. (16.26) and (16.30), we see that the necessary ingredients for computing the probability distribution at any location are $D(x)$, $G(x)$, and $\sigma_0(x)$.

The simplest strategy would be to implement the calculations, so much as possible, via post processing. The element variables D and G would come most naturally from a linear structural dynamics code, such as Salinas [8] or NASTRAN [9]. Because D is diagonal and has at most 5 rows, the storage of it at each quadrature point is not an issue. Matrix G has at most 5 rows and 6 columns, and storage space at each quadrature point should be quite manageable. Salinas is mentioned specifically because it lends itself to modification by the authors and MSC NASTRAN is mentioned because of its DMAP capability [10]. The static stresses, σ_0 – and there might be ensembles of them – can come from a linear or nonlinear quasi-static analysis code.

There are a few more considerations:

- One caveat in employing results from different finite element codes is the requirement that the meshes and coordinate systems must be identical. Additionally, conventions on stress orientation must be the same.
- The ordering of rows of D and G should be that of the development above: diagonal terms of D in decreasing order and each row of G as defined in Eq. (16.27).
- Because it is likely that D will be stored as a 5×1 vector and G will be stored as a 5×6 matrix, regardless of how many stress processes actually exist at the corresponding quadrature point, it would be helpful to store $N_p(x)$, the number of stress processes as well.

16.5 Example Problems

16.5.1 Example Problem 1

Consider the simply supported beam shown in Fig. 16.3, consisting of a beam subject to a static compressive load F_0 applied longitudinally and two dynamic loads $F_1(t)$ and $F_2(t)$ applied laterally. Loads F_1 and F_2 are assumed independent, stationary Gaussian processes with zero mean. The beam will be of length L , width $2w$, density ρ_B , cross-sectional area A_B , and Young's modulus E .

In general, each of F_1 and F_2 would excite many modes, but for the purpose of illustration, we assume that the frequency content of F_1 is band limited so as to excite only the first bending mode of the beam and that the frequency content of F_2 is also band limited, but so as to excite only the second bending mode.

The static stress at any place on the beam is

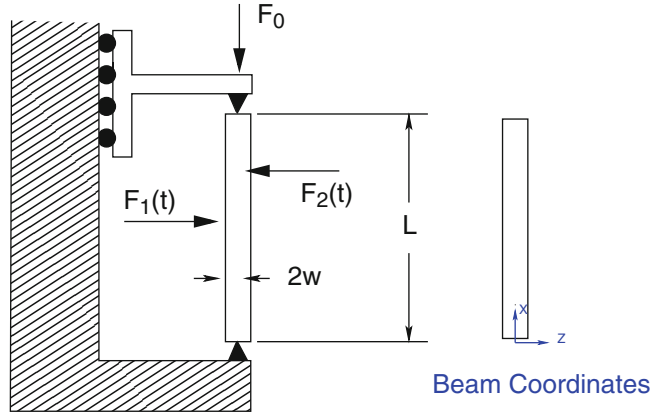


Fig. 16.3 Test case consisting of a simply supported beam of square cross section subject to a compressive longitudinal load F_0 and two random dynamic loads, $F_1(t)$ and $F_2(t)$ applied laterally

$$\sigma_0 = \begin{Bmatrix} -F_0/A_B \\ 0 \\ 0 \\ 0 \\ 0 \\ 0 \end{Bmatrix} \quad (16.40)$$

with $F_0/A_B = 1$. For convenience with respect to expressing the stresses associated with the bending modes, we assume that all constants are scaled such that

$$Ew \left(\frac{\pi}{L} \right)^2 \sqrt{\left(\frac{2}{\rho_B A_B L} \right)} = 1. \quad (16.41)$$

The stress due to bending of any mode $n \in (1, 2)$ is

$$\Psi(x, z) = \begin{Bmatrix} \sin\left(\frac{\pi x}{L}\right) \left(\frac{z}{w}\right) 4 \sin\left(\frac{\pi^2 x}{L}\right) \left(\frac{z}{w}\right) \\ 0 \\ 0 \\ 0 \\ 0 \\ 0 \end{Bmatrix} \quad (16.42)$$

where coordinates x and z are as indicated in Fig. 16.3. Note that because the random loads generate only one component of stress (σ_1) we anticipate at most one random process to show up in the calculation of von Mises stress. Again, for purpose of illustration for this problem, we assume

$$\Gamma_{qq} = \begin{bmatrix} 1 & 0 \\ 0 & 1/4 \end{bmatrix} \quad (16.43)$$

The spatial distribution of RMS von Mises stress, that is, $p_{\text{RMS}}(x, z)$ defined by Eq. (16.11), is illustrated on the leftmost portion of Fig. 16.4. Also shown on the right of the figure is $N_P(x, z)$, the rank of matrix $C(x, z)$ defined by Eq. (16.18), which describes the number of stress processes acting at that location. Because all of the modes associated with the random loads have nodal lines at the top and bottom of the beam, there are no random processes at those locations.

The RMS von Mises stress might be considered a nominal stress level, but one is perhaps more concerned about the probability of von Mises stress reaching high levels. The cumulative distribution function for von Mises stress is given by Eq. (16.33). Suppose we are interested in the 90th and 95th percentile of von Mises stress, that is, the values for Y such that the

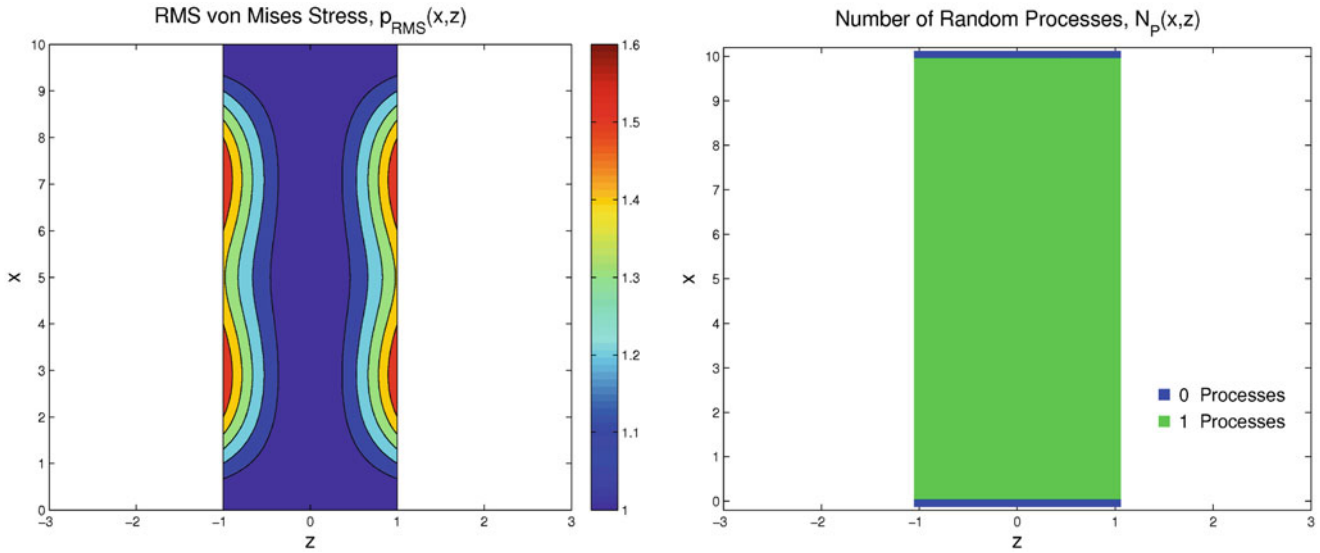


Fig. 16.4 The computed RMS von Mises stress resulting from the static pre-load and the lateral random dynamic loads is shown on the left. The distribution of the number of random processes is shown on the right

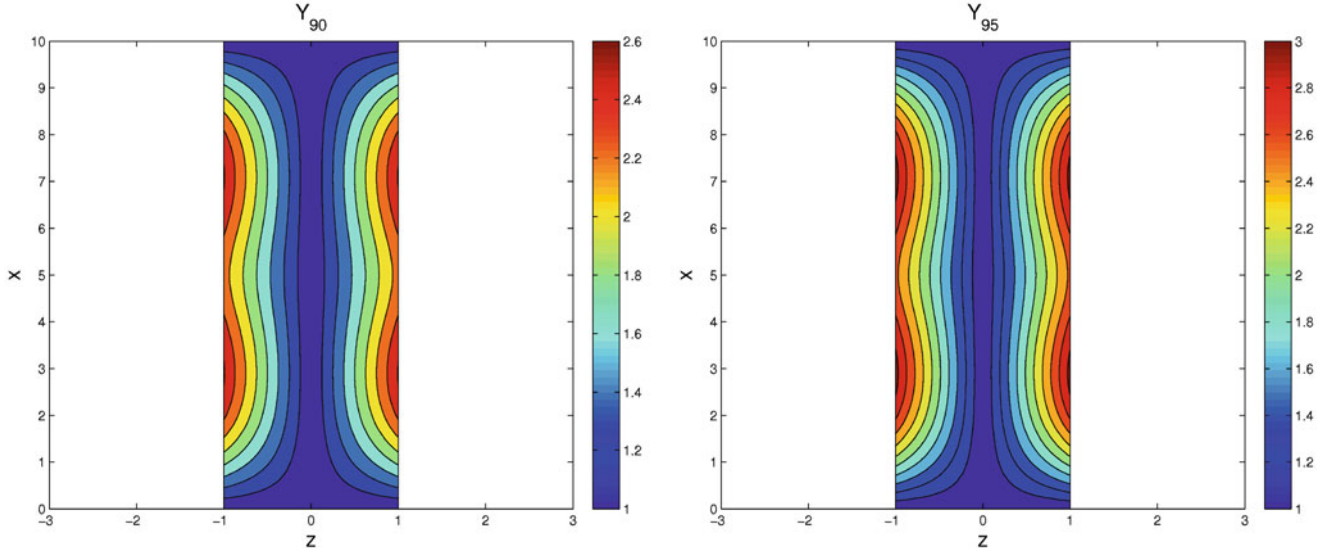


Fig. 16.5 The distribution of 90th percentile and 95th percentile von Mises stress are shown on the left and right contour plots, respectively

CDF defined by Eq. (16.33) equals 0.9 and 0.95, respectively. Let Y_{90} and Y_{95} denote these values. The distributions of 90th percentile and 95th percentile von Mises stress are shown in Fig. 16.5. The range of von Mises stress in Fig. 16.5 is about twice that of the plot of RMS von Mises stress.

16.5.2 Example Problem 2

Consider the cantilevered/simply supported beam shown in Fig. 16.6, subject to a static compressive load F_0 applied longitudinally, random dynamic load $F_1(t)$ also applied longitudinally, and random dynamic load $F_2(t)$ applied laterally at the free end of the beam. Loads F_1 and F_2 are assumed independent, stationary Gaussian processes with zero mean. The beam will be of length L , width $2w$, density ρ_B , cross-sectional area A_B , and Young's modulus E .

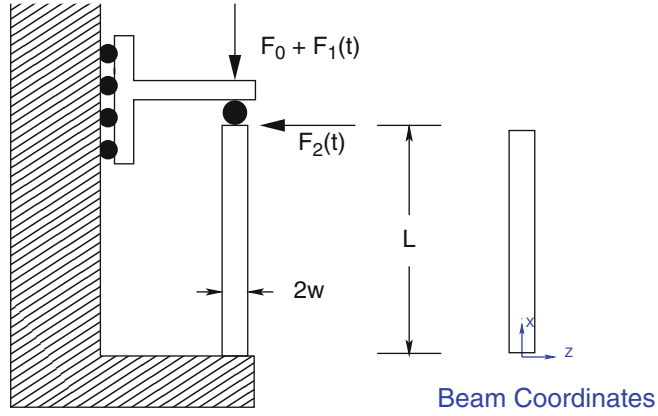


Fig. 16.6 Test case consisting of a cantilevered beam subject to a static compressive load F_0 applied longitudinally, random dynamic load $F_1(t)$ also applied longitudinally, and random dynamic load $F_2(t)$ applied laterally at the free end of the beam

We consider two axial modes excited by load F_1 and one bending load excited by F_2 . Each of F_1 and F_2 excite many modes, but for the purpose of illustration, we associate the first two axial modes with F_1 and the first bending mode with F_2 , and ignore the rest. Here we assume that the beam is sufficiently short so that shear stresses associated with that bending mode are significant.

Again, for convenience, we scale all constants such that Eq. (16.41) holds, but this time to simplify the expression for stress associated with axial deformation. The first bending mode can be approximated by

$$u(x) = \frac{1}{24} \left(\frac{x}{L} \right)^2 \left[\left(\frac{x}{L} \right)^2 - 4 \left(\frac{x}{L} \right) + 6 \right] \quad (16.44)$$

and we assume that the geometric features permit the scaling of bending stress shown below. The matrix of modal stresses $\Psi(x, z)$ is a 6×3 array with only 4 non-zero elements:

$$\begin{aligned} \Psi_{11}(x, z) &= \frac{1}{2} \cos \left(\frac{\pi x}{2L} \right), & \Psi_{12}(x, z) &= \frac{3}{2} \cos \left(\frac{\pi 3x}{2L} \right) \\ \Psi_{13}(x, z) &= \frac{1}{2} \left[1 - \left(\frac{x}{L} \right)^2 \right] - \left(\frac{x}{L} \right) \left[1 - \left(\frac{x}{L} \right) \right] \frac{z}{w} \\ \Psi_{43}(x, z) &= \delta \left[1 - \left(\frac{x}{L} \right) \right] \left(1 - \left(\frac{z}{w} \right)^2 \right) \end{aligned} \quad (16.45)$$

where $\delta = I_B / (2Lw_B A_B)$, which for this example we set to 1/2.

The static stress at any place on the beam is again

$$\sigma_0 = \begin{Bmatrix} -F_0/A_B \\ 0 \\ 0 \\ 0 \\ 0 \\ 0 \end{Bmatrix} \quad (16.46)$$

where $F_0/A_B = 1$. Again, for purpose of illustration for this problem, we assume a simple form for Γ_{qq} :

$$\Gamma_{qq} = \begin{bmatrix} 1 & 0 & 0 \\ 0 & 1 & 0 \\ 0 & 0 & 3 \end{bmatrix} \quad (16.47)$$

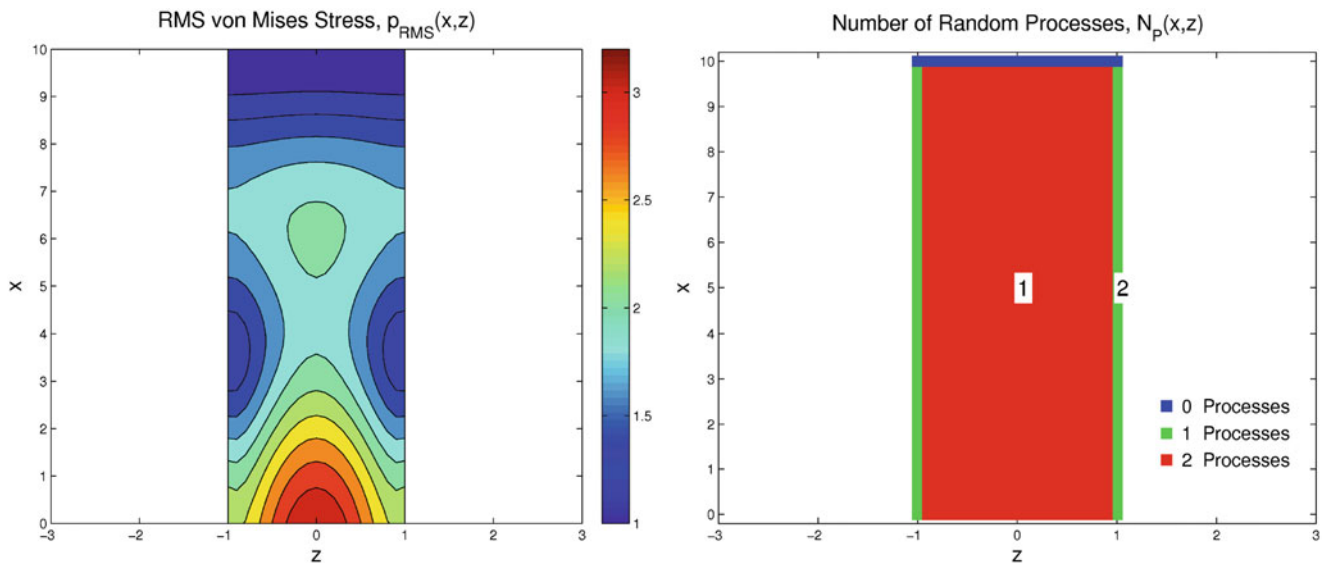


Fig. 16.7 The computed RMS von Mises stress resulting from the static pre-load and the lateral random dynamic loads is shown on left graphic. The distribution of the number of random processes is shown on the right. The locations marked “1” and “2” are discussed above

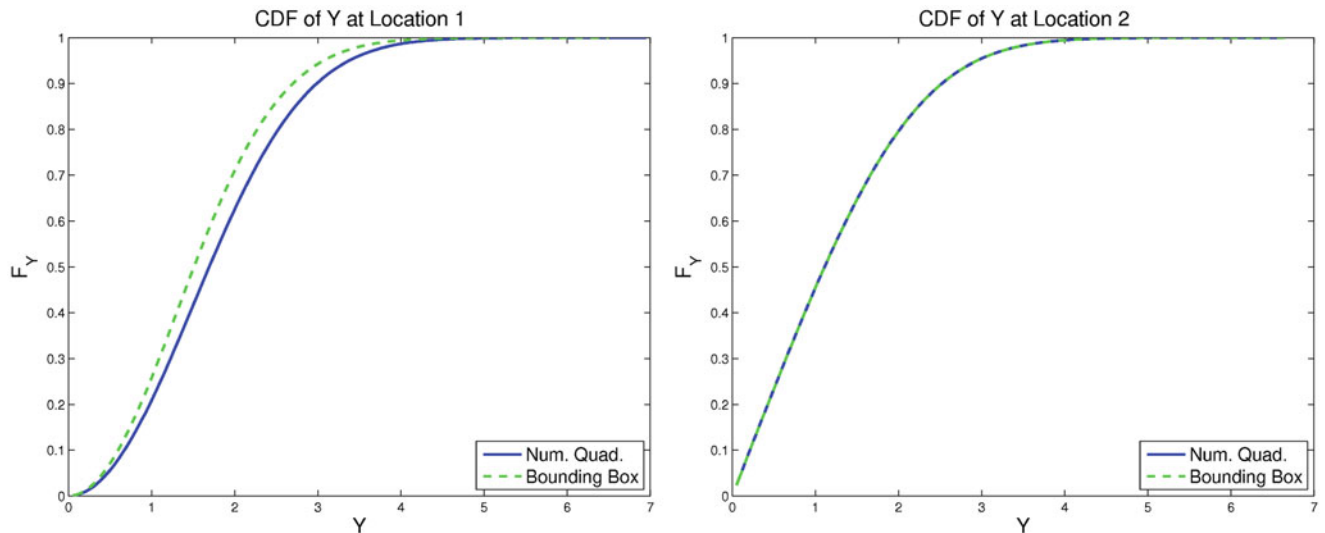


Fig. 16.8 The cumulative distribution functions (CDF) of von Mises stress at locations 1 and 2 are shown on the left and right graphics, respectively. Also shown are upper bounds obtained via Eq. (16.39). For the case of a single random stress process (such as location 2), the upper bound is exact

The RMS von Mises stress distribution for this case is shown on the left part of Fig. 16.7 and the distribution of the number of random processes is shown on the right portion of that figure. Because all of the vibration modes associated with the random loads have nodal lines at the top of the beam, there are no random processes there. On the left and right sides of the beam, there are only axial stress components, so there can be at most one process. In the interior of the beam, there are axial stress components due to the axial modes and the bending mode and there is a shear component associated with the bending, making two random stress processes possible.

Again, we are interested in the RMS von Mises stress, but also concerned about the probability of von Mises stress reaching high levels. The cumulative distribution function (CDF) for von Mises stress defined by Eq. (16.33) are illustrated by Fig. 16.8 for locations 1 and 2. For the case of a single random stress process (such as location 2), the upper bound as described by Eq. (16.39) is exact. More of the character of these distributions are indicated by the Probability Density Functions (PDF) shown in Fig. 16.9 for locations 1 and 2 noted in Fig. 16.7. The PDF for location 1 has a shape typical

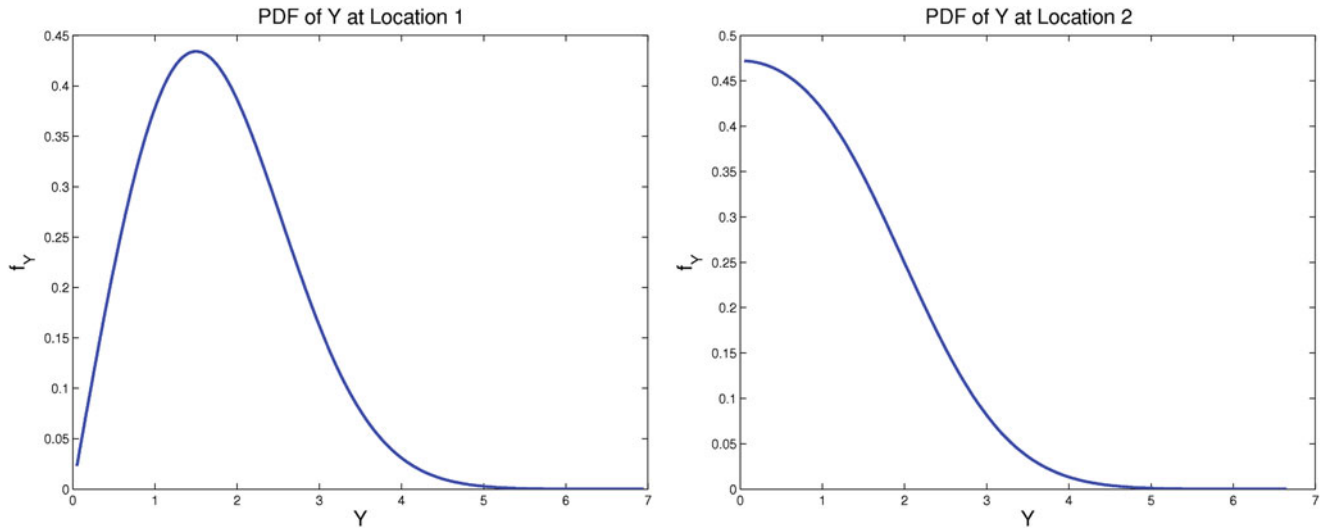


Fig. 16.9 The probability density functions (PDF) of von Mises stress at locations 1 and 2 are shown on the left and right, respectively

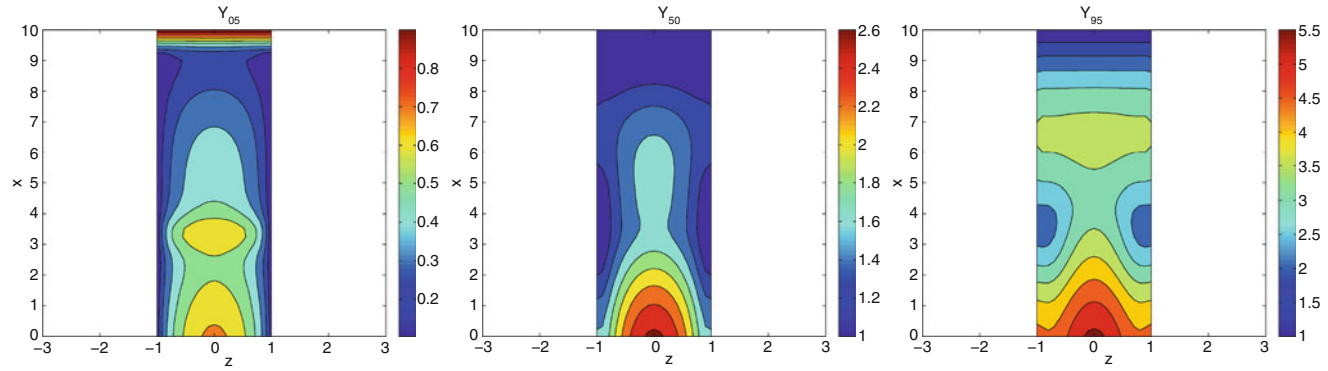


Fig. 16.10 The distribution of 5th percentile, 50th percentile, and 95th percentile von Mises stress are shown on the left, middle, and right contour plots, respectively

where there are two random stress processes and the PDF for location 2 has a shape typical where there is only one random stress process [3].

The spatial distributions of 5th percentile, 50th percentile, and 95th percentile von Mises stress are shown in Fig. 16.10. As expected, the range of von Mises stress in the 95th percentile plot (right side of Fig. 16.10) is substantially larger than those of the plot of RMS von Mises stress. The 5th percentile plot is particularly interesting; because the random loads excite vibration that result in stresses that are co-linear with the static stresses, there will be occasion when the random stresses act in direction opposite to the static stresses resulting in von Mises stresses less than that associated with the static loads alone. The plot of 50th percentile von Mises stress is very different from the RMS von Mises stress; this is the difference between the square root of the time average of a quadratic or a random variable, and the median of the absolute value of that variable.

16.6 Summary

The necessity of considering the von Mises stress (effective stress) in cases of random vibration is long known. Incorporating predictive mechanics of random vibration into modern engineering decision making requires expressing the stress response in a probabilistic manner. Though some progress in this direction has been reported in the literature, there are serious gaps with respect to the technology necessary to address random vibrations under pre-load – such as the random vibration of decelerating space structures in atmospheric re-entry.

A significant improvement in capability is presented here. With the use of the standard elements of random vibration analysis (cross spectral density matrix of loads, the modal frequency response matrices, assumption of a stationary and Gaussian load, etc.), a formulation is presented to express the probability distribution of von Mises stress at any location on a linear structure even for cases where the structure is subject to an arbitrary distribution of in situ stress.

The formulation is not complicated and implementation in a finite element context appears to be straightforward. On the other hand, evaluation of the necessary integrals can be compute intensive. A preferred implementation might involve the initial calculation of the full field of RMS von Mises stress and then calculation of the probability distribution of von Mises stress only at the “hot spots”.

Finally, it should be emphasized that the validity of the approximation embodied in Eq. (16.24) is still an issue for investigation.

Acknowledgements The authors express our appreciation to David Day, of Sandia National Laboratories, for very helpful mathematical discussion about the approximation central to this work.

References

1. Miles, J.W.: On structural fatigue under random loading. *J. Aeronaut. Sci.* **21**(11), 753–762 (1954)
2. Segalman, D.J., Fulcher, C.W.G., Reese, G.M., Field, R.V.: An efficient method for calculating R.M.S. von Mises stress in a random vibration environment. *J. Sound Vib.* **230**(2), 393–410 (2000)
3. Segalman, D.J., Reese, G., Field, R., Jr., Fulcher, C.: Estimating the probability distribution of von Mises stress for structures undergoing random excitation. *J. Vib. Acoust.* **122**(1), 42–48 (2000)
4. Tibbits, P.A.: Application of algorithms for percentiles of von mises Stress from combined random vibration and static loadings. *J. Vib. Acoust.* **133**(4) (2011)
5. Segalman, D.J., Field, R.V., Reese, G.M.: Probability distribution of von Mises stress in the presence of pre-load. Technical report SAND2013–3429, Sandia National Laboratories, Albuquerque (2013)
6. Roberts, J., Spanos, P.: Random Vibration and Statistical Linearization. Dover Publications, Mineola (2003)
7. Tibbits, P.A.: Percentiles of von Mises stress from combined random vibration and static loading by approximate noncentral Chi square distribution. *ASME J. Vib. Acoust.* **134**(4), 41009 (2012)
8. Reese, G., Bhardwaj, M.K., Walsh, T.: Salinas theory manual. Sandia report SAND2004-4079, Sandia National Laboratories, Albuquerque (2004)
9. Lahey, R., Miller, M., Reymond, M.: MSC/NASTRAN reference manual, version 68. The MacNeal-Schwendler Corporation (1994)
10. Bella, D., Reymond, M.: MSC/NASTRAN DMAP Module Dictionary. MacNeal–Schwendler, Los Angeles (1997)

Chapter 17

Damage Detection Integrating ISHM and LWSHM Techniques



Lucas Altamirando de Andrade da Rocha, Roberto Mendes Finzi Neto, and Valder Steffen, Jr.

Abstract Currently, structural health monitoring (SHM) represents one of the main areas of interest in engineering, being applied both for maintenance cost reduction and operational safety. In this contribution, a hybrid SHM system is proposed as a complementary methodology for the damage diagnosis of a typical aeronautical material panel (aeronautical aluminum plate 2024-T3), through the integration of two SHM techniques, namely the electromechanical impedance technique and the Lamb waves. For the diagnosis, a damage metric extracted from the impedance signatures of the structure was used in conjunction with an algorithm for localization of the damage by considering Lamb waves. In addition, temperature compensation techniques were systematically employed to avoid false diagnoses and a statistical model was developed to establish threshold indices according to a predefined confidence level. Thus, this work presents an evaluation of the sensitivity of the proposed techniques, considering a success rate. Finally, the results show the great potential for the integration of the two techniques together with statistical approach.

Keywords Structural integrity monitoring · Electromechanical impedance · Lamb waves · Temperature compensation · Fault diagnosis

17.1 Introduction

SHM systems will handle structures that experience changes in operating and environmental conditions. These changes influence the measured response and it is fundamental that they are not interpreted as evidence of damage (false positives). The variation of the ambient temperature is a common condition that must be accounted for during the process of damage detection [37].

Two examples of active local sensing for damage detection using PZT sensors are the Lamb Wave-based SHM (LWSHM) [49, 51–53] and the impedance-based SHM (ISHM) [4, 35, 36]. Advantageous features of these transducers include low cost, they generally require low power consumption and operate at higher frequency ranges (typically above 30 kHz) providing high sensitivity for the sensors. However, high-frequency signals also reduce the area of sensitivity of the sensors [43]. The LWSHM method monitors the properties of elastic mechanical waves that travel in the structure carrying information for damage along their path. On the other hand, the ISHM method monitors variations in the electromechanical impedance of a piezoelectric sensor bonded to (or embedded into) the monitored structure. The ISHM method generally uses the real part of the impedance since the imaginary part, which corresponds to the capacitive part of the response, is more sensitive to temperature variation. It is worth mentioning, however, that the imaginary part is used in a number of applications in order to assess the sensor's integrity [38].

Many studies have been performed in SHM for damage detection, especially for metallic structures using LWSHM and ISHM; review articles can be found in [8, 34]. The authors An and Sohn [2] employed LWSHM and ISHM methods for delamination detection in a composite wing mock-up specimen with stringers. To accomplish this, an active sensing data interrogation algorithm must be implemented [29].

A major drawback for active SHM systems that use piezoelectric transducers is the influence of temperature. Small temperature variation can lead the SHM system to give false positive diagnostics where no mechanical damage exists in the monitored structure [31]. Therefore, temperature compensation is imperative to obtain a reliable diagnostic of the structural integrity [5, 7, 14, 17, 18, 19, 37, 39, 46, 54].

L. A. de Andrade da Rocha (✉) · R. M. F. Neto · V. Steffen, Jr.

LMEst – Laboratory of Structural Mechanics, INCT (EIE) – National Institute of Science and Technology, Federal University of Uberlândia, Uberlândia, MG, Brazil

e-mail: lucasaarocha@ufu.br

For the ISHM technique, the effective frequency shift (EFS) through correlation analysis is the most commonly used temperature compensation method. Sun [54] first proposed the use of cross-correlation between two impedance signatures to compensate for frequency shifts caused by temperature variation. Park [37] compensated for both the frequency and the magnitude shifts through a modified damage metric. Koo [18] modified the method developed by Park [37] to develop EFS to compensate for temperature effects through the maximization of the correlation coefficient. The frequency shift for temperature compensation through this technique is usually chosen from the result of a simple optimization problem aiming at maximizing the correlation coefficient. Consequently, the damage metric (DM) is always minimized even when damage is found in the impedance signature. As the impedance signatures are well correlated, this characteristic can mitigate the low sensitivity of the technique since the DM is always minimized in the temperature compensation procedure, as shown by Rabelo [40]. In the present work, the authors propose the use of a pre-recorded set of measurements corresponding to the pristine condition encompassing several temperatures to apply only a frequency shift that corresponds to the temperature gradient of each measurement. As a result, the horizontal frequency shift due to temperature change will be compensated according to the optimization result.

In the LWSHM technique, a review of the different methods is presented in the literature [46]. The technique of temperature compensation selected for the Lamb Wave method is the reconstruction of the baseline signal to the analysis temperature, presented by Liu [23]. The method was developed to compensate the baseline signal for the current signal temperature. The Hilbert transform is used to compensate for the phase of the baseline signal. Orthogonal Match Search (OMP) is used to compensate for the amplitude of the baseline signal. Temperature compensation methods based on numerical modeling have been studied by many researchers. Marzani and Salamone [25] propose a comprehensive Lamb wave propagation model to predict the full pitch-catch signals under varying temperature. Numerical versus experimental studies demonstrate that the high accuracy of temperature compensation of Lamb waves signals can be obtained on metallic structures. However, regarding applications on composite structures, an accurate physical model is difficult to be derived.

Recently, a physics-based temperature compensation model combined with matching pursuit signal analysis has been introduced [47]. The performance of this model is found to be at par with the optimal baseline subtraction added to the baseline signal stretch compensation method. A cointegration approach presented by Dao and Staszewski [9], which has been widely used in econometrics, has been proposed to remove the undesired temperature effect from Lamb wave data. This method is partially built on the analysis of the non-stationary behavior of Lamb wave signal acquired at different stages. The procedure and computation associated with this method are quite complex.

The statistics analysis in the decision-making process is one of the main tools of a SHM system. Previous research works on LWSHM, such as the ones by [24, 26, 33, 44, 50, 51, 52] and others on ISHM [3, 10, 28, 31, 32, 34] have been typically used to identify structural damage in different contexts.

This paper investigates the use of the interaction between two SHM techniques, namely the electromechanical impedance technique and the Lamb waves, since such interaction has not yet been explored enough. The interaction is based on the actuator efficiency [21] so it is possible to select an optimal frequency from the impedance curve of the structure, reducing the error in the location of the damage. A limiting factor is that there is no commercial equipment that allows this interaction, therefore, this work used a hardware capable of using both cited techniques simultaneously (developed for this application), in addition the present paper took into account the condition of variable temperature to improve system performance when diagnosing structure damage. Next, a statistical model was developed to determine the damage threshold indices according to a predefined confidence level. In addition, this work seeks to bring to light the importance of the interaction of the two techniques, especially in cases where there is variation of temperature during the monitoring.

17.2 Lambwave-based Structural Health Monitoring (LWSHM)

In this section, the principles on which the technique of Lamb waves are based on are discussed in conjunction with the methodology through which structural damage is detected. Problems related to temperature variation are also presented.

17.2.1 Physical Principles of The Lamb Wave (LW) Technique

Basically, Lamb waves are elastic waves that propagate through solid media and thus are subject to reflections and attenuations imposed by this propagation medium. When considering the monitored structure as the propagation medium,

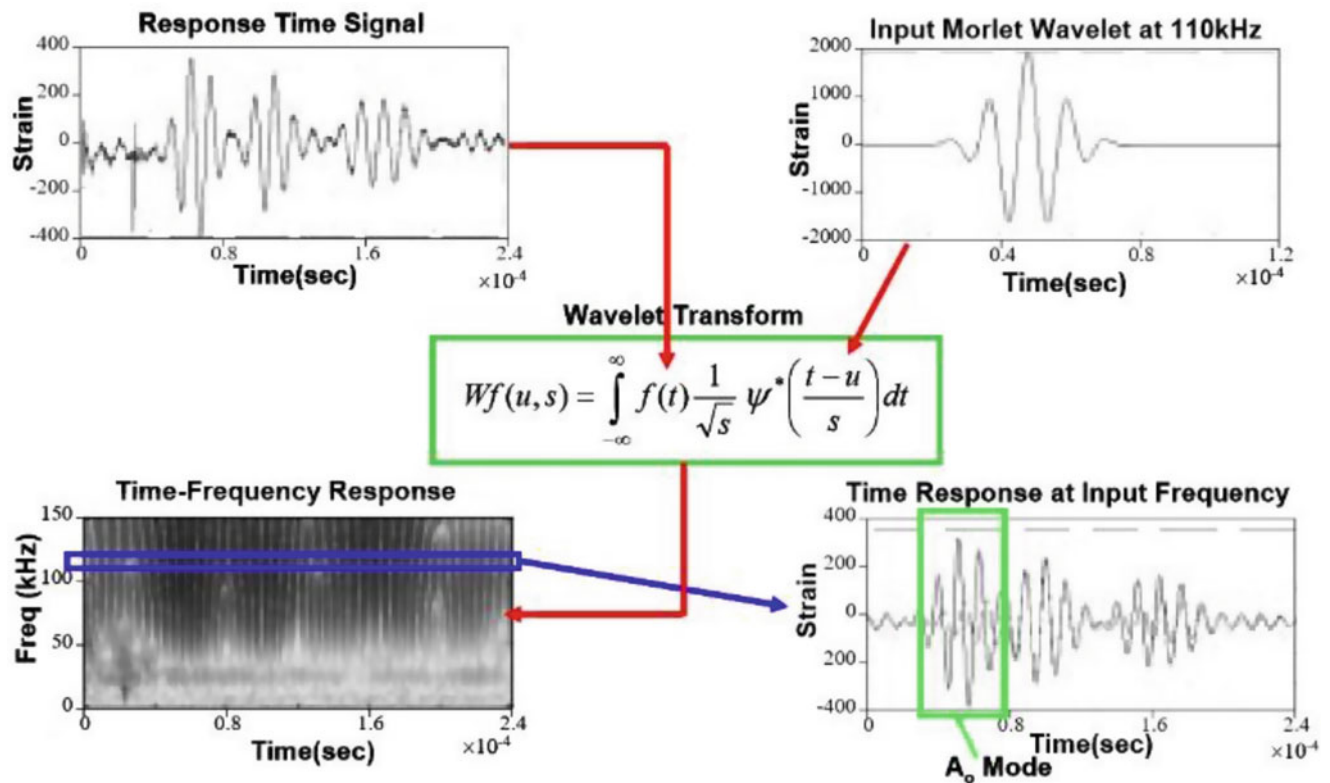


Fig. 17.1 A wavelet analysis procedure to extract a damage sensitive feature

structural damage also changes this medium. This technique has proven to be a reliable method to detect the presence of damage in structures, including its location, severity, and the type of damage [42].

Raghavan and Cesnik [42] define two usual methods of diagnosis associated with the LW technique, namely, the pulse-echo and the pitch-catch methods. In both methods, the actuator excites the structure with a pulse signal, typically a single tone modulated. The pulse echo method of the same actuator is used as a sensor to monitor the echoes of the signal along the propagation path. In the pitch-catch approach, the pulse signal is generated by an actuator and propagates through the structure; then, a sensor located in a different location of the structure receives the signal.

Both LW approaches make use of digital signal processing algorithms in order to extract features related to the propagation medium of the acquired signal. Thus, one can use the Fast Fourier Transform to detect characteristic frequencies [20]; alternatively, it is possible to use the Continuous Wavelet Transform (CWT) to extract the required features [49].

This work uses CWT for extracting the signal features [11], and the diagnostic method used herein is the pitch-catch. This methodology has been successfully applied to identify delaminations and fiber breaks in composite structures with carbon fiber/epoxy [11]. Additionally, this technique can also be applied to metal structures, such as in railway rails [35] or in metallic plates [15].

Figure 17.1 outlines the methodology used in the present work, from a pulsed excitation at a given frequency until the signal decomposition into frequencies through the CWT.

Thus, by analyzing the data window and looking for the peak of the signal, one can define the time instant at which the so-called Time of Flight (TOF) occurs and the peak value at a given instant. In addition, the signal energy can be used for characterization purposes [49]. Since the signal is classified as transient, transient analysis tools such as the CWT is used to extract additional information from the acquired data [55].

17.2.2 Damage Index

In the works of Sohn [49] and Lu [24] the damage index (DI) described by Eq. (17.1) was used to quantify damage. The DI is based on the comparison between the energy of the baseline and the signals processed by CWT [1, 12, 22, 24, 45].

$$DI = 1 - \frac{\int_{x_1}^{x_2} Wft(x, S_0) dx}{\int_{x_1}^{x_2} Wfb(x, S_0) dx} \quad (17.1)$$

where, $Wft()$ Wavelet Transform of the sampled signal; $Wfb()$ Wavelet Transform the baseline signal; x translation of wavelet used in CWT; S dilation of the wavelet used in CWT; x_1 and x_2 translation intervals (linked to time) analyzed by CWT.

LW technique uses low frequencies as compared with those normally used in the impedance technique. This makes the necessary hardware (data acquisition card, computer memory, etc.) less sophisticated. The excitation frequency is affected by the attenuation along the propagation path and is usually determined experimentally.

17.2.3 Temperature Compensation

The temperature effects on the time variant signal can be observed as a change in signal amplitude and phase [14]. Based on these effects, it can be assumed that a temperature effect on a LW signal can be approximated by a time-stretch signal and amplitude.

It was used temperature compensation method based on the baseline signal reconstruction for monitoring the temperature of the damage detection signal based on Lamb wave [23]. So, Liu used the Hilbert transform to compensate for the signal phase of the baseline. Orthogonal matching pursuit (OMP) is used to counterbalance signal amplitude. In Fig. 17.2 is the flowchart proposed by Liu for the reconstruction of the baseline to the desired temperature.

One can find more details on Liu's approach in [23].

In the present study, the temperature dependence is highlighted showing that a temperature variation can influence on decision-making, leading to a false interpretation of the current structural health state.

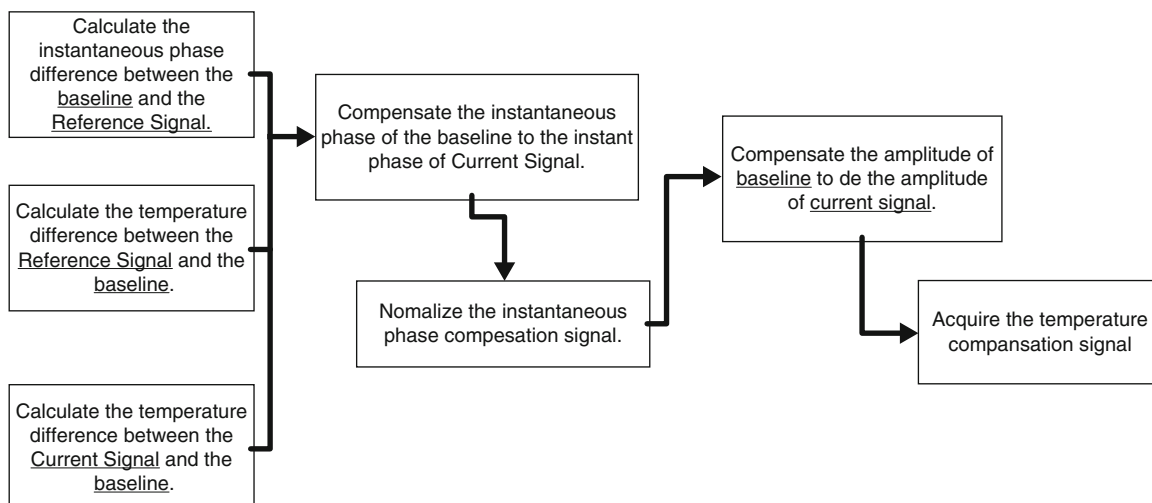


Fig. 17.2 The flowchart of the proposed temperature compensation method (Adapted from Liu [23])

17.3 Impedance-Based Structural Health Monitoring

In this section, the basics of the Impedance-based SHM technique is briefly described in conjunction with the methodology used to detect structural damage. Problems related to temperature variation are also discussed.

17.3.1 Physical Principle of ISHM Technique

The ISHM technique uses the piezoelectric properties of the PZT patch that is installed in the structure being monitored. The PZT patch is bonded to (or embedded into) a structure and a low electric voltage is applied [43], generating a strain in the PZT patch. Then, the response of the mechanical vibration is transmitted to the sensor in the form of an electrical response. If a structural modification occurs, such as damage, the electric response of the PZT patch will change accordingly. The well-known mechatronic model that describes the measurement process is shown in Fig. 17.3 for a single-degree-of-freedom (DOF) system:

For this system, Liang [21] demonstrated that the PZT's admittance, $Y(\omega)$, which is the inverse of the impedance, can be written as a function of the combined PZT actuator and structure mechanical impedance, as given by Eq. (17.2):

$$Y(\omega) = j\omega a \left[\bar{\varepsilon}_{33}^T (1 - j\delta) - \frac{Z_S(\omega)}{Z_S(\omega) + Z_a(\omega)} d_{3x}^2 \hat{Y}_{xx}^E \right] \quad (17.2)$$

where $Z_a(\omega)$ and $Z_S(\omega)$ are the actuator's and structure's mechanical impedances, respectively. \hat{Y}_{xx}^E is the complex Young's modulus of the PZT with zero electric field, d_{3x}^2 is the piezoelectric coupling constant in the arbitrary x direction, $\bar{\varepsilon}_{33}^T$ is the dielectric constant at zero stress, δ is the dielectric loss tangent of the PZT, ω is the excitation frequency, a is a geometric constant of the PZT and j is the imaginary unit. Assuming that the mechanical properties of the PZT patch do not vary during the measurement procedure, Eq. (17.2) shows that the electrical impedance of the PZT patch is directly related to the structure's impedance. Damage leads to changes in the structure's mechanical impedance, thus modifying local dynamic features. Hence, the electrical impedance is measured in order to monitor the so-called health state of the structure, through a comparison with a previous *baseline* measure, *i.e.*, the pristine condition. The real part of the electrical impedance is more reactive to damage since the imaginary part contains the capacitive portion of the PZT patch, which is more sensitive to temperature variation [19]. Therefore, the ISHM technique usually takes the real part of impedance signatures for damage assessment.

17.3.2 Damage Index

The curve that represents the impedance response provides a qualitative assessment of the damage. For a quantitative assessment of the failure, a previously defined Damage Metric (DM) is used [30]. In the present contribution, the damage

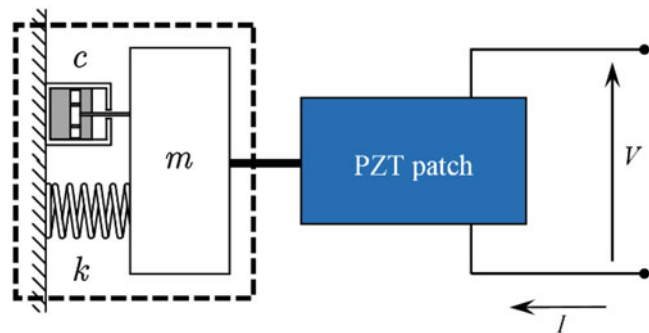


Fig. 17.3 Single DOF model illustrating the ISHM method

metric used is the Correlation Coefficient Deviation (CCD). This DM uses two signals, where the first corresponds to the baseline and the second corresponds to the test measurement. The CCD is given by Eq. (17.3):

$$CCD = 1 - \frac{1}{n} \sum_{i=1}^n \left\{ \frac{[\operatorname{Re}(Z_{1,i}) - \operatorname{Re}(\bar{Z}_1)][\operatorname{Re}(Z_{2,i}) - \operatorname{Re}(\bar{Z}_2)]}{S_{Z_1} S_{Z_2}} \right\} \quad (17.3)$$

where $\operatorname{Re}(Z_{1,i})$ and $\operatorname{Re}(Z_{2,i})$ are the real parts of the impedance from the baseline and test measurement at frequency i , respectively; n is the number of frequency points, $\operatorname{Re}(\bar{Z}_1)$ and $\operatorname{Re}(\bar{Z}_2)$ are the average of the baseline and test measurements, respectively; S_{Z_1} and S_{Z_2} are the standard deviations of the baseline and test measurements, respectively.

17.3.3 Temperature Compensation: Effective Frequency Shift (EFS)

The shifts caused by temperature variation may be considered uniform for a determined and limited frequency band. The changes due to a structural damage do not follow the same trend. This feature allows the mitigation of temperature variation effects through a data normalization procedure [39].

At first, the vertical shift is corrected simply by the difference in overall average value of the *baseline* and the test signature pattern according to Eq. (17.4):

$$\Delta_v = \frac{1}{n} \left[\sum_{i=1}^n \operatorname{Re}(Z_{2,i}) - \sum_{i=1}^n \operatorname{Re}(Z_{1,i}) \right] \quad (17.4)$$

Next step, the correlation coefficient $CC_{Z_1 Z_2}$ is utilized to determine the extension of the frequency shift. The $CC_{Z_1 Z_2}$ is obtained according to Eq. (17.5), which is part of the CCD damage index:

$$CC_{Z_1 Z_2} = \frac{1}{n} \sum_{i=1}^n \left\{ \frac{[\operatorname{Re}(Z_{1,i}) - \operatorname{Re}(\bar{Z}_1)][\operatorname{Re}(Z_{2,i}) - \operatorname{Re}(\bar{Z}_2)]}{S_{Z_1} S_{Z_2}} \right\} \quad (17.5)$$

If the test measurement Z_2 is shifted of n frequency points from the *baseline* Z_1 , then its correlation coefficient will be maximized. After this procedure, both signatures should be fully correlated, except for the portion associated with damage. Thus, an optimization procedure is performed, searching for the maximum correlation coefficient as a function of the frequency shift of n data points (delayed or advanced). Therefore, this technique searches for the optimum frequency shift Δf and the corrected impedance signature is written according to Eq. (17.6):

$$\operatorname{Re}(Z_{corr,i}) = \operatorname{Re}(Z_{2,i \pm \Delta f}) + \Delta_v \quad (17.6)$$

where $\operatorname{Re}(Z_{corr,i})$ is the real part of the impedance corrected at frequency i , $\operatorname{Re}(Z_{2,i \pm \Delta f})$ is the real part of the test measurement shifted by Δf data points.

In the frequency axis, the shift will be applied to the right if the test measurement's temperature is greater than the *baseline*'s temperature; otherwise, the shift will be oriented to the left. Therefore, it is important to have temperature readings for all measurements performed as close as possible to the sensors in the structure being monitored by an ISHM system.

17.4 Determination of Threshold with Statistical Control of Processes and Confidence Intervals

In SHM, it is highly desirable that a reliable threshold level is established based on the information acquired for the pristine condition of the structure. After the data is acquired and processed, next step is the preparation of the raw data for analysis. The first data operation is data editing. This refers to the pre-analysis operations that are designed to detect and eliminate spurious or degraded data signals that might have resulted from acquisitions and recording processes such as excessive noise, signal dropouts, or even from an external cause such as a power supply failure [6].

17.4.1 Normality Test

Several normality tests can be performed to verify a sample for normality [41]. In this study, the Jarque-Bera (JB) test is chosen since it is statistically rigorous as compared with the graphical methods. This test is a two-sided goodness-of-fit test suitable for the cases in which a fully-specified null distribution is unknown and its parameters have to be estimated. Equation (17.7) defines the JB test:

$$JB = \frac{N}{6} \left[S_k^2 + \frac{(k_t - 3)^2}{4} \right] \quad (17.7)$$

17.4.2 Threshold Determination with Statistical Process Control and Confidence Intervals

As normality has been confirmed, a concept from Statistical Process Control (SPC) was used to determine the Upper Control Limit (UCL) and the Lower Control Limit (LCL) of the damage indexes, since the SPC technique assumes successive deviations from a normally distributed function. Since this is not always the case and we are interested on the upper limit value for the threshold, this work proposes a methodology for the determination of the threshold by using the concept of confidence interval.

A more meaningful procedure for estimating parameters of random variables involves the estimation of an interval, as opposed to a single point value, which will include the parameter being estimated with a known degree of uncertainty. For the estimation of the mean value, a confidence interval can be established for the mean value μ_x based on the sample mean \bar{x} , according to Eq. (17.8):

$$\left[\bar{x} - \frac{\sigma_x Z_{\alpha/2}}{\sqrt{N}} \leq \mu_x < \bar{x} + \frac{\sigma_x Z_{\alpha/2}}{\sqrt{N}} \right] \quad (17.8)$$

where μ_x and σ_x are the population mean and standard deviation, respectively; \bar{x} is the sample mean, N is the sample size, v is the number of DOF, and $Z_{\frac{\alpha}{2}}$ is the standardized variable given by Eq. (17.9) associated with the significance level α :

$$z = \frac{x - \mu_x}{\sigma_x} \quad (17.9)$$

As σ_x is unknown, the confidence intervals for the mean μ_x and variance σ_x^2 have to be determined. For a sample of size N , one can show that Eqs. (17.10 and 17.11) [6] give the confidence intervals for the mean and variance values as, respectively:

$$\left[\bar{x} - \frac{st_{v;\alpha/2}}{\sqrt{N}} \leq \mu_x < \bar{x} + \frac{st_{v;\alpha/2}}{\sqrt{N}} \right], \quad v = N - 1 \quad (17.10)$$

$$\left[\frac{vS^2}{\chi_{v;\alpha/2}^2} \leq \sigma_x^2 < \frac{vS^2}{\chi_{v;1-\alpha/2}^2} \right], \quad v = N - 1 \quad (17.11)$$

where S^2 is the sample variance, $t_{v;\alpha/2}$ is a student t variable with v DOF and $\chi_{v;\alpha/2}^2$ is a chi-square variable with v DOF.

Therefore, after obtaining these intervals the threshold was determined according to Eq. (17.12):

$$DI_{threshold} = \mu_{x_{max}} + 3\sigma_{x_{max}} \quad (17.12)$$

where $\mu_{x_{max}}$ is the upper limit of the population mean and $\sigma_{x_{max}}$ the upper limit of the population standard deviation, both obtained choosing a significance level $\alpha = 1\%$ applied to Eqs. (17.10 and 17.11). It should be noted that the choice of the decision threshold influences both the detectable size and the probability of a false positive. Additionally, the confidence interval obtained from Eq. (17.10) is generally wider than the one obtained from Eq. (17.8); however, the difference decreases as the sample size increases. Equation (17.8) provides a confidence interval of the mean with the assumption that the sample variance is equal to the population variance. In this work, Eq. (17.10) was used to estimate the mean confidence interval since normality has been previously checked for this equation.

17.5 Experimental Design and Setup

For testing the methodology presented in this contribution, a 2024-T3 aeronautical aluminum plate, with dimensions $500 \times 500 \times 1.6$ mm and mass of 1120 kg was selected. This panel was instrumented with eight PZT patches (diameter 10 mm \times 0.5 mm thickness, of type 5H). The actuator sensors were bonded using an epoxy-based adhesive (Hysol EA9320NA). The test specimen was prepared as shown in Fig. 17.4a).

The arrangement of the PZT patches was chosen so that the damage localization procedure is facilitated, thus covering a large area of the structure. The idea is not to interfere with the functionality of the structure (the sensors are grouped in the center of the plate). In addition, the position of the inserts was inspired by the CLoVER sensor architecture developed by Salas and Cesnik [48]. In Fig. 17.4b) we can observe the architecture of the instrumentation used on the panel.

To simulate the damage in the structure, a structural modification was made by adding a small mass to the plate. To this end, a pair of NdFeB, Grade N52 (B444-N52) magnets of dimensions $6.35 \times 6.35 \times 6.35$ mm and 1.92 g weight were used. For signal generation, a National Instruments function generator (PXI-5412 with 14 bits resolution and sampling rate of 100 MS/s with maximum amplitude of $\pm 12V_{pk-pk}$) was used. Digitizer (PXI-5105, with 12 bits of resolution and sampling rate of 60 MS/s, with 8 independent channels) was used to acquire the signal. This description refers to the maximum configurations of the equipment, the equipment configuration is adjusted second the need of the analysis. These devices (PXI-5412 and PXI-5105) are embedded in the PXI-1033 chassis, which is a robust controller capable of operating both devices in real time.

For temperature control a climate chamber EPL-4H series Platinous was used, which employs a system BTCH (Balanced Temperature and Humidity Control) for controlling temperature and humidity. The BTCH system regulates the temperature and humidity inside the camera to reproduce the conditions desired by the user. This is done by continuously controlling the capacity of a cooler (dehumidifier) high-heat load and low humidification heater heat load in real time. Thus, EPL-4H chamber operates at temperatures ranging from -40°C to 180°C with a resolution of $\pm 0.5^{\circ}\text{C}$ (note that the humidity will not be used for control, it is not a parameter of interest in this article).

All tests were performed in free-free situation, to minimize interference from other sources of noise during the experiment (for example, any vibration of the climatic chamber, among others). The cable stiffness that connects the structure to the data acquisition equipment is another important factor when considering the repeatability of the experiment, especially when the impedance analysis is made. Thus, an intermediate connector with low rigidity is used.

The time to stabilize the temperature inside the environmental chamber was set to 45 min [16]. Thus, with the stable temperature, the baselines of the healthy structure were acquired at the target temperatures.

The impedance frequency range was selected according to the highest peak density to have the best sensitivity to damage [27].

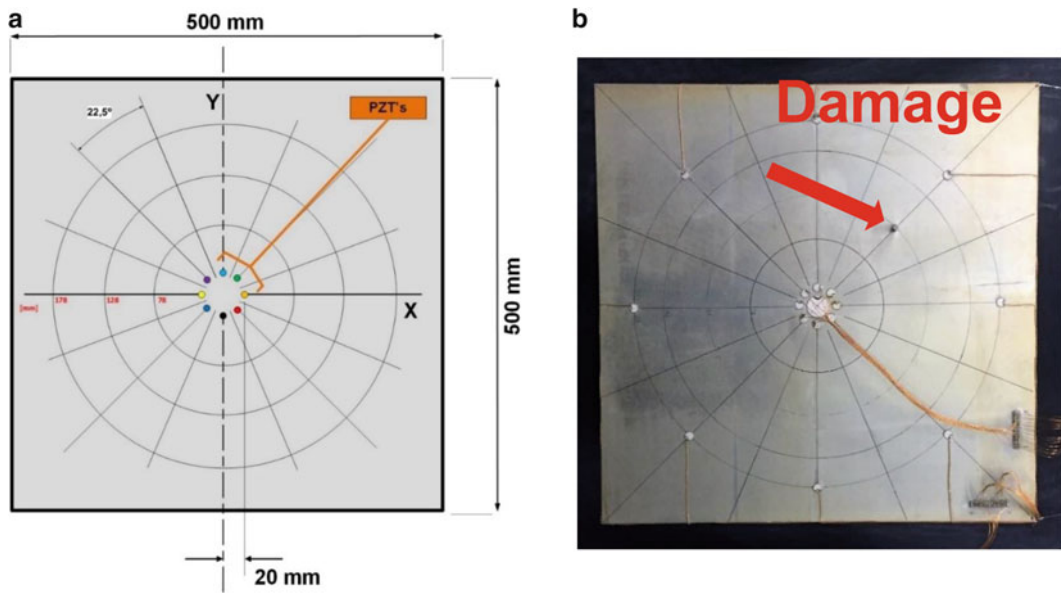


Fig. 17.4 (a) Positions of the sensor network, (b) Structure of instrumented aeronautical material

The settings required for the collection of database signals are presented below for the integrated SHM techniques:
For the electromechanical impedance:

Frequency range: 80,000 Hz to 90,000 Hz;
500 points per frequency;
100 samples per average frequency point;
30 signatures for temperature readings.

For the Lamb waves:

Frequency selected in the impedance step for each PZT;
Sampling rate 6 ms / s to 3000 samples (may vary, to meet the frequency of the signal generator);
Amplitude of actuation of $20V_{pk - pk}$;
Hann modulation of 3.5 (SOHN, 2005);
Readings interval of 100 ms;
Number of readings equal to 100 per PZT.

The proposed SHM system uses multiplexers similar to the topology proposed by Finzi Neto [13]. In addition, hardware has been implemented in a second network enabling multiplexers to operate simultaneously with the two SHM techniques considered here (LWSHM and ISHM).

17.5.1 Hybrid SHM System

The focus of this article is to incorporate the interaction of two techniques (ISHM and LWSHM) in the task of diagnosing damage in the analyzed structure (Fig. 17.5), thereby reducing the false negative responses.

For this task, it is acquired the impedance curves of each of the 8 PZT's; from these curves, it is possible to identify the presence of damage to the structure (item 3.2), but does not locate. With the impedance curves are selected the best frequency for each sensor to implement the analysis with the waves of Lamb. Accordingly, the frequency is selected where the impedance curve has the smallest value within the frequency range selected, in other words, where the elastic Lamb wave will have greater amplitude, facilitating damage locating algorithm (where the actuator efficiency is maximum - according to Liang [21]). This step has the function of estimating and locating the damage by the triangulation method from the TOF of the wave (note also that the effect of temperature is considered in this step and compensated). With identified and localized damage begins to statistical analysis that will lead finally to the diagnosis of the state of the structure.

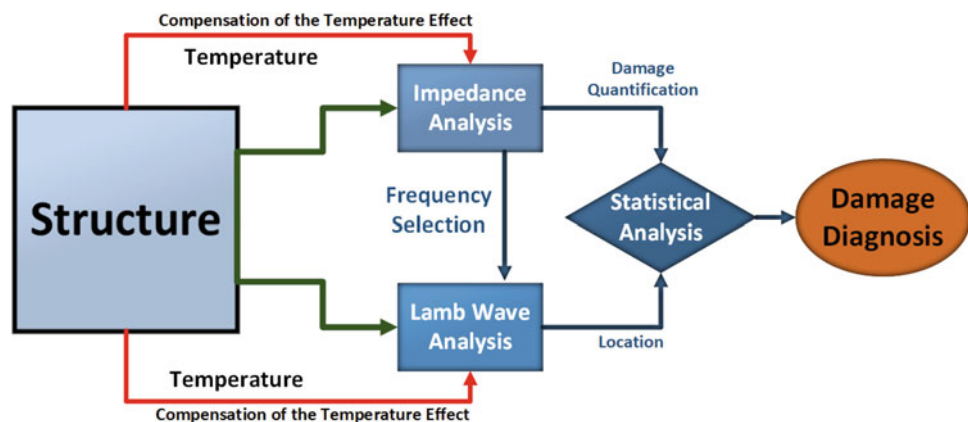


Fig. 17.5 Functional diagram of the proposed SHM system

17.6 Results

With the available database, it is possible to analyze the structure to any temperature within the range studied. To test the system, a temperature of 25 °C and a random damage in the structure at the position given by 73 × 64 mm was selected, as shown in Fig. 17.4b).

Then the impedance signatures of all PZT pellets were collected. In Fig. 17.6 are present in the average (30 signatures) signatures of eight PZT wafers already offset the effect of temperature. Also note that the trend curves of signatures have already been subtracted to demonstrate the selection of frequencies for the evaluation through the Lamb waves.

In Fig. 17.7 it can be noted that the CCD damage index structure with a random damage point to the existence of damage. Also in Fig. 17.7, “N D” represents the structure without giving and “D” the damage condition, since the threshold value is calculated independently for each actuator.

For the analysis with the Lamb waves it is necessary to select the best frequency within the selected range (80 kHz to 90 kHz). From Fig. 17.7 it is possible to select the excitation frequency of each of the PZT to generate Lamb waves. Table 17.1 shows the frequencies selected in Fig. 17.7.

With the selected frequencies, 100 readings were performed for each PZT sensor, in addition to the readings of four PZT sensors neighboring the PZT actuator. To exemplify the procedure, consider PZT#2 as the actuator. PZT#2 is then responsible for the excitation and the signal is collected by PZT#n-2, that is, by PZT # 8. After completing the 100 readings, the same process is repeated, but now using PZT#1 (PZT#n-1) as the sensor, until you reach PZT#4 (PZT#n + 2).

As in impedance, the effect of temperature in this case is also an error factor to be considered, especially when determining the TOF of each signal. Considering the temperature compensation algorithm for Lamb waves, based on the reconstruction of the baseline signal for the temperature of the monitoring signal, all the baselines are compensated for the temperature of 25 °C. The signals then pass through a high-pass FIR filter with a cutoff frequency of 1 kHz to minimize the effects of the thermal chamber vibration.

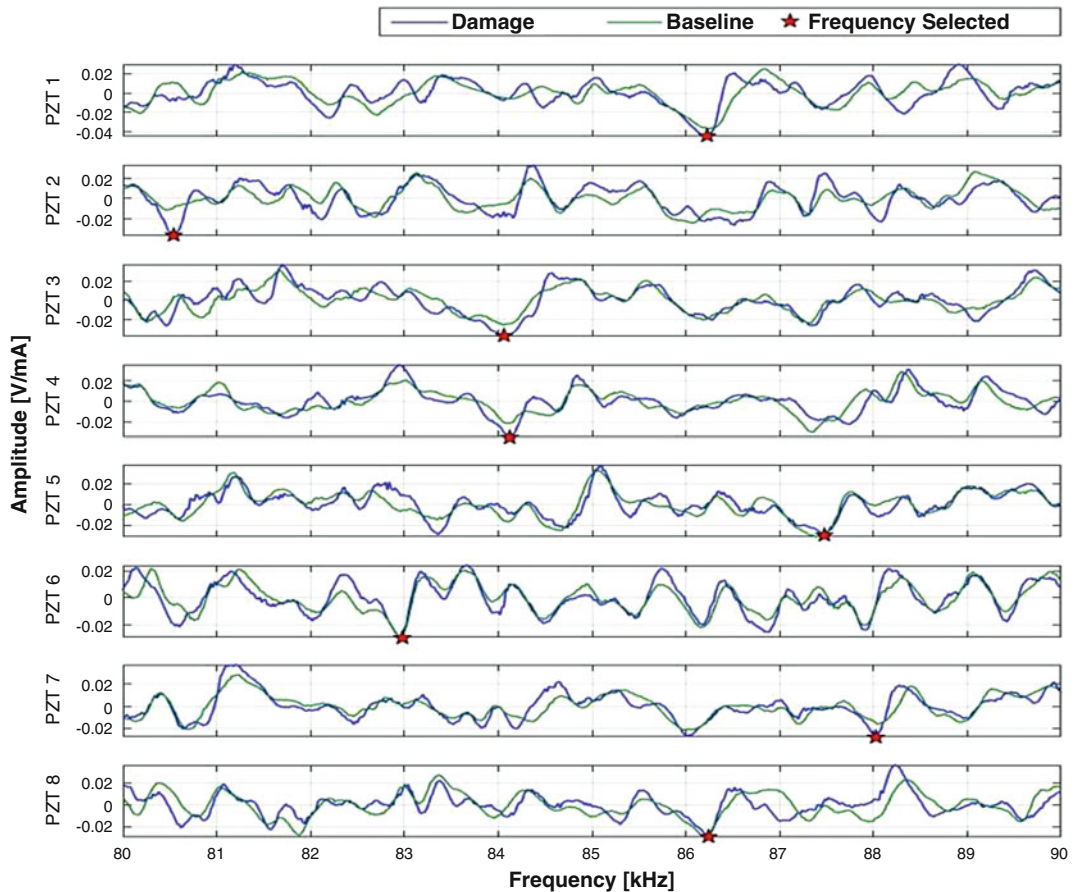


Fig. 17.6 Impedance curves with random damage

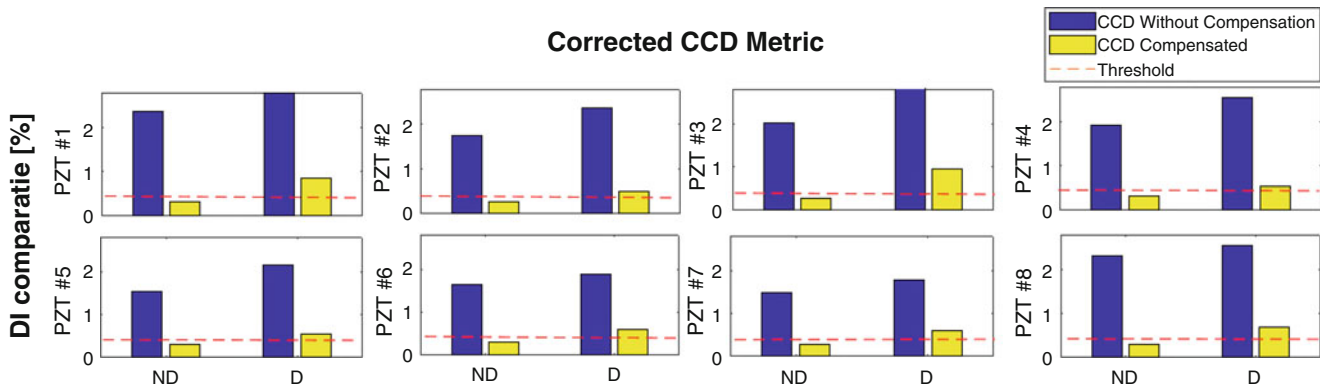


Fig. 17.7 CCD values in the complete analysis for the conditions with and without temperature compensation, for the condition with random damage

Table 17.1 Selection of frequencies for the random damage

Selected frequencies [kHz]							
PZT 1	PZT 2	PZT 3	PZT 4	PZT 5	PZT 6	PZT 7	PZT 8
86.22	80.54	84.06	84.12	87.48	82.98	88.02	86.24

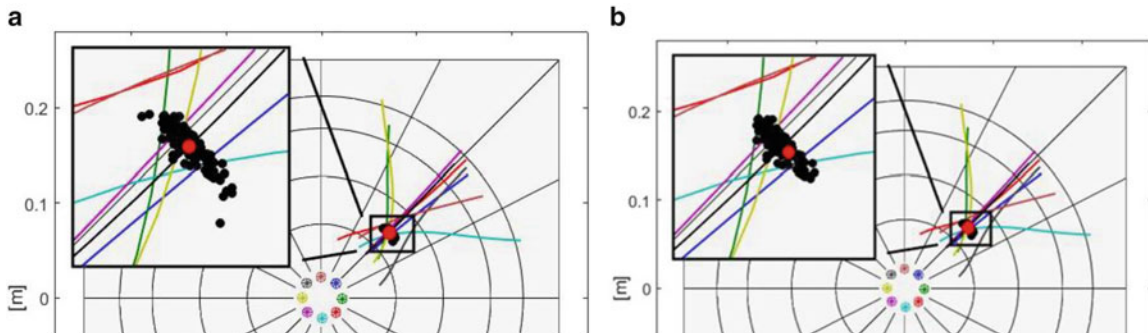


Fig. 17.8 (a) possible locations for the damage, (b) the damage location results after statistical processing

Table 17.2 Results of the normality test for the lamb waves technique

Skewness	Kurtosis	H_0	p-value [%]	Lim. Val.	Crit. Val.
0,0278	2,9831	0	0,5000	0,4032	5,8581

Figure 17.8a shows a collection of the possible locations (black point) of the damage and their average position (red point).

At this point of processing, the error value can still be reduced by applying the Chauvenet criterion and excluding outliers. In addition, it is necessary that the sample has a normal distribution and, for that, the JB test was applied. Table 17.2 shows the result of the normality test.

In Table 17.2, the skewness and kurtosis are the statistical moments of the sample analyzed. A simple normality test was performed to verify the asymmetry (skewness) of the sample (this should be close to zero), characterizing the PDF symmetry (Gauss probability density). It is also seen that the value of kurtosis is of the order of 3.0, indicating the peak shape similar to a classical bell-shape of a Gaussian distribution - corresponds to the null hypothesis, i.e., the sample follows a normal distribution (the result being 0 means that the null hypothesis should not be rejected). The p-value indicates the result for the hypothesis test. If the value of p is less than the level of significance, (in this case,) it indicates that the null hypothesis should not be rejected. The last two columns correspond to the limit values and the critical values of the normality tests. To accept the null hypothesis, the critical value must be greater than the limit value. These results follow the notation used in the MATLAB® statistical toolbox. Therefore, it can be concluded that the sample originates from a Gaussian distribution with 99% confidence.

Figure 17.8b shows the possible Cartesian location of the damage after the statistical treatment, being estimated in 72.3 mm in the X axis and 66.4 mm in the Y axis, which corresponds to a relative error percentage of 1,14%.

Considering Figs. 17.7 and 17.8b it is possible to make a fault diagnosis of the structure, where the damage was detected by the impedance signatures and quantified by the CCD metric. Since the location can be estimated from Lamb waves with error less than 2%. Note that the relative error of the location of the damage is not 2% for the entire structure, because when moving away from the sensor network the error increases significantly.

17.7 Conclusions

Considering that the integration of the two SHM techniques is considered somewhat new, this paper presents a combination between the technique known as electromechanical impedance and Lamb waves, with the purpose of obtaining better diagnostics of damaged structures (aeronautical structure, in the present case). One of the main limitations of studies and applications in this area is the requirement of specific instrumentation that meet the needs of the techniques involved.

Statistical methods were proposed in order to verify the success rate of damage detection considering the barely-visible impact damage introduced under the influence of varying temperature. Temperature compensation procedures were applied to reduce undesired effects in the signal analysis as due to temperature change.

This method takes into account concepts of statistical process control and confidence interval from statistical theory. The decision limit obtained with the proposed method was used to perform a sensitivity analysis by success rate (above the threshold values in Figs. 17.8b).

The detection system successfully detected the damage introduced with an error of less than 2%. The tests were verified using experimental data obtained from an aeronautical aluminum plate 2024-T3.

A method for performing data cleansing was performed to perform aberrant value detection using the Chauvenet criterion to eliminate false positives and improve overall results.

The experiment conducted through this study used a temperature compensation method for both SHM techniques. These procedures showed good results in the considered temperature (25 °C). Statistical analysis included normality tests to ensure that the samples followed a Gaussian distribution for all sensors.

The experiment conducted through this study used a temperature compensation method for both SHM techniques. These procedures showed good results in the considered temperature (25 °C). Statistical analysis included normality tests to ensure that the samples followed a Gaussian distribution for all sensors.

The proposed hybrid monitoring system was able to identify and locate the damage with a 1.14% error. The temperature chosen for the experiments was 25 °C with the aid of the climatic chamber EPL-4H. Clearly, the choice of this temperature range does not correspond to the full temperature range of an aircraft wing surface (-55 °C to +60 °C). However, the intention was to provide an illustration of the proposed method.

Finally, the combination of the two SHM techniques considered not only detect damage in the aeronautical structure, but also locate the damage. The present contribution demonstrated that both techniques (LW and ISHM) present interesting characteristics when working together to achieve successful SHM.

References

1. Abbate, A., Koay, J., Frankel, J., Schroeder, S.C.N., Das, P.: Signal detection and noise suppression using a wavelet transform signal processor: application to ultrasonic flaw detection. *IEEE Trans. Ultrason. Ferroelectr. Freq. Control.* **44**, 14–26 (1997)
2. An, Y.K., Sohn, H.: Integrated impedance and guided wave based damage detection. *Mech. Syst. Signal Process.* **28**, 50–62 (2012)
3. Annamdas, V.G.M., Ian, L.S., Pang, H.L.J., Soh, C.K.: Monitoring of fatigue in welded beams using piezoelectric wafer based impedance technique. *J. Nondestruct. Eval.* **33**(1), 124–140 (2014)
4. Annamdas, V.G.M., Sohn, C.K.: Application of electromechanical impedance technique for engineering structures: review and future issues. *J. Intell. Mater. Sys. Struct.* **21**(1), 41–59 (2010)
5. Baptista, F.G., Budoya, D.E., Almeida, V.A.D., Ulson, J.A.C.: An experimental study on the effect of temperature on piezoelectric sensors for impedance-based structural health monitoring. *Sensors* **14**, 1208–1227 (2014)
6. Bendat, J.S., Piersol, A.G.: *Random Data – Analysis and Measurement Procedures*. 4th ed. ISBN: 978-0470248775. Wiley, New York (2000)
7. Cavalini Jr., A.A., Oliveira, D.D., Rabelo, D.S., Finzi Neto, R.M., Steffen Jr., V.: Fault detection in a rotating shaft by using the electromechanical impedance method and a temperature compensation approach. In: *Proceedings of the XXXVI Ibero-Latin American congress on computational methods in engineering (CILAMCE 2015)*, Rio de Janeiro (2015)
8. Cesnik, C.: Review of guided-wave structural health monitoring. *Shock Vib. Dig.* **39**(2), 91–114 (2007)

9. Dao, P.B., Staszewski, W.J.: Cointegration approach for temperature effect compensation in lamb-wave-based damage detection. *Smart Mater. Struct.* **22**, 095002 (2013)
10. Davis, G.D., Rich, M.J., Drzal, L.T.: Monitoring moisture uptake and delamination in CFRP reinforced concrete structures with electrochemical impedance sensors. *J. Nondestruct. Eval.* **23**(1), 1–9 (2004)
11. Debnath, L.: *Wavelet Transforms & Their Applications*. Birkhäuser Press, Boston (2001)
12. Farrar, C.R., Lieven, N.A.J., Benent, M.T.: An Introduction to Damage Prognosis. In: *Damage Prognosis for Aerospace, Civil and Mechanical System*, p. 449. Wyle, Inglaterra (2005)
13. Finzi Neto, R.M.: A Low-cost electromechanical impedance-based SHM architecture for multiplexed piezoceramic actuators. *J. Struct. Heal. Monit.* **10**(4), 391–402 (2010)
14. Harley, J., Moura, J.: Scale transform signal processing for optimal ultrasonic temperature compensation. *IEEE Trans. Ultrason. Ferroelectr. Freq. Control.* **59**(10), 2226–2236 (2012)
15. Huynh, D., He, J., Tran, D.: Damage location vector: a non-destructive structural damage detection technique. *Comput. Struct.* **83**(28–30), 2353–2367 (2005)
16. Incropera, F.P., Dewitt, D.P., Bergann, T.L.: *Fundamentals of Heat and Mass Transfer*. Wiley edition 6, p. 272–275, California (2006)
17. Kijanka, P., Radecki, R., Packo, P.W., Staszewski, J., Uhl, T.: GPU-based local interaction simulation approach for simplified temperature effect modelling in Lamb wave propagation used for damage detection. *Smart Mater. Struct.* **22**(3), 035014 (2013)
18. Koo, K.Y., Park, S., Lee, J.J., Yun, C.B.: Automated impedance-based structural health monitoring incorporating effective frequency shift for compensating temperature effects. *J. Intell. Mater. Syst. Struct.* **20**(4), 367–377 (2009)
19. Krishnamurthy, K., Lalande, F.; Rogers, C. A.: Effects of temperature on the electrical impedance of piezoelectric sensors. In: *Proceedings of SPIE 2717, Smart Structures and Materials 1996: Smart Structures and Integrated Systems*, 302 (mai. 1996); San Diego (1996). doi: <https://doi.org/10.1117/12.239033>
20. Lemistre, M., Gouyon, R., Kaczmarek, H., Balageas, D.: Damage localization in composite plates using wavelet transform processing on lamb wave signals, *Second International Workshop on Structural Health Monitoring*, Stanford (1999)
21. Liang, C., Sun, F.P., Rogers, C.A.: Coupled electromechanical analysis of adaptive material system – determination of actuator power consumption and system energy transfer. *J. Intell. Mater. Syst. Struct.* **5**, 21–20 (1994)
22. Lind, R., Kyle, S., Brenner, M.: Wavelet analysis to characterize non-linearities and predict limit cycles of an aeroelastic system. *Mech. Syst. Signal Process.* **15**, 337–356 (2001)
23. Liu, G., Xiao, Y., Zhang, H., Ren, G.: Baseline signal reconstruction for temperature compensation in Lamb wave based, damage detection. *Sensors.* **16**(8), 1273 (2016)
24. Lu, Y., Ye, L., Wang, D., Zhong, Z., Herszberg, I.: Damage detection in a large composite panel of five stiffeners using lamb wave signals. *Mater. Forum* **33**, 16 (2009)
25. Marzani, A., Salamone, S.: Numerical prediction and experimental verification of temperature effect on plate waves generated and received by piezoceramic sensors. *Mech. Syst. Signal Process.* **30**, 204–217 (2012)
26. Monnier, T.: Lamb waves-based impact damage monitoring of a stiffened aircraft panel using piezoelectric transducers. *J. Intell. Mater. Syst. Struct.* **17**(5), 411–421 (2006)
27. Moura Jr., J.R.V.: Uma Contribuição aos Sistemas de Monitoramento de Integridade Estrutural Aplicada a Estruturas Aeronáuticas e Espaciais. 264f. Tese de Doutorado – Universidade Federal de Uberlândia, Uberlândia (2008)
28. Moura Jr., J.R.V., Steffen Jr., V.: Impedance-based health monitoring for aeronautic structures using statistical meta-modeling. *J. Intell. Mater. Syst. Struct.* **17**(11), 1023–1036 (2006)
29. Overly, T., Jacobs, L.D., Farinholt, K., Park, G., Farrar, C.R., Flynn, E., Todd, M.D.: Developing an integrated software solution for active-sensing SHM. *Smart Struct. Syst.* **5**(4), 457–468 (2009)
30. Palomino, L.V.; Steffen Jr., V.: Damage metrics associated with electromechanical impedance technique for SHM applied to a riveted structure. In: *Proceedings of the 20th International Congress of Mechanical Engineering – COBEM2009*. Porto Alegre (2009)
31. Palomino, L.V., Tsuruta, K.M., Moura Jr., J.R.V., Rade, D.A., Steffen Jr., V., Inman, D.J.: Evaluation of the influence of sensor geometry and physical parameters on impedance-based structural health monitoring. *Shock. Vib.* **19**, 811–823 (2012)
32. Palomino, L.V., Steffen Jr., V., Finzi Neto, R.M.: Probabilistic neural network and fuzzy cluster analysis methods applied to impedance-based SHM for damage classification. *Shock. Vib.* vol. Article ID 401942 1–12 (2014)
33. Park, C.Y.: Damage index comparison for a composite stiffened panel using lamb wave. *Adv. Mater. Res.* **26–28**, 1265–1268 (2007)
34. Park, G., Cudney, H., Inman, D.J.: Based structural health monitoring using a miniaturized impedance measuring chip for corrosion detection. *Am. Soc. Nondestruct. Test. Pesqui. Nondestruct. Eval.* **18**, 139–150 (2007)
35. Park, G., Cudney, H., Inman, D.J.: Feasibility of using impedance-based damage assessment for pipeline systems. *Earthq. Eng. Struct. Dyn. J.* **30**(10), 1463–1474 (2001)
36. Park, G., Inman, D.J.: Smart bolts: an example of self-healing structures. *Smart Mater. Bouletin.* 5–8 (2001)
37. Park, G., Kabeya, K., Cudney, H.H., Inman, D.J.: Impedance-based structural health monitoring for temperature varying applications. *JSME Int. J.* **42**(2), 249–258 (1999)
38. Park, S., Lee, J.-J., Yun, C.-B., Inman, D.J.: Electro-mechanical impedance-based wireless structural health monitoring using PCA-data compression and k-means clustering algorithms monitoring and path forward. *J. Intell. Mater. Syst. Struct.* **19**, 509–520 (2008)
39. Rabelo, D.S.; Finzi Neto, R. M.; Steffen Jr., V.: Impedance-based Structural Health Monitoring incorporating compensation of temperature variation effects. In: *Proceedings of the 23rd ABCM International Congress of Mechanical Engineering*. Rio de Janeiro (2015b)
40. Rabelo, D.S., Guimarães, C.G., Cavalini Jr., A.A., Steffen Jr., V.: A comparative study of temperature compensation techniques for impedance-based structural health monitoring systems In: *Proceedings of the 1st Workshop in Industrial Mathematics, Modelling and Optimization*. Catalão (2015c)
41. Rabelo, D.S., Steffen Jr., V., Finzi Neto, R.M., Lacerda, H.B.: Impedance-based structural health monitoring and statistical method for threshold-level determination applied to 2024-T3 aluminum panels under varying temperature, *Structural Health Monitoring*, Online First, (2016). doi:<https://doi.org/10.1177/1475921716671038>

42. Raghavan, A., Cesnik, C.E.S.: Lamb-Wave Based Structural Health Monitoring. Damage Prognosis for Aerospace, Civil and Mechanical System, Wiley, Cap. 11, pp. 235–274 (2005)
43. Raju, V.: Implementing Impedance-based Health Monitoring. Dissertation, Virginia Tech (1997)
44. Ramadas, C., Balasubramaniam, K., Joshi, M., Krishnamurthy, C.V.: Interaction of Lamb mode (A0) with Structural Discontinuity and Generation of “Turning modes” in a T-joint. Elsevier. (2011)
45. Rizzo, P., Di Scalea, F.L.: Wavelet-based feature extraction for automatic defect classification in strands by ultrasonic structural monitoring. *Smart Struct. Syst.* **2**(3), 253–274 (2006)
46. Rocha, L.A.A., Rabelo, D.S., Steffen Jr., V.: Identification of Damage in Structures with Rivets using Impedance techniques and controls of Lamb waves, CONEM 2014 no. 0503 (2014)
47. Roy, S., Lonkar, K., Janapati, V., Chang, F.K.: A novel physics-based temperature compensation model for structural health monitoring using ultrasonic guided waves. *Struct. Health Monit.* (2014). <https://doi.org/10.1177/1475921714522846>
48. Salas, K.I., Cesnik, C.E.S.: Design and Characterization of the CLoVER transducer for structural health monitoring. In: Proceedings of the 15th SPIE Symposium on Smart Structures and Materials & Nondestructive Testing and Health Monitoring, March 2008, Paper #6935–11, San Diego (2008)
49. Sohn, H.: Statistical Pattern Recognition Paradigm Applied to Defect Detection in Composite Plates in Damage Prognosis – for Aerospace, Civil and Mechanical Systems. Wiley, Hoboken (2005)
50. Sorohan, S., Constantin, N., Gavan, M., Anghel, V.: Extraction of dispersion curves for waves propagating in free complex waveguides by standard finite element codes. *Ultrasonics*. **51**, 503–515 (2011)
51. Su, Z., Ye, L., Lu, Y.: Guided lamb waves for identification of damage in composite structures: a review. *J. Sound Vib.* **295**, 753–780 (2006)
52. Su, Z., Ye, L.: Identification of Damage Using Lamb Waves from Fundamentals to Applications, Springer, e-ISBN:978-1-84882-784-4, (2009)
53. Su, Z., Ye, L.: Lamb wave-based quantitative identification of delamination in CF/EP composite structures using artificial neural algorithm. *Compos. Struct.* **66**, 627–637 (2004)
54. Sun, F.P., Chaudhry, Z., Liang, C., Rogers, C.A.: Truss structure integrity identification using PZT sensor–actuator. *J. Intell. Mater. Syst. Struct.* **6**, 134–139 (1995)
55. Wang, C.S., Chang, F.K.: Diagnosis of Impact Damage in Composite Structures with built-in piezoelectric networks. In: Proceedings of SPIE, vol. **3990**, pp. 13–19 (2000)



Chapter 18

Structural Health Monitoring of Additively Manufactured Parts Using Fiber Bragg Gratings

Carlisle Fauver, David Petrushenko, Elon Gordon, Michelle Lockhart, Scott Ouellette, and Alexandria Marchi

Abstract Many industries are moving toward the opportunities afforded by additive manufacturing (AM) techniques as a primary manufacturing method for components. Additionally, AM continues to be an effective option for rapid prototyping in many applications. Some advantages AM processes have over traditional manufacturing include the ability to create highly complex and multi-material parts with little or no restriction on the geometry of the object at a relatively low price point. However, one of the main challenges that from AM techniques is the relatively high variation, in both material properties and exact geometry, from part to part. This variation calls for structural health monitoring of each individual part. In this paper, fiber Bragg gratings (FBGs) – chosen because they can be embedded with minimal effect on the desired structure – are inserted into AM geometries between layers, allowing for strain readings to be taken in situ. These measurements provide empirical data of incipient failure as AM parts tend to fail between layers. Fused deposition modeling (FDM) is used, as it is relatively common and inexpensive, to create parts into which the FBGs are embedded. Measurements taken under a variety of tests are compared to analogous finite element as well as analytical models allowing for model accuracy evaluation for AM parts. This work provides experimental data to validate models, in addition to forming a better understanding of the validity and procedure of embedding FBGs into FDM parts. Additionally, this work serves as a proof of concept and calls for more work to be done in the field.

Keywords Additive manufacturing · Structural health monitoring · 3D printing · Fiberoptic · Fiber Bragg Grating

Nomenclature

ABS	Acrylonitrile Butadiene Styrene
AM	Additive manufacturing
FBG	Fiber Bragg grating
FDM	Fused deposition modeling
FEA	Finite element analysis
PLA	Polylactic Acid
2D	Two-dimensional
3D	Three-dimensional

18.1 Introduction

Additive manufacturing (AM) processes have grown in popularity over the past decade for many reasons; some of which include:

- The ability to create complex geometries
- The saved expense of a casting or forging apparatus

C. Fauver · D. Petrushenko · E. Gordon · M. Lockhart · S. Ouellette (✉) · A. Marchi
Los Alamos National Laboratory, Los Alamos Dynamics Summer School, Los Alamos, NM, USA
e-mail: souellette@lanl.gov

- The ability to rapidly prototype a concept to test design validity
- The flexibility to make various parts without needing to rotate tools
- The increased number of open-sourced and inexpensive machines

A subset of these processes known colloquially as three-dimensional (3D) printing are commonly used across both industry and academia. In general, 3D printing processes fabricate parts by assembling layers parallel to the build-plate in a Cartesian coordinate system, with many methods now developed to manufacture with various of materials.

The 3D printing process used in this paper is fused deposition modeling (FDM). FDM is a relatively inexpensive, process in which spooled thermoplastics are fed through a heated nozzle forcing the polymer to flow. The more compliant polymer is then extruded onto the previous layer to create the desired geometry by stacking two-dimensional (2D) lamina of material. As the next layer is applied, heat transfers through the polymer to the layer below, allowing them to fuse.

Along with the many opportunities afforded by AM technologies, there exist several inherent variabilities in the resultant parts.

Due to these unavoidable variabilities between parts, structural health monitoring (SHM) can be implemented to detect changes in behavior. SHM is the process in which a damage identification strategy is implemented to observe a structure throughout its operational lifetime [1]. The purpose behind SHM is, in many cases, to prevent catastrophic failure by alerting the stakeholders to any damage as defined by a quantifiable change in system behavior prior to it reaching a critical threshold. The definition of damage may vary depending on the system (e.g. corrosion of a bridge gusset plate versus delamination of an aircraft wing).

To this end, sensors are needed to monitor system behavior. Fiber Bragg gratings (FBGs) provide a means to measure the internal strains, both mechanical and thermal, of the part. An FBG is a fiber-optic sensor, fabricated to have high reflectivity at a specific wavelength due to the spacing of disks, known as gratings, written into the fiber with intense ultraviolet light. Broad spectrum light is then passed through the fiber resulting in a clear peak, at the designed wavelength which moves based on the strain experienced by the grating. This moving peak provides strain measurements over time. FBGs are chosen for embedding due to their small size, negligible mass, and electrically passive nature (non-conductive and immune to electromagnetic interference) [7].

One of the main reasons indicating internal sensors would be useful is AM parts commonly fail between layers. Due to this failure mode, embedded sensors are increasingly necessary, and as a result increasingly popular in literature. Sbriglia et al. printed parts with an opening for an accelerometer built into the geometry. The authors describe in detail the variations they attributed to various build parameters including layer height, print speed, and tool path [2]. Additionally, groups have examined the feasibility of embedding optical sensors into parts produced through AM for various purposes. Wiegmann et al. explored the survivability and performance of FBGs embedded into “printed packaging,” made with FDM. They found embedding FBGs to be a suitable methodology for future works in SHM [3]. Havermann et al. produced a process to embed FBGs into stainless steel parts by coating the fibers in nickel and inserting them into a groove. They utilized a different AM process, selective laser melting, for working with metals [4]. These collective works provide a starting point from which the procedure discussed in this paper is developed.

This work focuses on the embedding procedure of FBGs into FDM prints, the accuracy of models based on this method, and the applications of such parts. To this end, a simple, rectangular-prism, geometry is used to allow for closed form solutions of simple loading conditions in addition to finite element analysis (FEA). Ideally, these models will describe the part’s behavior under all expected loading conditions. Calibrating these models to the known solution provides confidence in solutions gathered from geometries too complex to be solved analytically. This more complex model could then be validated with experimental data.

18.2 Methodology

The general approach of this study is described in the experimental approach section introducing the study scope followed by a fiber embedding summary. Modeling and testing complete this section describing the FEA details and implemented testing practices.

18.2.1 Experimental Approach

First, FBGs are embedded into the FDM parts during the 3D print. This mid-print embedding allows the FBG to be placed between layers. Various engineering controls, discussed in the next section, keep the placement precise. Computer models are created to represent the created geometry as closely as possible. The physical parts then undergo bend testing, which is mirrored in the FEA of the computer models. Upon validation of the model's performance under the simple loading conditions, the beams are damaged and tested once again. The model is updated to portray the more complex geometry as accurately as possible and analyzed.

18.2.2 Fiber Embedding

The final embedding apparatus is labelled and shown in Fig. 18.1. This figure shows the modified build plate of the Lulzbot TAZ 6 used in this study. The given coordinate axes denote the axes of the TAZ 6 itself.

Shown in the center of the figure is the beam that is being printed. Moving along the length of the part, the thin strip shows where the fiber is being held and embedded. At either end the upright fiber clamps keep the fiber centered on the created plane. The centering bars provide a more rigid centering structure as they are much closer to the beam. These are attached to the build plate using a mounting rail, added for this purpose. Finally, the glue trough is shown where it would be during the minute-long embedding process. The fiber clamps, centering bars, and adhesive apparatus are all 3D printed and could be modified to attach to any build plate setup. This setup is inspired by the figures in [5, 6].

The apparatus described above is utilized during the embedding process. To implement this process, a pause of 75 seconds is included the G-code, the line by line instructions controlling the 3D printer. This pause was added by manually editing the .gcode file that was being input to the 3D printer via SD card. Before starting the print, the operator marks and secures the FBG in one of the fiber clamps taping down the rest of it on to the build plate but out of the way of the toolpath. During the pause, two people would embed the fiber (though one would likely be sufficient). The first person un-tapes the FBG, dips the center in the glue trough, and tensions it through the remaining fiber clamp. Meanwhile, the second person places the glue trough in position and tightens the second fiber clamp. Finally, either person snaps the cable into the centering bars to secure it. The print then continues through to conclusion.

The printing process for each beam takes [time value] to complete. Each beam has a 5 mm square cross-section and a length of 60 mm (50 mm between supports). The dimensions of the beam including damage are shown in Fig. 18.2. In principle, this methodology can be reproduced for any thermoplastic in any FDM machine. This study uses Polylactic Acid (PLA) as the beam material due to availability and PLA's performance compared to Acrylonitrile Butadiene Styrene

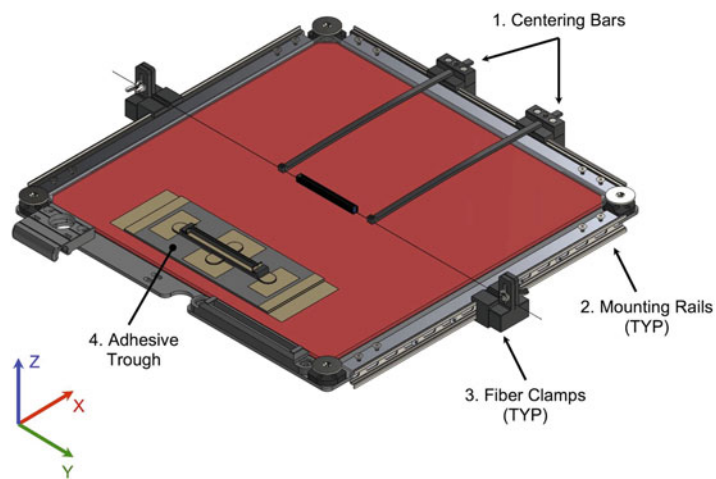


Fig. 18.1 Embedding control apparatus mounted to the bed of the Lulzbot TAZ 6 printer. Three systems were developed and used to assist in the embedding process: centering bars (1), fiber clamps (3), and the adhesive trough (4). 1) Centering Bars: maintained constant distance to center FBG along the x (transverse) direction. 2) Mounting Rails: provided adjustable positioning system to align to each component of (1) & (3). 3) Fiber Clamps: maintained sufficient tension within the fiber optic to disallow movement due to additional material. 4) Adhesive trough: assisted the consistent application of adhesive around the FBG

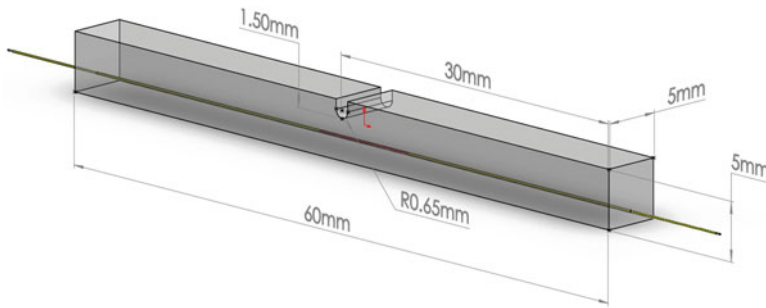


Fig. 18.2 Dimensioned rendering of a damaged beam with an embedded FBG sensor

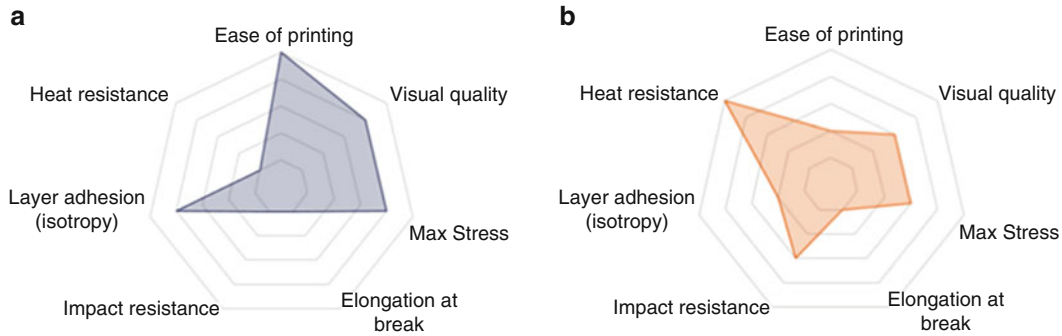


Fig. 18.3 Comparing the relative material properties of PLA (left) and ABS (right). PLA and ABS were used in different applications reflecting their respective advantages. Note: Reprinted from 3D HUBS: FDM 3D Printing Materials Compared

Table 18.1 Tensile test data

	Axial	Transverse
Mean [MPa]	1531	953.7
Standard deviation [MPa]	121.6 (7.9%)	79.43 (8.3%)

(ABS) as shown in Fig. 18.3. Inherent to FDM is the part to part variation of properties. Some of which, such as mechanical properties, can be better controlled than others [8].

18.2.3 Modeling

The FEA modeling is done in ABAQUS. Requiring the material properties to be defined, several dummy (non-embedded) beams are tensile tested resulting in what can be found in Table 18.1, [9]. Two methods of modeling are observed and compared in this study: brick and shell. The fundamental difference between the two is shown below in Fig. 18.4. The brick element method takes 3D elements into the analysis, while in shell element modeling the user defines the layer interactions between each 2D slice. Brick modeling is very common and shell modeling may be able to accurately take into account the inherent layering of FDM parts, [10, 11]. Therefore, both models are created. Each of the above methods produced significantly different models for the damaged case as shown in Figs. 18.5 and 18.6.

18.2.4 Specimen Testing

Bend tests, both three and four-point, provide well-known testing conditions that have analytical solutions available. These tests are especially sensitive to the type of damage being applied to the beams. Three-point bend testing provides a basis from which one can observe the upper limit of the elastic region. Four-point bend testing is used as a proof of concept: FBGs can be used to detect damage. All testing in this study is done statically.

Brick Element Method			Shell Element Method		
Element Type	Element Size (mm)	Number of Elements	Element Type	Element Size (mm)	Number of Elements
C3D8R	0.2 x 0.5 x 2	~ 7,500	S4R	0.5 x 2	~ 7,500

Fig. 18.4 Comparison of brick and shell element methods

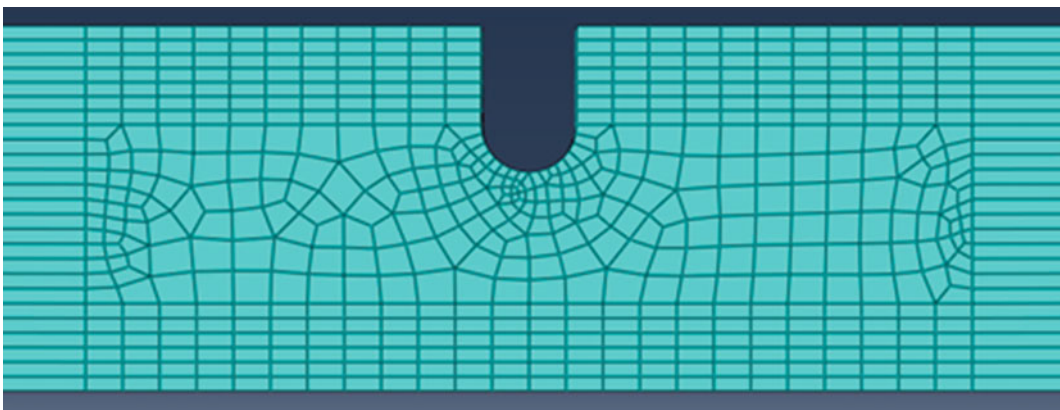


Fig. 18.5 Irregular geometry propagation in brick element meshing of damage

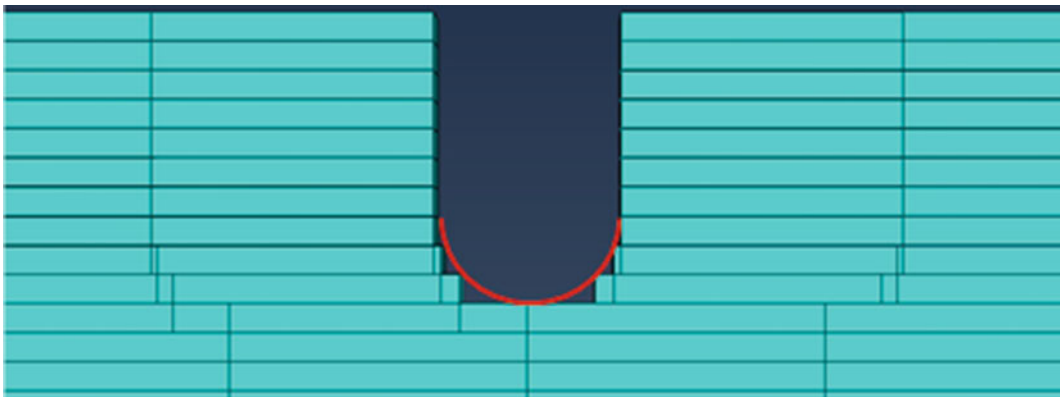


Fig. 18.6 Discretization of curve in shell element meshing of damage

Three-point bend testing is well-established. Testing calls for a simply supported beam and application of a point load. Data is collected every 7 min for 20 s and averaged out to minimize uncertainty. Upon collection the load mass is stepped up 200 g starting at 0 g and ending at 4000 g. The aforementioned 7 min give the system time to equilibrate to the new load, a concern in a laboratory setting which would not be present in a more static application.

Four-point bend testing is similarly well-established and calls for the same support structure. However, as the name implies, this test mode requires two point-loads be applied. Data is again collected 7 min after the application of the load. The loading is 3000 g split between two points (1500 g at each point). Once the data is collected, the load is removed allowing the system to spring back to its resting position. For consistency, the beams equilibrate back for 7 min. This process is repeated ten times for each beam.

The apparatus for both types of testing is shown in Fig. 18.7.

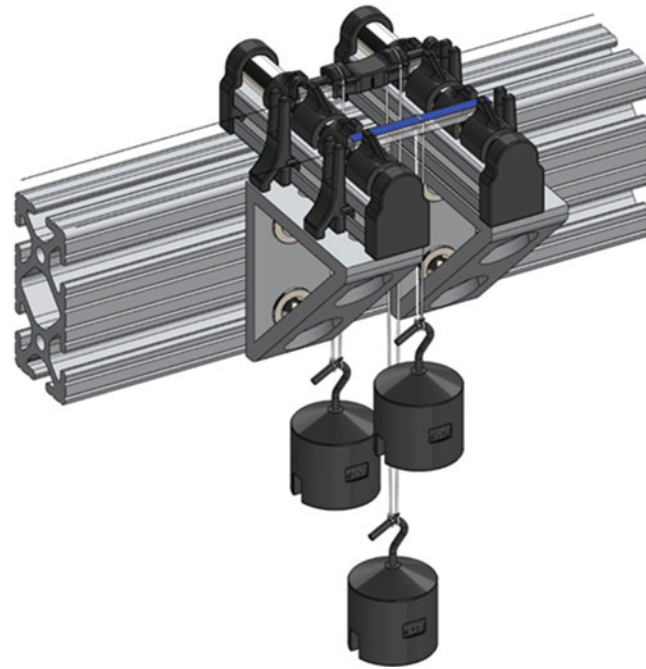


Fig. 18.7 Bend testing apparatus with three and four-point bend tests shown. To achieve point loads, fishing line is used in addition to the manufacture of a four-point alignment device with supports as shown

These bend tests are performed both before and after the beams are damaged. The undamaged beams undergo three and four- bend testing. Damaged beams undergo only four-point bend testing, due to expected inelastic responses in three-point bending after damage.

18.3 Results

This section of the study focuses on the results, showing both experimental and model values. Graphs from both cases display the findings of the study.

18.3.1 Model Predictions

Figures 18.8, 18.9 and 18.10 show the models' predictive visualizations for three and four-point bend testing respectively. Each contain brick and shell model results.

Figure 18.11 compares the brick and shell models' respective predictions for three-point bend testing. The mean prediction for each is displayed with the dark central lines. The shaded area indicates the region of uncertainty due to the unknown, but bounded, Poisson's ratio.

Figure 18.12 similarly compares the two models' predictions for four-point bend testing.

18.3.2 Experimental Results

Figures 18.13 and 18.14 mirror Figs. 18.11 and 18.12 with the experimental data added for direct comparison.

Figure 18.15 provides a more in-depth image of the experimental data for the four-point bend testing. The values used to create these plots are shown in Table 18.2.

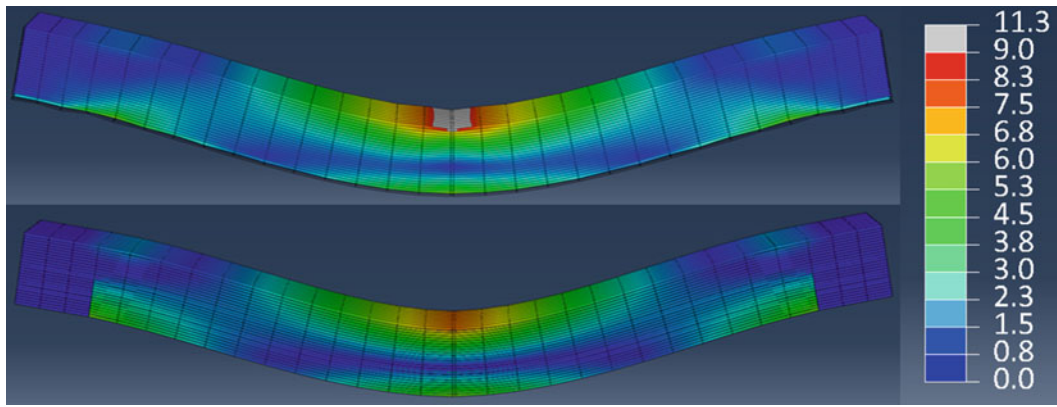


Fig. 18.8 Visualizations of brick (top) and shell (bottom) for a three-point bend test (scale in MPa)

18.4 Analysis

The analysis section underscores the implications of the experimental data comparing it to the model data.

18.4.1 Model Validation

The experimental results generally support the predictions made by the models.

The three-point bend test experiment, shown in Fig. 18.12, mostly falls between the two model predictions. This finding implies a more refined FEA model could accurately describe the beam's behavior. In combination with Fig. 18.10, this variation can be attributed to the unknown Poisson's ratio. In three-point bending, the two models perform quite similarly. This similarity implies a majority of the underlying physics are being captured in each model, [12].

The four-point bend test experiment, shown in Fig. 18.13, matches the models well, except for the damaged brick case. The damaged brick model predicts more than twice as much strain as the maximum experienced experimentally. This implies some physics is missing from this model, which could not be addressed due to time restraints. Strangely, the shell model predicts less strain in the damaged case as compared to the undamaged case. This may be due to the discretization of the damage geometry shown in Fig. 18.5. This lower strain may be counterintuitive, as a damaged beam would be expected to flex more under a given load. However, three of the seven tested beams exhibited this behavior.

18.4.2 Damage Detection

Comparing the beams from the undamaged state to themselves after damage provides promising results for future application of FBGs in SHM works with AM parts. To compare these beams, the sensor strain is normalized to be 0 in the undamaged case, as shown in Fig. 18.13. The strain discussed is in relation to each beam's individual undamaged mean.

In all seven beams there is a shift in the mean. Four of these lead to a significant difference of three standard deviations. Four of the seven beams experience more strain, three of which are significant. The remaining three experience less strain, one of which is significant. The variability in which direction the mean shifts is likely due to the inaccuracy of the damage itself. The negative relative strain may be due to the sensor being inadvertently moved closer to the neutral axis than intended. All seven beams also display a greater variance after damage, which is likely due to the nonlinearities introduced by the damage. This is shown in Fig. 18.14 in the height and width of each distribution.

18.5 Conclusions

With many industries moving toward AM, it is becoming increasingly important manufacturers be able to predict and monitor part behavior. This study indicates FEA as a promising method of prediction with further refinement. The models used were validated in the case of three-point bend testing, and the failure to validate for four-point bend testing is due to time

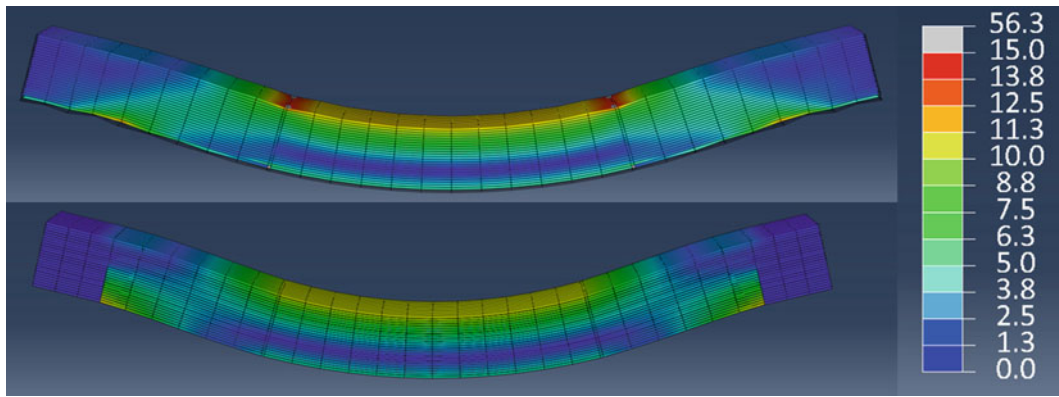


Fig. 18.9 Visualizations of undamaged brick (top) and shell (bottom) for four-point bend test (scale in MPa)

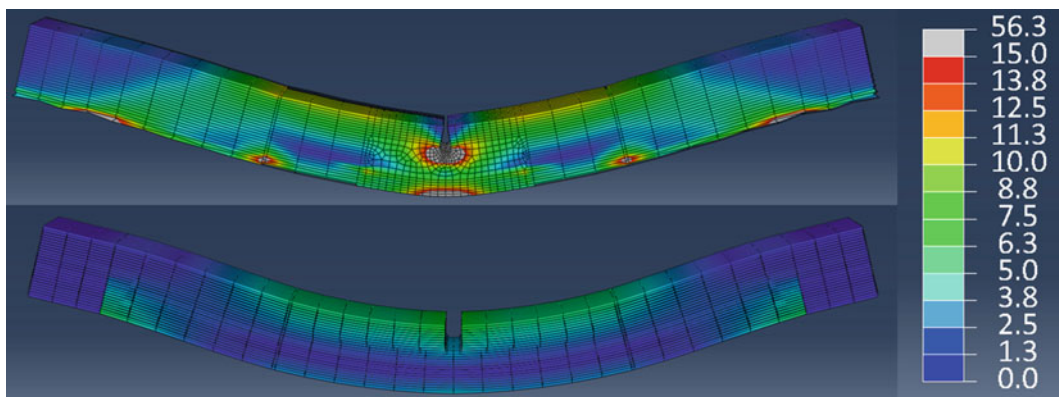


Fig. 18.10 Visualizations of damaged brick (top) and shell (bottom) for four-point bend test (scale in MPa)

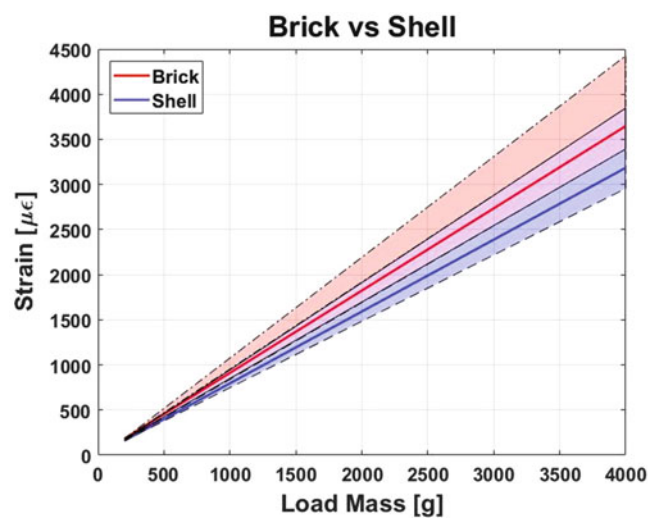


Fig. 18.11 Three-point bend test predictions for both brick and shell models

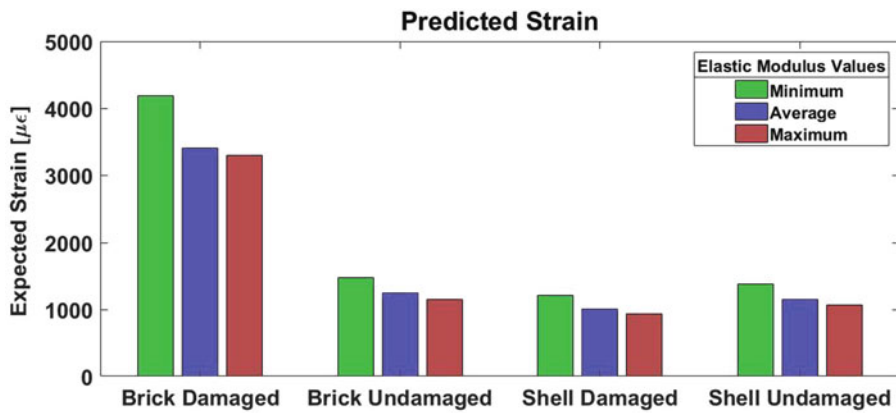


Fig. 18.12 Four-point bend test predictions for both brick and shell models

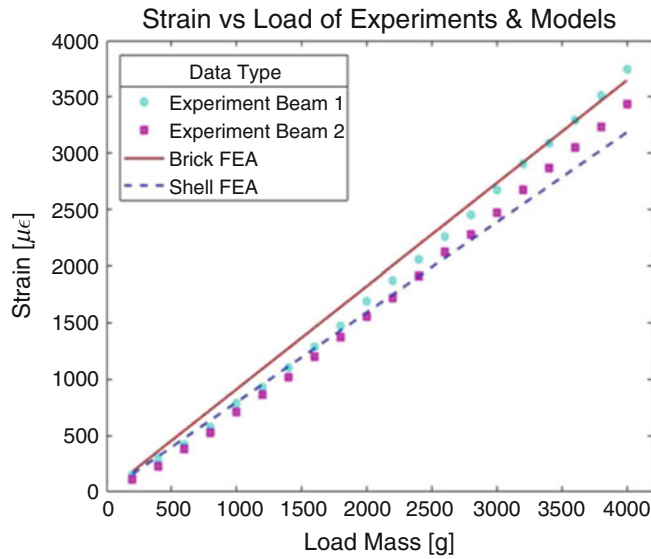


Fig. 18.13 Three-point bend test continuous model predictions compared to the discrete experimental data

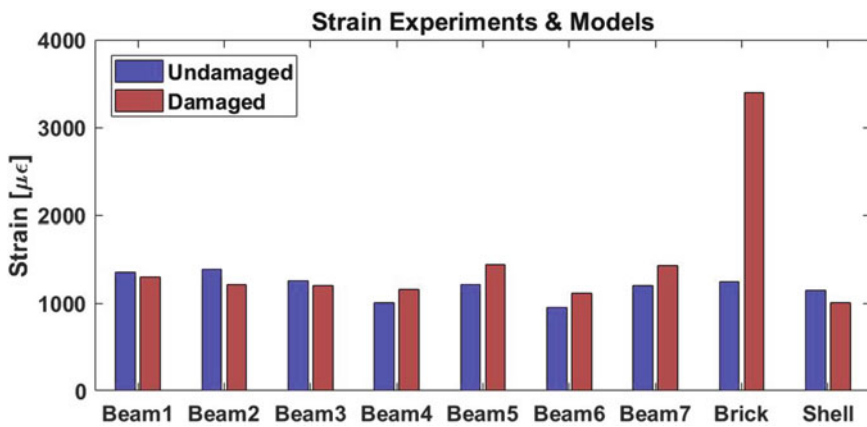


Fig. 18.14 Four-point bend model predictions compared to the experimental data

constraints. This study provides further proof of concept for the future use of FBGs in SHM of manufactured components. Specifically, the results indicate FBGs could be applied in damage detection. This study provides a starting point for future works researching the application of embedded fiber Bragg gratings in additively-manufactured parts for various purposes. Some such future works could include: dynamic loading, sensitivity analysis, and robotic fiber embedment.

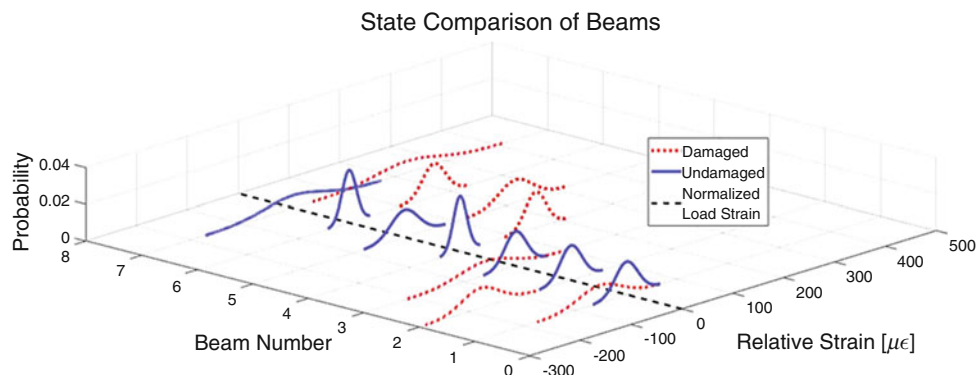


Fig. 18.15 Normal distributions created from the experimental four-point bend data (each plotted three standard deviations above and below the mean)

Table 18.2 Mean and standard deviation shift for each beam damaged compared to undamaged

Beam Number	1	2	3	4	5	6	7
Mean shift [micro strain]	-52.4	-178.0	-57.8	148.5	218.6	166.9	224.4
Standard deviation shift [micro strain]	20.0	15.3	30.4	7.1	5.4	8.5	4.5

Acknowledgements The authors would like to acknowledge, and thank, the following for their respective contributions to the study:

- The Los Alamos Dynamics Summer School under the Engineering Institute at Los Alamos National Laboratory
- Charles Farrar, Ph.D.
- Eric Flynn, Ph.D.
- Brittany Ouellette
- John Benardin, Ph.D.

References

1. Worden, K., Farrar, C., Manson, G., Park, G.: The fundamental axioms of structural health monitoring. Proc. Royal Soc. A. **463**, 1639–1664 (2007)
2. Sbriglia, B., et al.: Embedding sensors in FDM plastic parts during additive manufacturing. Top Modal Anal. **10**, 205–214 (2016)
3. Wiegmann, K., Bremer, K., Roth, B.: Utilizing 3D printing for the packaging of fiber optic sensors. Proc DGaO. B12 (2016)
4. Havermann, D., et al.: Temperature and strain measurements with Fiber Bragg gratings embedded in stainless steel 316. J. Lightwave Technol. **33**(12), 2474–2479 (2015)
5. Kantaros, A., Karalekas, D.: Fiber Bragg grating based investigation of residual strains in ABS parts fabricated through fused deposition modeling process. Mater. Des. **50**, 44–50 (2013)
6. Maier, R.R.J., et al.: Embedded fiber optic sensors within additive layer manufactured components. IEEE Sensors J. **13**(3), 969–979 (2013)
7. Economidou, S.N., Karalekas, D.: Optical sensor-based measurements of thermal expansion coefficient in additive manufacturing. Polym. Test. **51**, 117–121 (2016)
8. Torres, J., et al.: Mechanical property optimization of FDM PLA in shear with multiple objectives. JOM. **67**, 1183–1193 (2015)
9. Baker, A.M.: Measurement and modeling of thermal and mechanical anisotropy of parts additively manufactured using fused deposition modelling (FDM). Struct. Health. Monit. **2017**(1), 612–620 (2017)
10. Zhang, Y., Chou, K.: A parametric study of part distortions in fused deposition modeling using three-dimensional finite element analysis. Proc. IMechE. **222** B, 959–967 (2008)
11. Zhang, Y., Chou, Y.K.: Three-dimensional finite element analysis simulation of the fused deposition modelling process. Proc. IMechE. **220** B, 1663–1671 (2006)
12. Roy, C.J., Oberkampf, W.L.: A comprehensive framework for verification, validation, and uncertainty quantification in scientific computing. Comput. Methods Appl. Mech. Eng. **200**, 2131–2144 (2011)



Chapter 19

Multipoint Control for Single Axis Vibration Testing

Alan Williams, Vivian Cai, Michael Maestas, John Heit, and Stuart Taylor

Abstract In mechanical testing for system qualification, test engineers often face the challenge of representing a multi-axis vibration environment using a single-axis shaker table with only one degree of freedom for control. On large, complicated systems, the target environments are often defined as power spectral densities (PSDs) of a random vibration signal at multiple locations. These PSDs are almost invariably defined such that they are not physically realizable in any boundary condition. If one location responds with exactly its target PSD, another location will respond with a PSD that is different from its respective target. This paper presents a control strategy that minimizes an error between the responses and their respective targets, given a single actuation input. By estimating a model in real-time, an optimal input can be solved for each iteration of the control loop to adjust the excitation input and properly track responses. Implementing this control algorithm on a linear time invariant system by filtering the feedback sent to standard shaker controller hardware, there was a 4.3 dB and 3.5 dB variance in filter magnitude when using a 2.5 s model history and 5 s model history respectively. When applying this scheme to the LTV model, we noticed a stable change in filter magnitude. This paper has been approved for release as LA-UR-17-29695.

Keywords Adaptive · Control · Optimal · Qualification · Random vibration

19.1 Introduction

19.1.1 Background

Many complicated systems face equally complicated transportation and working environments. This produces a need for the qualification testing of these systems to withstand the vibrations incurred from their environments. Such qualification testing can be done with a single axis vibration shaker that attempts to recreate the random vibration produced by a specified environment. These environments can be simulated using an enveloping process that encapsulates multiple environments. The vibration in these environments is measured and specified by power spectral densities (PSDs). Multiple target PSD profiles are defined independent from each other, and therefore perfect tracking cannot be guaranteed given a single input. One input can cause a desired output at one location but disrupt an output at another location. This mismatch creates an over constrained problem that needs to be solved through an optimization method.

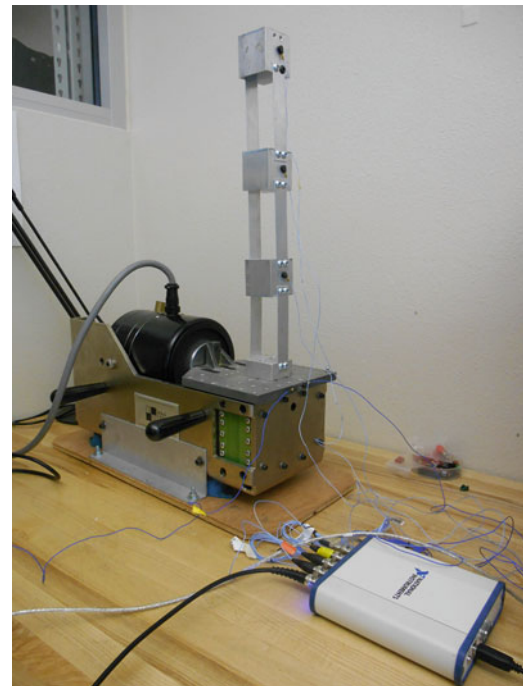
Qualification testing of this sort falls under two categories: input driven testing and output driven testing. Input driven testing requires directly measuring the vibration profile of the environment under question and using this measurement as the input to the shaker controller. This input can be used for single or multiple DOF shakers and the output response of the device under test (DUT) will be evaluated. Conversely, output driven testing requires measuring the DUT's response to the environment. The input solved using this test will elicit a response to match the actual response. If the number of output

A. Williams · J. Heit · S. Taylor (✉)
Los Alamos National Laboratory, Los Alamos, NM, USA
e-mail: sgtaylor@lanl.gov

V. Cai
University of California San Diego, La Jolla, CA, USA

M. Maestas
Colorado School of Mines, Golden, CO, USA

Fig. 19.1 Test setup with DUT on shaker table



locations is equal to the number of inputs the shaker can produce, then the input can be solved within the shaker. This project is a type of output driven testing as the target responses will be defined and the goal is to find the optimal input to meet those responses.

The DUT used in this experiment is an aluminum three-story block model, one on top the other, separated by bolted thin-plate columns. Each block is noted as “Node 1”, “Node 2”, and “Node 3”, successively from bottom to top. In this paper, “nodes” will also correspond to “locations” as those are points of interest in assessing responses from the model. The words “node” and “location” are used interchangeably. Figure 19.1 below shows the three-block model.

19.1.2 Defining Environments

In order to define the targets response PSDs, it is necessary to first determine the environments of interest. For this experiment, three transportation excitations were chosen from MIL-STD-810G, and are shown below:

1. US highway truck vibration exposure
2. Composite two-wheeled trailer
3. Composite wheeled vehicle (60% off-road)

Each environment input was transmitted to the base of the shaker and the PSD responses from each of the three locations were overlaid on the same plots. Once that is obtained, a smooth linear envelope is drawn on top of the overlaid plots, per location, becoming the target PSDs of interest. Figure 19.2 illustrates the process for “Node 1”, resulting in a conservative target PSD (shown in the green top solid line).

19.1.3 An Overly Constrained Problem

Since the target PSDs are enveloped, and are each arbitrarily defined, there is no single input that will match all responses to their respective target PSDs. Thus, the resulting problem is over constrained and underactuated.

Currently, solutions to this problem exist but are less than optimal. The prime reason these methods need improvement is that they require a human in the loop to define the input to the system. Given a target PSD for each desired location, a simulation is run to determine a “limit” profile that resembles each target PSD for each location, which will dictate the input.

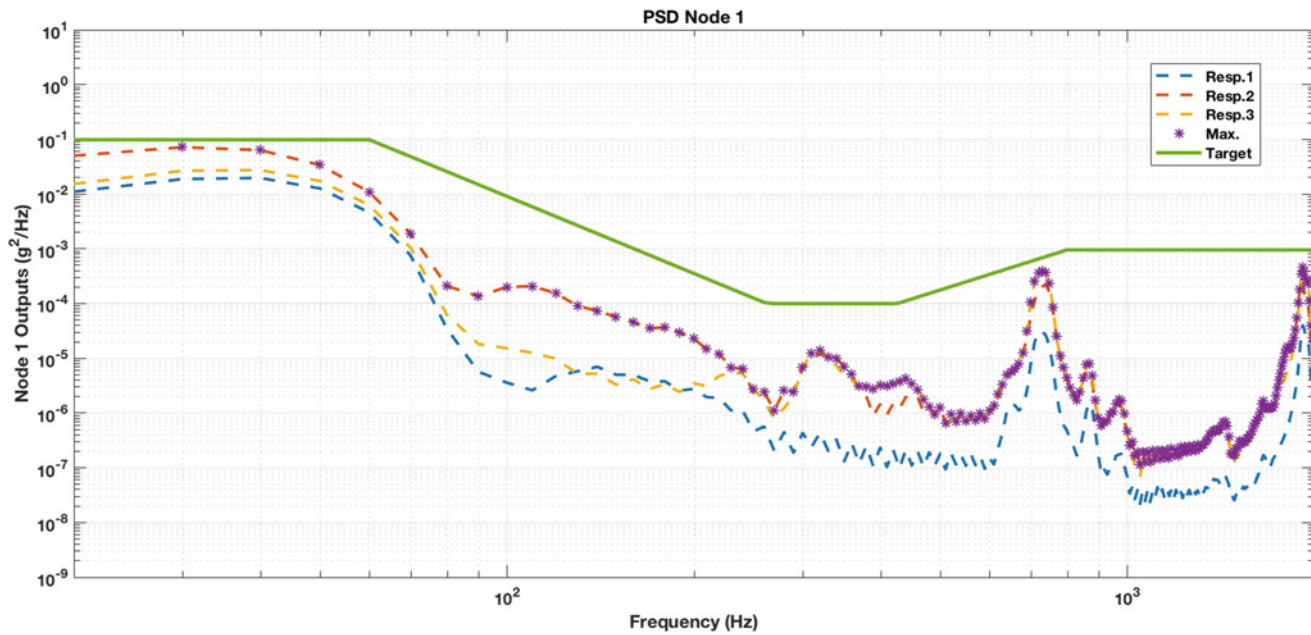


Fig. 19.2 Plot of environment envelope of node 1

The engineer continually adjusts the limits set on the response profile and simulates the system until he/she is satisfied with the tracking. This method is less than optimal because an engineer determines when to constrict the live model response to the limits, adjusting the needed input simultaneously.

The intent of this research is to also obtain a consistent input for the same DUT, eliminating the operator-to-operator variability that occurs in the current method.

19.2 Approach

19.2.1 Experimental Setup and Current Practices

The standard test setup consists of The Modal Shop 2075E electrodynamic exciter attached to a slip table that connects to the LASERUSB shaker control system (Fig. 19.3). The controller drives the shaker through the Labworks PA-138 linear power amplifier. With a standard setup, the controller is designed to shake the slip table such that a single random vibration profile is met, which is specified by feedback from a single accelerometer mounted on the testing apparatus. In the standard setup, the controller attempts to track the acceleration profile given a reference profile and the feedback it receives from the accelerometer.

19.2.2 Modification of Hardware

In order to incorporate a new feedback loop to the system, the test setup has to be modified to be able to adjust the input in real time. To change the actual response sent to the device under test (DUT) and apply a desired excitation, the signal generated from the feedback accelerometer is manipulated before being sent into the shaker controller. In order to “spoof” this signal, a National Instruments USB-4431 data acquisition device (DAQ) with four input ports and a single output port is placed in between the accelerometer and the controller (Fig. 19.4). The DAQ unit was chosen because feedback over multiple target objectives will be possible up to four dimensions, which correspond to the four accelerometer ports. Its single output port mimics the control accelerometer of the LASER controller. The NI DAQ can also be programmed with Matlab, which has libraries for filtering and transforming the signals coming from the testing locations.

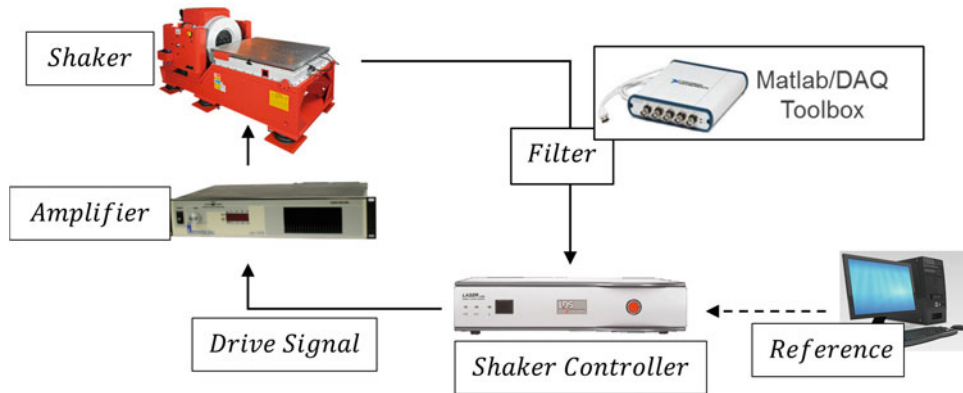


Fig. 19.3 Diagram of unmodified test setup

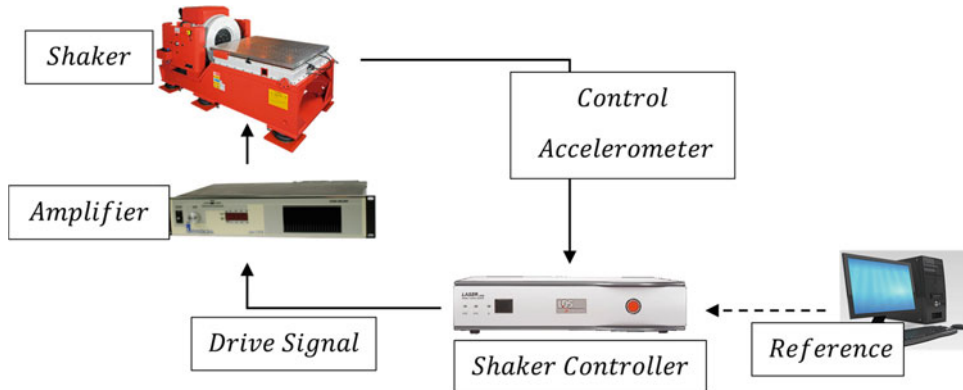


Fig. 19.4 Diagram of modified test setup

In order to control the output from the controller to the slip table, a filter was needed to be able to ensure the signal coming from the DAQ to the shaker controller would drive the intended excitation as needed. This allows a desired excitation at the base, at any point in the vibration test, to be specified different from that of the set reference excitation. To design a filter to achieve this goal, the reference PSD profile, initialized in the controller software, must be considered. The filter magnitude is equal to the reference PSD divided by the desired excitation PSD. If the excitation PSD at the base is exactly equal to that of the reference PSD, then the filter magnitude will be equal to 1. However, if the reference and the DAQ output do not equal each other then this will prompt the filter to amplify or attenuate the gain in those frequency bands. Equating the filter magnitude to the low pass filter, the relationship between this filter magnitude, reference PSD and desired excitation PSD is observed. The predicted signal coming from the base is expected to be higher at the frequencies that are attenuated. In this demonstration, the reference signal is set to a magnitude of $10e-4 \text{ g}^2/\text{Hz}$ and the low-pass filter has a cut-off frequency of 100 Hz and attenuates linearly to a magnitude of $10e-5 \text{ g}^2/\text{Hz}$ at 2000 Hz. The resulting base excitation appears to be the filter mirrored over the $10e-4 \text{ g}^2/\text{Hz}$ magnitude line. The result from testing the simple filter is shown below in Fig. 19.5.

The DAQ is limited in the number of inputs, which could cause a problem when encountering a more complicated system with more desired target locations. The other limitation the NI DAQ has is the delays that will occur when calculating “real-time” data. If a system is changing with time, then the delay has to be shorter than the time variation for the results to be accurate. A system that varies faster than the program can calculate the input will have ever increasing delays that will not allow the input to be optimized. In addition, there is a delay that occurs on the end of the LDS shaker controller as it updates the feedback information it is receiving to match its reference profile. This delay from the controller can be compounded if the delay of data going in and out the DAQ is too high.

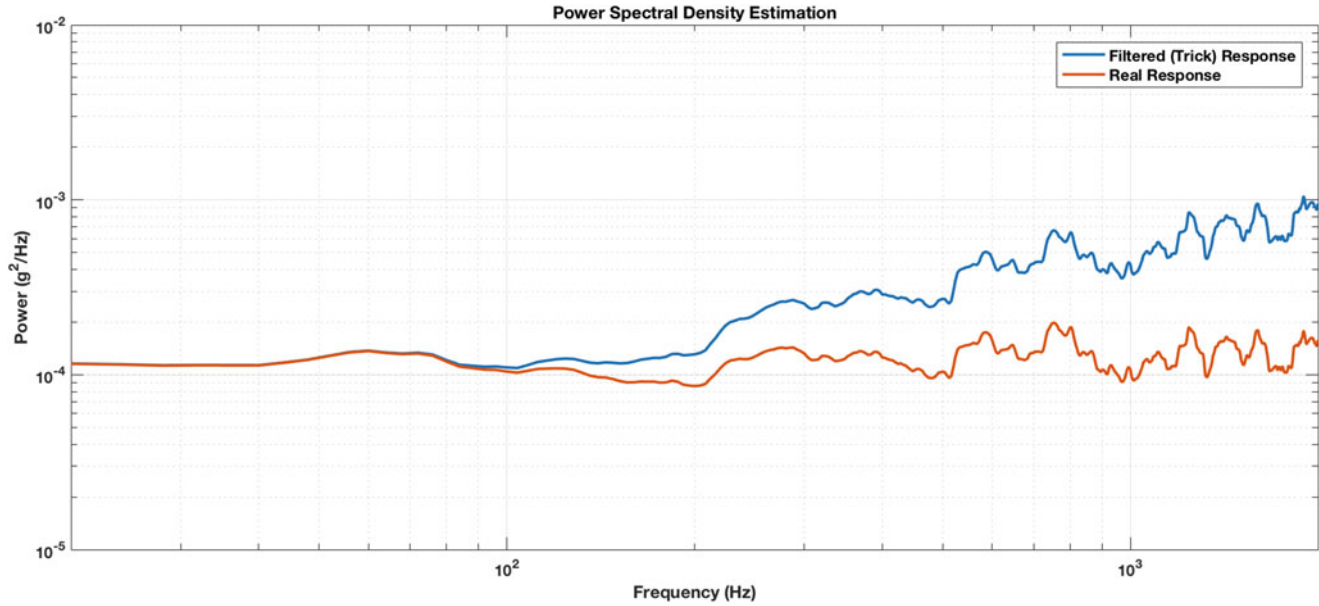


Fig. 19.5 Plot showing the response of the system with a low-pass filter

Table 19.1 Description of variables

Symbol	Description	Units
$H_i(\omega)$	The transfer function describing the relationship between the base excitation input and the output at node i	g/g
K	A constant used in the conversion from magnitude to power spectral density	1/Hz
f_s	Sampling rate	Samples/sec
N	Sample length	Samples
$\mu(\omega)$	Base excitation input	g
$\mu^*(\omega)$	Optimal base excitation input	g
$X_i(\omega)$	Power spectral response at node i	g^2/Hz
$X_{target i}(\omega)$	Power spectral target response at node i	g^2/Hz

19.2.3 Optimal Input Design

Most real structural systems are nonlinear, but can be simplified to a linear system, especially at low levels of vibration. Because operations are performed with a discrete filter, the signals are converted into the frequency domain through the Fast Fourier transform (FFT). After performing the FFT and transforming the data into the Fourier domain, the output of the system is equal to the frequency response function multiplied by the input (Eq. 19.1).

Note that all of the bolded variables in Table 19.1 are given as a function of frequency and denote a vector of values that correspond to the discrete vector of frequencies used in the Fourier analysis. The resolution of the discrete Fourier transform (DFT) or size of the bin is equal to the sampling rate divided by the sample length.

$$x(\omega) = H_i(\omega) \mu(\omega) \quad (19.1)$$

Given a target PSD profile and a PSD response generated from a random input, a cost function is required to minimize the offset of the target to the response signals. Note that the signal PSD is the square of the signal FFT divided by the frequency increment. In order to transform Eq. 19.1 into a PSD, the equation for each output PSD, X_i , becomes:

$$X_i = K \left(|\mathbf{H}_i|^\circ \mu \right)^2 \quad (19.2)$$

where $K = 1/(fs/N)$.

The cost function is the summation of the amplitude difference squared between the target ($X_{target i}$) and the response (X_i) PSD for each location. The optimal input, μ^* , is equal to the minimization of that cost function shown below.

$$\mu^* = \underset{\mu}{\operatorname{argmin}} \sum_{i=1}^3 \left(\log_{10} X_{target i} - \log_{10} K \left(|\mathbf{H}_i|^\circ \mu \right)^2 \right)^2 \quad (19.3)$$

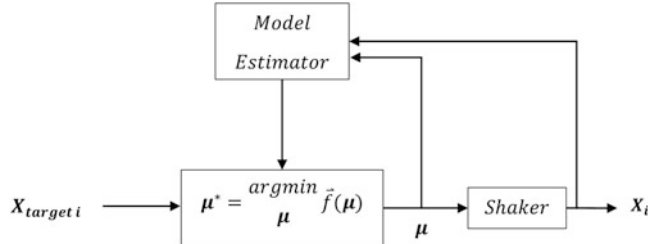
To analytically find where μ^* is the minimum, Eq. 19.3 can be solved closed form and only the positive solution will be used. The solution for μ^* becomes,

$$\mu^* = \frac{\sqrt[6]{X_{target 1}^\circ X_{target 2}^\circ X_{target 3}^\circ}}{\sqrt[6]{K^3 |\mathbf{H}_1|^2 \circ |\mathbf{H}_2|^2 \circ |\mathbf{H}_3|^2}} \quad (19.4)$$

and is a vector of length N where each element is the input magnitude at each frequency bin that minimizes the error between the target and response.

19.2.4 Model Estimation

The optimal input calculation relies on a model, denoted by the transfer functions ‘H’ at each node, that implies a model estimation step within the control loop. The complete control diagram is now shown below.



In the control iteration the model estimator performs an Hv estimation of the FRF between the shaker input and each other outputs over the course of the previous 5 s. If the model is known to be linear and time invariant, the value of FRF can be initialized once at the beginning of the test.

19.3 Results and Performance

19.3.1 Predicted Results

The optimal input was solved without implementing the DAQ hardware into the shaker controllers’ feedback loop. The DAQ accepts data from each node as well as from the base and calculates the model’s transfer function. This optimal input was used as the reference excitation initialized in the shaker controller in testing performance of the model estimation step with a LTI system (see part III section b).

To verify that the input did in fact produce the least error possible between the targets and the responses at each target location, a study was done using multiple methods of designing the input including the way it is currently done. The error is the sum square of the difference between the response and the targets summed across all frequency bins. The nonoptimal

methods were simulated within Matlab and the error of each was compared to the error of the optimal method. The sum square error between the targets and response across all three nodes for the optimal input was **5.2692e + 4 dB^2**. Figures 19.6, 19.7, and 19.8 below show the responses of Nodes 1, 2, and 3, respectively, due to the optimal input.

The first method tested only controlled for the response of the first node so as to match the response to the target perfectly. This produced perfect tracking on the first node and very erroneous tracking on nodes two and three. The sum squared error produced by this method is **7.4919e + 4 dB^2**.

The second verification method tested is similar to the current standard in determining an input for an invariably defined multiple output system. Again, the first node's response was set to attempt to match the target perfectly but with the addition of limits set on nodes two and three. These limits were set at those node's target profiles so the responses could not exceed the magnitude of those targets at any frequency band. The result: the first node was unable to track its target because the limits on nodes two and three caused the response of node one to be below its target. This method yielded a sum squared error of **1.3415e + 5 dB^2**.

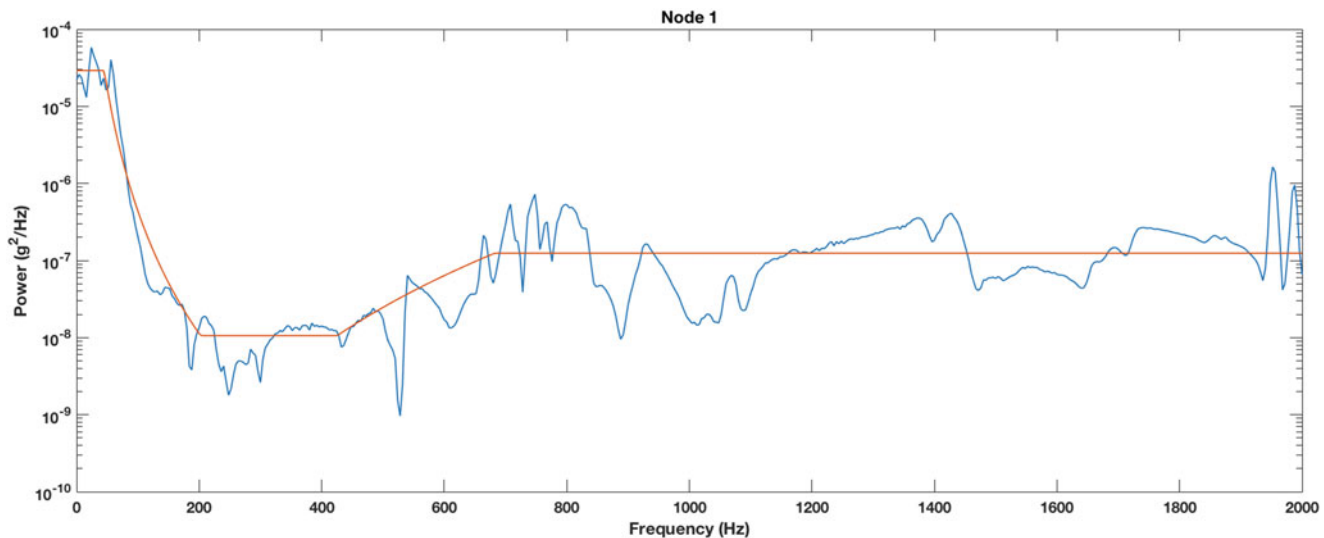


Fig. 19.6 Plot showing the response at node 1 superimposed over the target at node 1

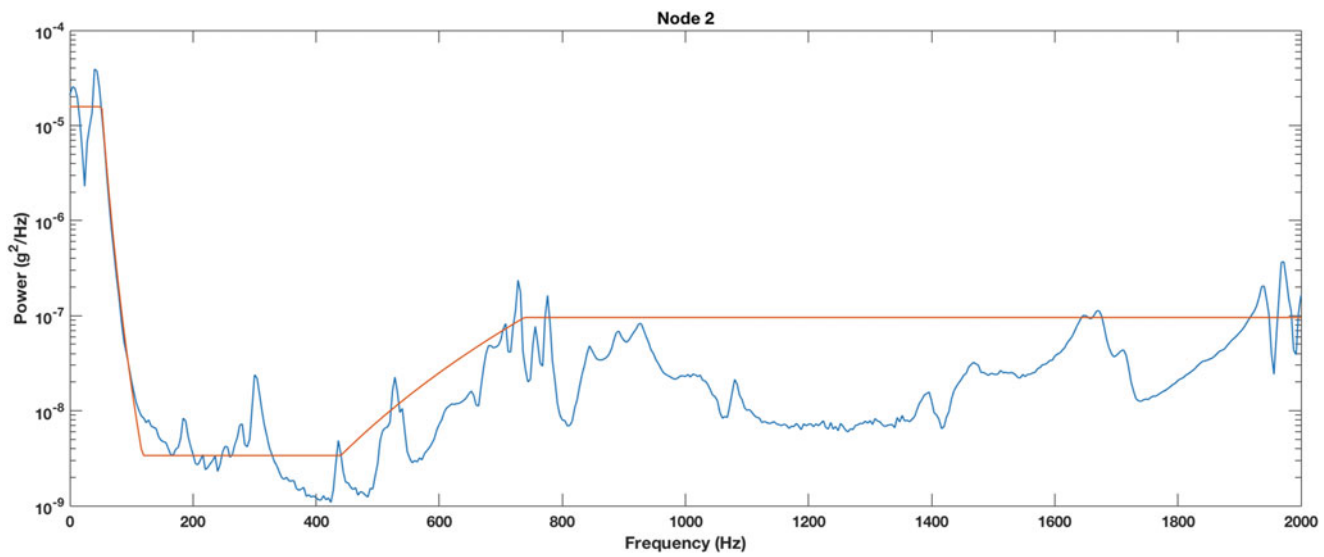


Fig. 19.7 Plot showing the response at node 2 superimposed over the target at node 2

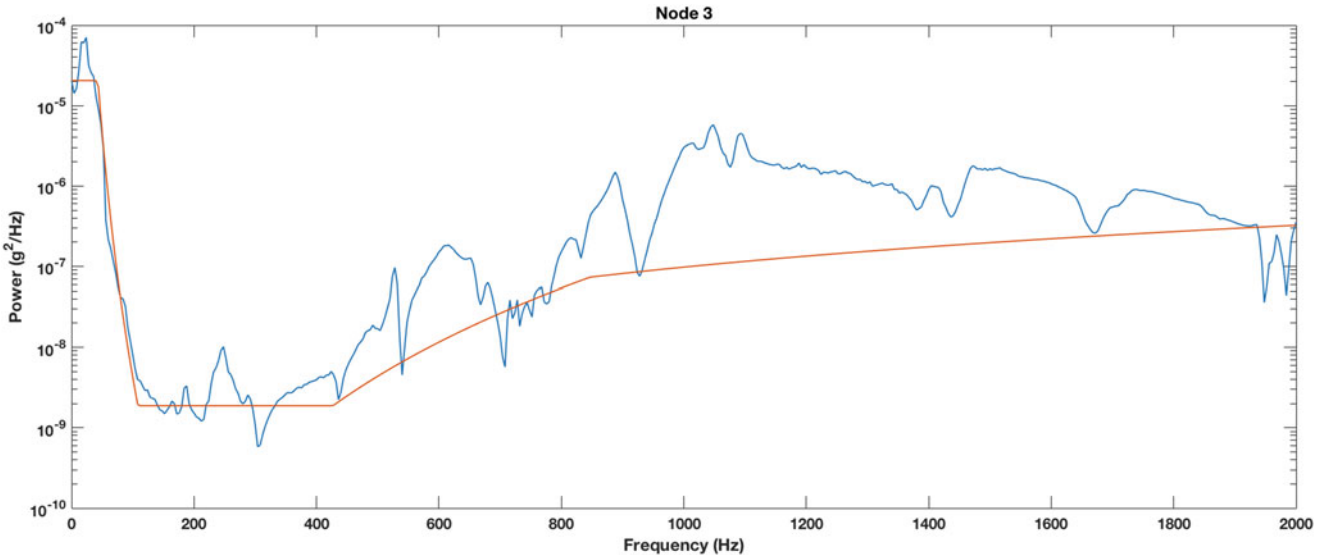


Fig. 19.8 Plot showing the response at node 3 superimposed over the target at node 3

19.3.2 Performance on an LTI System

The performance of the LTI system was then evaluated by changing parameters within the model estimation step. The length of time used for each model estimation iteration was adjusted from a time history of 2.5 seconds to 5 seconds. The two methods were compared using their mean filter magnitude over the course of a minute long test. The filter as mentioned previously is the reference excitation data divided by the desired shaker excitation data. **The 2.5 second model yielded a max standard of deviation of 4.3 dB and the 5 second model yielded a max standard of deviation of 3.5 dB.** This shows that a longer time step produces more consistent model estimation for a LTI system. It is important to note however, that for a linear time variant system a longer estimation may not allow the estimation to accurately show the change as the system varies with time. Equally as important, using a longer time history for estimation causes delays in feedback, which increase instability.

19.3.3 Performance on an LTV System

To create a linear time variant system (LTV) a magnetic mass was added to node one (lowest node) then after running the shaker for 30 seconds the mass was removed. The results show the filter profile shift from a constant value to a different value at the 30-second mark. Note, especially at higher frequencies the heat map in Fig. 19.9 shows a noticeable shift in magnitude after the mass was removed.

19.4 Conclusion and Future Work

This paper details an approach to optimize the input of a single-input, multi-output system. This method can be applied to both LTI and LTV systems and can be tuned further to lead to a more overall stable system. For LTI systems, a longer time block used for the model estimation produces a more reliable estimation and therefore a more reliable solution for the input. Conversely a longer block time can increase delays and therefore introduce instability.

In future work, all of the computing would be done in one device. Combining the LASER shaker controller and the DAQ would make the process of finding an input simpler and faster, and minimize instability in controlling these two feedback systems separately. In the current hardware used in this research, a change in the intercepted signal is perceived as a disturbance by the LASER system. One option to consider would entail having a commercial manufacturer design a shaker

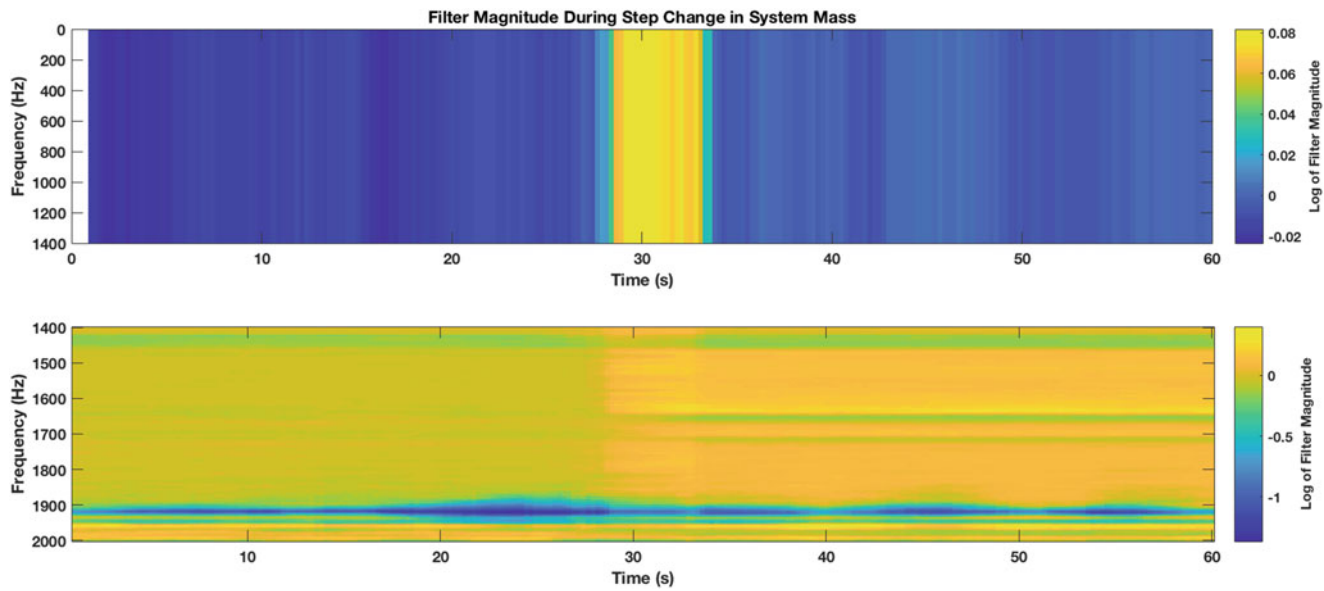


Fig. 19.9 Heat map of filter magnitude change during transition in the LTV system

controller that can use feedback from multiple accelerometers and perform the optimization of the input given multiple references. Other work might include incorporating a parameter updating nonlinear model into the optimization stage of the proposed algorithm, which will be applicable to a wider range of structures.

Appendix (Tables 19.2 and 19.3)

Table 19.2 Control parameters

Parameter	Description	Value
Sampling frequency	Rate at which NI DAQ system samples data	4000 samples/sec
Sample length	Number of samples on which the FFT was performed	1000 samples
Bin size	Width of the frequency bin on data in Fourier domain	4 Hz
Number of outputs	The number of nodes being controlled	3
FRF estimator	The type of estimator used to calculate the FRF	Hv
Window size	The window applied to data undergoing the FFT	1000 samples
Window type	The type of window applied to data undergoing the FFT	Hanning
Input queue trigger length	The number of samples required to trigger the processing routine	1000 samples
Output queue trigger length	The number of samples required to trigger the output routine	400 samples

Table 19.3 Structure parameters

Parameter	Description	Value
Height	Height of the structure	20 inches
Node distance	Distance between each node	6 inches
Node weight	The weight of each of the three nodes	354 grams
Added weight	The weight added to the lower node during the LTV test	70 grams



Chapter 20

Driving a Motion Platform with a Vibration Control Software for Multi-axis Environmental Testing: Challenges and Solutions

Umberto Musella, Ludovico Zanellati, Marco Grottoli, Francesco Celiberti, Bart Peeters, Francesco Marulo, and Patrick Guillaume

Abstract Multiple-Input Multiple-Output (MIMO) vibration control testing is nowadays recognized, in the environmental testing community, as an effective test methodology to accurately replicate the vibration environment a structure needs to withstand during its operational life. For these applications, the control process typically takes place in the frequency domain, within the data acquisition hardware's embedded processor. Multiple analog voltages (the so called drives) are computed and streamed to the exciters in order to obtain a controlled response of a Unit Under Test (UUT) for a set of multiple control channels (the so called Controls, typically acceleration recordings). The multi-input excitation can be simultaneously applied with a set of multiple independent shakers or with multi-degrees of freedom (DOFs) shaking tables. In this case the drives are translated in the shaking tables DOFs in the three dimensional space. Advanced state-of-the-art hydraulic and electrodynamic multi-axis shakers are nowadays available to excite the UUT in all the six DOFs. On the other hand six DOFs motion platforms are widely used in motion simulation, where the aim is to use the platform to replicate the motion of an object in the three dimensional space. This is typically performed with dedicated algorithms, running on real time hardware that communicates with the platforms internal controller via Internet Protocol. Theoretically, the only step to combine this type of hardware with a data acquisition system and a vibration control software is to translate the drives in actuator displacements. However, adding layers to the communication chain, brings practical challenges. First of all, in order to establish any communication, it is mandatory to cope with the platforms protocol and real time requirements. Then, for any environmental testing application, it is fundamental to guarantee that the information sent is not inconsistently distorted or delayed in the communication process. This work aims to show the challenges and the solutions to combine a six DOFs motion simulation platform with an advanced off-the-shelf MIMO vibration control software and data acquisition hardware. Case studies will show the possibility of effectively using the motion simulation platform for both multi-axis random vibration control (MIMO Random) testing and time waveform replication (TWR).

Keywords MIMO vibration control · Multi-axis environmental testing · Six-DOF motion platform · MIMO random control · Time waveform replication

U. Musella (✉)

Siemens Industry Software NV, Leuven, Belgium

Acoustics and Vibration Research Group, Vrije Universiteit Brussel, Elsene, Belgium

Department of Industrial Engineering, University of Naples Federico II, Naples, Italy

e-mail: umberto.musella.ext@siemens.com

L. Zanellati

University of Ferrara, Ferrara, Italy

M. Grottoli · F. Celiberti · B. Peeters

Siemens Industry Software NV, Leuven, Belgium

F. Marulo

Department of Industrial Engineering, University of Naples Federico II, Naples, Italy

P. Guillaume

Acoustics and Vibration Research Group, Vrije Universiteit Brussel, Elsene, Belgium

20.1 Introduction

Environmental vibration control tests are performed to prove that a system and all its sub-components will withstand the vibration environment during the operational life. These tests aim to replicate with an high degree of fidelity the structural responses of a Unit Under Test (UUT) in the in-service conditions. This brings the need for exciting the UUT in all the possible axes [1]. Nowadays the common practice, when more than one axis of excitation is needed, is to perform sequential single-axis tests (sequential Single-Input Single-Output [SISO] tests). This practice has known limitations and drawbacks [2]. The most critical aspect is that a sequential SISO test can lead to an unacceptable UUT time to failure overestimation [3] and different failure modes [4]. The main reasons lay on the fact that (i) an increased number of control points is essential to guarantee that the response levels match also in location that are not controlled [5, 6], (ii) with these tests it is impossible to guarantee that the cross-axis interaction the structure experiences in the in-service conditions will also be replicated and (iii) the number of excited degrees of freedom is crucial to replicate the actual stress state the test article is subjected to in the operational conditions. On top of more practical aspects that make difficult (or even impossible) to perform sequential SISO tests, this is the main reason why simultaneous multi-axial excitation, and more generally Multi-Input Multi-Output (MIMO) vibration control tests, are nowadays the *go for* in the environmental testing community [2, 7, 8].

In the recent years state-of-the-art three-axis and six-axis servo-hydraulic and electrodynamics shakers can be found on the market covering a wide range of loads and frequency bands. This is driving the multi-axial vibration research towards innovative solution to optimize their use [9–12], as testified by the persistent updates on the multi-axial testing standards [2] and recommended practices. On the other hand six-DOF motion platforms have been largely used in motion simulation since the 1965 [13] and exponentially improve their capabilities since then. Typically, the scope of these applications is to use the platform to mimic as close as possible the real vehicle accelerations as the inertial feedback to the driver via dedicated motion cueing algorithms seeking for the optimal compromise between realistic accelerations fidelity and motion system restrictions. This is performed with dedicated algorithms, running on real time hardware that communicates with the platform's internal controller via Internet Protocol.

The main aim of this work is to try to combine an advanced off-the-shelf vibration controller for environmental testing with a latest solution in the motion systems.

A first challenge comes from the typical communication architecture of the two hardware. On one side the vibration controller voltages driving the exciter systems are analog signals sent via standards BNC connectors; on the other side, the motion platform requires information via UDP/IP through Ethernet crossover cables. The datagram needs to be structured in such a way that the information carried can be interpreted correctly by the platform's control logic.

Once the connection has been established, a second step will be the on-line control of the motion platform with an off-the-shelf vibration control software for environmental testing. There are different types of MIMO vibration control tests, differing from the nature of the excitation environment the UUT needs to be subjected to, MIMO random tests are performed to replicate the response of the test article to a broadband random Gaussian vibration environment. Typical scenarios are the road excitation or the responses to a diffuse acoustic field. For the SISO case, the test specification is a Power Spectral Density (PSD) profile that needs to be replicated in a user defined control location by exciting the UUT with a single shaker. In the MIMO case, it is possible to define required test levels for multiple control channels that will be controlled simultaneously. Additional information about the cross-talk between the control channels is also included. This information must be provided in terms of Cross Spectral Densities (CSDs) between the control channels defining desired phase and coherence profiles. This feature is essential to also replicate the cross-talk that naturally exists between difference responses. The control target for a multi-axis random control test is thus a full Spectral Density reference matrix (SDM). Defining the target with no a-priori knowledge of the cross-correlation between control channels is already very challenging and subject of recent studies [10–12, 14–16]. With respect to this type of tests, the use of a six-DOF excitation mechanism opens the suggestive possibility of defining the control target in terms of virtual channels representing the degrees of freedom of the shaking system [17, 18]. This approach, known in the multi-axis vibration control literature as *DOF Control* requires the definition of the so called *Input Transformation* to transform the target from the motion space to the space defined by the acceleration control channels.

If on one hand, MIMO random tests can be used to on-line control the responses to all the gaussian random vibrations associated with the target SDM, Time Waveform Replication tests can be used to simultaneously replicate multiple arbitrary time histories [2, 19–21] with an off-line control approach (Iterative Learning Control).

After this brief introduction, Sect. 20.2 introduces the hardware used and the solution proposed to establish the communication between an off-the-shelf vibration controller and a six-axis motion platform. In Sect. 20.3 the bases of multi-axis random control (together with a detailed derivation of the Input Transformations) and Time Waveform Replication are covered. Section 20.5 shows the results from a series of tests run with the motion platform driven with a MIMO random vibration controller to match control targets in the motion space, showing thus the potentiality of both the

communication architecture established and the solution developed for MIMO random DOF control. Furthermore, Time Waveform Replication test results will show the possibility of replicating, with the motion platform, scaled accelerations recordings of the 1940 El Centro earthquake. Section 20.6 finally summarizes the main conclusions and the future directions.

In this work vectors are denoted by lower case bold letters, e.g. \mathbf{a} , and matrices by upper case bold letters, e.g. \mathbf{A} . An over-bar is used to indicate the complex conjugate operation and the apex \square^H to indicate the complex conjugate transpose of a matrix, e.g. $\bar{\mathbf{a}}$ and \mathbf{A}^H are the complex conjugate and the complex conjugate transpose of the vector \mathbf{a} and the matrix \mathbf{A} , respectively.

20.2 Six-DOF MOOG Platform Driven by Siemens LMS Environmental Testing Solutions

This work aims to combine a six degrees-of-freedom platform, typically used for driving simulation purposes, to an advanced multi-axis vibration controller and data acquisition system for environmental testing and (or) as a test bench to test prototype solutions for MIMO vibration control tests.

20.2.1 MOOG Motion Platform

The six-axis motion platform considered in this work is the MOOG MB-E-6DOF/24/1800KG at the Siemens LMS HQ facility in Leuven (Belgium). The platform's single DOF performances, considering the maximum allowed gross moving load of 1800 kg [22], are reported in Table 20.1.

Typical applications for this motion system are driving simulation of rail vehicles, cars, trucks and tanks driving, but also riding simulation as shown in Fig. 20.1a.

Figure 20.1b illustrates the communication architecture for a MOOG platform's typical use. A full dynamic model of the vehicle (e.g. modeled using Siemens Simcenter 3D + Simcenter Imagine.Lab Amesim) runs on an hard Real Time Operative System (RT OS) connected via Ethernet to an host computer and the MOOG Controller. The host computer is used to provide the inputs to the dynamic model (steering torque, throttle, break, ...) that will derive the accelerations of a specific point in the space (for example the platform centroid or the driver's head). These accelerations are fed in real time via UDP/IP to the MOOG controller that computes the three translations and the three rotations resulting in the desired acceleration values, through internal motion cueing algorithms. In the MOOG controller are also implemented the inverse kinematics, and therefore the estimations of required actuator displacements provided as inputs to the low level control logic that finally activates the actuators. At this point, from the measured actuator displacements, the MOOG controller evaluates the actual realized degrees of freedom via direct kinematics, used as feedback for the motion cueing algorithms.

The MOOG controller communicates with the RT OS via UDP/IP, providing in this way a simple, fast and connectionless data transmission. The UDP datagram structures allow the possibility of controlling the platform in different *Simulation Modes* by opportunely filling in specific bytes in the datagram's payload [26]:

- *Motion Cueing*. The RT OS running the vehicle's model, provides the accelerations of a reference point in the space. A proprietary motion cueing algorithm scales and filters these information so that they can be reproduced with the platform.
- *PVA Control*. The RT OS forwards in real-time the Position, Velocities and Accelerations (PVA set) of a moving reference frame to the MOOG Controller. This simulation mode includes the possibility of the PVA set, leaving to the MOOG Controller the freedom to derive the remaining information.

Table 20.1 MOOG MB-E-6DOF/24/1800KG single DOF performances

Translations	Excursions (m)	Velocities (m/s)	Accelerations (m/s ²)
Surge (Tx)	±0.69	±0.51	±3.92
Sway (Ty)	±0.66	±0.51	±3.92
Heave (Tz)	±0.56	±0.41	±5.88
Rotations	Excursions (deg)	Velocities (deg/s)	Accelerations (deg/s ²)
Roll (Tx)	±20	±15	±75
Pitch (Ty)	±20	±15	±75
Yaw (Tz)	±25	±15	±75

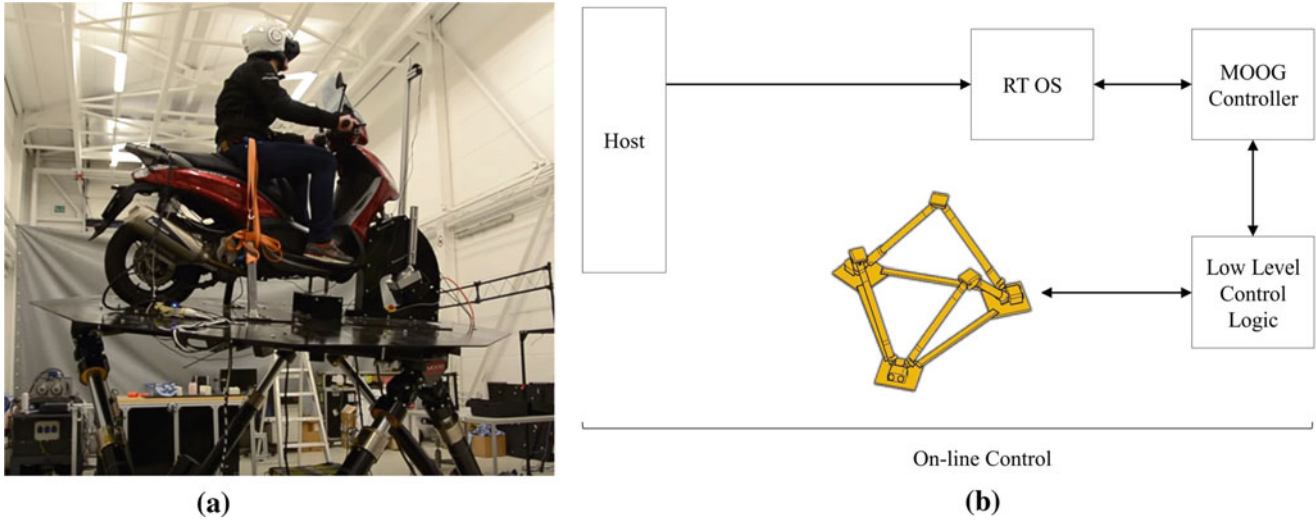


Fig. 20.1 Six-DOF MOOG platform used as driving or riding simulator. **(a)** Riding simulation with the MOOG platform. **(b)** Block scheme of the typical communication scheme for driving simulations

- *Special Effects.* The host can set the parameters of pre-defined waveform to be used together with the Motion Cueing, the PVA Control or standalone.
- Additionally, a *Test Mode* is also available to directly control the actuators or replay pre-defined waveforms using an in-house MOOG software.

20.2.2 Communication Architecture for Environmental Multi-axis Vibration Control Tests

Compared with the typical driving simulation applications the MOOG platform is meant for environmental testing deals with conceptually different scenarios. The test objective is to replicate with the vibration exciter(s) the dynamic environmental condition a Unit Under Test would experience during its operational life. The responses to be controlled typically come from acceleration measurements (the *control channels*), used as feedback to generate (and correct) the analog voltages (the *drives*) that drive the excitation system. The whole control loop runs in the vibration controller software and hardware. In this work the Siemens Simcenter LMS Test.Lab and a Siemens SCADAS Mobile with vibration control capabilities have been used. Also for these applications, a model of the system (from voltages to accelerations) is needed. Typically low-level random signals are used in a pre-test System Identification phase in order to have an estimate of the system's Frequency Response Functions (FRFs). Using this information and the accelerometers' feedback, during the control process the analog drives are continuously streamed via standard BNC connectors. To directly drive the platform's DOF, the voltages can be transformed in the three rotations and the three translations of a moving reference frame by considering the maximum ranges provided by the manufacturers for each degree of freedom and calculating the corresponding values per unit volt. The PVA Simulation Mode can then be used, providing to the RT OS (and then the MOOG Controller) the position-only information. A necessary step to communicate with the RT OS is then to convert the analog voltages sent from the SCADAS DACs in a digital representation and forward the information via Ethernet to the MOOG Controller. An UDP socket needs to be created with the RTOS. The UDP datagrams shipped must have a structure that can be interpreted by the MOOG controller. For these functions it is necessary to add an additional layer to the typical communication architecture illustrated in Fig. 20.1b. The solution adopted in this work has been to include a 32-bit Programmable Logic Controller (PLC) with Ethernet capabilities in pair with two multi-input analog modules. The final communication architecture is shown in Figs. 20.2 and 20.3. The PLC has been programmed with a structured text main program that sequentially executes two tasks:

1. Read the six analog inputs and convert them in the three translations and the three rotations of a moving reference system (5 ms).
2. Create an UDP datagram with the six positions in the payload and send it through the UDP socket established between the PLC and the RT OS (5 ms).

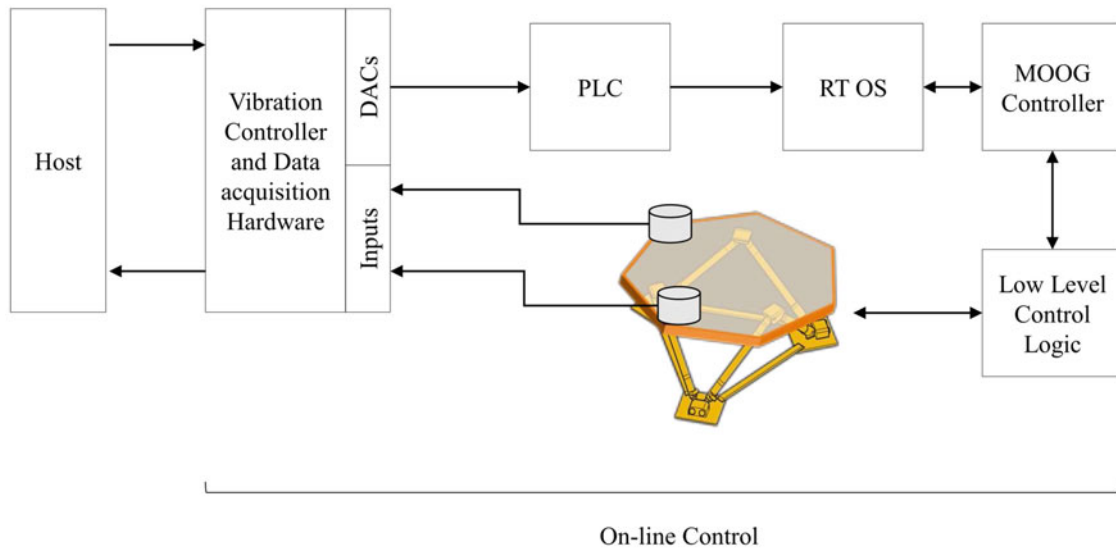


Fig. 20.2 MOOG platform used for vibration control testing: block scheme

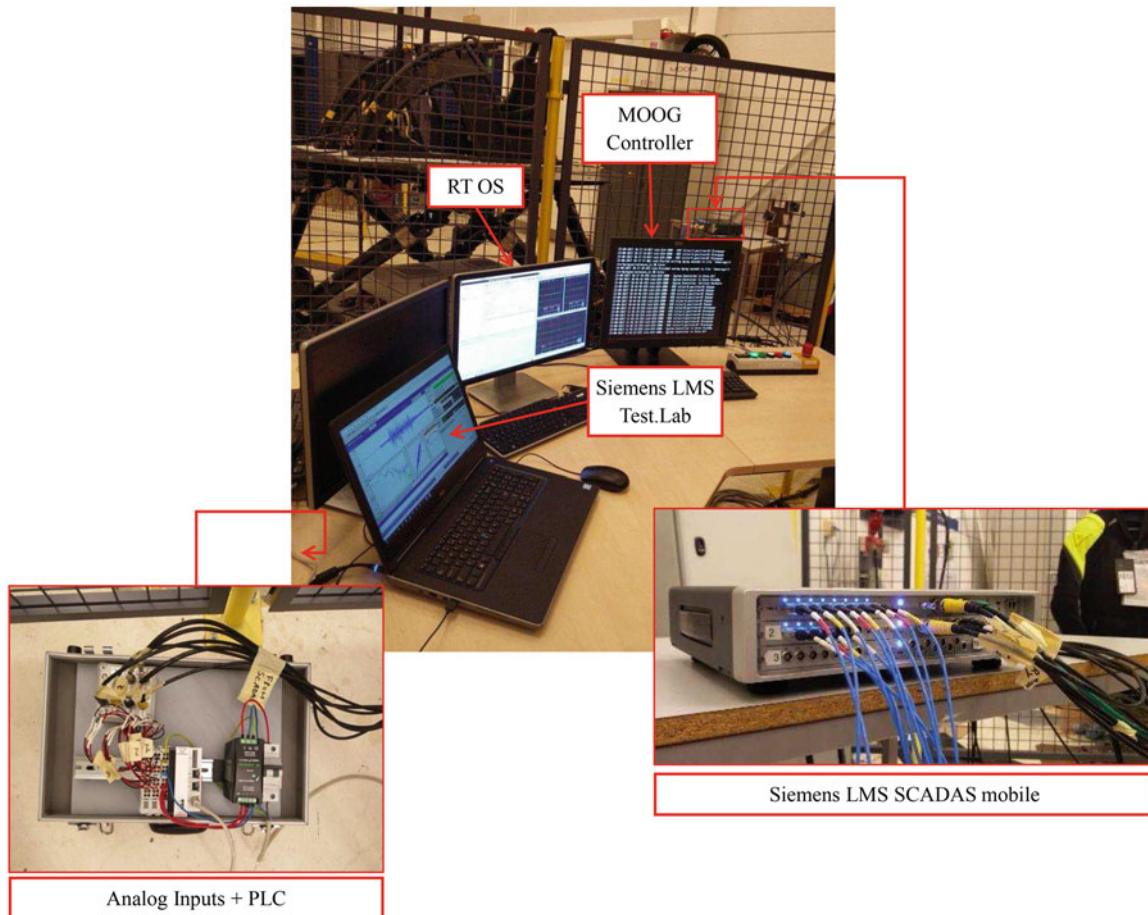


Fig. 20.3 The different hardware used to drive the MOOG platform for vibration control testing

The program can be loaded as boot project in the PLC, that will continuously stream via Ethernet the data in input to the analog input modules. The only operation needed to use the MOOG platform as a vibration exciter is at this point just connecting the SCADAS DACs to the PLC's analog input module and run the vibration control application.

As mentioned in the Sect. 20.1, there are different types of vibration control tests, depending on the nature of the excitation the structure needs to withstand in operational conditions. In the following the capabilities of two different environmental testing approaches will be shown: MIMO random vibration control (random gaussian excitation) and Time Waveform Replication.

20.3 Multi-axis Random Vibration Control (MIMO Random)

In this section it is considered the scenario where the control targets are random profiles (PSDs) specified in terms of degrees of freedom. Most of the derivations are in the frequency domain, hence all the quantities need to be considered as function of the frequency, if not specified otherwise.

The block scheme of a general MIMO Random Vibration Control test is illustrated in Fig. 20.4. The structure under test is excited driving m electrodynamic or hydraulic shakers and the system's response is recorded in $\ell \geq m$ control points. In the hypothesis of the structure under test behaving linearly and being time invariant, the system is represented by the Frequency Response Function (FRF) matrix $\mathbf{H} \in \mathbb{C}^{\ell \times m}$

$$\mathbf{Y} = \mathbf{H}\mathbf{U} \quad (20.1)$$

where $\mathbf{Y} \in \mathbb{C}^{\ell \times 1}$ and $\mathbf{U} \in \mathbb{C}^{m \times 1}$ are the spectra of the control channels recordings $\mathbf{y}(t) = \{y_1(t), \dots, y_\ell(t)\}^T$ and the input drives $\mathbf{u}(t) = \{u_1(t), \dots, u_m(t)\}^T$, respectively. In case of rectangular systems, i.e. $\ell \geq m$, the impedance matrix \mathbf{Z} is generally obtained via a Moore-Penrose pseudo-inverse, $\mathbf{Z} = \mathbf{H}^\dagger \in \mathbb{C}^{m \times \ell}$. In all the vibration control tests, a System Identification pre-test phase is needed to estimate the system's transfer functions; this is usually performed by running a low-level random test and using the so called H_1 estimator

$$\hat{\mathbf{H}} = \hat{\mathbf{S}}_{yu} \hat{\mathbf{S}}_{uu}^{-1} \quad (20.2)$$

where $\hat{\mathbf{S}}_{yu} \in \mathbb{C}^{\ell \times m}$ and $\hat{\mathbf{S}}_{uu}^{-1} \in \mathbb{C}^{m \times m}$ are spectral density matrices estimated via the Welch's averaged periodogram.

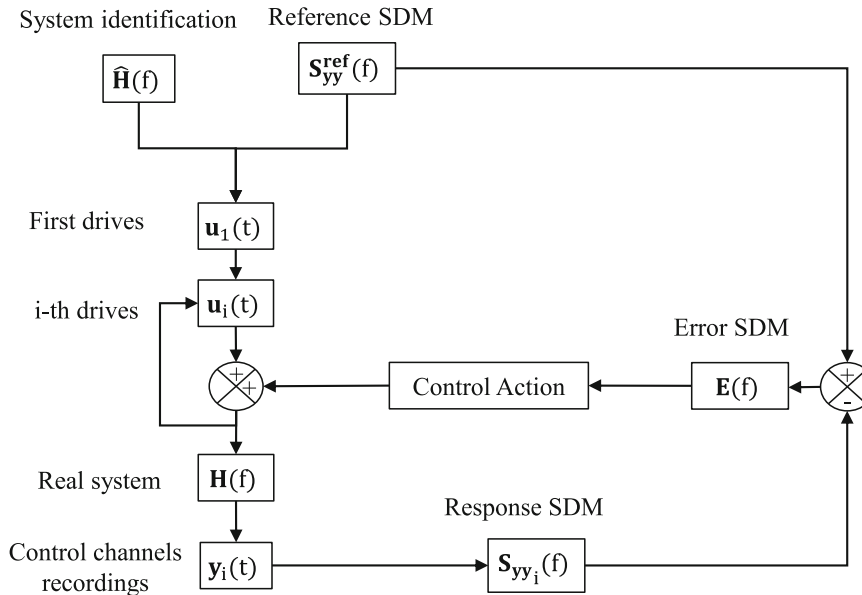


Fig. 20.4 MIMO random control general block scheme

The objective of MIMO Random Control vibration tests is to replicate a full Power Spectral Density matrix $\mathbf{S}_{yy}^{\text{ref}}$. Theoretically the test target could be directly achieved by sending the input drives that have the specified input spectral density matrix

$$\mathbf{u}(t) = \text{ifft}(\mathbf{U}) : \mathbf{S}_{uu} \triangleq E[\mathbf{U}\mathbf{U}^H] = \hat{\mathbf{Z}}\mathbf{S}_{yy}^{\text{ref}}\hat{\mathbf{Z}}^H \quad (20.3)$$

Nevertheless, due to the possible non-linear behavior of the unit under test and noise in the measurements, the system estimated in the pre-test phase will inevitably differ from the actual one ($\hat{\mathbf{H}}\hat{\mathbf{Z}} \neq \mathbf{I}$, where \mathbf{I} is the $\ell \times \ell$ identity matrix)

$$\mathbf{S}_{yy} = (\hat{\mathbf{H}}\hat{\mathbf{Z}})\mathbf{S}_{yy}^{\text{ref}}(\hat{\mathbf{H}}\hat{\mathbf{Z}})^H \neq \mathbf{S}_{yy}^{\text{ref}} \quad (20.4)$$

and a control action is needed to reduce the error

$$\mathbf{E} = \mathbf{S}_{yy}^{\text{ref}} - \mathbf{S}_{yy} \quad (20.5)$$

All the error correction strategies for MIMO Random Vibration Control tests (mainly due to the work of Underwood [7], Peeters [23] and Smallwood [24]) rely on the possibility of applying the so called *Cholesky Decomposition* to one of the spectral matrices in the game (either $\mathbf{S}_{yy}^{\text{ref}}$ or \mathbf{S}_{uu}) [25] and then iteratively correct the resultant *Cholesky Factor*. This operation is perfectly allowed because of the positive semi-definite nature of the spectral density matrices [11].

20.3.1 MIMO Random Reference Matrix

The reference matrix $\mathbf{S}_{yy}^{\text{ref}}$ to set as target of a multi-exciter random control test must be positive semi-definite to have a physical meaning. Beside the algebraic definition, there are some important properties to consider for practical applications. Particularly, all the eigenvalues of $\mathbf{S}_{yy}^{\text{ref}}$ are semi-positive and it has a unique Cholesky Decomposition, meaning that it can be decomposed in the product of two triangular hermitian matrices, referred as the Cholesky Factors: $\mathbf{S}_{yy}^{\text{ref}} = \mathbf{L}\mathbf{L}^H$;

20.3.1.1 Multiple Control Channels

Most of the MIMO vibco software have the possibility of setting the control target specifying the reference matrix $\mathbf{S}_{yy}^{\text{ref}}$ for the multiple control channels. The diagonal terms of $\mathbf{S}_{yy}^{\text{ref}}$ are usually known levels for the environmental test engineer, provided as test specifications. The CSDs are specified in terms of coherence and phase profiles between pairs of controls. For computational reasons linked to the control process stability [2, 7], coherence values of 0 and 1 are usually avoided [7]. Typical values of low coherence and high coherence are 0.05 \div 0.08 and 0.95 \div 0.98, respectively. All the CSDs are then easily computed via

$$CSD_{ij} = |CSD_{ij}| \exp(i\phi_{ij}) = \sqrt{\gamma_{ij}^2 PSD_i PSD_j} \exp(i\phi_{ij}) \quad (20.6)$$

where i is the imaginary unit and i and j are the i -th and the j -th control channels.

Filling in the MIMO random reference matrix *element by element* in terms of the $\ell(\ell + 1)/2 - \ell$ coherence and phase profiles could result in $\mathbf{S}_{yy}^{\text{ref}}$ being non positive semi-definite, following the fact that none of the necessary and sufficient conditions for this property to hold, have been taken into account in the completion process, as shown in [10] and [11]. The same publications highlight how the phase information between all the pairs of controls is fundamental in case the coherence is greater than zero, and increases with the coherence approaching the unity.

20.3.1.2 DOF Control

The use of a six-axis motion platform for multi-axis random vibration testing is directly linked to the possibility (and the necessity) of controlling the six DOF motion of the unit under test through the shaking system (the MOOG motion platform in this case) [17, 18]. This means on one hand to be able to transform the control channels acceleration recordings in the

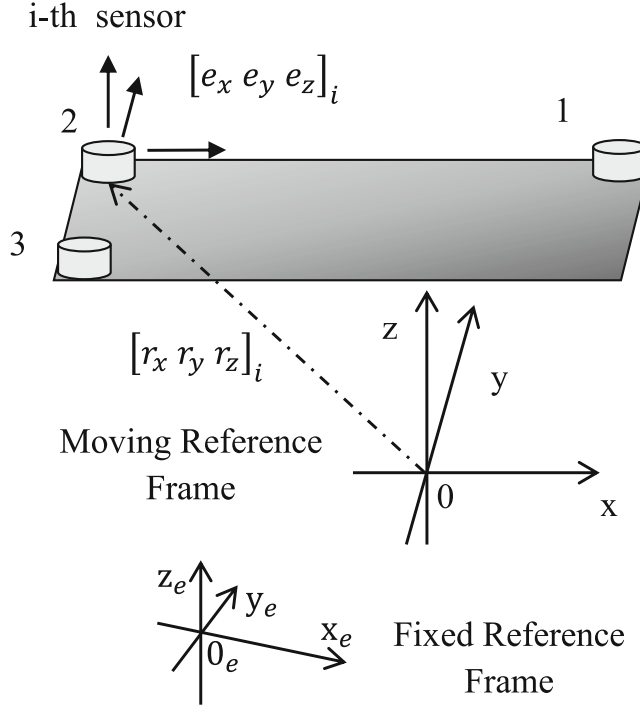


Fig. 20.5 Moving and fixed coordinate systems

linear and angular accelerations of a moving reference frame, on the other to translate the required motion in the actuator displacements (inverse kinematics). In the multi-axis shaker control community [17, 18] these transformations are known as Input and Output Transformations, respectively.

In the case study, the solution of the inverse kinematics and therefore the drives output transformation is left to the MOOG internal control logic. The aim of this subsection is then to find an adequate transformation law from the motion space to the measurement space (and backwards) in order to be able to define the MIMO Random reference matrix in the motion space and then transform it in terms of standard control channels PSDs, coherence and phase profiles in the frequency domain, therefore generating a target that can be processed by the Siemens Simcenter LMS Test.Lab Multi-Axis Random Control.

Let's consider a moving reference frame centered in a point 0, as shown in Fig. 20.5. Without lack of generality, for the case studied, it will be considered the Moving Platform Reference Frame (MPRF), with the origin in the Moving Platform Centroid (MPC). This point is located at the geometric center of the triangle with vertexes in the upper joint axes [26].

The i -th control sensor, fixed to the MOOG platform's plate, records the components (as many as the sensors sensitivity axes) of the acceleration $\mathbf{a}_i(t)$

$$\mathbf{a}_i(t) = \ddot{\mathbf{r}}_i(t) + \mathbf{a}_0(t) + \boldsymbol{\alpha}_0(t) \times \mathbf{r}_i(t) + \boldsymbol{\omega}_0(t) \times [\boldsymbol{\omega}_0(t) \times \mathbf{r}_i(t)] + 2\boldsymbol{\omega}_0(t) \times \dot{\mathbf{r}}_i(t) + \boldsymbol{\epsilon} \quad (20.7)$$

where

- $\mathbf{a}_0(t)$ is the linear acceleration of the point 0.
- $\mathbf{r}_i(t)$, $\dot{\mathbf{r}}_i(t)$ and $\ddot{\mathbf{r}}_i(t)$ are the position, velocity and acceleration of the sensor i relative to the Moving Reference Frame. Since the controls are fixed to the platform's plate, $\mathbf{r}_i(t)$ is time-invariant and the first and the second time derivatives nullify. Therefore it is possible to assume $\mathbf{r}_i(t) = \mathbf{r}_i$ and $\dot{\mathbf{r}}_i(t) = \ddot{\mathbf{r}}_i(t) = 0$.
- $\boldsymbol{\alpha}_0(t) \times \mathbf{r}_i$ is the tangential acceleration of the i -th sensor. $\boldsymbol{\alpha}_0(t) = \dot{\boldsymbol{\omega}}_0(t) = \frac{d}{dt}\boldsymbol{\omega}_0(t)$ and $\boldsymbol{\omega}_0(t)$ are the angular acceleration and angular velocity of the Moving Reference Frame.
- $\boldsymbol{\omega}_0(t) \times [\boldsymbol{\omega}_0(t) \times \mathbf{r}_i(t)]$ is the centrifugal acceleration. For vibration testing typically $\|\boldsymbol{\omega}_0\|^2 \ll \|\boldsymbol{\alpha}_0\|^2$ and the influence of this contribution can be neglected.
- $2\boldsymbol{\omega}_0(t) \times \dot{\mathbf{r}}_i(t)$ is the Coriolis's acceleration. Also this contribution nullifies since $\dot{\mathbf{r}}_i(t) = 0$.

With these considerations, the Eq. (20.7) becomes

$$\mathbf{a}_i(t) = \mathbf{a}_0(t) + \boldsymbol{\alpha}_0(t) \times \mathbf{r}_i \quad (20.8)$$

In order to find the transformation matrix that will allow to get the desired motion reference matrix in terms of control channels reference matrix, it is advantageous to write a vectorial equation for each component of $\mathbf{a}_i(t)$, representative for the acceleration control channels [17]. The canonical basis can be used to select the k -th measurements component

$$\mathbf{a}_i(t) = \begin{cases} a_{i,x}(t) = \mathbf{e}_x^T [\mathbf{a}_0(t) - \mathbf{r}_i \times \boldsymbol{\alpha}_0(t)] \\ a_{i,y}(t) = \mathbf{e}_y^T [\mathbf{a}_0(t) - \mathbf{r}_i \times \boldsymbol{\alpha}_0(t)] \\ a_{i,z}(t) = \mathbf{e}_z^T [\mathbf{a}_0(t) - \mathbf{r}_i \times \boldsymbol{\alpha}_0(t)] \end{cases} \quad (20.9)$$

where $\mathbf{e}_x = [1 \ 0 \ 0]^T$, $\mathbf{e}_y = [0 \ 1 \ 0]^T$, $\mathbf{e}_z = [0 \ 0 \ 1]^T$. Extending Eq. (20.9) to all the control channels it is possible to write

$$\mathbf{a}_{\text{ctrls}}(t) = \begin{cases} a_1(t) = [\mathbf{e}_1^T, (-\mathbf{e}_1^T \times \mathbf{r}_1)][\mathbf{a}_0^T(t), \boldsymbol{\alpha}_0^T(t)]^T \\ a_2(t) = [\mathbf{e}_2^T, (-\mathbf{e}_2^T \times \mathbf{r}_2)][\mathbf{a}_0^T(t), \boldsymbol{\alpha}_0^T(t)]^T \\ \dots \\ a_N(t) = [\mathbf{e}_N^T, (-\mathbf{e}_N^T \times \mathbf{r}_N)][\mathbf{a}_0^T(t), \boldsymbol{\alpha}_0^T(t)]^T \end{cases} \quad (20.10)$$

where N is the total number of the control channels. A closer look at Eq. (20.10) shows that the vector containing the linear and angular acceleration of the global reference frame $\mathbf{a}_{\text{DOF}} = [\mathbf{a}_0^T(t), \boldsymbol{\alpha}_0^T(t)]^T$ is transformed in the linear acceleration recordings measured by the control channels via a time-invariant matrix, depending only on the position of the j -th control channel (i.e. the control channel) and its orientation.

$$\mathbf{a}_{\text{ctrls}}(t) = \mathbf{T}^\dagger \mathbf{a}_{\text{DOF}}(t) \quad (20.11)$$

where the pseudo-inversion is the common case where the number of control channels is greater than six. The transformation from the motion space to the measurement space is known in literature as *Input Transformation* and the matrix $\mathbf{T} \in \mathbb{R}^{N \times 6}$ as *Input Transformation Matrix*

$$\mathbf{a}_{\text{DOF}}(t) = \mathbf{T} \mathbf{a}_{\text{ctrls}}(t) \quad (20.12)$$

$$\mathbf{T} = \begin{bmatrix} \mathbf{e}_1^T, (-\mathbf{e}_1^T \times \mathbf{r}_1) \\ \dots \\ \mathbf{e}_N^T, (-\mathbf{e}_N^T \times \mathbf{r}_N) \end{bmatrix} \quad (20.13)$$

From (20.11), (20.12) and the definition of SDMs [27] it is possible to obtain the same relations in terms of SDMs

$$\mathbf{S}_{yy\text{DOF}} = \mathbf{T} \mathbf{S}_{yy\text{ctrls}} \mathbf{T}^T \quad (20.14)$$

$$\mathbf{S}_{yy\text{ctrls}} = \mathbf{T}^\dagger \mathbf{S}_{yy\text{DOF}} \mathbf{T}^{\dagger T} \quad (20.15)$$

and therefore to transform a Multi-Axial random control target defined in the motion space in terms of control channels PSDs, coherence and phases. From Eq. (20.14) it is easy to check that, in case the reference matrix, defined in terms of degrees of freedom is positive semi-definite, also the corresponding matrix in terms of control channels is positive semi-definite.¹

¹It follows the definition of positive semi-definite matrices that, if \mathbf{A} is positive semi-definite, the matrix $\mathbf{C} = \mathbf{B}\mathbf{A}\mathbf{B}^H$, resulting from the bracket product operation, preserves the property. Obviously the same consideration applies if \mathbf{B} is a matrix with real entries and $\mathbf{B}^H = \mathbf{B}^T$.

20.4 Time Waveform Replication (TWR)

Time Waveform Replication (TWR) is used to replicate multiple time histories, for a user defined number of control channels, by driving multiple shakers or the multiple degrees of freedom of a multi-axis shaking system.

The control target is a set of reference time recordings (e.g. acceleration time histories) to be replicated. Also in this case, before the actual control test, a System Identification is run to get a low level random estimation of the system's FRFs. With this information and the spectra of the target $\mathbf{r}(f)$, the drives that theoretically return the reference time histories can be easily computed as

$$\mathbf{u}(t) = \text{iFFT}[\hat{\mathbf{Z}}(f)\mathbf{r}(f)] \quad (20.16)$$

However, inevitable mismatches between the estimated system and the real system's dynamic behavior, bring the necessity of iterative correcting the drives, as shown in Fig. 20.6, in order to compensate for the error between the recorded responses and the reference signals [21].

The complete error time histories need to be used to correct the drives. The control loop, contrarily to the MIMO random's one, takes place off-line and the full re-play of the corrected drives needs to be performed before the next iteration. It is remarkable to notice that, as shown in the block scheme of Fig. 20.6, a control gain diagonal matrix \mathbf{K} (with entries between 0 and 1) weights the error to be corrected in the next iteration, in order to prevent control instabilities.

Different metrics can be used to define the convergence rate of the process. A meaningful choice is to have as metric a *Composite Error*, combining the peak and the rms error

$$\mathbf{e}_{comp}(t) = \frac{\text{rms}[\mathbf{e}(t)]}{\text{rms}[\mathbf{r}(t)]} \alpha + \frac{\text{peak}[\mathbf{e}(t)]}{\text{peak}[\mathbf{r}(t)]} (1 - \alpha) \quad (20.17)$$

where α is a tunable weighting factor between 0 and 1. The threshold set on the defined metric determines the *Convergence Reached* status of the test. A user-defined maximum number of iterations can also be set as limit to end the test.

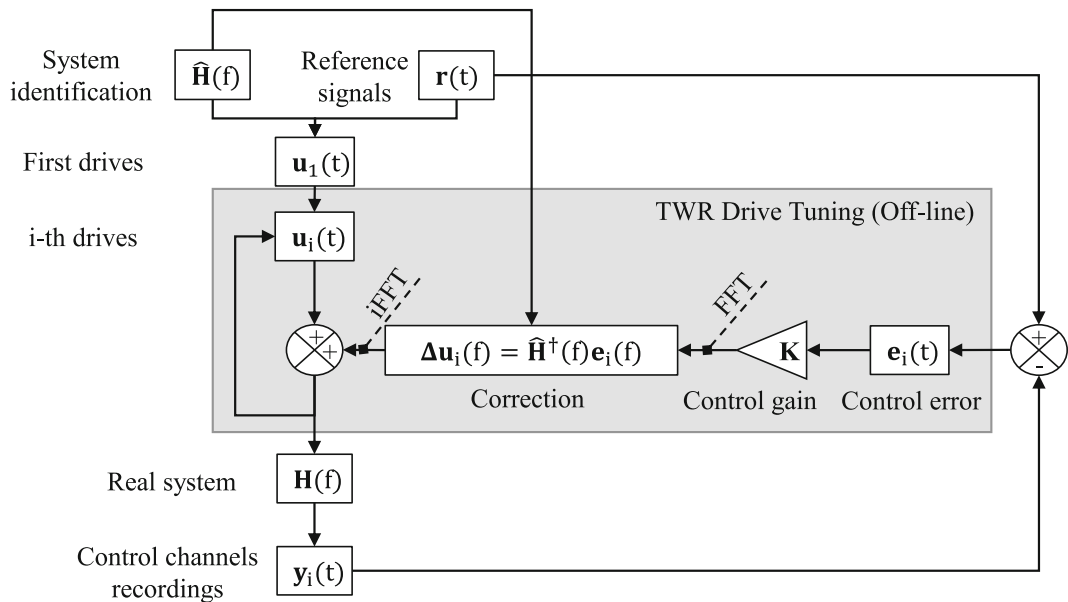


Fig. 20.6 Time waveform replication general block scheme

20.5 Environmental Testing with the MOOG Platform

The MOOG platform is driven with a Siemens LMS SCADAS mobile via the applications Siemens Simcenter LMS Test.Lab Multi-Axis Random Control (MIMO Random Control) and Time Waveform Replication (TWR). The communication architecture designed for controlling the MOOG platform is explained in detail in the Sect. 20.2.

20.5.1 MIMO Random Control of the MOOG Platform

MIMO Random Control requires the specification of the target in terms of control channels, as discussed in the Section 20.3.1.1. The platform's DOF Control is possible by taking the coordinates of the control sensors, defining the reference matrix in the motion space, building the Input Transformation Matrix for the sensors configuration chosen and retrieving the reference matrix in terms of control channels using Eq. 20.15. Once the control results are known in terms of the control channels SDM, the achieved DOF SDM can be computed with a backward transformation, as shown in Eq. 20.14. The block scheme of the entire process is illustrated in Fig. 20.7.

For these preliminary experiments, the frequency band of interest has been set to [0.1 – 15.6] Hz and the accelerations rms levels kept low (0.03 g_{RMS}). The moving reference frame is the MPRF, with center in the MPC. In order to accurately measure and control also in the very low frequencies, DC accelerometers have been selected as control sensors. The approximate coordinates of the accelerometers (DC1, DC3 and DC4) in the MPRF, are reported in Fig. 20.8b and listed in Table 20.2. The six control channels chosen are the DC1:+X, DC1:-Y, DC1:-Z, DC3:-Y, DC3:-Z and DC4:-Z as reported in Fig. 20.8. The control channels selection needs to be able to fully capture the six degrees of freedom motion. For the translations, it is obviously necessary to have at least one channel per axis. Less trivial is to unequivocally be able to assess the roll, pitch and yaw rotations. Since the drive signals are the six degrees of freedom, a wrong choice of the control channels or misplaced sensors influence the FRFs matrix's conditioning with respect to the pseudo-inversion. A useful tool to check upfront if the configuration chosen is able to capture the full six-degrees of freedom motion is the rank of transformation matrix \mathbf{T} . A matrix \mathbf{T} with rank smaller than six indicates that two or more DOFs are linearly dependent with the configuration chosen. The setup used for the tests, as shown in Fig. 20.8 returns a full rank transformation matrix.

A rank-deficient sensor configuration can be obtained by selecting the control channel DC3:+X in place of the control channel DC4:-Z. The resulting transformation matrix has rank five. A closer analysis of this configuration shows that the only two channels able to capture the roll and the pitch rotations (DC3:-Z and DC1:-Z) can only identify a rotation around a skewed axis in the XY plane of the MPRF, therefore a linear combination of roll and pitch. The control channel DC4:-Z will solve the issue (the pitch and roll are unequivocally identified by the pairs DC3:-Z, DC4:-Z and DC1:-Z, DC4:-Z, respectively).

In Fig. 20.9 the Singular Values of the FRF matrix obtained with a low level random system identification and the matrix Condition Number are reported in the frequency band of interest. To have a control configuration with a low condition number is fundamental for the MIMO Random vibration control test, since a (pseudo-) inversion operation is always needed to calculate and then correct the drives. Figure 20.9a, b correspond to the used control channel configuration (full rank input

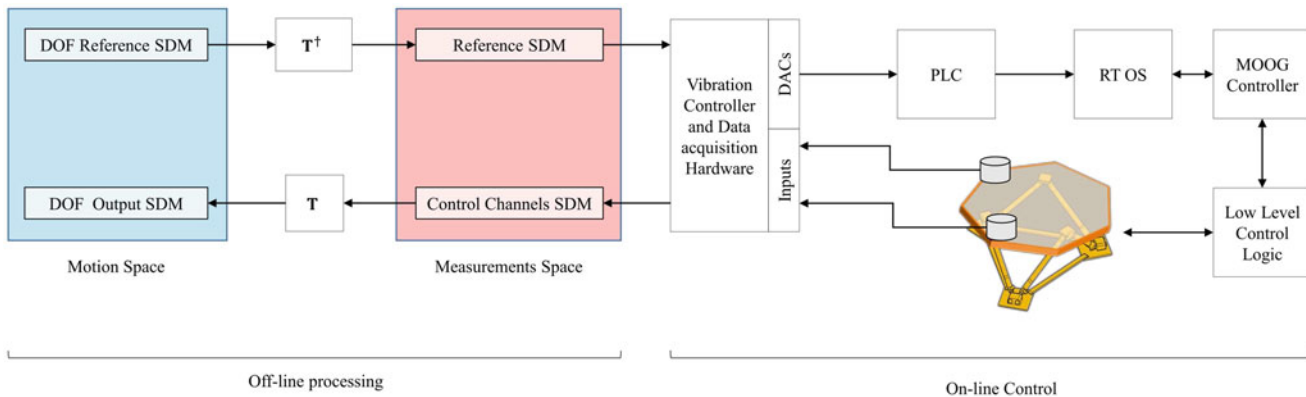


Fig. 20.7 Multi-axial random vibration control of the MOOG platform: block scheme

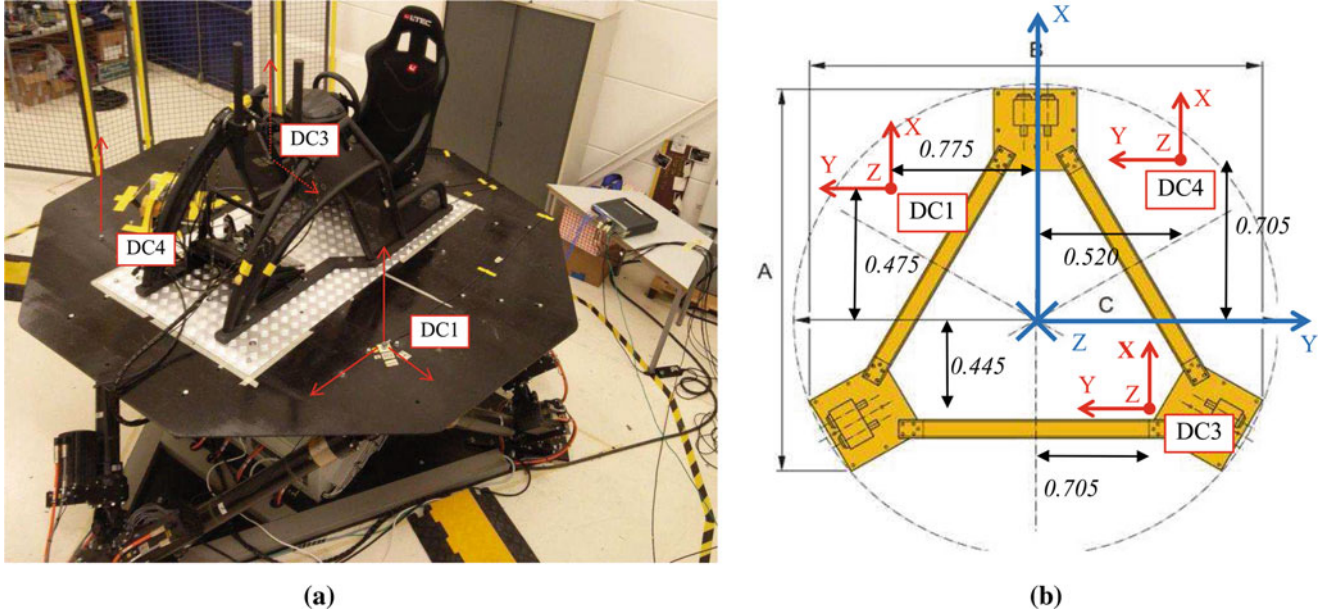


Fig. 20.8 MIMO random control test setup. (a) Sensors configuration. (b) Sensors positions in the MPRF (blue axes). The plate top surface is approximately 0.148 m above the MPC. All distances in meters

Table 20.2 Position of the control sensors in the moving platform reference frame

MPRF	DC1	DC3	DC4
X	0.475	-0.445	0.705
Y	-0.775	0.705	0.520
Z	-0.148	-0.148	-0.148

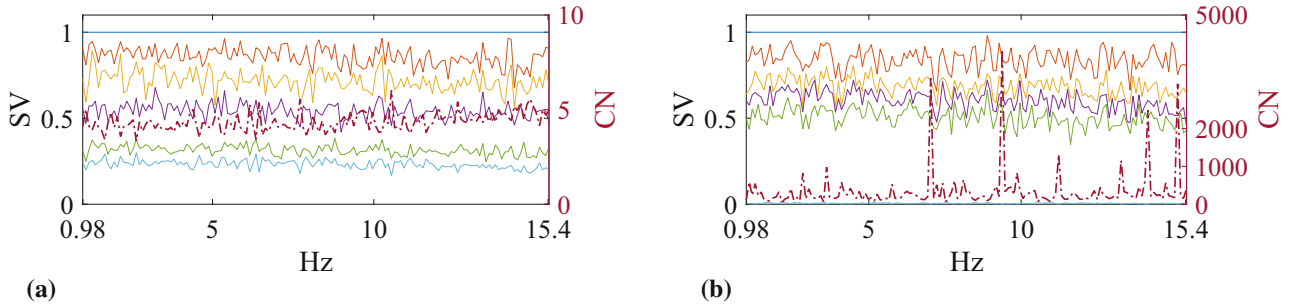


Fig. 20.9 Influence of the control channels selection on the system's FRFs matrix conditioning. (a) Singular values ratio and condition number of the system's FRF matrix for the sensor configuration shown in Fig. 20.8a. The corresponding matrix \mathbf{T} is full rank. (b) Singular values ratio and condition number of an ill-conditioned system's FRF matrix. Compared with the sensors configuration of Fig. 20.8a, the control channel DC4:+Z is replaced by DC3:+X. The corresponding matrix \mathbf{T} is rank deficient

transformation matrix), and the aforementioned configuration with a rank-deficient transformation matrix. From the figures it is possible to see that the rank-deficient configuration is associated to an FRF matrix with a very small singular value (close to zero) and it is inherently ill-conditioned in the whole frequency band. On the other hand, the Condition Number of the FRF matrix associated to the full-rank transformation matrix, shows that the smallest singular value is approximately just one-fifth of the biggest one in the whole frequency band of interest.

MIMO random tests have been run setting six different targets in the frequency band [0.98 – 15.4] Hz, defined in the motion space. Each target corresponds to a single degrees of freedom excitation scenario (*pure* surge, sway, heave and roll, pitch, yaw). For each degree of freedom, a classic segmented PSDs has been used, corresponding to an overall response level at the control locations of $0.03 \text{ g}_{\text{RMS}}$ and $0.03 \text{ (rad/s}^2\text{)}_{\text{RMS}}$ whereas all the other DOF profiles are scaled down to get overall response levels three order of magnitude smaller (a value of zero cannot be used for numerical reasons). In the motion space the reference spectral density matrix has been filled in considering independent DOF responses (the coherence between the different degrees of freedom is set to 0.01).

In order to run the tests, from the targets defined in the motion space, the corresponding target in terms of control channels are calculated using Eq. (20.11) with the Frequency Response Functions obtained in the pre-test low level random System Identification. Before the actual tests, the expected drives and response levels can be obtained with a pre-test system verification. These levels are shown in the bar plots of Figs. 20.10 and 20.11 for the MIMO random targets corresponding to the pure translations and pure rotations in the motion space, respectively. It is worthwhile to remark that the system verification is run on the reference matrix transformed from the motion space to the space of the control sensors and therefore the verified levels show before hand which control channels contributes the most to the DOF response targeted. For the translations, the control channels that will record the highest levels are indeed the ones with the sensitive axis parallel to the main axis of excitation. For the rotations

1. the roll motion accelerations are recorded by the control channels DC1:-Z, DC3:-Z, DC4:-Z and the levels reflect the sensor's distance from the surge axis in the MPRF;

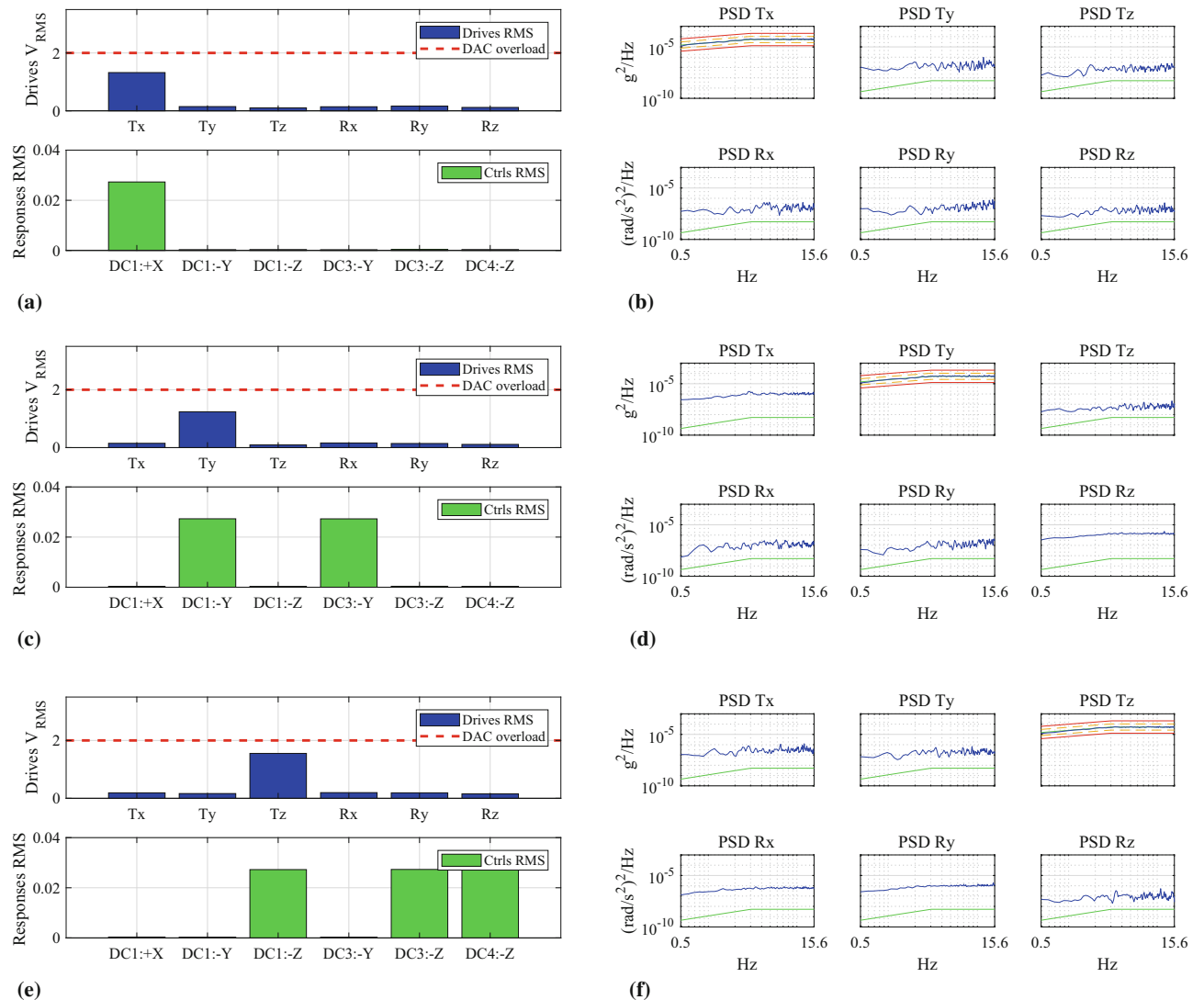


Fig. 20.10 Pre-test level verification and control results for the three MIMO random test with the targets set as pure translations. **(a)** Predicted levels (drives and responses) for the pure surge (Tx) MIMO random test. **(b)** Pure surge (Tx) MIMO random test results at the normal end. **(c)** Predicted levels (drives and responses) for the pure sway (Ty) MIMO random test. **(d)** Pure sway (Ty) MIMO random test results at the normal end. **(e)** Predicted levels (drives and responses) for the pure heave (Tz) MIMO random test. **(f)** Pure heave (Tz) MIMO random test results at the normal end

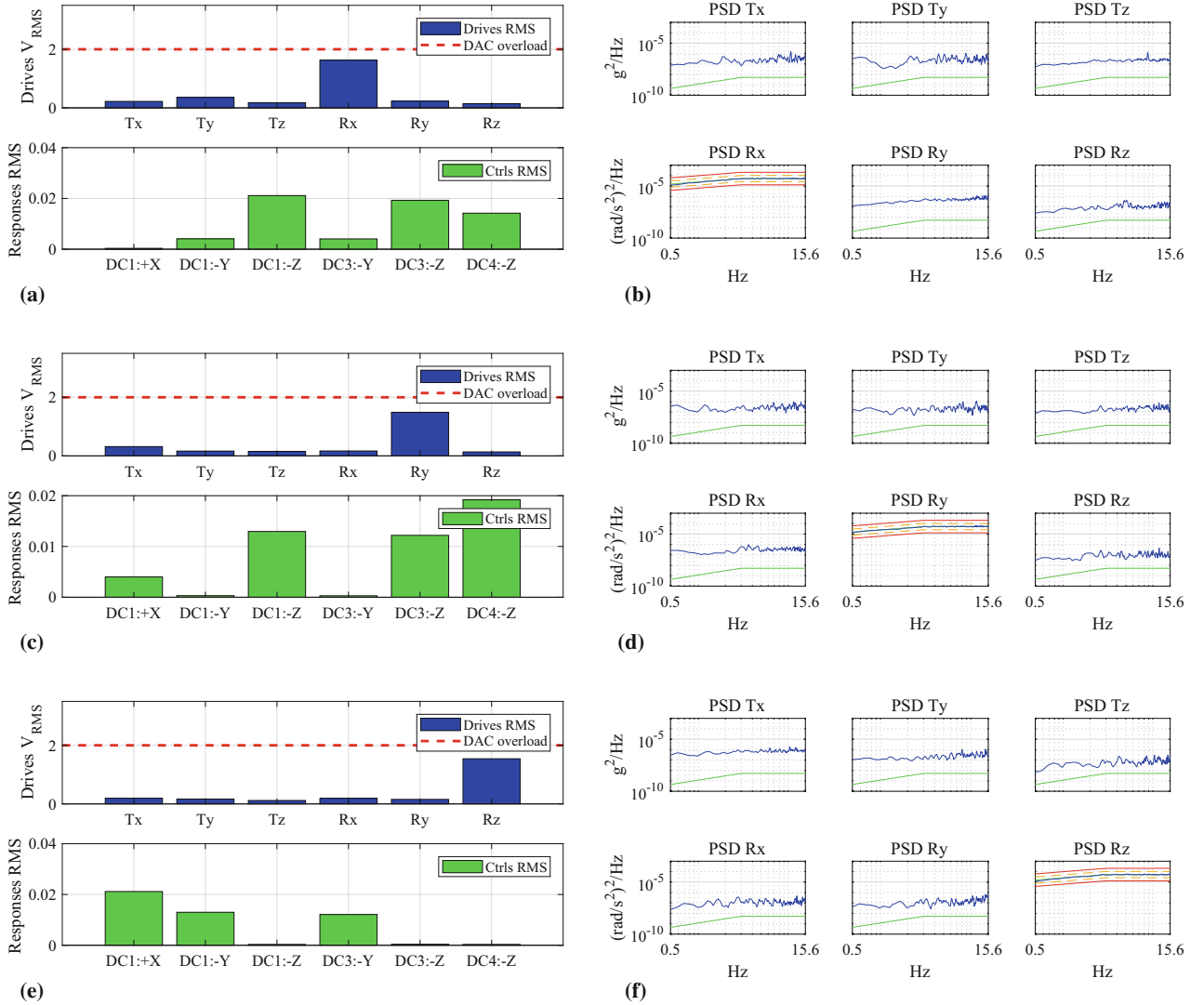


Fig. 20.11 Pre-test level verification and control results for the three MIMO random test with the targets set as pure rotations. **(a)** Predicted levels (drives and responses) for the pure roll (Rx) MIMO random test. **(b)** Pure roll (Rx) MIMO random test results at the normal end. **(c)** Predicted levels (drives and responses) for the pure pitch (Ry) MIMO random test. **(d)** Pure pitch (Ry) MIMO random test results at the normal end. **(e)** Predicted levels (drives and responses) for the pure yaw (Rz) MIMO random test. **(f)** Pure yaw (Rz) MIMO random test results at the normal end

2. the same sensors records the highest levels for the pure pitch motion. It is interesting to notice that also the predicted levels for the channel DC1:+X are not negligible, possibly indicating that the Z coordinates of the control sensors are . This can be due to small errors in retrieving the exact location of this point (the MPC is not easily accessible).
3. The X and Y control channels levels are finally recording the highest levels for the yaw motion. To notice that the predicted responses for the control channels DC1:-Y and DC3:-Y are approximately the same, as expected given the almost same distances from the yaw axis, whereas the DC:+X predicted response is higher.

Figures 20.10 and 20.11 also show the MIMO random control results in the motion space after transforming the response Spectral Density Matrix at the normal end of the test in the motion SDM through Eq. (20.12). All the results show that the main degree of freedom excited perfectly follows within the alarm limits the reference profile whereas all the others are kept to much lower values (with narrowband PSD values at least two order of magnitude smaller).

20.5.2 Time Waveform Replication: Earthquake Replication with the MOOG Platform

A TWR test is performed using the MOOG platform as three-axis exciter and the Siemens LMS SCADAS mobile driven by the Simcenter LMS Test.Lab Time Waveform Replication. The test set-up is the one reported in Fig. 20.8, using as control channels the three sensitive axes of the accelerometer DC1.

The chosen targets are the North-South (X direction in the fixed reference frame), East-West (Y direction) and Up-Down (Z direction) acceleration recordings of the 1940 El Centro earthquake (El Centro, California, 18 May 1940), publicly available on the web. According to the US earthquake database [28] and web sources, *it was the strongest recorded earthquake to hit the Imperial Valley, and caused widespread damages to irrigation systems and nine fatalities*. For safety reasons, the recorded waveforms used as targets are scaled down of a factor 10. The first drives are also calculated by using just the 60% of the target, in order to gradually achieve the test levels. The control gains are set to 0.8.

Figure 20.12 shows the control results of the test run. Figure 20.12a shows the responses after the first iteration, gradually brought to convergence (composite error threshold set to 0.1) in ten iterations. The accelerations time histories at the end of the test are shown in Fig. 20.12b, together with a detail plot of the time windows [2–6] s. The evolution of the composite error during the control process is shown in Fig. 20.13.

The results shown in this section highlight two main achievements of the current work: primarily, with the proposed communication architecture the on-line multi-axis control of the MOOG platform is with the Siemens Simcenter LMS Test.Lab environmental solutions is realizable. Easily implementable coordinate transformations allow the possibility of controlling the SDM associated with virtual channels representing the degrees of freedom of the moving reference frame, rather than the classical control channels reference SDM.

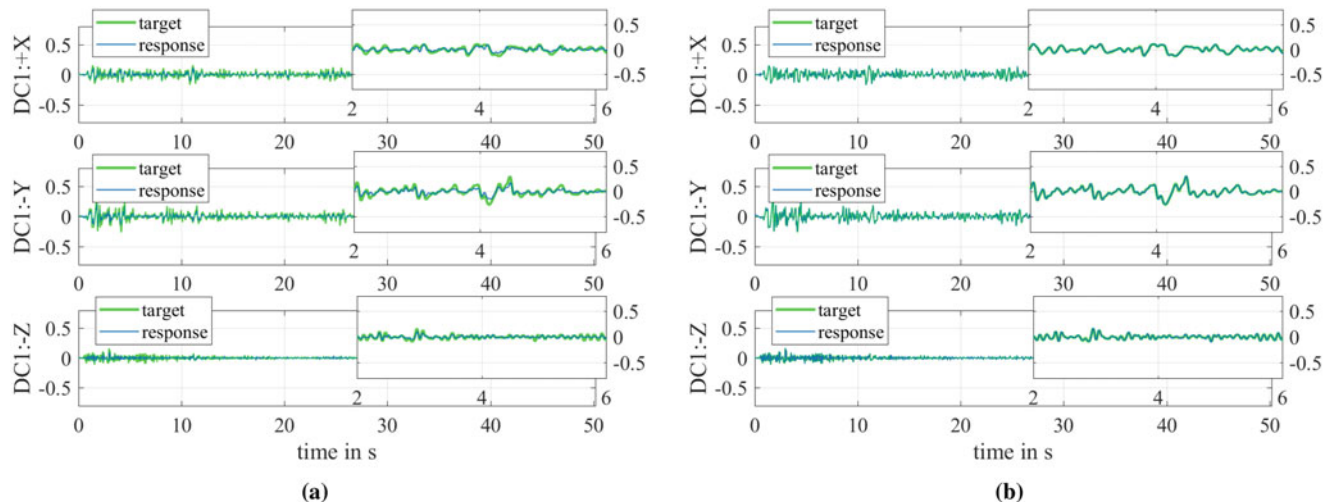


Fig. 20.12 Scaled El Centro earthquake waveform replication. Accelerations in g. (a) First iteration. Full time histories (50 s) and detail (2–6 s). (b) Last iteration. Full time histories (50 s) and detail (2–6 s)

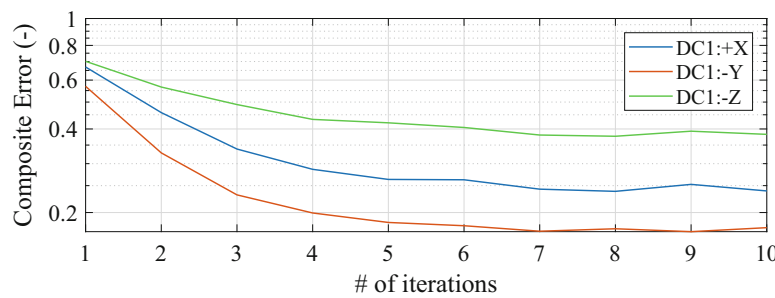


Fig. 20.13 Evolution of the composite error during the time waveform replication test

The capabilities of the software and the hardware of replicate arbitrary time histories in user-defined control channels have been also shown by successfully replicating with the MOOG platform and the Simcenter LMS Time Waveform Replication application (scaled) accelerations recordings of the 1940 El Centro earthquake.

20.6 Conclusions

In this paper an advanced state-of-the-art vibration controller typically used for environmental testing with traditional shakers, has been combined with a six degrees of freedom motion platform. The necessity of sending the analog drives, generated with the vibration controller, via UDP/IP in order to communicate with the platform's control logic, has been tackled by including in the communication chain a Programmable Logic Controller (PLC). In the PLC a main program runs continuously, reading the drives and creating an UDP datagram that can be read by a real time operative system and then forwarded to the platform. Once the communication between the two hardware has been established, the possibility of performing Multi-Input Multi-Output random vibration control tests by setting the control target in the motion space rather than the control channels, has been investigated. Off-line Input Transformations commuting the target from the motion space to the control channels have been theoretically exploited and implemented for the motion platform's DOF control. The input Transformation matrix shows also to be an useful tool to evaluate before hand the system conditioning with respect to the system's FRF matrix inversion. A series of MIMO random control experiments has been successfully run to test the capabilities of the solutions developed. Finally, the capabilities of using the six-DOF motion platform together with a state-of-the-art Time Waveform Replication software have been exploited to replicate the publicly available acceleration recordings of the 1940 El Centro Earthquake, opportunely scaled.

Acknowledgements The financial support of VLAIO is gratefully acknowledged (research grant *ADVENT: ADvanced Vibration ENvironmental Testing*).

References

1. United States Standard 810G: Method 514: vibrations (2008)
2. United States Standard 810G: Method 527.1: multi-exciter tests (2008)
3. Ernst, M., Habtour, E., Abhijit, D., Polhand, M., Robeson, M., M. Paulus: Comparison of electronic component durability under uniaxial and multiaxial random vibrations. *J. Electron. Packag.* **137**, 165–80 (2015)
4. Gregory, D., Bitsie, F., Smallwood, D.O.: Comparison of the response of a simple structure to single axis and multiple axis random vibration inputs. In: Proceedings of the 79th shock and vibration symposium (2008)
5. Daborn, P.M., Ind, P.R., Ewins, D.J.: Enhanced ground vibration testing for aerodynamic environments. *Mech. Syst. Signal Process.* **49**, 165–80 (2014)
6. Daborn, P.M., Ind, P.R., Ewins, D.J.: Next-generation random vibration tests. *Top. Modal Anal. II* **8**, 397–410 (2014)
7. Underwood, M.A.: Multi-exciter testing applications, theory and practice. In: Proceedings of Institute of Environmental Sciences and Technology (2002)
8. Underwood, M.A., Keller, T: Recent system developments for multi-actuator vibration control. *Sound Vib.* **35**, 16–30 (2001)
9. Smallwood, D.O.: Multiple-input multiple-output (MIMO) linear system extreme inputs/outputs. *Shock Vib.* **14**(2), 107 (2007)
10. Musella, U., D'Elia, G., Manzato, S., Peeters, B., Guillaume, P., Marulo, F.: Analyses of target definition processes for MIMO random vibration control tests. In: Proceedings of the XXXV IMAC Conference (2017)
11. Musella, U., D'Elia, G., Manzato, S., Peeters, B., Guillaume, P., Mucchi E., Marulo, F.: Tackling the target matrix definition in MIMO random vibration control testing. In: Proceedings of the 30th Aerospace Testing Seminar (2017)
12. Musella, U., Peeters, B., Guillaume, P., Carrella, A.: Minimum drives spectral density matrix for MIMO random vibration control tests: application cases. In: Proceedings of the Institute of Environmental Science and Technology (2017)
13. Stewart, D.: A platform with six degrees of freedom. *Proc. Inst. Mech. Eng.* **1**, 180 (1965)
14. Underwood, M.A., Ayres, R., Keller, T.: Filling in the MIMO matrix part 1 – performing random tests using field data. *Sound Vib.* **45**, 8–14 (2011)
15. Daborn, P.: Scaling up the impedance-matched multi-axis test (IMMAT) technique. In: Proceedings of the XXXV IMAC (2017)
16. Jacobs, L., Ross, M., Tipton, G., Cross, K., Hunter, N., Harvie, J., Nelson, G.: Experimental execution of 6-dof tests derived from field tests. In: Proceedings of the XXXV IMAC (2017)
17. Fitz-Coy, N., Nagabhushan, V., Hale, M.T.: Benefits and challenges of over-actuated excitation systems. *Shock Vib.* **17**, 285–303 (2010)
18. Underwood, M.A., Keller, T.: Applying coordinate transformations to multi-DOF shaker control. *Sound Vib.* **40**, 14–20 (2006)
19. De Cuyper, J.: Linear feedback control for durability test rigs in the automotive industry. Ph.D. thesis, KU Leuven (2006)
20. Moten, S.: Enhancing model based system engineering for mechatronic systems. Ph.D. dissertation, KU Leuven, Leuven (2017)

21. Cornelis, B.: Adaptive modelling for improved control in durability test rigs. In: Proceedings of the 20th International Congress on Sound and Vibration (2013)
22. MOOG: Electric and hydraulic motion bases for a wide range of payload applications: system specification. PSS26853 Issue 3.0 (2014)
23. Peeters, B., Debillie, J.: Multiple-input-multiple-output random vibration control: theory and practice. Proc. Int. Conf. Noise Vib. Eng. **1**, 507–16 (2002)
24. Smallwood, D.O.: Multiple shaker random vibration control – an update. In: Proceedings of the Institute of Environmental Sciences and Technology (1999)
25. Musella, U., Manzato, S., Peeters, B., Guillaume, P.: CR-calculus and adaptive array theory applied to MIMO random vibration control tests. J. Phys. Conf. Ser. **744**, 012175 (2016)
26. MOOG: Interface manual: motion real-time software. CDS27206, Issue 2.0 (2013)
27. Bendat, J., Piersol, A. G.: Random data. Wiley, Hoboken (2011)
28. Southern California Earthquake Data Center at CalTech: Imperial Valley earthquake (July 2010)



Chapter 21

The Yellow Frame: Experimental Studies and Remote Monitoring of the Structural Health Monitoring Benchmark Structure

A. Mendler, C. E. Ventura, and S. Allahdadian

Abstract This paper provides a summary of the various vibration tests that have been recently conducted on the test frame that has been used for various studies, starting from the IASC-ASCE benchmark for vibration damage identification technologies created in the early 2000s. The tests conducted include ambient-vibrations of various configurations of the test frame, which simulate different levels of structural damage. A detailed description of the conducted tests, as well as modal analyses of selected damage scenarios are included in the paper. This system will be online by mid-2018, and will allow interested parties to acquire real-time data from ambient vibration tests. Long term damage detection studies are also possible to be conducted.

Keywords Benchmark · Modular frame · Continuous monitoring · SSI-PC · Statistical subspace damage detection

21.1 Introduction

From the beginning, a major challenge in structural health monitoring research has been the acquisition of damage-corrupted data of real structures. To lay the foundations for future studies, the Earthquake Engineering Research Facility (EERF) established a modular frame structure at the University of British Columbia (UBC) in 1997 [1, 2]. Two years later, the frame was tested on the shake table, and later it was moved to the courtyard of the research facility and set up for continuous monitoring and numerous vibration tests. In an effort to unite the international research on SHM technology, the versatile frame structure was declared a baseline model in 1999, and numerous damage detection studies on the benchmark problem—of numerical and experimental nature—were initiated by the U.S. task group that had formed under the auspices of the American Society of Civil Engineers (ASCE) and the International Association for Structural Control (IASC) [3]. In 2000 and 2002, a series of shaker, hammer and ambient vibration tests were performed, while gradually removing brace elements, or by losing the bolted connections, [4]. However, the acquisition of damage-corrupted data remained challenging, and that is why the Yellow Frame remains in heavy use to date (Fig. 21.1).

21.2 Purpose

This paper pursues two objectives, it is meant to summarize the most recent tests conducted on the Yellow Frame, and to demonstrate how suitable the frame is to train, test and validate modern damage detection algorithms. In other words, it is an invitation to the engineering community to collaborative research on the benchmark structure. It is organized in five subsequent sections. First, the Yellow Frame structure is described, giving detailed information on the individual modules, cross sections and materials, as well as applied modelling simplifications. Secondly, the instrumentation is documented for the most recently conducted ambient vibration tests, describing the sensor layout as well as all data acquisition and signal processing units. Thirdly, it is explained how damage can be simulated by removing braces, and next, the basic modal properties are juxtaposed for several damage scenarios. Ultimately, a cutting-edge damage assessment method is applied to the recorded ambient vibration data showcasing the results from a recent research project at UBC.

A. Mendler · C. E. Ventura · S. Allahdadian (✉)
Department of Civil Engineering, University of British Columbia, Vancouver, BC, Canada



Fig. 21.1 Photo of the Yellow Frame [4]

Table 21.1 Material and cross sectional values [1]

Module	Type	Material	b [mm]	h [mm]	t [mm]	w [mm]	A [mm ²]	I _y [mm ⁴]	I _x [mm ⁴]
Column	B100 × 9 typ.	W300	100	99	4.76	3.2	1133	1.97×10^6	6.46×10^5
Beam	S75 × 11 typ.	W300	64	76	6.6	9.9	1430	1.22×10^6	2.49×10^5
Braces	Threaded rod	N/A	12.5	12.5				N/A	N/A
Stiffener	Square tube	N/A	51	51	6.4			N/A	N/A

21.3 Frame Description

In this section, it is explained how versatile the test structure is, and details are given on the configuration used in recent damage assessment tests [5].

21.3.1 Frame Modules

The Yellow Frame is a steel frame construction kit consisting of column, beam and brace modules which can be assembled arbitrarily to model any real structure scaled down by a factor of approximately three. The I-shaped beam and column modules are S75 × 11 and B100 × 9 sections, respectively, made of hot rolled steel with a nominal yield strength of 300 MPa. The modular nature of the Yellow Frame allows it to be tested in multiple configurations, both braced and unbraced, and different sets of diagonal or crossed braces can be added to each bay, e.g. 25 × 25 × 3 L-profiles or 12.5 mm steel rods. It is also possible to redistribute the applied floor masses as desired. The cross sections and materials are further specified in Table 21.1.

21.3.2 Benchmark Test Configuration

In the current test configuration, the frame serves as a benchmark structure for structural health monitoring defined by the IASC and ASCE taskforce in 1999. The frame replicates a four-story building with two bays in each direction. The double-

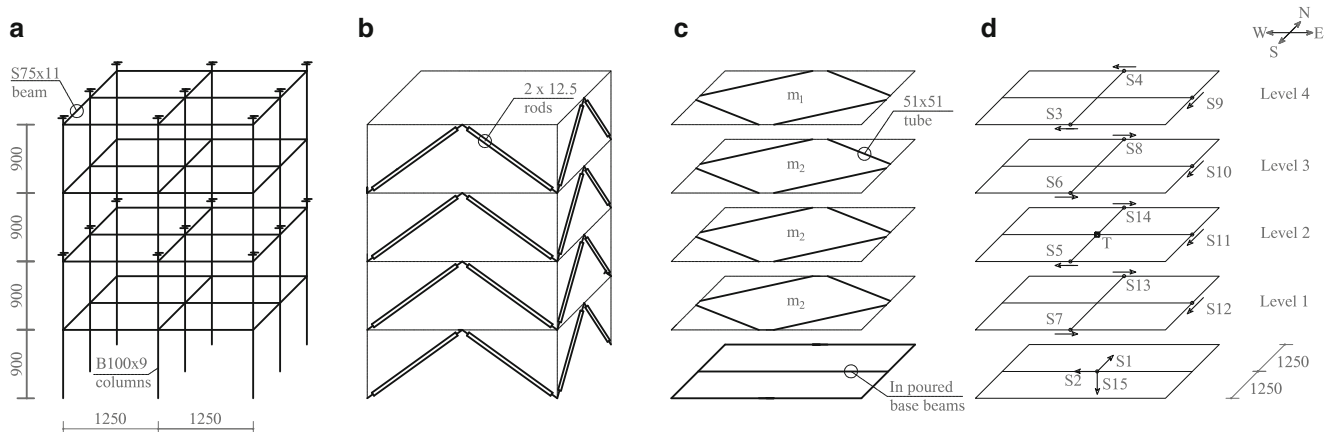


Fig. 21.2 Yellow Frame wireframe (a) gravity system, (b) chevron bracing, (c) in-plane stiffener, (d) instrumentation

symmetrical layout has a width of 2.5 m, and the two stacked column modules create a total height of 3.6 m, or 0.9 m per storey (Fig. 21.2a). The gravity system, therefore, consists of 12 identical beam modules per level, and a total number of nine steel columns which are resting on steel base beams partially encased in concrete (Fig. 21.2a). To add lateral stiffness, the four exterior walls are braced in a chevron configuration, with two concentrically placed pairs of threaded steel rods for each wall and level (Fig. 21.2b). In addition, four 51 mm square steel tubes are added to each level above ground providing in-plane stability (Fig. 21.2c). The I-shaped columns also contribute to the lateral stiffness, and cause the N-S direction to be the strong axis; however, the lateral stiffness is dominated by the stiffness of the braces, and therefore, the stiffness in the N-S and E-W direction are almost identical in the reference configuration. Four $1.5 \text{ m} \times 0.65 \text{ m}$ steel plates are added to each level above ground to simulate the dead load. From the 1st Level to the 3rd Level, a mass of $m_2 = 1815 \text{ kg}$ is applied, and for the 4th Level, it is reduced to $m_1 = 1360 \text{ kg}$ (Fig. 21.2c). To activate torsional modes, a slightly eccentric arrangement is pursued.

21.3.3 Modelling Simplification

In preparation for both the modal analysis and damage localization, a finite element model has been prepared in Abaqus® [6]. Since the model is merely used to estimate the frequency range of interest and to obtain spatial information on the stiffness distribution, it appears that radical modeling assumptions can be made. These assumptions are (a) braces are pinned axial members (b) with the exception of the braces, all beam-column connections are rigid, (c) the connection to the base beam and ground is fixed, (d) the modal damping is set to 2% critical damping. For other studies not mentioned in this paper, more complex models have also been prepared in SAP2000® considering the flexibility in the joints.

21.4 Instrumentation

This section will concisely summarize the instrumentation during recent tests [5]. First, the sensor layout and the data acquisition systems are described, followed by two sections on the data acquisition and remote monitoring capabilities.

21.4.1 Sensor Layout

To fully capture the vibration behaviour of the Yellow Frame, wired force balance accelerometers are placed on both the structure and the ground. A clear instrumentation plan is provided in Fig. 21.2d. On each level above ground, three uni-axial sensors are aligned in horizontal direction, with an acceleration range of $\pm 1.0 \text{ g}$ and a frequency range of up to 50 Hz. This sums up to a total number of 12 sensors on the structure. Another tri-axial EPISensor is placed centrally on ground level with

Table 21.2 Accelerometer specification

Measurand	Orientation	Type	Frequency range	Acceleration range	Brand
Acceleration	Uni-axial	FBA-11	DC to 50 Hz	$\pm 1.0 \text{ g}$	Kinemetrics®
	Tri-axial	EPISensor	DC to 200 Hz	$\pm 0.25 \text{ g}$ up to $\pm 4 \text{ g}$	Kinemetrics®

a higher frequency range of up to 200 Hz, and is capable of measuring up to $\pm 4 \text{ g}$ accelerations. This sensor is used to record ground motions and for studying the soil structure interaction. In addition to the accelerometer, a temperature or moisture sensor can be included at any location. In recent tests, it was placed below the 2nd Level, and denoted with the letter “T” in Fig. 21.2d. A summary of the sensor specifications is given in Table 21.2.

21.4.2 Data Acquisition

To acquire the signals, the DASYLab® software is used in combination with the IOTech DaqBook/216, which is a PC-based data acquisition unit with up to 16 programmable input channels. The 100 kHz unit has a 16 bit analogue-to-digital converter, and allows 16 signals to be sampled with a frequency of up to 1200 Hz. The signal conditioning modules (IOTech DKB18) inside the unit include low-pass filters as well as instrumentation amplifiers, which can be set to a gain of 10, 100, 200, or 500. The software used for the signal processing is the included DaqView® Version 5.0.

21.4.3 Remote Continuous Monitoring

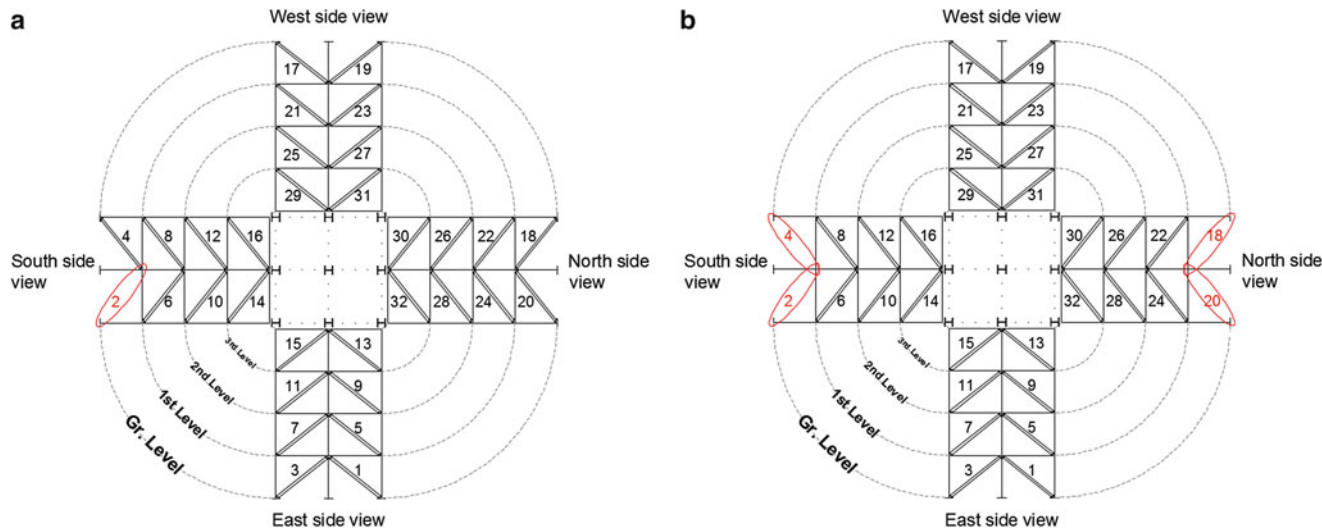
The structure is equipped with accelerometers as well as with ambient temperature or moisture sensors. Therefore, it is suitable for both short-term tests under laboratory conditions as well as long-term test studying the changes in the modal solution due to temperature and humidity effects, changing excitation mechanisms and noise levels. These external variables are also referred to as environmental and operational variables (EOV) [7]. Remote access to the system will be available to interested parties in mid-2018. Please contact the second author at ventura@civil.ubc.ca for further information.

21.5 Test Description

The conducted damage simulations follow a well-established pattern which is almost identical to former tests on the Yellow Frame [4]. However, the most recent arrangement with pairs of threaded braces instead of L-shaped braces allows a larger number of simulated damage scenarios. The general idea is to gradually remove braces, and thus, modify the seismic force resisting system in a strategic manner, including several symmetrical and asymmetrical damage scenarios on one and multiple levels. Earthquake loads create high shear forces on the ground level, and often damage concentrates here. That is why in the first nine damage scenarios, C1-C9, several sets of braces have been removed on this level, simulating a total failure. In scenarios C10-C11, and in scenario C12, braces fail on the 2nd level and on the 1st level above ground, respectively, while the failing braces are widely distributed over the structure in all other cases. The first nine scenarios, C1-C9, will be examined in this paper, and all following considerations will be built upon the damage scenarios described in Table 21.3. Herein, a damage scenario is characterized by the element location label followed by the number of removed braces at that location in superscript. In damage scenario C1, for example, one brace is removed at location two, denoted by 2^1 , and the corresponding element location at the south side of the frame can be found in Fig. 21.3. A drawing for each of the first nine damage scenarios can be found in Appendix A, with red circles indicating the location of the removed braces.

Table 21.3 First nine damage scenarios on the ground level

Damage scenarios		C1	C2	C3	C4	C5	C6	C7	C8	C9
S		2 ^I	2 ^{II}	2 ^I – 4 ^I	2 ^{II} – 4 ^{II}	2 ^{II} + 4 ^{II}	2 ^{II} + 4 ^{II}	2 ^{II} + 4 ^{II}	2 ^I + 4 ^I	2 ^{II} + 4 ^{II}
N						18 ^I + 20 ^I	18 ^{II} + 20 ^{II}		18 ^I + 20 ^I	18 ^{II} + 20 ^{II}
W								17 ^{II} + 19 ^{II}	17 ^I + 19 ^I	17 ^{II} + 19 ^{II}
E									1 ^I + 3 ^I	1 ^{II} + 3 ^{II}

**Fig. 21.3** (a) Damage scenario C2, (b) damage scenario C6 [5]

21.6 Operational Modal Analysis

In this section, the results from the operational modal analysis for both the reference configuration as well as several damage scenarios are given. The results will help to understand the dynamic behaviour of the Yellow Frame and how it changes for several damage scenarios, but they will only indirectly be used for the damage assessment method introduced in Sect. 21.7.

21.6.1 Mode of Vibration in the Reference Configuration

For research purposes, the team at the Earthquake Engineering Research Facility (EERF) has developed an automated stochastic subspace identification (SSI) principal component (PC) algorithm, based on a mean value-based clustering approach described in the literature [8–10]. To guarantee accurate modal estimates, a very long measurement duration of 160 min was chosen for the reference configuration. This value was estimated based on a conservative rule of thumb for the required minimal measurement duration, with $T_{\min} = 200/(f_{\min}\zeta)$ [8].

Looking at the cross-spectral density of the ambient vibrations, which is plotted in Fig. 21.4, it becomes clear that the first two modes are closely spaced, as well as modes 4 and 5. Thus, it appears that the frame has very similar stiffness values in the E-W and N-S directions. To visualize the effect, the mode shapes of the first five modes are plotted in Fig. 21.5—before uncoupling mode 1 and 2 as well as mode 5 and 6 in preparation for the damage detection. The first mode vibrates at a frequency of 7.44 Hz and describes a translation in the E-W direction, which was defined as the weak direction. The second mode, at 7.90 Hz, has a very similar mode shape, but it is vibrating in the N-S direction. The third mode shape at 15.54 Hz is a rotation about the vertical axis, and the fourth and fifth modes are translations in the E-W and N-S direction, respectively. Higher modes and damping ratios are affected by more uncertainties [11], which is why they are not further discussed. To validate the accuracy of the developed SSI-PC, however, the modal estimates are compared to documented values from a peak picking procedure in the first column of Table 21.4 [5], as well as ARTeMIS® results [12], which in turn, are verified through the customary validation techniques. With a maximal deviation of 0.07% for the estimated natural frequencies, it

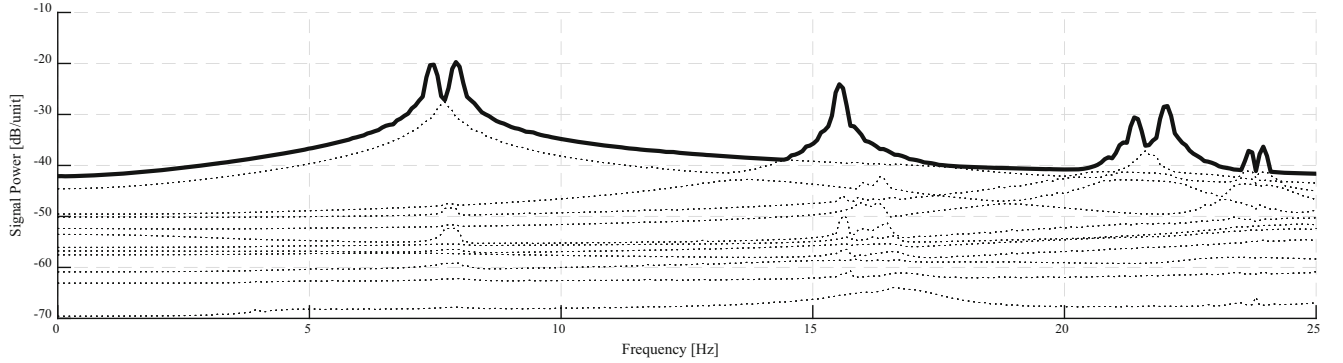


Fig. 21.4 Half spectrum – singular values of the low noise cross-spectral density matrix for the reference configuration

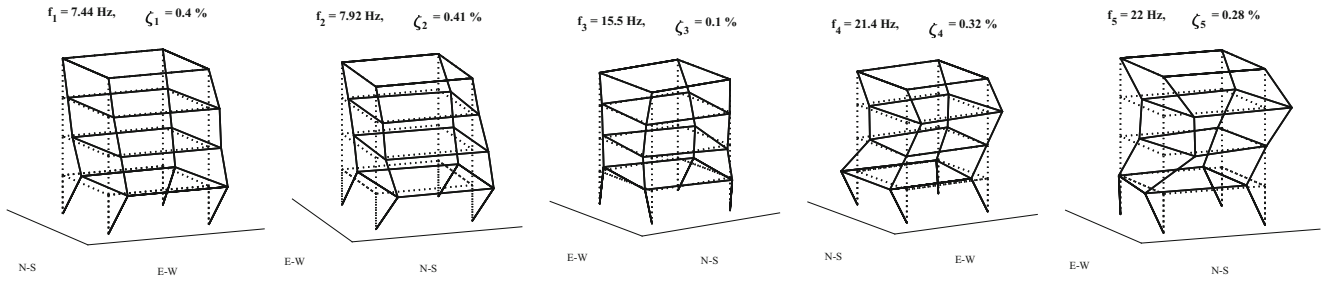


Fig. 21.5 Mode shapes and modal frequencies for the reference configuration

Table 21.4 Modal parameters of the reference configuration

No.	Description	Frequency [Hz]				Damping [%]		
		PP [5]	SSI-PC (EERF)	SSI-PC (ARTeMIS)	Dev. [%]	SSI-PC (EERF)	SSI-PC (ARTeMIS)	Dev. [%]
1	1st mode, E-W	7.44	<u>7.442</u>	7.442	0.00	<u>0.40</u>	0.41	2.44
2	1st mode, N-S	7.90	<u>7.921</u>	7.919	0.03	<u>0.41</u>	0.42	2.38
3	1st mode, torsion	15.54	<u>15.543</u>	15.542	0.01	<u>0.10</u>	0.12	16.67
4	2nd mode, E-W	21.41	<u>21.411</u>	21.422	0.05	<u>0.32</u>	0.42	23.81
5	2nd mode N-S	22.02	<u>22.015</u>	22.031	0.07	<u>0.28</u>	0.36	22.22

can be said that the developed SSI-PC yields reliable results and can be used for further studies on the Yellow Frame. It should be noted that only global modes are documented and local ones are discarded. For data integrity reasons, damping ratio estimates are also given, despite the high deviations.

21.6.2 Modal Parameters for Several Damage Scenarios

Following the procedure described in the previous section, brace elements are gradually removed. For practicability, the measurement duration is reduced to 20 min, following a less conservative rule of thumb with $T_{\min} = 10/(f_{\min}\zeta)$ [8]. The ambient vibration of each damage scenario is analyzed through the developed SSI-PC algorithm, and all frequency estimations are plotted in Fig. 21.6, where the underlying values can be found in Table 21.5. Each modal frequency corresponds to the mode shapes described in Fig. 21.5 above.

As a result, mode 1, mode 3 and mode 4 show clear decays in the modal frequency for the first six damage scenarios C1 – C6. The estimated frequencies are connected through a solid black line in Fig. 21.6. The reason why this trend cannot be observed for mode 2 and 5 is because, in these six cases, braces have only been removed in the E-W direction affecting the 1st and 2nd translational modes in the E-W direction (mode 1 and 3) as well as the torsional mode (mode 4). In the same light, the increase in the modal frequency from damage scenario C6 to scenario C7 and C8 is to be expected. In all three damage scenarios, a total number of eight braces are missing. However, in scenario C6, all eight braces have been removed in the E-W direction, where in scenario C7, four braces on both the West and the South side have been removed. The

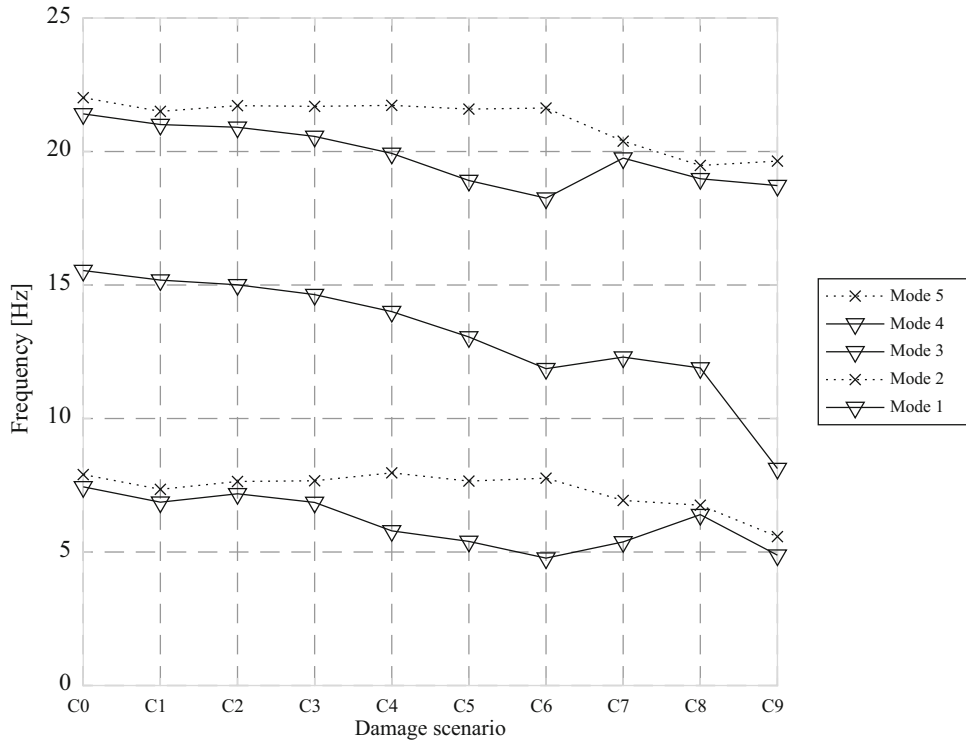


Fig. 21.6 Modal parameters of the damaged structure

Table 21.5 Modal frequencies in [Hz] of the damaged structure

F [Hz]	Mode 1	Mode 2	Mode 3	Mode 4	Mode 5
C1	6.87	7.35	15.19	21.01	21.51
C2	7.18	7.64	15.01	20.91	21.72
C3	6.86	7.67	14.64	20.57	21.69
C4	5.79	7.97	14.00	19.93	21.73
C5	5.40	7.66	13.06	18.91	21.59
C6	4.77	7.77	11.87	18.25	21.63
C7	5.38	6.93	12.30	19.75	20.39
C8	6.40	6.75	11.89	18.98	19.48
C9	4.88	5.58	8.13	18.72	19.64

redistribution of stiffness within the ground level leads to similar torsional frequencies but higher translational frequencies in the E-W direction (mode 1 and mode 4) and lower ones in the N-S direction (mode 2 and mode 5). It is fair to say that for all five modes of vibration, the lowest frequencies could be measured while all braces have been removed on the ground level (C9). The average decrease in the modal frequencies for the affected modes (modes 1, 3 and 4) is 4.42 Hz, with the highest sensitivity for the torsional mode (mode 3) and a maximum drop in the frequency of 7.42 Hz. For the damping ratios of modes, on the other hand, no clear trends could be observed, and they are only documented for the reference case.

21.7 Subspace-Based Damage Assessment

The statistical subspace damage detection (SSDD) [13] and localization (SSDL) techniques [5, 14, 15] evaluate the global condition of a structure by identifying changes in the eigenstructure of the system. This change can be identified by detecting the variations in the mean of a residual. This residual is built from the current measurements of the structure and a data-driven subspace from the reference state, *i.e.* undamaged structure. Subsequently a statistical test, *i.e.* χ^2 -test, is used to define a damage index by testing the residual. The effect of practical testing factors such as noise and measurement length were also investigated for this method in [5, 16, 17].

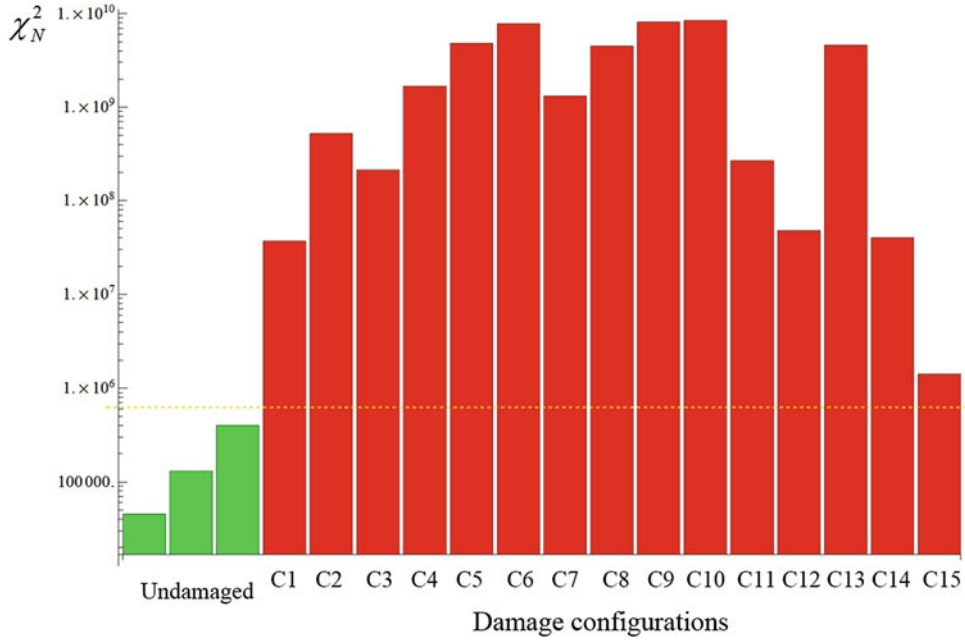


Fig. 21.7 Damage detection of the damage scenarios (the yellow line represents the 99% percentile threshold) [5]

21.7.1 Damage Detection

The damage scenarios introduced before were tested using the SSDD method. In three of the tests, the structure is not damaged, and therefore, they are used in evaluating a safety threshold based on the 99th percentile of their distribution. The resultant χ^2 -values are illustrated on a log-scale in Fig. 21.7 from testing all the damage scenarios. It can be seen in this figure that all the damage scenarios are detectable. It should be noted that the scale of the χ^2 -value is not a representative of the amount of damage.

21.7.2 Damage Localization

Following the detection of existence of damage in a structure, the second level of damage assessment is to locate the damage. Since all the scenarios are detectable, they are used in the damage localization. The damage will be localized using the MinMax test [5, 18]. A clustering approach, *i.e.* HFC, will be used to cluster the elements. Furthermore, The Jacobians constructed from analytical modal parameters introduced in [5, 18] will be employed. The results for the first and sixth damage scenarios are shown in the following figure. It is seen that almost in all of the damage scenarios, the damaged brace/s can be identified with great accuracy. Therefore, the Yellow Frame test proved to be a excellent specimen to assess the robustness of the SSDD and SSDL techniques under real and noisy testing conditions (Fig. 21.8).

21.8 Conclusion

Although it was commissioned in 1997, the Yellow Frame is still a suitable structure to provide test data for structural health monitoring research under real and noisy testing conditions. The frame is braced in a chevron configuration, and each brace consists of two threaded rods. This way minor and major damage events can be simulated by removing individual rods or by removing brace pairs and groups of braces, respectively. It showed to be an excellent test specimen for training, testing and validating cutting-edge SHM methods. Exemplarily, the results from a research project at UBC were summarized, showcasing both the efficiency of the statistical subspace damage detection (SSDD) and localization (SSDL) method and the appropriateness of the test specimen. However, another collaborative research projects could be mentioned here, where

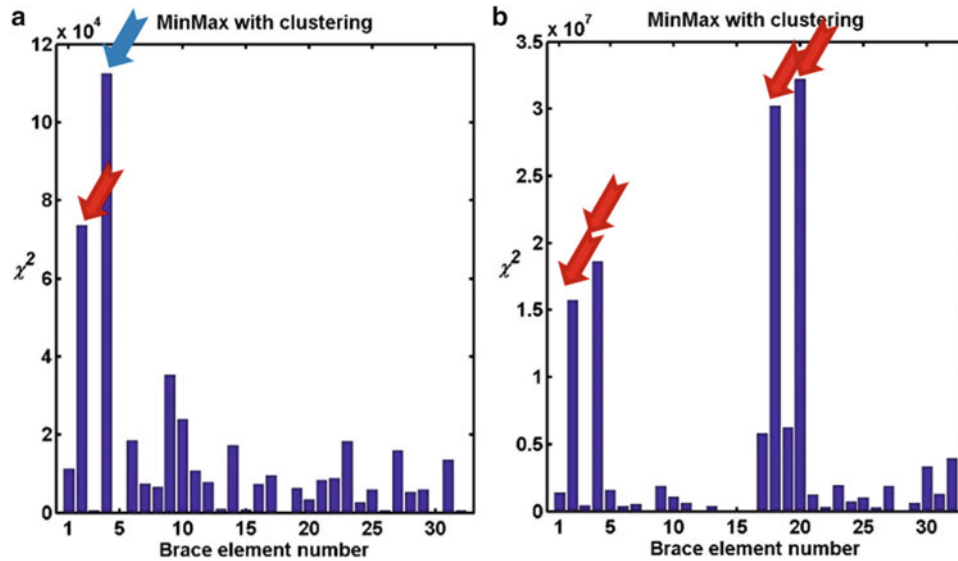


Fig. 21.8 Damage localization with HFC clustered Jacobians for (a) damage scenario C1, and (b) damage scenario C6 (red arrow: location of the damage, blue arrow: location of the element in the same cluster as the damaged element) [5]

a method based on the modal flexibility has been successfully applied using the same test setup [11]. The frame is equipped with accelerometers, as well as temperature and humidity sensors, which is why it is most suitable for long-term structural health monitoring considering several environmental and operational conditions.

Appendix A

Damage Scenarios C1-C9 (Fig. 21.9)

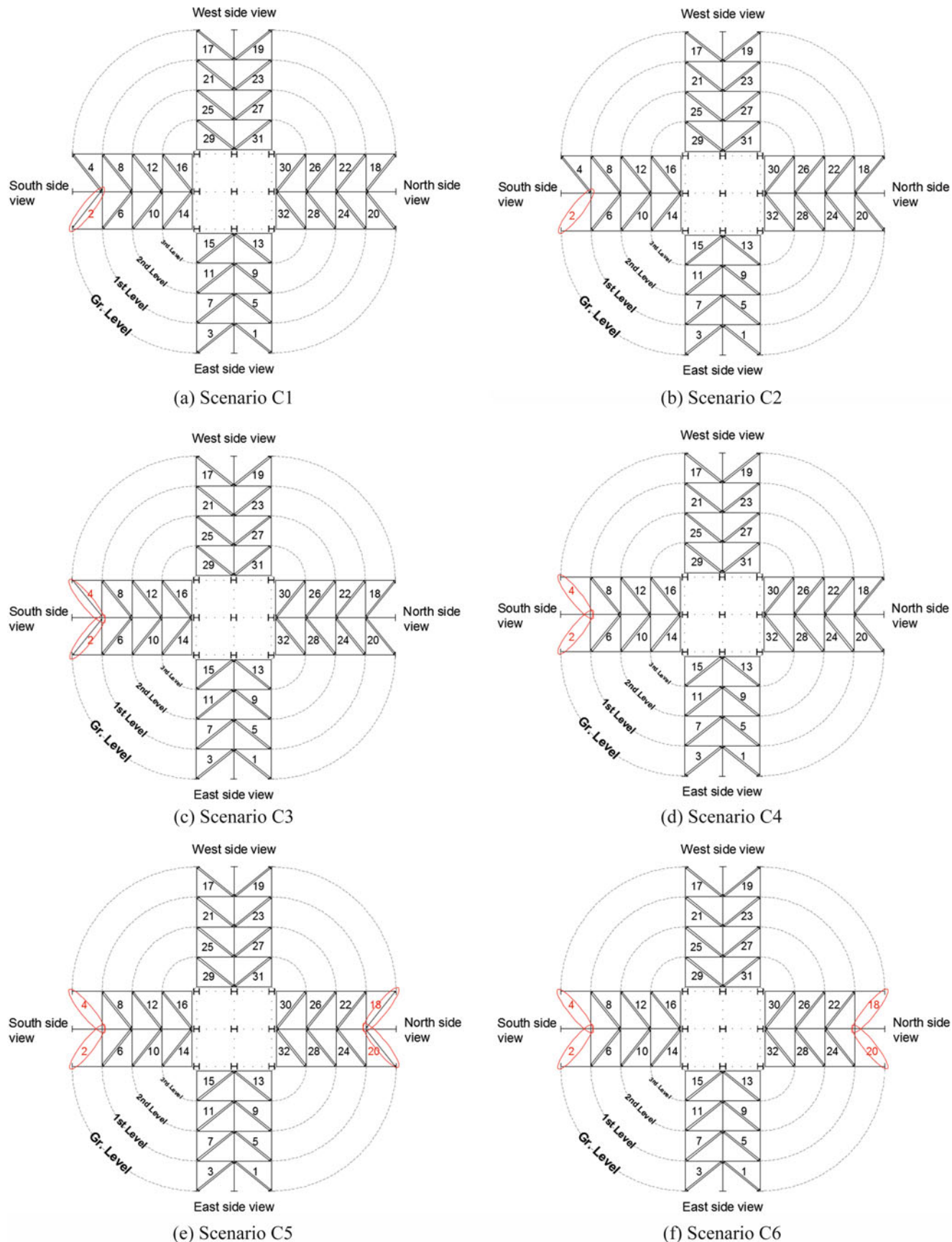


Fig. 21.9 First nine damage scenarios C1-C9 on the ground level of the Yellow Frame [5]

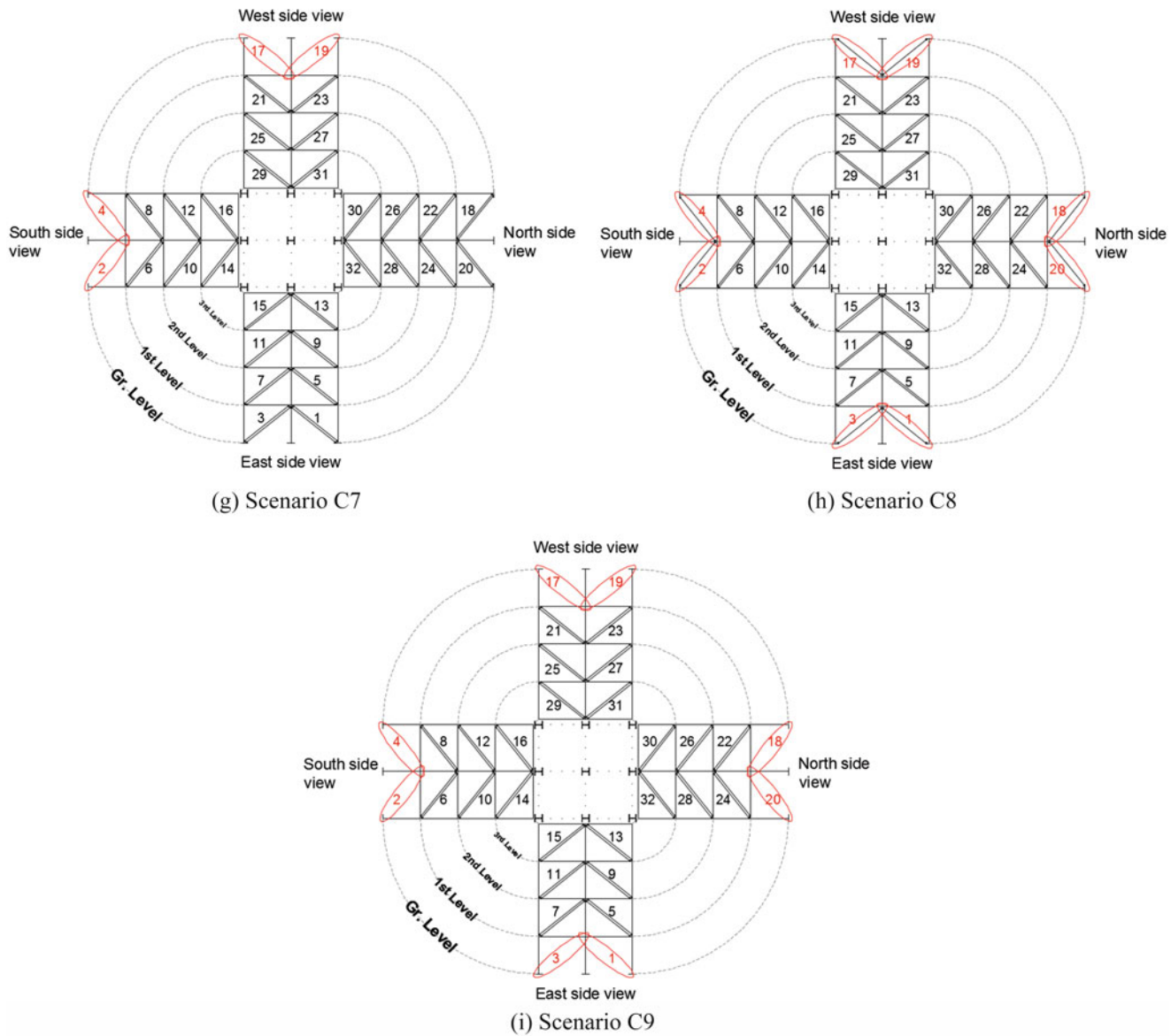


Fig. 21.9 (continued)

References

- Black, C.J., Ventura, C.E.: Blind Test on Damage Detection of a Steel Frame Structure In: IOMAC proceedings, International Operational Modal Analysis Conference (1998)
- Ventura, C.E., Prion, H., Latendresse, V., et al.: Modal properties of a steel frame used for seismic evaluation studies. Proc. of the Intl. Society for Optics and Photonics. **2**, 1885–1891 (1997)
- Dyke, S.J., Bernal, D., Beck, J.L., et al.: An experimental benchmark problem in structural health monitoring. In: Proceedings of the 3rd International Workshop on Structural Health Monitoring (IWSHM 3), pp. 488–497 (2001)
- Ventura, C.E., Lord, J.F., Turek, M., et al.: Experimental studies and remote monitoring of IASC-ASCE benchmark test frame. In :Proceedings of the IMAC XXI International Modal Analysis Conference, pp. 3–6 (2003)
- Allahdadian, S.: Robust statistical subspace-based damage assessment, Doctoral dissertation, University of British Columbia (2017)
- Hibbett, Karlsson, and Sorensen, ABAQUS: User's Manual, Dassault Systems Software, Abaqus(C) (1998)
- Farrar, C.R., Worden, K.: Structural Health Monitoring: A Machine Learning Perspective. Wiley, Oxford (2012)
- Brincker, R., Ventura, C.E.: Introduction to Operational Modal Analysis. Wiley, New York (2015)
- van Overschee, P., de Moor, B.: Subspace Identification for Linear Systems: Theory-Implementation-Application. Springer Science & Business Media, Berlin (2012)

10. de Almeida Cardoso, R., Cury, A., Barbosa, F.: A clustering-based strategy for automated structural modal identification. *Structural Health Monitoring*, no. 1475921716689239, SAGE (2017)
11. Bernagozzi, G., Ventura, C.E., Allahdadian, S., et al.: Application of modal flexibility-based deflections for damage diagnosis of a steel frame structure. *Procedia Eng.* **199**, 2026–2033 (2017)
12. Structural Vibration Solutions A/S., ARTeMIS Modal, Denmark (2015)
13. Basseville, M., Benveniste, A., Goursat, M., Hermans, L., Mevel, L., Van der Auweraer, H.: Output-only subspace-based structural identification: from theory to industrial testing practice. *J. Dyn. Syst. Meas. Control*. **123**(4), 668–676 (2001)
14. Allahdadian, S., Ventura, C.E., Andersen, P., et al.: Sensitivity evaluation of subspace-based damage detection method to different types of damage. *Struct. Health Monit. Damage Detect.* **7**, 11–18 (2015)
15. Allahdadian, S., Ventura, C., Andersen, P., Mevel, L., Döhler, M: Investigation on the sensitivity of subspace based damage detection technique to damage and noise levels. In: IOMAC proceedings, International Operational Modal Analysis Conference (2015)
16. Allahdadian, S., Ventura, C.E., Andersen, P., et al.: Subspace based damage detection technique: investigation on the effect of number of samples. In: Proceedings of 11th Canadian Conference on Earthquake Engineering (11 CCEE) (2015)
17. Allahdadian, S., Döhler, M., Ventura, C.E., et al.: On the influence of sample length and measurement noise on the stochastic subspace damage detection technique. *Struct. Health Monit.* **7**, 35–46 (2016)
18. Allahdadian, S., Döhler, M., Ventura, C., et al.: Damage localization of a real structure using the statistical subspace damage localization method. In: Proceedings of 11th International Workshop on Structural Health Monitoring (IWSHM 11) (2017)



Chapter 22

Developing a Passive Vibration Absorber to Generate Traveling Waves in a Beam

Seyedmostafa Motaharibidgoli, V. V. N. S. Malladi, and Pablo A. Tarazaga

Abstract Sound waves enter the outer ear and pass into the ear canal where the waves cause the eardrum to vibrate. Those acoustics are transmitted to the middle ear, and then pass through the innermost part of the ear, called the cochlea. The basilar membrane (BM), the main structural element of the cochlea, analyzes the waves propagating through it much like a biological Fourier analyzer. The waves travel from the base of the cochlea through the BM and get absorbed at the apex of the cochlea. These latter feature of the human auditory system is the inspiration to study waves propagating from one end of a beam to the other without reflections at the boundary.

Inspired by this the work herein numerically studies the dynamics of a uniform beam connected to a spring-damper system, in order to study some of the observed phenomenological behaviors of the basilar membrane. The location of the spring-damper system divides the beam into two dynamic parts: one which exhibits traveling waves and the other with standing waves. The various structural parameters of the setup have effects on the frequency bandwidth of the absorber and the portion of the beam with traveling waves. These parameters are numerically studied in this paper. These results lead us to new applications of the linear vibration absorber and possible explanation of the functionality of the Helicotrema in the cochlea.

Keywords Traveling waves · Standing waves · Vibration · Absorber · Helicotrema

22.1 Introduction

There are multiple studies on generating traveling waves in beams, plates, strings, etc. [1–5]. Loh, *et al.* used two-mode excitation method [1] and Avirovik *et al.* generated traveling waves in beams using piezoceramics as the actuator in piezo-structural-coupled systems [3]. In a study by Blanchard *et al.*, traveling waves were generated in a string with fixed boundary conditions using base excitation and a spring-damper attached to the string [5]. These studies showed that by changing the spring and damper parameters they can produce pure traveling and standing waves in different locations of the finite structure given a steady state input.

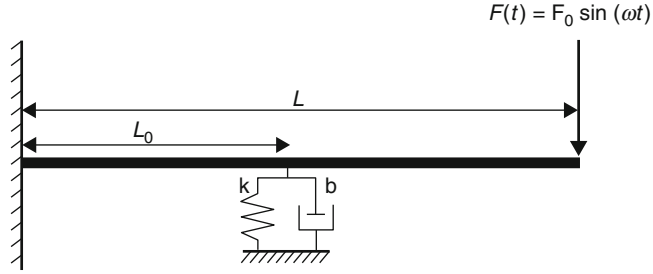
In this study, instead of using two actuators to excite two points of a beam with a phase difference, we use one actuator at the free end of a cantilever beam and a spring-damper system attached at another location along the length of the beam. Using this method, we are able to produce travelling waves passively on a portion of the beam. The traveling waves are generated between the excitation and the spring-damper location while standing waves are produced between the clamp and spring-damper. In this study, we develop a finite element model of the system and investigate the effect of the location of the spring-damper system on the produced traveling and standing waves. For each location, a set of damper parameter is chosen based on the location of the spring-damper system. We keep the excitation frequency and the spring stiffness constant in all of the simulations.

S. Motaharibidgoli (✉) · V. V. N. S. Malladi · P. A. Tarazaga

Vibration, Adaptive Structures, and Testing Laboratory, Department of Mechanical Engineering, Virginia Tech, Blacksburg, VA, USA
e-mail: mostafa4@vt.edu

Table 22.1 Beam parameters

Length	Width	Thickness	Density	Elasticity
46 cm	2.446 cm	0.32 cm	2700 kg/m ³	71 GPa

**Fig. 22.1** Schematic picture of the system**Table 22.2** First eight natural frequencies of the model

f_{n1}	f_{n2}	f_{n3}	f_{n4}	f_{n5}	f_{n6}	f_{n7}	f_{n8}
34.4 Hz	219.6 Hz	247.8 Hz	534.3 Hz	712.1 Hz	1104.2 Hz	1485.7 Hz	1998.7 Hz

22.2 Development of a Passive Vibration Absorber

In the present work, we modeled a 460 mm \times 24.46 mm \times 32 mm aluminum cantilever beam with a spring-damper system attached to it at a length L_0 using a finite element method (FEM). The equation of the motion of the system through this approach is given by,

$$M\ddot{x} + (C + b B_{sd})\dot{x} + (K + k B_{sd})x = B_f F,$$

where, x is the displacement vector of the beam, M and K are mass and stiffness matrices of the beam calculated using the beam parameters tabulated in Table 22.1, C is the damping coefficient matrix of the beam, b is the damping coefficient of the attached damper and k is the stiffness of the spring, F is input force applied to the tip of the beam, B_f is the force influence term, and B_{sd} is the spring-damper influence matrix. Matrix C is considered as a linear combination of mass and stiffness matrices, $C = \alpha M + \beta K$, where α and β are obtained experimentally and have the values of 1.0793 and 7.317×10^{-8} , respectively. Matrix B_{sd} is calculated based on the location of the spring-damper system on the beam. It adds the damping and stiffness of the passive absorber to the damping and stiffness of the corresponding node in the model.

Figure 22.1 shows a schematic picture of the system with passive absorber attached to it.

A harmonic force with the frequency ω and amplitude F_0 is applied to the tip of the beam ($L = 0.46 m$) to excite the system. Based on the previous work by Malladi *et al.*, traveling waves are generated at frequencies midway between two consecutive natural frequencies [2]. We follow a similar approach in this work to study the effects of passive absorber location on the produced waves. The first eight natural frequencies of the model are listed in Table 22.2.

The excitation frequency is chosen to be 1700 Hz ($w = 10681.415 \text{ rad/s}$) which is halfway between the 7th and 8th natural frequencies. In this study, we change the location of the spring-damper system (L_0) and choose the damper coefficient (b) in a way to produce traveling waves in the beam. The spring stiffness (k) is set to 150 kN/m is all of the cases we study.

22.3 Traveling Wave Generation

We obtained the response of the system to the input force for various absorber location and corresponding damping coefficient for five cases. In each case the traveling waves envelop is plotted for visual inspection of the waves generated. By changing the location of the spring-damper (L_0) we can generate different length of traveling and standing waves in the vibrating beam.

Figure 22.2a shows the areas swept by the steady state velocity of the beam plotted over time. The spring damper location is shown on the plots as a vertical line (purple color) and the input force is applied at the free end (L). The corresponding envelope of the area swept is plotted in Fig. 22.2b. In this case, the absorber system is attached to $L_0 = 0.23 m$ very close to the third node of the 7th mode and b is 210 N. s/m. As the figures show, a combination of traveling waves and standing waves

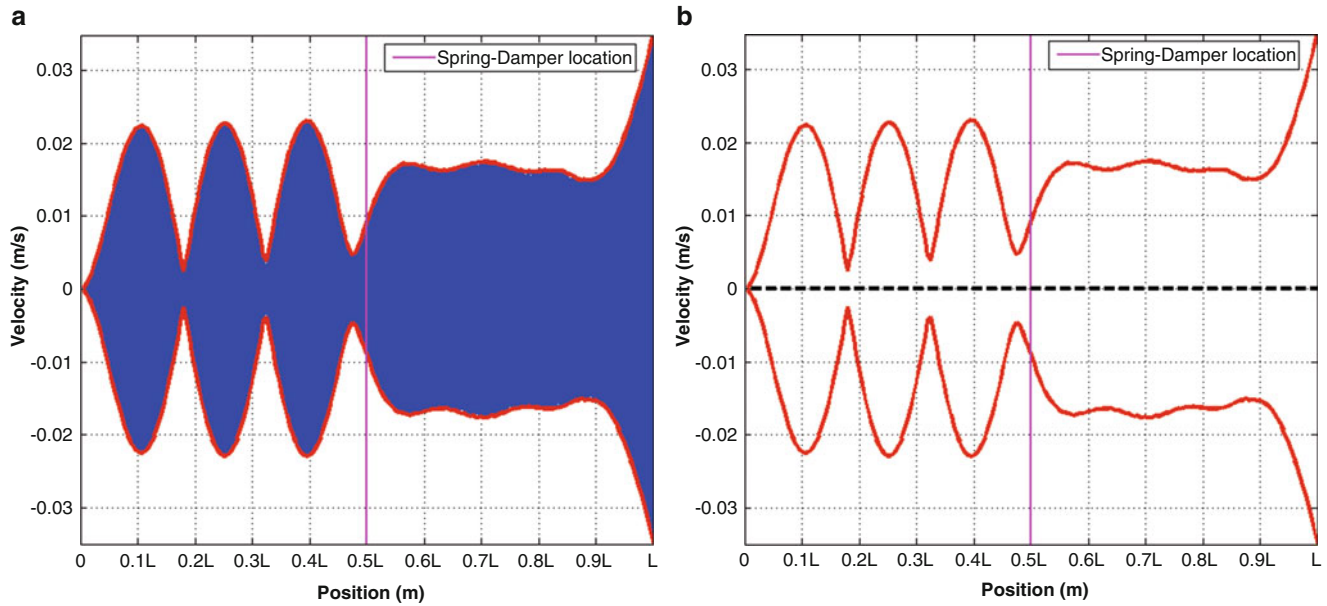


Fig. 22.2 (a) Displacement of elements of the beam, (b) envelope of velocity with $L_0 = 0.23 \text{ m}$, and $b = 210 \frac{\text{N.s}}{\text{m}}$

are generated on both sides of the spring-damper with different qualities. The waves generated between $0.55L$ to $0.9L$ have high traveling wave content, while the waves between the absorber system and the clamped end mostly consist of standing waves. The effects of boundary conditions are also seen in the plots.

In the second case seen in Fig. 22.3a, the absorber is attached to $L_0 = 0.322 \text{ m}$ between the 4th and 5th vibration node of the mode 7 and b is equal to 50 N.s/m . In this case the waves produced between $0.7L$ to $0.9L$ are combinations of both traveling and standing waves and further calculations are needed to determine the portion of each types of waves in this part of the beam. Figure 22.3b shows the effect of spring-damper system placed close to the 5th node of the 7th mode at 0.368 m . The damping coefficient is 175 N.s/m in this simulation. Between $0.85 L$ and $0.9 L$ the produced waves are almost pure traveling waves. Compared to the previous cases, the portion of the traveling waves produced in the beam between the clamp and absorber location (specially between $0.3L$ and $0.7L$) increased significantly. In the system of Figure 22.3c, L_0 is equal to 0.092 m and it is very close to the first node of the mode 7. Coefficient b is chosen to be 300 N.s/m . The results show that a combination of traveling and standing wave is produced between the absorber and the free end. In the last simulation seen in Fig. 22.3d, the absorber is placed close to the second node of mode 7 and the damping coefficient is set to 350 N.s/m . The waves generated after the spring-damper location are mostly traveling waves and the pure standing waves are seen between the clamp end and $0.175 L$.

22.4 Conclusion

In this study, we developed a finite element model of a cantilever beam with an attached spring-damper. A harmonic force with an excitation frequency midway of the 7th and 8th natural frequency of the system, was applied to the tip of the beam. The work has shown that traveling and standing waves on the beam are generated by changing the location of the spring-damper system and tuning the stiffness and damping of the absorber. The location of the spring-damper system affects the quality of standing and traveling waves such that mostly pure traveling waves are generated on one part of the system and coexist with mostly pure standing waves on the other part.

In the future work will focus on the effect of all the variables on the produced waves. A function will be defined to evaluate the quality of the traveling and standing waves on each part of the beam. Moreover, the work will validate the simulations experimentally, thus we are able to predict the responses of the system.

Acknowledgment The authors would like to acknowledge the support of the Air Force Office of Scientific Research through the Young Investigator Program (FA9550-15-1-0198). Dr. Tarazaga would also like to acknowledge the support provided by the John R. Jones III Faculty Fellowship.

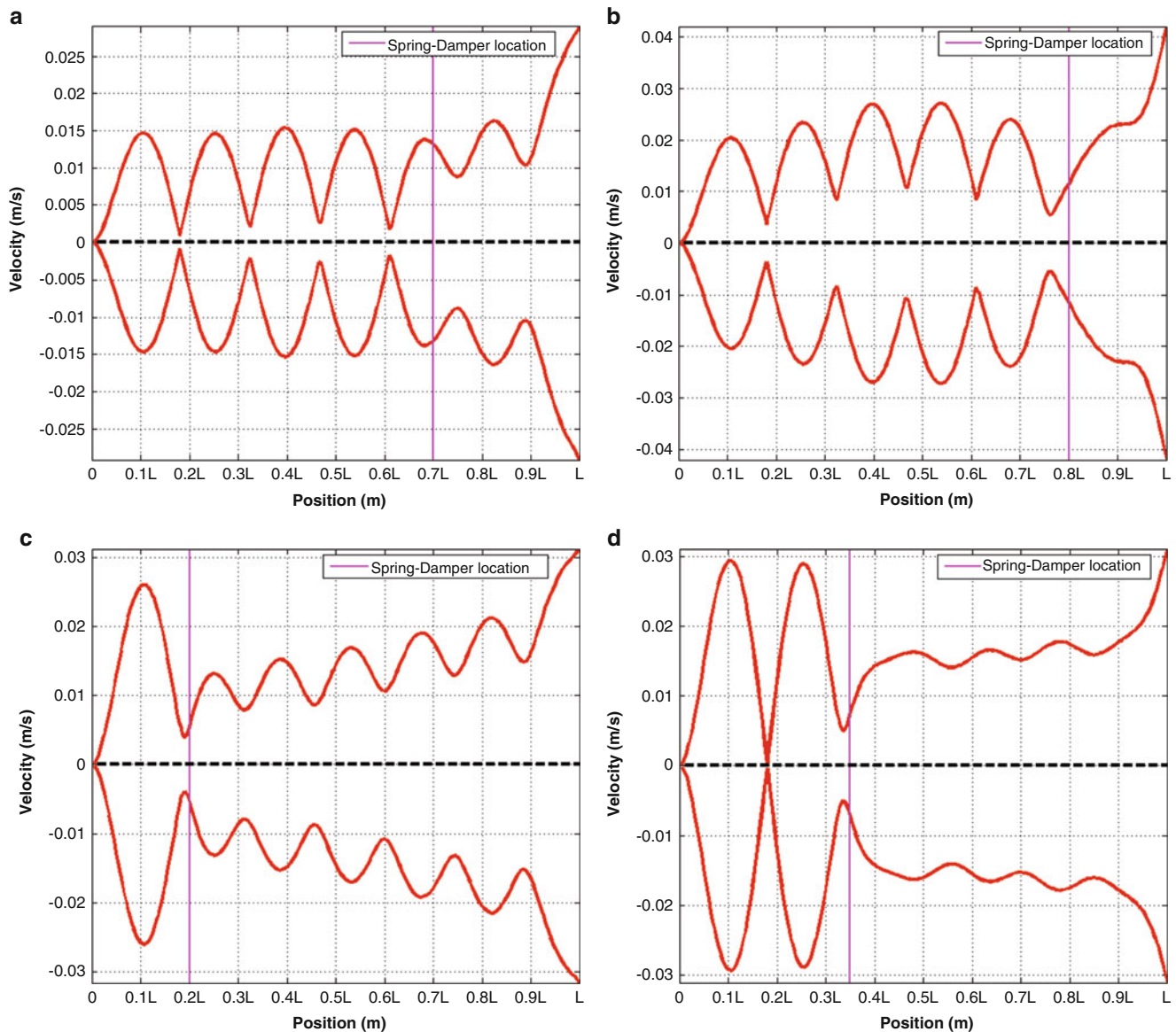


Fig. 22.3 Traveling wave envelop for four cases, with constant stiffness ($k = 150 \text{ kN/m}$) and varied spring-damper location (L_0) and damping coefficient: **(a)** $L_0 = 0.7L$ and $b = 50 \text{ N.s/m}$, **(b)** $L_0 = 0.8L$ and $b = 175 \text{ N.s/m}$, **(c)** $L_0 = 0.2L$ and $b = 300 \text{ N.s/m}$, **(d)** $L_0 = 0.35L$ and $b = 350 \text{ N.s/m}$

References

1. Loh, B.-G., Ro, P.I.: An object transport system using flexural ultrasonic progressive waves generated by two-mode excitation. *IEEE Trans. Ultrason. Ferroelectr. Freq. Control.* **47**(4), 994–999 (2000)
2. Malladi, V.V.N.S., Avirovik, D., Priya, S., Tarazaga, P.: Characterization and representation of mechanical waves generated in piezo-electric augmented beams. *Smart Mater. Struct.* **24**(10), 105026 (2015)
3. Avirovik, D., et al.: Theoretical and experimental correlation of mechanical wave formation on beams. *J. Intell. Mater. Syst. Struct.* **27**(14), 1939–1948 (2016)
4. Malladi, V.V.S., Albakri, M., Tarazaga, P.A.: An experimental and theoretical study of two-dimensional traveling waves in plates. *J. Intell. Mater. Syst. Struct.* **28**(13), 1803–1815 (2017)
5. Blanchard, A., McFarland, D.M., Bergman, L.A., Vakakis, A.F.: Damping-induced interplay between vibrations and waves in a forced non-dispersive elastic continuum with asymmetrically placed local attachments. In *Proc. R. Soc. A.* **471**(2176), 20140402. The Royal Society (2015)



Chapter 23

Experimental Assessment of the Effect of Different Tires on Comfort of Construction Truck Operators

S. Cinquemani, M. Cutini, G. Abbati, G. Meloro, and E. Sabbioni

Abstract Operators of construction trucks (such as wheel loaders, excavators, etc.) are often exposed to severe whole body vibrations induced by road/soil unevenness. Most of construction trucks are not equipped with any cabin suspensions unless seat and tires. Especially these latter are of paramount importance since they also govern the natural frequencies and the modes of vibration of the vehicle. Specific care has thus been paid to tires during the years and different technologies were adopted for their construction.

The present paper compares different methodologies to assess comfort of construction truck operators. In particular, outdoor tests prescribed by the standards to evaluate whole body vibrations experienced by operators are compared with ad hoc designed indoor tests carried out using a four-post test rig. Four sets of tires having the same dimensions but differing for type of construction. Tires were selected to evaluate potential differences, advantages and drawbacks of applied methodologies.

Keywords Wheel loader · Whole body vibrations · Comfort · Indoor and outdoor testing · Four-post test rig · Tires

23.1 Introduction

Operators of construction trucks (such as wheel loaders, excavators, etc.) are exposed to prolonged and intense multi-axis vibrations in the frequency range 0–20 Hz mainly induced by road/soil irregularity. Particularly critical from the operator comfort/health point of view are the low frequency vibrations, which are usually characterized by large amplitudes [1–8, 12]. The consequences of excessive exposure to vibrations may be loss of concentration, tiredness, decrease of effectiveness of the work being performed and eventually injuries (e.g. back pain).

One possibility for reducing vibrations is through the vehicle suspension system [1, 2]. However even nowadays a lot of construction trucks are not still equipped with any suspension system except the seat and the tires. Unfortunately, traditional passive seat suspensions amplify vibrations at frequencies close to their natural frequencies, which is generally in the range 1.5–4.5 Hz [3, 5, 6]. Thus their efficiency is generally poor at low frequencies and high amplitudes [3–8].

Tire stiffness is instead characterized by a large variance since different technologies are applied for the construction both of pneumatic and solid tires (tread pattern; compounds' characteristics; number of compound's layer; cushion, and hard base characteristics). Clearly, especially solid tires can present a different comfort level depending on compound characteristics and adopted technological solution.

It is straightforward to understand that tires of different type may significantly affect operator comfort, since they dramatically change vehicle natural frequencies and modes of vibration and consequently how road/soil vibrations are transmitted to the seat [2].

The present paper investigates different methodologies to assess the effect of different tires on operator comfort. Specifically, outdoor experimental tests prescribed by the standards to evaluate whole body vibrations experienced by operators [9–11] and ad-hoc designed indoor tests carried out using a four-post test rig are compared and systematically

S. Cinquemani · E. Sabbioni (✉)
Dipartimento di Ingegneria Meccanica, Politecnico di Milano, Milan, MI, Italy
e-mail: edoardo.sabbioni@polimi.it

M. Cutini
Consiglio per la ricerca in agricoltura e l'analisi dell'economia agraria (CREA), Treviglio, BG, Italy

G. Abbati · G. Meloro
Trelleborg Wheel Systems Italia, Tivoli, RO, Italy

analyzed. More in details, random tests and field tests (i.e. tests reproducing the accelerations the vehicle would experience on the field) were reproduced at the four-post test rig. Moreover frequency sweep tests were performed to individually excite the modes of vibration of the vehicle.

On purpose, a large wheel loader was instrumented with mono-axial and tri-axial accelerometers placed at the vehicle hubs, cabin and seat. During the tests, the wheel loader was equipped with four sets of tires having the same dimensions but differing for type of construction. Tires were selected to evaluate potential differences, advantages and drawbacks of applied methodologies.

23.2 Experimental Setup

The tested vehicle is shown in Fig. 23.1, while its main characteristics are reported in Table 23.1. During the experimental tests, the vehicle was equipped with four different sets of tires, which in the following will be referred as T1, T2, T3 and T4. All the tires have dimensions 20.5×25 . All the tests were repeated using the four sets of tires.

During the experimental tests the vehicle has been instrumented using mono-axial and tri-axial accelerometers. In particular, mono-axial accelerometers were placed on the vehicle chassis in correspondence of the four hubs and of the silent-blocks (Fig. 23.2). Mono-axial accelerometers were also placed in the cabin in correspondence of the front left and the rear left silent-blocks. Tri-axial accelerometers were placed in the cabin in correspondence of the rear right silent-blocks and the seating position. Only during indoor tests, a mono-axial accelerometer was placed at the bucket (Fig. 23.2b). All mono-axial accelerometers measured vertical accelerations.



Fig. 23.1 Tested vehicle on the four-post test-rig

Table 23.1 Main characteristics
of tested vehicle

Mass (empty)	[kg]	15,650
Front axle mass	[kg]	7160
Rear axle mass	[kg]	8490
Mass (loaded)	[kg]	17,900
Front axle mass	[kg]	10,600
Rear axle mass	[kg]	7300
Wheelbase	[m]	3.0
Track	[m]	1.93

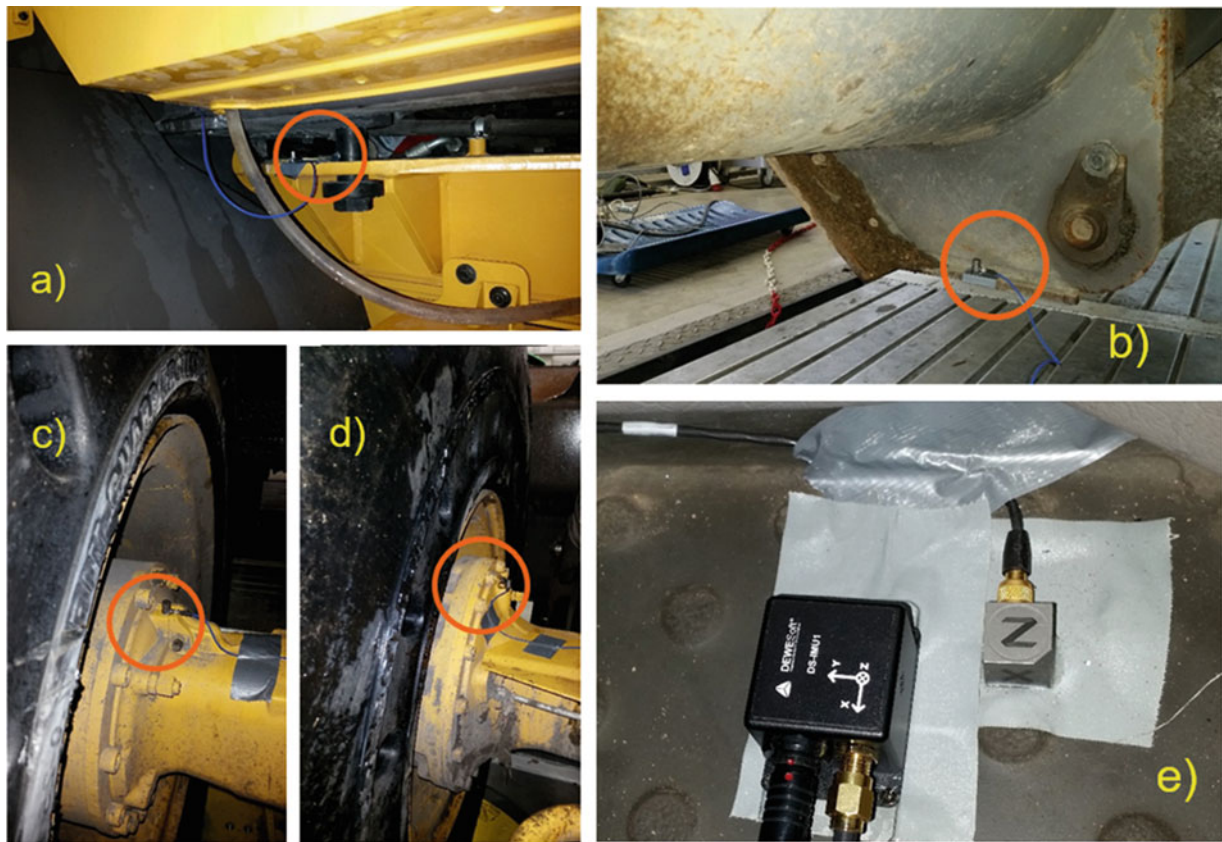


Fig. 23.2 Position of accelerometers: (a) silent-block connecting chassis and cabin, (b) bucket (c) front hub (d) rear hub, (d) cabin



Fig. 23.3 Outdoor tests: comfort test using ISO 5008 smooth track

23.3 Outdoor Tests

Outdoor tests were carried out using normalized tracks prescribed by standard ISO 5008 (Fig. 23.3). For each set of tires, tests were performed by keeping the speed of the vehicle constant (10, 12, and 14 km/h). Each test was repeated four times to have a statistical significance.

As an example, Figs. 23.4 and 23.5 show the spectra of vehicle and seat accelerations measured during the tests carried out at 10 km/h on the ISO 5008 smooth track [9] with the four sets of tires. Specifically Fig 23.4 shows heave (average of acceleration of the four hubs), pitch (difference between acceleration of front and rear hubs) and roll (difference between left

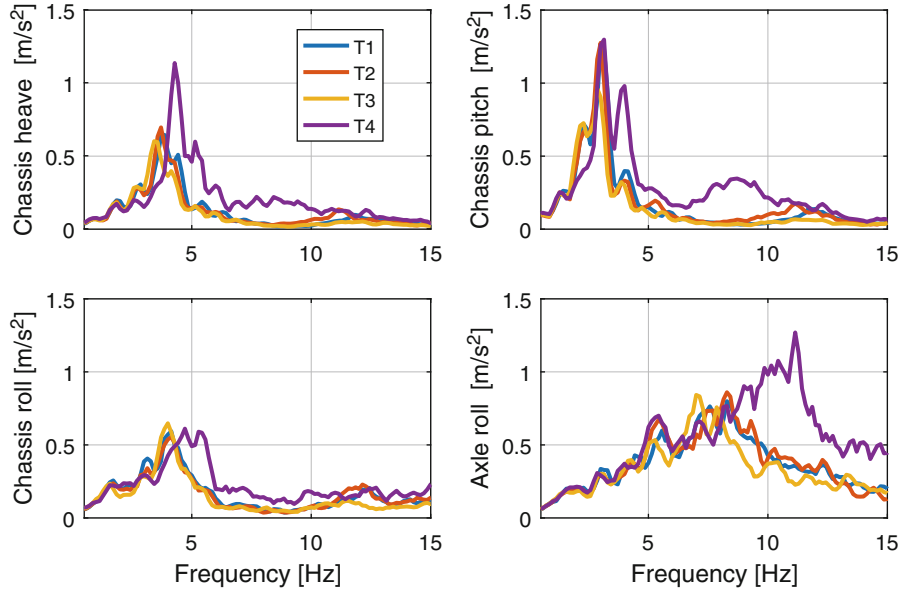


Fig. 23.4 ISO 5008 smooth track, speed 10 km/h-Spectra of chassis accelerations of heave, pitch, roll and rear axle roll acceleration

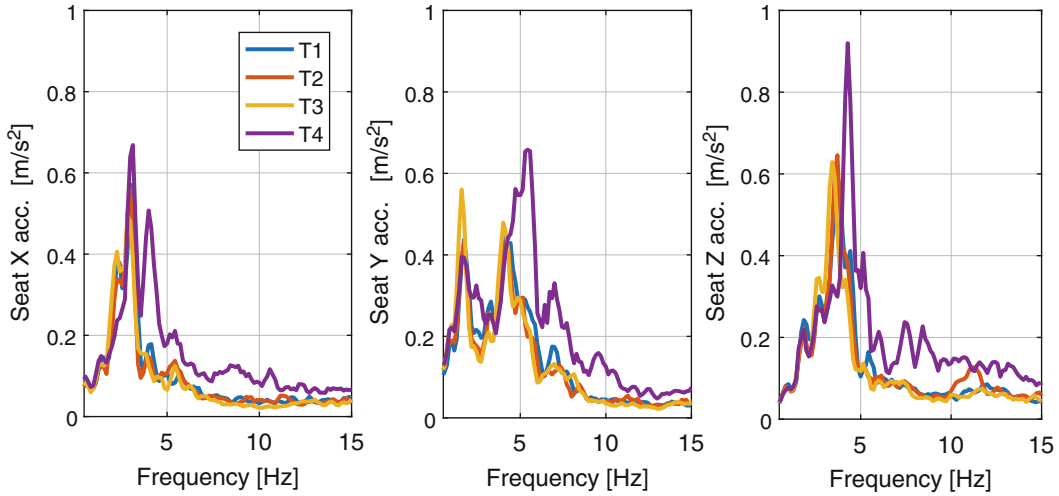


Fig. 23.5 ISO 5008 smooth track, speed 10 km/h-Spectra of seat accelerations

and right acceleration of the front hubs) acceleration of vehicle chassis, and roll acceleration of the rear axle (difference between left and right acceleration of the rear hubs). Figure 23.5 instead depicts the acceleration of the seat along x (longitudinal), y (lateral) and z (vertical) axes.

Operational modal analysis was applied to estimate the natural frequencies of the vehicle. Specifically, the least squares complex exponential method (LSCE, [15]) was used. On the purpose of obtaining a wide-band excitation (which can be considered similar to a random process), time histories of accelerations measured on the vehicle during all the performed tests were joined together.

Estimated natural frequencies are reported in Table 23.2. Although modes of vibration can be roughly estimated, their contribution to vibrations transmitted to the driver seat cannot be distinguished. This leads to a lack of information on most critical components in terms of vibration transmissibility and on main causes of discomfort.

Looking at the results collected in Table 23.2, the effect of the tested tires on vehicle modes of vibration appears evident: T1, T2 and T3, although different in construction type, are comparable. T4 instead yields to a significant increase of vehicle eigenfrequencies.

To evaluate comfort, the synthetic index proposed into ISO 2631 [10] to assess whole body vibrations was adopted. It is defined as the root means square value of the acceleration weighted according to specific weighting curves to consider

Table 23.2 Natural frequencies identified using outdoor tests

Natural frequency		T1	T2	T3	T4
1st	[Hz]	2.96	3.02	2.78	3.24
2nd	[Hz]	3.82	3.95	3.75	4.44
3rd	[Hz]	4.35	4.58	4.14	5.35
4th	[Hz]	8.57	8.72	7.28	8.88
5th	[Hz]	11.93	11.54	11.28	10.34

Table 23.3 Weighted rms vertical acceleration at the seat for different operating speeds

	a_v				
		T1	T2	T3	T4
Speed: 10 km/h		1.31	1.33	1.19	2.04
Speed: 12 km/h		1.76	1.86	1.97	2.01
Speed: 14 km/h		2.29	2.12	1.84	–

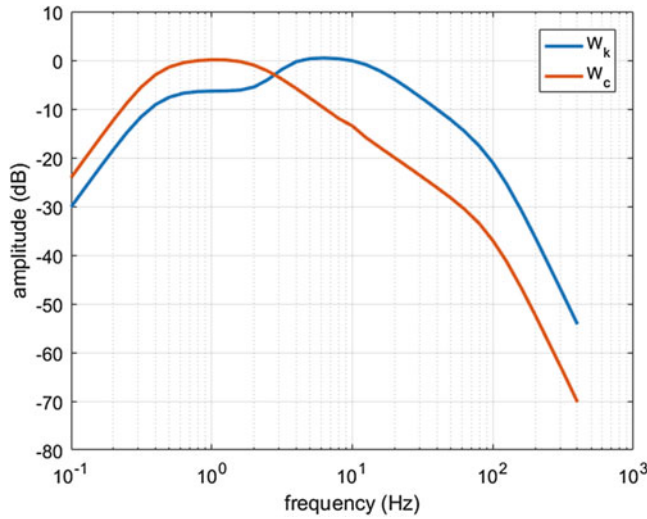


Fig. 23.6 Frequency weighting curves prescribed by ISO 2631 [10]

the different ability of the human body to withstand accelerations at different frequencies. Figure 23.5 shows the curves W_k and W_c used to respectively weight the vertical and horizontal (both longitudinal and lateral) accelerations transmitted to the operator. It's important to observe that curve W_k gives a higher weight to acceleration in the range between 4 and 10 Hz, while contributions at other frequency have fewer effects on comfort. Table 23.3 resumes comfort indexes calculated for each set of tires.

As previously observed, T4 seems to have a worse behavior in terms of comfort (test at 14 km/h was not executed due to excessive discomfort of the operator). This is mainly due to the fact that vibrations transmitted to the operator have a significant frequency content up to 10 Hz. Performance of T1, T2, T3 is instead comparable (inside the test variability) and significantly better than the one of T4.

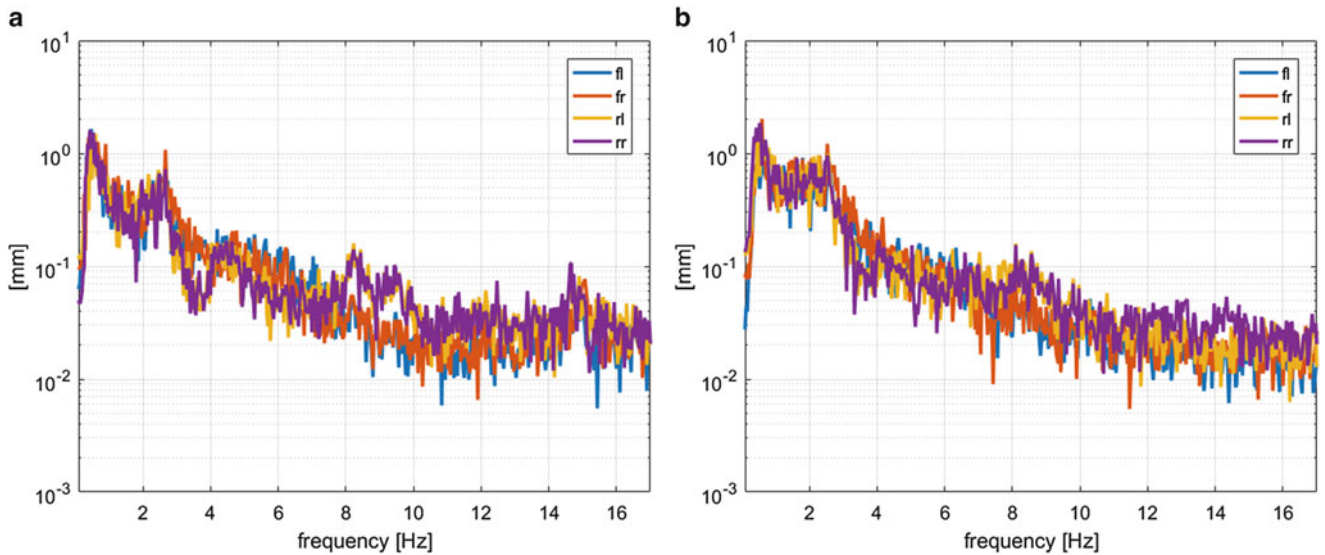
23.4 Indoor Tests

The same wheel loader (Fig. 23.1) was tested using the four-post test-rig placed at the CREA-Unità di Treviglio. Different kinds of tests can be performed using the four-post test-rig: sine tests, sweep sine tests, ramp tests, random input tests, etc.

Specifically, sweep sine tests in the frequency range 0.1–18 Hz were used to characterize the vertical dynamics of the vehicle. Sweep sine tests consist in a chirp signal with a constant imposed amplitude, while the frequency is linearly increased with a rate of 0.1 Hz/s. Performed tests are reported in Table 23.4. As can be seen, sweep sine tests were carried out in order to excite the vehicle modes of vibration of heave, roll and pitch separately. Tests reproducing the accelerations measured during real working condition (field test) were also carried out and their spectra in terms of pad displacement are depicted in Fig. 23.7 (a logarithmic scale is used for the y-axis).

Table 23.4 Performed tests on the four-post test-rig

Signal	Test type	Name	Amplitude	Frequency range
Sweep	Four actuators in phase	Heave	1,2 mm	0–18 Hz
Sweep	Only front actuators in phase	Pitch	2 mm	0–18 Hz
Sweep	Only left actuators in phase	Roll	2 mm	0–18 Hz
Sweep	Only rear left actuator	FL	3 mm	0–14 Hz
Sweep	Only front left actuator	RL	3 mm	0–14 Hz
Field	Input reproducing the acceleration measured during real working conditions	Grass, stones	Up to 30 mm	Mainly in the range 0.5–3 Hz (Fig. 23.7)

**Fig. 23.7** Spectra of imposed pad displacements: grass (a), stones (b)**Table 23.5** Vibration total value, four-post test rig tests

		T1	T2	T3	T4
a_{wz}	Grass	1.10	1.12	0.99	1.63
a_{wz}	Stones	1.09	1.20	1.01	1.75

Comfort indexes have been calculated for each test and are reported in Table 23.5. It is worth noting that the absolute values are different from those in Table 23.3 as they strongly depend on the amplitude of the imposed wheel displacement, but the relative values remain very similar. In particular, once again T4 results to have the worst behavior, while performance of T1, T2 and T3 is instead comparable (inside the test variability).

Results are confirmed by spectra of accelerations measured during the test and depicted in Fig. 23.8, where a significant contribution of accelerations up to about 15 Hz is noted for the T4 wheel set.

Indoor tests allow to force the vehicle at specific frequencies and observe its response so to have a more in depth knowledge on the behavior of tires in terms of transmissibility of vibration and to investigate more in details the modes of vibration of the system and how they contribute to the operator comfort. By knowing the displacement imposed at each tire, it is in fact possible to evaluate the frequency response functions (FRFs) of the system. Main results are depicted in Fig. 23.9 for the heave test (all the test-rig pads are moved in phase), while Fig. 23.10 shows the results of the pitch test (front wheel pads are moved in phase). In the figures, the FRFs between the imposed pad acceleration (input to the system) and the heave and pitch motions of the vehicle chassis are shown for the four tested tires. FRFs were calculated applying H1 estimator [13] to the time histories of the acceleration measurements. Both the tests demonstrate a similar behavior for T1, T2 and T3, while T4 looks very different, having a first resonance peak at higher frequency and amplifying acceleration in the 5–12 Hz band of frequency. This result suggests that, to enhance operator comfort, it is more effective, at least up to a certain extent, to shrink the frequency range of vibrations transmitted to the seat and filter out high frequency components (higher than 4 Hz) rather than reducing the resonance peak. Similar considerations can be done looking at Fig. 23.10, related to the pitch test. Even in this test, T4 shows a worse behavior in terms of width of involved frequencies, even if the peak is lower. In other words, although T4 lowers the amplitude of resonance peaks, it spreads and shifts towards higher frequencies

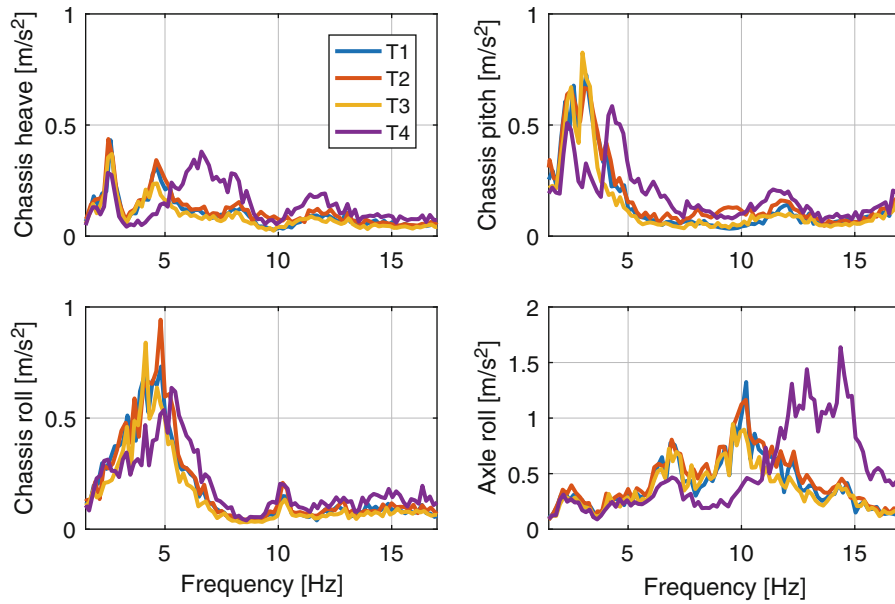


Fig. 23.8 Spectra of chassis accelerations of heave, pitch, roll and rear axle roll acceleration-Test: stones

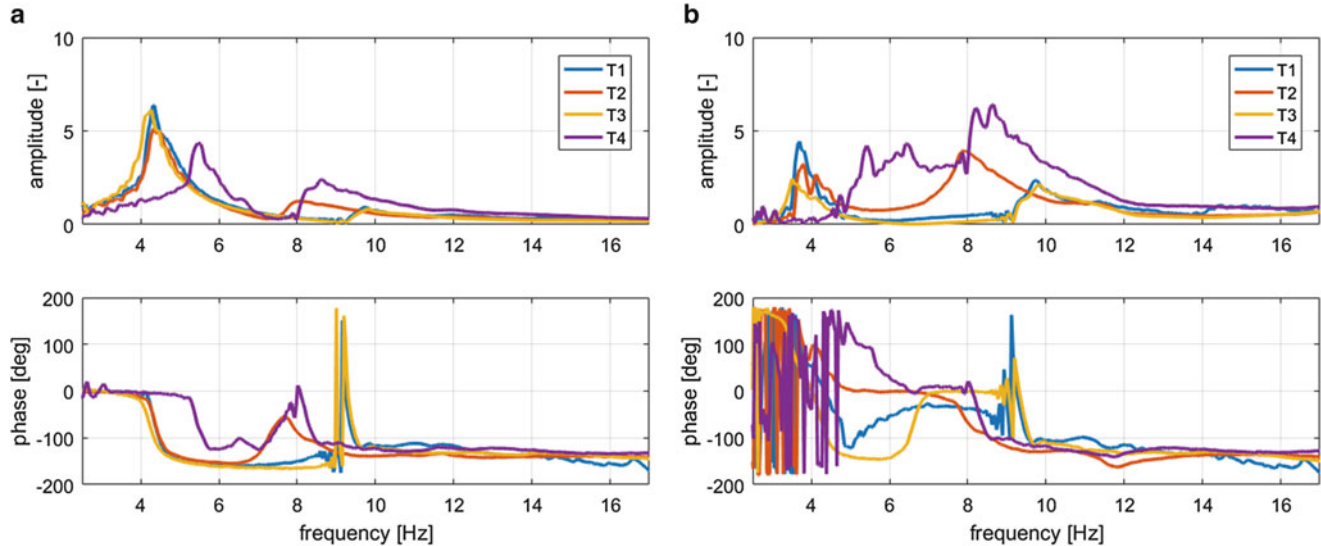


Fig. 23.9 Heave test: TFs between front left pad (input) and chassis heave and pitch (outputs) accelerations

the range of vibrations transmitted to the operator (i.e. T4 shifts the frequency of vibrations to a range at which human body is more sensible, see Fig. 23.6).

Table 23.6 collects the natural frequencies and the modes of vibration of the vehicle equipped with the four sets of tires.

To compare results between outdoor (Table 23.2) and indoor tests (Table 23.6) it should be reminded that tire dynamic stiffness is overestimated when the wheel does not rotate and this leads to an overestimation of vehicle natural frequencies of about 20%. This difference is consistent with literature data showing the tire dynamic stiffness sharply decreases (about 26% for tractor tires) as the tire is rolling (see Fig. 23.11). However, beyond a certain speed (which depends on tire type), this effect becomes negligible. Moreover, it must be pointed out that frequency range and the amplitude change significantly between indoor sweep tests and outdoor tests and this may lead to additional differences in the identified the natural frequencies due to tire nonlinear behavior [15]. This frequency shift, although not affecting results in the considered case, must be accounted for when four-post test rigs are used to evaluate comfort of operators.

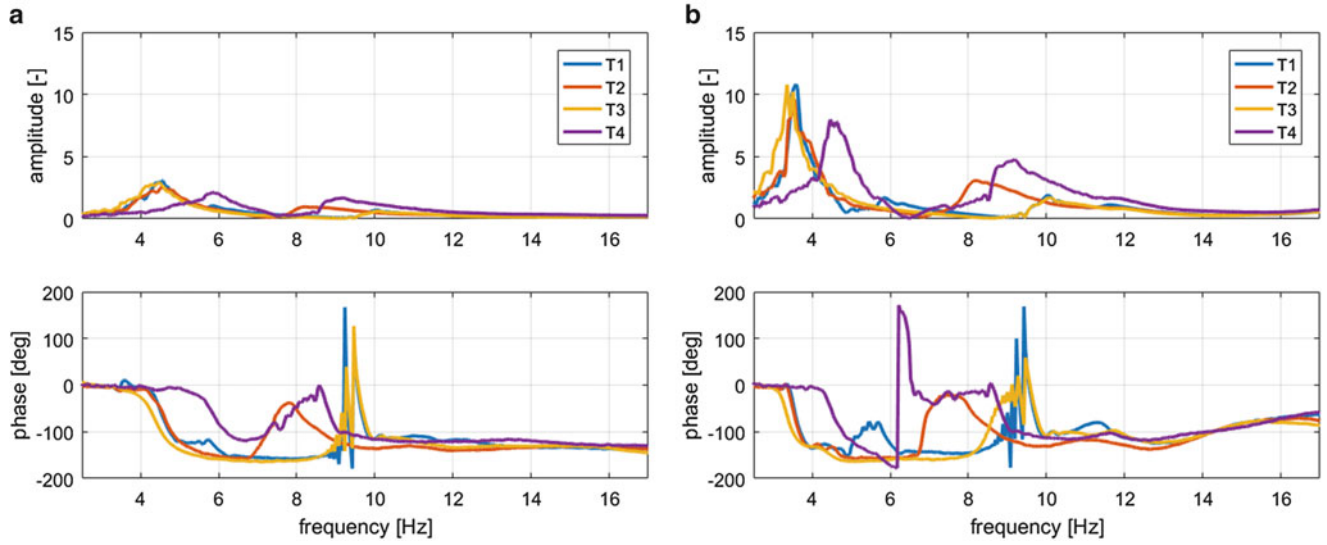


Fig. 23.10 Pitch test: TFs between front left pad (input) and chassis heave and pitch (outputs) accelerations

Table 23.6 Natural frequencies and modes of vibration identified during indoor tests

		T1	T2	T3	T4
Chassis pitch	[Hz]	3.58	3.68	3.50	4.62
Chassis heave	[Hz]	4.40	4.48	4.30	5.60
Chassis roll	[Hz]	4.66	4.78	4.57	5.76
Rear axle roll	[Hz]	10.22	10.45	9.99	13.01
Seat heave	[Hz]	3.88	3.88	3.88	3.86

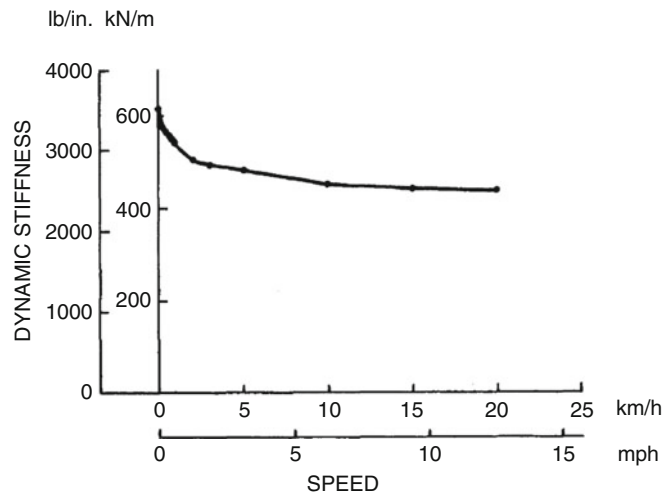


Fig. 23.11 Effect of speed on dynamic stiffness of a radial-ply tractor tire [14]

23.5 Conclusion

This work analyzed different methodologies for evaluating whole body vibrations experienced by operators of construction trucks and how it is affected by tires differing for type of construction. Specifically outdoor tests prescribed by directives and ad-hoc designed tests carried out using a four-post test rig were considered.

On purpose, a large wheel loader has been instrumented and tested at the CREA-Unità di Treviglio repeating both indoor and outdoor tests with four different sets of tires (all having the same dimensions).

Outdoor tests, performed according to ISO 5008 standard, allowed to have a preliminary evaluation of main eigenfrequency of the system and an estimation of the comfort index, calculated according to ISO 2631, for each set of tires. A more

in-depth understanding of the system can be obtained through indoor tests carried out using a four-post test-rig, as it allows to evaluate the frequency response function and to highlight modes of vibration of the vehicle by applying suitable inputs.

Results from tracks and test rig are coherent and allow to highlight differences between tested tires. Tires T1, T2 and T3, which are characterized by a similar dynamic stiffness, provide comparable results. On the contrary, T4 is characterized by an higher stiffness leading to the transmission of forces in a range of frequency (up to 10 Hz) that is considered critical for comfort.

Acknowledgement The research was carried out in the frame of the An.Ec.Oi.C. project (Experimental analysis of the effect of different wheel loader's tires on operator's comfort) funded by Trelleborg Wheel Systems Italia S.p.A.

References

1. Braghin F., Genoese A., Sabbioni E., Bisaglia C., Cutini M.: Experimental evaluation of different suspension systems for agricultural vehicles through four-poster test bench. In: Proceedings of the Mini Conference on Vehicle System Dynamics, Identification and Anomalies, pp. 491–498, Budapest, Hungary, 10–12 November (2008)
2. Braghin F., Cheli F., Genoese A., Sabbioni E., Bisaglia C., Cutini M.: Experimental modal analysis and numerical modelling of agricultural vehicles. In: Conference Proceedings of the Society for Experimental Mechanics Series (2009), Orlando, FL; USA; 9–12 February (2009)
3. Drakopoulos, D.: A review of the current seat technologies in agricultural tractors. National AgrAbility Project- Assistive Technol. **8**(3), 1–21 (2008)
4. Hostens, I., Deprez, K., Ramon, H.: An improved design of air suspension for seats of mobile agricultural machines. J. Sound Vib. **276**, 141–156 (2004)
5. Burdoff, A., Swuste, P.: The effect of seat suspension on exposure to whole-body vibration of professional drivers. Ann. Occup. Hyg. **37**(1), 45–55 (1993)
6. Mayton A.G., DuCarme J.P., Jobes C.C., Matty T.J.: Laboratory investigation of seat suspension performance during vibration testing. In: Proceedings of the ASME-IMECE conference, Chicago, IL, USA, 5–10 November (2006)
7. Stein, G.J., Zahoransky, R., Gunston, T.P., Burstro, L., Meyer, L.: Modelling and simulation of a fore-and-aft driver's seat suspension system with road excitation. Int. J. Ind. Ergon. **38**, 396–409 (2008)
8. Braghin F., Cheli F., Facchinetto A., Sabbioni E.: Design of an active seat suspension for agricultural vehicles. In: Conference Proceedings of the Society for Experimental Mechanics Series, 3 (PART 2), Jacksonville, FL; United States; 1–4 February 2010 (2011)
9. ISO 5008, Agricultural wheeled tractors and field machinery – Measurement of whole-body vibration of the operator (2002)
10. ISO 2631-1: Mechanical vibration and shock-Evaluation of human exposure to whole-body vibration Part 1: General requirements (1997)
11. ENI EN 13059, Safety Of Industrial Trucks – Test Methods For Measuring Vibration (2008)
12. Fornaciari L., Pochi D., Vassalini G., Gallucci F.: Investigation of the vibrations transmitted by agricultural tractor to the driver under operative conditions. In: Proceedings of International Conference on Innovation Technology to Empower Safety, Health and Welfare in Agriculture and Agro-food Systems, Ragusa, Italy, 15–17 September (2008)
13. Bendat, J.S., Piersol, A.G.: Engineering Applications of Correlation and Spectral Analysis. Wiley, New York (1993)
14. Wong, J.Y.: Theory of Ground Vehicles. Wiley, Hoboken (2001)
15. Brown, D., Allemand, R., Zimmerman, R., Mergeay, M.: Parameter estimation techniques for modal analysis, SAE Technical Paper 790221 (1979)



Chapter 24

Tool Wear Inspection of Polycrystalline Cubic Boron Nitride Inserts

Chandula Wickramarachchi, T. E. McLeay, S. Ayvar-Soberanis, W. Leahy, and E. J. Cross

Abstract In industry, highly frequent inspection of tooling used to machine safety critical components is common place. Worn or damaged tools produce undesirable surface finishes leading often to early failure of the part due to fatigue crack growth. In the development stages of polycrystalline boron nitride tools, the tool wear inspection technique is an off-line run-to-failure method. This approach interrupts the cutting process intermittently, to measure the tool wear using optical and scanning microscopy. This method is time consuming and expensive, causing bottlenecks in production. The overall aim in industry is to develop an on-line, automated system capable of informing the operator of the tool's imminent failure. This paper focuses on treating this process as a preventative maintenance problem by studying whether acoustic emission can be used as an indirect measurement of tool wear at any given time. Acoustic emission measurements taken from the machining process of face turning are investigated here. Basic analysis in the frequency domain using principle component analysis reveals a number of interesting insights into the process. Relationships between the sharpness of the tool and the magnitude of the frequencies suggests promising link between acoustic emission and tool wear.

Keywords Acoustic emission · Tool wear · PCBN · Principle component analysis · Turning

24.1 Introduction

Polycrystalline Cubic Boron Nitride (PCBN) is the second hardest material in existence [1]. For this reason, and due to low wear rates, PCBN is utilised as a cutting tool material. Wear resistance is a crucial property, which allows the tool to operate for longer periods under harsh environments such as high cutting forces, high temperatures, shock loading and plastic deformation[2]. PCBN also has low chemical wear rates, especially when machining ferrous material, as it does not contain carbon molecules, which tend to burn in high temperatures or diffuse into other carbon base workpieces [3]. Subsequently, PCBN can be used for machining hardened steel. At high cutting temperatures (700°C or higher), the high thermal conductivity of PCBN permits the fast dissipation of heat whilst its toughness and strength aids with resisting fracture [4]. These material properties allow PCBN to be used in finish turning which is a way of securing a desirable surface finish of a machined part. This process is capable of replacing grinding in the final machining stage, and consequently, of reducing the cost and time required for finishing [5].

Owing to the aforementioned material characteristics, PCBN is expensive compared to carbide tooling [6]. Therefore, the preventative method used in industry where tools are discarded at constant time intervals can be costly. Currently, this technique is used because it is not possible to directly measure the tool during a cut to investigate its wear state. During the cutting process, the tool is always in contact with the workpiece, and the area of contact is very small. Hence, accessibility poses the main obstruction for the direct measurement of tool wear. However, studies undertaken on tooling materials such as carbides and ceramics for example, have found tool wear to influence the forces, temperatures, acoustic emissions and

C. Wickramarachchi (✉)

Dynamics Research Group, Department of Mechanical Engineering, University of Sheffield, Sheffield, UK

Industrial Doctorate Centre in Machining Science, Rotherham, UK

e-mail: cwickramarachchi1@sheffield.ac.uk

T. E. McLeay · S. Ayvar-Soberanis

Advanced Manufacturing Research Centre, Rotherham, UK

W. Leahy

Element Six Global Innovation Centre, Didcot, UK

E. J. Cross

Dynamics Research Group, Department of Mechanical Engineering, University of Sheffield, Sheffield, UK

vibrations generated in machining [7–9]. Therefore, by measuring these outputs, tool wear can be studied indirectly. The approach taken here is to use the indirect measurements in conjunction with tool wear data taken at certain time intervals, for supervised learning, as a first step of automation. In this work, acoustic emission of a PCBN insert was collected during a turning operation. The resulting data were studied in the time and frequency domain, to understand whether this output can be used as an indirect measurement of tool wear of PCBN.

24.1.1 Acoustic Emission During Turning

Acoustic Emission (AE) is the release of elastic energy during the deformation of a material. These stress waves can be captured by piezoelectric transducers. As a non-destructive evaluation method, AE is often used in predictive maintenance of structures and machinery [10]. Although AE is not usually adapted into continuous monitoring systems, it has been employed in attempts to predict tool wear in metal cutting in the past [11–13]. AE signals obtained during machining are made up of both continuous and transient components. The continuous signal is produced by plastic deformation and frictional effects occurring in the cutting zone [14]. Transient signals are an indication of collisions and breakages of chips and tool [15, 16].

Numerous studies have been conducted on examining the AE signal during a tool's life and many have found that flank wear has a correlation with changing features of AE such as root mean square (RMS), skewness, kurtosis, AE count rate, amplitude and frequency. In literature, it was found that low values of AE amplitude were caused by worn tools, whereas the high values are present owing to sharp tools [17]. Furthermore, as the tool wear increases, the high temperatures generated in the cutting zone leads to a formation of a white layer which could in turn increase the AE values once more, as white layers are harder than the original workpiece surface [17]. It has also been suggested that whilst this is the case, increasing thermal loads leads to lower damping and therefore lower AE amplitude [18].

The use of acoustic emission measurements to understand tool wear in hard turning using PCBN has only been conducted once previously. The study in question was based on basic time domain analysis where the skewness and kurtosis of the signal's RMS values were compared against flank wear. The author found the shape of the bursts coupled with its amplitude can give an idea of the severity of flank wear but concluded that the results were not reliable or robust enough for practical implementation [19]. Subsequently, this work was carried out in order to understand whether AE signals taken from PCBN tooling, could provide information regarding tool wear states, when analysed in the frequency domain.

24.2 Experimental Set-Up

The experimental set up for this work used diamond shaped inserts manufactured with 55% CBN content. The workpiece used was a true hardened steel (AISI 4340) bar with a hardness value between 54 and 57 HRC. In one pass of the face turning operation, the tool travels from the outer diameter (120 mm) of the workpiece to the inner diameter (48 mm). A CNC lathe, Gildemeister CTX400 was used for this experiment. Piezoelectric AE transducers (Kistler 8152B111) were used with 1 MHz sampling rate. The sensor was placed at the back of the tool holder, to minimise the amount of noise captured. A Kistler A5125 pre-amplifier was used without any filters. Figure 24.1 displays the machine and sensor set-up. Wear measurements were taken after every 10 passes. Crater wear images were taken using a 3D surface scanner and flank wear images using an optical microscope. The tools were tested in face turning conditions under standard machining parameters.

24.3 Results

24.3.1 Time Domain Observations

The face turning operation produces AE bursts continuously throughout each machining pass. Figure 24.2a displays the data captured during a cut length of 1 mm. When studying data corresponding to 1 mm, roughly 3 wave packets can be seen. These vary in amplitude and duration. When observing the raw data at the 10 mm scale (Fig. 24.2b), the wave packets seen in the 1 mm scale are grouped together at different time scales. At this scale, the literature suggests that the transient, high amplitude pulses are due to collisions of the chips against the tool and the low amplitude continuous waves are due to deformation of the workpiece [20]. In passes from later on in the trial, during a metre of a cut, the amplitude of the AE

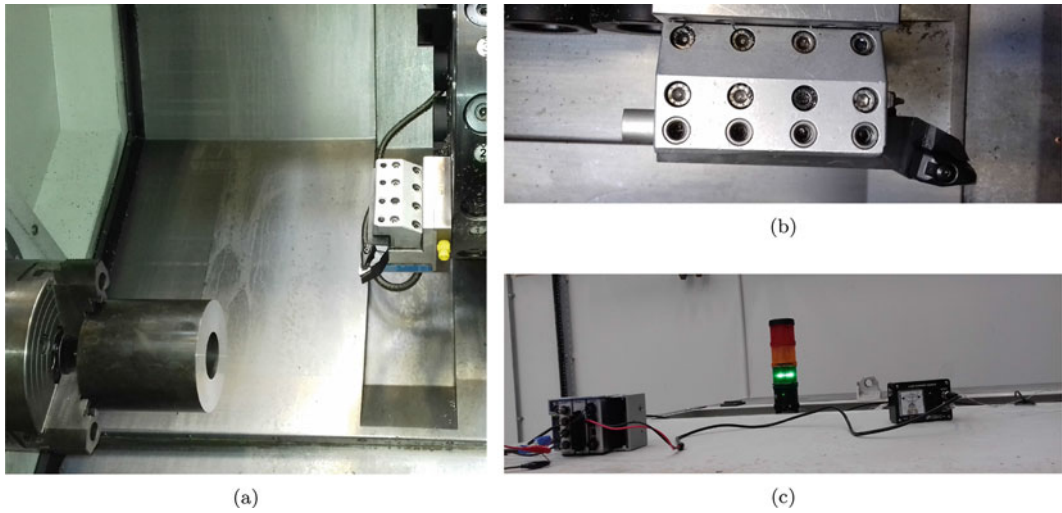


Fig. 24.1 (a) The lathe with the workpiece and tool holder dynamometer with tool holder in place. (b) AE sensor placed at the back of the tool holder. (c) The compact DAQ system (left)

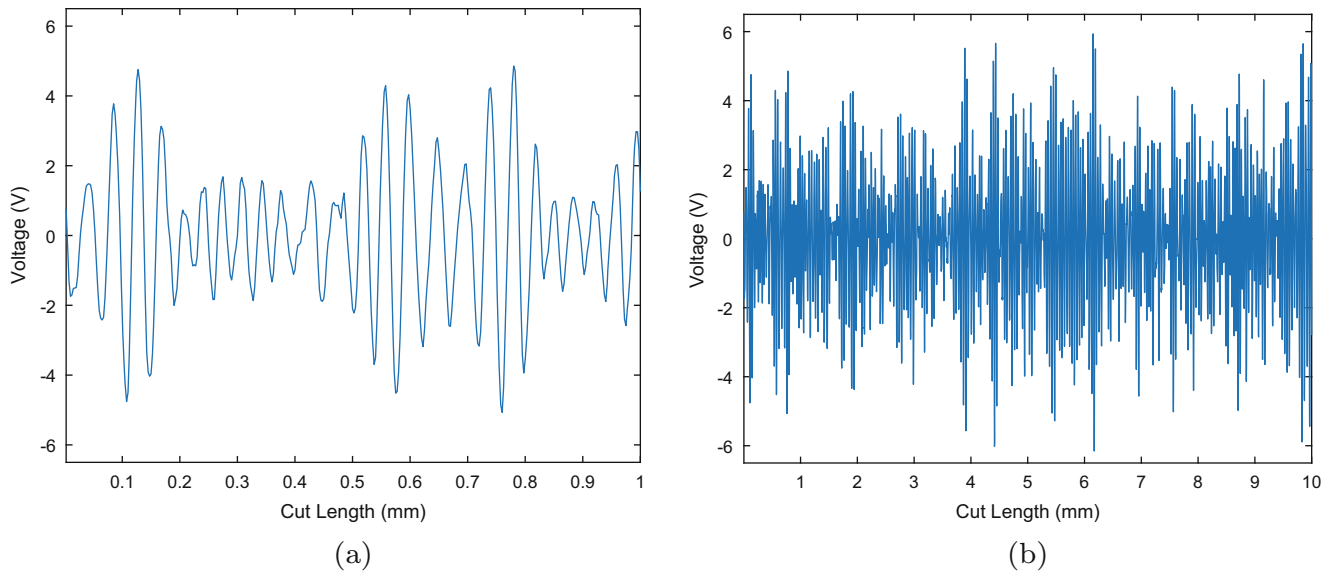


Fig. 24.2 Data produced at cut length of (a) 1 mm and (b) 10 mm

signal, which represents around 160 mm, periodically increases and decreases roughly 6 times (Fig. 24.3b). This behaviour is not evident in the early stages of the tool (Fig. 24.3a) suggesting it is directly linked to tool wear. The root mean square of the signal at the early stages of tool life and the signal from a worn tool displays this effect clearly.

The cause of each AE oscillation at the 1 mm (Fig. 24.2a) scale has not been explained in literature. In the past, these signals have been studied at larger scales than 1 mm. However, many studies have been conducted on chip formation when machining hardened steel with cubic Boron Nitride tools. It has been found that at the constant cutting speed of 2.5 m/s as used here, the chips produced are saw toothed [21]. This means in the primary shear zone, the chip periodically fails [22]. The frequency of the force oscillation as the saw tooth is formed is around 20–50 kHz [23]. Past studies have captured this sawtooth shape and it can be seen in Fig. 24.4a. For these cutting tools and workpieces, the chip shape is continuous for lower cutting speeds and the sawtooth is sharper for higher cutting speeds. When comparing this chip formation information from literature with the AE data collected in this trial at the cutting speed of 2.5 m/s, an interesting relation can be seen. The saw tooth chip formation examined in previous studies occur around every 50 μm (i.e. the distance between two teeth at the peaks), and the periodicity of the oscillations seen in Fig. 24.2a also occur around every 50 μm . The corresponding signal showing 100 μm can be seen in Fig. 24.4b. Subsequently, it could be presumed that one wavelength of the AE signal is produced by the adiabatic shear band growing and breaking in the primary shear zone. However, at this early stage, not enough evidence is available to confirm this assumption completely as chips were not collected in this study.

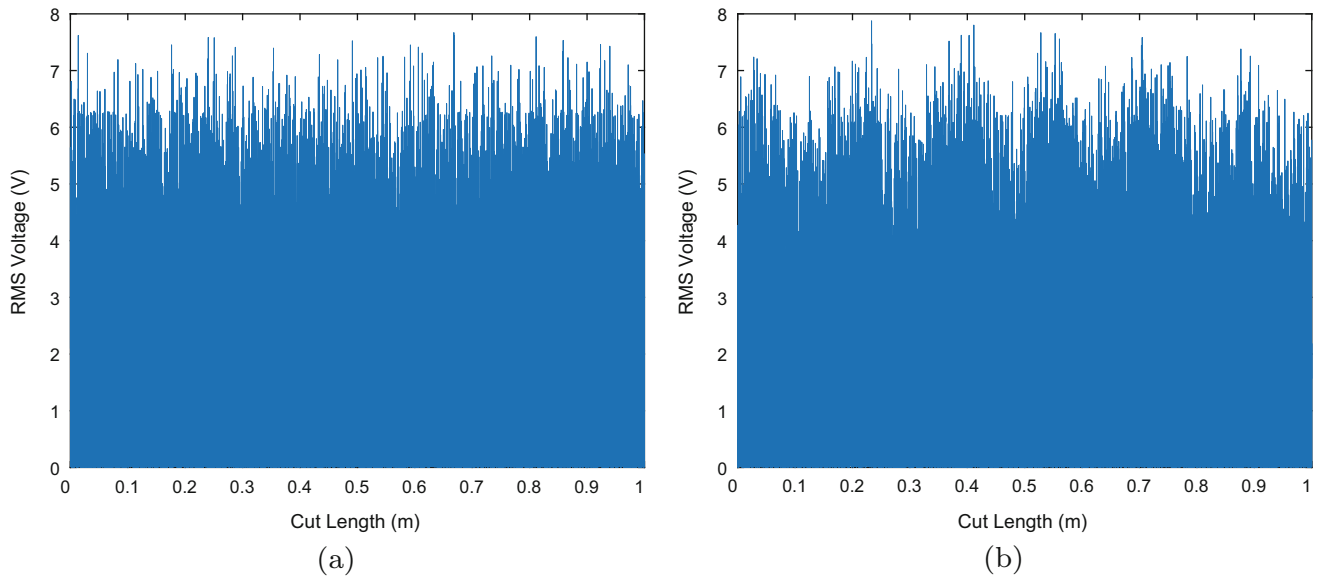


Fig. 24.3 Data produced at cut length of 1 m (a) new tool and (b) worn tool

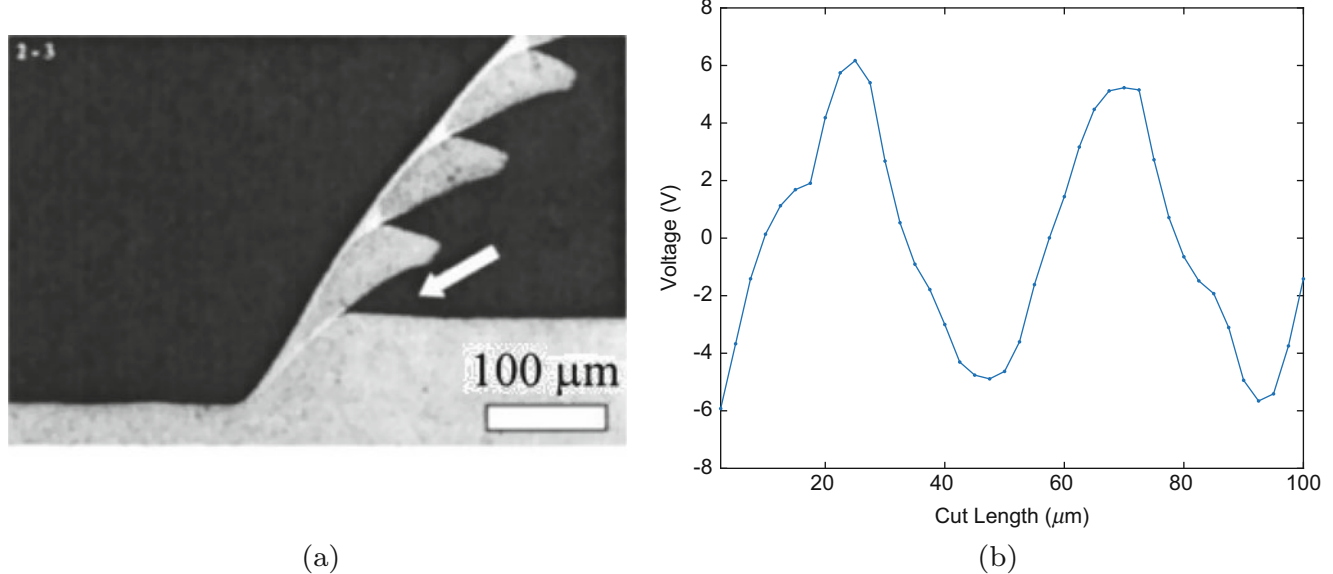


Fig. 24.4 (a) Sawtooth chip and its formation taken from cutting conditions ($V_c = 2.5$ m/s, Hardness_{workpiece} = 56 HRC)[24] (b) Signal captured during 100 μm

24.3.2 Frequency Domain Observations

The AE signal produced during the entire tool life was split into over 1600 sections to reduce computational cost. The frequency component of an AE signal which provides the content of the waveform was calculated using a short time Fourier transform for each section (Fig. 24.5). The magnitude is shown in decibels. Principle component analysis was conducted on the magnitude of the AE frequencies of each section. The percentage of variance of the scores (or axis) indicate that almost 90% of the variance can be captured by the first 2 scores which are plotted in Fig. 24.6 where the colour bar represents the pass number.

The frequency with the highest power ($F_{highest}$) lies at 58.59 kHz. Given the saw tooth chip formation, it is plausible to assume the $F_{highest}$ frequency corresponds to shear deformation of the workpiece. For a new tool, a second peak of high power can be seen up to pass 40. This could be due to the transition stage of the cutting edge where the chamfer with a negative

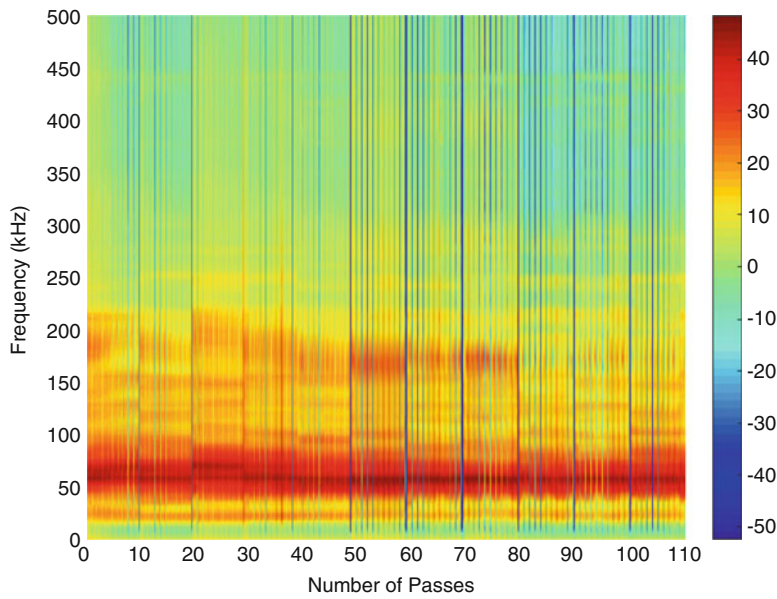


Fig. 24.5 Spectrogram of the AE signal

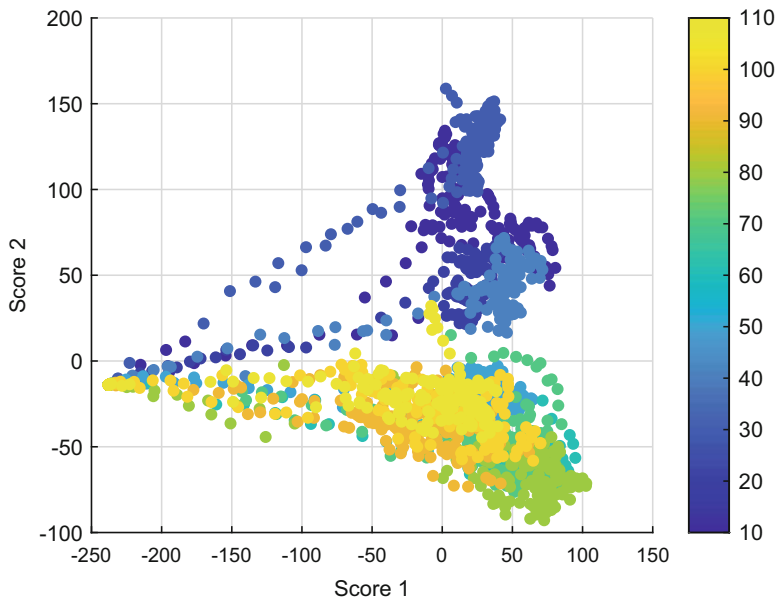


Fig. 24.6 PCA of the frequencies

rake angle A (Fig. 24.7a) is completely worn and the cumulation of crater and flank wear produces a sharp cutting edge with a positive rake angle B (Fig. 24.7b). Moreover, these passes are also clearly separable from others by eye in the PCA graph. Consequently, this suggests that PCA of AE signals in the frequency domain can be used for classification of wear states for PCBN tools.

The $F_{highest}$ frequency is most powerful during the middle of the tool life, owing to the sharpness of the tool. The sharpness of the tool has been calculated here as a ratio of crater radius and cutting edge radius (Fig. 24.8). These radii were found by examining the cutting edge circle and crater circle as seen in Fig. 24.7c.

The frequency which is exactly 3 times the $F_{highest}$ (58.59 kHz) at 175.77 kHz, has a high amplitude, and is present in the middle of tool life and dissipates, though it does not completely disappear. Traces of it can be seen during passes 100 to 110. It could be assumed that this frequency component is caused by the collision of the tool with the chip and/or the chip curl. This is on the grounds that the rate of curl depends on the segmentation frequency (the frequency at which the

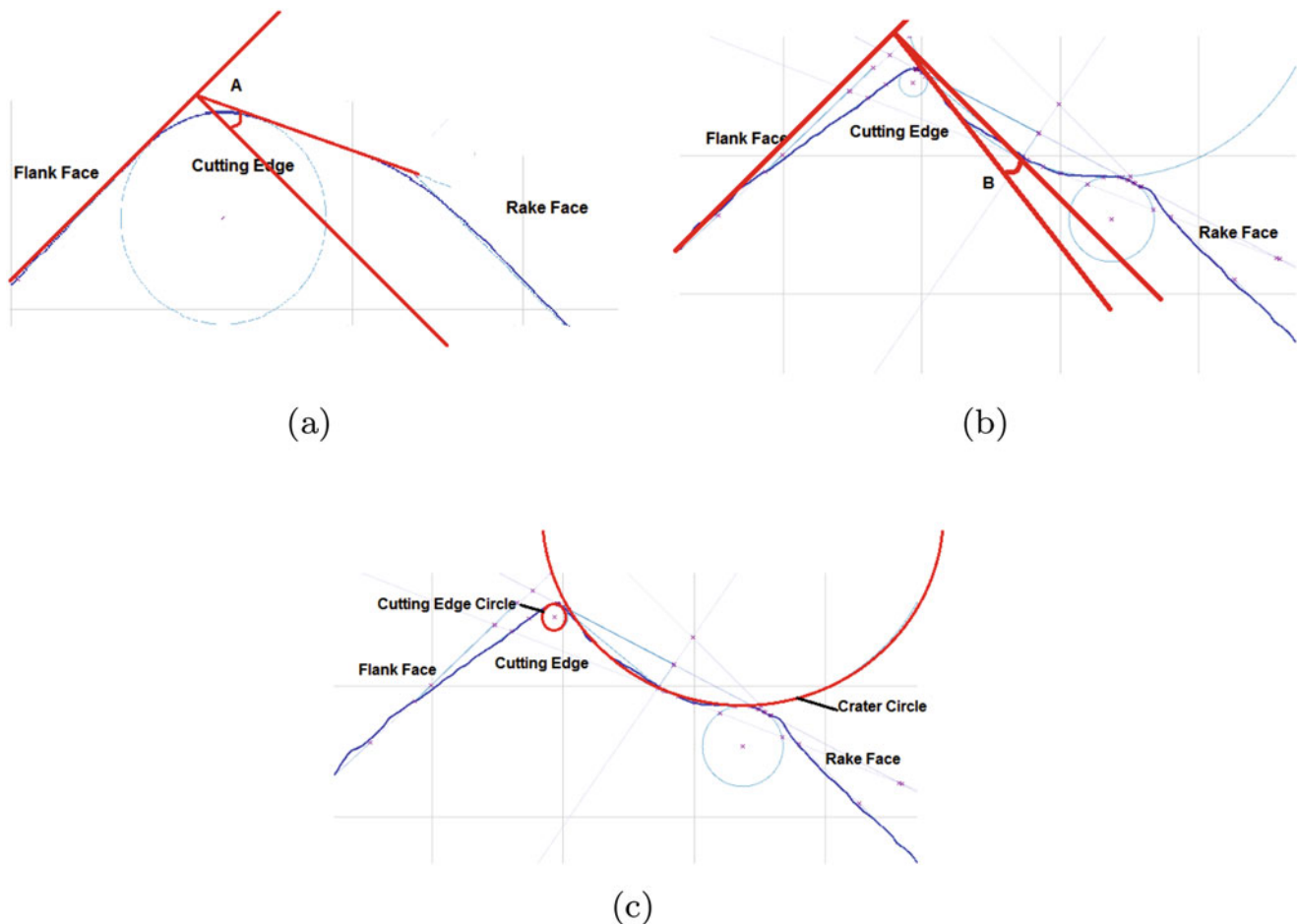


Fig. 24.7 Profile of a (a) new tool (b) worn tool (c) worn tool with circles highlighted

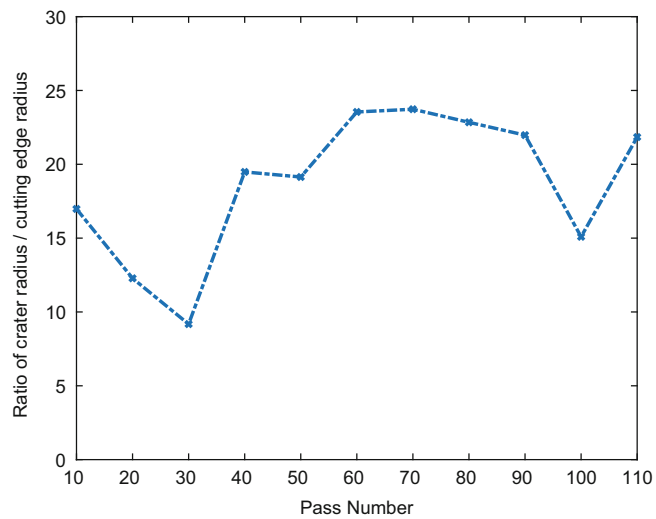


Fig. 24.8 Sharpness of tool over time

saw tooth behaviour occur – the $F_{highest}$ frequency in this case). The curling of a chip can occur naturally or as a result of force being applied to the chip [25]. The curling in this case is a product of crater wear which changes the rake face and produces a surface for the chip to collide against [26]. In the trial, it was seen that during the middle section of the tool's life, it has very little ability to clear swarf from the cutting zone. The swarf is tangled and gathers around the cutting zone. This is because the crater wear is deep and the chamfer which directs the chips away (Fig. 24.7a) from the cutting edge is almost non-existent (Fig. 24.7b). It was witnessed that at this point, the chip does not break away hence affecting the number of tool – chip collisions as well.

24.4 Conclusions

Due to the challenges of measuring tools directly, machining outputs such as AE can be used as indirect measurements of tool wear. It is possible to use these indirect measurements with machine learning algorithms to automate the tool wear measurement process. Spectral analysis of AE signals collected during a face turning operation was carried out in order to understand whether acoustic emission from machining can be used as an indirect measurement of tool wear of PCBN inserts.

It was found that, the variation of the frequency component of the AE signals with the highest power is caused by tool wear, as all other machining conditions are kept constant. This frequency component is assumed to be due to shear deformation of the workpiece to produce a chip. This will be examined further in a future study by collecting chips and also by analysing force in the frequency domain. The sharpness of the tool affects the magnitude of the frequency band with the highest power significantly.

The change in tool profile from a negative rake angle to a positive rake angle is thought to correspond to two frequencies with similar high amplitudes at the start of tool life. The clusters found in the PCA results corresponding to these early passes can be easily separable from the rest by eye. Consequently, principle component analysis can be utilised as an initial step towards classification of tool wear states.

Curling of chips at the tool cutting edge may be responsible for a frequency band with high amplitude at three times the frequency with the largest power. This needs to be investigated further by studying chip segmentation frequency through force data and also by collecting chips during machining.

These findings suggests that AE can be used as an indirect measurement of tool wear for PCBN inserts. The results from the principle component analysis conducted on the spectral information of the AE signal can be fed through classification algorithms as the next step of automating tool wear measurements.

Acknowledgements The research facilities of Element Six Ltd. in Oxford funded this work and also provided the machine, workpieces and tools used in this experiment. This work was also part funded by the EPSRC. The Advanced Manufacturing Research Centre (AMRC) in Rotherham extended a lot of help and guidance throughout this experiment.

References

- Lin, Z.-C., Chen, D.-Y.: A study of cutting with a CBN tool. *J. Mater. Process. Technol.* **49**, 149–164 (1995)
- Tönshoff, H., Arendt, C., Amor, R.B.: Cutting of hardened steel. *CIRP Ann. Manuf. Technol.* **49**, 547–566 (2000)
- Lahiff, C.M., Sc, B., Gordon, S.S., Phelan, P.: An investigation into the effect of high speed cutting on the wear behaviour of PCBN tools in continuous cutting of hardened steel. In: Masters Thesis (2008)
- ElementSix: PCBN Metalworking Brochure. Technical report. Element Six Ltd, Shannon (2008)
- Liu, C.R., Mittal, S.: Single-step superfinish hard machining: feasibility and feasible cutting conditions. *Robot. Comput. Integrat. Manuf.* **12**, 15–27 (1996)
- Dogra, M., Sharma, V.S., Sachdeva, A., Suri, N.M., Dureja, J.S.: Tool wear, chip formation and workpiece surface issues in CBN hard turning: a review. *Int. J. Precis. Eng. Manuf.* **11**, 341–358 (2010)
- Ravindra, H., Srinivasa, Y., Krishnamurthy, R.: Acoustic emission for tool condition monitoring in metal cutting. *Wear* **212**(1), 78–84 (1997)
- Emel, E., Kannatey-Asibу, E.: Acoustic emission and force sensor fusion for monitoring the cutting process. *Int. J. Mech. Sci.* **31**(11), 795–809 (1989)
- Dolinský, S., Kopač, J.: Acoustic emission signals for tool wear identification. *Wear* **225**, 295–303 (1999)
- Miller, R.K., Hill, E.V.K., Moore, P.O.: Acoustic Emission Testing. American Society for Nondestructive Testing, Columbus (2005)
- Uehara, K., Kanda, Y.: Identification of chip formation mechanism through acoustic emission measurements. *CIRP Ann. Manuf. Technol.* **33**(1), 71–74 (1984)
- Kannatey-Asibу, E., Dornfeld, D.: A study of tool wear using statistical analysis of metal-cutting acoustic emission. *Wear* **76**(2), 247–261 (1982)

13. Diniz, A., Liu, J., Dornfeld, D.: Correlating tool life, tool wear and surface roughness by monitoring acoustic emission in finish turning. *Wear* **152**(2), 395–407 (1992)
14. Li, X.: A brief review: acoustic emission method for tool wear monitoring during turning. *Int. J. Mach. Tools Manuf.* **42**(2), 157–165 (2002)
15. Moriwaki, T., Okushima, K.: Detection for cutting tool fracture by acoustic emission measurement. *CIRP Ann. Manuf. Technol.* **29**(1), 35–40 (1980)
16. Liang, S.Y., Dornfeld, D.A.: Tool wear detection using time series analysis of acoustic emission. *J. Eng. Ind.* **111**(3), 199 (1989)
17. Guo, Y., Ammula, S.: Real-time acoustic emission monitoring for surface damage in hard machining. *Int. J. Mach. Tools Manuf.* **45**(14), 1622–1627 (2005)
18. Tönshoff, H., Jung, M., Männel, S., Rietz, W.: Using acoustic emission signals for monitoring of production processes. *Ultrasonics* **37**, 681–686 (2000)
19. Bhaskaran, J., Murugan, M., Balashanmugam, N., Chellamalai, M.: Monitoring of hard turning using acoustic emission signal. *J. Mech. Sci. Technol.* **26**(2), 609–615 (2012)
20. Jiaa, C., Dornfeld, D.: Experimental studies of sliding friction and wear via acoustic emission signal analysis. *Wear* **139**(2), 403–424 (1990)
21. Halpin, T., Barry, J., Byrne, G.: The performance of PCBN in hard turning. Technical report (2005)
22. Ståhl, J.-E., SECO Tools AB (Fagersta): Metal Cutting: Theories and Models. Lund University, Lund (2012)
23. Barry, J., Byrne, G.: Cutting tool wear in the machining of hardened steels part I: alumina/TiC cutting tool wear. *Wear* **247**, 139–151 (2001)
24. Barry, J., Byrne, G.: The mechanisms of chip formation in machining hardened steels. *J. Manuf. Sci. Eng.* **124**(3), 528 (2002)
25. Fang, Y.: Theoretical Modelling and Animation of the Chip Curling Process in 3-D Metal Cutting. Retrieved from <http://ro.uow.edu.au/theses/1600> (1998)
26. Stabler, G.V.: The fundamental geometry of cutting tools. *Proc. Inst. Mech. Eng. Part H, J. Eng. Med.* **210**(4), 259–266 (1996)



Chapter 25

A New Approach to Dynamic Analysis of a Multi-Span Beam Structure with Multiple Moving Oscillators

Bingen Yang, Hao Gao, and Shibing Liu

Abstract A multi-span beam structure carrying multiple moving oscillators is seen in a variety of engineering applications, including highway bridges, elevated guideways and railways with moving vehicles, and tubes conveying fast-moving pods. With the oscillators having different speeds and varying inter-distances, the dynamic interactions between the supporting structure and the moving oscillators are usually complicated. Indeed, the number of moving oscillators on the structure is time-varying, and as such, a conventional solution method must frequently check the number of oscillators on the structure and adjust the numerical algorithm accordingly. Because of this, most investigations have been limited to just one or a few moving oscillators. Proposed in this paper is a new semi-analytical method that can systematically handle a beam structure with an arbitrary number of moving oscillators, without tedious number checking and algorithm adjustment. In the development, an extended solution domain (ESD) is firstly defined and a generalized assumed-mode method is then developed based on the ESD, which eventually yields a set of time-varying state equations. Solution of the state equations by a standard numerical integration algorithm gives the dynamic response of the coupled beam-oscillator system. Because the proposed method makes use of the exact eigenfunctions of the multi-span structure that are obtained by a distributed transfer function method, it is highly accurate and efficient in computation, as shown in a numerical study.

Keywords Multi-span beam structures · Moving oscillators · Fast transit systems · Distributed transfer function method · Semi-analytical solution method

25.1 Introduction

A multi-span beam structure carrying multiple moving subsystems has various engineering applications, including highway bridges, elevated railways with moving vehicles [1, 2], cable transport systems [3, 4], high speed trains on viaducts, and recently envisioned hyperloop systems (a multi-span tube structure conveying fast-moving pods). In general, subsystems moving over a multi-span structure have different speeds and inter-distances. Consequently, dynamic interactions between the multi-span beam structure and subsystems are complicated, and can generate large deflection of and stress in the multi-span beam structure. These effects can reduce reliability of the multi-span beam structure, increasing the possibility of failure. Therefore, accurate dynamic analysis is vital to reliability and safety of this kind of coupled flexible-rigid body dynamic systems.

In early research efforts, researchers mainly focused on moving load problems [5–9] during the 1960s and 1970s, and moving mass problems [10–15] from the 1970s to 1990s. In a moving load problem, a subsystem that moves along the supporting beam structure is modeled as a concentrated force due to gravity with the inertia effect of subsystem being neglected. In a moving mass problem, the connection between the moving subsystem and the beam structure is assumed to be rigid, but the inertia of the moving subsystem is considered. However, in many engineering applications, the inertia effect of moving subsystems and the elastic coupling between the moving subsystem and a supporting structure cannot be ignored. Under the circumstances, the moving oscillator problems should be considered, in which the moving subsystem is modeled as a spring-mass-damper oscillator that is elastically connected to the supporting beam structure during its motion.

Dynamic analysis of a beam structure carrying a single moving oscillator has been studied since the 1990s. Different modeling techniques and solution methods for moving oscillator problems have been developed. A modal expansion

B. Yang (✉) · H. Gao
University of Southern California, Los Angeles, CA, USA
e-mail: bingen@usc.edu

S. Liu
Controls and Dynamics Engineer, Hyperloop One, Los Angeles, CA, USA

approach was proposed by Klasztorny and Langer [16] to study the dynamics of a simply supported Euler-Bernoulli beam carrying moving oscillators. With a finite element formulation, Lin and Trethewey [17] found that the moving oscillators could excite higher order modes of a supporting beam, and rotary inertia should be considered in analysis. Pesterev and Bergman [18, 19] proposed a kernel integral equation method for beams with oscillators moving at constant speed or with acceleration. Yang et al. [20] and Bergman et al. [21] developed a numerical procedure to study the dynamic response of a single-span and one-dimensional continuum with moving oscillators. In addition to aforementioned studies, other issues in moving oscillator problems have been addressed as well, such as moving oscillators with random parameters [22], a single-span beam with flexible boundaries [23], and separation and reattachment of an oscillator moving on a supporting beam structure [24]. In most previous studies on moving oscillator problems, a single-span beam is considered. Most recently, Ebrahimi et al. [25] studied the dynamics of a simply supported multi-span Euler-Bernoulli beam with one oscillator moving at a constant speed. Nevertheless, these studies are limited to one or a few moving oscillators.

Although many studies on moving oscillator problems are available in the literature, dynamic analysis of a multi-span beam structure with arbitrarily many oscillators moving at different speeds and with different inter-distances has not been well addressed. Firstly, having different speeds and inter-distances, oscillators can be entering, travelling on, or leaving the supporting beam simultaneously. Consequently, the number of oscillators traveling on the structure is time-varying, which makes the formulation, analysis, and solution of moving oscillator problems tremendously difficult by conventional methods, if not impossible. Secondly, the dynamic response of a beam structure with many moving oscillators may be significantly different from that of a beam structure with only several moving oscillators. For instance, under certain conditions, repeated passage of many oscillators can generate ever-increasing vibration amplitude of the support beam structure. Hence, to address these issues, an accurate and efficient modeling and solution approach is essential for this kind of coupled beam-oscillator dynamic systems.

This paper proposes an original method to determine the dynamic response of a multi-span beam structure carrying an arbitrary number of moving oscillators with different speeds and varying inter-distances. In the development, an extended solution domain (ESD) is defined, which completely resolves the time-varying number of oscillators issue. There is no need to check the number of oscillators on the beam structure, allowing convenient formulation and efficient solution of the moving oscillator problem. With the ESD, a generalized assumed mode method is used to formulate the coupled system, in which the eigenfunctions of a multi-span beam structure as comparison functions are obtained in exact closed-form by the distributed transfer function method (DTFM). The generalized assumed mode method yields a set of time-varying state equations, whose solution by numerical integration gives the dynamic response of the coupled multi-span beam-oscillator system. As shall be shown by a numerical example, the proposed semi-analytical method can model a multi-span beam structure with arbitrarily many moving oscillators with high efficiency and accuracy in computation.

The remainder of the paper is organized as follows. In Sect. 25.2, the moving oscillator problem is described. The proposed modeling and solution method is presented in Sect. 25.3. In Sect. 25.4, numerical examples are presented to demonstrate the accuracy and efficiency of the proposed approach. The main results and contributions from this investigation are summarized in Sect. 25.5.

25.2 Problem Statement and Modeling

Shown in Fig. 25.1 is a schematic of a multi-span beam carrying n moving oscillators. The beam structure is modeled as a piecewise uniform Euler-Bernoulli beam of length L being divided into $(p + 1)$ segments or spans by p elastic supports located at nodes $x_{s,1}, x_{s,2}, \dots, x_{s,p}$. For convenience of analysis and solution, the origin of the coordinates ($x = 0$) is set at the left end of the beam. In general, at both ends of the beam structure ($x = 0$ and $x = L$), the boundary conditions are specified as clamped or hinged. As summarized in Fig. 25.2, the coupled beam-oscillator system has three basic types of components: (a) beam segments, with transverse displacement $w_l(x, t)$, density ρ_l , cross section area A_l , Young's modulus E_l , area moment of inertia I_l , and length L_l ; (b) elastic column supports with height h_j , Young's modulus $E_{s,j}$, cross section area $A_{s,j}$ and area moment of inertia $I_{s,j}$; and (c) moving oscillators or mass-spring-damper subsystems, with mass m_i , stiffness k_i , damping coefficient c_i , constant moving speed v_i , and vertical displacement $y_i(t)$.

To derive the governing equations of the coupled system, each elastic column support is modeled as a pair of translational and torsional springs, as shown in Fig. 25.3. Here, without loss of generality, the inertia of the support is ignored. By structural mechanics [26], the equivalent translational stiffness ($k_{t,j}$) and torsional stiffness ($k_{r,j}$) of the j th elastic support are of the form

$$k_{t,j} = \frac{E_{s,j}A_{s,j}}{h_j}, \quad k_{r,j} = \frac{E_{s,j}I_{s,j}}{h_j} \quad (25.1)$$

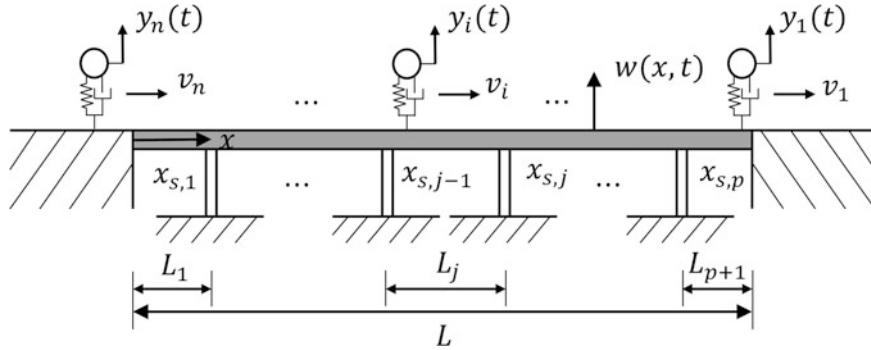


Fig. 25.1 Schematic of a multi-span beam carrying multiple moving oscillators

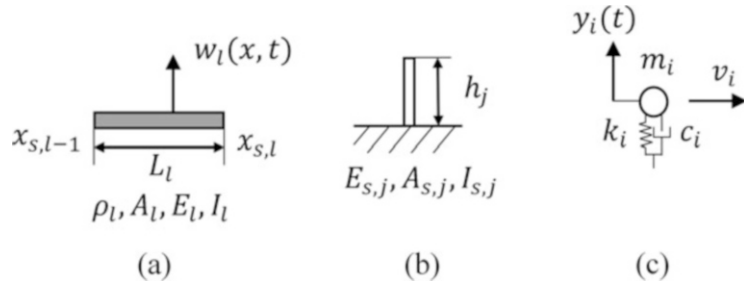
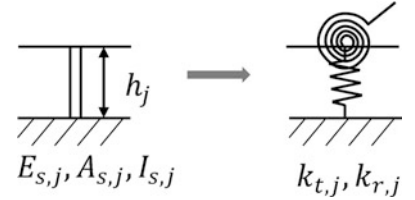


Fig. 25.2 Basic components of the coupled beam-oscillator system: (a) beam segment; (b) elastic column support; (c) moving oscillator

Fig. 25.3 A simplified model of elastic column supports



By the Euler-Bernoulli beam theory [27], the transverse displacement $w(x, t)$ of the multi-span beam structure with multiple translational and torsional springs (i.e. elastic supports) is governed by

$$\rho A(x) \frac{\partial^2 w(x, t)}{\partial t^2} + \frac{\partial^2}{\partial x^2} \left[EI(x) \frac{\partial^2 w(x, t)}{\partial x^2} \right] = -f_s + f_o, \quad 0 < x < L \quad (25.2)$$

where ρ, A, E, I are the parameters of the multi-span beam, f_s is the resultant constraint force generated by the support springs, and f_o is the resultant force due to interactions between the moving oscillators and the beam. The resultant constraint and interaction forces are given by

$$f_s = \sum_{j=1}^p k_{t,j} w(x_{s,j}, t) \delta(x - x_{s,j}) - \sum_{j=1}^p k_{r,j} \frac{\partial w(x_{s,j}, t)}{\partial x} \frac{d\delta(x - x_{s,j})}{dx} \quad (25.3)$$

$$f_o = \sum_{i=1}^n \left\{ k_i [y_i(t) - w(x_{o,i}, t)] + c_i \left[\frac{dy_i(t)}{dt} - \frac{dw(x_{o,i}, t)}{dt} \right] \right\}_i \Delta_i(t) \delta(x - x_{o,i})$$

where $\Delta_i(t) = [h(x_{o,i}) - h(x_{o,i} - L)]$; $\delta(\bullet)$ and $h(\bullet)$ are the Dirac delta function and Heaviside step function, respectively; and $y_i(t)$ is the vertical displacement of the i th oscillator governed by

$$m_i \frac{d^2 y_i(t)}{dt^2} + c_i \left[\frac{dy_i(t)}{dt} - \frac{dw(x_{o,i}, t)}{dt} \Delta_i(t) \right] + k_i [y_i(t) - w(x_{o,i}, t) \Delta_i(t)] = -m_i g \quad (25.4)$$

with g being the gravity acceleration. The boundary conditions of the multi-span beam structure are of the form [28]

$$B_{L,r}[w(0, t)] = 0, \quad B_{R,r}[w(L, t)] = 0, \quad r = 1, 2 \quad (25.5)$$

where $B_{L,r}$ and $B_{R,r}$ are appropriate operators. Assume each oscillator is in its equilibrium position under gravity with zero vertical velocity at $t = 0$. Thus, the initial conditions for the coupled beam-oscillator system are described as follows

$$\begin{aligned} w(x, 0) &= u_0(x), \quad \frac{\partial w(x, 0)}{\partial t} = v_0(x) \\ y_i(0) &= \frac{-m_i g}{k_i}, \quad \frac{dy_i(0)}{dt} = 0, \quad i = 1, 2, \dots, n \end{aligned} \quad (25.6)$$

where $u_0(x)$ and $v_0(x)$ are the initial displacement and velocity of the beam structure, respectively. Accordingly, the dynamic response of the coupled beam-oscillator system is the solution of governing equations 25.2, 25.3 and 25.4 with boundary conditions 25.5 and initial conditions 25.6.

25.3 Semi-Analytical Solution Method

Three issues exist in solution of the coupled beam-oscillator dynamic problem. First, the partial differential equation 25.2 is coupled with a set of ordinary differential equation 25.4, and they must be solved simultaneously. Second, the coupled system is time-varying, as implied by Eq. 25.3, which implies that analytical solutions of the system response in general is almost impossible to obtain. Third, because the speeds and inter-distances of the moving oscillators (as shown in Fig. 25.1) are different, there are numerous possibilities of the number of oscillators on the beam structure at any given time. This is especially true when the number of moving oscillators (n) is fairly large. Utility of conventional numerical methods thus encounters the need to count the number of oscillators on the beam structure at each calculation step and subsequently to change the solution algorithm, which inevitably increases computation loads. To address these issues, a new semi-analytical method is proposed in this section.

The proposed method takes the following four steps to determine the dynamic response of the coupled beam-oscillator system.

- Step 1. Obtain the exact eigenfunctions of the multi-span beam structure by the distributed transfer function method (DTFM);
- Step 2. Define an extended solution domain (ESD);
- Step 3. Construct a state equation via application of the generalized assumed-mode method in the ESD; and
- Step 4. Solve the state equation with numerical integration.

These steps are detailed in sequel.

25.3.1 Exact Eigensolutions

The exact eigensolutions of the $(p + 1)$ -span beam structure are obtained by the distributed transfer function method (DTFM) [28–30]. By means of the DTFM, the state space form of the governing equation of the l th beam segment in s -domain is [28, 30]

$$\frac{\partial}{\partial \xi} \hat{\eta}_l(\xi, s) = \mathbf{F}_l(s) \hat{\eta}_l(\xi, s) + \hat{\mathbf{p}}_l(\xi, s), \quad \xi \in [0, L_l] \quad (25.7)$$

where $\hat{\eta}_l$ is a state vector given by

$$\hat{\eta}_l(\xi, s) = \left\{ \hat{w}_l(\xi, s), \frac{\partial}{\partial \xi} \hat{w}_l(\xi, s), \frac{\partial^2}{\partial \xi^2} \hat{w}_l(\xi, s), \frac{\partial^3}{\partial \xi^3} \hat{w}_l(\xi, s) \right\}^T \quad (25.8)$$

with $l = 1, 2, \dots, p + 1$; ξ being the local spatial coordinate defined on the segment; $\hat{w}_l(\xi, s)$ being the transverse displacement of the l th uniform beam segment; $\mathbf{F}_l(s)$ being a four-by-four matrix consisting of the parameters of the l th beam segment; $\hat{\mathbf{p}}_l(\xi, s)$ representing the external force and initial disturbances; s being the Laplace transform parameter; and the hat ($\hat{\cdot}$) standing for Laplace transformation with respect to t . The boundary conditions 25.5 of the beam structure can be written as

$$\mathbf{M}\hat{\eta}_1(0, s) + \mathbf{N}\hat{\eta}_{p+1}(L_{p+1}, s) = 0 \quad (25.9)$$

where \mathbf{M} and \mathbf{N} are the boundary condition matrices consisting of the coefficients in Eq. 25.5. The matching conditions at the j th node, where a pair of translational and torsional springs is located, can be written as

$$\hat{\eta}_{j+1}(0, s) = \mathbf{T}_j \hat{\eta}_j(L_j, s) \quad (25.10)$$

where matrix \mathbf{T}_j consists of the parameters of the involved beam segments and column support. See Refs. 28–30 for further details on formulation of the state matrix $\mathbf{F}_l(s)$, boundary condition matrices \mathbf{M} and \mathbf{N} , and matching condition matrix \mathbf{T}_j .

By setting $s = i\omega$, with $i = \sqrt{-1}$, the characteristic equation of the beam structure is [28, 30]

$$\det(\mathbf{M} + \mathbf{N}\Lambda(L, i\omega)) = 0 \quad (25.11)$$

where $\Lambda(x, i\omega)$ is a state transition matrix given by

$$\Lambda(x, \omega) = \begin{cases} e^{\mathbf{F}_1 x}, & x \in (0, x_{s,1}) \\ e^{\mathbf{F}_j(x - x_{s,j-1})} \mathbf{T}_{j-1} e^{\mathbf{F}_{j-1} L_{j-1}} \dots \mathbf{T}_1 e^{\mathbf{F}_1 L_1}, & x \in (x_{s,j-1}, x_{s,j}), j = 2, 3, \dots, p \\ e^{\mathbf{F}_{p+1}(x - x_{s,p})} \mathbf{T}_p e^{\mathbf{F}_p L_p} \dots \mathbf{T}_1 e^{\mathbf{F}_1 L_1}, & x \in (x_{s,p}, L) \end{cases} \quad (25.12)$$

With ω determined by Eq. 25.11, the mode shape $\varphi(x)$ of the beam structure is determined by

$$\varphi(x) = [1 \ 0 \ 0 \ 0] \Lambda(x, \omega) \alpha \quad (25.13)$$

where α , a vector associated with an eigenvalue ω , is a non-trivial solution of

$$(\mathbf{M} + \mathbf{N}\Lambda(L, \omega)) \alpha = 0 \quad (25.14)$$

As can be seen from the above solution process, no approximation or discretization has been made. The eigensolutions are in *exact* and *closed-form* as shown in Eq. 25.13.

25.3.2 Extended Solution Domain

To resolve the issue of the time-varying number of oscillators on the beam structure, an extended solution domain (ESD) is defined in this subsection. Assume all oscillators are located on the left-hand side of the beam structure at initial time ($t = 0$), with the first oscillator at the left end of the beam structure ($x = 0$); see Fig. 25.4. Then, the distance between the first and the last oscillator (D_L), as well as the location of the last (far-left) oscillator ($x = -D_L$), is defined as

$$D_L = \sum_{l=1}^{n-1} d_l^0 \quad (25.15)$$

where d_l^0 is the initial inter-distance between the l th and $(l + 1)$ th oscillators.

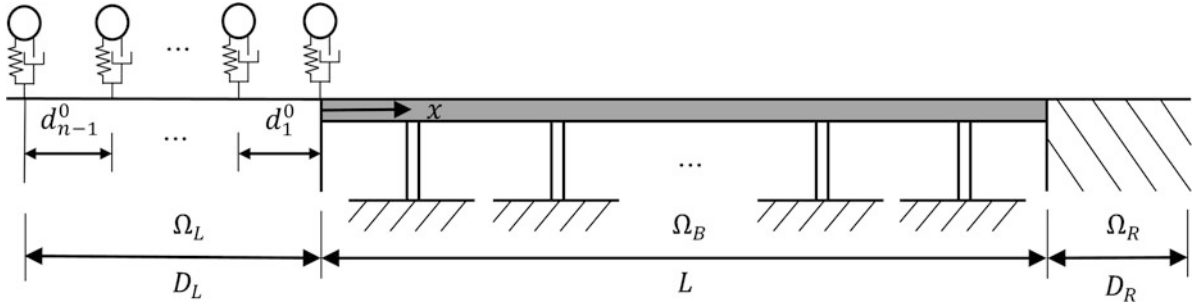


Fig. 25.4 The extended solution domain of a coupled beam-oscillator system

When the last oscillator just leaves the beam structure ($t = (L + D_L)/v_n$), the distance between the first and the last oscillator (D_R) becomes

$$D_R = \frac{v_1}{v_n} (L + D_L) - L \quad (25.16)$$

And the location of the first oscillator is $x = L + D_R$. Define an extended solution domain Ω as the union of three subdomains

$$\Omega = \Omega_B \cup \Omega_L \cup \Omega_R \quad (25.17)$$

where the subdomains are shown in Fig. 25.4, and are listed as follows

$$\begin{aligned} \text{Beam structure domain: } \Omega_B &= \{x \mid 0 \leq x \leq L\} \\ \text{Left extended domain: } \Omega_L &= \{x \mid -D_L \leq x < 0\} \\ \text{Right extended domain: } \Omega_R &= \{x \mid L < x \leq L + D_R\} \end{aligned} \quad (25.18)$$

It follows that the extended solution domain is given by

$$\Omega = \{x \mid -D_L \leq x \leq L + D_R\} \quad (25.19)$$

The subdomains Ω_L and Ω_R can be viewed as two virtual domains being rigid surfaces, between which the beam structure is installed. In the extended solution domain, the number of moving oscillators is fixed, which is always n . Therefore, a solution procedure that is developed in the ESD does not need number checking on moving oscillators.

25.3.3 Generalized Assumed-Mode Method

In this subsection, a generalized assumed-mode method is used to formulate a state equation in the extended solution domain (ESD). Solution of the state equation gives the dynamic response of a coupled beam-oscillator system.

Define an extended beam displacement in the ESD Ω by

$$W(x, t) = \begin{cases} w(x, t), & x \in \Omega_B \\ 0, & x \in \Omega_L \cup \Omega_R \end{cases} \quad (25.20)$$

where $w(x, t)$ is the transverse displacement of the beam structure governed by Eq. 25.2. Likewise, define an extended eigenfunction in Ω by

$$\Phi(x) = \begin{cases} \varphi(x), & x \in \Omega_B \\ 0, & x \in \Omega_L \cup \Omega_R \end{cases} \quad (25.21)$$

where $\varphi(x)$ is an eigenfunction (mode shape) of the beam structure determined by Eq. 25.13.

With the above definitions, the extended displacement $W(x, t)$ is approximated by m -term series

$$W(x, t) \approx \sum_{k=1}^m \Phi^{(k)}(x) q^{(k)}(t) = \boldsymbol{\Gamma}(x) \mathbf{q}(t), \quad x \in \Omega \quad (25.22)$$

where $\Phi^{(k)}(x)$ is the k th extended eigenfunction defined by Eq. 25.21, $q^{(k)}(t)$ are generalized coordinates, and $\boldsymbol{\Gamma}(x)$ and $\mathbf{q}(t)$ are vectors of the form

$$\begin{aligned} \boldsymbol{\Gamma}(x) &= [\Phi^{(1)}(x), \Phi^{(2)}(x), \dots, \Phi^{(m)}(x)] \\ \mathbf{q}(t) &= [q^{(1)}(t), q^{(2)}(t), \dots, q^{(m)}(t)]^T \end{aligned} \quad (25.23)$$

With the series (Eq. 25.22), a discretized model of the coupled beam-oscillator system can be obtained by the extended Hamilton's principle, as follows

$$\left[\begin{array}{cc} \mathbf{M}_b & \mathbf{0} \\ \mathbf{0} & \mathbf{M}_o \end{array} \right] \left\{ \begin{array}{c} \ddot{\mathbf{q}}(t) \\ \ddot{\mathbf{y}}(t) \end{array} \right\} + \left[\begin{array}{cc} \mathbf{C}_s & \mathbf{C}_c^T \\ \mathbf{C}_c & \mathbf{C}_o \end{array} \right] \left\{ \begin{array}{c} \dot{\mathbf{q}}(t) \\ \dot{\mathbf{y}}(t) \end{array} \right\} + \left[\begin{array}{cc} \mathbf{K}_b + \mathbf{K}_s & \mathbf{K}_{c,1}^T \\ \mathbf{K}_{c,1} + \mathbf{K}_{c,2} & \mathbf{K}_o \end{array} \right] \left\{ \begin{array}{c} \mathbf{q}(t) \\ \mathbf{y}(t) \end{array} \right\} = \left\{ \begin{array}{c} \mathbf{0} \\ \mathbf{f}_g \end{array} \right\} \quad (25.24)$$

where

$$\begin{aligned} \mathbf{y}(t) &= [y_1(t), y_2(t), \dots, y_n(t)]^T, \quad \mathbf{M}_b = \int_0^L \rho A(x) \boldsymbol{\Gamma}^T(x) \boldsymbol{\Gamma}(x) dx \\ \mathbf{K}_b &= \int_0^L EI(x) \boldsymbol{\Gamma}''(x)^T \boldsymbol{\Gamma}''(x) dx + \sum_{j=1}^p \left[k_{t,j} \boldsymbol{\Gamma}(x_{s,j})^T \boldsymbol{\Gamma}(x_{s,j}) + k_{r,j} \boldsymbol{\Gamma}'(x_{s,j})^T \boldsymbol{\Gamma}'(x_{s,j}) \right] \\ \mathbf{M}_o &= \text{diag}[m_1, m_2, \dots, m_n], \quad \mathbf{K}_o = \text{diag}[k_1, k_2, \dots, k_n] \\ \mathbf{f}_g &= [-m_1 g, -m_2 g, \dots, -m_n g]^T, \quad \mathbf{K}_s = \sum_{i=1}^n [v_i c_i \boldsymbol{\Gamma}^T(x_{o,i}) \boldsymbol{\Gamma}'(x_{o,i}) + k_i \boldsymbol{\Gamma}^T(x_{o,i}) \boldsymbol{\Gamma}(x_{o,i})] \\ \mathbf{C}_s &= \sum_{i=1}^n c_i \boldsymbol{\Gamma}(x_{o,i})^T \boldsymbol{\Gamma}(x_{o,i}), \quad \mathbf{K}_{c,1} = \begin{bmatrix} -k_1 \boldsymbol{\Gamma}(x_{o,1}) \\ \vdots \\ -k_n \boldsymbol{\Gamma}(x_{o,n}) \end{bmatrix}, \quad \mathbf{K}_{c,2} = \begin{bmatrix} -v_1 c_1 \boldsymbol{\Gamma}'(x_{o,1}) \\ \vdots \\ -v_n c_n \boldsymbol{\Gamma}'(x_{o,n}) \end{bmatrix}, \quad \mathbf{C}_c = \begin{bmatrix} -c_1 \boldsymbol{\Gamma}(x_{o,1}) \\ \vdots \\ -c_n \boldsymbol{\Gamma}(x_{o,n}) \end{bmatrix} \end{aligned} \quad (25.25)$$

with $\boldsymbol{\Gamma}' = d\boldsymbol{\Gamma}/dx$. Here $\mathbf{y}(t)$ is the vector of oscillator displacements; \mathbf{f}_g is the vector of gravitational forces applied to the oscillators; \mathbf{M}_b and \mathbf{K}_b are the inertia and stiffness matrices of the multi-span beam; \mathbf{M}_o and \mathbf{K}_o are the inertia and stiffness matrices of the moving oscillators; \mathbf{K}_s , $\mathbf{K}_{c,1}$, $\mathbf{K}_{c,2}$, \mathbf{C}_s and \mathbf{C}_c are stiffness and damping matrices of the beam due to its coupling with the moving oscillators.

Now, define a state vector

$$\mathbf{z}(t) = [\mathbf{q}(t), \mathbf{y}(t), \dot{\mathbf{q}}(t), \dot{\mathbf{y}}(t)]^T \in R^{2(m+n)} \quad (25.26)$$

Then Eq. 25.24 can be converted into a state equation as follows

$$\dot{\mathbf{z}} = \mathbf{A}(t) \mathbf{z} + \mathbf{b} \quad (25.27)$$

where

$$\begin{aligned} \mathbf{A}(t) &= \begin{bmatrix} \mathbf{0} & \mathbf{I} \\ \mathbf{P} & \mathbf{Q} \end{bmatrix}, \quad \mathbf{Q} = \begin{bmatrix} \mathbf{M}_b^{-1} \mathbf{C}_s & \mathbf{M}_b^{-1} \mathbf{C}_c^T \\ \mathbf{M}_o^{-1} \mathbf{C}_c & \mathbf{M}_o^{-1} \mathbf{C}_o \end{bmatrix} \\ \mathbf{P} &= \begin{bmatrix} \mathbf{M}_b^{-1} (\mathbf{K}_b + \mathbf{K}_s) & \mathbf{M}_b^{-1} \mathbf{K}_{c,1}^T \\ \mathbf{M}_o^{-1} (\mathbf{K}_{c,1} + \mathbf{K}_{c,2}) & \mathbf{M}_o^{-1} \mathbf{K}_o \end{bmatrix}, \quad \mathbf{b} = \begin{bmatrix} \mathbf{0} \\ \mathbf{0} \\ \mathbf{M}_o^{-1} \mathbf{f}_g \end{bmatrix} \end{aligned} \quad (25.28)$$

with \mathbf{I} being the identity matrix. The initial condition of the state equation is

$$\mathbf{z}(0) = [\mathbf{q}^T(0) \quad \mathbf{y}^T(0) \quad \dot{\mathbf{q}}^T(0) \quad \dot{\mathbf{y}}^T(0)]^T \quad (25.29)$$

with

$$\begin{aligned} \mathbf{q}(0) &= \int_0^L \rho A(x) u_0(x) \mathbf{\Gamma}^T(x) dx \\ \dot{\mathbf{q}}(0) &= \int_0^L \rho A(x) v_0(x) \mathbf{\Gamma}^T(x) dx \end{aligned} \quad (25.30)$$

and $u_0(x)$ and $v_0(x)$ are given by Eq. 25.6. Finally, the dynamic response of the coupled system is the solution of the state equation 25.29 with the initial condition (25.30), which can be obtained by standard numerical integration method such as Runge-Kutta method.

In the four steps of the proposed semi-analytical solution method, the number of oscillators in the ESD is always a constant (n). There is no need to check the number of oscillators on the beam structure for the solution of the state equation. Furthermore, instead of admissible functions, exact eigenfunctions obtained by the DTFM are used as comparison functions in the generalized assumed mode method. As such, the proposed semi-analytical method is efficient and accurate for dynamic analysis of a multi-span beam structure with arbitrarily many oscillators having different speeds and inter-distances, which will be demonstrated in the next section.

25.4 Numerical Example

In this section, the procedure, accuracy and efficiency of the proposed approach are demonstrated through investigation of the dynamics of a three-span Euler-Bernoulli beam carrying multiple oscillators. Assume the beam structure with fixed-fixed boundary conditions is an UIC60 high-speed rail [31], which is divided into three spans by two elastic columns. With the definitions given in Sect. 25.2 and shown in Fig. 25.2, the parameters of the coupled system are as follows: (a) beam segments: $\rho_l = 7.85 \times 10^3 \text{ kg/m}^3$, $E_l = 200 \text{ Gpa}$, $A_l = 76.86 \text{ cm}^2$, $I_l = 3.06 \times 10^3 \text{ cm}^4$, and $L_l = 20 \text{ m}$; (b) elastic column supports: $E_{s,j} = 20 \text{ Gpa}$, $h_j = 5 \text{ m}$, $A_{s,j} = 0.2 \text{ m}^2$ and $I_{s,j} = 0.01 \text{ m}^4$; and (c) moving oscillators: $m_i = 100 \text{ kg}$, $k_i = 1 \times 10^6 \text{ N/m}$ and $c_i = 1 \times 10^3 \text{ N s/m}$.

25.4.1 Transient Response

As stated in Sect. 25.3, the proposed method takes four steps as follows.

Step 1: Obtain the exact eigensolutions of the multi-span beam structure by the DTFM. By the DTFM in Sect. 25.3.1, the first 30 natural frequencies of the three-span beam structure are listed in Table 25.1, whose corresponding modes are used in the assumed mode method to construct the state equations.

Step 2: Define an extended solution domain (ESD). Consider nine oscillators with different velocities and initial inter-distances as follows.

$$\begin{aligned} v_1 = v_2 = v_3 = 100 \text{ m/s}, \quad v_4 = v_5 = 80 \text{ m/s}, \quad v_6 = v_7 = 60 \text{ m/s}, \quad v_8 = 80 \text{ m/s}, \quad v_9 = 100 \text{ m/s} \\ d_1^0 = 20 \text{ m}, \quad d_2^0 = d_3^0 = 30 \text{ m}, \quad d_4^0 = d_5^0 = d_6^0 = 40 \text{ m}, \quad d_7^0 = d_8^0 = 100 \text{ m} \end{aligned}$$

Following Sect. 25.3.2, the length of each subdomain can be determined as $D_L = D_R = 400 \text{ m}$ and $L = 60 \text{ m}$. The last (the ninth) oscillator leaves the beam structure at $t = 4.6 \text{ s}$. During this period ($0 \leq t \leq 4.6 \text{ s}$), the inter-distances between two adjacent oscillators varies with time. Consequently, the number of oscillators on the beam domain (Ω_B) can be zero, one, two, or three. However, the number of oscillators in the extended domain (Ω) is fixed, which is nine.

Step 3: Construct a state equation via application of the generalized assumed-mode method in the ESD. In the ESD defined in Step 2, the state equations can be obtained by Eq. 25.27 in Sect. 25.3.3.

Table 25.1 Natural frequencies of the multi-span beam structure (rad/s)

Mode	Natural frequency	Mode	Natural frequency
1	17.074344	16	320.787888
2	17.561597	17	327.956473
3	17.811998	18	331.305442
4	47.155067	19	427.611342
5	48.436481	20	436.700280
6	49.089406	21	440.769300
7	92.601259	22	549.857862
8	94.999218	23	560.968024
9	96.205849	24	565.671384
10	153.318119	25	687.536316
11	157.099638	26	700.735170
12	158.968996	27	705.926087
13	229.367048	28	840.640962
14	234.753151	29	855.967890
15	237.352027	30	861.433607

Step 4: Solve the state equation with numerical integration. In this study, the Runge-Kutta method of order four is used to solve the transient response of the coupled system. To avoid accumulation of numerical integration errors, proper step size should be chosen in simulation. A time step size is suggested as follows, and will be used in the subsequent simulations.

$$\Delta t = \frac{1}{r} \left(\frac{2\pi}{\omega_{max}} \right) \quad (25.31)$$

where r is a constant named as step size ratio, and

$$\omega_{max} = \max \left(\omega_m, \sqrt{k_1/m_1}, \dots, \sqrt{k_n/m_n} \right) \quad (25.32)$$

with ω_m being the highest natural frequency of the beam structure selected in the assumed-mode method ($m = 30$ in this example). As can be seen in Eq. 25.31, larger step size ratio r yields finer simulation steps and higher accuracy, but leads to more computation effort. In general, r should be at least six to generate accurate numerical results. In this numerical example, the step size ratio is set as $r = 10$.

With above-described four steps, the transient response of the coupled system can be obtained. Fig. 25.5 shows the transient response of the beam displacement at $x = 10, 30$ and 50 m, which are the mid-points of each span. As can be seen from Fig. 25.5, after 2.5 s, the displacements of the beam structure keep increasing, which might become unacceptably large vibration. To further investigate this phenomenon, consider a sequence of 20 oscillators that have same parameters as the nine oscillators case. All the 20 oscillators are evenly spaced with inter-distance $d_i^0 = 100$ m and velocity $v_i = 300$ m/s. By the proposed approach, the transient displacement responses at the mid-point of each span are plotted in Fig. 25.6(a). From which, a resonance like vibration is shown after 2 s. If setting the damping coefficients of all oscillators as zero, this ever-intensified vibration can be clearly observed, as shown in Fig. 25.6(b). It is concluded that, with proper inter-distances and velocities, the oscillators traveling over the multi-span beam can generate ever-increasing vibration. Vibrations like this may become fatal to both the beam structure and moving oscillators. It certainly deserves further investigations.

25.4.2 Comparison with FEM

To compare the proposed method with the finite element method (FEM), consider the same three-span beam in Sect. 25.4.1 with only one oscillator moving at $v_1 = 100$ m/s. The governing equations of the multi-span beam by the FEM is obtained based on 1D elements with Hermitian polynomials as shape functions [32]. By casting the governing equations into a matrix state equation, the transient response is solved by the fourth order Runge-Kutta method.

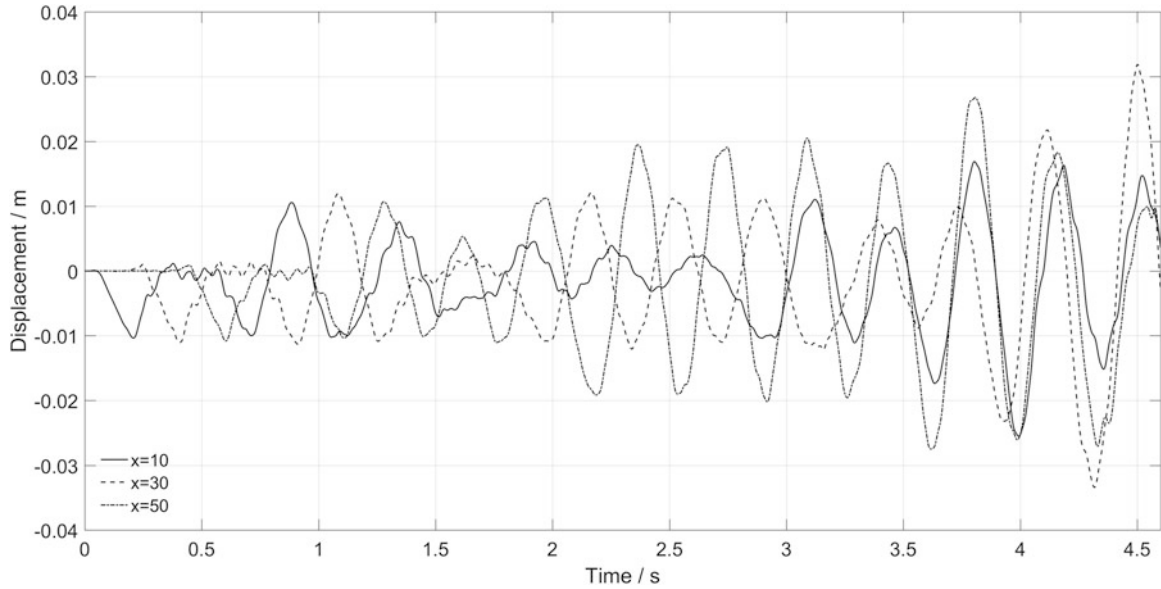


Fig. 25.5 Beam displacement at the mid-span points ($x = 10, 30$ and 50 m) for the nine oscillators case

Fig. 25.7 compares the transient displacement response at $x = 10$ by the proposed method with 30, 45 and 60 modes, and by the FEM with 30, 60, and 120 elements. As can be seen from Fig. 25.7(a), the transient responses by the proposed method and FEM are in good agreement. Taking a closer look of the response at $0.296984 \leq t \leq 0.296996$ s in Fig. 25.7(b), one can observe that result by the proposed method with 60 modes matches well with that by the FEM with 120 elements, which can be considered as a reference solution. Of course, with increasing number of modes in the proposed method or number of elements in the FEM, results that approaches to the reference solution indicate higher accuracy. For example, in Fig. 25.7(b), results by the proposed method with 30 assumed modes is considered as accurate as that obtained by the FEM with 60 elements.

To evaluate the computational efficiency, Table 25.2 lists the elapsed times in determination of dynamic response of the coupled system by the proposed method and the FEM. The simulations are run on a laptop with MS Windows, an Intel Core i7 processor and 8GB memory. A step size ratio $r = 10$ is set for both methods. It is seen from the table, with similar accuracy, the proposed method with 30 modes needs only 2% of the computation time by FEM with 60 elements. And the proposed method with 60 modes needs even less computation time (1%) of that by FEM with 120 elements. Therefore, the proposed method is much more efficient and accurate than the conventional FEM in solving the dynamic response of coupled beam-oscillator systems. It is worth pointing out that only one oscillator is considered for the computational efficiency comparison because the ESD cannot be directly applied to the convention FEM algorithm. In the case with multiple moving oscillators, it requires frequently checking of numbers of oscillators that coupled with the beam, which can significantly increase the computational load.

25.5 Conclusions

A new semi-analytical approach for dynamic modeling and vibration analysis of a multi-span beam structure carrying many moving oscillators has been presented. The main results in this paper are summarized as follows.

- (i) An extended solution domain (ESD) is established, by which the issue of the number checking of oscillators moving on a multi-span beam structure during solution process is completely resolved. With the ESD, the number of oscillators is a constant, and consequently number checking for moving oscillators is not necessary. This feature allows the proposed method to handle any number of moving oscillators in modeling and solution, without the limitation to one or a few oscillators as seen in the previous studies.

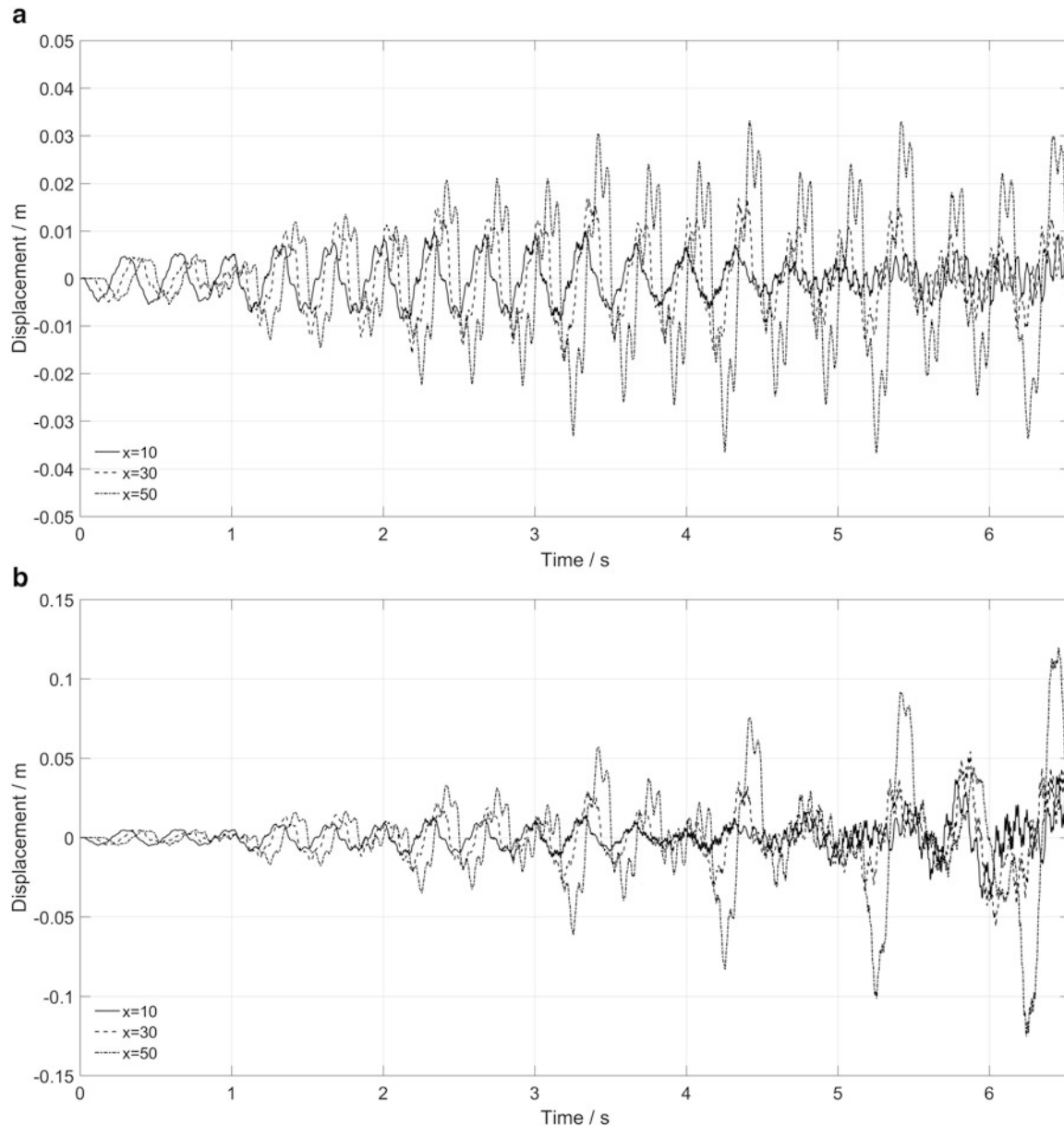


Fig. 25.6 Beam displacement at the mid-span points ($x = 10, 30$ and 50 m) for the twenty oscillators case **(a)** $c = 1000$ N s/m; **(b)** $c = 0$

- (ii) Different from conventional assumed-mode method, the generalized assumed-mode method uses the exact eigenfunctions of a multi-span beam structure by the distributed transfer function method as comparison functions. Unlike traditional admissible functions, these exact eigenfunctions satisfy all the boundary conditions and matching conditions of the beam structure, which makes the proposed method more accurate and efficient in numerical simulations. As demonstrated in the numerical examples, the computation time by the proposed method can be less than 2% of the time needed by the finite element method.
- (iii) As shown in numerical simulations, a periodic pattern of moving oscillators can induce resonance-like vibration, which could be dangerous to both the beam structure and moving oscillators. Further investigation on this phenomenon seems meaningful.

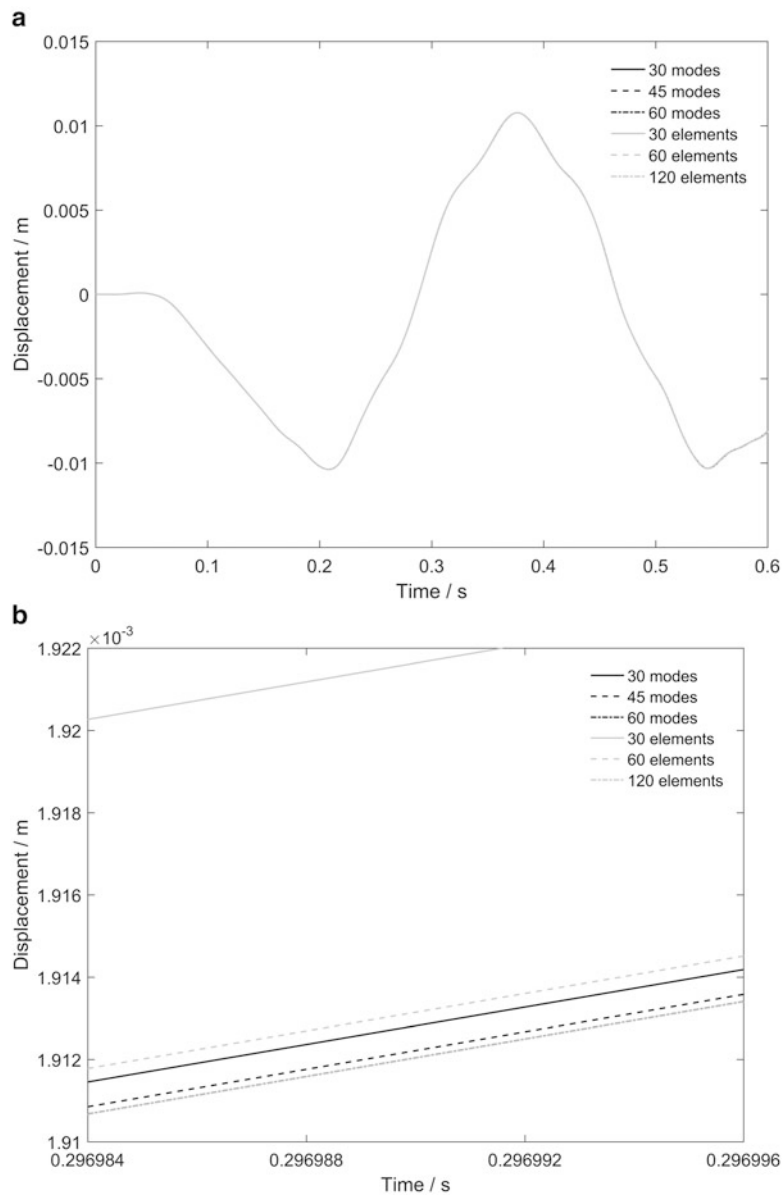


Fig. 25.7 Comparison of the beam displacement at $x = 10$ m by the proposed method and the FEM: (a) for $0 \leq t \leq 0.6$ s; (b) for $0.296984 \leq t \leq 0.296996$ s

Table 25.2 Comparison of elapsed computation time

Proposed method (No. of modes)	Elapsed time (second)	FEM (No. of elements)	Elapsed time (second)	Elapsed time percentage (Proposed method/FEM)
30	3.995	30	19.075	2%
45	10.652	60	181.68	6%
60	23.024	120	2977.8	1%

References

1. Diana, G., Cheli, F.: Dynamic interaction of railway systems with large bridges. *Veh. Syst. Dyn.* **18**(1–3), 71–106 (1989)
2. Cai, Y., Chen, S.S., Rote, D.M., Coffey, H.T.: Vehicle/guideway interaction for high speed vehicles on a flexible guideway. *J. Sound Vib.* **175**(5), 625–646 (1994)
3. Zhu, W.D., Mote, C.D.: Free and forced response of an axially moving string transporting a damped linear oscillator. *J. Sound Vib.* **177**(5), 591–610 (1994)
4. Nguyen, Q.C., Hong, K.S.: Simultaneous control of longitudinal and transverse vibrations of an axially moving string with velocity tracking. *J. Sound Vib.* **331**, 3006–3019 (2012)
5. Steele, C.R.: The finite beam with a moving load. *J. Appl. Mech.* **34**, 111–118 (1967)
6. Achenbach, J.D., Sun, C.T.: Moving load on a flexibly supported Timoshenko beam. *Int. J. Solids Struct.* **1**(4), 353–370 (1965)
7. Frýba, L., Steele, C.R.: *Vibration of Solids and Structures under Moving Loads*. Springer, Netherlands (1973)
8. Henchi, K., Fafard, M., Dhatt, G., Talbot, M.: Dynamic behavior of multi-span beams under moving loads. *J. Sound Vib.* **199**(1), 33–50 (1997)
9. Zheng, D.Y., Cheung, Y.K., Au, F.T.K., Cheng, Y.S.: Vibration of multi-span non-uniform beams under moving loads by using modified beam vibration functions. *J. Sound Vib.* **212**(3), 455–467 (1998)
10. Ting, E.C., Genin, J., Ginsberg, J.H.: A general algorithm for moving mass problems. *J. Sound Vib.* **33**(1), 49–58 (1974)
11. Lee, U.: Separation between the flexible structure and the moving mass sliding on it. *J. Sound Vib.* **209**(5), 867–877 (1998)
12. Blejwas, T.E., Feng, C.C., Ayre, R.S.: Dynamic interaction of moving vehicles and structures. *J. Sound Vib.* **67**(4), 513–521 (1979)
13. Akin, J.E., Mofid, M.: Numerical solution for response of beams with moving mass. *J. Struct. Eng.* **115**(1), 120–131 (1989)
14. Pesterev, A.V., Bergman, L.A.: A contribution to the moving mass problem. *J. Vib. Acoust. Transact. ASME.* **120**(3), 824–826 (1998)
15. Nikkhoo, A., Rofooei, F.R.: Shadnam, dynamic behavior and modal control of beams under moving mass. *J. Sound Vib.* **306**, 712–724 (2007)
16. Klasztorny, M., Langer, J.: Dynamic response of single-span beam bridges to a series of moving loads. *Earthq. Eng. Struct. Dyn.* **19**(8), 1107–1124 (1990)
17. Lin, Y.-H., Trethewey, M.W.: Finite element analysis of elastic beams subjected to moving dynamic loads. *J. Sound Vib.* **136**(2), 323–342 (1990)
18. Pesterev, A.V., Bergman, L.A.: Response of elastic continuum carrying moving linear oscillator. *J. Eng. Mech.* **123**(8), 878–884 (1997)
19. Pesterev, A.V., Bergman, L.A.: Vibration of elastic continuum carrying accelerating oscillator. *J. Eng. Mech.* **123**(8), 886–889 (1997)
20. Yang, B., Tan, C.A., Bergman, L.A.: Direct numerical procedure for solution of moving oscillator problems. *J. Eng. Mech.* **126**(5), 462–469 (2000)
21. Bergman, L.A., Yang, B., Tan, C.A.: Response of elastic continuum carrying multiple moving oscillators. *J. Eng. Mech.* **127**(3), 260–265 (2001)
22. Muscolino, G., Benfratello, S., Sidoti, A.: Dynamics analysis of distributed parameter system subjected to a moving oscillator with random mass, velocity and acceleration. *Probab. Eng. Mech.* **17**(1), 63–72 (2001)
23. Chen, Y., Tan, C.A., Bergman, L.A.: Effects of boundary flexibility on the vibration of a continuum with a moving oscillator. *J. Vib. Acoust.* **124**(4), 552–560 (2002)
24. Stăncioiu, D., Ouyang, H., Mottershead, J.E.: Vibration of a beam excited by a moving oscillator considering separation and reattachment. *J. Sound Vib.* **310**, 1128–1140 (2008)
25. Ebrahimi, M., Gholampour, S., Kafshgarkolaei, H.J., Nikbin, I.M.: Dynamic behavior of a multispan continuous beam traversed by a moving oscillator. *Acta Mech.* **226**(12), 4247–4257 (2015)
26. Hearn, E.J.: *Mechanics of Materials*. Butterworth-Heinemann, Oxford, UK (1985)
27. Rao, S.S.: *Vibration of Continuous Systems*. Wiley, Hoboken (2007)
28. Yang, B., Tan, C.A.: Transfer functions of one-dimensional distributed parameter systems. *ASME J. Appl. Mech.* **59**(4), 1009–1014 (1992)
29. Yang, B.: *Stress, Strain, and Structural Dynamics: an Interactive Handbook of Formulas, Solutions and MATLAB Toolboxes*. Elsevier Academic Press, Oxford, UK (2005)
30. Yang, B.: Distributed transfer function analysis of complex distributed parameter systems. *ASME J. Appl. Mech.* **61**(1), 84–92 (1994)
31. Cheng, Y.-H., Huang, Y.-H.: Dynamic characteristics of infinite and finite railways to moving loads, *ASME. J. Eng. Mech.* **129**(9), 987–995 (2003)
32. Cook, R.D.: *Concepts and applications of finite element analysis*, Wiley, New York (2007)